Organised By:

THE HONG KONG INSTITUTION OF ENGINEERS 香港工程師學會

Geotechnical Division 岩土分部

Supporting Organisations:

HKGES HONG KONG GEOTECHNICAL SOCIETY 香港岩土工程學會

THE HONG KONG INSTITUTION OF ENGINEERS 香港工程師學會 Civil Division 土木分部

THE HONG KONG INSTITUTION OF ENGINEERS 香港工程師學會 Environmental Division 環境分部

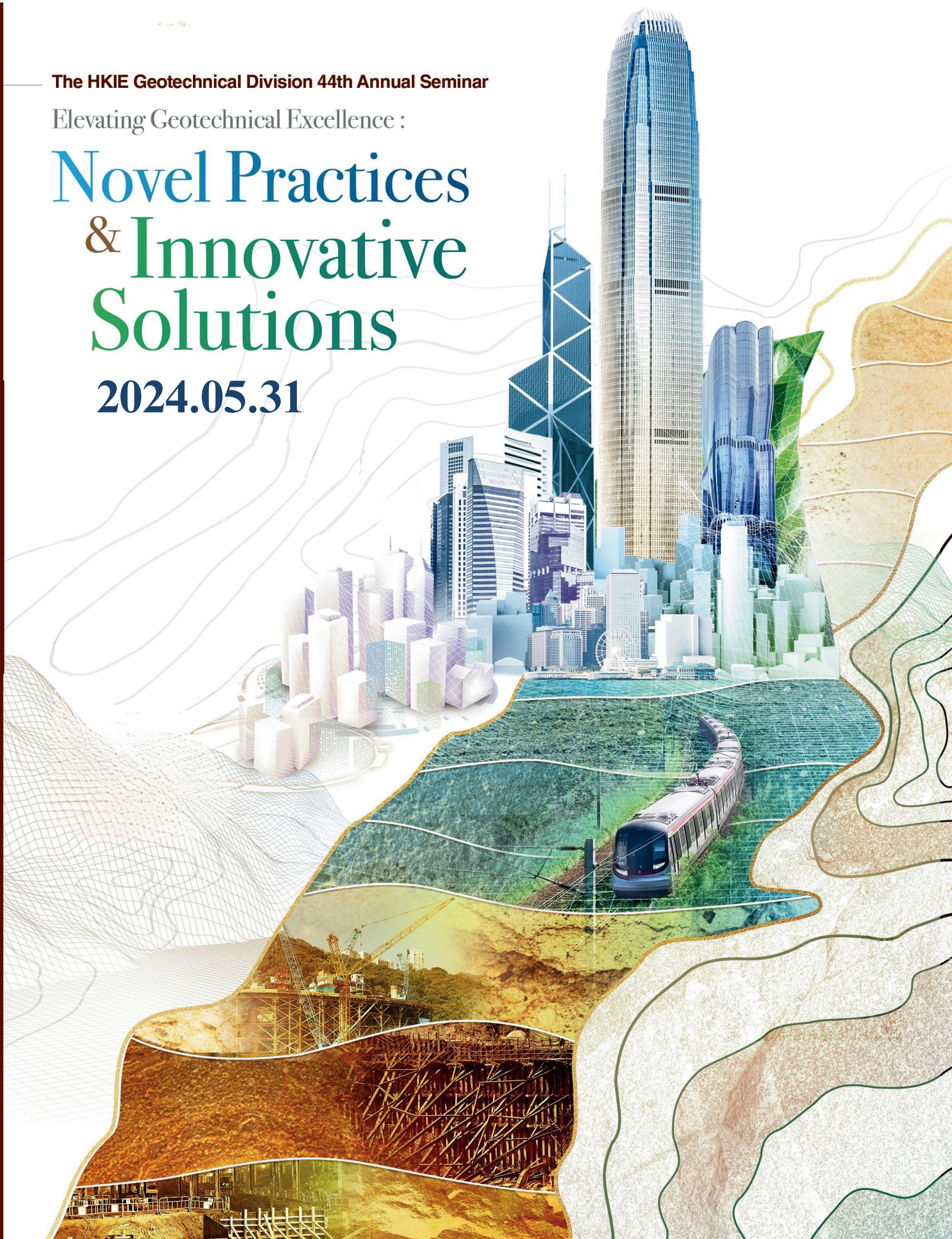
THE HONG KONG INSTITUTION OF ENGINEERS 香港工程師學會 Structural Division 結構分部

The HKIE Geotechnical Division 44th Annual Seminar

Elevating Geotechnical Excellence :

Novel Practices & Innovative Solutions

2024.05.31



aurecon
Bringing ideas to life

About Aurecon

Aurecon is an international design, engineering and advisory company that brings ideas to life to create a better future for people and the planet.

Our clients' ideas and aspirations drive all that we do. We work alongside them like no other firm to co-create clever, innovative solutions to some of the world's most complex challenges, adding value across the project lifecycle through deep technical and advisory expertise. We serve our clients across a range of markets and international locations. Hardwired in our DNA are engineering, design and the deep need to leave a legacy. We are as diverse as we are dynamic. As curious as we are clever.

We believe humanity depends on engineering; and we recognise we have a broader stewardship role to play. A deep responsibility to hold. As we continually strive for a life in balance, Aurecon clients will be both ready for the future and engineered for life.

Bridging Modernity and History

Aurecon's smart engineering solutions bridged modernity and history at the St Andrew's Church Life Centre in Hong Kong. The underground expansion preserved the heritage church while adding modern facilities such as an 850-seater auditorium and classrooms.

Aurecon's contributions encompassed various aspects, including excavation and lateral support, foundation design, and site formation works. Additionally, Aurecon provided geotechnical site supervision through the RGE Stream, ensuring the project's smooth execution. Meticulous engineering assessments and construction controls minimized damage.

The project received recognition for its architecture and environmental considerations. Aurecon successfully turned the vision of a modern community space within a heritage church complex into a reality, ensuring a legacy for future generations.



Anderson Road Quarry (ARQ) site, Hong Kong



St Andrew's Church Life Centre, Hong Kong

Transforming Historical Quarry into Residential Land

Aurecon played a pivotal role in the redevelopment of the Anderson Road Quarry (ARQ) site in Hong Kong. The project aimed to transform the site into a versatile area for both public and private housing, contributing to the overall development of Hong Kong. Aurecon provided a range of engineering services to facilitate the project, including geotechnical, tunnelling, and structural design.

The scope of the project encompassed several significant aspects:

- Site formation and geotechnical works: Creating approximately 40 hectares of land platforms on the ARQ site.
- Road works: Constructing around three kilometers of vehicular roads, a 130-meter road underpass, and a public transport terminus.
- Water supply system: Constructing an underground stormwater retention tank.
- Road improvement works: Implementing road improvements at key junctions and sections.
- Vehicular flyover: Constructing a flyover to enhance transportation connectivity.

Through its comprehensive engineering services, Aurecon contributed to the successful redevelopment of the ARQ site, facilitating its transformation into a multi-purpose land tract that supports Hong Kong's ongoing development.

Connect with us
aurecongroup.com

WENTX







FOR THE SUSTAINABILITY AND PROSPERITY OF HONG KONG

In line with ***Hong Kong's forward-thinking Climate Action Plan 2050*** and the ambitious ***Waste Blueprint for Hong Kong 2035***, the Hong Kong Resources Recovery Park (**HKRRP**) embarks on a transformative journey. **HKRRP** envisions the West New Territories Landfill Extension (**WENTX**) as an exemplary showcase of sustainable project development. **WENTX** plays a crucial role in making our city not only smarter and more livable but also incorporates elements of globally competitiveness. **HKRRP** is collaboratively moving towards a more sustainable and prosperous future.

HKRRP

FOR MORE INFORMATION

www.cscechk.com/en/index.php
www.veolia.com.hk

AECOM

Delivering a better world

AECOM offers comprehensive tunneling and underground structure design, as well as management services worldwide for clients in the public and private sectors. Our services cover project and construction management, feasibility studies, concept and detailed design, and risk management for various tunneling and underground works.

To enable a cost-effective planning and efficient implementation of future land use and infrastructure development, we have been appointed to conduct a regional geological and geotechnical engineering study for the geologically complex Northern New Territories (North), an integral part of the Northern Metropolis Development.



aecom.com

AtkinsRéalis

Here to make the extraordinary a reality



BAUER

MC96



Urban development close to residential area?

Experience the **power of silence** and **eco-friendly** solutions with BAUER electric equipment.

Low Noise

Eco-Friendly

bauerfe.com



Lok Ma Chau Ecological Enhancement



Photo for illustrative purpose only

Yuen Long Barrage Scheme



Tseung Kwan O Desalination Plant



ELS System of the In-situ Reprovisioning of Sha Tin Water Treatment Works



Photo for illustrative purpose only

Relocation of Diamond Hill Service Reservoirs to Cavern



Site Formation and Infrastructure Works for Public Housing Development at Ka Wai Man Road

100 years of Engineering Excellence

Binnies is a multidisciplinary engineering and consulting company providing comprehensive technical services, including water, environmental, civil, geotechnical, structural, urban development, transportation infrastructure and construction management. Operating in Hong Kong since 1930, we develop a full range of resilient and intelligent engineering solutions to deliver functional infrastructure that improves people's lives.

Find out more at binnies.com

binnies Enhancing lives, communities and the environment

中国地质工程集团有限公司
CHINA GEO-ENGINEERING CORPORATION

我們的主要業務包括：
Our Business includes:

- 基礎工程
  Foundation Works
- 斜坡及擋土牆長遠防治山泥傾瀉工程
  Construction of Landslip Preventive and Mitigation Works to Slopes and Retaining Walls
- 道路及渠務工程
  Roads and Drainage
- 水務工程
  Waterworks
- 地盤平整工程
  Site Formation













香港灣仔港灣道30號新鴻基中心24樓2421－25室
Rm. 2421-25, 24/F., Sun Hung Kai Centre, 30 Harbour Road, Wanchai, Hong Kong
TEL : (852) 2511 9001 FAX : (852) 2580 0697

CERTIFIED COMPANY HKQAA ISO 9001 : 2015 Certificate No.: CC 1776
CERTIFIED COMPANY HKQAA ISO 14001 : 2015 Certificate No.: CC 3492
CERTIFIED COMPANY HKQAA ISO 45001 : 2018 Certificate No.: CC 6799

中國港灣 CHINA HARBOUR

香港振華 HONG KONG ZHEN HUA

www.chechk.com



建造香港

Building Hong Kong's Future



1200+
全職員工

40
經營年資

335
個項目

100+
個獎項









China Road and Bridge Corporation (CRBC) mainly undertakes contracting, investment, development and operation of road, bridge, port, railway, airport, tunnel, real estate and industrial projects. With branch offices in nearly 60 countries and regions, CRBC has established an efficient and rapid market network.

CRBC has over 36 years' experience in Hong Kong construction market. It is registered on the List of Approved Contractors for Public Works for Group C kept by Development Bureau under all five categories including Buildings, Port Works, Roads and Drainage, Site Formation and Watermains.

中國路橋工程有限責任公司
CHINA ROAD AND BRIDGE CORPORATION

C M WONG & ASSOCIATES LTD
黃志明建築工程師有限公司

11/F Universal Trade Centre
3-5A Arbuthnot Road, Hong Kong
Tel: (852)2522-1068
Fax: (852)2526-3111
www.cmwal.com
cmwal@cmwal.com



C M Wong & Associates Ltd is a Hong Kong based consulting engineer in providing a full range of professional services including feasibility studies, planning, design and supervision in relation to building and infrastructure projects. Our clients include various Hong Kong Government departments, institutions and major developers.

We adopt a flexible approach to suit clients' needs. We are also renowned for providing innovative engineering solutions for challenging projects especially for those with difficult ground conditions.







ISO 9001 : 2015
Certificate No.: CC 801

ISO 14001 : 2015
Certificate No.: CC 5408

ISO 45001 : 2018
Certificate No.: CC 7033


FUGRO
Are you ready to shape the future?
Fugro is the world's leading Geo-data specialist, collecting and analysing comprehensive information about the earth and the structures built upon it.
Our talented people and sustainable innovations are pushing the transition towards net-zero, safe infrastructure and climate resilience to deliver on our promise: together we create a safe and liveable world.

fugro.com

40 years of experience

G&E ENGINEERING Since 1984



Sustainable construction, carbon credit, and climate change mitigation involve innovation and technology. However, not many people are aware of the contribution that geosynthetics can make towards these goals. Studies have shown that geosynthetic designs can reduce carbon emissions by 25-90%. For instance, geogrid reinforced fill requires less concrete and steel, while geomembrane and geosynthetic clay liner can replace quarry clay. Additionally, geotextile and geocomposite can reduce the use of granular material, decrease transportation fuel, better preserve natural resources, and control water loss. One example of geosynthetic design is the 68° RE fill slope at HKZBM.



Site Preparation, January 2017



Leveling of Formation, February 2017



Foundation Drainage, April 2017



Backfilling over Geogrid Reinforcement
June 2017



Geogrid Wrapped Back Facing
August 2017



Work Progress to Crest
October 2017



Hydroseeding, April 2018



Full Vegetation, July 2018



View, September 2018

G&E ENGINEERING Since 1984

G AND E COMPANY LIMITED

14/F, Kiu Yin Commercial Building,
361-363 Lockhart Road, Wanchai, Hong Kong
Tel: 2570 0103 Fax: 2570 0089
E-mail: info@g-and-e.com www.g-and-e.com

igs

ACT ISO 9001 : 2015

UKAS MANAGEMENT SYSTEMS 0273

VSL INTRAFOR

EXPERIENCE THE ELECTRIFYING SILENCE!



INTRAFOR ELECTRIC CUTTER
TUNG CHUNG WEST STATION
MTR EXTENSION

Intrafor is a specialized contractor in foundation engineering, retaining structures, ground improvement, horizontal directional drilling and coring. We provide turnkey solutions for geotechnical challenges across the entire construction spectrum. We have contributed to the most complex and ambitious projects in the world. Are you based in Hong Kong? We'd love to know more about your project! Please get in touch with us to discuss your needs.

Intrafor Hong Kong Ltd
20/F Eight Commercial Tower • 8 Sun Yip Street, Chai Wan, Hong Kong
Tel. 2590 2288 • www.intrafor.com

Gammon

LAMBETH

Gammon Construction and Lambeth Associates bring together the diverse experience of operations, planning, commercial, and design professionals – ensures it remains at the forefront of new techniques and new thinking in Geotechnical and Foundation Engineering Excellence. We are fully committed to building a better quality of life and living environment in a safe and sustainable manner.







Gambot











A member of the Gammon Group

22/F, Tower 1, The Quayside, 77 Hoi Bun Road, Kwun Tong, Kowloon, Hong Kong Tel: 2516 8790 Fax: 2516 6352

MEINHARDT

Facebook | LinkedIn | Instagram

Meinhardt China

With 1,200 staff in Hong Kong and China, our services cover all aspects of mechanical, electrical, civil and structural design for all types of construction projects, as well as project management and infrastructure such as bridges, tunnels, highways, ports, transportation, water services and waste management. We provide environmental consultancy across our projects and as standalone services. We also have a team of specialists providing services in all aspects of the façade of buildings and structures including curtain wall design, concrete repair and refurbishment.

Our clients include government bodies, agencies, private developers and end-users both in industrial and commercial enterprises.

Our award-winning projects have garnered recognition internationally and these awards serve to affirm our unrivalled reputation for innovative and inspiring engineering solutions.

Our Projects



Hong Kong Children's Hospital
(Civil & Structural)



Cross Bay Link, TKO
(Infrastructure & Environment)



Northwest Kowloon Long Span Footbridge
(Infrastructure & Environment)



Grand Central & Yue Man Square
(Mechanical & Electrical)



Hong Kong West Kowloon Station High Speed Rail
(Mechanical & Electrical)



HKSTP Advanced Manufacturing Centre
(Civil & Structural)

10/F, Genesis, 33-35 Wong Chuk Hang Road, Wong Chuk Hang, Hong Kong
www.Meinhardt-china.com | www.meinhardtgroup.com

商界展關懷 caringcompany 2023/24

ARUP

Novel solutions for complex challenges

Combining our domain knowledge with advanced technology, Arup delivers the most elegant and innovative geotechnical solutions for some of the most challenging projects from inception to operation and maintenance, shaping a greener, smarter and more resilient Hong Kong.

Image
Central Kowloon Route, Hong Kong



www.arup.com

SMEC

Member of the Surbana Jurong Group



A trusted partner on transformational infrastructure projects around the world

We combine the skills and experience of our global team with modern technology and state-of-the-art geotechnic and tunnelling techniques, to provide the most appropriate and innovative technical solutions for every project.

Explore our team and projects

We're redefining exceptional

Through our specialist expertise, we're challenging boundaries to deliver advanced infrastructure, energy and urban solutions.

smec.com

VIBRO 惠保

新創建集團成員
Member of NWS Holdings

COMMITTED
PROFESSIONAL
UNITED



New Acute Hospital at Kai Tak Development Area



Road Improvement Works in West Kowloon Reclamation Development

WWW.VIBRO.COM.HK

Delivering tailored solutions for a smart and resilient city

Combining our geotechnical expertise with digital technologies and innovative mindset, we developed our in-house automation tools to unlock insights from geo-data and streamline design process, improving overall efficiency and accuracy. Our ingenuity is the foundation to shape a digitally-enabled sustainable future for Hong Kong.

wsp.com

▼ Lead landfill designer of a strategic landfill extension project in Hong Kong



asia infrastructure solutions

DELIVERING THE FUTURE



Shape Tomorrow
Innovate with Digital Twins in Design and Engineering

Boost Efficiency
Unleash the Power of Robotic Process Automation (RPA)

Be a Pioneer
Drive Success with Tomorrow's Innovations

Follow Us:
@asiainfrastructuresolutions

Bridges and Civil Structures | Caverns and Tunnels | Geotechnics | Highway Design and Maintenance | Building Structures, Facades and MiC | Mechanical and Electrical Design | Urban Traffic and Transport Planning | Waste and Environmental Management | Project and Programme Management | Infrastructure: Rail and Railway Systems, Airports, Ports and Maritime Assets

asiainfrasolutions.com

亞洲聯合基建 ASIA ALLIED INFRASTRUCTURE | 俊和 CHUN WO



AAI ChunWo

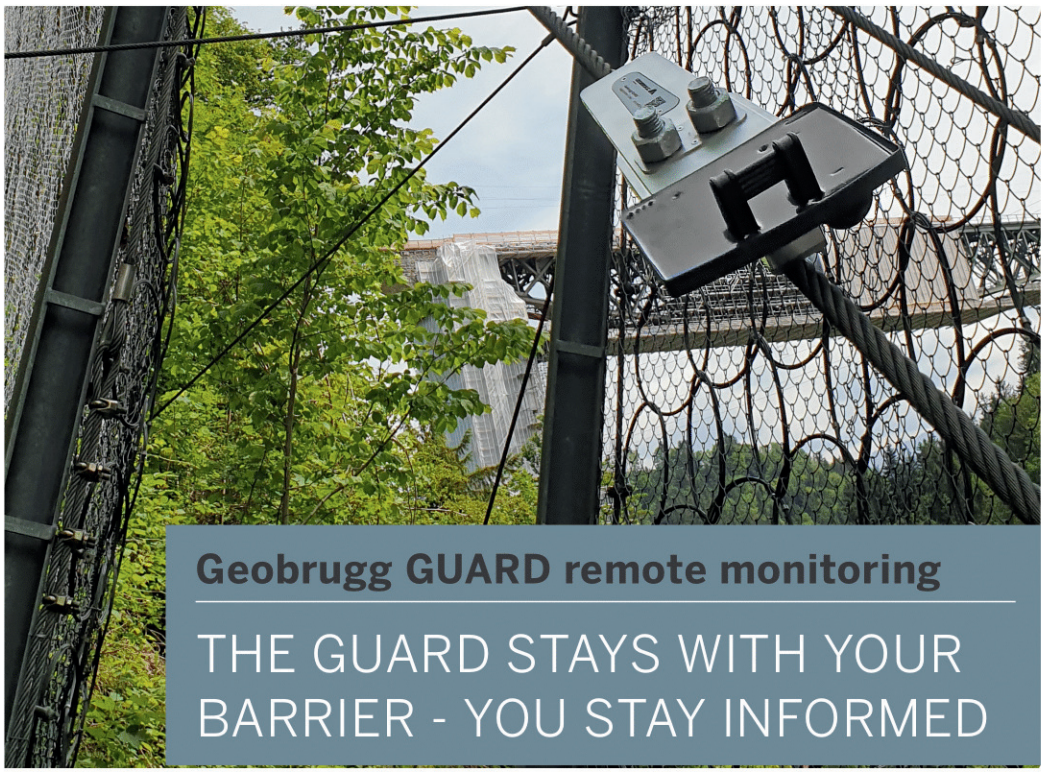
Geobrugg Guard

BRUGG
Geobrugg
Safety is our nature

Geobrugg Guard monitors your rockfall barrier, debris flow barrier, avalanche barrier or similar systems. No matter where they are.

Marketing Manager:
Thomas Mok
Tel: 2893 0444
Mobile: 9887 0410
Email: fog@fong-on.com.hk

CE European Technical Approval
www.eota.eu





KS 金城 1963 KUM SHING

營創更好未來 Brighter Future

Hong Kong
Energy Infrastructure
Specialist

2013 HKMA Quality Award GOLD

Power | Transportation | Environment | Power 2.0

www.KUMSHING.com.hk



Inspiration with Excellence

MANNINGS Consultants

Mannings (Asia) Consultants Limited
Wholly owned subsidiary of Boltek Holdings Limited (HKEX Stock Code 8601)
5/F, Winning Commercial Bldg., 46-48 Hillwood Rd., Tsim Sha Tsui, Kln., Hong Kong
Tel : (+852) 3168 2028 Fax: (+852) 3168 2022

http://www.manningsasia.com

MOTT MACDONALD



Tunnel in congested urban area
Central Kowloon Route



Double shield tunnel boring machine
Tsuen Wan Drainage Tunnel



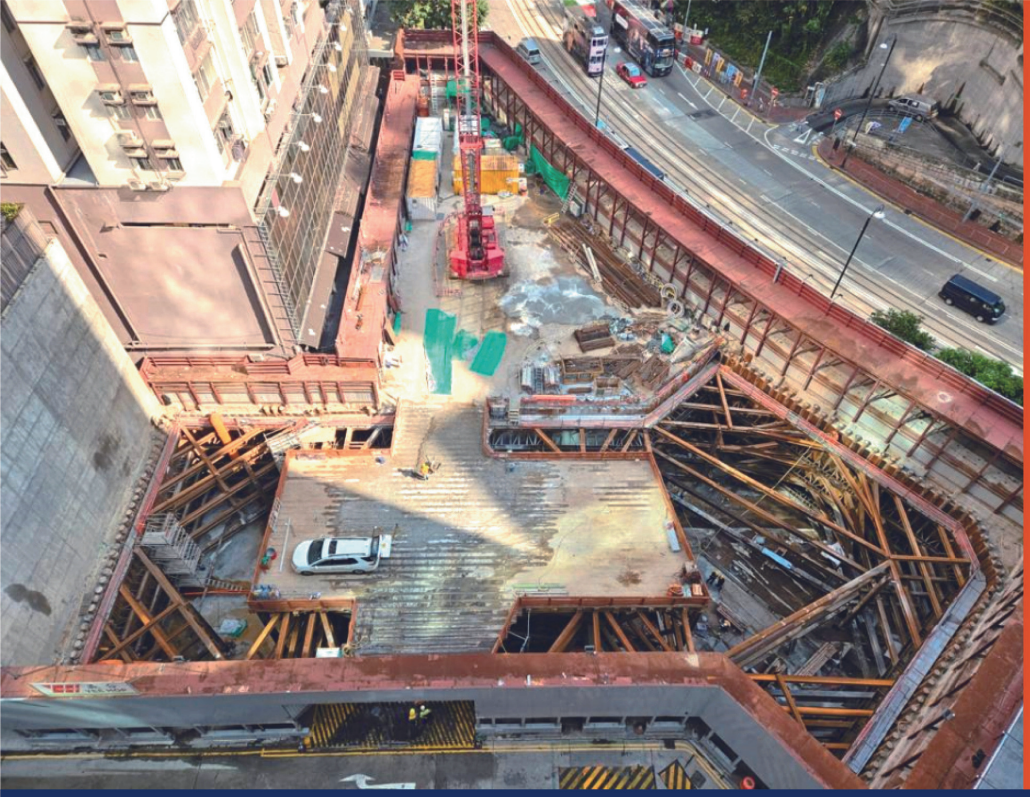
Site formation and infrastructure works
Lung Ping Road

Opening opportunities with connected thinking.













YEE HOP

Yee Hop Engineering Co., Ltd. was established in 1989, we are an established contractor in Hong Kong and are principally engaged in the provision of :

(i) foundation and earth lateral excavation works;
(ii) other civil works, including site formation works, port works and road and drainage works ;
(iii) tunneling works, including pipe jacking, hand dig tunnel and cut and cover tunnel works ; and
(iv) Superstructure.

Units 1104 -06 Nan Fung Commercial Centre, 19 Lam Lok St., Kowloon Bay

Proceedings of the 44th Annual Seminar
Geotechnical Division, The Hong Kong Institution of Engineers

Elevating Geotechnical Excellence: Novel Practices & Innovative Solutions

31 May 2024
Hong Kong

Organised by:
Geotechnical Division, The Hong Kong Institution of Engineers

Supported by:
Hong Kong Geotechnical Society
Civil Division, The Hong Kong Institution of Engineers
Environmental Division, The Hong Kong Institution of Engineers
Structural Division, The Hong Kong Institution of Engineers

ORGANISING COMMITTEE

Chairman
Ir Alvin LAM

Members
Ir Ray CHAN
Ir Warren DOU
Mr Dominic FUNG
Ir Marion KAN
Ir Carmen LAU
Ir Dr S W LEE
Dr Andy LEUNG
Ir Abby LIU
Ir Grace TAM
Ms Connie YAM
Ir Derek YU

Any opinions, findings, conclusions or recommendations expressed in this material do not reflect the views of the Geotechnical Division, Hong Kong Institution of Engineers.

Published by:
Geotechnical Division
The Hong Kong Institution of Engineers
9/F., Island Beverley, 1 Great George Street, Causeway Bay, Hong Kong

Tel: 2895 4446 Fax: 2577 7791
Prepared in Hong Kong

FOREWORD

It is my great pleasure to welcome all of you to the 44th Annual Seminar of the Hong Kong Institution of Engineers (HKIE) Geotechnical Division. Under the theme of "Elevating Geotechnical Excellence: Novel Practice and Innovative Solutions," this seminar serves as a platform for knowledge exchange, collaboration, and exploration of groundbreaking advancements in the field of geotechnical engineering.

The 2023 Policy Address highlighted a range of major development projects in Hong Kong, such as the Northern Metropolis, the Kau Yi Chau Artificial Islands, the Three Railways and Three Major Roads proposals together with other railway, green mass transit and road projects. These development projects, combined with other ongoing projects, present significant prospects for the construction industry. They also pose challenges such as timely completion of sheer number of projects for increasing the housing supply and enhancing resilience of the city in the face of climate change. Geotechnical engineers, plays a crucial role in ensuring the smooth delivery and sustainability of these development projects, and it is essential to continuously explore innovative ideas to push the boundaries of excellence. The time is nigh for us to elevate the professionalism of geotechnical engineers into new heights.

The 44th HKIE Geotechnical Annual Seminar brings together leading experts, researchers, and professionals for sharing invaluable insights, experiences, and discoveries that will shape the future of our profession. This Seminar is not only an opportunity to explore but also a chance to establish connections and foster collaborations. The power of collective wisdom and shared experiences cannot be underestimated, and it is through collaboration that we can truly elevate geotechnical excellence.

I would like to express my heartfelt gratitude to all the speakers and sponsors who have contributed their time, knowledge, and resources to make this seminar a reality. My special thanks go to the Organising Committee, led by Ir Alvin Lam, who have worked so hard to make this seminar a great success.

Lastly, I wish you all a memorable and enriching experience at this Seminar. May this event inspire us all to reach new heights of geotechnical excellence and create a future where innovative solutions transform the world we live in.

Thank you.



Ir Dr Gavin Toh
Chairman, Geotechnical Division
Hong Kong Institution of Engineers (2023/24 Session)

ACKNOWLEDGEMENTS

The Organising Committee would like to acknowledge the support of the following sponsors for their generous support of the Seminar:-

AECOM Asia Company Ltd
Asia Infrastructure Solutions Ltd
AtkinsRéalis
Aurecon Hong Kong Limited
BAUER Equipment HK Limited
Binnies Hong Kong Limited
China Geo-Engineering Corporation
China Harbour Engineering Company Limited
China Road and Bridge Corporation (Hong Kong & Macau)
Chun Wo Construction Holdings Company Limited
CM Wong & Associates Ltd
Fong On Geotechncis Ltd
Fugro Geotechnical Services Ltd
G and E Company Ltd
Hong Kong Resources Recovery Park
Intrafor Hong Kong Limited
Kin Wing Engineering Co., Ltd
Kum Shing Group
Lambeth Associates Ltd / Gammon Construction Limited
Mannings (Asia) Consultants Limited
Meinhardt Consulting Engineers
Mott MacDonald Hong Kong Ltd.
MTR Corporation Limited
Ove Arup & Partners Hong Kong Ltd.
SMEC Asia Limited
Vibro (HK) Limited
WSP (Asia) Limited
Yee Hop Engineering Co., Ltd

2024 HKIE Geotechnical Paper Award

The HKIE 2024 Geotechnical Paper Award has received 10 nominations. With the endorsement of the Geotechnical Division Committee (GDC), a 7-member Assessment Board is formed to look for the winning papers. It comprises Ir Dr Gavin Toh (Chairman), Ir Dr S W Lee (Deputy Chairman), Ir Dr Daman Lee, Ir Prof George Tham, Ir Y C Chan, Ir K W Leung and Ir Dr C K Lau (Coordinator). Ir Dr Gavin Toh and Ir Dr S W Lee are ex-officio members of the Board, who are the Chairman and Deputy Chairman of GDC. The other five members are selected from the 20-member Assessment Board Panel taking account of the subject nature of the contending papers and the need to avoid potential conflicts of interest.

The Assessment Board follows the practices set up since inauguration in 2014 to ensure the confidentiality of participants and fair but critical judgment on the contending papers. Hence, members would receive information on a need-to-know basis, and only the winning papers are made known publicly. The Board members share views through a hub that remove identity tags. Deciding winners in the Assessment Board meeting is by secret ballot.

I am pleased to announce that the Assessment Board has decided at a meeting held on 12 April 2024 to confer the Awards for 2024 to two papers:

"Predicting spatio-temporal man-made slope failures induced by rainfall in Hong Kong using machine learning techniques (2023)"

Te Xiao, Li Min Zhang, Raymond Wai Man Cheung and Suzanne Lacasse

Citation: Hong Kong is perhaps unique in the world in terms of keeping accurate and detailed inventory of all sizeable man-made slopes and rainfall records, and meticulous landslide records in the territory over the past 40 years. The authors make good use of such high-quality data in their machine learning exercise to train up an AI model to forecast spatio-temporal landslides in Hong Kong. The paper indicates that the logistic regression algorithm is the most suitable tool among 6 commonly used algorithms. The ability to forecast the 2008 notable landslide events infuses confidence into the readers. The paper is well-structured and clearly written. The trained AI model may be able to help upgrade the prevailing landslide warning criteria used in Hong Kong in anticipation of extreme weather conditions occurring in Hong Kong.

and

"Soil inertial factors for seismic bearing capacity (2019)"

Aslan S. Hokmabadi, Erin H. Y. Leung and Jack W. Pappin

Citation: The paper presents a literature review of applying the traditional bearing capacity equation to seismic design of shallow foundations. The study was thoughtful in regressing on discrete calculated values to trinomial empirical equations for applications of the study findings. The paper would be particularly relevant when Hong Kong seismic design requirements become mandatory as the paper findings fit harmoniously with the shallow foundation design framework of Hong Kong design codes. The paper is well written with illustrated diagrams and has adequate provision of references for readers who want to have a deeper understanding of the subject.

Prize presentation ceremony is to be held at the HKIE Geotechnical Annual Seminar on 31 May 2024. The authors of the winning papers will be presented with a trophy and a crystal plaque each. A certificate will also be presented to each of the co-authors. The authors of the winning papers will be invited to give presentation on the key findings of the papers.

For further information on the HKIE Geotechnical Paper Award, please visit the website of HKIE Geotechnical Division http://mobile.hkieged.org/geopapeer.vbhtml.



Ir Dr C K Lau
Coordinator, Assessment Board
2024 HKIE Geotechnical Paper Award

TABLE OF CONTENTS

PAPERS	Page No.
1. Elevating Geotechnical Excellence: Novel Practices and Innovative Solutions in Hong Kong C. M. Wong	1 - 43
2. Seismic Hazard Analyses of Northern Metropolis and Kau Yi Chau Artificial Islands in Hong Kong Zhengwei Chen, Gang Wang	44 - 52
3. Solution for Geotechnical Data Platform and BIM-based Foundation Design Automation Chen Xuewei, Cecilia Wan	53 - 60
4. Tunnels and Caverns Design in Rock Jason T. Y. Chin	61 - 78
5. Trial Piles with High Percentage GGBS Kian Y. K. Chiu, Eric H. Y. Sze	79 - 85
6. Case Study of Real-time Monitoring of Groundwater Levels and Rainfall Data for a Hillside Terrain Site Formation Works for Public Housing at Pok Fu Lam in Southern District, Hong Kong in Year 2023 Gary S. H. Kwok, Chester S. C. Lam	86 - 97
7. Digital twin visualization of distributed fibre optic strain data for a high-performance early warning system R.G. Laver, Y. F. Leung	98 - 109
8. The Establishment of a Safe Method of Offshore Pile Driving in Hong Kong Daman Lee, K. T. Hung, Victor Li	110 - 123
9. Use of Compressible Layer for Raft Footing Design with Winkler Method Ted Tse, Ka-Ming Lee, Ted Lan	124 - 135
10. The Use of Removable Ground Anchors in Deep Basement Excavation in Hong Kong Brian K.L. Ieong, Rupert K.Y. Leung	136 - 145

11. A New Era of Underground Construction in Hong Kong – From Ground Investigation to Construction 146 - 159
Simon C. M. Leung, Bridges Guy D.C., Franklin K. L. To, Michael W.K. Choi

12. Data-driven Site Supervision on Micro Tunnel Boring Machine (MTBM) on Hard Rock Performance - Objective, Analysis and a Case of Effluent Pipeline in a Caverns Project 160 - 172
Simon C. M. Leung, Elton M.Y. Ko

13. Energy geostructures for reducing energy consumption in Hong Kong: an example of energy diaphragm wall 173 - 188
Leung, A. K., Wang, Y. H., Yang, H. X., Zhou, H., and Zhou, C.

14. A Critical Review of Pile Acceptance Criteria 189 - 200
Victor Li

15. Digital Integration for Condition Assessment for Water Tunnels in Hong Kong 201 - 212
S.W. Millis, J.R. Connell, W.F Liu & C.W. Poon

16. Analytical Chloride Diffusion Model for Durability Assessment of Concrete-Lined Tunnels 213 - 225
P.L. Ng, S.J. Zhou, J. Wang

17. Effects of Vibration due to Piling in Proximity of MTR Structure and Mitigation Measures 226 - 238
Shawn Y.T. Shang, Y. Chen

18. Evolution of Three-Dimensional Geotechnical Information Infrastructure 239 - 249
Lawrence K.W. Shum, Sammy P.Y. Cheung, Chris S.C. Tang, Richard C.M. Ho, Raymond C.H. Koo

19. Advancements in Design and Construction Practice for Deep Excavation 250 - 261
Lawrence K.W. Shum, Sammy P.Y. Cheung, Raymond C.H. Koo, Ivan Li and J.C. Liu

20. An Innovative ELS System on Recently Reclaimed Land – Construction and Performance 262 - 272
Gavin S.H. Toh, C.N. Ho, Jack Yiu, Tom S.K. Chan, Chris C.F. Shum Oscar Y.N. Tse & Kimberly H.Y. Leung

21. Economical Design Approaches for Deep Excavation and Lateral Support (ELS) in Soil with Shallow Bedrock 273 - 284
Ted Tse & Kelvin Ng

22. Enhancing Pore Water Pressure Monitoring by Fully Grouted Piezometers: A Case Study of Crossrail and Prospects of Application in Hong Kong 285 - 296
M.S.P. Wan & F.L.C. Lo

23. Innovative Synergy between Slope Upgrading and Ecological Conservation in Preventive Maintenance Programme 297 - 308
Jay P. H. Wan, W. K. Yeung, Dr. C. C. Pang, Lawrence C. F. Leung, Ronald P. M. Li & Stanley K. M. Chung

24. Adopting Underslab Drainage System to Tackle Groundwater Uplift Force: A Holistic Overview and Experience Consolidation 309 - 320
Andrew T F Wong, Alvin K M Lam & Tony K S Mak

25. Ground Movements Caused by Diaphragm Wall Installation 321 - 332
L.W. Wong

26. Exploring Computer-based Rock Mass Characterization 333 - 345
Louis N.Y. Wong & K.K. Chan, S.N. Goh, Ivan H.H. Chan & Regis L.G. Chee

27. Development of an AI rock type classification and fracture state characterization web-based application 346 - 353
Louis N.Y. Wong, Keith K.C. Tse, Joseph S.H. Cheung Lequan Yu

28. A Showcase to Components Replacement in Existing Steel Flexible Barrier System 354 - 361
W.L. Wong, P. Cheng, K.K. Chan, C.Y. Tang

29. The Pathway to Decarbonisation in LPMitP: Carbon Management Framework 362 - 373
Ryan Yan, Ashley Cheng, David Mak, Thomas Tang, Kenny Yau, Martin Lee, Yan Tse, Roy Hung, Florence Chu, Jonathan Lau, Natalie Yim

30. Review on the End Bearing Capacity of Large Diameter Bored Piles founded on Meta-sedimentary Rock in Hong Kong 374 - 385
Terence L Y Yau, C K Lau

31. Fully Coupled Numerical Methods and a Simple Method for Calculating Settlements of Foundations and Reclamations on Clayey Soils 385 - 397
Jian-Hua Yin, Ze-Jian Chen, Pei-Chen Wu, & Kai Liu

32. An Innovative ELS System on Recently Reclaimed Land – Design and Analysis 398 - 408
Jack Yiu, Tom S.K. Chan, Chris C.F. Shum, Gavin S.H. Toh,
C.N. Ho, Oscar Y.N. Tse

Elevating Geotechnical Excellence: Novel Practices and Innovative Solutions in Hong Kong

C M Wong
C M Wong & Associates Ltd. Hong Kong

ABSTRACT

With nearly 50 years of experience as a geotechnical and structural engineer, the author aims to share his noteworthy expertise in this seminar. The paper will provide an overview of three key aspects of geotechnical engineering: Slope Works, Excavation and Lateral Support (ELS) Works, and Foundation.

Regarding slope works, the paper will discuss the design development of slope upgrading works and natural terrain mitigation works together with several actual examples showcasing successful approaches to address challenging site constraints. Additionally, the paper will introduce novel materials that are either currently used or under study for slope works.

Regarding ELS works, this paper will discuss the Enhanced Control System (5A system) for ground control during ELS. The author will also share his latest experiences in implementing sustained soil nailing as tie-backs, which represents the advancement in ELS design works.

For the foundation section, this paper will elucidate the development of "presumed allowable bearing pressures" for rock. Each section will feature actual examples under the author's supervision, showcasing his ability to

1 INTRODUCTION

Hong Kong is a densely populated city and its topography is mostly hilly. Due to the scarcity of flat land, many buildings and infrastructures have to be situated close to or even rightly on the hillside, which in most cases require the careful planning, design and construction of the geotechnical works to achieve safety and economic purposes.

In addition, the geology of Hong Kong comprises different types of soil and rock and the bedrock levels vary from ground to more than 100m depth. Wide varieties of foundations have been adopted to suit the different terrain conditions to safely support superstructures ranging from residential houses to high rise buildings.

To tackle the challenges comprising not only the technical issues but also the high demands for standards of safety and sustainability, the engineers of Hong Kong have been exercising their expertise and employing their experiences to achieve excellence in these aspects of design and construction.

This paper will provide an overview of three aspects of geotechnical engineering works – Slope Works, Excavation and Lateral Support Works and Foundations. This is followed by actual examples that are under the direction of the author and can exhibit excellence in overcoming both engineering difficulties and social issues.

2 GEOLOGY OF HONG KONG

As described by Sewell et al. (2000), more than three-quarters of the rock outcrops of Hong Kong are composed of igneous rocks, predominantly volcanic and granitic rocks, while the remaining are sedimentary rocks. Sedimentary rocks are occasionally interbedded and interlaminated with metamorphosed sedimentary rocks e.g. metasiltstone and metasandstone. (GEO, 1992) These rocks are typically deeply weathered, occasionally with weathering front reaching as deep as 100m. (Cheung, 2021) Superficial deposits overlying the bedrocks comprising alluvium, colluvium and other unconsolidated materials are found over the whole territory. These sediments are with weathered profiles of thicknesses varying from a few metres to several tens of metres but can also exceed 200m locally (Fyfe et al., 2000). There are also large reclamation areas along the coasts and in the Hong Kong International Airport at North Lantau with variable deposits comprising sand fill, mixed rock and soil fill as well as construction and demolition debris. A geological map of Hong Kong modified from Sewell et al. (2000) (Pappin et al., 2004) is extracted in Figure 2-1.

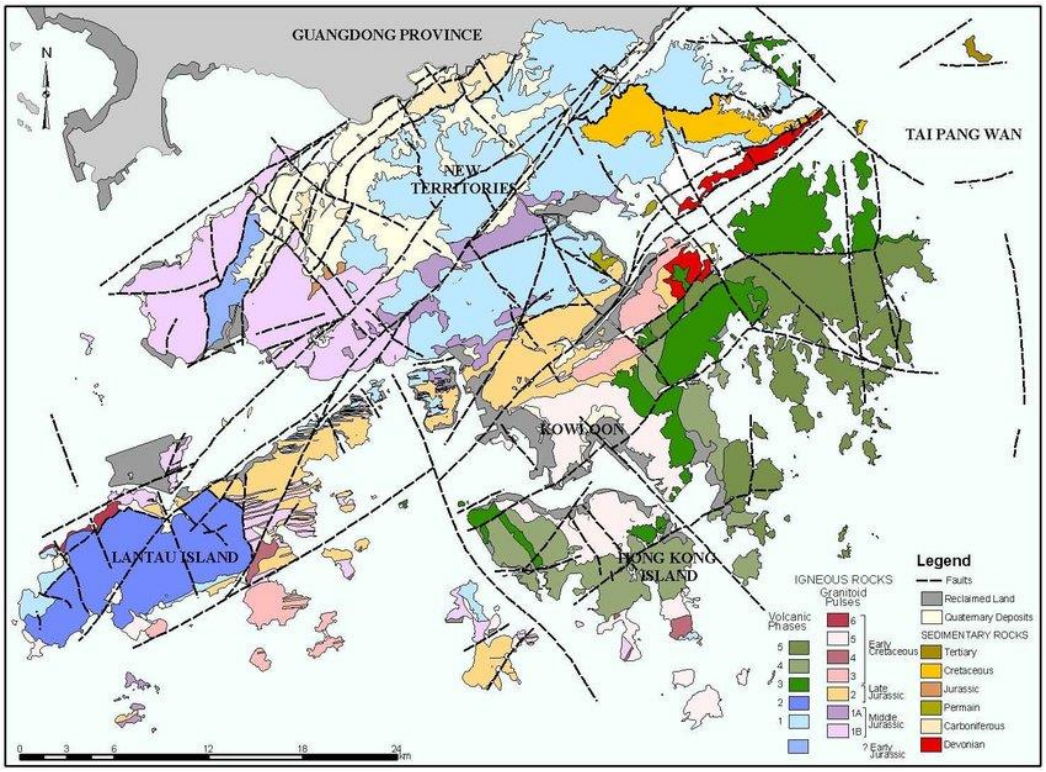


Figure 2-1: Simplified Geological Map of Hong Kong modified from Sewell et al. (2000) (Pappin et al., 2004)

3 Slope and Retaining Wall Upgrading Works and Slope Protection

Owing to the hilly terrains and lack of natural flat grounds in Hong Kong, over the years, plenty of cut slopes, fill slopes and retaining walls, collectively known as man-made features, had been constructed across the territories to create flat grounds for urban development and to house the growing population. The amount of geotechnical control, prevailing design standards and available technologies at the time of formation of these man-made features could be vastly different from the present day. Landslides associated with the man-made features formed in the old days prior to establishment of Geotechnical Control Office (GCO) in 1977(renamed as Geotechnical Engineering Office (GEO)) were not rare. Some notable cases of man-made feature landslides include fill slope landslides in Sau Mau Ping in 1972 and 1976, landslide at the hillside above a cut slope at Po Shan Road in 1972, failure of a masonry retaining wall and the fill platform behind at Baguio Villas in 1992 and failure of a masonry wall and the slope below at Kwun Lung Lau in 1994. A total of 156 people lost their lives in the three landslide events in the 1970s and a total of seven people lost their lives in the two landslide events in 1990s. (GEO, 2024)

In late 1970s, the government launched Landslip Preventive Measures (LPM) Programme, a long-term programme to upgrade the existing substandard government and private man-made features. (DEVB, 2021) In order to upgrade the existing man-made features to meet the current safety standards, different upgrading measures were adopted in public and private projects alike. Some typical examples of upgrading measures are regrading of slope, provision of structural supports and ground improvement. In 2010, GEO broadened the scope of the LPM Programme and launched Landslip Prevention and Mitigation (LPMit) Programme to include studies of natural hillside catchments. (CEDD, 2023)

Recent initiatives in reducing carbon footprint in construction works, as well as the challenges in association with frequent and extreme rainfall events, have prompted the necessity to adopt innovation and novel technology in LPMit Programme. This, together with continuous specialist works in upgrading of man-made features and mitigation of natural terrain hazards, are two of the key elements of the slope safety system in Hong Kong. (Cheung, 2021)

3.1 Early development

In the early days of Landslip Preventive Measures (LPM) Programme, i.e. late 1970s to 1980s, upgrading measures adopted for cut slopes and retaining walls were generally limited to cutting back to a shallower angle and supporting the existing slope or retaining wall with a new retaining wall and backfill. Prestressed ground anchors were sometimes used in steep cut slopes or retaining walls with significant height. Fill slopes were stabilized by recompaction of top 3m of loose fill with provision of surface treatments and drainage, based on the recommendations by the Independent Review Panel set up by the government following the major fill slope failure in Sau Mau Ping in 1976. (GCO, 1976 & GEO, 1998)

Each of these early day upgrading measures has its own shortcomings. For example, cutting back to a shallower angle or supporting the slope with a retaining wall and backfill, both involving permanent modification of the existing landscape. The available space at the slope toe or slope crest is modified. Existing trees on the feature and at the crest need to be removed due to excavation or backfilling. As for prestressed ground anchors, life time monitoring works including residual load measurements and special grease checks should be carried out at regular intervals throughout the design life, imposing extra workload on the maintenance party of the anchored slope, especially when the anchor forces were found to drop. Due to this monitoring requirement, permanent prestressed ground anchors have not been adopted since the early 1980s. As for fill slope recompaction, which was traditionally carried out by placing and compacting 200-400mm thick horizontal layers of fill on a benched excavated profile to form a 3 metre thick compacted fill capping, bulk excavation was involved and extensive works area were reserved for stockpiling the excavated ground material. Similar to cutting back mentioned above, the existing landscape of the surroundings was permanently modified while removal of trees were usually involved. In view of these shortcomings, new upgrading measures and construction methods were introduced to the industry.

In the late 1980s, soil nails were first applied in the upgrading measures of cut slopes and retaining walls. Studies were carried out on various aspects of soil nail design, including method of stability analysis, nail-soil interaction, design of soil nail head, durability, pullout resistance, reinforcement materials, drillhole forming techniques, potential damming effect of soil nail grouting and non-destructive testing. Soil nail design has been evolving over the years, with significant improvement in robustness. Efforts are still being made in recent years to improve the design details and materials. For example, studies have been carried out to reduce soil nail head sizes and increase the constructability, alongside studies on potential replacement of steel reinforcement with more sustainable or more durable substitutes.

In the 2000s, development of upgrading measures for fill slope went along two main separate ways- new methods and materials for fill replacement and soil nail with grid beam system. A new technique of fill recompaction emerged in this period. Excavation and recompaction of fill slope were carried out in a pit-by-pit manner (Chan and Chan, 2008). Each pit had a dimension of 1.5m x 1.5m on plan and depth of 3m. High temporary benched cuts can thus be avoided. Instead of using compacted soil as backfill, the use of cement stabilized soil (GEO, 2003a), mass concrete, no-fines concrete and light weight concrete were trialed and was demonstrated to be effective and has become the prevalent trend in the recent years, while new cementitious backfill materials with better performance were being developed and studied in the 2020s.

Meanwhile, on the account that soil nailing was the most commonly used slope upgrading measure in Hong Kong early in this century, the industry also explored the possibility of using soil nail in loose fill slopes. The Hong Kong Institution of Engineers (HKIE) published a study to establish a basic design framework for soil nails in loose fill in 2003. The study covered the following:

(i) laboratory tests for steady state shear strength of loose fill,

(ii) proposed use of surface grid beams,

(iii) recommended minimum relative compaction of 75% for loose fill to be upgraded by soil nails,

(iv)recommended lower bound shear strengths at the onset and during liquefaction and

(v) recommended minimum factor of safety for the checking of fill liquefaction using steady state parameters (FOS = 1.1).

In 2011 and 2013, Geotechnical Engineering Office (GEO) and HKIE co-published further studies on the use of soil nails in loose fill. These further studies built on the study in 2003 and further explored the following areas:

(i) arrangement and inclination soil nails based on numerical analysis,
(ii) recommended nominal grid beams embedment,
(iii) recommended method to delineate zones of liquefiable fill and non-liquefiable fill and
(iv) illustrated worked examples as per the recommendations.

3.2 Examples of innovative works

3.2.1 High strength steel bars as soil nails

The subject feature above a private lot along Po Shan Road is a 25m high cut slope formed before mid-twentieth century. Based on records, a total of 22 anchors were installed in 1978. Monitoring and measurement of residual loads of the anchors had been carried out in the 1980s and 1990s, till 2000. The monitoring data showed that there was a decline in anchor forces over the years. (Wong et al, 2011b)

As a long-term solution, soil nails were proposed to substitute the anchors in 2008 under LPM programme. Site constraints including thick layer of colluvial boulders, high groundwater table, existence of ground anchors with sizable anchor heads were carefully considered. Under the conventional approach, soil nails of 40mm diameter high yield steel bars would need to be spaced at less than 2m. This closely spaced arrangement would clash with the existing ground anchor heads. To facilitate widely spaced nails, high strength steel bars of 36mm diameter with yield strength of 1080MPa (the yield strength of normal soil nails was 460MPa at that time) was adopted. The allowable nail force for individual nail was thus increased from 385kN to 732kN, an escalation of 90% as compared to normal soil nails of 40mm. This enables the soil nail spacing to be increased to a range of 2.4m to 4m. Such wider spacing is also necessary in order not to cause damming up the groundwater table at the steep natural terrain behind the subject cut slope. (Wong et al, 2011b)

Owing to the wider soil nail spacing, instead of typical isolated soil nail heads, a grid beam structure was constructed to tie all soil nails together in order to prevent local instability of the feature.

Consideration was also made to the construction method for the soil nailing works. The prevalent drilling method for soil nail was eccentric drilling, also known as Overburden Drilling with EXcentric (ODEX) drilling, which was prone to jamming of drill bits in the layer of colluvial boulders and might lead to excessive ground loss. To prevent such situations from happening during construction at the feature with high geotechnical sensitivity, concentric drilling was adopted. The mechanism of concentric drilling has reduced the width of the gap between the casing pipe and drillhole to the minimum and, thus avoiding the flushing up of material outside the casing and any consequent ground loss. Also, there is no gap between the casing shoe and the pilot bit and therefore jamming of drill bit is highly unlikely. (Wong et al., 2011b) The upgrading works were completed in 2008.



Plates 3-1 & 3-2: Subject government cut slope: before upgrading works with heads of ground anchor exposed on slope surface (left); upgrading works with grid beams exposed on slope surface (right)

3.2.2 Retaining walls upgrading works under traffic constraint

The feature comprises two stacking cantilevered reinforced concrete walls – the height of the lower wall is about 10m and that of the higher wall is about 5m. At the toe of the feature is a narrow one way access road acting as an exit from Comfort Terrace to King's Road. The feature is located at the junction with King's Road where the access road is on a steep gradient with a sharp turn before turning onto King's Road.

The conventional upgrading measure for such retaining walls is the installation of soil nails as tie back for the walls. The nails would be spread uniformly on the wall stem. However, the nail heads in this case would make the already sub-standard access road narrower, and might cause encroachment upon the vehicular path.

In view of the above constraints, an innovative solution was proposed. First of all, the two stacking walls were structurally connected at the top of the stem of the lower wall and the toe of the upper wall. Then, tie back soil nails were installed mainly at the upper wall and even with a few at the lower wall, they were located at a minimum of 4m clearance above the road level. The soil nails would then be connected by tie beam and these tie beams would avoid the clashing of vehicles. The works were carried out smoothly in 2011.

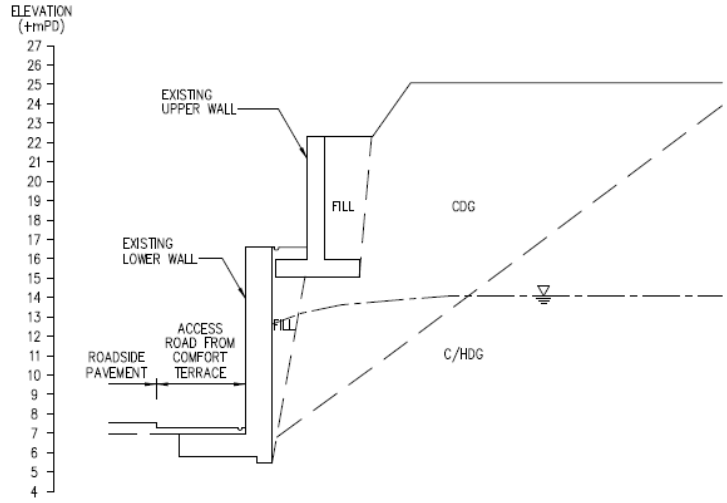


Figure 3-1: Typical section of the retaining wall before upgrading works

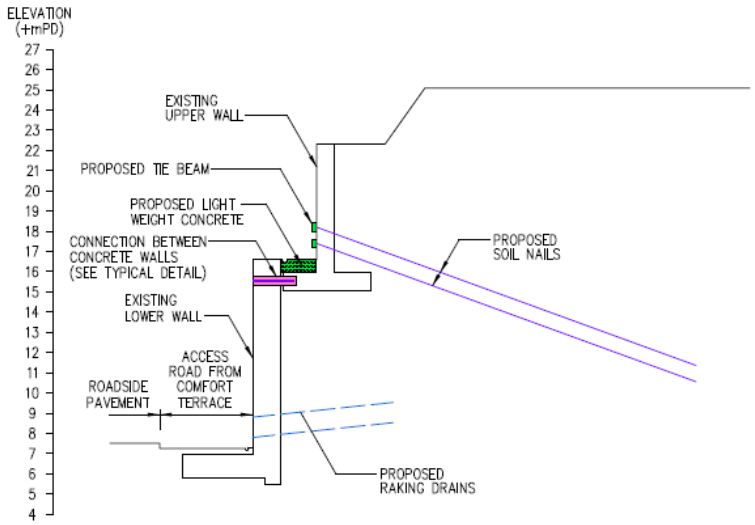


Figure 3-2: Proposed upgrading works at the retaining wall

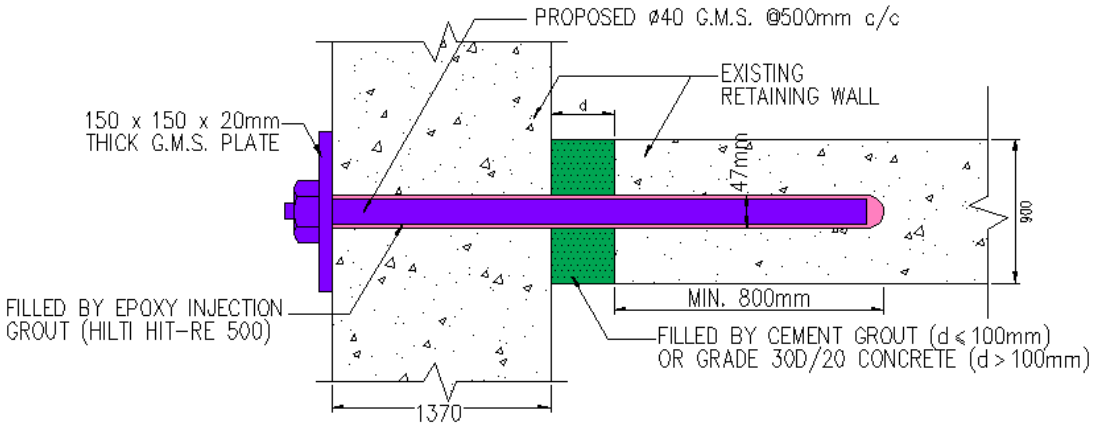


Figure 3-3 Typical details of connection between concrete



Plate 3-3: General view of the retaining wall after completion of upgrading works.

3.2.3 Preservation of stone wall tree on old masonry wall

The feature comprises a cut slope with a retaining wall at the toe overlooking Hornsey Road. The retaining wall has likely retained its original masonry appearance since its formation, with a stone wall tree protruding from the southern portion of the feature. The stone wall tree is of the species of ficus virens and has an overall height of 18m and average crown spread of 20m.

While designing the upgrading measures, considerations were made to preserve the valuable stone wall tree and the appearance of the masonry wall. Soil nails were adopted as the structural measure stabilize the masonry wall. Professor Jim Chi Yung, a stone wall tree expert, was invited to assess the condition of the tree and provide expert opinions on how to minimize disturbance to the tree. The water-cement ratio of the grout adopted was 0.35, which is lower than normal grout (with water-cement ratio about 0.4) to minimize migration of grout into surrounding soil. For each soil nail, permanent steel casing was provided for the first 5m of drillhole to control grout loss. Soil nail layout in close vicinity of the stone wall tree were handpicked on site together with Professor Jim. To construct the nail heads, - the masonry blocks of the wall affected by soil nails were removed from the wall one by one, and reinstated after the completion of the concealed nail head construction.

To abate sliding force and overturning moment to the masonry wall due to surcharge of the stone wall tree and to minimize the chance of stem failure and uprooting of the tree, pruning was carried out to reduce the tree crown. In future maintenance, the height and crown spread of the tree should be maintained within an allowable maximum value. The upgrading works were completed in 2018. The appearance of the stone wall tree and masonry wall was preserved. The feature won Special Merit in Sustainable Slope Excellence Award in 2020. As of to date, the stone wall tree is still thriving and providing a beautiful heritage-cum-vegetation appearance.

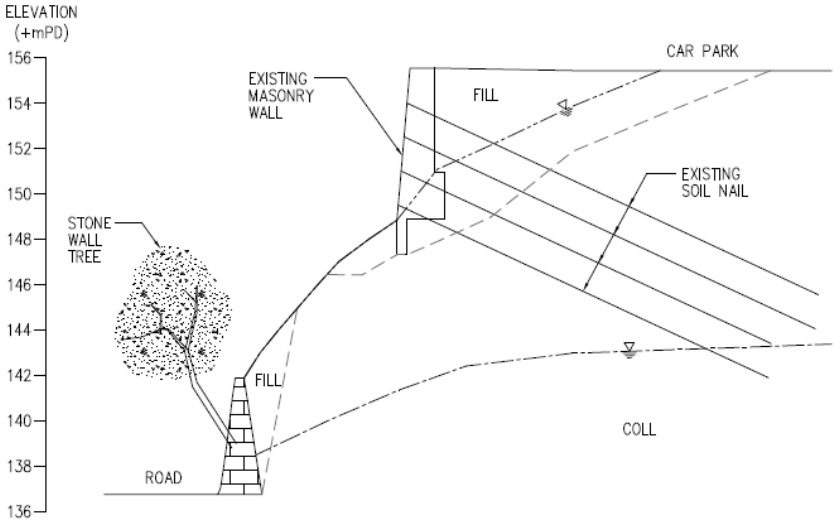


Figure 3-4: Typical section of the cut slope with retaining wall before upgrading work

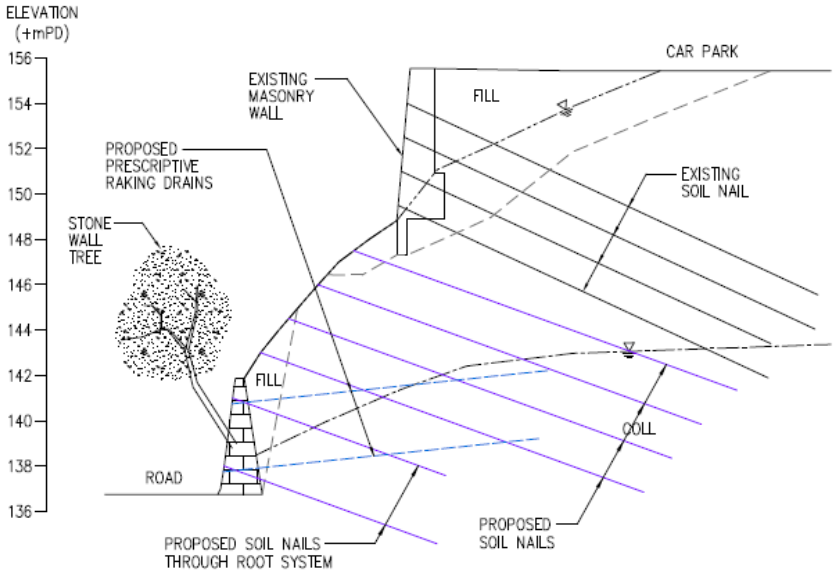


Figure 3-5: Proposed soil nails through root system of stone wall tree



Plates 3-4 & 3-5: Root portion of the stone wall tree: before installation of soil nails (left); after completion of soil nailing works. Locations are soil nail heads are circled in blue. (right)



Plate 3-6: Condition of the stone wall tree in May 2024

3.2.5 Rehabilitation of retaining wall with historical values

The subject retaining wall is located within an on-going construction site for private development. The feature was a ruin of a series of back-to-back tenement buildings (tong lau). As of 2018 when the development site was taken over by the private developer, only the back wall and small portions of the side walls of the tenement buildings remained intact in the ruin. The back wall, about 5m in height and 34m in length, retained a former building platform alongside Cochrane Street, while the remnant side walls were connected to the back wall. Composed of brickworks, these walls largely preserved their original appearance. The exact construction year of these tenement buildings is unknown, but Antiquities Advisory Board (AAB) (2016) puts the construction year at 1930s in a historical building appraisal. Although no grading is assigned to the remnant walls as confirmed by AAB in 2017 (AAB, 2024), AAB remarked in the appraisal that the remnant walls could serve as a reminder of a building and living style of pre-war Hong Kong (AAB, 2016).

During the design stage of the private development, efforts were made to preserve the remnant walls including the subject feature as far as possible, alongside their historical values. Assessment reveals that the stability of the subject feature was not up to the current safety standards and requires upgrading works. Typical

upgrading measures of a retaining wall of this height include installation of soil nails and/or thickening of the wall from the wall front. These two typical measures would have an adverse effect on appearance of the wall.

In order to preserve the appearance, upgrading measures could only be carried out behind the wall. In this case, pit-by-pit excavation followed by backfilling with mass concrete, were proposed. However, the current guidelines limit the depth of each excavated pit to 3m whereas the height of the brick wall is about 5m. In order for this scheme to be workable, open excavation was carried out to form a level platform about 2m below the wall crest. Pit excavation could then began at the level platform and the base of the 3m deep pit would meet the wall base. As of to date, the construction works are still on-going.



Plate 3-7: Condition of subject retaining wall and one of the connected side wall before commencement of construction works

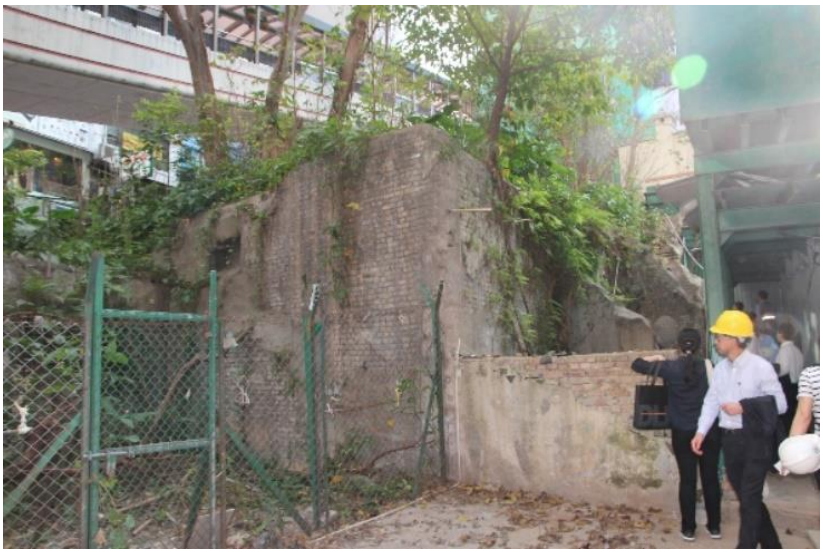


Plate 3-8: General view of condition of the subject retaining wall before commencement of construction works

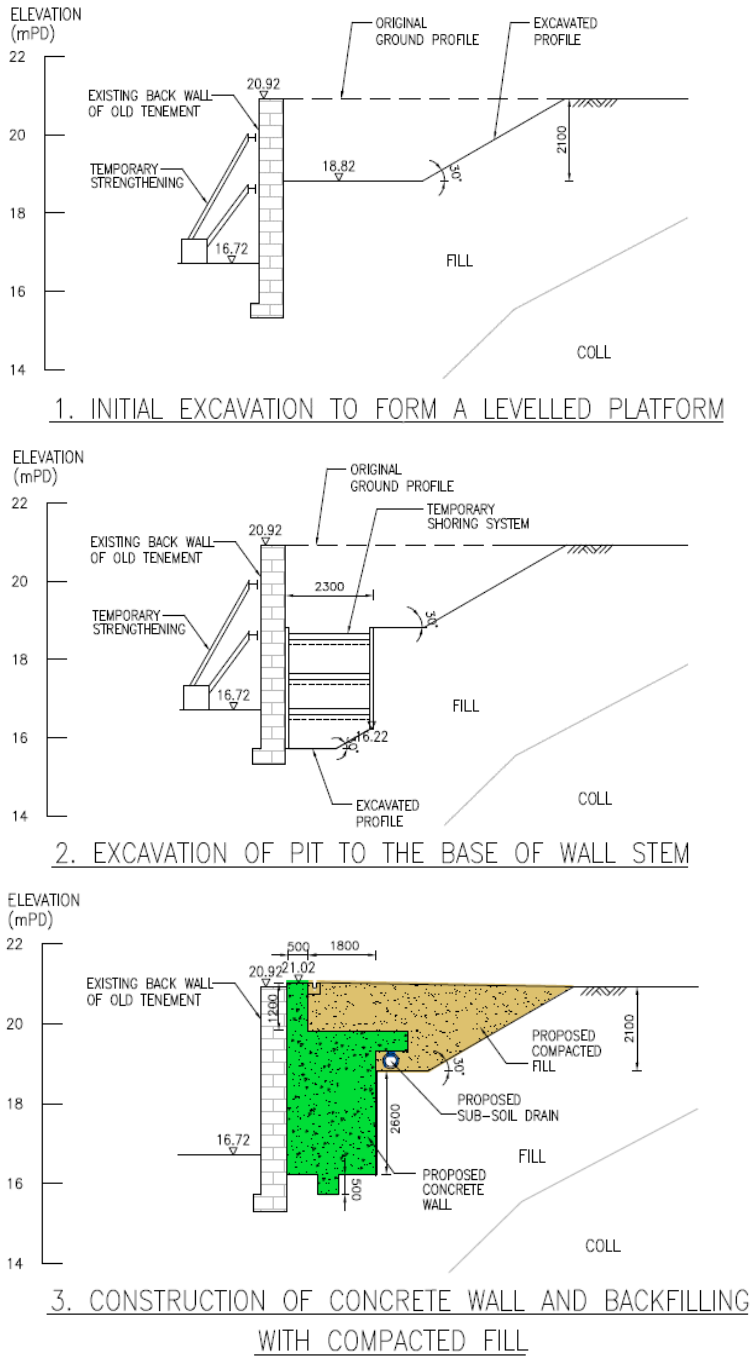


Figure 3-6: Typical section of the upgrading works.

3.3 Natural Terrain Hazard Study

Hong Kong is prone to natural terrain landslides, given its high seasonal rainfall, deep weathering soil profile and the vast extent of natural terrain areas (Ko and Lo, 2018). The natural terrain susceptible to landslides pose hazards to people and property in developed land nearby.

In the last century, severe rainstorm events occurred occasionally and caused widespread natural terrain landslides across the territory. Some notable rainstorm events include the June 1966 heavy rainstorm affecting Hong Kong Island of which the landslides and flooding together resulted in 64 fatalities and more than 2000 people homeless, the May and August 1982 rainstorms affecting the whole territory during which more than

1400 natural terrain landslides were triggered and squatter areas were severely damaged and, the November 1993 rainstorm affecting mostly Lantau Island during which more than 800 natural terrain landslides were triggered. In the 2000s, severe rainstorm events became more frequent and extreme. In the June 2008, Hong Kong was struck by the most severe rainstorm at that time, of which the return period of the rolling 4-hour and 24-hour rainfall were inferred to be in the order of 1,000 and 200 years respectively. On Lantau Island alone, more than 2400 natural terrain landslides occurred, resulting to blockage of some roads of sole access and the trunk road to Hong Kong International Airport, cut-off of water supply to villages and evacuation of village residents. (Ho et al., 2016)

In 2010, GEO broadened the scope of the LPM Programme and launched Landslip Prevention and Mitigation (LPMit) Programme to include studies of natural hillside catchments. (CEDD, 2023)

In September 2023, under a single severe rainstorm event, the government received a staggering number of 145 landslide reports within just two days. The 24-hour rainfall recorded in the Eastern and Southern District of Hong Kong exceeded more than 800mm, which was the highest record since rain gauges were installed in the areas. Increasing precipitation with greater extremes is expected in Hong Kong in the coming years, further increasing the landslide risk across the territory. Upscaling the government's LPMit Programme and speeding up the programme might be necessary for protecting public safety.

3.3.1 Recent development in NTHS

Guideline for natural terrain hazard studies (NTHS) was first compiled into GEO Report No. 138 (first edition) for practitioners to follow in 2003. The most popular approach for NTHS has been based on design event approach. Under the first edition of the report, a conservative event with a return period of 100 years and a worst credible event with return period of 1000 years are adopted as the design event for run out analysis of landslide debris (GEO, 2003b).

A major update on the design event approach was released in 2013 in Technical Guidance Note (TGN) No. 36 (GEO, 2013). In the new approach, an event with return period of 100 years based on recent landslides as well as relevant relict landslides with a high degree of certainly is adopted as the design event. This, together with other updates, were compiled into a second edition of GEO Report No. 138 in 2016. Detailed guideline on application of "react-to-known-hazard" principle on natural terrain catchments under LPMit programme is also presented in this new version of the report

3.3.2 Typical Mitigation Measures

Some common mitigation measures for natural terrain landslide hazards in Hong Kong include flexible debris resisting barrier, rigid debris resisting barrier and in-situ stabilization by soil nails. In natural terrain study area comprising numerous catchments and spanning across an extensive area, a hybrid approach consisting of more than one type of mitigation measures should be adopted.

On first look, in-situ stabilization with soil nails is a handy solution which can suit the condition of most natural terrain catchments. However, installation of soil nails involves erection of temporary platforms and access ladders, and might thus cause disturbances to flora and fauna residing in the area. Soil nailing across vast extent of the catchment should be avoided as much as feasible. If condition allows, debris-resisting barrier should be adopted as the mitigation measure instead of soil nailing.

An example including all the recent development on mitigation measures for natural terrain is a Study Area in Clearwater Bay. As shown in Figure 11, a total of 5 hillside catchments require mitigation works based on results of the NTHS. The toe areas of catchments D and E are composed of relatively gentle grounds, which are suitable for construction of debris-resisting barrier. Considering the actual design requirements and ease of access of construction plants and materials by road, rigid-debris resisting barrier is proposed for catchment D, while flexible debris-resisting barrier is proposed for catchment E. Soil nailing is proposed at the remaining catchments A, B and C. The extent of soil nails is confirmed to hazardous areas only, to minimize disturbance to flora and fauna as far as possible.

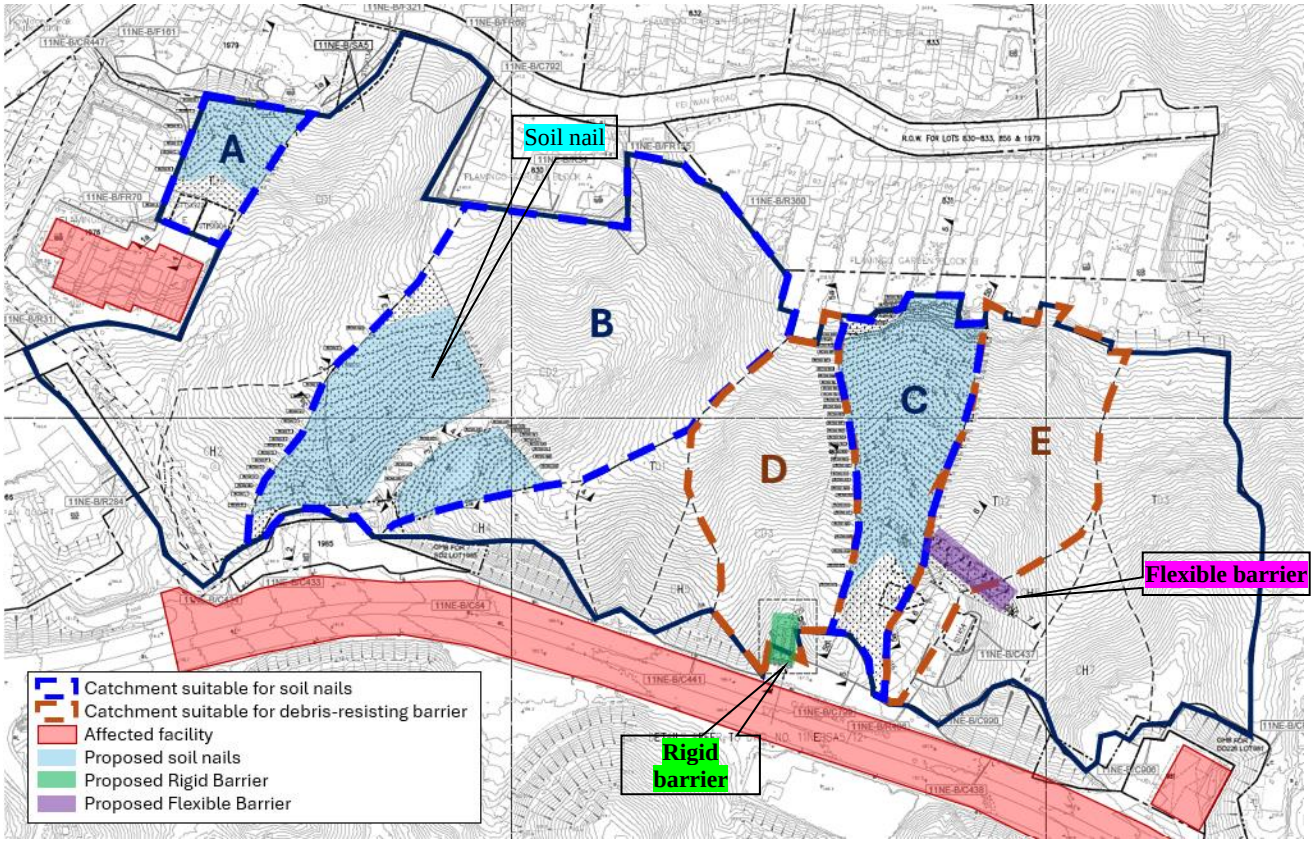


Figure 3-7: Layout of mitigation measures in a Study Area comprising 5 catchments which require mitigation works





Plates 3-9 & 3-10: General view of the rigid barrier at Catchment D of the Study Area in the example, from the facility at risk (left) and from the Study Area (right).



Plate 3-11: General view of the flexible barrier at Catchment E of the Study Area in the example

3.4 Prospective advancement in material

3.4.1 Potential use of fibre-reinforced polymer as reinforcement in soil nail

Traditionally, steel reinforcement bars are used in soil nailing works in Hong Kong. However, steel reinforcement bars are prone to corrosion and thus steel soil nails require corrugated plastic sheathing for corrosion protection in aggressive grounds. Studies have been carried out to explore possibilities in substituting steel soil nails with fibre-reinforced polymer, which is a composite material made of polymeric resin embedded with fibre and apparently more durable than steel. The initiative was that corrugated plastic sheath protection may not be required for the highly durable fibre-reinforced polymer soil nail in aggressive grounds. (Cheung & Lo, 2005) The light weight of these composite materials also adds to the advantages in the aspect of safety in manual handling. Carbon fibre-reinforced polymer (CFRP) and glass fibre-reinforced polymer (GFRP) were studied in the 2000s and 2020s respectively.

Under the study in the 2000s, a series of laboratory tests including tension test and CFRP-grout bond strength test, trial GFRP soil nail installation and trial GFRP soil nail pull-out test were carried out. Two types of GFRP reinforcement were tested: the flat strip type and the rounded type. The study reveals that the type of CFRP tested has tensile strength around 5 times conventionally used soil nail steel reinforcement bar. The results of CFRP-grout bond strength are comparable with the bond strength between steel reinforcement bar and grout. Trial installation was successful. However, results of the pull-out tests were considered inconclusive since, in some of the tests on flat strip type reinforement, the CFRP soil nail fails pre-maturely The pre-mature failure could be explained by damage of carbon fibres due to concentrated stress immediately behind the head adapter during transportation. No pre-mature failure was reported for CFRP soil nails with rounded type reinforcement.

Although the results in laboratory tests indicate a good prospect of CFRP soil nails, the study remarks that the brittle behaviour, low shear strength and low bending capacity have yet been explored, while cast in-situ head adapters are preferred for pull-out tests in further site trial. (Cheung & Lo, 2005)

With the experience on studying CFRP, laboratory studies and site trials on GFRP soil nails has been proposed in the 2023. Reinforcement bar tension tests and GFRP-grout bond strength tests have been proposed to specimens subject to an alkaline environment. GFRP by different manufacturers, resin of different types and reinforcement bars with different surface treatment will be explored. (PolyU, 2023) The site trial is proposed to include a total of 21 trial nails, some of which will be subject to pull-out tests, the remaining of which will be subject to long-term monitoring. All trial nails will be installed with optical fibre sensors for deformation monitoring (CMA, 2023). As of to date, the tests under the laboratory studies and site trial are still on-going.

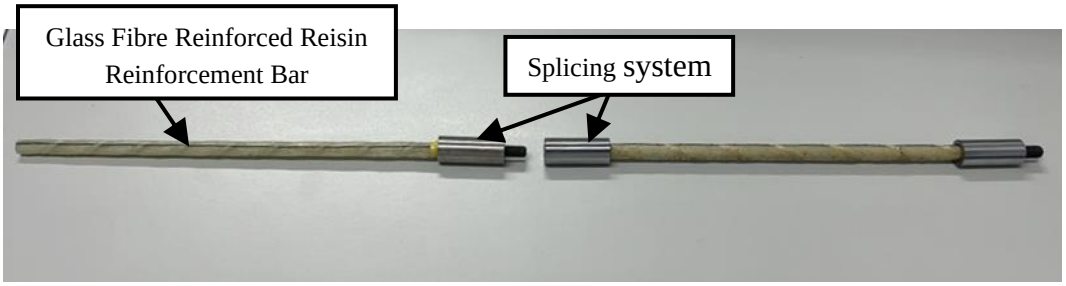


Plate 3-12: Components of glass fibre reinforced resin reinforcement bar

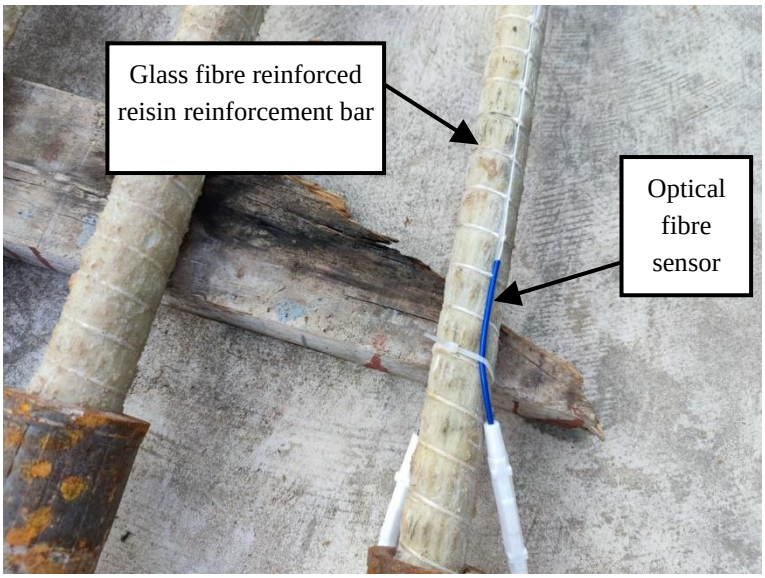


Plate 3-13: Glass fibre reinforced resin reinforcement bar fitted with optical fibre sensor used in site trial



Plate 3-14: Pull-out test for glass fibre reinforced resin soil nail

3.4.2 Potential use of engineered cementitious composite (ECC) grout to replace Portland cement grout in soil nail

The initiative of the studies related to ECC grout is similar to fibre-reinforced polymer reinforcement bar mentioned above. ECC, popularly known as bendable concrete, is a class of fibre-reinforced concrete material exhibiting excellent crack control under a strain of several percent. The reinforcement fibre is typically micro fibre and the distribution and flow direction are carefully controlled and monitored. When subject to high tensile load, instead of developing a single crack with macroscopic width, ECC develops numerous parallelly aligned cracks with very small width, typically less than 100 micrometers, in an orientation normal to the tensile loading axis. (Li, 2012) These tight crack width does not increase water permeability of the ECC beyond the level for the uncracked material. (Lepech & Li, 2009) Hence, ECC grout has the potential in protecting steel reinforcement bars against corrosion by limiting infiltration of water and the dissolved corrosive ions. Corrugated plastic sheath protection may not be required for soil nails with ECC grout installed in aggressive grounds.

Professor Victor Li from University of Michigan and Professor Christopher Leung from The Hong Kong University of Science and Technology were invited to carry out Laboratory studies to develop a suitable ECC grout for the use in soil nail construction. Mixes of ECC grout composing of difference mix proportions of fly ash, cement, water and fibre, fibre types and fibre suppliers were subject to workability tests (i.e. flow cone test and flow table test), bleeding test and strength tests (i.e. crushing strength test and direct tensile test). Cracking behavior of grout specimens under direct tensile test was closely monitored. (CMA, Leung & Li, 2018)

Among all mixes, the one showing the most promising laboratory test results, i.e. highest strain compatibility with steel reinforcement, was selected for site trial. Work procedures, work efficiency and workmanship were reviewed. (CMA, Li & Leung, 2019) The results of the study are promising, while further research on the durability of ECC grout in a longer monitoring period will be required. Also, during the site trial, a long ECC mixing and grouting time was noted. The skills required for ECC mixing is also significantly higher than that of conventional cement grout. Optimisation of the work flow for installing soil nails in ECC grout is crucial for its implementation.



Plates 3-15 & 3-16: Filled moulds for simulated grouting exercise (left), mixing of ECC grout during site trial (right).

3.4.3 Use of self-compacting cementitious materials for backfill in pit-by-pit works

Although using concrete as backfill in pit-by-pit works was demonstrated to be effective, it also comes with drawbacks like:

(i) long setting time,
(ii) difficult for material delivery in remote sites and steep terrain,
(iii) the need of compaction by concrete vibrator and
(iv) safety hazards associated with manual handling and working in pits.

In the 2020s, government departments carried out studies to explore the potential use of a self-compacting material (SCM) developed by Nano Advanced Materials Institute Limited (NAMI) as backfill material in road works and pit-by-pit works. The SCM developed by NAMI is composed of cementitious material, fine aggregate, crushed rock fines, water and admixtures. The proportions were adjusted for optimization of its mechanical behaviors. This material was originally developed for the use in road works in which re-excavation is common. The proportions are adjusted to achieve a low compressive strength, while maintaining high flowability and workability, self-levelling, self-compacting and homogeneity. (GEO, 2023a) The qualities of high flowability and self-compacting in SCM are highly favourable in pit-by-pit works, in view of the challenges listed at the beginning of this section.

A sizable loose fill slope was chosen as a pilot site to review the constructability of SCM. This fill slope was designed to be upgraded by pit-by-pit works and nearly 900 m^3 SCM were required for backfilling the excavated pits (Plates 3-17 and 3-18). This site is not close to public road and the works area is limited. The characteristic of high flowability of SCM solved the transportation of backfilling material for over 100-meter travelling distance with level difference exceeding 30-meter. This case is known to be the largest amount of SCM used for slope upgrading works in Hong Kong. This project has also won champion in slope category of HKIE Geotechnical Project Excellence Award in 2023.

The key findings of the studies and the pilot application include a good consistency of SCM and no observation of ground subsidence or signs of distress or detachment after application of SCM, no difficulty in site mixing, efficient placement of SCM due to its high flowability and self-leveling and self-compacting qualities, efficient horizonal pumping over 250m and vertical pumping of over 30m using common equipment, no difficulty in sampling for quality assurance tests. (GEO, 2023a)

In addition to these findings, an apparently much lower amount of heat release was reported during curing when compared to cement grout or concrete, possibly due to the low cement content. This quality, if well investigated and documented in further studies, may be favourable in backfilling works near sensitive utilities. Possibly due to the low cement content in the SCM, much less shrinkage cracks were found in cured SCM backfill than in cement grout or concrete backfill. GEO has issued a Technical Note giving recommendations on the design and use of SCM in upgrading works in 2023. With more successful cases, SCM has the potential to become the prevalent backfill material in pit-by-pit works.



Plate 3-17: Backfilling of a pit by self-compacting material during site trial



Plate 3-18: General view of the fill slope after completion of pit-by-pit excavation and backfilling with self-compacting material, followed by pit planting of shrubs and whips.

3.4.4 Concrete canvas for slope protection

Instead of the conventionally used shotcrete, Concrete Canvas has recently been adopted as slope surfacing materials under emergency works. Concrete Canvaswhich is known as Geosynthetic Cementitious Composite Mats (GCCMs), consists of three layers, including fibrous top surface, dry concrete mix with 3D fibre matrix PVC backing, and serves different purposes in relation to strength, water proofing and flexibility on the slope surface. (Concrete Canvas Ltd., 2022)

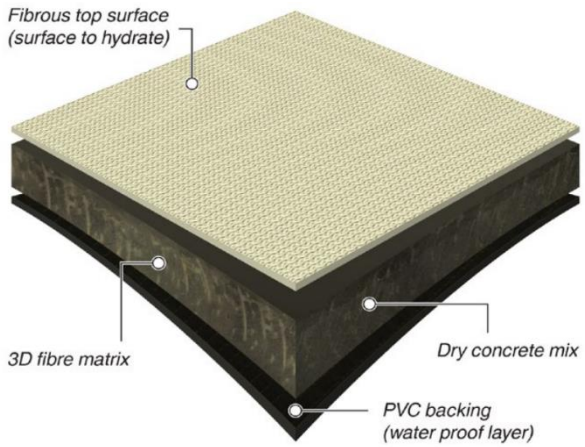


Figure 3-8: Composition of Concrete Canvas (Concrete Canvas Ltd., 2022)

In September 2023, landslides occurred on two man-made slopes in Lamma Island. Emergency repair works for providing hard cover to the failure slope surface are required. However, difficulties arise on carrying out shotcreting works in outlying island due to difficulties in plants mobilization, material delivery and limited working area. It is also required to complete the works in a short time to allow the re-opening of the footpath at the slope toe. Therefore, there was an opportunity of introducing Concrete Canvas as the slope surface cover under this case.

Batched rolls of Concrete Canvas could be delivered on site easily and the corresponding working procedures on handling the Concrete Canvas are relatively simple. Each roll is having roll width and roll length of 1 m and 10 m respectively with thickness of 5 mm and unit weight of 7kg/m^2. Concrete Canvas is laid on the slope

surface with at least 100 mm overlapping between layers and fixed with U-pins. After finish positioning Concrete Canvas, the covered surface is hydrated by spraying with water and bolts are used to fix the joints of Concrete Canvas after setting.

Concrete Canvas will harden to 80% of its 28 days strength in 24 hours and the slope surface could be thereby protecting the slope against erosion, water penetration and weathering effect within a short period of time. (Concrete Canvas Ltd., 2022)

Laying Concrete Canvas on the slope surface provides a quick temporary slope surface cover without involvement of heavy machinery items, such as air compressor and shotcrete machine, and overcome the difficulties on delivering the shotcreting materials to the outlying island.



Plates 3-19 & 3-20: Delivering batched rolls of Concrete Canvas on site (Left) and Fixation of Concrete Canvas on the slope surface (Right)



Plates 3-21 & 3-22: General view of the slope surface before (Left) and after (Right) emergency slope surfacing works using Concrete Canvas



Plate 3-23 : Extent of emergency slope surfacing works under Concrete Canvas

3.4.5 Fibre-reinforced shotcrete for slope protection

As mentioned previously, one of the critical issues on the adoption of hard slope surface cover is the crack propagation at the slope surface, resulting in high maintenance cost on cracks repairing works. For shotcreted slope, a layer of steel mesh reinforcement is laid on the slope surface prior to the shotcreting works as crack control measures. However, the laying works involve erection and dismantling of temporary working platforms, and it increases greatly on the time required for the slope surfacing works.

Moreover, the laying works rely heavily on the manual operation, and the corresponding safety risk, such as working at height, manual handling of mobilizing welded mesh and getting injured from protruded welded mesh, may be easily induced.

Therefore, fibre-reinforcement shotcrete is introduced as the slope surfacing cover. Fibre inside the shotcrete mixture may enhance the flexural strength of the slope surface cover and increase the ability of resisting crack propagation and maintaining structural integrity after initial cracking. (CMA, 2020) As such, the adoption of fibre-reinforced shotcrete neglects the need of laying welded mesh and the corresponding safety risks on handling the welded mesh at the slope surface are thereby eliminated.

Wet-mix fibre-reinforced shotcrete, which the shotcreting materials are mixed in the concrete plant and delivered to the construction sites, is commonly adopted in tunneling works. However, the available working space for carrying out the slope upgrading works is usually limited, and there may not be sufficient access and space for delivering the wet-mix fibre-reinforced shotcrete. Therefore, ‘dry-mix’ fibre-reinforced shotcrete, for which the fibre and shotcreting materials are mixed in a small mixing plant on site, is introduced. (CMA, 2020)

As shown in the plates below, fibre is mixed with the shotcrete material in the portable mixing machine on site, and the mixture is applied directly on the slope surface, similar to the working procedures of the shotcreting works. The study is still ongoing and further site trials will be carried out to review the use of ‘dry-mix’ fibre-reinforced shotcrete as the slope surface cover.





Plates 3-24 & 3-25: Mixing of fibre-reinforced shotcrete for shotcreting works



Plates 3-26, 3-27 & 3-28: Typical working procedures of shotcreting works using fibre-reinforced shotcrete. Original slope surface (left); application of shotcrete (middle); shotcreted slope surface (right).



Plate 3-29: Slope surface with covered with fibre-reinforced shotcrete.

4 EXCAVATION AND LATERAL SUPPORT WORKS (ELS WORKS)

Excavation and lateral support (ELS) works are commonplace in the building and infrastructure projects. In recent years, with the growing complexities of the deep excavation works, which are often pushed to the property boundaries and / or in the midst of sensitive structures and utilities, ELS works have become one of the major construction activities in Hong Kong under great concern. For years, the engineers have been exhibiting excellence in designing innovative systems and introducing sophisticated design methods to promote safety, economy and sustainability in the works.

An overview of the design approach in ELS works is first presented, followed by discussions of selected aspects that can demonstrate excellence of the geotechnical engineering practitioners.

4.1 Overview of the Design Approach in ELS Works

Before the computer era in the 1980s, excavations and lateral support systems in Hong Kong comprising either free or propped cantilever walls were mostly analyzed and designed by the Rankine and Coulomb's theories and other conventional approaches described in references such as Terzaghi (1967) and Bowles (1968). In the 1980s, the early editions of Geoguide 1 (GCO, 1982), NAVFAC Design Manual 7.2 (US Government, 1982), CIRIA Report 104 (Padfield and Mair, 1984), and others became the main references for the practitioners in the design of ELS works. In 1990, the then GCO has published the GCO Publication No. 1/90 titled "Review of Design Methods for Excavations". The publication comprises comprehensive descriptions of various ELS works systems and different design approaches as guidance for the engineers. Discussions of some advanced design concepts including the finite element method, elasto-plastic soil model have also been included.

The GCO Publication No. 1/90 (GCO, 1990) adopts the "Global Factor Method" in which unfactored soil strength parameters and loads are used in the stability checks (as described by PNAP APP-57 (BD, 2012)) of an ELS works for compliance with "global factors of safety specified in the guides / codes including Geoguide

1 (GCO, 1982) and Foundation Codes 2004 (CoPF) (BD, 2017). Nevertheless, the CIRIA Report No. C580 (Gaba et al., 2003) was published in 2003 which introduced a Limit State Partial Factor (LSPF) method for embedded retaining walls. In this method, soil structure interaction analysis is carried out for both the serviceability and the ultimate limit state conditions. Soil parameters and loads will be applied with pre-determined partial factors in the design of ELS works. In 2004, GEO of Hong Kong set up a Review Group comprising members from the Buildings Department, consultants and contractors to review the use of the LSPF. The author was a member of the Review Group. After the review, the Buildings Department has subsequently recommended that the method could be adopted for a trial period of two years as indicated in a letter dated 6 January 2005. Some modifications as to the partial factors given by CIRIA Report No. C580 to concur with the practice of Hong Kong are contained in the letter with the requirements including sensitivity analysis for singly propped excavations etc.

Wong & Yau (2005) has assessed the structural implications of the LSPF approach by CIRIA Report No. C580 as compared with the global factor method of GCO Publication No. 1/90 in 3 ELS works cases. The results reveal that the LSPF approach requires shorter embedment lengths of the walls, with reduction in the order of 40% while there are no significant differences in the structural steel contents in the shoring and strutting. Wong & Yau (2005) thus has demonstrated cost effectiveness of the LSPF approach. In addition, the shorter embedment length can result in lower risk incurred in construction, e.g. minimizing the risk of hard driving of sheet pile in difficult ground.

Upon expiry of the 2 years trial period as imposed by BD's letter dated 6 January 2005, the Buildings Department has further extended the trial period for 3 more years in a letter dated 18 January 2007 to allow time to collect sufficient data for assessing the suitability of the approach. A PNAP APP-57 was finally issued in 2011 which concludes that the LPSF method could be used as an alternative to the global safety method with conformance to the guidance and requirements given in Appendix A of the PNAP. The appendix has excluded the use of the method for walls entirely embedded in soft clay, contains modifications to some of the partial factors given in CIRIA Report No. C580, and requires sensitivity analysis for singly propped excavations etc.

CIRIA Report No. C580 was superseded by CIRIA Report No. C760 (Gaba et al., 2017) in which the contents were modified to be compatible with the relevant Eurocodes. Also its scope of application has been extended to cover soft clays and weak rocks. Contents on some aspects such as environmental protection, derivation of geotechnical parameters are enriched.

In December 2023, GEO published the GEO Publication No. 1/2023 titled "Deep Excavation Design and Construction" (GEO, 2023b) which is a revision to the Publication No. 1/90. The new publication serves to consolidate the experience gained and improvements made since 1990. Clearer and more comprehensive guidelines are given in the Publication. Some advanced design methods are discussed. In particular, the "Partial Factor Method" (Limit State Partial Factor Method) has been well incorporated into the Publication in its 6.4.2 with a full list of minimum partial factors consistent with the Geoguide 1 (2020 Version) (GEO, 2020) for the design of retaining wall. In addition, there is no longer a need to carry out sensitivity analysis and post-construction review, given the experience gained on using the LSPF method since 2005.

4.2 Water Pumping Test

Before commencing the Excavation and Lateral Support Works (ELS works) below groundwater table, pumping test is normally required to demonstrate the water tightness of the pile wall systems for deep excavation works and the surrounding implications due to dewatering works to ensure safety in construction works proceeding in dry conditions.

For large-sized construction sites with deep excavation, full-scale pumping tests are commonly adopted to study the performance of the pile wall systems and verify the test results if it tallies with the design groundwater drawdown. However, full-scale pumping tests require a long time to complete dewatering and may possibly induce adverse effect to the surroundings. Pumping test may induce a substantial differential piezometric pressure across the embedded wall, which could lead to undesirable settlement when the lateral shoring support has not been installed. Therefore, partial pumping test is often adopted to minimize the potential impacts to the surroundings during dewatering.

Figure 4-1 shows a residential development site at Tuen Mun with an approximate site area of 44,000 sqm and an average excavation depth of 12 m. In view of the sizable construction site, several representative locations are chosen for carrying out pumping tests.

In some cases, partial pumping tests may be considered inadequate for deep excavation with highly sensitive structures at surroundings of the construction site since the uncertainties and the potential risks inducing to the highly sensitive structures can be ascertained to the minimal through implementation of full-scale pumping tests.

A construction site with office development located at Central is having the same site constraints that the highly sensitive structures (i.e. MTR tunnels for Island Line and Tsuen Wan Line) are located only 3 m (minimum allowable for MTR structures) besides the deep excavation works with approximate depth of 25 m (See Figure 4-2).

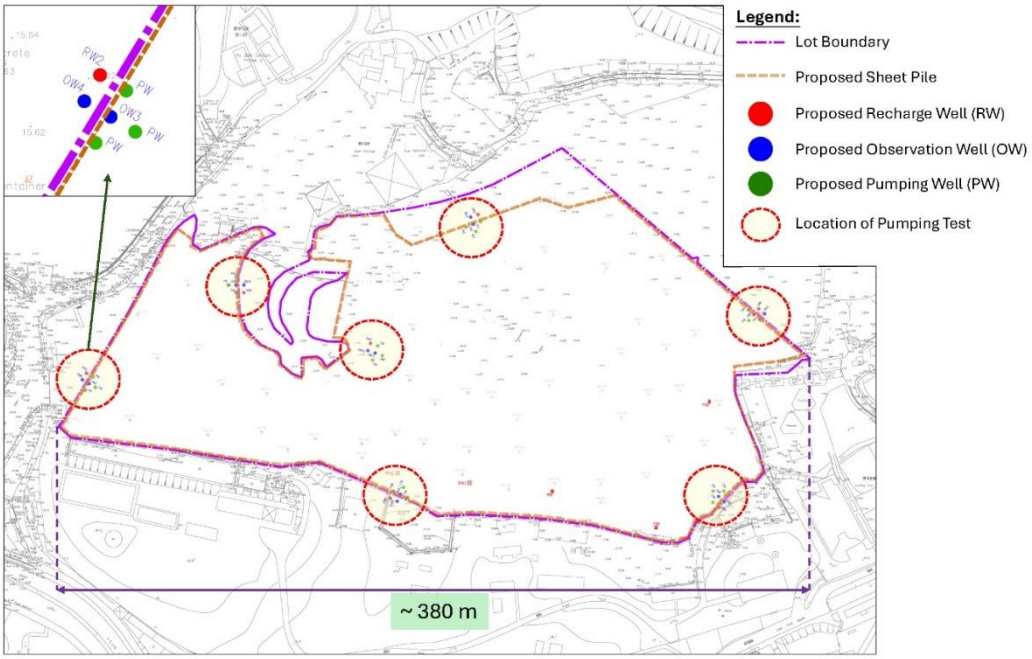


Figure 4-1: Layout Plan of Partial Pumping Tests at Construction Site in Tuen Mun Town

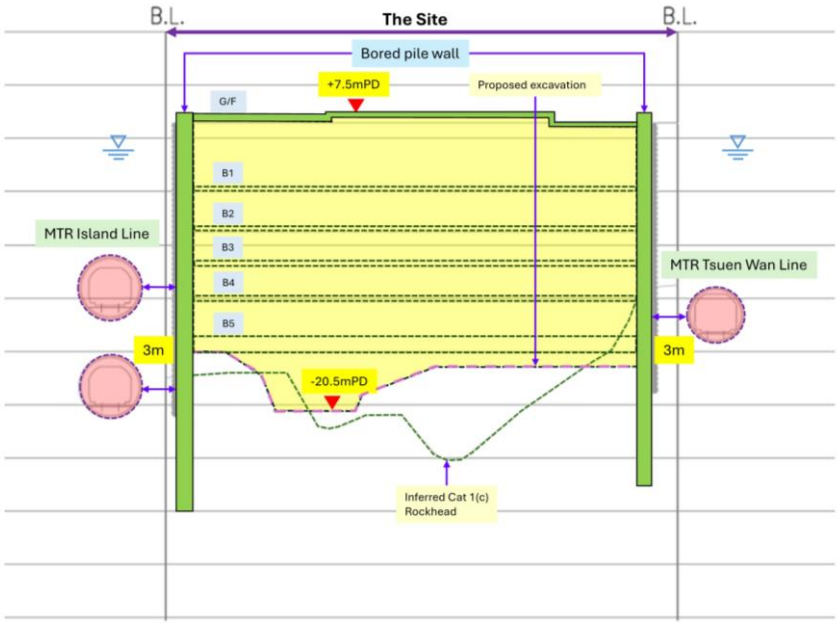


Figure 4-2: Section of Deep Excavation Works at Murray Road Site, Central

To verify the water tightness of the pile wall systems, as well as the implications to the surrounding structures, carrying out full-scale pumping tests in one go, in which the pumps shall be installed below the design excavation level for dewatering, would be the most direct approach for this case. However, the potential impacts to the MTR tunnels are unpredictable, and any excessive groundwater drawdown due to dewatering may induce uncontrollable ground settlement, significant stress changes and causing irrecoverable damages to the sensitive tunnel structures.

Having considered the sequence of work (top-down construction), tightness of the works programme and the safety concerns associated with nearby tunnels, the pumping tests for the development site at Central are divided into three stages. This approach aims to effectively control potential impacts resulting from dewatering but without hindering the progress of excavation works. The figures below illustrate the steps of staged pumping tests at different ELS stages.

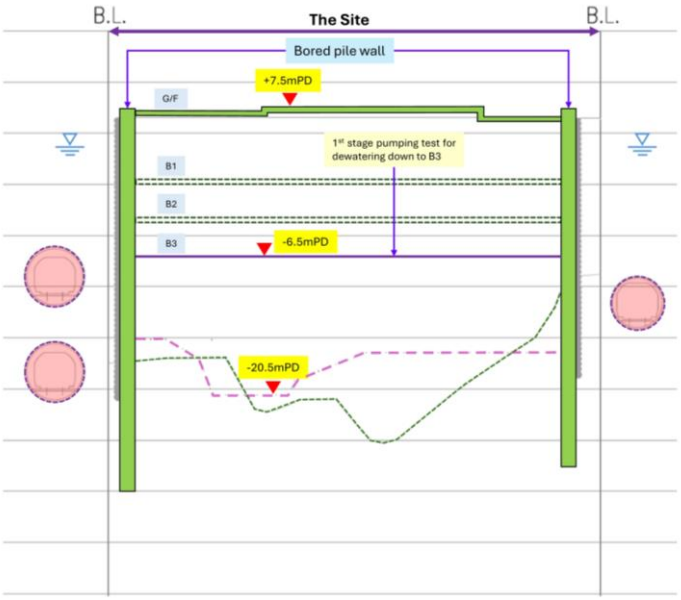


Figure 4-3: 1st Stage Full-scale Pumping Tests

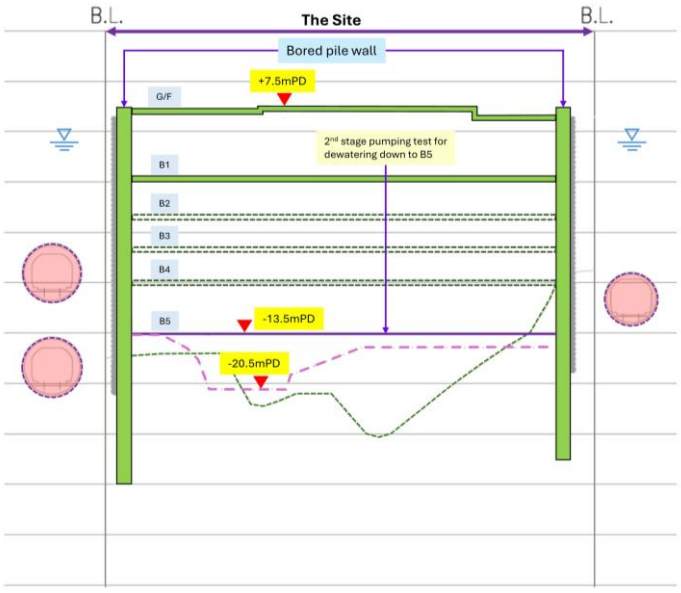


Figure 4-4: 2nd Stage Full-scale Pumping Tests

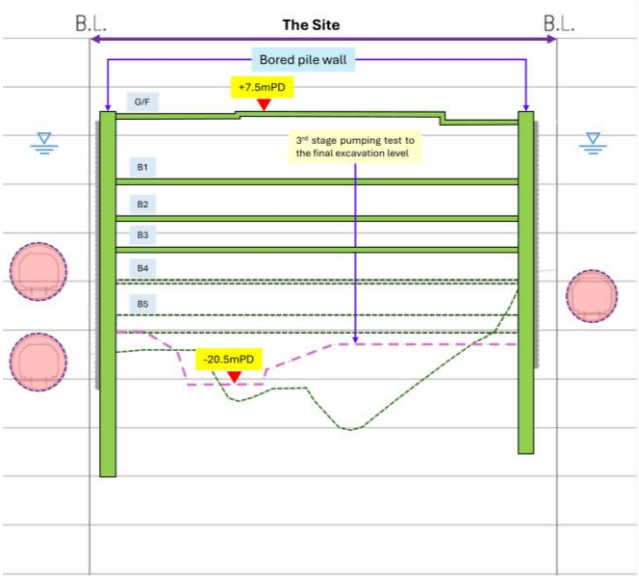


Figure 4-5: 3rd Stage Full-scale Pumping Tests

4.3 Excavation under Support by Tied-Back Wall

Comparing with the conventional excavation involving shoring and strutting, a retaining wall which is anchored or tied back into the unexcavated ground by rock anchors or soil nails is often a better solution as it provides construction space free of strutting, which is obviously a major benefit for the construction work. It is often a more economical option as large quantities of steel shoring and strutting can be avoided. However, as installation of the anchors beyond the site boundary is required, it often involves land matters which may be difficult to resolve. Therefore, tie back pile wall is much less commonly adopted in Hong Kong than other parts of China or other western countries.

In Hong Kong, the tied back forces of tie-back wall can be provided by soil nails or prestressed anchors which are either rods or strands of high strength steel. An anchor normally comprises a "grouted" length at its end penetrated into bedrock which derives the anchoring force and a "free" length between the bedrock and the wall. However, these anchors are seldom used as permanent supports to the retaining wall which would otherwise require long term monitoring if they are under prestress in accordance with Geospec 1 (GCO, 1989). Normally support to the excavation will finally be taken up by the permanent structure and the anchors are de-stressed and removed. The removal is to avoid obstructions to the future construction work below the adjacent grounds.

The followings are examples of development projects in Hong Kong involving deep excavation with tied-back wall system.

4.3.1 A Residential Development Site at Tsing Yi

The site is located at the foothill of a natural hillside consisting of granitic geology. The development comprises 2 residential towers of 30 storeys high on 2 levels of common podium and one level of basement. The bedrock level is high and the structure can be supported by footings directly founded on bedrock. Vertical excavation of about 23m in depth was required for the construction of the foundation and the podium structure. Behind the excavation is the natural slope which remains about 150m in height after the toe was removed for development.

The excavation was supported by pipe pile walls with prestressed rock anchor during the construction stage. A typical section showing the excavation are shown in Figure 4-6. A photo showing the completed anchor system is shown in Plate 4-1. In the permanent stage, the vertical excavation is supported by the lateral soil loads together with the wind loads are the reinforced concrete podium wall and basement wall. The enormous soil loads together with the wind loads are finally transferred through the podium and basement structures to

the footing and resisted by the friction between the footing and granitic bedrock. Sufficient friction is made possible by the weight of the heavy superstructure.

For the 30 storeys towers, it had been shown that when the superstructure reached 26 storeys, the self-weight of the partially completed building was great enough to mobilize sufficient friction to counteract the earth loads. Therefore the prestressed anchors were destressed and removed after the completion of 26 storeys.

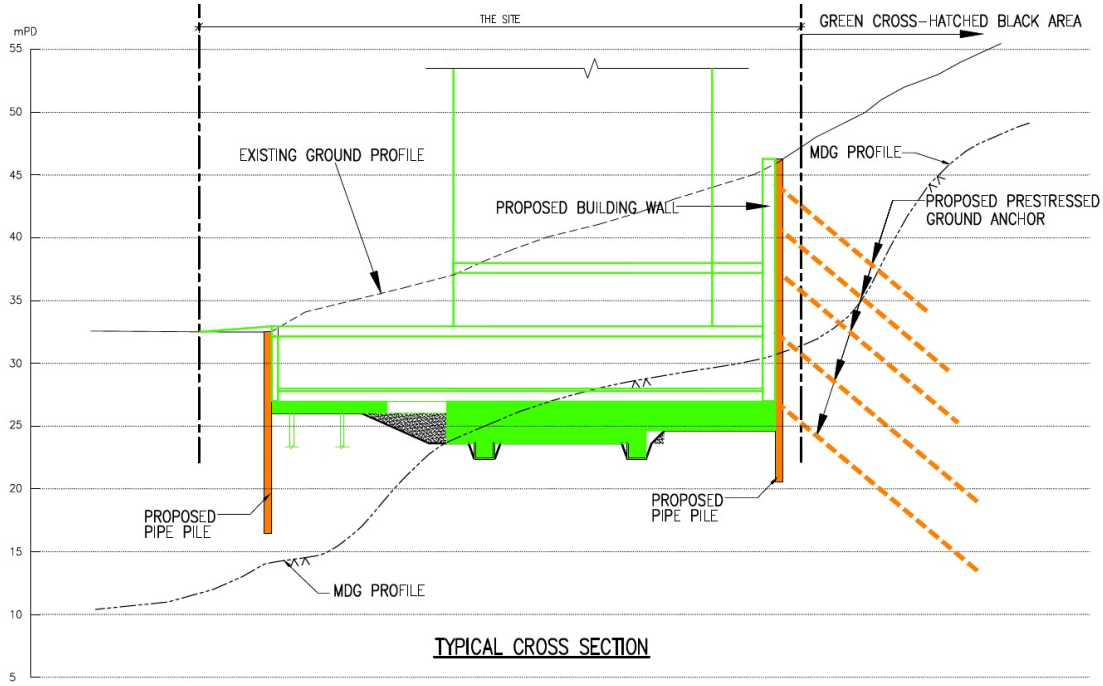


Figure 4-6: A Typical Cross Section of Tie Back Excavation of a Site in Tsing Yi



Plate 4-1: Photo Showing Completed Tie Back System in a Site in Tsing Yi

4.3.2 A residential development at Tai Wo Ping

The development site is at the foothill of Beacon Hill. It occupies an area of about 600000 sq. m. The site is entered via a cul de sac at the south and rise by 60m over a length of 250m to the northern lot boundary, the whole site being on hilly terrain. The development comprises 6 nos. of 23-storey buildings at the south and 26 nos. of houses of 3 to 4 storeys high at the north. Vertical excavation depth of 25m to 30m has to be carried out

along the northern boundary of the site. This cutting was temporarily supported by a bored pile wall comprising 3m to 3.5m diameter bored piles with tie backs in the form of prestressed ground anchors anchored from bedrock. A typical cross section across the bored pile wall, and a photo showing the completed bored pile wall are shown in Figure 4-7 and Plate 4-2 respectively.

In the long term, the 25-30m retained height of the anchored bored pile wall is reduced to 15m tall free cantilever wall. The reduction is made possible by casting a purposely 10m thick concrete block (as part of the pile cap) against the lower part of the pile wall, as shown in Figure 4-7. Upon completion of the bored pile foundations and pile caps, the prestressed rock anchors were destressed and removed. The development project was recently completed.

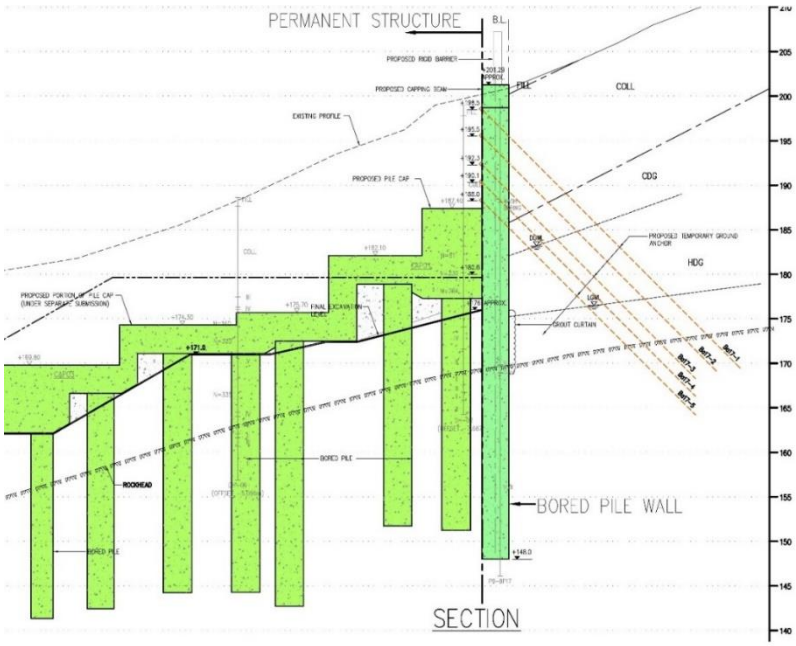


Figure 4-7: Typical Cross Section at the North Boundary of Residential Development in Tai Wo Ping



Plate 4-2: Photo Showing Completed Anchored Bored Pile Wall of Residential Development in Tai Wo Ping

4.3.3 A residential redevelopment at Deep Water Bay

The site is fronting onto the upper section of Deep Water Bay Road. It was occupied at the front portion by a single family house and at the rear portion by a series of stacking retaining walls and a cut slope before the redevelopment. The redevelopment comprises two houses and needs cutting into the rear slope to provide more level area. Thus, a vertical excavation of about 17m in height is required.

The proposed building plan layout leaves a space between the vertical cut and rear boundary. The granitic bedrock is also high at this site. Making use of these beneficial factors, a row of temporary soldier pile wall tied back by T40 rebars with anchorage from rock is constructed. A section is shown in Figure 4-8, together with a photo showing the completed tie back wall in Plate 4-3.

Footing foundations on bedrock are constructed to support the superstructure. A vertical cantilever reinforced concrete wall, which is supported by the footing is also cast against the soldier pile wall to replace its lateral load resistance in the long term. This scheme has resulted in significant saving in both time and cost as compared with the conventional shoring scheme.

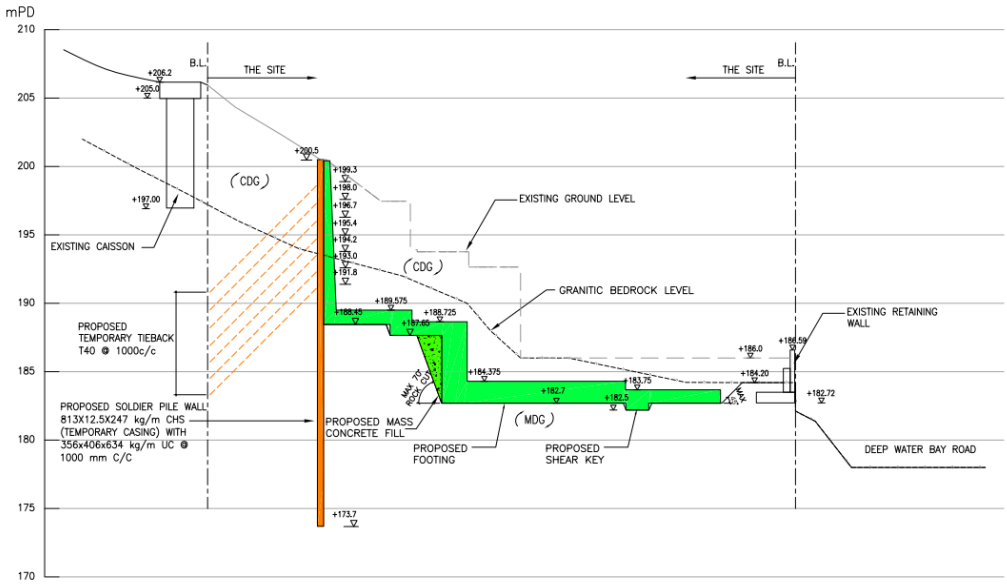


Figure 4-8: Typical Cross Section at the North Boundary of Residential Development at Deep Water Bay



Plate 4-3: Photo Showing Completed Anchored Soldier Pile Wall (with Tie Back) in Residential Development at Deep Water Bay

4.3.4 A residential development at Stanley

A Grade I Historic Building is situated on a platform at the top of the site and needs to be preserved. The platform is supported by fill slopes around it. The development comprises a series of low rise buildings on the fill slopes. In order not to obstruct the heritage building, the top of the proposed buildings around it cannot be higher than its lowest floor level. As such, excavation needs to be carried out deeply into the existing slopes, to result in a vertical cutting about 20m in height. Figure 4-9 shows a typical section showing the existing topography, site geology and proposed formation level.

To support the 20m vertical cut, a row of soldier piles tied back by prestressed ground anchors was proposed. Since the anchors need to be removed before completion of the development, a cantilever reinforced concrete retaining wall supported by the raft footing foundation was proposed to form an integrated structure with the soldier pile. Such integration serves two purposes. Firstly, the bending action to be caused by the enormous soil loads would be resisted mainly by the reinforced concrete cantilever wall, which in turn is supported by a raft footing. Secondly, the sliding resistance to the soil loads would be provided by the shear capacity of the solider pile wall. Figure 4-11 shows the proposed arrangement.

The issue with tie back walls was that the tie back, whether soil nails with sustainable loads or prestressed ground anchors, need to be monitored during its lifetime. This requirement was waived in 2023 through the revision of Geoguide 7 (GEO, 2023c). Monitoring is now only required during the construction period. Given this relaxation, a revised scheme is devised. This scheme comprises a row of 800mm diameter bored piles with tie back of 4T50 nails. This tied back wall will also act as permanent structure to retain the vertical cut. This will release the building foundation of the burden to resist the soil loads, resulting in a much lighter foundation. The heavy reinforced concrete cantilever wall in the original scheme is also not required. This revised scheme has resulted in significant saving in both time and cost as compared with the original scheme.

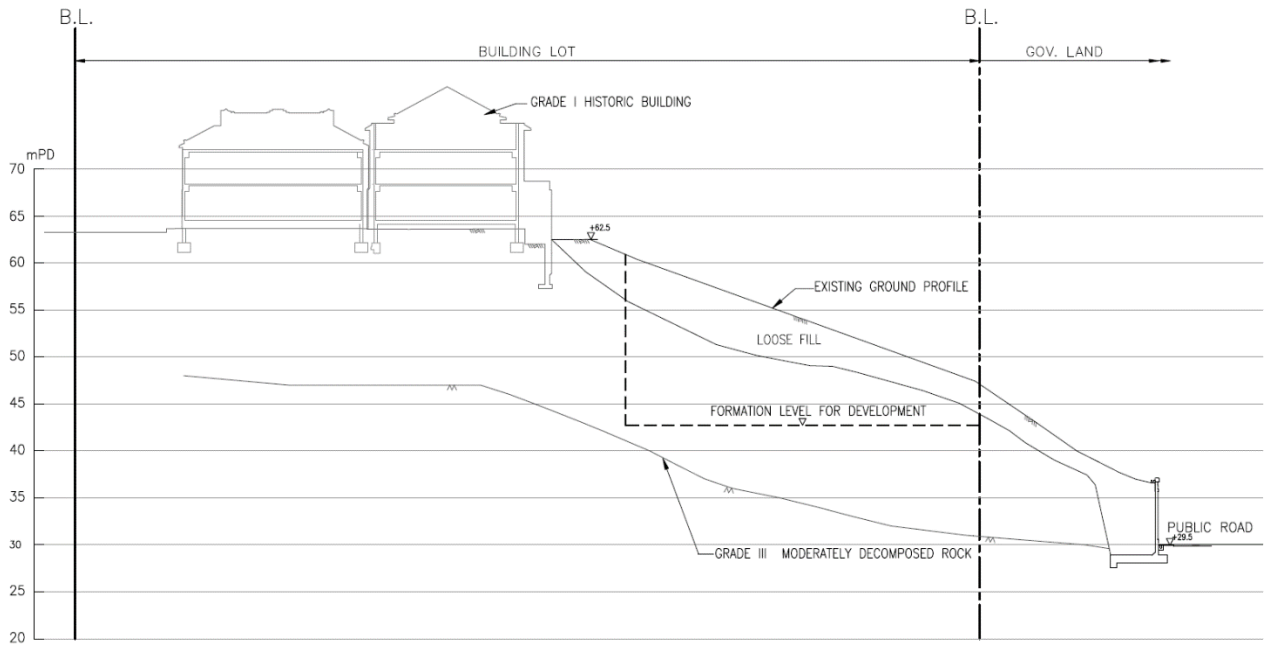


Figure 4-9: Geological Profile of Grade I Heritage Building and the Development in Stanley

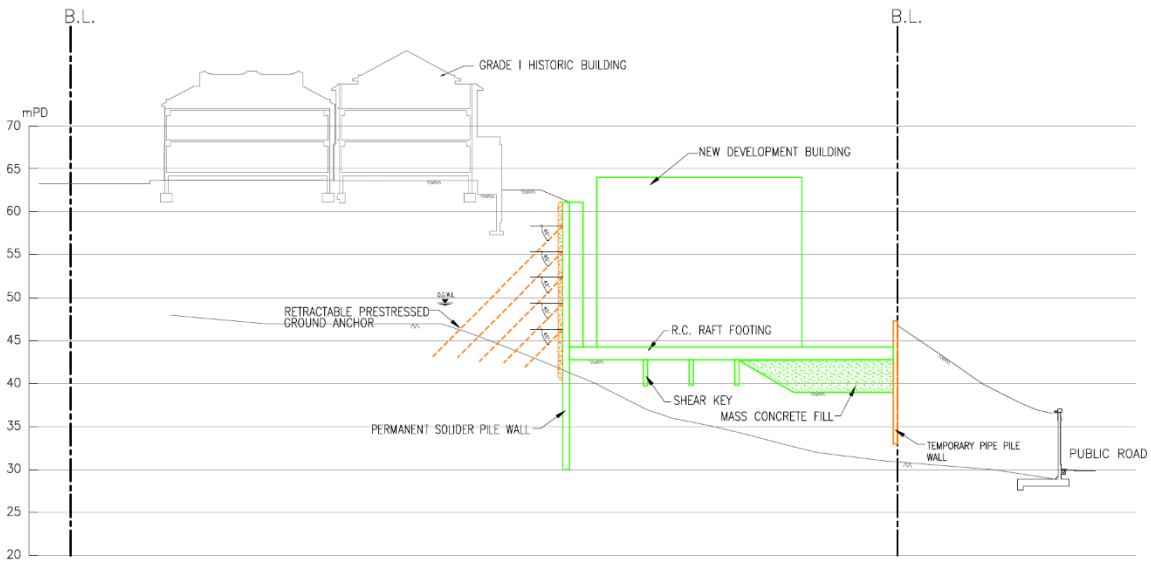


Figure 4-10: Grade I Heritage Building and the Development in Stanley - Scheme I Excavation Support

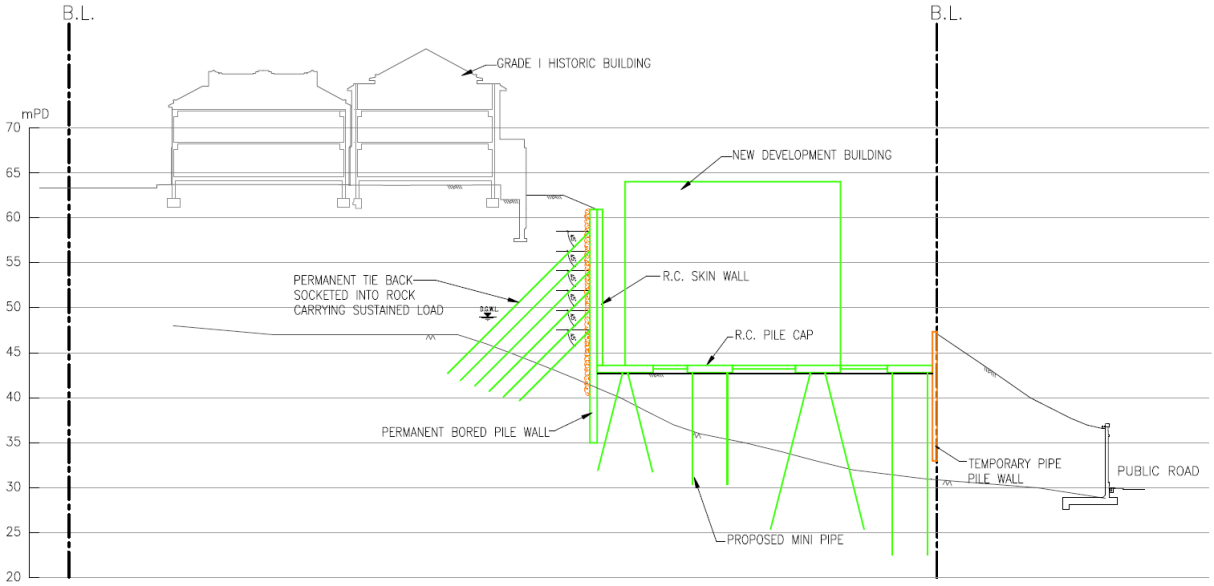


Figure 4-11: Revised Scheme II Support by Soil Nailing

4.4 Introduction of 5A Approach in ELS Works

Prior to the publication of GEO Publication No. 1/2023 (GEO, 2023b), the settlement limit for excavations was empirically set at 25 mm, irrespective of the excavation depth. This approach used a three-tier triggering control mechanism called Alert-Alarm-Action (AAA) Levels, referenced from PNAP APP-137 (BD, 2018), has been commonly adopted for ELS works to monitor if the works have adverse impacts to nearby facilities and pose hazards to the public. In general, the Alert and Alarm levels are set at 50% and 75% of the Action Level respectively, and the Action Level has been taken empirically as 25mm in typical ELS works in Hong Kong. However, the 25mm limit proved impractical for deep excavations in some cases, leading to unreasonable shoring designs, making ELS works impractical, prolong construction duration and sometimes dangerous for workers.

Response actions at Alert and Alarm Levels suffer from generality, reliance on the project team and contractor, and variability in promptness, adequacy, and significance. This lack of control undermines the purpose of providing advance warning. Stakeholders are often not promptly notified or consulted until the Action Level is reached, leading to unnecessary delays. Conversely, response actions at the Action Level can be overly broad, suspending all works, including essential works to maintain the stability of ELS works. The process of obtaining consent for remedial works after suspension further exacerbates delays. Furthermore, the absence of provisions for revising trigger values creates uncertainty after work resumes.

Since 2018, numerous ELS works projects in both the public and private sectors have encountered the "stop works" action limit. Once this limit is reached, all construction activities are suspended. Subsequent delays occur as time is needed to review the design based on the latest information about site conditions. This creates a snowball effect, as the resumption of construction activities depends on bringing the ground settlement situation under control. In certain projects, the process of resuming work and revising the trigger limit can span several hundred days. These delays have significant impacts on the economy and society, with the public inevitably facing the consequences of postponed construction activities.

The AAA limit is established to monitor the impact of ELS works on the surrounding ground and structures. Exceeding the AAA trigger values, predominantly due to ground settlement, can significantly affect roads and services. To effectively address these issues, specific response actions like repaving cracked road pavements, repairing damaged subgrade, and reinstating deformed pipelines can be easily implemented with prior agreements from stakeholders and authorities. Additionally, specific ground investigations using GCO probes and GPR surveys can be employed at different levels of ground settlement. This comprehensive approach not only addresses serviceability concerns for sensitive receivers but also considers stability requirements for ELS works, streamlining procedures, and improving the control mechanism's effectiveness and efficiency.

GEO (2023b) introduced an alternative 5A control mechanism (five-tier system by subdividing the third-tier response actions into three levels i.e. Alert-Alarm-Action Levels 1-3), to enhance the response actions according to the actual site conditions and increase the awareness of ground settlement monitoring by the stakeholders at different levels.

Table 9.1 of GEO Publication No.1/2023 provides recommended empirical limits for setting trigger values in the 5A approach. The Alert and Alarm levels are generally similar to the 3A approach. However, the Action levels are divided into three categories: Action Level 1, Action Level 2, and Action Level 3. For instance, the ground settlement limit for Action Level 1 is set at 20mm, Level 2 is defined as 0.3%He (limited to 60mm), and Level 3 is established at 0.5%He (limited to 100mm). This means that for a 20m deep excavation, the stop work action Level 3 is set at 100mm in the 5A approach, instead of the 25mm limit in the 3A approach. These revised limits are more reasonable and avoid the need for impracticably closely spaced strut arrangements.

By implementing the 5A approach, the control mechanism considers the actual site conditions and provides more appropriate trigger values. This approach ensures that response actions are tailored to the specific circumstances and allows for a more effective monitoring of ground settlement.

It is important to emphasize that the 5A approach is not simply to relax the "stop" works action limit, but to deal with ground settlement in a more rational way. At Action Level 1, the focus is primarily on addressing serviceability concerns related to road pavement and utilities. This entails carrying out necessary repair works to rectify and repave the pavement, as well as reinstating any deformed pipelines. Prior agreements with utilities undertakers and authorities are sought to ensure proper coordination and approval for these repair activities. Additionally, utilities undertakers and authorities will be notified and consulted if there is a need for repairs or continuous monitoring of the situation. This collaborative approach ensures that the necessary actions are taken to maintain the serviceability and integrity of road pavement and utilities in the face of ground settlement.

Upon reaching Action Level 2 (i.e. 0.3%He), additional investigations such as GPR surveys, CCTV inspections, and probing tests should be conducted to identify subgrade and service issues. The design should be evaluated to determine if cumulative settlement in subsequent excavation stages could exceed the estimated value and whether the performance of ELS remains acceptable.

When Action Level 3 is reached (i.e. 0.5%He), an Emergency Plan should be developed, which includes intermediate stage serviceability checks, a comprehensive investigation plan, and a Works Suspension Plan if necessary.

In comparison to the traditional 3A Approach, the adoption of the 5A Approach also emphasizes the importance of making engineering decisions based on the actual conditions of ELS works. Determining the action level by considering its correlation with the maximum excavation depth is a more practical approach than adopting the empirical value of 25mm as the Action Level. Moreover, the flexibility of the 5A Approach allows

for easier coordination of ELS works and remedial measures to address ground settlement concurrently with construction works, avoiding the need for complete works suspension at all times. The recommended empirical limits in the 5A Approach are summarized in Table 4-1:

Table 4-1 – Recommended Empirical Limits for Setting Trigger Values using 5A Approach in ELS Works, extracted and summarized from Table 9.1 of GEO (2023b)

		Criteria of				
Instrument	Criterion	Alert Level	Alarm Level	Action Level 1	Action Level 2	Action Level 3
Ground Settlement Monitoring Marker	Total settlement	10 mm (or 50% of Action Level 1)	15 mm (or 75% of Action Level 1)	20 mm (Shall be reviewed according to the actual site conditions and the corresponding requirements from the stakeholders)	$0.3\%H_e$ (Shall be bounded between 25 mm to 60 mm)	$0.5\%H_e$ (Shall be bounded between 30 mm to 100 mm)
Services monitoring marker	Angular distortion	1:600	1:500	1:400	1:350	1:300
Building monitoring marker	Angular distortion	1:1000	1:750	1:600	1:550	1:500
Note: H_e is the maximum excavation depth						

5 FOUNDATION WORKS

5.1 Historical Review

As rock is the strongest founding stratum for building structures, it has been a practice to determine its allowable bearing pressure as a statutory or codified value for safety and convenience in design. A historical review is first conducted on the statutory or codified provisions of the allowable bearing pressure of rock in Hong Kong.

5.1.1 Igneous Rock

The earliest stipulation of allowable bearing pressure of rock of Hong Kong is that in Building (Construction) Regulation (B(C)R) 1956 (Hong Kong Government, 1956). The B(C)R describes 3 types of rock in its Table VIII which are extracted as follows in Table 5-1.

The descriptions of the rock are too general. There would likely be ambiguity in assigning the type of rock to a founding rock stratum. It was not until 1975 that B(C)R 1975 (Hong Kong Government, 1975) classifies "rock (granite and volcanic)" into 4 types (a) to (d) with quantitative descriptions in terms of total core recovery (TCR) as extracted in Table 5-2.

Table 5-1 – Extract of Table VIII of B(C)R 1956 for Maximum Permissible Pressure on Rock under Foundations

Type of soil under foundation			Maximum permissible pressure
Rock	(a)	Hard, sound rock, massive	40T/sq.ft (4301kPa)
	(b)	Medium hard rock	25T/sq.ft (2688kPa)
	(c)	Soft rock	8T/sq.ft (860kPa)

Table 5-2 – Extract of Table IX of B(C)R 1975 for Safe Bearing Capacities of Rock under Foundations

Type of ground	Safe bearing capacity kPa
Rock (granite and volcanic)	
(a) massive crystalline rock in hard sound condition (core recovery greater than 85%)	5,000
(b) medium hard rock (core recovery greater than 50%)	3,000
(c) soft rock (core recovery of 50% and less)	1,000
(d) closely jointed and heavily shattered rock	To be assessed after inspection and testing

Under the heading "Rock (granite and volcanic)", the table applies only to granitic and volcanic rocks which are igneous rocks. The same table has been reproduced in B(C)R 1985 (Hong Kong Government, 1985).

The Buildings Department issued an AP/RSE Practice Note PNAP 141 in December 1990 and October 1995 which contained revisions in rock presumed bearing pressures as extracted in Table 5-3. An additional category of rock having presumed bearing pressure of 7,500kPa has been added. The requirements of rock to attain the presumed bearing values (pressure) are also more comprehensive by including rock grades and strengths as in addition to TCR.

The first Foundation Code of Hong Kong was promulgated in 2004 titled "Code of Practice for Foundations" (CoPF 2004) (BD, 2004). Comparing with PNAP141 for presumed bearing pressures of rock, one more category (1(a)) of igneous rocks (granite and volcanic) is added with the highest presumed allowable bearing pressure of 10,000kPa under more stringent requirements in rock grade, total core recovery and rock strengths. Details for rock are extracted in Table 5-4. For simplicity, only the new Category 1(a) of the CoPF 2004 is listed while the remaining grades 1(b), 1(c) and 1(d) are identical to 1(a), 1(b) and 1(c) of PNAP141 respectively.

In addition, CoPF2004 lists the presumed allowable bond or friction between rock and concrete for piles in its Table 2.2 reproduced in Table 5-5.

Table 5-3 – Extract of Appendix A of PNAP 141 for Rock

Category		Presumed Bearing Value, kPa
1.	Rock (granite and volcanic)	
	(a) Fresh to slightly decomposed strong rock of material weathering grade II or better, with a total core recovery of more than 95% of the grade and minimum uniaxial compressive strength of rock material (UCS) not less than 50MPa (equivalent point load index strength PLI_{50} not less than 2MPa).	7,500
	(b) Slightly to moderately decomposed moderately strong rock of material weathering grade III or better, with a total core recovery of more than 85% of the grade and minimum uniaxial compressive strength of rock material (UCS) not less than 25MPa (equivalent point load index strength PLI_{50} not less than 1MPa).	5,000
	(c) Moderately decomposed, moderately strong to moderately weak rock of material weathering grade III or IV or better, with a total core recovery of more than 50% of the grade.	3,000

Table 5-4 – Extract of Table 2.1 of the Code of Practice for Foundations (2004)

Category	Description of rock or soil	Presumed allowable Bearing Pressure (kPa)
1(a)	Rock (granite and volcanic) Fresh strong to very strong rock of material weathering grade I, with 100% total core recovery and no weathered joints, and minimum uniaxial compressive strength of rock material (UCS) not less than 75MPa (equivalent point load index strength PLI_{50} not less than 3MPa).	10,000

Table 5-5 – Extract of Table 2.2 of the Code of Practice for Foundations (2004)

Category of rock as defined in Table 2.1	*Presumed allowable bond or friction between rock and concrete or grout for piles (kPa)*	
	Under compression or transient tension	*Under permanent tension*
1(c) or better	700	350
1(d)	300	150

Wong (2014) summarized the development of the presumed rock bearing pressures used in the foregoing B(C)Rs, codes and PNAPs. The "Code of Practice for Foundations 2017" (CoPF 2017) promulgated in 2017 (BD, 2017) retains the same requirements for presumed allowable bearing pressures of the CoPF 2004 for igneous rock, except that fresh to slightly decomposed strong igneous rock is allowed when assessing the weathering grade of the Category 1(a) rock.

In 2023, the Geotechnical Engineering Office (GEO) issued GEO Technical Guidance Note No. 53 (TGN 53) to supersede the corresponding bearing pressure values in GEO Publication No. 1/2006. The presumed allowable bearing pressures of igneous rocks Categories 1(a), (b) and (c) in CoPF 2017 is increased to 12,500kPa, 10,000kPa and 7,500kPa respectively. In addition, the presumed allowable bond or friction with

rock for Categories 1(a) and 1(b) have also been increased to 1000kPa under compression or transient tension and 500kPa under permanent tension. The Guidance Note justifies the upgrading as follows:

"Over the years, instrumented pile loading tests have been carried out for piles founded on various rock formation, which included the comprehensive pile testing programme for Airport Railway, West Rail and the West Kowloon District Development and private development at Sai Sha. GEO has collected and analysed these pile test data for improving knowledge and practice in foundation engineering. The instrumented pile loading test results indicate that there are substantial safety margin of the proven bearing capacity and shaft friction when compared with the recommendations given in the publication. Hence, updated guidelines on the presumed allowable bearing capacity and bond friction on igneous rocks are derived."

5.1.2 Meta-sedimentary rock

Until the promulgation of CoPF 2017, the presumed allowable bearing pressure was applicable to igneous rock only. So before 2017 for sites with meta-sedimentary rock, the allowable bearing pressure need to be determined on a case by case basis. CoPF 2017 classifies meta-sedimentary rock as Category 2 rock with requirements extracted in Table 5-6:

Table 5-6 – Extract of Table 2.1 of the Code of Practice for Foundations 2017

Category	Description of rock or soil	Presumed Bearing Pressure, kPa
2	Meta-Sedimentary rock Moderately decomposed, moderately strong to moderately weak meta-sedimentary rock of material weathering grade III or better, and with not less than 85% TCR of the designated grade.	3,000

There are recent cases that allowable bearing pressures higher than 3000kPa are adopted, which will be elaborated in Section 5.2.1.

5.1.3 Marble

Marble is formerly limestone that has undergone metamorphosis under heat and pressure by which the rock becomes stronger by being denser and more compact. However, being reactive (though sparingly) with water containing carbon dioxide, marble is usually associated with a karstic upper surface with dissolution features. Large cavities with or without infilled material may also be present within the marble mass affecting foundation design and construction.

The discovery of extensive occurrence of marble rock in some locations of Hong Kong started from the piecemeal identifications of marble bedrock in Yuen Long, as pointed out by Houghton & Wong (1990) in which the special geological features of the district characterized by interbedded meta-sedimentary and marble rocks were described. In Houghton & Wong (1990), special site investigation requirements, construction of the geological site models, foundation design were discussed in detail, with reference to experiences gained from 5 number of sites in the district. With the contents and insights, Houghton & Wong (1990) highlights the appropriate approaches in foundation design and construction for sites with marble geology. Since 1990, the area in North-western New Territories underlain by karstic geology has been designated as Scheduled Area No. 2 and brought under special geotechnical control.

In 1994, GEO issued GEO Report No. 29, promulgating a system developed by Y C Chan for zoning and classification of marble sites. The system is primarily based on a parameter named "Marble Quality Designation" (MQD), which measures quality and extents of fractures of marble rock in individual drillholes. Upon determination of the range of MQD of a marble mass, the "marble class" of the rock mass can be assigned in accordance with a pre-established scale which ranks from "Very good" to "Very poor". So the system aims to facilitate interpretation of the possible degree and extent of dissolution zones, and assist in the assessment of the relative load-bearing characteristics. The applications of the system to 2 sites have been demonstrated in detail in GEO (1994b) and Chan et al. (1994).

The classification system was incorporated into the CoPF 2017. The Code further ranks suitability of the rock mass in acting as a bearing stratum in accordance with the "marble class" in the Notes under its Table 2.5.

Prescriptive allowable bearing pressures have not been assigned to marble in GEO Report 29 or CoPF 2017. GEO issued Technical Guidance Note No. 26 in 2022. It considers that the foundation properties of sound marble are similar to that of igneous rock and therefore assigns the presumed allowable bearing pressure of 7500kPa and 5000kPa, under the fulfilment of marble class, rock grade, TCR and rock strengths as identical to that of the igneous rocks. The Building Authority included these values of bearing pressure in August 2023 through amendments of CoPF 2017 and PNAP APP-18.

5.2 Case studies

5.2.1 Large Diameter Bored Piles on Meta-Sedimentary Rock at Kiu Tau Wai, Yuen Long

The bedrock of the site for founding of large diameter bored piles is meta-sedimentary rock, varying at 24m to 52m below ground. In accordance with CoPF 2017, the rock is designated as Category 2 and the presumed allowable bearing pressure is 3000kPa for rock of material weathering grade III or better, and with not less than 85% TCR of the designated grade. Rock strengths in terms of UCS and PLI_{50} do not form part of the criteria for attaining the presumed allowable bearing pressure of 3000kPa in accordance with CoPF 2017.

Nevertheless, UCS and PLI_{50} tests have been performed, giving results of 29.4MPa to 127.8MPa and 1.2MPa to 9.9MPa respectively. These rock strengths are higher than the threshold requirements of granite and volcanic rocks for attaining presumed allowable bearing pressure of 5000kPa, which are only 25MPa for UCS and 1MPa for PLI_{50} under Category 1(c) of the CoPF 2017. So, there should be good justification for increasing the presumed allowable bearing pressure from the codified value of 3000kPa to 5000kPa, so as to achieve economy in design.

Owing to the lack of test data on meta-sedimentary rock, it is considered prudent to include or enhance other criteria apart from strength tests for elevating the allowable bearing pressure to 5000kPa. The minimum TCR is raised from the normally adopted 85% to 90% to provide a higher level of confidence.

Another criterion is the introduction of Rock Mass Rating (RMR) approach. RMR is an integrated parameter for properties of a rock developed by Bieniawski (1973) and (1989). It is the sum of the rating of the rock for 5 aspects including rock core strength, rock quality designation, joint spacing, joint conditions and the presence of ground water which constitutes a comprehensive description of the quality of rock. High rating of RMR indicates strong rock generally. The GEO Publications No. 1/2006 (GEO, 2006) correlates RMR with allowable bearing capacity q_a in its Table 6.5 and Figure 6.8 extracted as follow. The recommended allowable bearing pressure is a conservative determination as compared with the existing test data. To achieve an allowable bearing pressure of 5000kPa, RMR of 50 is required. Therefore, the criterion of RMR ^{3} 50 is also included.

The following Table 5.7 summarizes the proposed criteria for determining allowable bearing capacity for the Kiu Tau Wai Site.

Table 5-7: Proposed Criteria for the Presumed Allowable Bearing Pressure of the Kiu Tau Wai Site

		Value	**CoPF 2017 Requirements**
Design Parameters	Allowable bearing Capacity	5000kPa	3000kPa
Acceptance Criteria	Uniaxial Compressive Strength (UCS) Or Point Load Index Strength (PLI_{50})	Min. 25MPa (UCS) Min. 1MPa (PLI_{50})	Nil
	Material Weathering Grade	Grade III or better	Grade III or better
	Total core recovery (TCR)	Min. 90%	85%
	Rock Mass Rating (RMR)	Not less than 50	Nil

Full scale load tests on 2 trial piles with full instrumentations were conducted, each under 3 times of its working load. Performances were satisfactory, showing that the ultimate bearing pressure was well in exceedance of 15000kPa. Based on the load test results, the actual factors of safety are greater than 3 for the allowable bearing pressure of 5000kPa.

Table 6.5 – Allowable Bearing Pressure Based on Computed RMR Value

Parameters	Rock Mass Rating (RMR)			
	< 40	**50**	**70**	**88**
Allowable bearing pressure, q_a (kPa)	3,000	5,000	10,000	14,500

Notes : (1) For RMR < 40, the rock mass should comprise at least 50% of moderately decomposed, moderately strong to moderately weak rocks. Refer to Table 2 of Geoguide 3 (GCO, 1988) for classification of the strength of rock materials. In common granitic and volcanic rocks in Hong Kong, this corresponds to a weathering grade better than IV.

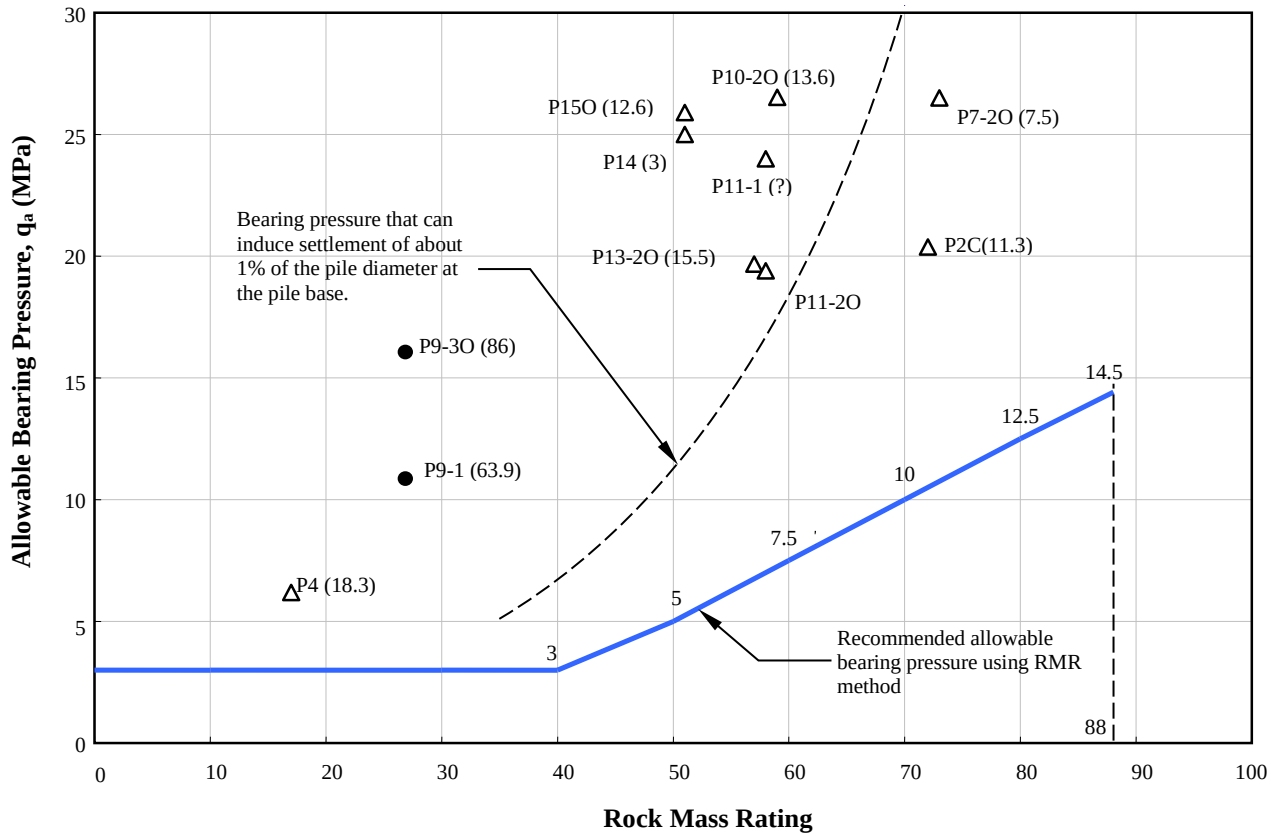
(2) The rock mass within the zone of influence of the foundation loads should be assessed when computing the RMR values. The minimum zone of influence should not be less than three times the diameter of the pile base.

(3) Interpolate between allowable bearing pressures for intermediate RMR values greater than 40.

(4) The ratings for individual parameters are given in Table 6.4.

(5) This table is applicable where the stability of the rock mass is not subject to the effect of adversely oriented discontinuities.

(6) If allowable bearing pressure, q_a, determined by RMR is greater than σ_c, use $q_a = \sigma_c$.



Legend :
- ● = End-bearing resistance substantially mobilised
-) = Degree of mobilisation of end-bearing resistance unknown (i.e. not fully mobilised)
- (64) = denotes the measured settlement at pile base in mm

Notes : (1) Refer to Appendix A for details of pile tests.
(2) Higher bearing pressure can be used when substantiated by pile loading tests.

Figure 6.8 – Allowable Bearing Pressure Based on RMR Value for a Jointed Rock Mass beneath Piles

Figure: 5-1: Extract of Table 6.5 and Figure 6.8 of GEO Publication No. 1/2006 (GEO, 2006)

5.2.2 Large Diameter Bored Piles on Sedimentary Rock at Pak Shek Kok

Large diameter bored piles were proposed for a site at Pak Shek Kok where sedimentary rock is at around 60m to 70m below ground. As CoPF 2017 has not included the presumed allowable bearing pressure for sedimentary rock, its value needs to be assessed.

As a start of the assessment, the criteria adopted for the Kiu Tau Wai site above were considered. Since sedimentary rock is generally weaker than meta-sedimentary rock, a smaller allowable bearing pressure of the same grade is anticipated. After careful consideration, for a minimum TCR of 90% and the same strength requirements for that of Category 1 (c) attaining an allowable bearing pressure of 5000kPa for granite and volcanic rock, an allowable bearing pressure of 3000 kPa was proposed. The RMR was lowered from 50 to 40 for 3000 kPa in accordance with Figure 6.8 of GEO Publication No 1/2006. An additional criterion by limiting the Fracture Index (FI) of rock to 16.6, which was based on site specific considerations, was also conservatively imposed. The proposed criteria are listed in Table 5-8 as follows:

Table 5-8: Proposed Criteria for Founding of Large Diameter Bored Piles in Pak Shek Kok Site

		Value
Design Parameters	Allowable bearing Capacity	3000kPa
Acceptance Criteria	Total core recovery (TCR)	Min. 90%
	Weighted-Average of Rock Mass Rating (RMR) from top of Inferred Engineering Rockhead to 5m below or three times the diameter of the pile base below the pile base whichever the deeper.	Not less than 40
	Fracture Index (FI) of Rock Materials below Inferred Engineering Rockhead of Grade III of better rock.	Not more than 16.6
	Uniaxial Compressive Strength (UCS) or Point Load Index Strength (PLI_{50}) within one time pile base diameter below the pile base	Not less than 25MPa (UCS), Not les s than 1MPa (PLI_{50})

5.2.3 Shaft Grouted Bored Pile at a Site at Caine Road, Mid-Levels

The bedrock level of the site at Caine Road, Mid Levels is from 80 to 100m below ground where end-bearing pile was not a practicable and economical foundation option. Shaft grouted bored pile was therefore proposed which derived its load bearing capacity mainly from the shaft friction with soil. A typical geological section is shown in Figure 5-2, indicating that the Site is overlaid in succession by fill, colluvium and CDG .

The soil friction on a plain pile shaft is low and the pile capacity with a constructible depth is too small to support the proposed 50-storey building. Therefore, shaft grouted technique was used to increase the pile shaft friction. Shaft grouting is carried out initially by cracking the concrete surface with high water pressure at the initial set of the concrete, and then followed by injecting cement grout into the surrounding soil. The permeation grout along the pile shaft will substantially increase the frictional capacity of the pile.

Shaft grouted bored piles had not been put into actual use in Hong Kong before this project. Several trial piles using the same technique were carried out under West Rail Project but had not been put into practical use (Ng, et al 2001). Shaft grouted barrette had been adopted for several other projects beforehand. Reference was therefore made to the data of those test piles to obtain the design parameters for the shaft grouted bored piles.

The proposed ultimate and allowable frictional coefficients for colluvium and CDG are listed in Table 5-9.

Two instrumented trial piles of 1.2m diameter were carried out in 2011 and the test results indicate that the above ultimate frictional values can be readily attained. (Wong, 2014)

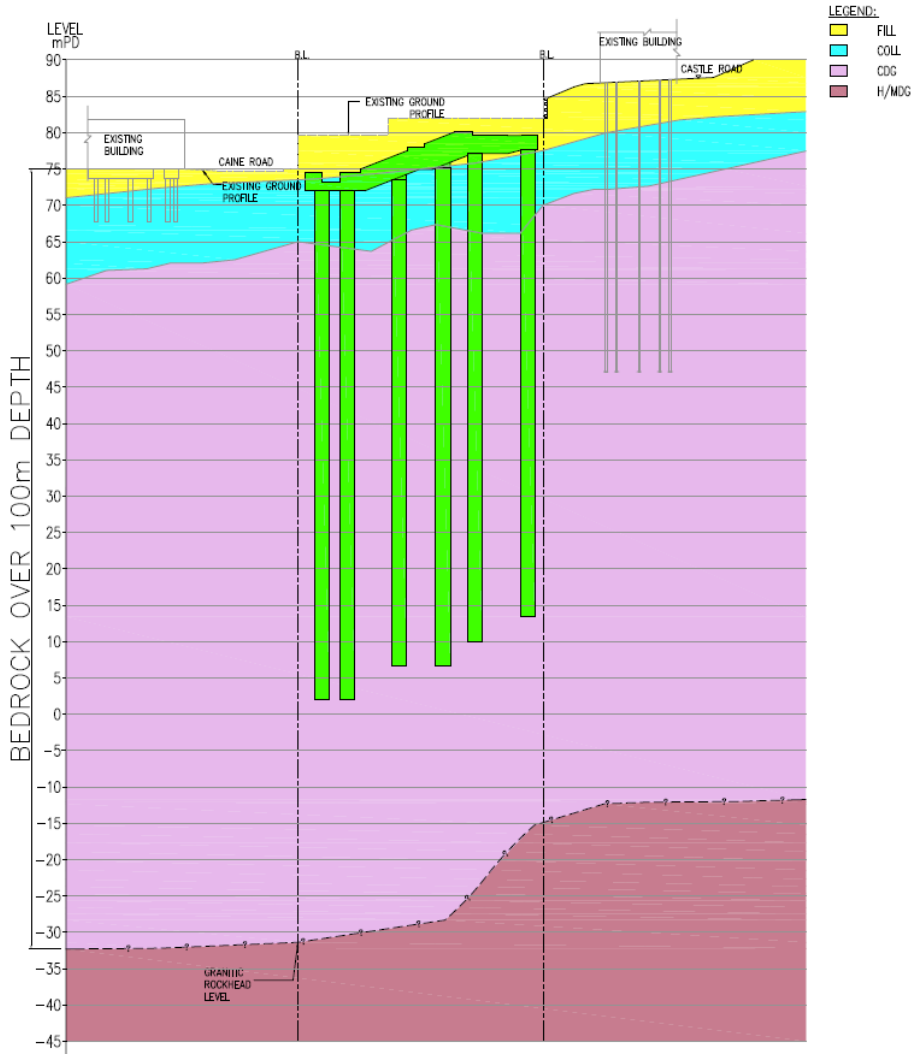


Figure 5-2: A Typical Geological Section through the Caine Road Project

Table 5-9: Proposed Parameters for Shaft Grouted Bored Piles at Caine Road Site

Soil Stratum	Allowable Friction (kPa)		Ultimate Friction (kPa)	
	Related to N	Capping Value	Related to N	Capping Value
Fill	0	0	0	0
Colluvium	1.8N	70	3.6N	140
CDG	1.2N	70	2.4N	140

5.2.4 Shaft Grouted Bored Piles at a site at Wellington Street

Shaft grouted bored piles was again proposed as a site at Wellington Street where the bedrock is more than 150m below ground.

With the test results obtained from the Caine Road site, a higher frictional values for CDG were proposed for this site. The ultimate friction increased from 2.4N to 4.5N with the maximum value also increased from 140kPa to 390kPa. Owing to the increase, the factor of safety was increased from 2 to 3. Two trial piles of 1.2m diameter were carried out to justify the proposed friction values. For one of the trial piles, soft toe was formed and it was intended to load test it to failure. The results show that even when the test load well exceeded 3 times the allowable working load and had reached the limit of the jacking machine, the trial pile was still behaving in a satisfactory manner. The proposed design parameters are summarized below in Table 5-10. If the design

parameters for the Caine Road site were adopted for the Wellington Street site, the pile length would have to be increased from 45m to 65m as indicated in Figure 5-4.

Table 5-10: Proposed Design Parameters for Shaft Grouted Bored Piles in Wellington Street Site

Soil Stratum	Allowable Friction (kPa)		Ultimate Friction (kPa)	
	Related to N	Capping Value	Related to N	Capping Value
Fill	0	0	0	0
CDG	1.5N	130	4.5N	390

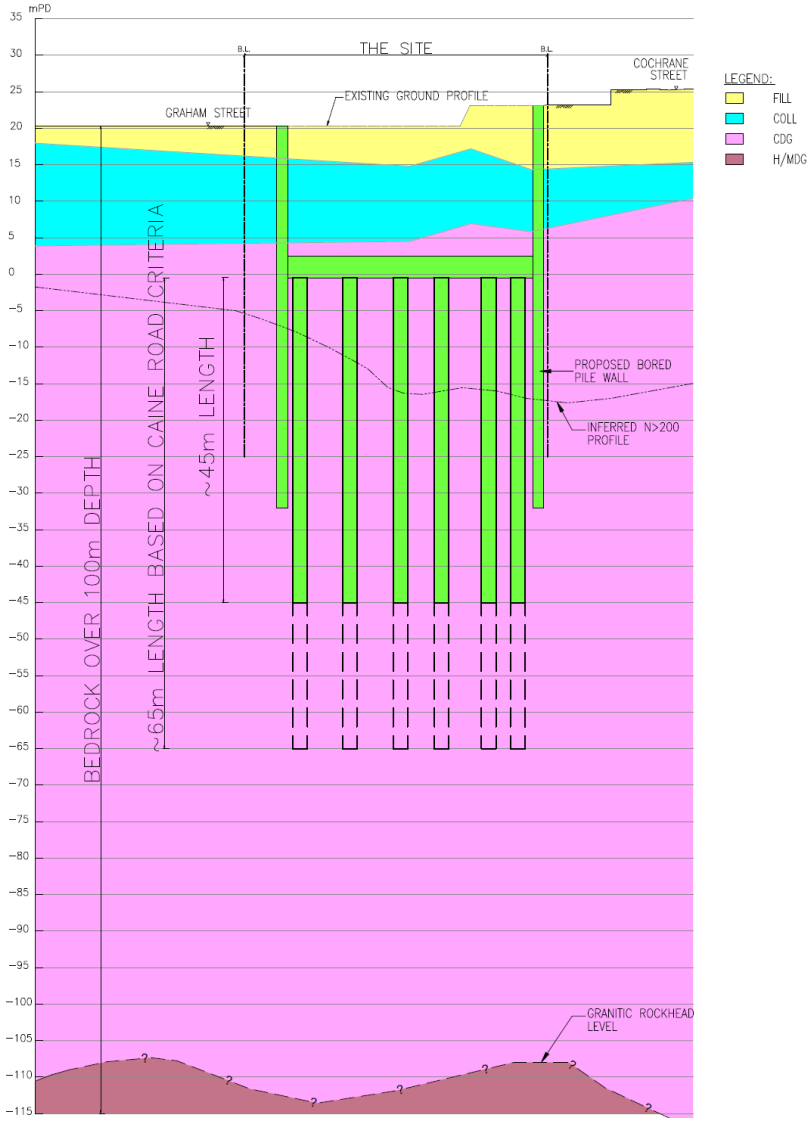


Figure 5-4: Shaft Grouted Bored Piles for Wellington Street Site

5.2.5 Shaft Grouted Pre-bored H-Piles at a Site at Staunton Street

Shaft grouted pre-bored H-pile was proposed for a small site at Staunton Street as the bedrock is more than 120m below ground. The shaft grouting technique was similar to that of bored pile. A typical geological section is shown in Figure 5-5.

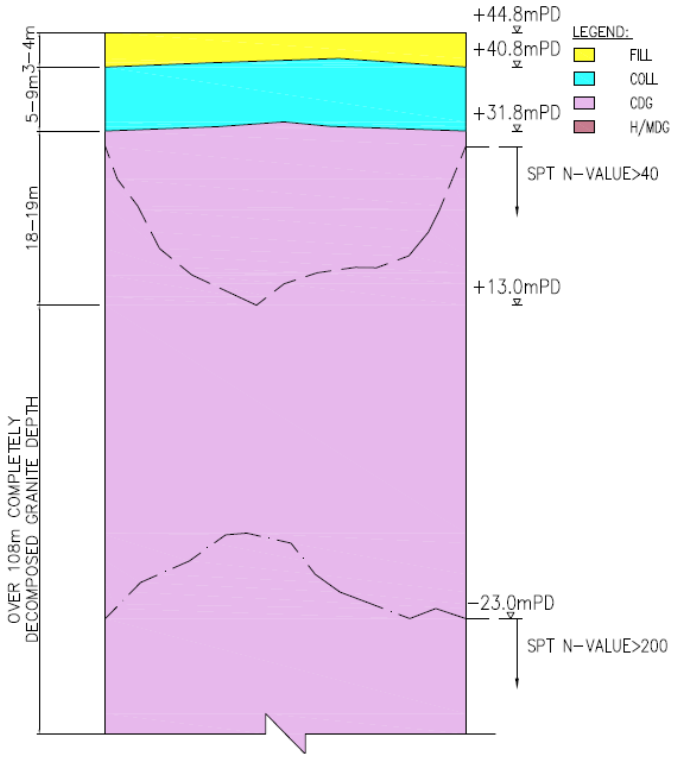


Figure5-5: Typical Geological Section for Site at Staunton Street

The piles comprise the installation of 305x305 x223Kg/m steel UBP embedded in cylindrical grout columns of 610mm diameter. They are similar to prebored H-piles socketed in rock except that the pile capacity is gained from the enhanced soil friction around the pile shaft.

In determining the friction values, reference was made to those for continuous flight auger pile (CFA pile), for which an allowable frictional coefficient of 1.6N kPa with N capped at 40 were adopted. CFA piles are constructed by a rotating a continuous flight hollow stem auger into the ground to the designed depth. Once the auger head reaches the pile toe level, concrete is pumped through the hollow stem to fill the drilled shaft to form the pile. This pile type was popular in Hong Kong in the 1970s and 1980s when the piling works were near very old buildings as the installation caused little vibration and disturbance. Wong & Tse (2001) has reported the use of CFA piles floating on karstic marble for a site at Yuen Long. The major drawback of CFA piles is when boulders are encountered, the auger has difficulties to go through. After down-the-hole ODEX drilling machine was available in 1980s, it has seldom been used in Hong Kong.

Two trial piles were installed and tested in 2013 to verify the design parameters. The working geotechnical pile capacity was taken as 6000kN and the test load was 3 times this value. The test results were satisfactory. The design parameters are listed in Table 5-11 below:

Table 5-11 – Proposed Design Parameters for Shaft Grouted Bored Piles in Staunton Street Site

Soil Stratum	Allowable Friction (kPa)		Ultimate Friction (kPa)	
	Related to N	Capping Value	Related to N	Capping Value
Fill	0	0	0	0
CDG	1.6N	64	4.8N	192

6 CONCLUDING REMARKS

Hong Kong is a densely populated city with limited land and is facing unique challenges with heavy development beside hilly terrain and with varying geology. Geotechnical engineers play an important role in overcoming these challenges effectively.

This paper has discussed progression of slope works, natural terrain hazard studies, excavation and lateral support works and deep foundations in Hong Kong. It is noted that the novel practices have been the results of

response to the site specific constraints and the initial solutions are normally on a conservative side to ensure safety. Examples are soil nails with sustainable loads, allowable bearing pressure for rock, friction values for shaft grouted piles, etc. As more experience and data are garnered, the initial parameters, which are normally on the conservative side, should be reviewed and updated, if the test data support such improvements. Such continuous evolution can facilitate the resilience and sustainability in the long run.

7 ACKNOWLEDGEMENT

This paper is published with the permission of the Head of the Geotechnical Engineering Office, Civil Engineering and Development, Government of the Hong Kong Special Administrative Region.

8 REFERENCES

Antiquities Advisory Board (AAB). (2016). Historic building appraisal building remains at Cochrane Street and Gutzlaff Street, Central, Hong Kong Island. Antiquities Advisory Board, Hong Kong Special Administrative Region Government.

Antiquities Advisory Board (AAB). (2024). Information on historic buildings. Antiquities Advisory Board, Hong Kong Special Administrative Region Government. Retrieved on 4 March 2024. [https://www.aab.gov.hk/en/historic-buildings/search-for-information-on-individual-buildings/index.html?kw=Cochrane%20Streetanddistrict=allanddm=allandpg=allandcg=allandyear=all]

Bieniawski, Z.T. (1973). Engineering classification of jointed rock masses. Trans S. Afr. Inst. Civ. Engrs 15, 335-344.

Bieniawski, Z.T. (1989). Engineering rock mass classifications. New York: Wiley.

Bowles, J.E. (1968). Foundation Analysis and Design 1st Edition New York McGraw-Hill.

British Standard Institution (2004). BSEN 1997-1:2004 Eurocode 7: Geotechnical design - Part 1: General rules.

British Standard Institution (2015). BS8004:2015 Code of Practice for Foundations.

Buildings Department (BD). (1995) Authorized Person/Registered Structural Engineer Practice Note PNAP141.

Buildings Department (BD). (2004) Code of Practice for Foundations. Buildings Department, Hong Kong Special Administrative Region Government.

Buildings Department (BD). (2012) PNAP APP-57 Requirement for an Excavation and Lateral Support Plan Building (Administration) Regulation 8(1)(bc). Buildings Department, Hong Kong Special Administrative Region Government.

Buildings Department (BD). (2017) Code of Practice for Foundations 2017. Buildings Department, Hong Kong Special Administrative Region Government.

Buildings Department (BD). (2018). PNAP APP-137 - Ground borne Vibrations and Ground Settlements Arising from Pile Driving and Similar Operations. Buildings Department, Hong Kong Special Administrative Region Government.

C M Wong and Associates Ltd. (CMA), Leung, K. Y. C. and Li, V. C. (2018). Special Study on the Use of Engineered Cementitious Composite (ECC) in Soil Nail Grouting. Geotechnical Engineering Office (GEO), Civil Engineering and Development Department, The Hong Kong Special Administrative Region Government, C M Wong and Associates Ltd., The University of Science and Technology. Unpublished.

C M Wong and Associates Ltd. (CMA), Li, V. C. and Leung, K. Y. C. (2019). Report on Development and Testing of ECC Grout for Soil Nail. Geotechnical Engineering Office (GEO), Civil Engineering and Development Department, The Hong Kong Special Administrative Region Government, C M Wong and Associates Ltd., The University of Science and Technology. Unpublished.

C M Wong and Associates Ltd. (CMA). (2020) Special Study on Adoption of Green Procurement for LPMit Works. Geotechnical Engineering Office (GEO), Civil Engineering and Development Department, The Hong Kong Special Administrative Region Government.

C M Wong and Associates Ltd. (CMA). (2023) Site trial of using GFRP reinforcing bars for soil nails - site trial proposal. Geotechnical Engineering Office (GEO), Civil Engineering and Development Department, The Hong Kong Special Administrative Region Government.

Chan, T.C.F. and Chan, D.C. (2008). A glimpse of the new technology applications in the landslip preventive measures programme. Proceedings of the HKIE Geotechnical Division 28th Annual Seminar. Geotechnical Division, The Hong Kong Institution of Engineers, Hong Kong, pp 73-81.

Chan, Y.C., Ho, K.K.S., Pun, W.K. (1994). A New Marble Rock Mass Classification System for the Interpretation of Karst Morphology in Hong Kong, HKIE Transactions Vol 1 No. 2 1994.

Cheung, R.W.M (2021). Landslide risk management in Hong Kong. Landslides, vol. 18, pp.3457-3473.

Cheung, W. M. and Lo, D. O. K. (2005). Use of carbon fibre reinforced polymer reinforcement in soil nailing works. Proceedings of the HKIE Geotechnical Division 25th Annual Seminar: Safe and Green Slopes. The Hong Kong Institution of Engineers, pp.175-184.

Civil Engineering and Development Department (CEDD). (2023) Landslip Prevention and Mitigation Programme (LPMitP). Civil Engineering and Development Department, Hong Kong Special Administrative Region Government. Retrieved on 19 April 2024. https://www.cedd.gov.hk/eng/our-projects/landslip/lpmitp/index.html

Concrete Canvas Ltd. (2022) Brochure of Concrete Canvas.

Davisson, M.T. (1972). High Capacity Piles. Proceedings. Lecture Series, Innovations in Foundation Construction, ASCE, Illinois Section, Chicago, March, 22 pp. 81-112.

Development Bureau (DEVB). (2021) The Landslip Preventive Measures (LPM) Programme in the Geotechnical Engineering Office, Civil Engineering Department. Development Bureau, Hong Kong Special Administrative Region Government. Retrieved on 4 March 2024. https://www.devb.gov.hk/filemanager/tc/content_429/lpm.pdf

Fyfe, J.A., Shaw, R., Campbell, S.D.G., Lai, K.W., Kirk, P.A. (2000). The Quaternary geology of Hong Kong. Geotechnical Engineering Office, Hong Kong Government, 2000.

Gaba, A.R., Hardy, S., Doughty, L., Powrie, W., Selemetas, C. (2017). CIRIA C760 Guidance on Embedded Retaining Walls - Construction Industry Research and Information Association.

Gaba, A.R., Simpson, B., Powrie, W., Beadman, D.R. (2003). CIRIA No. C580 Embedded Retaining Walls - Guidance for Economic Design, Construction Industry Research and Information Association.

Geotechnical Control Office (GCO). (1976) GEO Report No. 86 Report of the Independent Review Panel on Fill Slopes. First produced in 1976. First published in 1999. Geotechnical Engineering Office , Civil Engineering and Development Department, Hong Kong Special Administrative Region Government. 37pp.

Geotechnical Control Office (GCO). (1982) Geoguide 1 Guide to Retaining Wall Design. Geotechnical Engineering Office, Civil Engineering and Development Department, Hong Kong Special Administrative Region Government.

Geotechnical Control Office (GCO). (1990). GCO Publication No. 1/90, Review of Design Methods for Excavations. Geotechnical Engineering Office, Civil Engineering and Development Department, Hong Kong Special Administrative Region Government.

Geotechnical Engineering Office (GCO). (1989) Geospec 1 Model specification for prestressed ground anchors (second edition). Geotechnical Engineering Office , Civil Engineering and Development Department, Hong Kong Special Administrative Region Government. 165pp.

Geotechnical Engineering Office (GEO) and Hong Kong Institution of Engineers (HKIE). (2011) Design of soil nails for upgrading loose fill slopes.

Geotechnical Engineering Office (GEO) and Hong Kong Institution of Engineers (HKIE). (2013) Design illustrations on the use of soil nails to upgrade loose fill slopes.

Geotechnical Engineering Office (GEO). (1992) Geology of Yuen Long. 69pp.

Geotechnical Engineering Office (GEO). (1993) Geoguide 1 Guide to Retaining Wall Design (2nd Edition). Geotechnical Engineering Office, Civil Engineering and Development Department, Hong Kong Special Administrative Region Government.

Geotechnical Engineering Office (GEO). (1994a). GEO Report No. 29 Classification and Zoning of Marble Sites (originally produced in May 1989 as GCO Technical Note No. TN 4/89) Geotechnical Engineering Office, Civil Engineering and Development Department, Hong Kong Special Administrative Region Government.

Geotechnical Engineering Office (GEO). (1994b). GEO Report No. 32 Karst Morphology for Foundation Design. Geotechnical Engineering Office, Civil Engineering and Development Department, Hong Kong Special Administrative Region Government.

Geotechnical Engineering Office (GEO). (1998) GEO Report No. 58 Appraisal of Performance of Recompacted Loose Fill Slopes. Geotechnical Engineering Office , Civil Engineering and Development Department, Hong Kong Special Administrative Region Government. 87pp.
Geotechnical Engineering Office (GEO). (2003a) GEO Report No. 162. Methods other than recompaction for upgrading loose fill slopes. Geotechnical Engineering Office , Civil Engineering and Development Department, Hong Kong Special Administrative Region Government. 43pp.
Geotechnical Engineering Office (GEO). (2003b) GEO Report No. 138 (1st Edition) Guidelines for Natural Terrain Hazard Studies. Geotechnical Engineering Office, Civil Engineering and Development Department, Hong Kong Special Administrative Region Government.
Geotechnical Engineering Office (GEO). (2006) GEO Publication 1/2006. Geotechnical Engineering Office , Civil Engineering and Development Department, Hong Kong Special Administrative Region Government.
Geotechnical Engineering Office (GEO). (2008) Geoguide 7 The Guide to Soil Nail Design and Construction. Geotechnical Engineering Office , Civil Engineering and Development Department, Hong Kong Special Administrative Region Government. Special project report. Unpublished.
Geotechnical Engineering Office (GEO). (2013) Geotechnical Guidance Note No. 36 Guidelines on Enhanced Approach for Natural Terrain Hazard Studies under LPMitP. Geotechnical Engineering Office, Civil Engineering and Development Department, Hong Kong Special Administrative Region Government.
Geotechnical Engineering Office (GEO). (2016) GEO Report No. 138 (2nd Edition) Guidelines for Natural Terrain Hazard Studies. Geotechnical Engineering Office, Civil Engineering and Development Department, Hong Kong Special Administrative Region Government.
Geotechnical Engineering Office (GEO). (2020) Geoguide 1 Guide to Retaining Wall Design (2020 Version). Geotechnical Engineering Office, Civil Engineering and Development Department, Hong Kong Special Administrative Region Government.
Geotechnical Engineering Office (GEO). (2022) Geotechnical Guidance Note No. 26 Supplementary Guidelines for Foundation Design in Areas Underlain by Marble and Marble-bearing Rocks. Geotechnical Engineering Office, Civil Engineering and Development Department, Hong Kong Special Administrative Region Government.
Geotechnical Engineering Office (GEO). (2023a) Technical Note TN 1/2023 Pilot study on the use of self-compacting backfill material in slope and retaining wall works. Geotechnical Engineering Office, Civil Engineering and Development Department, Hong Kong Special Administrative Region Government.
Geotechnical Engineering Office (GEO). (2023b) GEO Publication No. 1/2023, Deep Excavation Design and Construction. Geotechnical Engineering Office, Civil Engineering and Development Department, Hong Kong Special Administrative Region Government.
Geotechnical Engineering Office (GEO). (2023c) Geoguide 7 The Guide to Soil Nail Design and Construction (2023 Version). Geotechnical Engineering Office , Civil Engineering and Development Department, Hong Kong Special Administrative Region Government. Special project report. Unpublished.
Geotechnical Engineering Office (GEO). (2023d) Technical Guidance Note No. 53 Supplementary Guidelines for Foundation Design and Construction. Geotechnical Engineering Office , Civil Engineering and Development Department, Hong Kong Special Administrative Region Government.
Geotechnical Engineering Office (GEO). (2024) Hong Kong Slope Safety Facts and Figures Past Notable Landslides. Geotechnical Engineering Office , Civil Engineering and Development Department, Hong Kong Special Administrative Region Government. Retrieved on 4 March 2024. https://hkss.cedd.gov.hk/hkss/en/facts-and-figures/past-notable-landslides/index.html
HKSAR Government Buildings Department (2005). Circulation Letter - Notes of Design of Excavation and Lateral Support Works Using CIRIA Report No. C580. (dated 6 January 2005).
HKSAR Government Buildings Department (2007) Circulation Letter - Design of Design of Excavation and Lateral Support Works by the Limit State Partial Factor Method Extension of the Trial Period (dated 18 January 2007).
Ho, K. K. S., Sun, H. W., Wong, A. C. W., Yam, C. F. and Lee, S. M. (2016) Enhancing slope safety preparedness for extreme rainfall and potential climate change impacts in Hong Kong. Slope safety preparedness for impact of climate change, ch. 4, pp 105-150. Taylor and Francis Group, CRC Press.
Hong Kong Government (1975). Building (Construction) Regulations 1975.
Hong Kong Government (1985). Building (Construction) Regulations 1985.

Hong Kong Government. (1956). Building (Construction) Regulations 1956.
Hong Kong Institution of Engineers (HKIE). (2003) Soil nails in loose fill a preliminary study.
Houghton, D. A. and Wong, C. M. (1990). Implications of the Karst Marble at Yuen Long for Foundation Investigation and Design, Hong Kong Engineer June 1990 pp19-27.
Ko, W. K. F. and Lo, L. C. F. (2018) From landslide susceptibility to landslide frequency: A territory-wide study in Hong Kong, Engineering Geology, Volume 242, Pages 12-22.
Lepech, M. D. and Li, V. C. (2009) Water permeability of engineered cementitious composites. Cement and Concrete Composites 31 (2009) 744-753.
Li, V. C. (2012) Can concrete be bendable? The notoriously brittle building material may yet stretch instead of breaking. American Scientist the magazine of Sigma Xi, The Scientific Research Society. Vol. 100(2013) 484-493.
Padfield, C.J. and Mair, R.J. (1984). CIRIA Report 104 Design of Retaining Walls Embedded in Stiff Clay.
Pappin, J., Free, M., Bird, J., Koo, R. (2004). Evaluation of site effects in a moderate seismicity region, Hong Kong.
PolyU Technology and Consultancy Co. Limited (PolyU). (2023) Study on using glass fibre-reinforced polymer reinforcement in soil nails for slope works - laboratory studies proposal.
Sewell, R.J., Campbell, S.D.G., Fletcher, C.J.N., Lai, K.W., Kirk, P.A. (2000). The Pre-Quaternary geology of Hong Kong. Geotechnical Engineering Office, Hong Kong Government, 2000.
Terzaghi, Karl and Peck, Ralph B. (1967). Soil Mechanics in Engineering Practice, Wiley.
United States (US) Government (1982). NAVFAC Design Manual 7.2 Foundations and Earth Structures.
Wong, C. M. (2014). Overview of Development and Challenges in Foundation Design and Construction in Hong Kong. The HKIE Geotechnical Division Annual Seminar 2014, pp27-52.
Wong, C. M., Lee, T. L. C. and Ting, R. C. M. (2011b). Innovative materials and drilling method adopted for soil nailing works at Po Shan Road. Proceedings of the HKIE Geotechnical Division 31th Annual Seminar. Geotechnical Division, The Hong Kong Institution of Engineers, Hong Kong.
Wong, C.M. and Tse, Y.P. (2001). Auger-injection Pile Floating above Karstic Marble, Proceedings of the Fourteenth Southeast Asian Geotechnical Conference, Hong Kong, pp 1067-1070.
Wong, C.M. and Yau, T.L.Y. (2005). Structural Aspects of Excavation and Lateral Support Works Using Ultimate Limit State Approach, Seminar on Excavation and Lateral Support Works on 18 June 2005 Proceedings jointly organized by Hong Kong Geotechnical Society, Hong Kong Institution of Engineers Geotechnical Divisions and City University of Hong Kong.

Seismic Hazard Analyses of Northern Metropolis and Kau Yi Chau Artificial Islands in Hong Kong

Zhengwei CHEN
WSP Asia Limited, Hong Kong
Gang WANG
Hong Kong University of Science and Technology, Hong Kong

ABSTRACT

Northern Metropolis and Lantau Tomorrow are two major projects to alleviate the acute shortage of land in Hong Kong. The Northern Metropolis is a planning area consisting of North District and Yuen Long District in northern New Territories to provide an integrated living and economic region, while the Lantau Tomorrow targets to create a third core business district by constructing artificial islands with a total area of around 1,000 hectares through land reclamation near Kau Yi Chau. Hong Kong is a densely populated city with a moderate level of earthquake risk; however, there is still a lack of seismic hazard study and yet no seismic design code.

In this study, seismic hazard assessment is conducted for Northern Metropolis and Kau Yi Chau Artificial Islands, based on Hong Kong uniform hazard spectrum for the 2% probability of exceedance in 50 years. For Tuen Mun and Yuen Long, 591 drilling boreholes are collected and interpreted to build the 3D regional geological model (20km × 20km); the physics-based simulation of wave propagation is performed to investigate the complicated effect of deep sedimentary layers and mountainous terrains. On the other hand, 104 boreholes around the Kau Yi Chau Artificial Islands are collected and interpreted, and 1D nonlinear site response analyses are conducted to evaluate the seismic hazard level before and after land reclamation.

1 INTRODUCTION

1.1 Northern Metropolis at Tuen Mun - Yuen Long

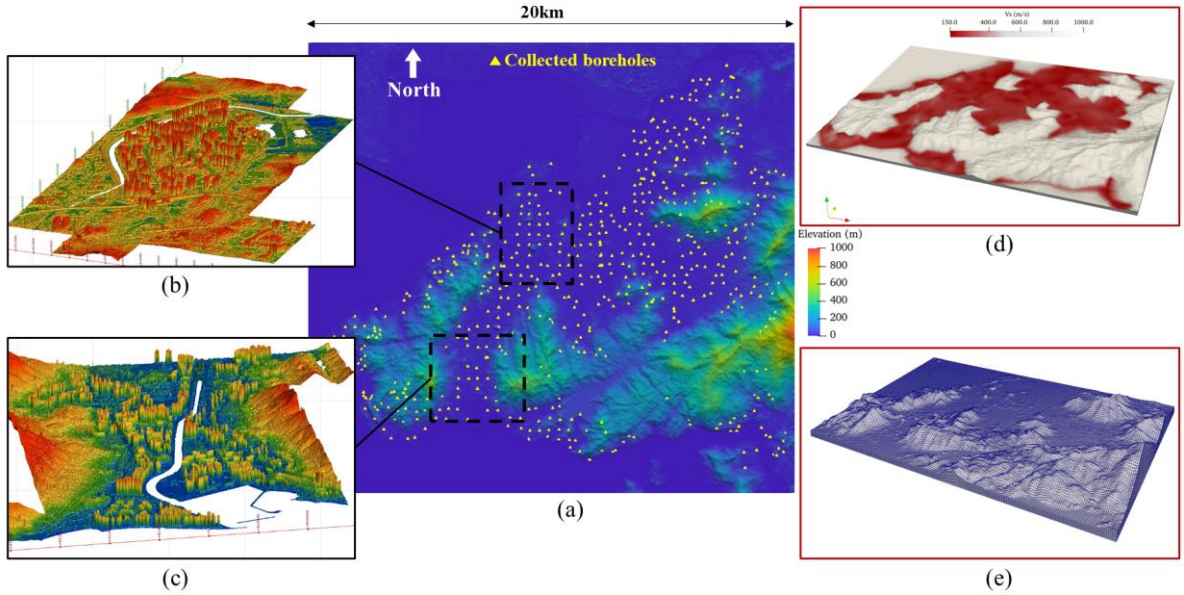


Figure 1. (a) Collected boreholes in the study region; (b) buildings located at Yuen Long; (c) buildings located at Tuen Mun valley around Tuen Mun river; (d) shear wave velocity distribution; (e) 3D physics-based model.

The Tuen Mun-Yuen Long in the North-West New Territories are mainly formed of late Jurassic to Cretaceous granitic and volcanic rocks surrounding Quaternary deposits (basin) (GEO, 2012). The Yuen Long formation in the north consists of siltstone and karstic marble with large sinkholes, while to the east of it is the Lok Ma Chau formation consisting of sandstone and siltstone. The Quaternary deposits on the top of the basin mainly consists of the alluvium around the Tuen Mun river.

The study region is 20km (north-south) × 20km (east-west), as shown in Figure 1(a). A total of 591 boreholes are collected in the study region, each of the selected borehole stations contains the underlaying strata as well as the standard penetration test (SPT) results. Figure 1(b)&(c) show the densely distributed buildings along the Tuen Mun river, at the Yuen Long and Tuen Mun districts respectively. The SPT-N values at each borehole are used to estimate the shear wave velocity V_S, based on the correlation between V_S and SPT-N provided in (GEO, 2012). The available V_S values are adopted to interpolate the 3D V_S distributions shown in Figure 1(d). Usually SPT-N smaller than 15 are estimated with a V_S less than 200 m/s, and SPT-N of 50 are assigned with a V_S of around 300 m/s, based on the empirical correlation. SPT-N=100 is regarded as the boundary between the grade IV and grade III rocks with V_S of 400 m/s. Fresh or slightly decomposed rocks are assigned a V_S of 1000 m/s for simplicity. Note that the compressional wave velocity $V_P = 2V_S$ is adopted for our simulation model. Figure 1(e) shows the constructed physics-based model using the spectral element method, which will be discussed in the following sections.

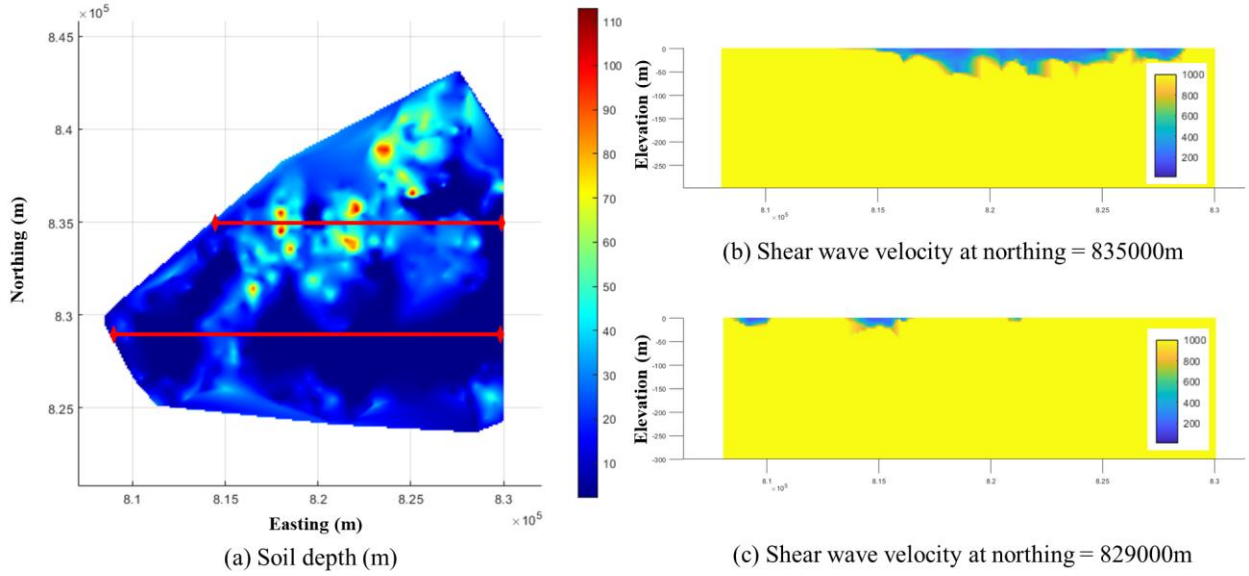


Figure 2. (a) soil depth distribution across the study region; Shear wave velocity distributions at two cross sections (b) northing = 835000 and (c) northing = 829000.

Figure 2 shows the detailed interpolation of soil structure within the study region. The soil depth distribution is depicted in Figure 2(a). At the Tuen Mun region, the two major mountain groups, Tsing Shan and Kau Keng Shan, have very shallow soil layers; the soil layer at the valley between them is approximately 20m, as shown in Figure 2(c). Yuen Long has a soil depth at around 30-50m, with a few sinkholes as deep as around 100m (Figure 2a&b). The complicated topography and soil distributions at the study region could significantly affect the ground motion responses during seismic activities. Mountains could amplify the ground motions due to the focusing effect of the convex terrains (Chen et al., 2023a, 2023b); on the other hand, the subsurface soils will further give rise to the ground seismic level due to the soil amplification (Huang et al., 2020).

1.2 Kau Yi Chau Artificial Islands in Central Waters

In June 2021, the Civil Engineering and Development Department (CEDD) and Planning Department of Hong Kong began a joint consultancy agreement to investigate artificial islands in the central waters. The study aims to conduct a detailed planning and engineering analysis for around 1,000 hectares of artificial islands near Kau Yi Chau (Figure 3a).

The three islands in our studied area are divided into three subzones based on the Island (I), the shore (II) and the sea (III) areas surrounding the three islands and a total of 104 boreholes have been collected from the ground investigation database archive at GEO as shown in Figure 3 (b). To perform 1D site response analysis, 30 representative boreholes (RBHs) have been chosen based on its locations, ground/seabed levels and BHs that have minimum values of SPT-N. The locations of these 30 representative boreholes are shown in Figure 3 (b) by big dots (the rest shown by small dots).

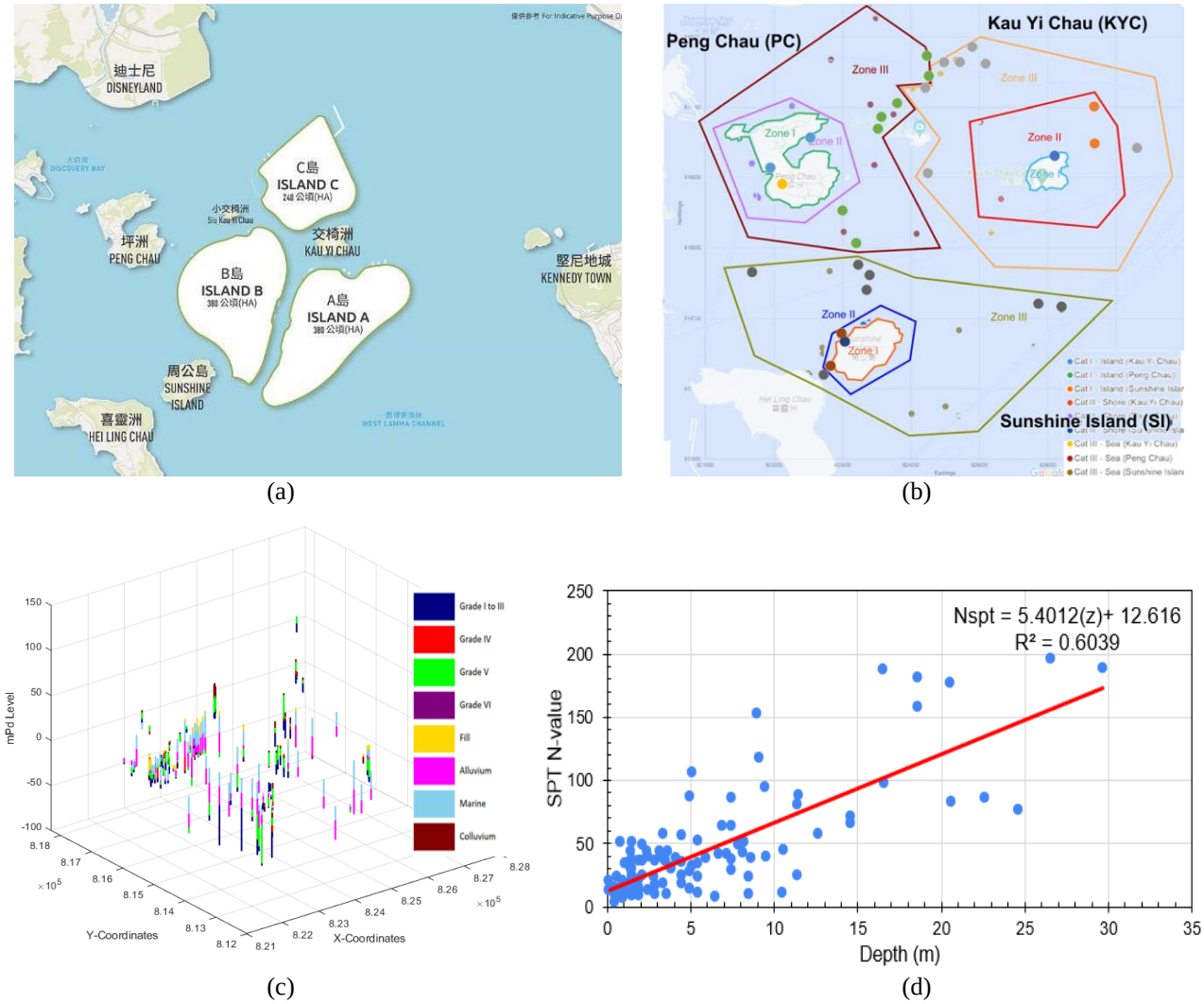


Figure 3. (a) Lantau Tomorrow reclamation scheme (CEDD); (b) zones classifications, all BHs and representative BHs (big dots) at the reclamation site; (c) 3D visualization of all collected boreholes; (d) SPT-N vs Depth.

The main geological formation, based on these boreholes, consists of volcanic rocks and rhyolites from grade I to grade VI, fills, alluvium, and marine deposit. The 3D visualization of all boreholes showing top, bottom levels and type of rock and soil is shown in Figure 3 (c). The number of blows, SPT-N, of the standard penetration test results have been collected for all the soil layers at different depth and a relation between the SPT-N and depth has been developed to depict the variation of shear-wave velocity with depth, as shown in Figure 3 (d). The relationship between SPT-N value and shear-wave velocity is used to construct the 1D nonlinear seismic model to calculate the ground response under seismic excitations. Both the Equivalent Linear (EQL) model via Strata software and the nonlinear (NL) model via DEEPSOIL, are used to evaluate the ground response and to study the soil nonlinear effect. Note that for zones in the sea (II and III in Figure 3b), ground responses before and after land reclamation (to +7 mPD) are both investigated.

1.3 Seismic input in the study region

Figure 4(a) shows the uniform hazard spectrum (UHS) at the rock outcrop of Hong Kong, based on the probabilistic seismic hazard analysis, for 2%, 10%, and 63% probabilities of exceedance in 50 years (GEO, 2018). In this study, seven sets of ground motions (14 recordings in total) have been selected and applied as rock-outcrop input motion and its mean spectral accelerations (of two horizontal components) are fitted with the UHS of 2% probability of exceedance, as shown in Figure 4(b). Figure 4 (c) shows an example of the selected earthquake motion as the seismic input for this study; this motion is recorded along the east-west direction at LPCC station during the Darfield earthquake in New Zealand in 2010. The peak ground acceleration of this motion is approximately 0.2 g and the peak ground velocity is 0.19 m/s showing a clear velocity pulse.

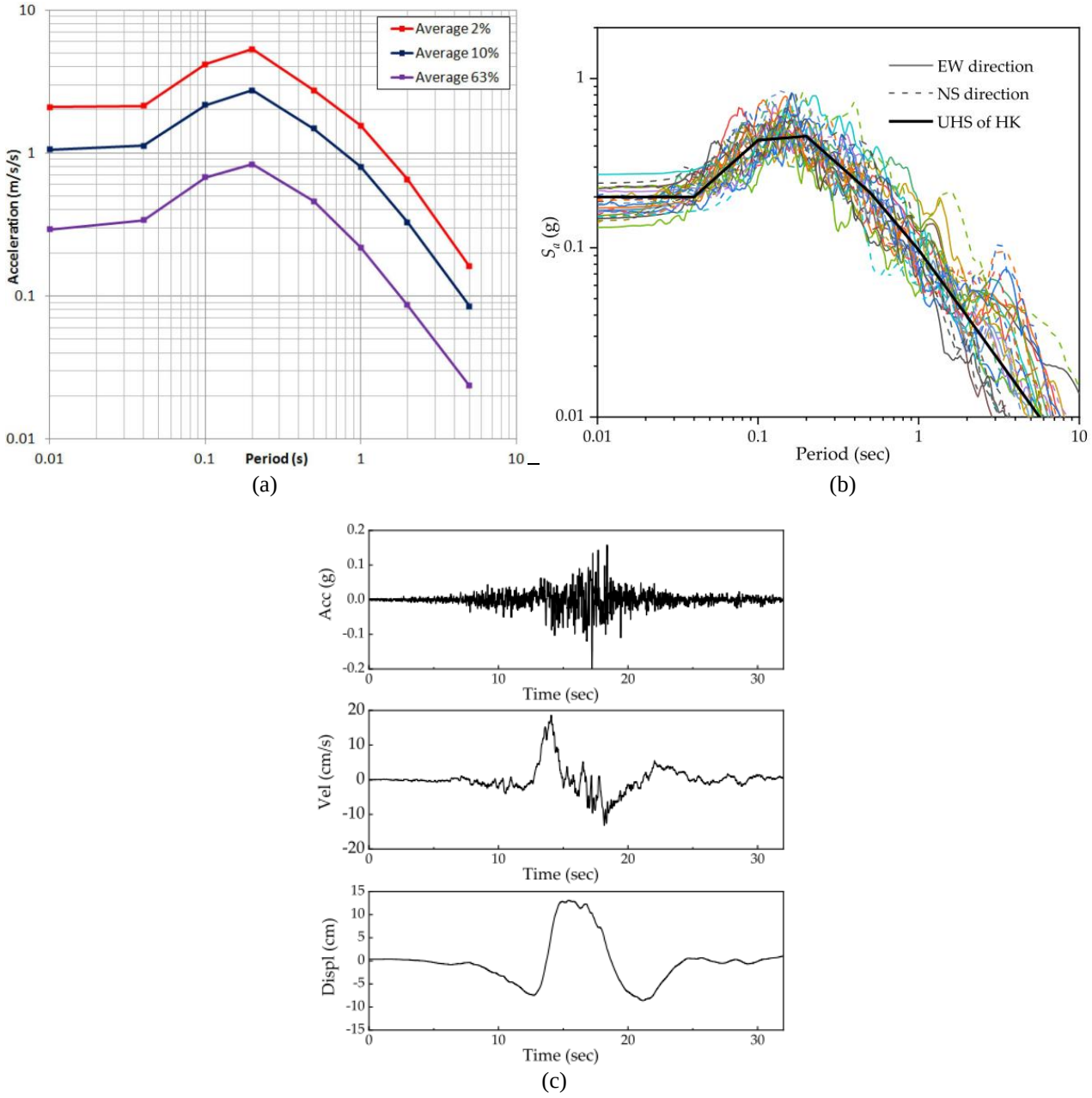


Figure 4. (a) Uniform hazard spectra of Hong Kong at 2%, 10% and 63% probabilities of exceedance in 50 years; (b) Selected earthquake motions fitting 2% probability of exceedance in 50 years; (c) acceleration, velocity and displacement time-histories.

2 3D SEISMIC ANALYSIS AT TUEN MUN - YUEN LONG

2.1 Spectral element model

The spectral element method (SEM) is a high-order finite element method, with specially designed interpolation points and integration scheme. It combines the advantages of FEM for the geometrical flexibility and the Pseudo Spectral Method for accuracy of wavefield simulation (Poursartip et al., 2020). The SEM discretizes the elements using high-order Lagrange interpolants, and integrates over elements based on the Gauss-Lobatto- Legendre integration rule (Komatitsch and Vilotte, 1998). This scheme yields a systematic diagonal mass matrix, suitable for parallel computation. The SEM was first introduced into the seismology by Komatitsch and Vilotte (1998) in the early 1990s. As for the time integration, SPECFEM3D adopts the second-order classical explicit finite difference scheme, benefited from the systematic diagonal mass matrix. The constructed SEM model for the study region has a resolution of 40m × 40m horizontally, with more than 2 million high-order spectral elements and over 100 million grid points (Figure 1e).

The Lysmer-Kuhlemeyer transmitting boundary is implemented as the bottom boundary, which is composed of two terms: (1) the absorbing term that dissipates waves outward the domain; (2) the second term can be regarded as a force acting at the bottom, to simulate waves travelling into the study region (Lysmer and Kuhlemeyer, 1969). In this study, the selected earthquake recordings as introduced in the previous section have been adopted as the seismic input.

2.2 Seismic responses considering topographic and site effects

Firstly, the SEM model is adopted to examine the topographic effect on ground motion distribution, without considering the soil amplification at the basin region. The topographic amplification factor (*TAF*) is calculated through dividing the S_a on topographies by S_a on flat ground (Wang et al., 2018). It reflects the focusing effect of mountain terrains on seismic waves that leads to unexpectedly severer ground responses.

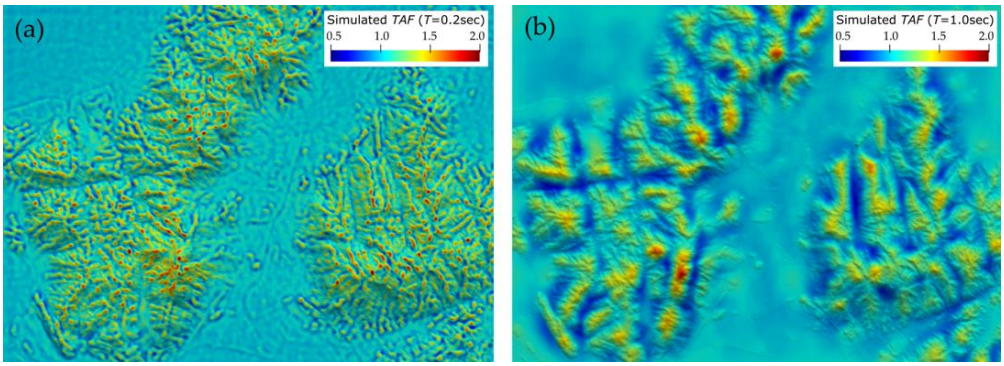


Figure 5. Ground amplification due to the topographic effect at periods of (a) 0.2 sec and (b) 1 sec.

Figure 5 shows the topographic amplification factor of two local mountain groups around Tuen Mun and Yuen Long, at two periods of 0.2 sec and 1 sec. Note that when studying the topographic effect, the soil effect is yet not considered and the region is simulated as uniformly distributed grade V rocks. It is found that both periods have a similar range of *TAF* between 0.5 and 2.0. However, the S_a at 1 sec (Figure 5b) shows significantly larger terrain features of amplification and de-amplification than S_a at 0.2 sec (Figure 5a). This is because larger periods correspond to larger wavelengths, and thus show stronger focusing effect from regional terrains. On the other hand, smaller periods indicate shorter waves that respond to more locally terrain features (Figure 5a). This is consistent with another seismic study for Hong Kong Island by Wang et al. (2018).

Secondly, the soil amplification at the basins is studied, by using the interpreted borehole data to construct a 3D SEM model (Figure 2). Figure 6 shows the ground spectral acceleration S_a distributions at a wide range of periods from 0.05 sec to 5 sec. It is found that S_a at different periods show significantly different patterns, which is attributed to different soil depths, as illustrated in Figure 2(a). Sites with deeper soil thickness (H) have greater soil amplification at larger periods, with site period equaling to $4H/V_S$. S_a at 0.05 sec shows more amplification at areas with shallower soil (~20m) like the edge of basins (Figure 6a). S_a at 0.2 sec shows the

largest area of amplification, because site period of 0.2 sec takes the largest proportion within the basins with depth between 20 m and 50 m (Figure 6b). On the other hand, only a few deep-soil areas (with soil > 50 m) show notable amplification at larger periods of 1 sec and 5 sec (Figure 6 c&d). Overall, the soil amplification factors (S_a on soil divided by S_a on rock outcrop) can be as high as 3 to 5 (5 for 0.2 sec and 1 sec).

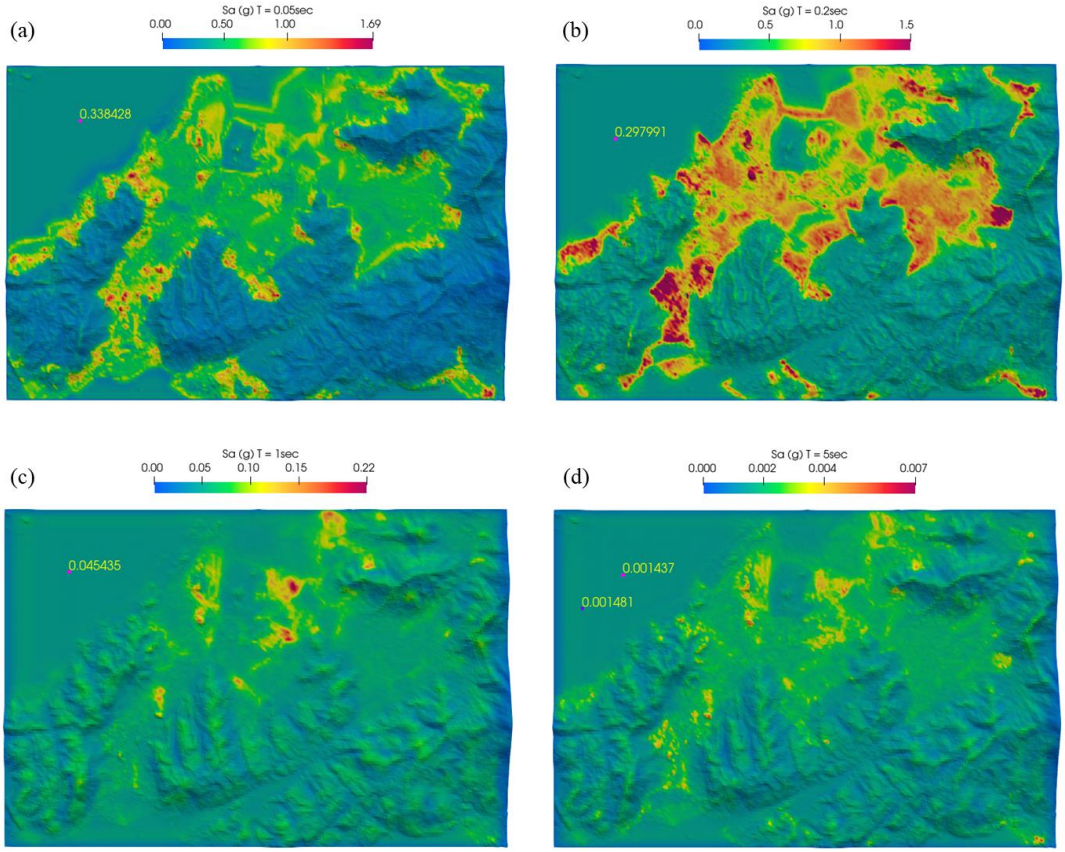


Figure 6. Ground response spectra at periods (a) 0.05 sec, (b) 0.2 sec, (c) 1 sec, and (d) 5 sec.

3 NONLINEAR SITE RESPONSE ANALYSIS AT KAU YI CHAU ARTIFICIAL ISLANDS

3.1 Soil strata

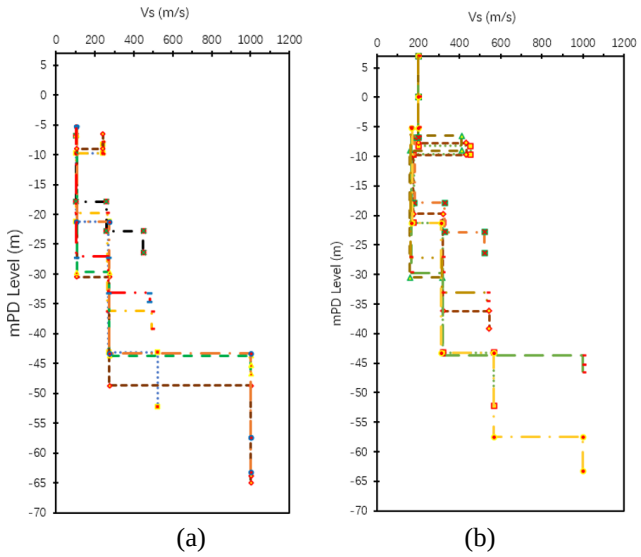


Figure 7. Shear wave velocity profile of boreholes within the sea near Kau Yi Chau (a) before and (b) after reclamation

Figure 7 presents the shear wave velocity profiles before and after reclamation for the seven representative borehole samples in the sea. The original seabed level is around -10 mPD (before reclamation), whereas the final formation level is set as + 7 mPD assuming 200 m/s as the shear-wave velocity for fill materials. The analyzed soil profiles extend deep to rock with grade III or better and represented by V_S of 1000 m/s (at a level of -40 mPD to -70 mPD). Both strata before and after reclamation will be used to conduct seismic analysis. The degradation G/G_{max} and Damping Ratio (D%) with shear strain are selected for the studied soils (both cohesive and non-cohesive), depending on: over consolidation ratio, confining pressure, plasticity index (PI), number of cycles and frequency, and details can be found in Darendeli (2001). In this study, we adopted a plasticity index of 30 for marine deposit to determine the degradation and damping ratio curves.

3.2 Nonlinear seismic analysis

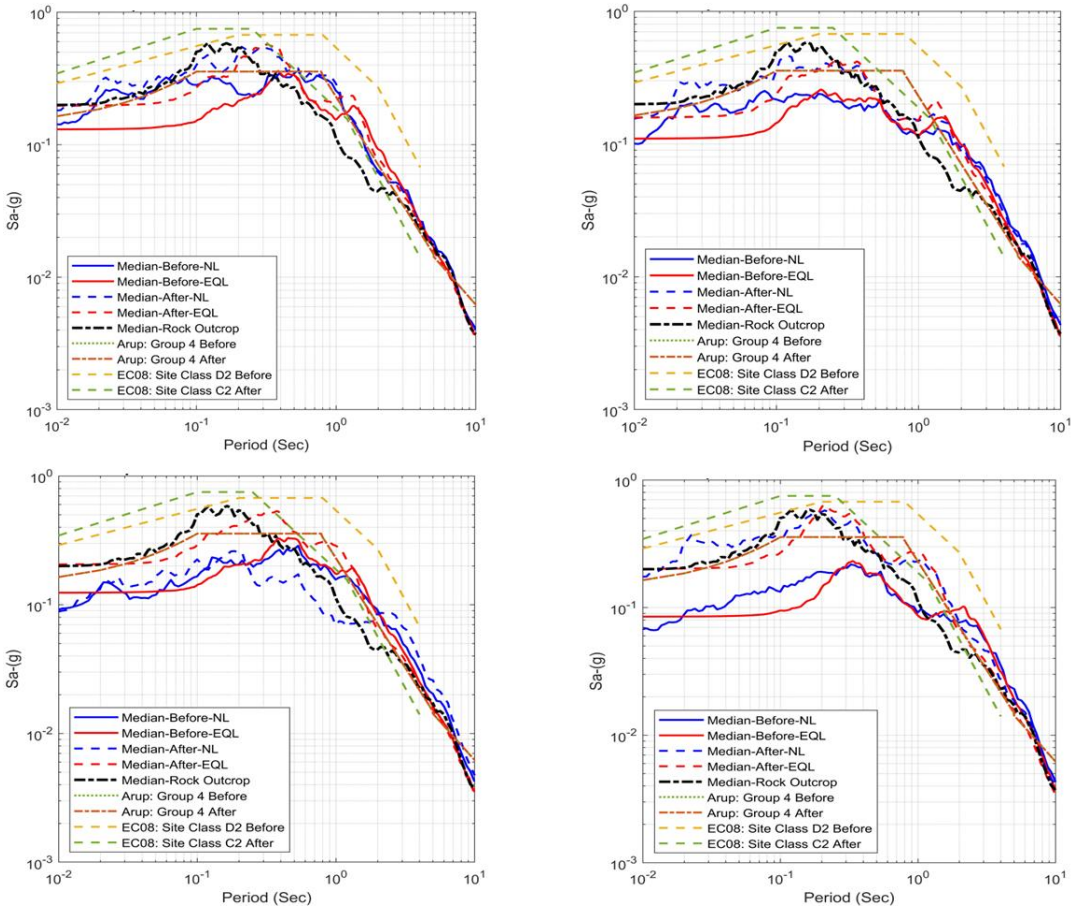


Figure 8. Spectral acceleration in the sea around the Kau Yi Chau island, before and after land reclamation.

Figure 8 shows the ground spectral responses (median results from the 14 earthquake recordings) at sea regions near Kau Yi Chau island, before and after reclamation. Note that seismic analysis results from Euro Code type 2 (denoted by EC2, for low to moderate seismic zones) and Arup are also presented for comparison (Pappin et al., 2015). Both EC2 and Arup estimate seismic hazard levels based on site classifications V_{S30} which represents the average shear wave velocity within 30 m below ground level. Detailed classifications criteria can be found in Pappin et al. (2015). The results show that compared to rock outcrop, the studied sites show de-amplification at short periods (< 0.5s) before reclamation for both Equivalent Linear (EQL) and nonlinear (NL) analyses, but not in the same trend (EQL and NL) especially in very short periods <0.1s; the spectral acceleration is amplified at longer periods > 0.6s. After reclamation, the spectral acceleration sees notable amplifications, mainly at periods of 0.1 sec to 1 sec.

In general, EC2 over-estimates the seismic hazard level over the studied period ranges at both before and after reclamation. On the other hand, Arup over-estimates seismic hazard level before reclamation, but under-estimates seismic hazard level after reclamation at period between 0.1 sec and 0.4 sec.

4 CONCLUSIONS

In this study, seismic hazard assessment is conducted for Northern Metropolis and Kau Yi Chau Artificial Islands, based on Hong Kong uniform hazard spectrum for 2% probability of exceedance in 50 years. In-situ borehole data have been collected to interpret the geological model at the study regions. The 3D physics-based model (20km × 20km) is constructed to perform regional scale seismic wave propagation at Tuen Mun and Yuen Long regions (Northern Metropolis), to investigate the effects of local topographies and basins on ground seismic responses. Besides, 1D nonlinear seismic analyses are performed to study the seismic levels at the Kau Yi Chau Artificial Islands in Central Waters.

It is found that topographies at Tuen Mun and Yuen Long regions contribute to a topographic amplification factors of 0.5 – 2.0, and larger periods show ground amplification at larger terrain scales. The deep sedimentary soil layers at the Yuen Long regions contribute to a soil amplification factor as high as 3-5 depending on the studied period. On the other hand, studies on the Kau Yi Chau artificial island show similar ground responses by using equivalent linear and nonlinear soil models, due to the relatively moderate seismic level in Hong Kong. The soil deposits around Kau Yi Chau artificial islands lead to de-amplification at short periods (high frequencies) before reclamation due to large damping ratio from the marine deposits, while the filling material would lead to notable amplification of ground responses at period between 0.2 sec and 2sec. Besides, the obtained seismic responses are compared against those estimated by Euro Code and Arup.

ACKNOWLEDGEMENTS

The authors acknowledge financial support from Hong Kong Research Grants Council through General Research Fund 16214322.

REFERENCES

Chen, Z., Huang, D., Wang, G., 2023a. Large-scale ground motion simulation of the 2016 Kumamoto earthquake incorporating soil nonlinearity and topographic effects. *Earthq. Eng. Struct. Dyn.* 52, 956–978. https://doi.org/10.1002/eqe.3795.

Chen, Z., Huang, D., Wang, G., 2023b. A regional scale coseismic landslide analysis framework: Integrating physics-based simulation with flexible sliding analysis. *Eng. Geol.* 315, 107040. https://doi.org/10.1016/j.enggeo.2023.107040.

Darendeli, M.B., 2001. Development of a new family of normalized modulus reduction and material damping curves. *The University of Texas at Austin*.

GEO, 2018. Seismic hazard analysis of the Hong Kong region. Rep. No. 311.

GEO, 2012. Landslip prevention and mitigation programme pilot seismic microzonation study in north-west new territories for the study of potential effect of earthquake on natural terrain investigation. Agreem. No. CE49/2008(GE).

Huang, D., Wang, G., Du, C., Jin, F., Feng, K., Chen, Z., 2020. An integrated SEM-Newmark model for physics-based regional coseismic landslide assessment. *Soil Dyn. Earthq. Eng.* 132, 106066. https://doi.org/10.1016/j.soildyn.2020.106066.

Komatitsch, D., Vilotte, J.P., 1998. The spectral element method: An efficient tool to simulate the seismic response of 2D and 3D geological structures. *Bull. Seismol. Soc. Am.* 88, 368–392. https://doi.org/10.1785/BSSA0880020368.

Lysmer, J., Kuhlemeyer, R.L., 1969. Finite Dynamic Model for Infinite Media. *J. Eng. Mech. Div.* 95, 859–877. https://doi.org/10.1061/JMCEA3.0001144.

Pappin, J.W., Koo, R.C.H., Jiang, H., Kwan, J.S.H., Yu, Y.B., So, M.M.L., Shiu, Y.K., Ho, K.K.S., Pun, W.K., 2015. A rigorous probabilistic seismic hazard model for Southeast China: a case study of Hong Kong. *Bull. Earthq. Eng.* 13, 3597–3623. https://doi.org/10.1007/s10518-015-9798-y.

Poursartip, B., Fathi, A., Tassoulas, J.L., 2020. Large-scale simulation of seismic wave motion: A review. *Soil Dyn. Earthq. Eng.* 129, 105909. https://doi.org/10.1016/j.soildyn.2019.105909.

Wang, G., Du, C., Huang, D., Jin, F., Koo, R.C.H., Kwan, J.S.H., 2018. Parametric models for 3D topographic amplification of ground motions considering subsurface soils. *Soil Dyn. Earthq. Eng.* 115, 41–54. https://doi.org/10.1016/j.soildyn.2018.07.018.

Solution for Geotechnical Data Platform and BIM-based Foundation Design Automation

Chen Xuewei & Cecilia Wan
WSP Asia Ltd, Hong Kong

ABSTRACT

This paper introduces two automated tools developed by the author for foundation engineering: GI_Inventory, a geotechnical data integration platform, and ETE_Foundation, an automated foundation design tool. Leveraging geotechnical public data from the Hong Kong Common Spatial Data Infrastructure (CSDI), including geotechnical borehole locations and AGS files, the author developed GI_Inventory—a GI data platform. The software automates the retrieval and organization of AGS documents for Hong Kong, generates geotechnical data tables and drawings programmatically, the author developed ETE_Foundation, an automated tool for pile foundation design. Engineers can establish pile foundation analysis models based on BIM models and geotechnical data. ETE_Foundation automatically generates models and conduct analysis and design for pile foundations. The tool integrates geotechnical data, enabling automatic calculation of pile lengths and adjustment of soil spring parameters in the model. This facilitates rapid design results for piles, accommodating changes and modifications in engineering design. Overall, these automation tools, GI_Inventory and ETE_Foundation, streamline foundation engineering processes by automating geotechnical data integration, organization, retrieval, and analysis. They enhance efficiency, accuracy, and adaptability in foundation engineering projects.

1 INTRODUCTION

The main content of this article is to introduce two automated tools developed by the author for foundation engineering: the geotechnical data integration platform, GI_Inventory, and the automated foundation design tool, ETE_Foundation. Based on the geotechnical public data provided by Hong Kong Common Spatial Data Infrastructure (CSDI), including the planar locations of geotechnical boreholes and digital documents of geotechnical data (AGS documents), the author developed a comprehensive geotechnical data application platform called GI_Inventory. This article describes the implementation method of the software and the functionalities that have been completed so far, including the automated retrieval and organization of AGS documents provided by CSDI for the entire Hong Kong region, the generation of geotechnical data tables and drawings through programming, and the creation of CAD drawings and BIM models using geotechnical data.

The author also developed the automated foundation design tool, ETE_Foundation. Engineers can establish pile foundation analysis models with geotechnical data based on BIM models. Through finite element calculations, the tool automatically generates models and performs analysis and design for pile foundations. The automated program for pile foundation design integrates geotechnical data and can automatically calculate pile lengths and adjust soil spring parameters in the model, providing quick design results for piles. The high level of automation in the entire pile foundation design process accommodates inevitable changes and modifications in engineering design.

2 THE DEVELOPMENT OF GI_INVENTORY

2.1 Conventional Approach

The traditional workflow for using geotechnical data involves querying borehole data from the Geotechnical information infrastructure (GeoInfo) website for the vicinity of a project site. Then, based on the GeoInfo index, relevant site reports or laboratory reports in PDF format are searched and downloaded. Subsequently, geotechnical engineers analyze and process the data.

In addition to providing PDF documents, both CSDI and GeoInfo also offer corresponding AGS data files. AGS data is a standardized digital format introduced by GEO in 1993 and published by the Association of Geotechnical and Geo-environmental Specialists (AGS). Similar AGS data requirements are also adopted in most government geotechnical investigation contracts.

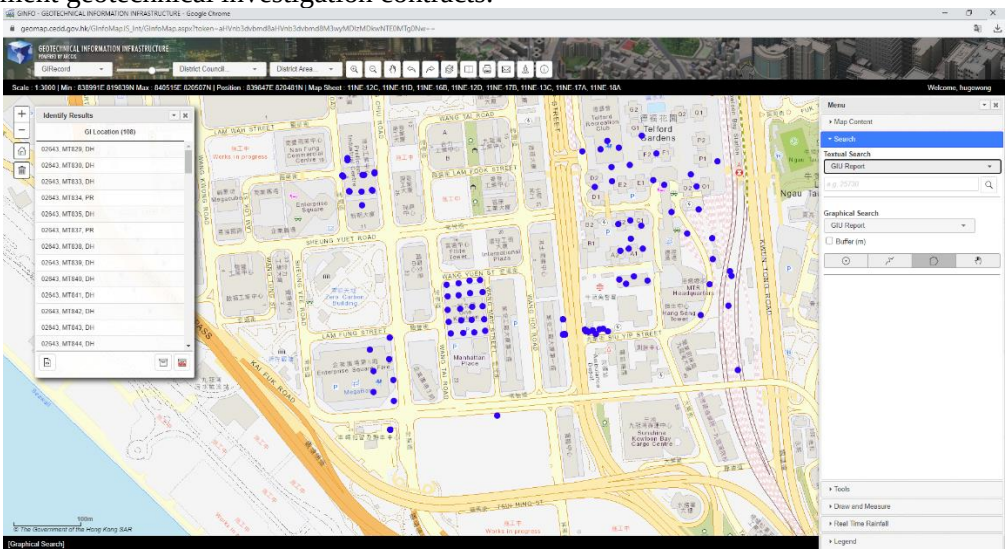


Figure 1: GeoInfo website user interface

Currently, the GeoInfo website only provides download links for AGS data documents of the respective boreholes, without integrating detailed AGS data into the GeoInfo platform for users to search through webpages. The current procedure involves downloading relevant AGS files or PDF documents and manually organizing the geotechnical information by engineers. This entire process requires significant data processing time and does not utilize the existing AGS data files.

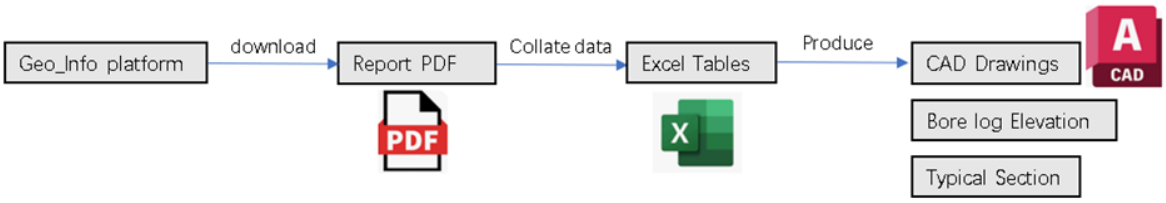


Figure 2: The traditional workflow for handling GI Data

After organizing the geotechnical information, As shown in Figure 2, engineers determine different soil or rock layer types, elevations, and thicknesses through textual descriptions of the geotechnical layers. They then convey this information to draftsmen for the preparation of geotechnical plan drawings, rock head contours, and profiles of critical sections. Alternatively, engineers can establish a Civil3D model to create relevant profiles, which can be used by foundation design engineers.

2.2 Problem Statement

To address the aforementioned challenges and make the entire process more intelligent, the author of this paper aims to integrate data from the AGS digital files provided by CSDI and establish a comprehensive geotechnical data platform called GI Inventory. This platform enables engineers to directly access and apply geotechnical data in foundation design. Within GI Inventory, engineers can obtain information such as the planar location, type, and depth of borehole, classification and elevations of geotechnical layers, and relevant

laboratory data (e.g., Triaxial Test data), as shown as Figure 3. GI Inventory can directly generate AutoCAD drawings, including plan views and cross-sectional views of the boreholes. Additionally, it can generate a BIM model of the geotechnical data (based on the Revit platform) for engineers to coordinate and use collaboratively.

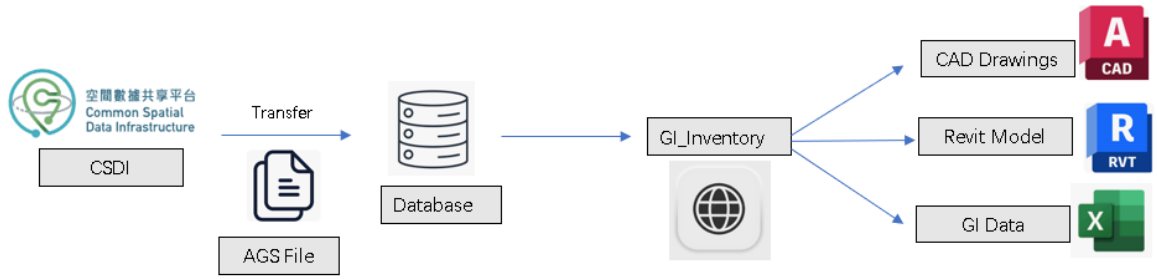


Figure 3 The design concept of GI_Inventory for extracting GI Data

During the development of the comprehensive geotechnical data platform GI Inventory, the following challenges are encountered:

Using AGS files to process geotechnical data does come with some challenges. One problem is the compatibility issue between AGS files and existing software or systems. Not all geotechnical software applications or databases are designed to handle AGS files seamlessly. This can create difficulties in importing and manipulating the data, potentially leading to errors or incomplete analysis. Another issue is the lack of uniformity in AGS file formats. While AGS is a standardized format, there can be variations in how different organizations or software vendors implement it. This can result in inconsistencies in data interpretation and compatibility issues when exchanging AGS files between different systems or projects. Furthermore, AGS files may not always capture all the necessary information or details required for comprehensive geotechnical analysis. Some critical data points or parameters may be missing or not adequately represented in AGS files, limiting the accuracy and reliability of the analysis.

The complete set of AGS files provided by CSDI consists of two types of data: site data and laboratory data. However, CSDI has not classified these two types of data nor provided any information on their interrelationships. In order to establish the correlation between the two, it is necessary to employ artificial intelligence to carry out the analysis, e.g. project names in the AGS files. Additionally, a comprehensive evaluation can be conducted by taking into account the boreholes names, which will aid in determining the association between the two types of data.

2.3 Digital Solutions

One of the key technical challenges in developing a comprehensive geotechnical data platform is determining the category of a geotechnical layer based on the textual description in the AGS. After obtaining the attribute descriptions of soil layers and the grading of rock layers from the AGS, a preliminary classification is performed using a specific mechanism. However, even after the preliminary classification, there are still some cases where the category of a layer cannot be uniquely determined based solely on the text and grading. These cases are initially marked as "unknown" types. For a subset of samples, engineers use their expertise to identify the layers, and these manually identified results are used to train an AI model. Eventually, a geotechnical layer classification with a certain level of accuracy is achieved.

For example, Lithology essentially classifies materials into two groups: solid geology and superficial deposits. Superficial deposits primarily describe the type of soil, such as fill, alluvium, or marine deposits. Solid geology, on the other hand, describes the type of rock, including tuff, granite, granodiorite, quartz monzonite, and more. However, merely identifying the material type is not sufficient for lithology; it should also encompass the size of the materials. Soil, for instance, can be classified into various sizes, including gravel, sand, clay, silt, cobble, and boulder. Rocks, on the other hand, can be characterized by their degree of decomposition, such as completely decomposed, slightly decomposed, or fresh. To extract the relevant

information from the description sentence, we need to identify and extract the following elements: capital letters, words enclosed in brackets, and the degree of decomposition level.

The AGS files provided by CSDI do not explicitly indicate the relationship between site reports and laboratory reports. The laboratory reports only specify the names of different boreholes without providing the plan coordinates of the boreholes. As a result, the CSDI platform does not display the positions of laboratory reports in relation to the boreholes. The only way to determine the relationship between laboratory reports and site reports is by matching the project names and borehole names in both reports. The names of laboratory reports associated with site reports are shown in Figure 4. The pairing of project names requires the use of artificial intelligence for approximate string comparison and scoring. By combining the results of borehole pairing, the corresponding relationship between the two can be determined.

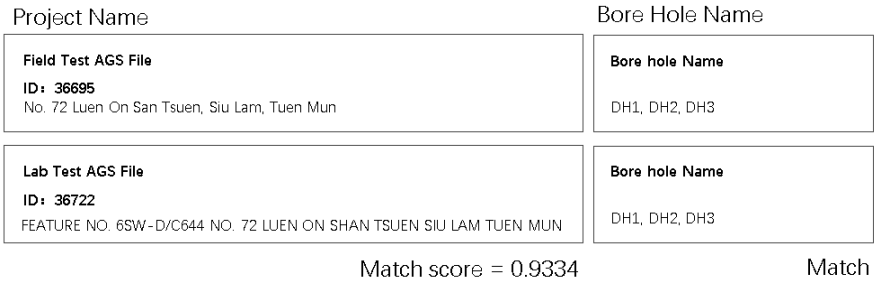


Figure 4. To compare and find the relationship between two AGS Files

GI_Inventory is a form-based program developed on the Delphi platform, as shown as Figure 5. The program organizes a large amount of geotechnical data from AGS files into a database format using Python scripts. The GI_Inventory program is called directly in the background and does not require re-identification or computation. As indicated in the diagram below, the program reads the database, and users can select the area of interest by drawing a box. The program automatically displays the relevant boreholes. By clicking on "Show Selected GI Data," users can access the next-level form. In this form, users can query spatial information and geotechnical data for all boreholes within the selected area. They can also view the project numbers and directly download the source AGS files. Users can also directly view the geotechnical data for specific boreholes associated with a specified Project_ID.

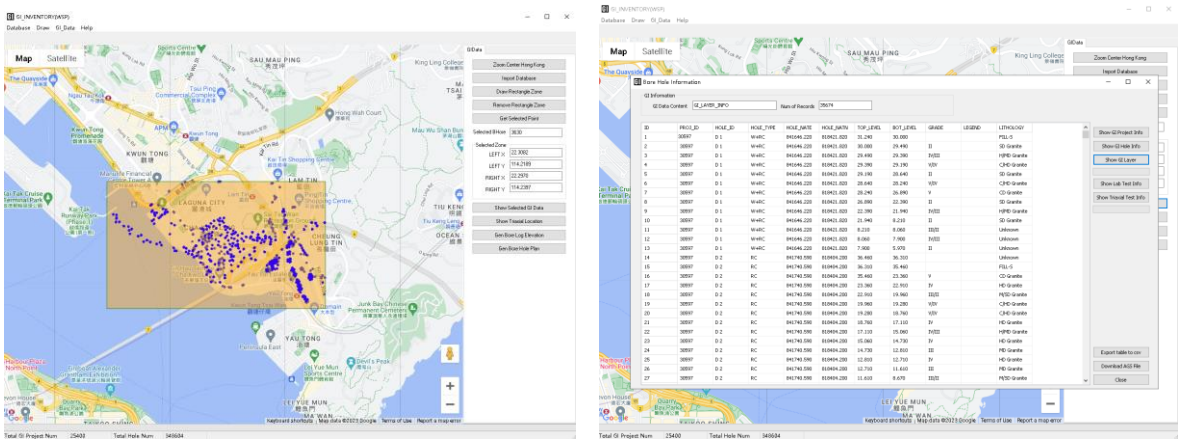


Figure 5. Graphical User Interface (GUI) of GI_Inventory

GI_Inventory has also been developed for post-processing. After selecting the desired data for querying, users can click on "Gen Bore Log Elevation" and "Gen Bore Hole Plan." Using ActiveX technology, the program generates CAD drawings through AutoCAD, creating borehole elevation and plan views, as shown in the diagram. These drawings are available for engineers to use, as shown as Figure 6.

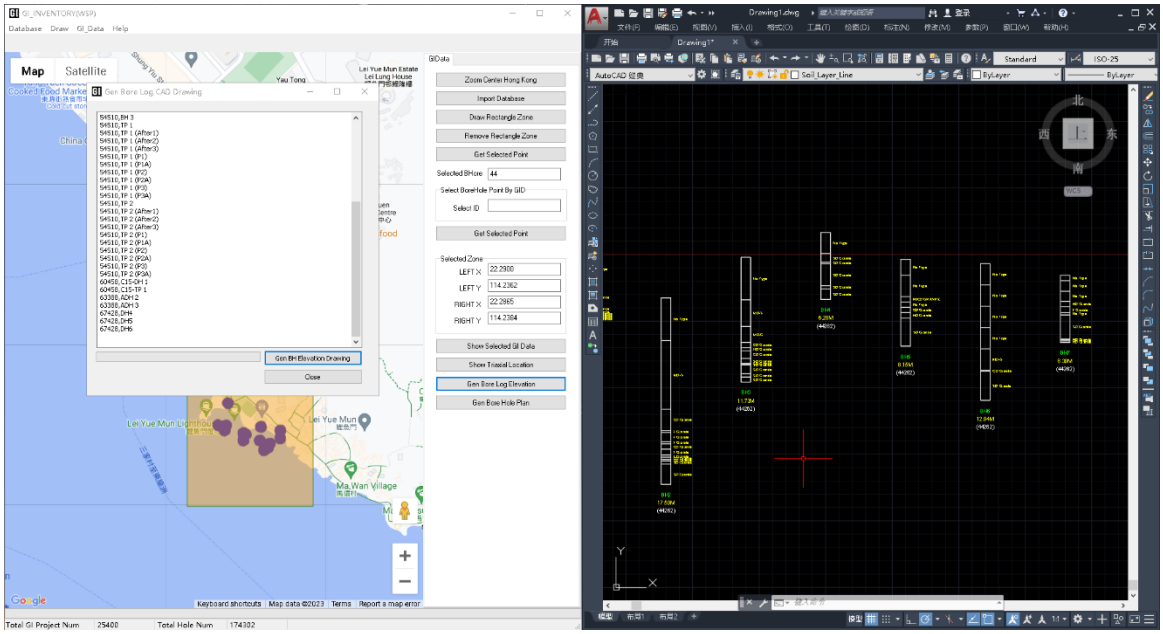


Figure 6. GI_Inventory generates bore log elevation drawings

3 FOUNDATION DESIGN PROGRAM ETE_FOUNDATION

3.1 Conventional Approach

In traditional foundation design methods, engineers are required to organize a large amount of geotechnical data and manually create the foundation model. The foundation model consists of four main components: piles and pile caps, loads on the superstructure, and soil linear springs. The length of the piles is influenced by the depth of the rock surface, while the parameters of the soil linear springs depend on the distribution and thickness of the soil layers. After conducting finite element analysis to determine internal forces, reinforcement calculations based on the internal forces of the piles are performed (which cannot be adequately handled by finite element analysis software alone, requiring additional reinforcement calculations). This is the complete process of pile foundation design, as shown as Figure 7. As design and geotechnical exploration work progress, the parameters need constant adjustment. This requires a significant amount of manpower and can lead to a decrease in accuracy. Sometimes, to save time on repetitive iterations, conservative values are used for certain geotechnical parameters, resulting in material waste during the design phase. The author of this paper aims to improve the efficiency of foundation design by developing a BIM-based foundation design software.

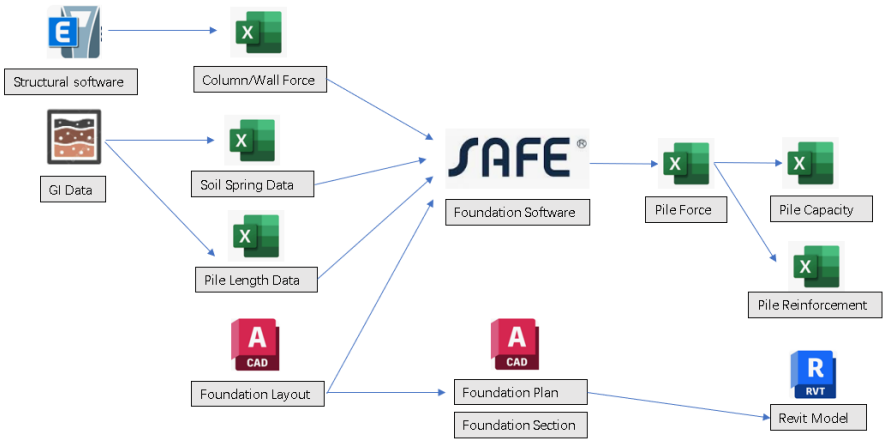


Figure 7. Traditional calculation processes for foundation analysis and design

3.2 Problem Statement

Currently, commercial software available on the market cannot handle the entire process of foundation design. When using software in conjunction with the foundation design process, the overall workflow is as shown in Figure 7. Throughout the foundation design process, which includes modeling, handling loads from the superstructure, pile reinforcement calculations, and pile bearing capacity verification, most of the steps require engineers to manually create Excel spreadsheets for calculations and batch processing.
Commercial software such as SAFE is only responsible for calculating the stress on the pile cap and the internal forces of the piles. Moreover, the modeling process in SAFE, which involves the concept of soil springs, is complex, and engineers often resort to using spreadsheets for batch processing. Therefore, in this article, the author proposes modeling the foundation model using a BIM-based platform, ensuring that most of the information can be imported into SAFE software, including geotechnical information. Additionally, BIM can assist engineers in generating CAD drawings, tables, and pile schedules during the post-processing phase.

3.3 Digital Solutions

GI_Inventory can assist engineers in gaining preliminary understanding of the geotechnical data near a project during the early stages. With GI_Inventory, elevation surfaces for multiple soil layers can be generated. The ETE_Foundation software can directly import the topological surface data of key soil layers, enabling the calculation of stiffness for all soil springs based on specifications. The geotechnical data provided by GI_Inventory can be used to preliminarily determine pile lengths. Based on engineering experience, the approximate cost range of the project can also be estimated. These preliminary assessments are of significant importance in the early stages of project planning and selection.

In order to enhance the digital application in the foundation design process, the entire foundation model is created using BIM technology. Since the foundation model includes piles, pile caps, soil springs, and loads from the superstructure, utilizing BIM modeling allows for the preservation of data within the foundation model. When there are updates in geotechnical information, the model can be instantly updated as well. Another benefit of BIM modeling is the ability to directly generate foundation plan layouts and cross-sections from the BIM model, reducing the workload of draftsmen. The workflow of ETE_Foundation is depicted in the Figure 8.

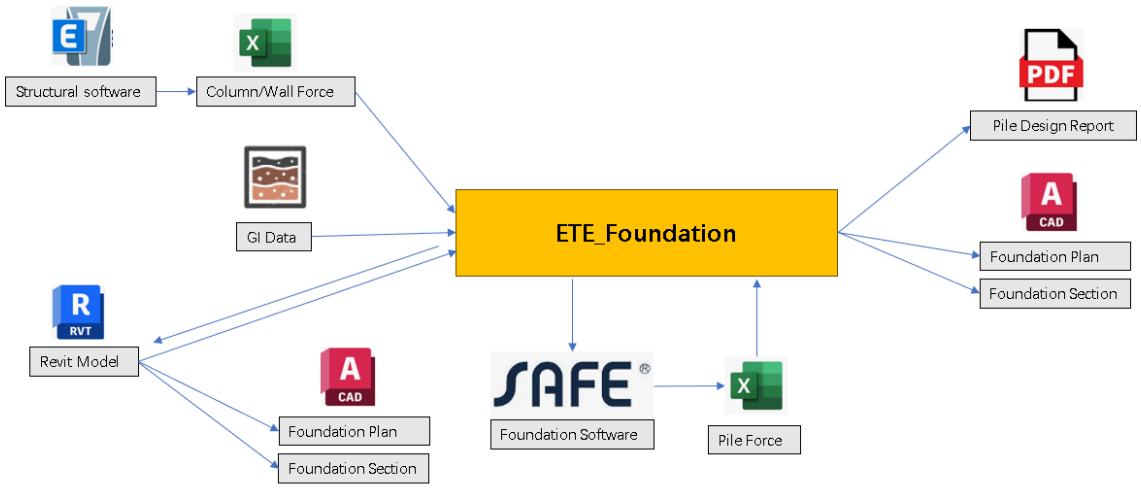


Figure 8. The design process of ETE_Foundation

The BIM-based foundation design software brings about the following innovations in the entire design process:

In the early stages, GI_Inventory provides borehole data that can be input into the ETE_Foundation software. The surface data of the rock layers can be imported into ETE_Foundation to determine the final pile length.

The lateral stiffness of the soil springs is also related to the data of the soil layers. As shown in the Figure 9, automating the generation of pile spring properties can improve the efficiency of engineer modeling.

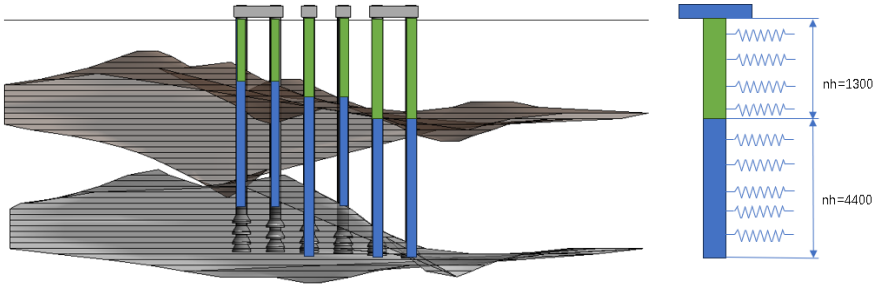


Figure 9. The relationship between soil layers and soil lateral springs

ETE_Foundation is a pile foundation design software based on the Revit model. This means that pile foundation can be created in Revit, including piles, pile caps, base slabs, rock layers, and more, all of which can be modeled in Revit, as shown as Figure 10. The model can then be imported into the ETE_Foundation for further processing and subsequently imported into the SAFE software for structural analysis. The interface of ETE_Foundation is shown in Figure 11.

After determining the soil spring parameters and pile length based on geotechnical data, the SAFE finite element model can be directly generated. Internal force analysis can be performed in the SAFE software. After the internal force analysis, users can import the internal force data into ETE_Foundation for reinforcement calculation of the piles and automatically generate calculation reports, as shown in Figure 12. ETE_Foundation uses the Load Fraction method for quick bearing capacity verification of bored pile reinforcement calculations. This method allows for a rapid assessment of whether the bearing capacity of the reinforcement section meets the requirements.

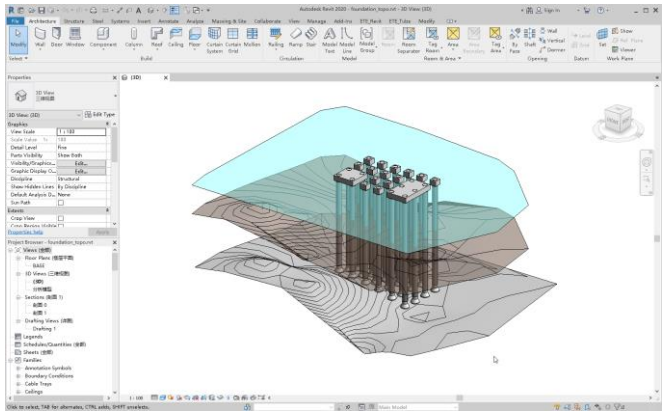


Figure 10. Foundation model in Revit

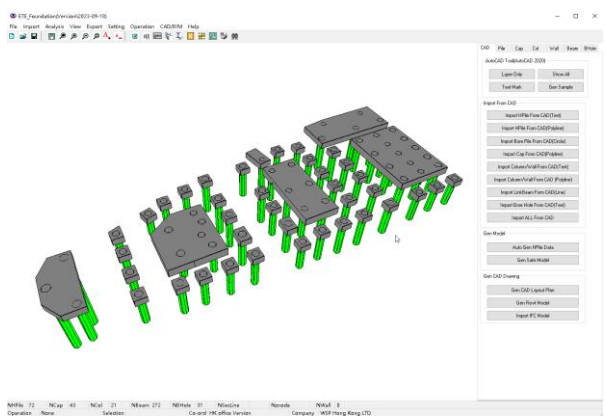


Figure 11. GUI of ETE_Foundation

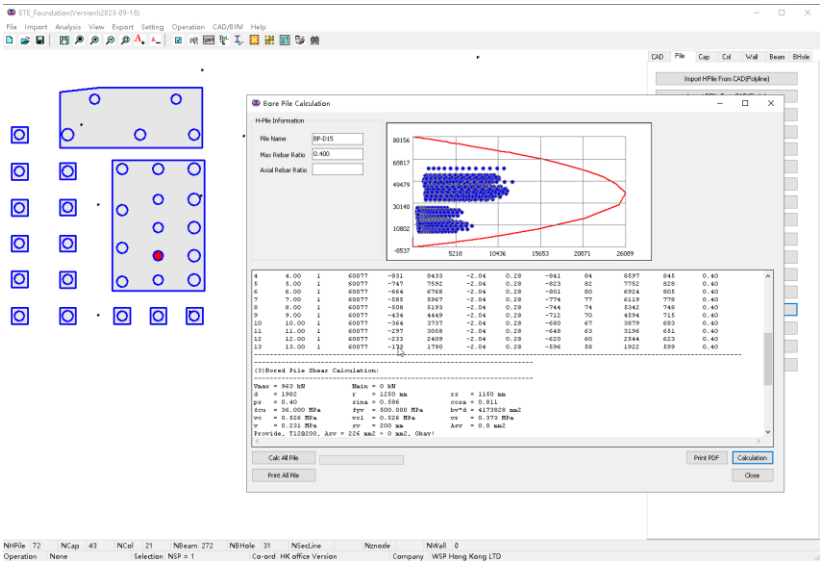


Figure 12. The reinforcement design function for pile foundations in ETE Foundation

4 CONCLUSIONS

The Development Bureau and the Lands Department launched the CSDI Platform on December 29th. The CSDI Platform provides a vast amount of geotechnical survey data for government infrastructure projects. In this article, the author utilized the AGS format files containing extensive geotechnical data provided by CSDI to develop the comprehensive geotechnical data platform, GI_Inventory. Unlike the GeoInfo platform, GI_Inventory directly extracts the contents of AGS data files, including borehole data, soil layer information, and laboratory data, reducing the time required for manual processing of geotechnical data. Additionally, the platform can generate borehole plan views and cross-sectional views, reducing the drafting time for draftsmen. The key surfaces generated by GI_Inventory can be imported into the foundation design software, ETE_Foundation, for foundation design. With the development of digital solutions and BIM technology, more and more projects are incorporating BIM technology. However, there is currently no integrated foundation design software based on BIM technology. This article discusses the traditional foundation design process and proposes a new digital solution tailored for foundation design. The software, ETE_Foundation, has been developed, allowing engineers to establish accurate BIM models, enabling subsequent design and analysis work to adapt to changes in the data model, meeting the requirements for continuous modification and updating in practical engineering projects. The entire digital workflow reduces manual processing time and errors.

REFERENCES

Geotechnical engineering office, 2006, Design of single piles and deformation of piles, Foundation design and construction: 81-160. CEDD Hong Kong.
KWAN K H, LIAUW T C. Computerized ultimate strength analysis of reinforced concrete sections subjected to axial compression and biaxial bending. Computers &Structures, 1985, 21(6): 1119-1127.
Computers & Structures, Inc.2016, CSI Analysis Reference Manual. Computers & Structures, Inc.

Tunnels and Caverns Design in Rock

Jason T.Y. Chin
Aurecon Hong Kong Limited

ABSTRACT

In the field of underground space design, numerous publications, design theories and software are readily available and easily accessible in the market. But it can be unclear as to which software to use, or which design approach to adopt to complete a tunnel or cavern design. Factor in varying ground conditions and tunnels with different sizes, the experience will become overwhelming. As such, it is necessary to adopt a design approach that is acceptable by the industry and recognizes the appropriateness of the engineering application that was first developed (so called "first principal"). Such design approach shall not only be safe, but also understand the limit of the applied theories or software. This paper aims to present one general and complete design approach for drill and blast or mechanically excavated tunnels and caverns in rock of all qualities (using one completed project as example), that would eliminate such ambiguities. This paper will also be a useful reference for those pursuing a career in tunnelling. The design approach follows the three general stages below.

I. Derive initial support (rock bolt and shotcrete) from empirical approach.
II. Check the adequacy of support from Step 1 using theory of reinforced rock arch (RRA).
III. Verify and modify the support design by numerical method.

1 BACKGROUND

Numerous design guidelines and approaches for tunnels and caverns have been extensively discussed and published. While each of these publications are mostly supported by case studies to demonstrate validity, it is important to realise that there is no one single design approach, or factor of safety, that would fit all cases of tunnels or caverns support. In one of his most widely referenced publication "Practical Rock Engineering" (Hoek, 2023), Dr. Evert Hoek wrote the following:

"*…there are no simple universal rules for acceptability nor are there standard factors of safety which can be used to guarantee that a rock structure will be safe and that it will perform adequately. Each design is unique and the acceptability of the structures has to be considered in terms of the particularly set of circumstances, rock types, design loads and end users for which it is intended… Tables 1 to 4 summarise some of the typical problems, critical parameters, analysis methods and acceptability criteria which apply to a number of different rock engineering structures. These examples have been drawn from my own consulting experience and I make no claims that this is a complete list nor do I expect readers to agree with all of the items which I have included under the various headings.*"

Figure 1 shows one of the tables mentioned by Dr Hoek which is captured unedited in its entirety.

2 INTRODUCTION

The design approach presented in this paper is by no means a one-solution-fit-all approach. But this is one that is overall most suitable for the conditions and rock types in Hong Kong. Adaptation of this approach elsewhere should be done with appropriate consideration and modification according to local conditions and rock types.

In the subsequent sections, each of the three general design stages outlined in abstract will be elaborated in more details with figures and diagrams. The three general design stages can be expanded in the following seven sub-steps.

1. Assessed all available information (geotechnical investigation and laboratory testing result) to determine relevant design parameters. The outcome of this assessment included qualitative and quantitative

assessment of the rock mass such as intact rock unconfined compressive strength (UCS), jointset data, joint strengths etc.

2. Carried out initial tunnel temporary lining design based on Q-System (NGI, 2015). The outcome of this is a temporary support table of tunnel such as thickness of sprayed concrete lining, length and spacing of rock bolts, reinforced ribs (this is Stage I outlined in abstract).

3. The next step involved kinematic analysis. At the end of this, the largest possible rock blocks can be determined. And the bolt length and spacing determined from previous step 2 above can be verified to be sufficient to stabilize these blocks.

4. With the initial support derived from empirical method, the next stage involved the checking of the support design using the reinforced rock arch (RRA) method (stage II outlined in abstract). At the end of this step, the pattern rock bolts, together with the rock mass holding these bolts, will be checked, and assessed as a collective structural beam.

5. The next step involved the use of finite element program with assumption of certain rock-structure interaction behaviors (such as arching effect of rock, relaxation factor etc.) and determine the state of stress of the sprayed concrete lining (bending moment and hoop force) (stage III outlined in abstract).

6. The next step is to determine if this state of stress is within the structural capacity of the tunnel lining. This is achieved by plotting the characteristic interaction diagram of the lining and plotting the data points (bending moment and hoop forces obtained from previous step 5) on this curve. If all the data points are located within this interaction curve, the lining is structurally sufficient. Otherwise the tunnel lining needs to be further strengthened.

7. The next and final step of tunnel support design involves determining the largest unsupported span and the longest unsupported time of the tunnel.

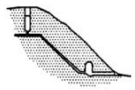
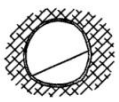
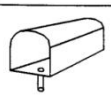
STRUCTURE	TYPICAL PROBLEMS	CRITICAL PARAMETERS	ANALYSIS METHODS	ACCEPTABILITY CRITERIA
 Pressure tunnels in hydro-power projects.	Excessive leakage from unlined or concrete lined tunnels. Rupture or buckling of steel lining due to rock deformation or external pressure.	• Ratio of maximum hydraulic pressure in tunnel to minimum principal stress in the surrounding rock. • Length of steel lining and effectiveness of grouting. • Groundwater levels in the rock mass.	Determination of minimum cover depths along pressure tunnel route from accurate topographic maps. Stress analyses of sections along and across tunnel axis. Comparison between minimum principal stresses and maximum dynamic hydraulic pressure to determine steel lining lengths.	Steel lining is required where the minimum principal stress in the rock is less than 1.3 times the maximum static head for typical hydroelectric operations or 1.15 for operations with very low dynamic pressures. Hydraulic pressure testing in boreholes at the calculated ends of the steel lining is essential to check the design assumptions.
 Soft rock tunnels.	Rock failure where strength is exceeded by induced stresses. Swelling, squeezing or excessive closure if support is inadequate.	• Strength of rock mass and of individual structural features. • Swelling potential, particularly of sedimentary rocks. • Excavation method and sequence. • Capacity and installation sequence of support systems.	Stress analyses using numerical methods to determine extent of failure zones and probable displacements in the rock mass. Rock-support interaction analyses using closed-form or numerical methods to determine capacity and installation sequence for support and to estimate displacements in the rock mass.	Capacity of installed support should be sufficient to stabilize the rock mass and to limit closure to an acceptable level. Tunnelling machines and internal structures must be designed for closure of the tunnel as a result of swelling or time-dependent deformation. Monitoring of deformations is an important aspect of construction control.
 Shallow tunnels in jointed rock.	Gravity driven falling or sliding wedges or blocks defined by intersecting structural features. Unravelling of inadequately supported surface material.	• Orientation, inclination and shear strength of structural features in the rock mass. • Shape and orientation of excavation. • Quality of drilling and blasting during excavation. • Capacity and installation sequence of support systems.	Spherical projection techniques or analytical methods are used for the determination and visualization of all potential wedges in the rock mass surrounding the tunnel. Limit equilibrium analyses of critical wedges are used for parametric studies on the mode of failure, factor of safety and support requirements.	Factor of safety, including the effects of reinforcement, should exceed 1.5 for sliding and 2.0 for falling wedges and blocks. Support installation sequence is critical and wedges or blocks should be identified and supported before they are fully exposed by excavation. Displacement monitoring is of little value.
 Large caverns in jointed rock.	Gravity driven falling or sliding wedges or tensile and shear failure of rock mass, depending upon spacing of structural features and magnitude of in situ stresses.	• Shape and orientation of cavern in relation to orientation, inclination and shear strength of structural features in the rock mass. • In situ stresses in the rock mass. • Excavation and support sequence and quality of drilling and blasting.	Spherical projection techniques or analytical methods are used for the determination and visualization of all potential wedges in the rock mass. Stresses and displacements induced by each stage of cavern excavation are determined by numerical analyses and are used to estimate support requirements for the cavern roof and walls.	An acceptable design is achieved when numerical models indicate that the extent of failure has been controlled by installed support, that the support is not overstressed and that the displacements in the rock mass stabilize. Monitoring of displacements is essential to confirm design predictions.
 Underground nuclear waste disposal.	Stress and/or thermally induced spalling of the rock surrounding the excavations resulting in increased permeability and higher probability of radioactive leakage.	• Orientation, inclination, permeability and shear strength of structural features in the rock mass. • In situ and thermal stresses in the rock surrounding the excavations. • Groundwater distribution in the rock mass.	Numerical analyses are used to calculate stresses and displacements induced by excavation and by thermal loading from waste canisters. Groundwater flow patterns and velocities, particularly through blast damaged zones, fissures in the rock and shaft seals are calculated using numerical methods.	An acceptable design requires extremely low rates of groundwater movement through the waste canister containment area in order to limit transport of radioactive material. Shafts, tunnels and canister holes must remain stable for approximately 50 years to permit retrieval of waste if necessary.

Figure 1: Original Table 3 in Dr Hoek's publication "Practical Rock Engineering" (Hoek, 2023)

3 DESIGN STEPS FOR TUNNELS AND CAVERNS IN ROCK

The following sections will elaborate in detail each of the seven design steps outlined in Section 2 with supporting documents and examples. For purpose of avoiding repeated term, the term "tunnel" instead of "tunnel and cavern" will be used throughout this paper but both are equal for topics presented in this paper unless otherwise mentioned.

3.1 Geological Review

The first task for any tunnel projects is to always collect and review all available geological and geotechnical data including aerial photo interpretation, whether project specific or non-project specific. This task is best to be carried out by a qualified engineering geologist, where key parameters such as rock types, weathering grades, uniaxial compressive stress (UCS) results along the depth of each log are summarized into a spreadsheet.

Concurrently, relevant borehole televiewer data must be reviewed to determine dip angle and dip direction of rock jointsets. This data is entered into the program DIPS which will be used by the program UNWEDGE explained later in Section 3.3.

After all the review and analyses were completed, the most representative and characteristic jointset orientation (total of 4 major, 1 minor jointset in the example used in this paper) and engineering parameters of rock mass (UCS of intact rock, joint shear strength) can be determined to be adopted in subsequent design of tunnel support.

Another geological information that will be extremely helpful in early stage of a project is the expected rock mass quality (the *Q*-value) along the tunnel complex. The success of this highly depends on few things: quality of horizontal directional coring (HDC) along the alignment, meticulous focus on HDC details, and unbiased application of Q-system parameters. One of the most common ways to estimate *Q*-value along the tunnel is by varying the parameters *RQD*, J_n, J_a and J_r in Equation (1) based on data obtained along the HDC. *RQD*, J_a and J_r can be estimated directly from HDC core samples, supplemented by boreholes and televiewer along the alignment. These three parameters are to be grouped along the alignment from direct observation. J_n, which relates to number of jointsets, can be estimated according to rock type. In Tuff, where rock mass is expected to be more fractured than Granite, the J_n value will be higher. Jw is assumed to be 1.0 because any groundwater seepage observed through joints is expected to be grouted. *SRF* relates to in-situ stress condition or overburden and can be estimated from any UCS results along the alignment. In highly fractured or fault zones, *SRF* will be locally adjusted accordingly. When all these parameters are being properly assessed, the expected *Q*-value along the alignment can be estimated using Equation (1).

3.2 Initial Support System using Empirical Method

One of the most widely used rock classification and support system is an empirical approach developed by the Norwegian Geotechnical Institute, the Q System (NGI, 2015), first developed in 1971 for use in metamorphic rock. This has been widely adopted due to its simplicity and reliability when used correctly on site. Over the years of application and improvement from experience, several factors were introduced for better representation on the scale and complexity of underground projects.

This method has been developed based on data collected through direct observations and historical failures from past projects and experience. The fundamental concept of classification method is to recognize the fact that the quality of rock mass as construction material in underground excavations cannot be measured by strength tests alone but have to be characterized by several controlling geological parameters. These parameters and correlations are derived for classification purpose, and grouped into different classes accordingly, to estimate rock mass behaviour and support requirements for prediction of tunnel supports.

The classification involves grouping areas of consistent geological structures based on the generality of observed features such as groundwater inflow condition, intact rock volumes, density and orientation of discontinuities, and infilling within discontinuities. By grouping the types of conditions likely to be encountered, it enables designers to prescribe a handful of generalized support types to cover those conditions. As result, the classification allows an engineer an invaluable understanding of the rock mass quality.

The general form of *Q*-value is determined by the estimation of the following six (6) rock mass parameters. The *Q* values range from 0.001 to 1,000 and represents an empirical and quantitative classification system showing the rock mass quality with respect to tunnel stability and support. On site, the *Q* values are mapped through direct observation of the exposed tunnel excavation face.

$$Q_{mapped} = \frac{RQD}{J_n} \times \frac{J_a}{J_r} \times \frac{J_w}{SRF} \quad (1)$$

Where *RQD* = rock quality designation, J_n = jointset number, J_a = joint alteration number, J_r = joint roughness number, J_w = joint water pressure number, *SRF* = stress reduction factor.

These six factors are used to classify rock mass quality on site, in different degrees of direct observation. Figure 2**Error! Reference source not found.** is a table directly extracted from NGI handbook as a guideline of rating each of these parameters.

NGI also developed a *Q*-chart intended for use to determine the appropriate support system within predefined ranges of *Q*-values (Figure 2). In order to use this *Q*-chart the tunnel effective span (D_e) is first calculated, which is the ratio of tunnel span to *ESR* factor and used this across the chart to determine the required support for each class of rock mass quality. Each class of rock mass quality is represented by an upper and lower bound *Q*-values. The tunnel span (either the width or height of tunnel) is determined from the tunnel cross section and the *ESR* factor is determined based on the definition from NGI. Figure 2**Error! Reference source not found.** is the original *Q*-chart extracted from the NGI handbook.

There are other factors that need to be applied to the *Q* ranges determined directly from the *Q*-chart. These factors are summarized in the following paragraphs.

The original *Q* chart was developed as permanent support for tunnel. For temporary support, the design *Q*-value for roof (Q_{roof}) is adjusted to five times the mapped *Q*-value Q_{mapped}, i.e. this factor of 5 is either applied directly on-site on the *Q* values mapped by the engineering geologist, or a factor of 1/5 is applied on the design values of *Q* support table. It is recommended to apply factor of 1/5 on design values and clearly mention this on the drawing, so to avoid accidental omission on site.

$$Q_{roof} = 5 \times Q_{mapped} \quad (2)$$

At tunnel junction or intersection, e.g. cross passages connecting two main tunnels in parallel, the mapped joint set number (J_n) should be adjusted by factor of 3.0 with *ESR* taken as 1.0. This factor is also recommended to apply on design drawing for the same reason.

$$Q_{roof} = \frac{Q_{mapped}}{3.0} \quad (3)$$

The *Q* value determined from the *Q*-chart is intended for tunnel crown. For tunnel sidewall support, the design *Q*-value for wall (Q_{wall}) is related to design Q_{roof} as shown in Table 1.

Table 1: Factors to be applied on Q_{roof} to determine Q_{wall}

$Q_{mapped} \geq Q_{roof}$		$Q_{mapped} < Q_{roof}$	
Q_{roof}	Q_{wall}	Q_{mapped}	Q_{wall}
> 10	$5 \times Q_{roof}$	> 10	$5 \times Q_{roof}$
0.1 – 10	$2.5 \times Q_{roof}$	0.1 – 10	$2.5 \times Q_{roof}$
< 0.1	$1 \times Q_{roof}$	< 0.1	$1 \times Q_{roof}$

For *Q*-value less than 0.1, the design rock dowel length of both the roof and wall should be the same even if the wall dowel lengths are shorter. This is to avoid the risk of potential rock bursting from wall. An *ESR* value of 1.0 has been adopted for calculating the dowel lengths due to the large span of tunnel.

In general, the relationship between the design *Q*-value for roof support and the mapped *Q*-value can be summarized as follow:

$$Q_{roof} = f^* \times f_{Jn} \times Q_{mapped} \quad (4)$$

Where f^* = the factor on support condition (temporary or permanent), f_{Jn} = the factor on joint set number (J_n) for the support location

These two coefficients account for all the factors given above, and the Q_{mapped} value determined on site can be used directly to determine the support classes and related requirements according to the drawings.

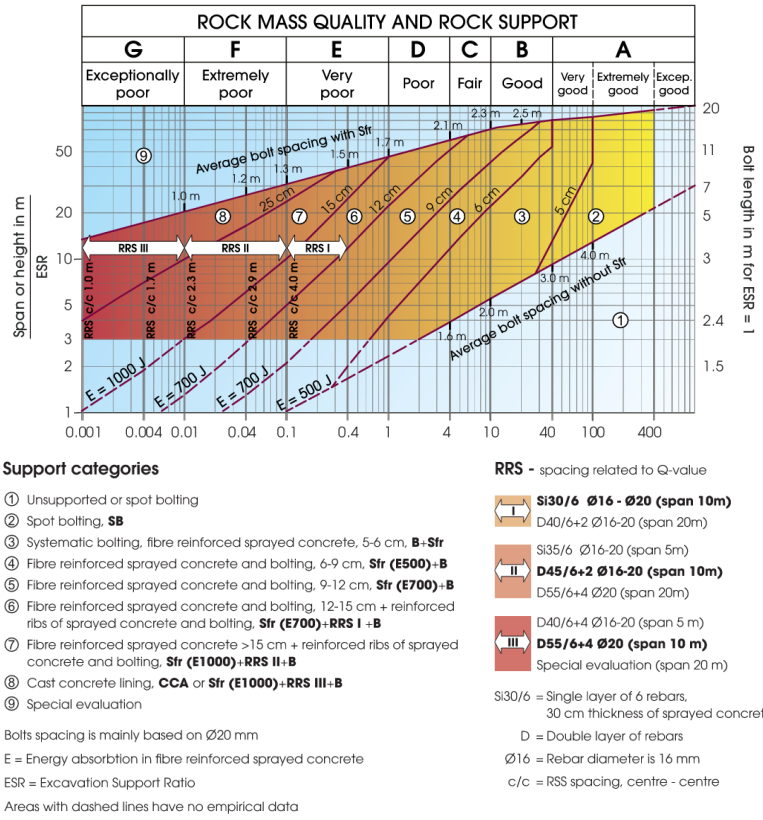


Figure 2: The *Q*-chart and support categories from the NGI *Q*-System (NGI, 2015) handbook

The dowel length L_d can be determined directly from the *Q* chart above or using the following equation (Barton, et al., 1974). It is recommended to use the following equation because it is slightly more accurate than directly reading off from chart.

$$L_d = 2 + 0.15D/ESR \quad (5)$$

3.3 Kinematic Analysis of Wedge Failure

A stiff support system needs to be provided after tunnel excavation to limit any rock wedge movement. Only a very small movement is needed to trigger the failure of a wedge. Sliding of a few millimeters along one plane or the line of intersection of two planes is generally sufficient to overcome the peak strength of the joint surfaces. Tensioned mechanically anchored rock bolts, untensioned-fully-grouted rock dowels and other continuously coupled devices can be used to support the wedges.

For roof wedges, the rock bolts should be capable of supporting the entire self-weight of the rock wedge. And the bolts should be placed uniformly about the wedge centroid to prevent rotation that reduces the factor safety. For sidewall wedges, the bolts can be placed in the sliding plane to increase the shear resistance of the joints.

The program UNWEDGE is used next to verify the preliminary support determined from Section 3.2. This requires the size and orientation of the tunnel, combined with the jointset data (dip and dip direction of each

set), as input into the program. Based on all these input parameters, the program determined the largest possible size and weight of rock wedges at the exposed tunnel wall and crown. These wedges are formed by physically intersecting the planes from jointsets and tunnel.

After the input into UNWEDGE the material property (capacity), spacing and length of rock dowels determined from the *Q*-chart, the program will calculate the factor of safety (FOS) of the provided support system (pattern dowels) against the failing wedges. The dowels must physically penetrate beyond the wedges in order for an FOS to be determined. Otherwise, the dowels will fall off together with the wedges yielding an FOS of zero.

The FOS for each wedge is calculated as the ratio of total support pressure provided by all intersecting dowels to the weight of the wedges. There are two other key parameters that would affect the FOS, namely joint water pressure and joint cohesion. The higher the joint water pressure, the more unstable the block, hence yielding a lower FOS. This is because joint water pressure directly contributes to the causal effect for wedge to fall off. Joint cohesion, on the other hand, has the opposite effect of joint water pressure. A small presence of joint cohesion (say 5 to 10 kPa) would yield very stable wedges that requires low support pressure, hence higher FOS.

In Hong Kong, pressurized joints from full groundwater head are seldom observed but minimal joint water pressure is often assumed to account for unforeseen groundwater inflow. For joint cohesion, friction does exist regardless of joint infilling. However, as a conservative approach, joint friction cohesion is assumed to be zero.

An example of UNWEDGE output findings is shown in Figure 3. In this example joint water pressure equivalent to 1.0 m of water head is adopted. This is to account for any transient groundwater through open joints that are not being effectively grouted by fissure grouting when measurable inflow is observed from probe holes. Joint cohesion is ignored due to difficulty in justifying its presence and the magnitude.

From the findings, the most critical rock wedges are found to be the ones at the crown (wedge no. 7s and 8), formed by prescribed jointsets at the project site.

In the case where the dowels capacity is found to be insufficient (i.e., FOS < 1.5 from UNWEDGE), one of the following can be done to increase the FOS: bolt spacing needs to be reduced, length of bolts to be increased or use bolts with higher capacity. Several iterations are needed in this step to determine the most optimised bolt spacing and length that yielded the desired FOS.

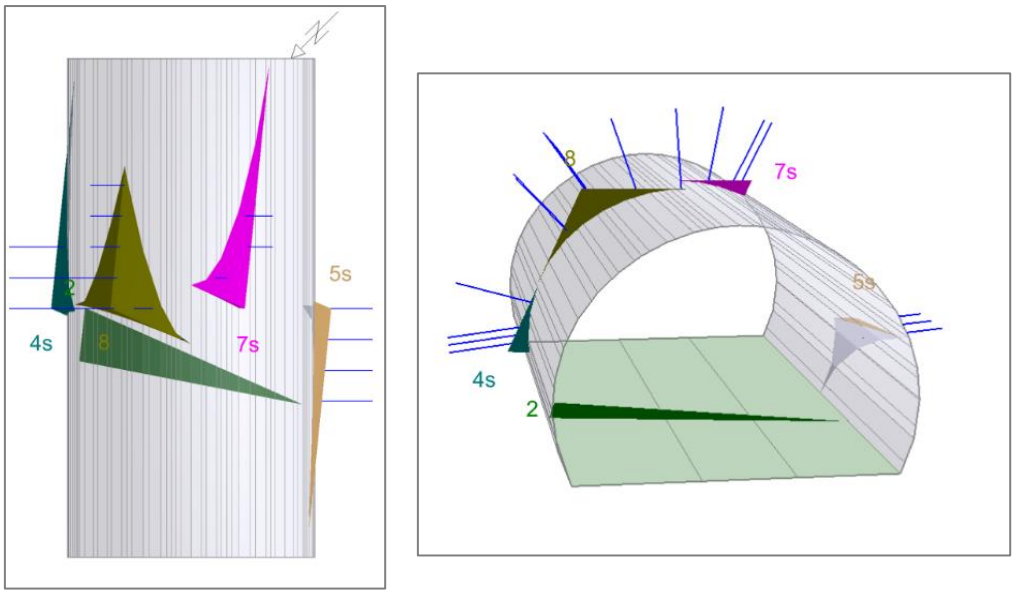


Figure 3: The Q-chart and support categories from the NGI Q-System *(NGI, 2015)* handbook

Due to its ease of use, UNWEDGE is a program that is most often being misused for purpose other than FOS of failing wedges. Below are some of the main points of misuse that the author has noticed that must be reminded to young engineers:

- UNWEDGE is intended for use in situation where the in-situ stresses are low or not critical, where their influence can be largely neglected without the introduction of significantly errors. Where high in-situ stress levels occur in blocky rock masses, the FOS predicted by the program can be incorrect.
- The wedge analysis is considered part of the tunnel support system verification. However, the findings from UNWEDGE should not be used to replace typical tunnel design from empirical approach or numerical analysis.
- As sliding of a few millimeters is generally sufficient to overcome the peak strength of the joint surfaces, rock wedge will fail when only small displacement occurs mobilizing its effective strength. As such, peak strength of discontinuities should not be used because this may overestimate the joint shear strength. And residual strength should be adopted instead.
- At deeper rock mass, the rate of increase of joint shear strength decreases. Therefore, using a constant joint friction angle for all depth of rock mass may overestimate the FOS leading to unconservative design especially for deep rock tunnels.

3.4 Support System as Reinforced Rock Arch (RRA)

After an initial support system has been developed and verified with kinematic approach, the next step in the design process involves checking the collective effect of pattern bolts. When pattern rock bolts are installed around tunnels, they are providing reinforcement effect to the rock mass, rather than as support to the rock mass. The reinforcement concept treats the rock mass with pattern bolts collectively as an arch under compression; whereas the old fashion concept of "support" would treat the rock mass as loading supported by the bolts. This shift in tunnel design concept resulted in a different analysis approach called reinforced rock arch (RRA) approach. This concept of tunnel rock mass reinforcement has been demonstrated excellently by Dr Evert Hoek's educational experiment shown in Figure 4. The small pieces of rocks in the inverted bucket did not fall out because they were being held firmly by the equally spaced bolts forming a collective slab under compression.

In order for the bolts to hold the slab of rock pieces together, the spacing, *s*, of the bolts must not be too large compared to the average size of rock pieces, *a*. However, there is common misconception about how rock bolts contribute to creating a linear zone of compression that keeps the rock pieces from falling. The arching effect is not due to the clamping action of the end plates but rather due to its reinforcement effect allowing stresses to arch linearly to the adjacent rocks thus creating a confinement effect. As such, this arched beam of reinforced rock mass can be considered as a structural element supporting the rock mass above it.

The most common analytical approach that allows the reinforced rock arch strength to be calculated is the design approach proposed by Bischoff and Smart (Bischoff & Smart, 1977). In this computational method, the increased in the capacity of thrust of the reinforced arch is being compared with the rock pressure acting on the arch. If the acting pressure is less or equal to the thrust capacity of the reinforced arch, then the tunnel is considered stable. The equations to calculate the increased thrust capacity of reinforced arch is as follow:

$$\Delta T_A = q\frac{\sigma_b A_b}{s^2}(L - s) \tag{6}$$

ΔT_A represents the increase in unit thrust of the reinforced arch zone; σ_b is the yield strength of bolts; A_b is the cross-sectional area of the bolts; s is the spacing of the reinforcing pattern bolts both transverse and longitudinally to the tunnel axis. Parameter q is the function of internal friction angle, φ, of the rock mass that correlates between effective increase in the allowable stress of the rock mass and rock reinforcement confining pressure ($\Delta\sigma_1/\Delta\sigma_3$) and can be calculated using the following equation:

$$q = \tan^2\left(45^\circ + \frac{\varphi}{2}\right) \tag{7}$$

The rock mass pressure acting on the reinforced arch (P_{arch}) can be estimated using calculation method proposed by Grimstad and Barton (Grimstad & Barton, 1993), which is also the calculation method

recommended by GeoGuide 4 (GEO, 2018). The equation to estimate rock pressure of tunnel is as follow, where J_n, J_r, and Q are parameters determined in step 2 (page 62) using Q-System (NGI, 2015).

$$P_{arch} = \frac{2J_n^{\frac{1}{2}}(Q)^{-\frac{1}{3}}}{3J_r} \quad (8)$$

The tunnel is considered sufficient as reinforced rock arch when the condition $\Delta T_A \geq P_{arch}$ is fulfilled.

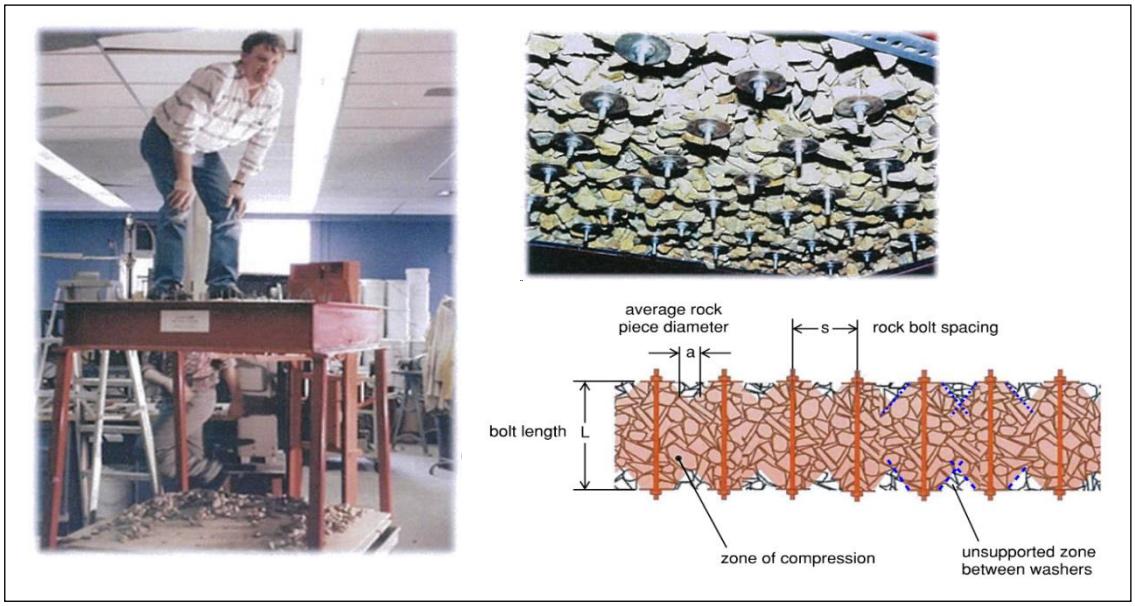


Figure 4: Demonstration on the concept of reinforced rock arch with pattern bolts *(Hoek, 2023)*

One of the most common misconception when calculating P_{arch} is whether factor f_{Jn} from Equation (4) needs to be applied to Equation (8). It should be clarified that f_{Jn}, which is a factor to account for additional exposed jointsets at junction and portal, is only intended for mapping purpose and not to be applied in calculation of P_{arch} at junction or portal.

3.5 Finite Element Analysis (FEA)

This last step in the tunnel design perhaps is one of the more complicated steps throughout the entire design and involves several sub-steps to yield any representative results. In general, numerical analysis program *RS2* (previously *Phase2*) was used to further verify and optimise tunnel support in highly jointed ground developed from all previous steps.

In the project example for this paper, continuum numerical modelling has been adopted for highly jointed ground condition for two main reasons: (1) in highly jointed rock mass condition, the rock bolts and rock mass surrounding the tunnel opening behave collectively as reinforced medium and form part of the support system. Where other empirical approaches consider surrounding rock as a load that requires support, the concept of rock reinforcement is best represented as continuum model in RS2 program; and (2) it is recommended by GeoGuide 4 (GEO, 2018) that in ground condition with mapped Q value of less than 0.1, the support system must be verified by numerical modelling.

In order to build a representative numerical model, there are several key parameters that need to be determined: (1) horizontal to vertical stress ratio at design depth of rock formation, and (2) relaxation factor of surrounding rock mass of the tunnel opening. The following are detailed explanation and determination of these parameters. There are other key parameters such as shear strength of the rock joint (joint roughness coefficient JRC, and joint compressive strength, JCS) however they are not applicable in continuum model because discontinuities

are not being modelled in continuum model, where failure criteria is stress related rather than rock blocks related.

The rock head cover of the project tunnel is greater than 100m, and in such deep and highly fractured ground condition it is anticipated that the ground would behave as isotropic and homogeneous material. In the published paper by Kwong and Wong (Kwong & Wong, 2013), the results from 124 hydraulic fracturing test carried out in Hong Kong have been analysed and summarized to show that at this depth, the lower bound in-situ stress ratio is about 1.0. Therefore, the FEA ground model and in situ stress field is assumed to be isotropic and horizontal to vertical stress ratio of 1.0 is adopted for the numerical analysis.

3.5.1 Degree of Relaxation

The second critical rock mass parameter is the degree of relaxation of the surrounding rock mass when a tunnel opening is formed. The degree of relaxation of a tunnel directly contributes to the amount of stress being transferred to the tunnel lining. When the rock mass surrounding a tunnel opening relaxes, some of the energy stored in the rock mass is being released and dissipated through deformation of the tunnel. The higher the deformation of a tunnel, the less stress is being transferred from the ground to the lining. However, if the deformation gets excessive, the deformation could become plastic resulting in potential caving or collapse. On the other hand, if the tunnel is only allowed to deform very slightly (e.g., in the case of immediate support installation), the support pressure required to stabilize the tunnel will be very high and unnecessarily costly to do so. As such, a balance between cost and safety must be reached.

In order to achieve this, convergence-confinement analysis is carried out to determine the degree of ground relaxation and to determine the resultant support pressure that applies to the lining. In general, the degree of relaxation can be determined from the following two equations published in the 2008 Kersten Lecture by Hoek et al. (Hoek, et al., 2008). These two equations combined to determine the level of convergence of excavated tunnel behind the tunnel face.

$$\frac{u}{u_{max}} = 1 - \left(1 - \frac{u_0}{u_{max}}\right) \cdot e^{-\frac{3d_t}{2P_r}} \tag{9}$$

$$d_t = -\frac{2}{3} P_r \cdot ln\left(\frac{u_{max}-u}{u_{max}-u_o}\right) \tag{10}$$

where u = convergence behind tunnel excavation face, u_{max} = maximum short-term tunnel convergence (determined from FEA model), u_0 = convergence at tunnel excavation face, d_t = ratio of x / tunnel radius, x is distance behind tunnel face, P_r = ratio of plastic radius/tunnel radius (measured from FEA model)

The above two equations can be represented by Figure 5 to determine u / u_{max}. The following steps explain how to use numerical modelling to determine tunnel convergence and degree of relaxation.

1. Set up an *RS2* model with an unsupported, unlined tunnel opening. Right after excavation of the tunnel, apply 100% of support pressure to the tunnel opening then allow the support pressure to gradually reduce to zero. The result of this is shown in Figure 6 where tension and shear failure points formed around the deformed tunnel opening. The extend of this plastic zone is measured directly from the model, which is 13.1 m on average.

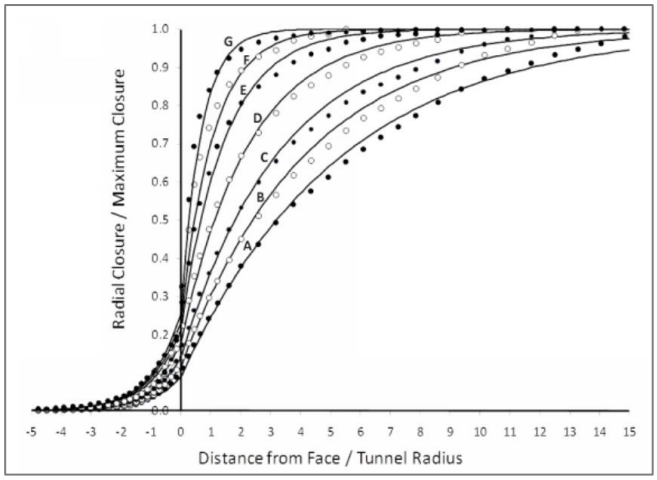


Figure 5: Normalised tunnel convergence behind tunnel excavation face *(Hoek & Marinos, 2000)*

2. Determine the maximum displacement from the same model, which is approximately 95.2 mm at tunnel crown from Figure 6.

3. Assuming a 1.0 m excavation advance length of tunnel, the values determined from steps 1 and 2 are used to calculate the tunnel convergence, *u*, either from the two equations above or the curve in Figure 5. The curves representing Equation (9) and (10) can be re-created using spreadsheet. Figure 7 shows one of these plots at day 0 when excavation length is 1.0 m. The convergence value determined from the curve is approximately 28.1 mm. The longitudinal displacement profile of the tunnel at day 1, 3, and 7, which corresponds to advance length of 2 m, 4 m, and 8 m respectively, is 35.4 mm, 47.6 mm, and 65.2 mm, respectively. In this calculation, the tunnel radius, plastic radius, and maximum displacement of the tunnel are all obtained from the *RS2* model, which is shown in Figure *6*. The tunnel advance length in the calculation of convergence is at the mid-point of the excavated length, therefore at day 0 when tunnel excavated 1.0 m, advance length in the calculation is 0.5 m.

4. Next, a ground reaction curve (GRC) is created from the stress and deformation values obtained from the FEA model. Right after the tunnel is excavated, 100% of ground stress is applied radially outward on the tunnel perimeter. This ground stress is gradually reduced to zero. At each step of the decrement the displacement value at crown is recorded and plotted against the corresponding ground stress. For this example, the blue curve in Figure 8 shows the specific GRC for the tunnel.

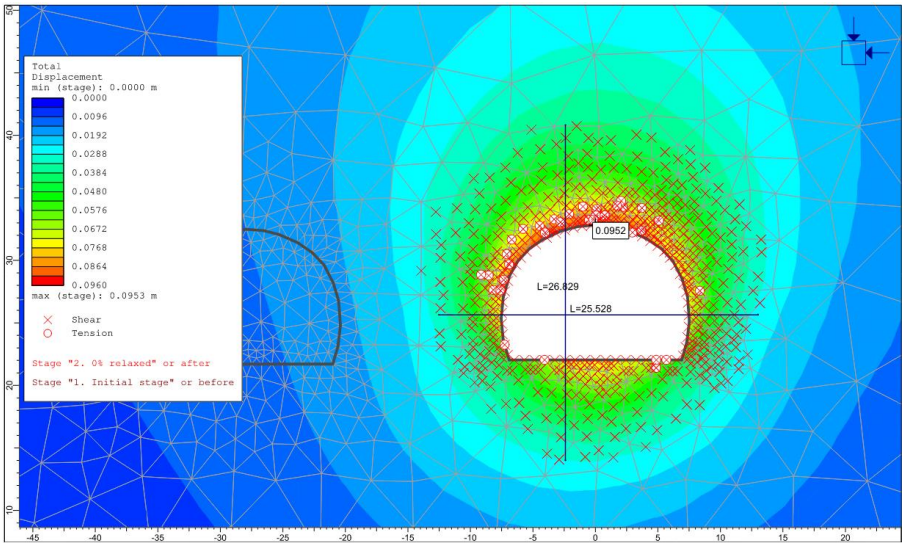


Figure 6: FEA model output with plastic shear points around tunnel opening to determine the radius of plastic zone.

5. Using the radial convergence determined from step 3 and plotting this on the X-axis of the GRC, the percentage of support pressure required for this particular tunnel is found to be approximately 19% of in-situ stress. This means that for this particular tunnel when 1 m is excavated, the tunnel crown will converge approximately 28.1 mm, and consequently approximately 19% of ground stress is transferred to the lining. The summary of the GRC and relaxation at day 1, 3, and 7, which corresponds to advance length of 2 m, 4 m, and 8 m respectively, is being plotted on the same curve on Figure *8*.

6. The degree of relaxation for 1.0 m advance is therefore 1 – 0.19 = 81% (say 80% approximately). This relaxation factor will then be adopted on a second FEA model, applied after excavation and before tunnel lining installed. The bending moment and hoop force extracted directly from the second FEA model will be used to check against the flexural capacity of tunnel lining as shown in Section 3.6.

The phenomenon of ground relaxation is a key observation and concept to represent the behavior of ground-structure interaction for tunnel, especially in rock. This can be *loosely* thought of the percentage of in-situ rock mass loading being transferred to and supported by the lining. In the above example when tunnel is excavated 1.0 m ahead, it will converge an average of 28.1 mm radially, consequently only approximately 19% of the in-situ rock stress will be transferred to the tunnel lining. Hence the lining is subject to approximately 19% of the in-situ rock mass loading; the other 81% has been "relaxed" and dissipated by stress redistribution around the opening and the "softening" of rock stiffness due to deformation.

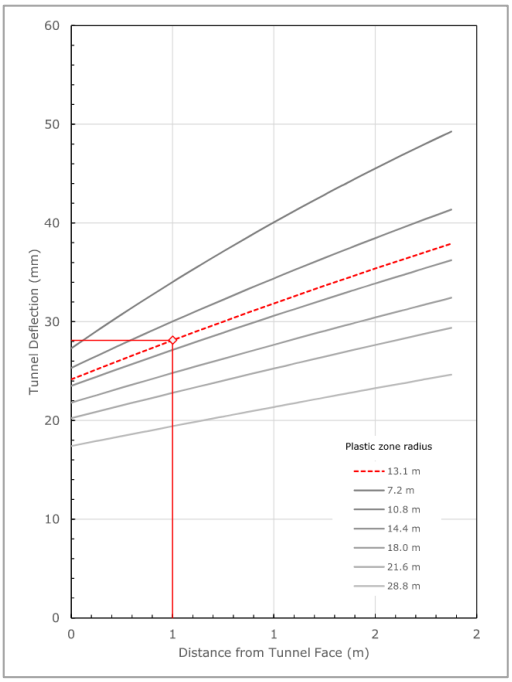


Figure 7: Longitudinal displacement profile at day 0 with excavation length of 1.0 m (recreated based on original curve (Figure 5) and Hoek et al. *(Hoek, et al., 2008)*)

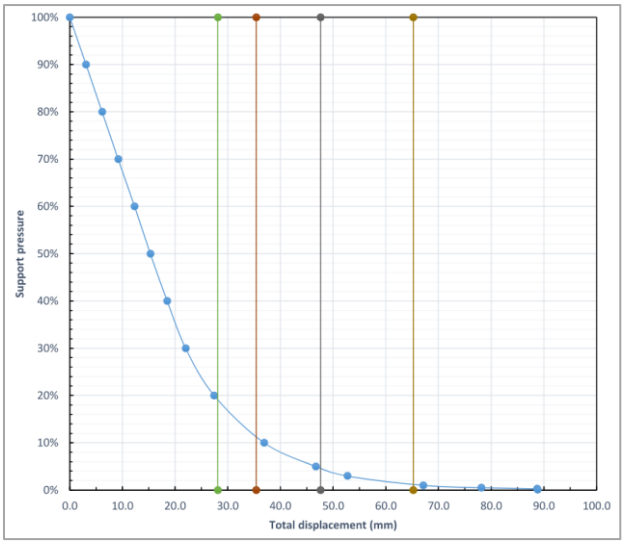


Figure 8: Ground reaction curve (GRC) of tunnel with maximum displacement of tunnel as input to determine the percentage of support pressure.

The degree of relaxation to be adopted in the design of tunnel lining has always been the subject of heavy discussion and shall be verified. Despite having a healthy amount of experience in similar ground and size of tunnel excavation in Hong Kong, and supported by solid scientific theory and data, the perception of relaxation is often based on anything but. The main reason for this is relaxation is often being misunderstood as under-design of the lining simply because the relaxed support pressure is lower in value compared to full unrelaxed load. And designer is often being requested to adopt a lower relaxation factor or just simply ignore it. This cannot be any farther than the truth. Ground stress redistribution and relaxation factor around underground openings is a physical phenomenon that must be properly considered in design and construction of underground space. Failing to do so would result in overdesign with unnecessary additional support requiring additional effort to install. The potential exposure to unnecessary safety risk from ignoring the relaxation of underground space must be avoided by properly considering and including relaxation in the design.

3.5.1 Engineering Model and Rock Mass Parameters for FEA

In setting up the numerical model for the analysis of the tunnel support, an important consideration is the selection of appropriate computer program that suits the subject and purpose of the analysis. The most commonly used geotechnical FE program in Hong Kong is PLAXIS, applicable for design of excavation and lateral support (ELS) and tunnels in soft ground. However, for tunnelling in weak or jointed rock mass, the program *RS2* (previously *Phase2*) is generally more preferable.

The geotechnical parameters for the analysis and design for tunnel in jointed rock mass are heavily depending on the presence of discontinuities and orientation of jointsets, where joint spacings, widths, infillings are some of the critical factors that will alter the behavior of tunnel. The most widely adopted engineering model for jointed rock mass is the failure criterion developed by Dr Evert Hoek and Professor E.T. Brown (Hoek & Brown, 1980) for the design of underground excavation. This criterion was derived from the research findings on brittle failure of intact hard rock by Hoek, combined with model studies of jointed rock mass by Brown. In 2002, there was a major update where the correlation between the model criterion and the geological strength index (GSI) was further improved (Hoek, et al., 2002). There was another major update in 2018 where, among others, the paper discussed the use and application of GSI; expanded guidelines for the selection of disturbance factor *D*; and set out a recommended sequence of calculations for use in applying the Hoek-Brown criterion. The detail derivation of these equations will not be discussed, but in the following sections, the equations for Hoek-Brown failure criterion based on the 2002 version (Hoek, et al., 2002) will be presented, and the numerical values of the model parameters adopted for the FEA will be presented.

The generalized Hoek-Brown criterion can be expressed in the following equation:

$$\sigma_1' = \sigma_3' + \sigma_{ci}\left(m_b \frac{\sigma_3'}{\sigma_{ci}} + s\right)^a \tag{11}$$

Where σ_1' and σ_3' are major and minor principal effective stresses at failure; and σ_{ci} is the uniaxial compressive strength (UCS) of intact rock; a and s are material constant given by the following equations, and m_b is a reduced value of the material constant m_i determined by the following equation:

$$s = e^{\left(\frac{GSI-100}{9-3D}\right)} \tag{12}$$

$$a = \frac{1}{2} + \frac{1}{6}\left(e^{-GSI/15} - e^{-20/3}\right) \tag{13}$$

$$m_b = m_i\, e^{\left(\frac{GSI-100}{28-14D}\right)} \tag{14}$$

The material constants m_i and σ_{ci} can be determined from triaxial tests. The recommended values of m_i for various rock type is summarized in the following table. In Hong Kong, the recommended values of m_i for granitic and tuff rock are 32 and 13 respectively.

The UCS of the jointed rock mass can be obtained by assuming $\sigma_3' = 0$ in the generalized H-B equation, which resulted in the following relationship:

$$\sigma_c = \sigma_{ci} s^a \tag{15}$$

The tensile strength of the jointed rock mass is obtained by assuming $\sigma_1' = \sigma_3' = \sigma_t$ in the generalized H-B equation, which resulted in the following relationship:

$$\sigma_t = -\frac{s\sigma_{ci}}{m_b} \tag{16}$$

Rock type	Class	Group	Texture			
			Coarse	Medium	Fine	Very fine
SEDIMENTARY	Clastic		Conglomerates* (21 ± 3) Breccias (19 ± 5)	Sandstones 17 ± 4	Siltstones 7 ± 2 Greywackes (18 ± 3)	Claystones 4 ± 2 Shales (6 ± 2) Marls (7 ± 2)
	Non-Clastic	Carbonates	Crystalline Limestone (12 ± 3)	Sparitic Limestones (10 ± 2)	Micritic Limestones (9 ± 2)	Dolomites (9 ± 3)
		Evaporites		Gypsum 8 ± 2	Anhydrite 12 ± 2	
		Organic				Chalk 7 ± 2
METAMORPHIC	Non Foliated		Marble 9 ± 3	Hornfels (19 ± 4) Metasandstone (19 ± 3)	Quartzites 20 ± 3	
	Slightly foliated		Migmatite (29 ± 3)	Amphibolites 26 ± 6		
	Foliated**		Gneiss 28 ± 5	Schists 12 ± 3	Phyllites (7 ± 3)	Slates 7 ± 4
IGNEOUS	Plutonic	Light	Granite 32 ± 3 Granodiorite (29 ± 3)	Diorite 25 ± 5		
		Dark	Gabbro 27 ± 3 Norite 20 ± 5	Dolerite (16 ± 5)		
	Hypabyssal		Porphyries (20 ± 5)		Diabase (15 ± 5)	Peridotite (25 ± 5)
	Volcanic	Lava		Rhyolite (25 ± 5) Andesite 25 ± 5	Dacite (25 ± 3) Basalt (25 ± 5)	Obsidian (19 ± 3)
		Pyroclastic	Agglomerate (19 ± 3)	Breccia (19 ± 5)	Tuff (13 ± 5)	

Figure 9: Recommended values of material constant m_i from Hoek *(Hoek, 2023)*.

The modulus of deformation for the rock mass is given by the following equation with unit of *GPa*.

$$E_m = \left(1 - \frac{D}{2}\right)\sqrt{\frac{\sigma_{ci}}{100}} \cdot 10^{((GSI-10)/40)} \tag{17}$$

The two parameters in the H-B criterion equations above, *GSI* and *D*, were introduced to the H-B failure criterion to estimate the reduced rock mass strength in different geological conditions. The *GSI* is more of a descriptive and qualitative representation of the rock mass, which can be estimated from the chart in Figure 10. The parameter *D* is disturbance factor that depends on the degree of damage at the perimeter of the tunnel from blasting works. It varies from 0 for undisturbed in-situ rock mass to 1.0 for very disturbed rock mass.

GSI has been introduced to consider site specific condition, and GSI values for any specific project must be adjusted accordingly. The shaded area in Figure 10 represents the most common range of rock mass quality and *GSI* in Hong Kong.

Due to the fact that ground condition is not discrete and different degrees of weathering is always observed, *GSI* for each project shall always be a range of values to represent any geological variation. The wider the range of *GSI*, the higher the variation of ground condition, and hence the higher the likelihood to encounter worse than expected ground condition. This has been in good agreement among practicing tunnel engineers and engineering geologist. To cover all possible ground condition, the support system for tunnel will be split into different classes (according to the *Q* ranges determined from Section 3.2, and each support classes will be associated with a single *GSI* value for purpose of numerical analysis. And the *GSI* values are calculated from the following equation, first proposed by Hoek et al. (Hoek, et al., 1995), to be used as input to *RS2* FEA.

$$GSI = 9 \ln Q' + 44 \tag{18}$$

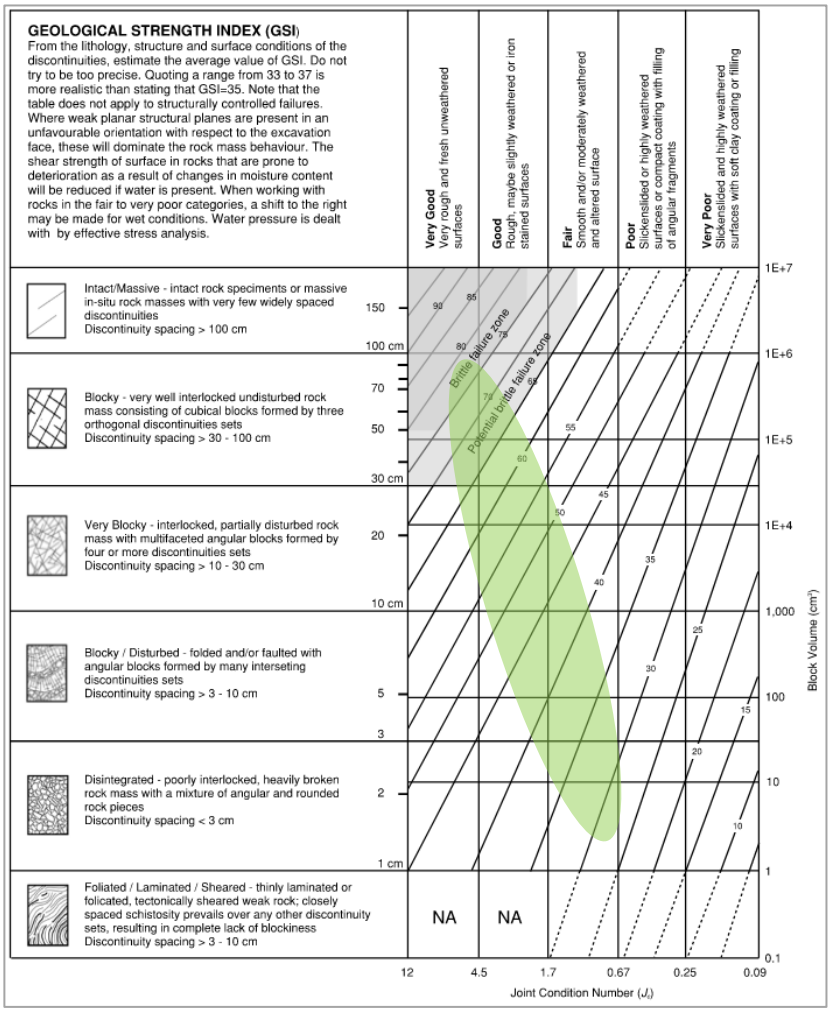


Figure 10: Reproduced geological strength index (GSI) by Cai et al. *(Cai, et al., 2004)* showing common range of GSI for rock in Hong Kong in green shade.

3.6 Structural Capacity of Tunnel Lining

In the last step of tunnel lining design, the structural capacity of tunnel lining is being checked using a separate numerical model (step 6 in Section 3.5). The setting up of the model and stages of analyses are largely the same as the steps described in Section 3.5, except in this FE model, liner structure and rock bolts have been added to the excavation for purpose of design check and optimisation.

Due to the fact that sprayed concrete lining takes time to build up its strength, it is necessary to check intermediate stages or early strength of the sprayed concrete capacity. While concrete is gaining strength, ground load to be supported by the lining also increases gradually. Therefore, in the numerical model, early sprayed concrete strength of 1, 3, and 7-day (with corresponding relaxation values at 1, 3, and 7-day) have been checked, in addition to the final 28-day full strength. The following table summarized the material properties of sprayed concrete in accordance with EC2 (BSI, 2004).

The steps to determine the relaxation factors corresponding to the early strength of the sprayed concrete is the same as the six steps outlined in the previous section, except in step 3, the x-axis value of the load displacement profile chart (correspond to distance from excavated face) are adjusted to reflect the number of days, assuming that daily excavation round length is 1.0 m. The result of the structural check where the state of stresses is plotted against the flexural capacity of the lining (axial force-bending moment diagram) is attached in Figure 11 for each stage.

Table 2: Material properties of sprayed concrete lining

Age (day)	Characteristic compressive strength f_{ck} (MPa)	Elastic Modulus E (MPa)	Poisson's Ratio	Corresponding relaxation factor of ground stress (%)
0	0	3	0.2	80
1	9	13	0.2	90
3	15	16	0.2	96
7	21	18	0.2	99
28	30	22	0.2	100

It can be observed from the four charts that maximum axial force of the lining increases from approximately 900 kPa at day 1 to slightly less than 4,000 kPa at day 28. This increasing trend in the hoop force of the lining correspond well with the increase of stiffness of the lining; whereas the bending moment of the lining remains at or below approximately 50 kNm due to deformation of the lining, which is relatively flexible at 300 mm thick.

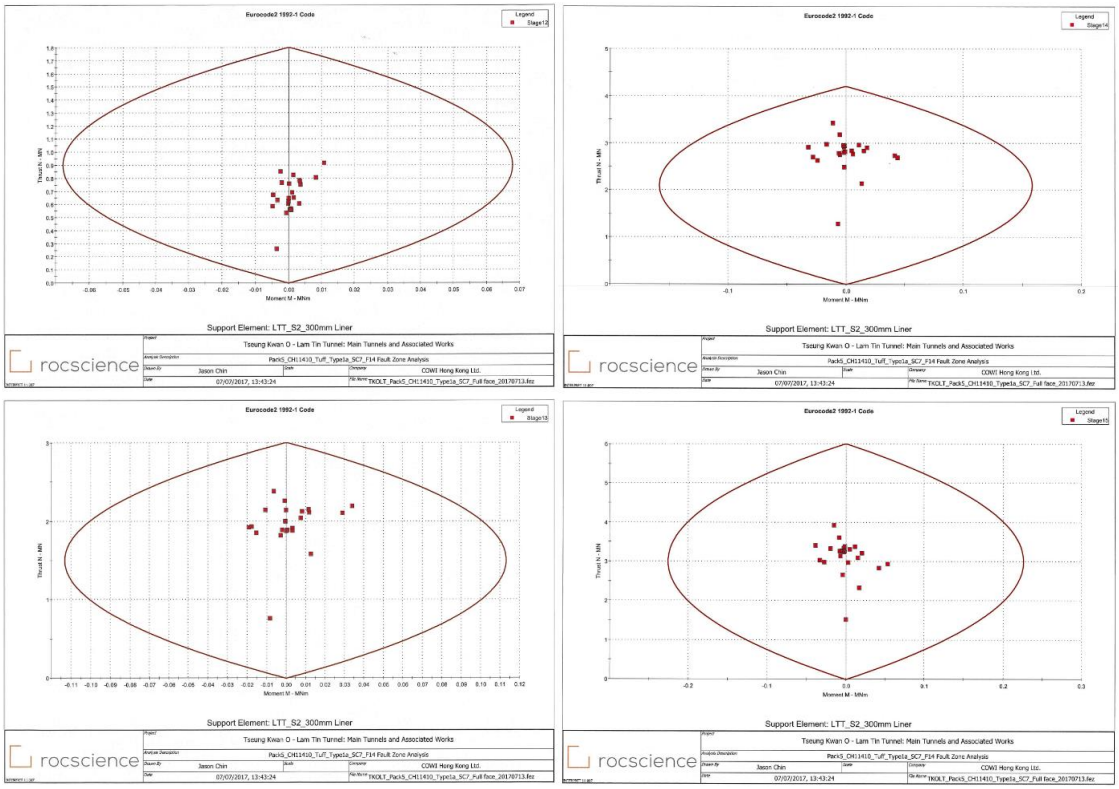


Figure 11: Structural interaction diagram for tunnel lining. Top left: 1-day; bottom left: 3-day; top right: 7-day; bottom right: 28-day strength.

The example and results presented are the final product after numerous rounds of discussion with the contractor in attempt to optimise the design. To provide a safe while economical tunnel support system, it is always more preferable to reduce the thickness of the lining because reduced lining means smaller excavation profile and lower mucking volume. This would have much more impact to the project program compared with adopting lower concrete strength or different excavation staging.

3.7 Unsupported Span and Stand-up Time

The last step of tunnel support design is to determine the corresponding stand-up time of a tunnel with a certain span. In theory this stand-up time can be viewed as the time within which the tunnel will remain self-standing, after which the tunnel will collapse. However, I would advise young engineers that this overly simplified and seemingly easy to use chart is more than just drawing vertical (or horizontal) line to determine the corresponding value but should instead be applied cautiously and not blindly. This is being explained in subsequent paragraphs. Figure 12 is a typical chart I replicated from the original chart from Bieniawski (Bieniawski, 1989) applicable to the example for this paper.

The term "stand-up time" was first used in the late 1950s and further developed and modified by Bieniawski (Bieniawski, 1993). To use this chart, the RMR value is first determined from the equation below proposed by Bieniawski (Bieniawski, 1989). For the example used in this paper, the adopted Q value is 0.05 and $RMR = 17$ calculated from the following equation:

$$RMR = 9 \ln Q + 44 \tag{19}$$

Along the line of $RMR = 17$ there are different combination of unsupported roof span and stand-up time, and different combinations can directly change the decision on method of construction, excavation cycle, tunnel reinforcement system, and duration of the reinforcement system installation. Short unsupported span (short tunnel excavation round length) and long stand-up time would favor construction method that could take longer to excavate (e.g., roadheader, mechanical breaking); while long unsupported span and short stand-up time could favor shorter than allowed excavation round length limited by the duration of sprayed concrete and rock bolts

installation. Therefore, unsupported span and stand-up time must be discussed with the contractor to take into consideration the cycle time and available equipment for the works.

In this project, the unsupported length of 1.0 m (light blue circle in Figure 12) is simply too short for the excavation program, while the unsupported span of 2.5 m (light pink circle) is right at the upper bound line with very short stand-up time, which is impractical to carry out any physical works. It should be cautioned not to adopt the unsupported span right at the upper bound especially in ground with low rock mass quality. This is to avoid potential collapse due to unexpected adverse ground condition, overexcavation of tunnel face, and/or bad workmanship – all of which may result in larger span causing the actual point falling beyond the upper bound of the chart. As such, it is recommended to adopt a boundary line which is slightly lower than the upper bound line (blue line in Figure 12) to minimize the aforementioned risks and fixed the unsupported span at 2.0 m (red circle) with stand-up time of less than 1.0 hour specified.

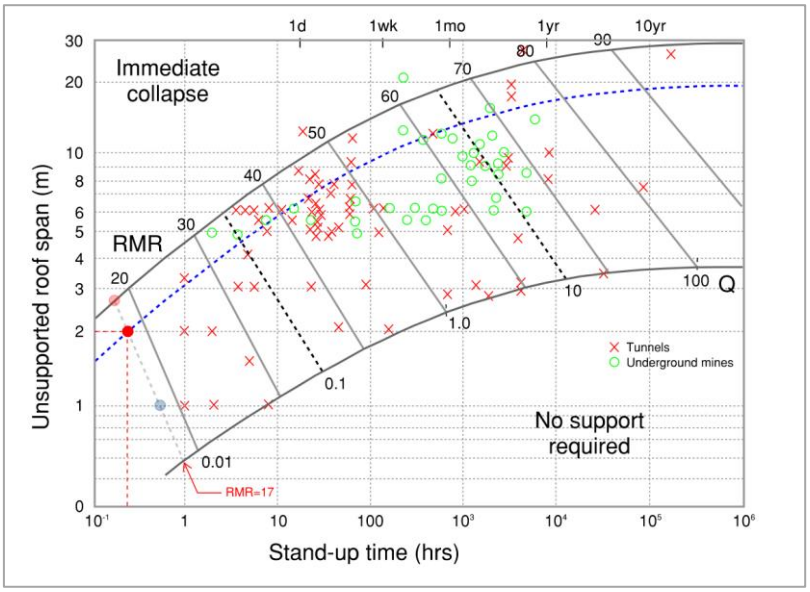


Figure 12: Reproduced unsupported roof span and stand-up time chart from Bieniawski *(Bieniawski, 1989)* showing the adopted excavation round length.

4 CONCLUSIONS

There are many published literatures on tunnel and cavern design in rock, the design process presented in this paper is by no mean the only one, but it is one that has been adopted and accepted in Hong Kong. The design process presented in this paper is intended to be a guideline for new or experienced professionals, and it is supplemented with background theories, detailed examples, practical experience and clarification on limitation and common misunderstandings.

REFERENCES

Barton, N., Lien, R. & Lunde, J., 1974. Engineering Classification of Rock Masses for the Design of Tunnel Support. *Journal of the International Society for Rock Mechanics*, pp. 189-236.

Bieniawski, Z., 1989. *Engineering Rock Mass Classifications: A Complete Manual for Engineers and Geologists in Mining.* Hoboken: John Wiley & Sons.

Bieniawski, Z., 1993. Classification of Rock Masses for Engineering: The RMR System and Future Trends. In: J. A. Hudson, ed. *Rock Testing and Site Characterization - Priciples, Practice and Projects.* s.l.:Pergamon, pp. 553-573.

Bischoff, J. & Smart, J., 1977. *Method of Computing a Rock Reinforcement System Which is Structurally Equivalent to an Internal Support System.* New York, ASCE, pp. 279-284.

BSI, 2004. *BS EN 1992-1-1:2004 Eurocode 2: Design of Concrete Structures.* s.l.:Bristish Standards Institute.

Cai, M. et al., 2004. Estimation of Rock Mass Deformation Modulus and Strength of Jointed Hard Rock Masses Using the GSI System. *International Journal of Rock Mechanics and Mining Sciences,* 41(1), pp. 3-19.

GEO, 2018. *GEOGUIDE 4: Guide to Cavern Engineering,* Hong Kong: CEDD HKGOV.

Grimstad, E. & Barton, N., 1993. *Updating of the Q-System for NMT.* Fagernes, s.n., pp. 46-66.

Hoek, E., 2023. *Practical Rock Engineering.* [Online] Available at: https://www.rocscience.com/assets/resources/learning/hoek/Practical-Rock-Engineering-Full-Text.pdf
[Accessed 2024].

Hoek, E. & Brown, E., 1980. *Underground Excavations in Rock.* London: Institution of Mining and Metallurgy.

Hoek, E., Carranza-Torres, C. & Corkum, B., 2002. *Hoek-Brown Failure Criterion - 2002 Edition.* Toronto, s.n., pp. 267-273.

Hoek, E., Carranza-Torres, C., Diederichs, M. & Corkum, B., 2008. *The 2008 Kersten Lecture: Integration of Geotechnical and Structural Design in Tunneling.* Minneapolis, University of Minnesota.

Hoek, E., Kaiser, P. & Bawden, W., 1995. *Support of Underground Excavations in Hard Rock.* Rotterdam: A.A. Balkema.

Hoek, E. & Marinos, P., 2000. Predicting Tunnel Squeezing Problems in Weak Heterogeneous Rock Masses. *Tunnels and Tunneling International,* 32(11), pp. 45-51.

Kwong, A. K. & Wong, B. M., 2013. An assessment of in-situ rock stress ratio in Hong Kong. *HKIE Transactions,* 20(1), pp. 52-61.

NGI, 2015. *Handbook of Using the Q-system.* Oslo: Norwegian Geotechnical Institute.

Trial Piles with High Percentage GGBS

Kian Y.K. Chiu & Eric H.Y. Sze
Geotechnical Engineering Office, Civil Engineering and Development Department, Government of the Hong Kong Special Administrative Region, Hong Kong SAR, China

ABSTRACT

With a view to reducing carbon emissions, there is a pressing need to promote wider application of low-carbon concrete in construction works. The use of Ground Granulated Blastfurnace Slag (GGBS) as a supplementary cementitious material has been proven effective in reducing the total carbon emission of the concrete production process. While the application of GGBS concrete is not uncommon in the construction of superstructure and precast facades, it is rare to see the use of GGBS concrete in piling works nowadays in Hong Kong. Recent communications with relevant stakeholders revealed a general lack of knowledge of the effects of using GGBS concrete, especially those with high percentage of GGBS, in the construction operation and quality control of piling works. In order to collect more field data and site operation observations in respect of adopting high percentage GGBS in piling works, two full-scale trial piles were constructed with over 75% GGBS replacement level. The entire construction process was carefully monitored and recorded, together with a well-designed testing and monitoring plan, to identify any potential issues during site operation and quality control, and to gain better understanding of the performance of GGBS concrete in-situ. The successful completion of these trial piles would provide technical evidence to support a wider application of GGBS concrete in piling works, thus contributing to the achievement of carbon neutrality in Hong Kong.

1 INTRODUCTION

The use of Ground Granulated Blastfurnace Slag (GGBS), a by-product of the iron manufacturing industry, as a supplementary cementitious material (SCM) has been proven effective in reducing the total carbon emission of the concrete production process by lowering the use of Ordinary Portland Cement (OPC). Taking cognisance of the goal to achieve carbon neutrality under the Hong Kong's Climate Action Plan 2050, there is a pressing need to promote a wider application of low-carbon concrete in construction works.

Since 2012, the General Specification for Civil Engineering Works (GS) published by the Government of the HKSAR has allowed the use of GGBS as SCM in concrete production for public works projects, with a replacement level between 35% and 75% for normal concrete. Since then, GGBS concrete has been used, albeit not very common, in the construction of superstructure and precast facades, etc. The durability aspects of GGBS concrete were studied by Leung & Wong (2011). Kwok & Leung (2023) evaluated the performance of GGBS concrete mixes, which were found generally on-par with OPC concrete mixes and were considered suitable for general civil and geotechnical engineering works.

Despite the proven performance of GGBS concrete, its use is rarely seen in the construction of piles in Hong Kong. Recently, Chu (2023) reported the trial use of GGBS concrete with a replacement level of 50% in deep foundation works under an urban renewal project. Recent communications with relevant stakeholders, including piling contractors and concrete suppliers, etc., have revealed various practical concerns of adopting GGBS concrete with a high replacement level (i.e. more than 50%) in piling works. For example, the potential high adhesiveness of the concrete due to the fineness of GGBS could pose challenges to the tremie

concreting process and the pile casing extraction process. Other hesitations include workability, retention of slump, temperature evolution in the pile, and the long-term strength development have also been discussed.

In view of the general lack of understanding of the effects of using GGBS concrete in the construction operation and quality control of piling works on site, the Geotechnical Engineering Office (GEO) of Civil Engineering and Development Department (CEDD) initiated a series of full-scale trial piling works in 2023 to examine this matter in a systematic manner. The first two trial piles with different GGBS replacement levels were successfully constructed in early 2024. While monitoring work and data interpretation are still in progress, this paper presents some of the key observations made during the construction operation and discusses the preliminary results regarding the performance of GGBS concrete used in these trial piles.

2 TECHNICAL DETAILS OF TRIAL PILES

2.1 The Trial Piles

With the support of the West Development Office of the CEDD, two trial bored piles of 3 m in diameter and 63 m and 52 m in length respectively, namely GGBS-YLS-P1 and GGBS-YLS-P2, with different replacement levels of GGBS were constructed at a site near Lam Tai West Road at Yuen Long South, New Territories. In order to mimic the actual situation of large concreting volume and long concreting time, full-scale trial on concreting of bored piles was proposed. The replacement level of GGBS for GGBS-YLS-P1 was 75%, which is the ceiling of the allowable portion of the total cementitious content in the GS. For GGBS-YLS-P2, in view of the success of the first trial pile, a slightly higher replacement level of 80% was adopted in the second pile. Construction of the two trial piles was completed in February and March 2024 respectively. The technical details of these two trial piles are summarised in Table 2.1. Figure 2.1(a) gives an overview of the trial piling works.

Table 2.1: Technical details of GGBS-YLS-P1 and GGBS-YLS-P2

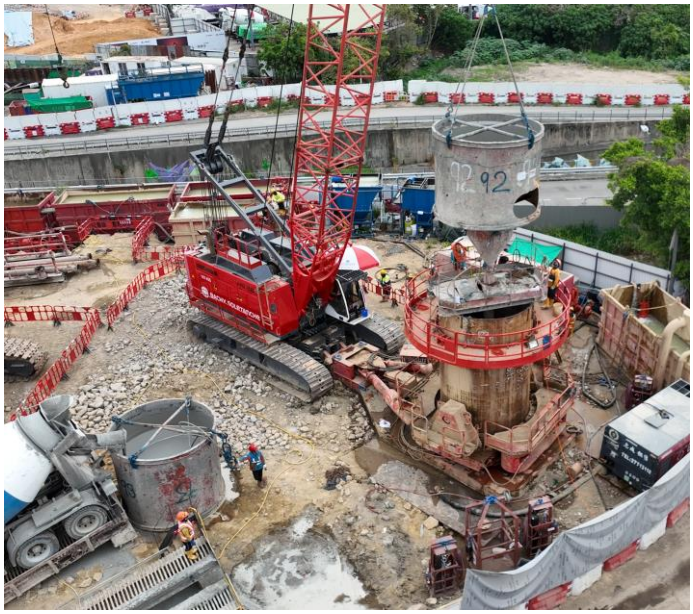
	GGBS-YLS-P1	**GGBS-YLS-P2**
Pile shaft diameter	3.0 m (2.85 m in rock)	3.0 m (2.85 m in rock)
Pile shaft length	63 m (300 mm toe-in into rock)	52 m (300 mm toe-in into rock)
Steel reinforcement ratio	1.8% to 2.6%	1.8% to 2.6%
Proportion of GGBS to total cementitious content in concrete	75%	80%
Concrete grade strength	60D/20	60D/20
Designed slump value	200 mm	200 mm

2.2 Testing and monitoring

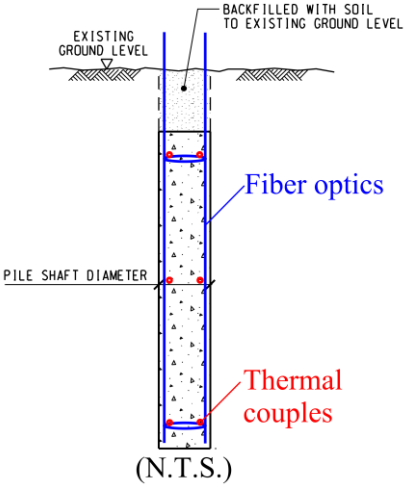
To properly identify any potential construction issues during site operation and quality control, the entire construction process, including tremie concreting and pile casing extraction, was carefully monitored and recorded. The conventional construction, testing and monitoring procedures of a typical bored pile apply to the two trial piles, which include slump test, cubes for 28-day compressive strength tests, sonic logging test, interface core drilling, full-length core drilling and associated unconfined compressive strength tests of concrete cores. The following additional testing and monitoring were also proposed to better understand the performance of tremie concrete with high percentage GGBS:

- slump retention tests at every 2 hours for a period of 10 hours after the commencement of concreting works for the retention of workability;
- extra concrete cubes for 3-, 7-, 10-, 14-, 56- and 90-day compressive strength tests for capturing the strength development from early age to long term;
- additional full-length core drilling for unconfined compressive strength (UCS) test at 56^{th} and 90^{th} day;

- Temperature Rise Evaluation Test (TRET) for evaluating the heat development properties; and
- temperature evolution monitoring along pile shaft and across pile diameter using thermal couples and fiber optics (see Figure 2.1(b)).



(a)



(b)

Figure 2.1: (a) Overview of the trial piling works; (b) Instrumentation arrangement within the trial pile

3 RESULTS AND DISCUSSIONS

3.1 Laboratory trials and plant trials

To provide basis for selection of suitable concrete mixes for the trial piles, laboratory trials were conducted for mixes with GGBS content ranging from 65% to 85% (see Table 3.1). Compressive cube strength tests and slump tests were conducted, and the results of which met the acceptance criteria (i.e. 60 MPa and 200 mm respectively). For control, concrete mix with 25% Pulverised Fly Ash (PFA) content was also tested.

Table 3.1: Summary of concrete mixes tested in laboratory trials

Concrete Grade [Design Slump]	GGBS Content (SCM %)	Water-Cement Ratio	Aggregate-Cement Ratio	Average Cube Strength [Average Slump value]	Selected for Plant Trials	Trial Pile ID
Grade 60D/20 [200 mm]	65%	0.34	2.99	81 MPa [220 mm]	-	-
	70%	0.34	2.98	68 MPa [210 mm]	-	-
	75%	0.34	2.98	69 MPa [220 mm]	Yes*	GGBS-YLS-P1*
	80%	0.35	2.98	66 MPa [235 mm]	Yes**	GGBS-YLS-P2**
	85%	0.34	2.98	70 MPa [235 mm]	-	-
	25% PFA	0.35	2.96	84 MPa [200 mm]	-	-

* *The plant trial of 75% GGBS concrete was normal and the same mix was applied to the trial pile GGBS-YLS-P1.*

** *During the plant trial of 80% GGBS concrete, a premature stiffening of the concrete ("false set") was observed which occurred within a short period after mixing (about 5 to 15 minutes). As a result, a new concrete mix with another set-retarding admixture was adopted, which was also applied to the trial pile GGBS-YLS-P2.*

3.2 Tremie concreting and pile casing extraction

One of the major concerns of using GGBS concrete in piling works is the high adhesiveness of the GGBS concrete with a high replacement level (i.e. ≥ 50%). This issue poses significant challenge to the tremie concreting process (e.g. longer concrete pouring, clogging of tremie pipe) as well as the pile casing extraction process (e.g. difficulty in casing extraction, up-dragging of steel cage). Therefore, these processes were carefully examined during the construction of trial piles.

Figure 3.1 compares the observed different degrees of adhesiveness of the concrete mixes with and without GGBS. While PFA concrete could slide down the plate relatively smoothly when the plate was placed upright, GGBS concrete appeared more adhesive to the plate.



(a) (b)

Figure 3.1: Different degrees of adhesiveness of concrete observed during slump tests: (a) 80% GGBS (GGBS-YLS-P2); (b) PFA concrete (observed at another site)

Comparing with the typical concreting time of a bored pile with PFA concrete (observed at another site), a longer pouring time of concrete from the concrete bucket to the tremie pipe was observed when a high percentage of GGBS was adopted (see Figure 3.2). This is particularly notable for 75% GGBS concrete. The reduced concrete pouring time observed in 80% GGBS was probably due to the use of a different set-retarding admixture (see Section 3.1), which could have made the concrete less adhesive.



(a) (b)

Figure 3.2: Pouring of concrete from concrete bucket to tremie pipe and the approximate observed pouring time: (a) 75% GGBS (GGBS-YLS-P1); (b) 80% GGBS (GGBS-YLS-P2)

As reflected by the contractors and the concrete supplier, other concreting stages (e.g. concrete pouring from the mixing plant to the agitator of trucks at the plant, and the transfer from the agitator of trucks to the concrete bucket at the site) could have also taken a slightly longer time due to the adhesiveness of GGBS concrete, especially at the early stage of the construction works due to a lack of experience with the new concrete mix. As experience accrued, the situation was found to be improved.

Other aspects of the construction process for both trial piles were found to be normal. Despite the relatively higher adhesiveness of the GGBS concrete, no clogging of the tremie pipe was observed. There was also no difficulty during pile casing extraction. As reported by the piling contractor, comparing with the typical operation when OPC or PFA concrete was used, no extra power was required to extract the casing, and no up-dragging of the steel cage was observed throughout the process.

The construction process was reviewed among different parties, including resident site supervision staff, contractors and concrete supplier. In hindsight, there are various measures to mitigate the prolonged concrete pouring time when a high percentage of GGBS is used. For examples, the construction site arrangement can be suitably adjusted to tighten the loading/unloading cycle of the concrete trucks, more manpower for field concrete testing and more machinery / equipment (e.g. additional crane, concrete bucket, ramp for concrete trucks to unload) could be deployed on-site (subject to site availability). From the material point of view, further study to tackle the increased adhesiveness of GGBS concrete could be explored. In this study, the observed improved performance of 80% GGBS concrete could be attributed to the use of a different set-retarding admixture. With the developing concrete admixture technology, there is room for further alleviating the adhesiveness issue of GGBS concrete. Despite the above-mentioned issues, for sites where the concreting volume is less (e.g. smaller pile diameter, shorter pile depth), such added concrete pouring time should not be critical to the construction process.

3.3 Testing and monitoring

For workability, apart from carrying out slump tests for each truck of concrete, slump retention test was also carried out every 2 hours for a period of 10 hours due to the typically long concreting time for bored pile construction. To summarise, the measured average slumps for both trial piles fulfilled the design requirements. The slump for 75% GGBS concrete dropped from 250 mm to 240 mm at the 10th hour (of a 4% decrease), while that for 80% GGBS concrete remains at 250 mm after 10 hours. This may probably be due to the use of a different set-retarding admixture for 80% GGBS concrete (see Section 3.1).

For strength, by the time of preparing this paper, only the concrete cube compressive strength test results for GGBS-YLS-P1 up to the 28-day were available (as shown in Figure 3.3).

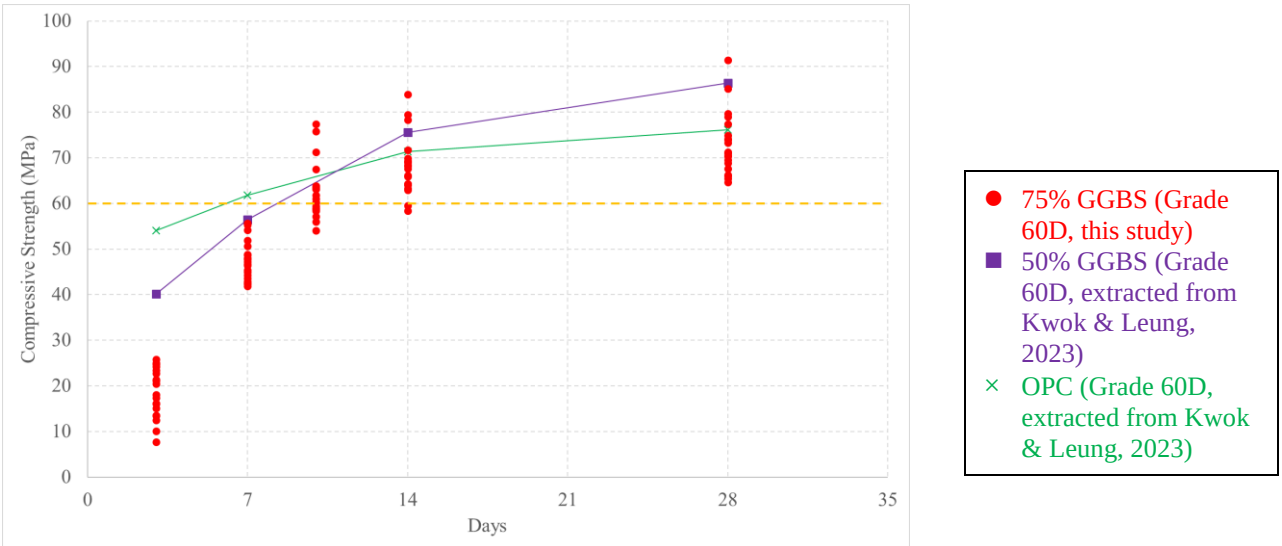


Figure 3.3: Compressive strength test results (up to 28-day) for 75% GGBS content (GGBS-YLS-P1 of this study) in comparison with 50% GGBS concrete and OPC concrete (both results extracted from Kwok & Leung, 2023)

For early strengths, the measured 3-day early age compressive strengths of 75% GGBS concrete were found to be about 11% to 36% of the measured mean 28-day strength. In comparison, those of 50% GGBS concrete and OPC concrete were found to be 47% and 71% respectively (results presented by Kwok & Leung (2023), which are also plotted in Figure 3.3). This indicates a slower strength development at the early age for 75% GGBS concrete as compared with 50% GGBS concrete and OPC concrete. It should, however, be remarked that the GGBS concrete mix used in this study was specifically designed for a slower initial setting time (for tremie concrete in bored pile construction) as compared with the concrete tested in Kwok & Leung (2023). The strength gain for GGBS concrete and OPC concrete became more comparable at 7th day and after.

As can be seen from the test results of 75% GGBS concrete, there were some variations among the measured concrete cube strengths at different ages. For 3-day strength, the variation is not unexpected as the effect of workmanship on preparing, dismantling and testing the cubes became more prominent when the cubes were still at a very low strength. For 28-day strength, the calculated standard deviation was within the tolerance specified in the GS. Further work will be carried out to evaluate the strength variations when more test data (e.g. further concrete cube tests, UCS tests of full-length concrete cores) become available later.

To verify the concrete cube strengths and supplement the strength evolution with time, especially for longer term, full-length core drilling will be carried out for the trial piles at 28th, 56th and 90th day for core strength testing. For viewing the concrete core quality, Figure 3.4 shows the concrete cores extracted from GGBS-YLS-P1 after 28 days of concreting. Further results will be studied and presented later.



Figure 3.4: Full-length concrete core drilled from GGBS-YLS-P1 after 28 days of concreting

For temperature, in-situ measurements of the concrete in the constructed trial piles using both thermal couples and fiber optics (see Figure 2.1(b)) are still on-going by the time of preparing this paper. Preliminary results indicate that the measured temperature rise was up to about 30°C and the peak temperature of about 75°C was reached on the 3rd day after concreting. More monitoring results would be collected and analysed for better understanding the temperature evolution of in-situ GGBS concrete along the pile shaft and across the pile diameter in future.

4 CONCLUDING REMARKS AND WAY FORWARD

4.1 Key observations

Two full-scale trial piles (3 m diameter, over 50 m long) using tremie concrete with high percentage GGBS (75% and 80% GGBS replacement levels respectively) were successfully constructed in Hong Kong. The construction works, including the tremie concreting process and the pile casing extraction process, were carefully monitored. These trial piles were also systematically tested and monitored with a view to better

understanding the performance using GGBS concrete in piling works. While some monitoring work and data interpretation are still in progress, key observations from the preliminary results of this study are summarised below:

(a) The cube compressive strength, workability and its retention of both 75% and 80% GGBS concrete met the design requirements of tremie concrete for trial piles (Grade 60, 200 mm slump). Longer-term strength of in-situ concrete cores up to 90 days is being monitored and will be reported in the future.

(b) Compared with PFA concrete, higher adhesiveness was observed in GGBS concrete rendering a generally longer pouring time during the concreting process. Different means to alleviate this issue has been discussed in the paper.

(c) Other aspects of the construction process for both trial piles were found to be normal, e.g. no clogging of the tremie pipe, no difficulty in pile casing extraction and no up-dragging of the steel cage was observed throughout the process.

(d) Temperature evolution along the pile shaft and across the pile diameter is being monitored using both thermal couples and fiber optics, and the results will be reported in the future.

4.2 Way forward

The trial piles presented in this paper form part of the trial pile study programme of the GEO in the Northern New Territories of Hong Kong. To facilitate the design and construction of pile foundation works in meta-sedimentary rocks, which are commonly found in the Northern Metropolis, another series of trial piles are being undertaken at various sites. Full-scale loading tests using bi-directional loading equipment installed at the pile base will be carried out for these trial piles. The test results will be studied with a view to enhancing the foundation design guideline for meta-sedimentary rocks. The study findings once available will be reported in the future.

ACKNOWLEDGEMENTS

This paper is published with the permission of the Head of the Geotechnical Engineering Office and the Director of Civil Engineering and Development, the Government of the Hong Kong Special Administrative Region of the People's Republic of China. The support from the West Development Office of the CEDD in undertaking the trial piling works is appreciated. The authors would like to thank the Public Works Central Laboratory and Housing Department for the technical advice and support.

REFERENCES

Chu K.Y. 2023. Adoption of Ground Granulated Blast Furnace Slag (GGBS) Concrete in Deep Foundation (abstract and presentation). *Annual Concrete Forum 2023 - Towards Climate-Friendly Concrete Construction*. HKSAR.

Kwok J.Y. & Leung J.C.K. 2023. Evaluation of the Performance of GGBS Concrete Used in Civil and Geotechnical Works. *Proceedings of the HKIE Geotechnical Division 43rd Annual Seminar - Towards a Smart-Green-Resilient Geo-Future for World-class City Development*, 292-304.

Leung P.W.C. & Wong H.D. 2011. Final Report on Durability and Strength Development of Ground Granulated Blastfurnage Slag Concrete. *GEO Report No. 258*. HKSAR.

Case Study of Real-time Monitoring of Groundwater Levels and Rainfall Data for a Hillside Terrain Site Formation Works for Public Housing at Pok Fu Lam in Southern District, Hong Kong in Year 2023

Gary S.H. Kwok & Chester S.C. Lam
Asia Infrastructure Solutions Limited, Hong Kong

ABSTRACT

A record-breaking extreme rainfall event happened in early September 2023 raised the public concern on the design safety of infrastructural works and geotechnical works to withstand the inclement weather. Real-time monitoring has become an effective tool nowadays to provide accurate and comprehensive information to record both the rainfall data and groundwater level for design review for civil engineering projects. This paper is to picturize the impact of extreme rainfall event on the groundwater table by case study on a hillside site formation project at Pok Fu Lam in Year 2023 via observations from the real-time rolling rainfall depth together with groundwater level. The groundwater levels have risen 3m to 18m from their long-term average level during the extreme rainfall event which the groundwater level rose with unprecedented magnitude especially for those located near existing natural drainage line identified from the aerial photo interpretation study. Superposition effect is also observed from two successive extreme rainfall events in September and October. Recommendations are then suggested to respond to the findings observed from the real-time monitoring information.

1 INTRODUCTION

1.1 Background

In recent decades, global warming turns the weather of the subtropical zone, like Hong Kong, becoming more familiar to the topical weather than before. Although the code of practices for drainage design recently updated the rainfall increase to 16.0% due to climate change for design life reached the end of 21st Century, the extreme weather becomes more frequent and keeps breaking the extreme weather record which threatens the factor of safety for the infrastructure design.

This case study provides valuable insights into geotechnical engineering for site formation works especially for the case with existing nature drainage lines. The analysis of real-time monitoring data offers a comprehensive understanding of the groundwater behavior and its relationship with rainfall events.

2 RAINFALL ANALYSIS

2.1 Rainfall in Hong Kong

Generalized extreme value (GEV) distribution is commonly adopted to estimate magnitude of rainfall extreme events for design purposes which is well defined in Stormwater Drainage Manual which adopted the hourly rainfall data was recorded at Hong Kong Observatory (HKO) headquarter since 1884. It is revealed

that the extrapolation of design rainfall intensity for very long return periods, says 200 years, would be based on limited amount of historical data which are clustered at the side with shorter return periods. As such, the uncertainty at high levels would increase drastically (Tang et al. 2011).

The tendency of extreme rainfall events continues to increase, as reflected in the HKO data shown in Figure 1. To address this concern, the Drainage Services Department (DSD) Stormwater Drainage Manual (SDM) 2018, with Corrigendum No. 1/2022 & 1/2024, and the Geotechnical Engineering Office (GEO) technical guidance note TGN-30 (issue no. 3) recommend increasing the mean rainfall intensity given by the IDF curves by 16.0% and 28.1% to incorporate the climate change effects projected up to the end of the 21st century. Overall, the predicted mean rainfall intensity by storm constants by TGN-30 (issue no. 3) is about 1.19 to 1.96 times higher than the one predicted by DSD SDM (Corr. 1/2024) with climate change effect projected up to the end of the 21st century for Intensity-Duration-Frequency (IDF) relationship curves of HKO headquarters, with time of concentration ranged from 1 to 240 minutes and return period from 2 years to 1000 years.

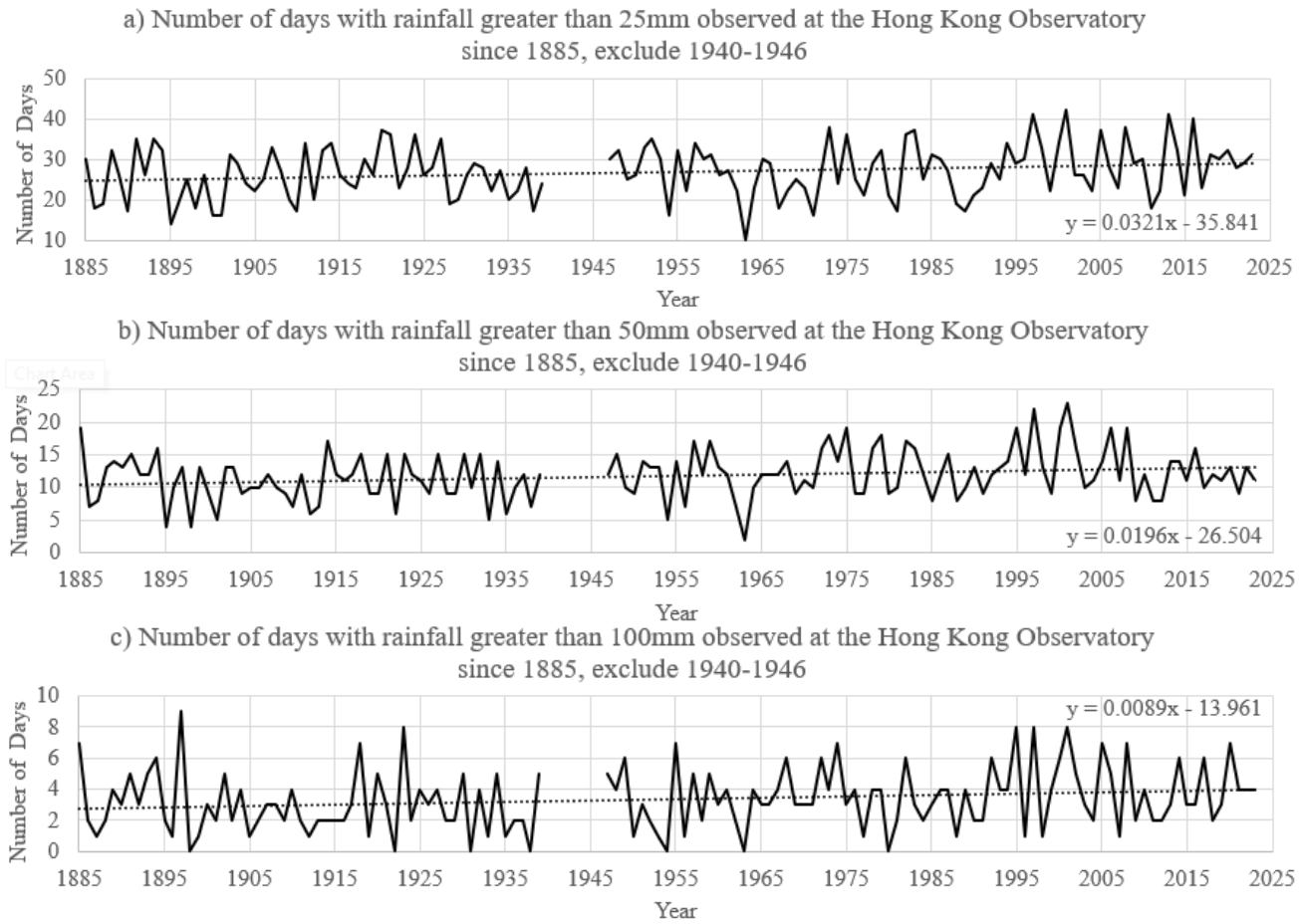


Figure 1: Number of Days with rainfall greater than (a)25mm, (b)50mm and (c)100mm observed at HKO since 1885, exclude 1940-1946 (HKO, 2024)

2.2 Summary of Rainfall in 2023

The year 2023 was identified as the warmest year on record, with an established El Niño event that persisted throughout the year. The annual total rainfall in Hong Kong reached 2774.5mm, representing a 14% increase compared to the 1991-2020 normal of 2431.2mm. There are 47 rainstorm warning signals, consisting of 37 amber, 8 red and 2 black, recorded in 2023. Notably, the rainfall concentrated in wet season in 2023, i.e. 1st April to 31st October, which contributed the annual rainfall depth from 95.4% (Yuen Long) to 98.1% (Islands District) for all districts in Hong Kong such that the discussion of dry season in 2023 would be neglected in following study.

The rainfall pattern in 2023 generally followed the trend of the previous 30 years, with the exception of a record-breaking event in early September. The measured rainfall varied across different districts, with Tai Po and Lantau Island recording the highest rainfall throughout the year. However, the extreme event in early September had a significant impact on the Hong Kong Island, particularly the Southern District and Eastern District. Over 400 mm of rainfall was recorded in many parts of the territory, with the Eastern District and Southern District of Hong Kong Island receiving over 800 mm of rainfall on 7th – 8th September. These two days contributed an average of 16.5% to the annual rainfall depth, with a range of 8.7% (Tuen Mun) to 22.3% (Eastern District).

Table 1: Summary of Record-breaking Events in Year 2023 (HKO, 2024)

Record-breaking Events (since records began in 1884)	Date / Period	New HKO Record
Highest 1-Hour Total Rainfall (All Months)	7 September 2023 23:00 to 24:00	158.1 mm
Highest 2-Hour Total Rainfall (All Months)	7 September 2023 23:00 to 8 September 2023 01:00	201.0 mm
Highest 12-Hour Total Rainfall (All Months)	7 September 2023 22:00 to 8 September 2023 10:00	605.8 mm

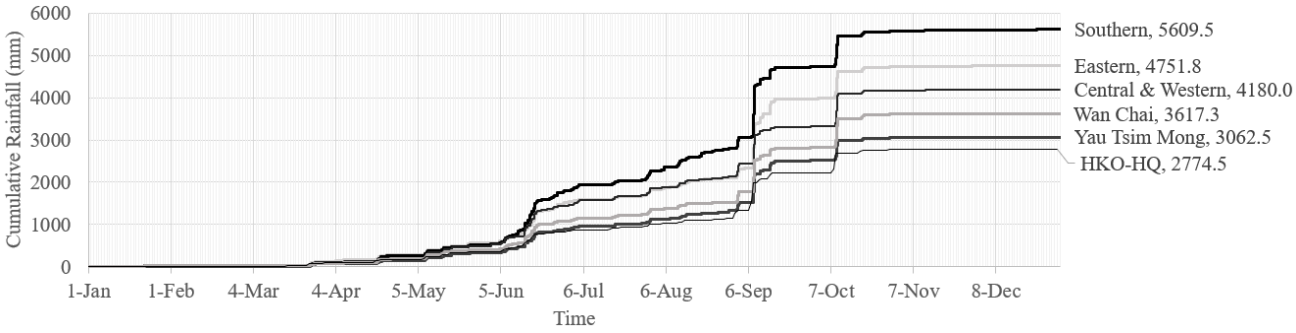


Figure 2: Rainfall Record in Different District in Year 2023 (i-lens, 2024 and HKO, 2024)

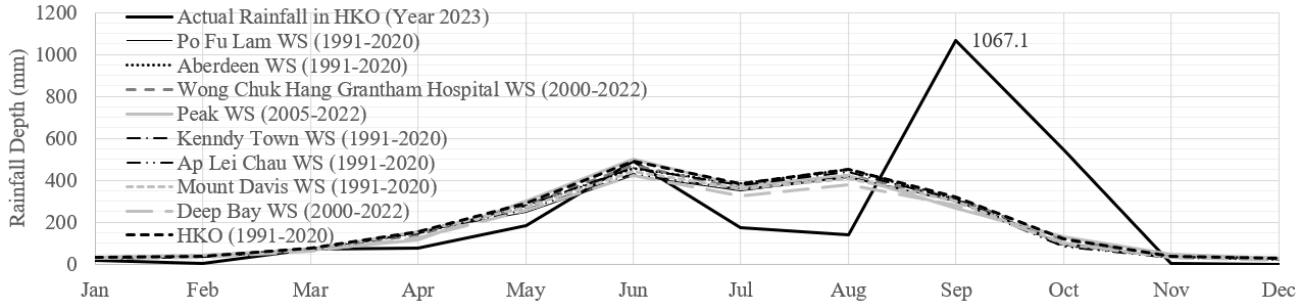


Figure 3: Comparison of Rainfall Record of HKO in 2023 amongst the Average Rainfall Record in Various Weather Stations in Central & Western and Southern District of Hong Kong Island (i-lens, 2024 and HKO, 2024)

To compare with the extreme rainfall depth information from DSD SDM, as illustrated in Figure 4, it is revealed that the rolling rainfall record of the 7th – 8th September event far exceeded the required design return period of 50 years for the urban drainage branch system in the area of concern. This suggests that the surface water may spill over the drainage system, resulting in potential localized flooding issues, especially in areas near the natural drainage line in the territory.

In this study, the real-time respond of the groundwater level is to be illustrated to provide insights how the extreme rainfall affects the groundwater table in hillside territory. Notwithstanding, there is no clear correlation between the return period of rainfall depth and the return period of observed groundwater level.

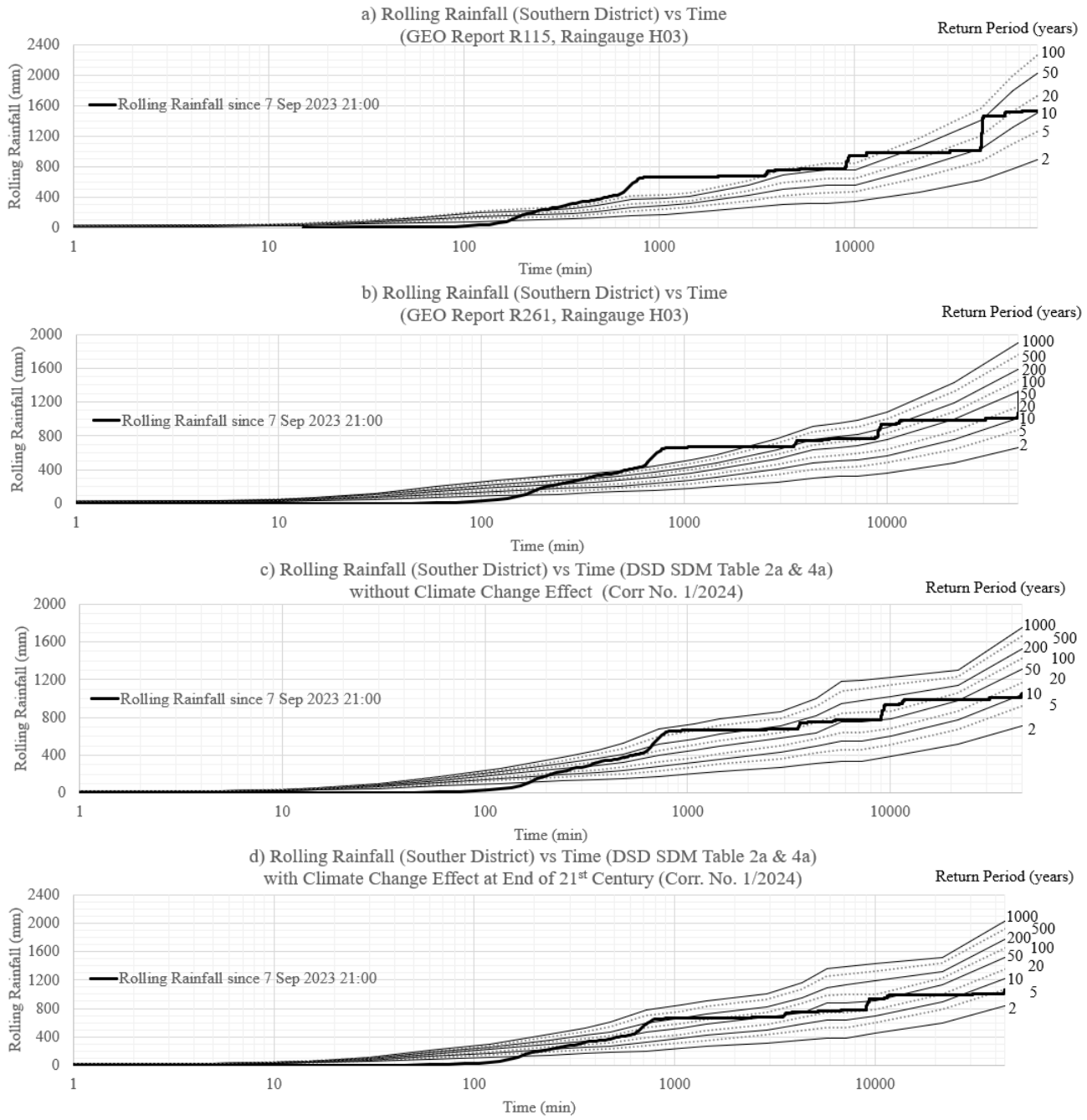


Figure 4: Comparison of Rolling Rainfall Record of Southern District to (a) GEO Report R115 Rain Guage H03; (b) GEO Report R261; (c) DSD SDM 2018 (Corr. No. 1/2024) and (d) DSD SDM 2018 (Corr. No. 1/2024).

3 CASE STUDY FOR REAL-TIME MONITORING

3.1 Background

The study area is located at the south-west of Hong Kong Island of size 2.6-hectare for hillside site formation works which is up to 67m high rising from approximately +85mPD at the toe on the northern flank up to +152mPD at the crest, with slopes generally dipping at approximately from 10° to up to 30°. The site is underlain by the fine ash vitric tuff and an NNE-SSW orientated band of coarse ash crystal tuff is present to the west of the study area. Both the fine ash vitric tuff and coarse ash crystal tuff are assigned to the Ap Lei Chau Formation of the Repulse Bay Volcanic Group.

The study site is characterized by a south-west facing hillside with predominantly planar slopes between two rounded spurlines. The crest area has a gentle incline (<15°), which becomes steeper (20°–30°) at mid-slope, and the slopes are gentler (<15°) towards the toe of the study area. A small depression is present at the lower central part of the study area, containing slightly steeper slopes, up to 30° locally. The depression is the head of a valley up to 45 m long and 45 m wide. The study area is covered with thick vegetation, with trees and bushes on the gentler slopes, and ferns and grasses on the upper slopes.

The majority of rock outcrops and boulders found within the study area are composed of coarse ash crystal tuff with local exposures of fine ash tuff limited to the small depression at the lower central part of the study area. Intermittent rock outcrops of coarse ash crystal tuff, with moderately to closely spaced joints, are exposed along the spurline of the northern side of the study area. The rock is found to be weak to moderately strong, greyish brown, highly to moderately decomposed. Exhumed corestones of very strong, slightly decomposed, coarse ash crystal tuff are located on the southern spurline. The largest is approximately 3m high and 2.4m wide. The corestones are subangular to subrounded and relatively blocky due to the widely spaced joints. The exposed subrounded boulders of coarse ash crystal tuff may also be locally displaced exhumed corestones now part of the general slope colluvium.

Saprolite of extremely weak, moist, orangish brown, completely decomposed coarse ash crystal tuff is exposed at the upper part of the study area and forms a stiff, moist, brown, mottled white, sandy silt/clay soil. Residual soil is exposed at the crest of the study area and in the lower part of the spurline at the northern side of the study area where it is composed of stiff to very stiff, moist, orangish brown, sandy silt/clay.

The upper part of the regional catchment of the study area has been modified by the formation of extensive agricultural terraces. These terraces have been formed by localized cutting and filling activities and associated with the construction of small rubble walls. Stepped terraces range from 1.5m to 4m wide but are typically 2m to 3m wide and 0.5m to 1.5m high. For drainage estimation, the surface characteristics of the catchments involve excavated surfaces, paved surfaces and steep grassland natural slopes where the majority of site area is underlain by an impervious rock layer. The groundwater monitoring system consisted of 36 standpipes or piezometers strategically placed across the site area and these devices were equipped with real-time monitoring sensors to accurately record groundwater fluctuations in 5-minute intervals to match with rain gauge data in 15-minute intervals for Southern District for reference.

3.2 Observations

Except for the extreme events recorded on 7th – 8th Sep & 9th Oct and site-specific local activities in affected areas, all measured groundwater levels remained steady which fluctuated within 2m throughout the year. The groundwater level did not rise significantly despite that several red rainstorm intensity events are encountered from May to July 2023; however, the extreme rainfall events in September and October incurred significant changes in groundwater levels. The groundwater levels rose with range from 3 to 5m for the majority of the monitoring points during this record-breaking event whereas the groundwater level of remaining monitoring points generally rose 5 to 8m from its long-term average especially for those located near existing natural drainage lines.

Apart from the above, the groundwater level raised up to approximately 18m from its long-term average for piezometer BP05P was highlighted as shown in Figure 5. This unprecedented observation is most likely incurred by combination of superposition effect of two successive extreme rainfall events and surface water collected along the drainage line. Overall, once groundwater levels rise, they eventually return to the long-term average level which the rate of decreasing of groundwater levels are generally consistent after rainfall events. Given the consistent decreasing behavior, if another heavy rainfall occurs before full recession to the long-term average, groundwater levels will start from the prior elevation and potentially reach a new maxima measurement point exceeding the previous peak by superposition as illustrated in Figure 5. On the contrary, the groundwater levels would only rise by independent rainfall event if it has returned to its long-term average level as illustrated in Figure 6. It suggests that the recession rate of groundwater level interferes in the degree of superposition for continuous rainfall events which the superposition effect may incur unprecedented rise of groundwater resulting in catastrophic consequence.

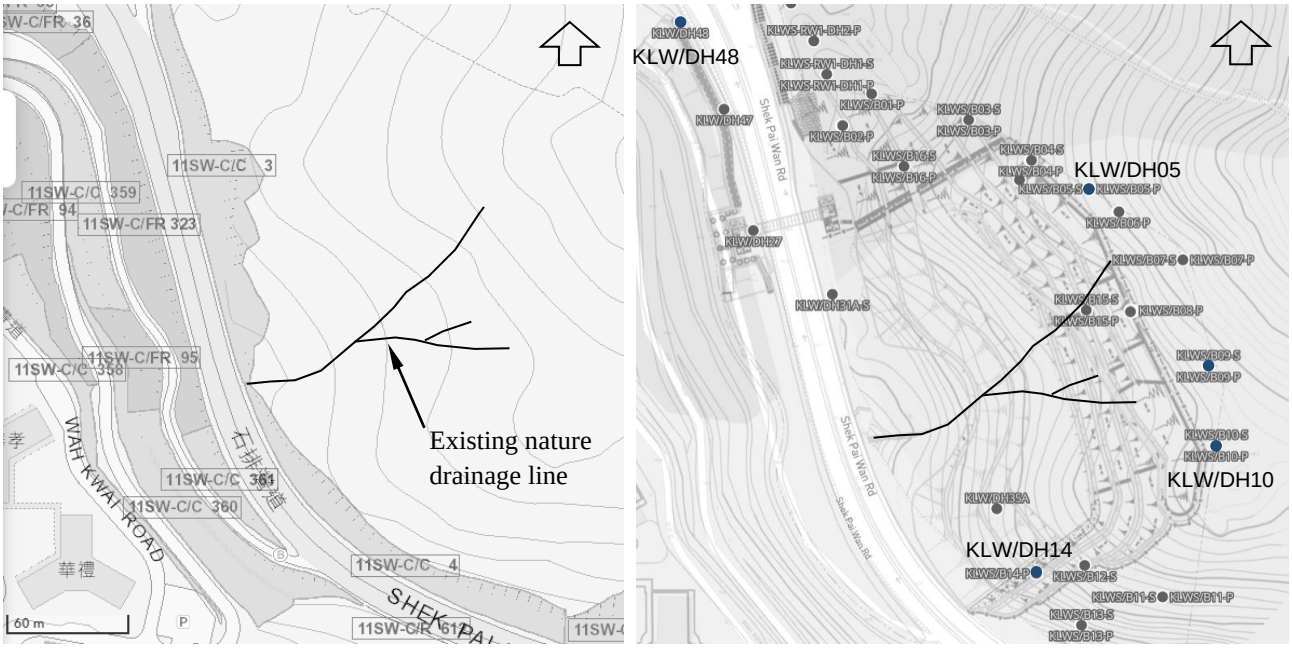


Plate 1: Location Map and Groundwater Monitoring Plan

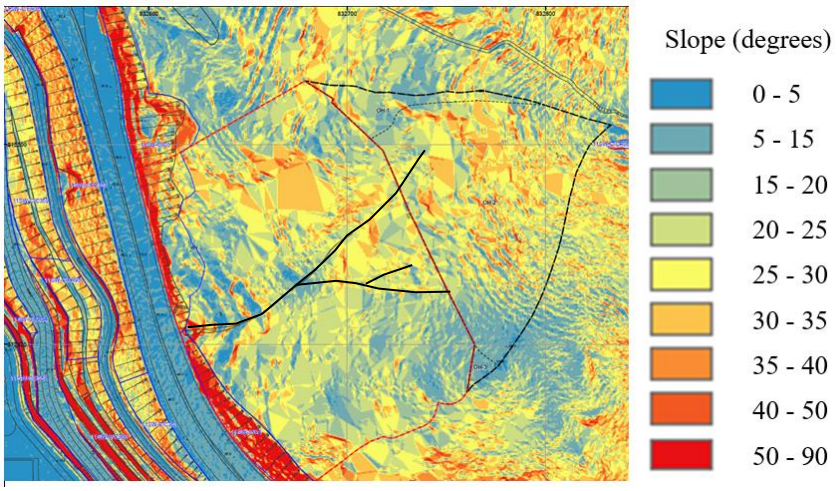


Plate 2: Slope Angle Map

The permeability of the soil layers in the study area ranged from 5.4E-6 m/s to 1.8E-7 m/s, as measured by in situ falling head permeability tests. The decreasing rate of groundwater level after extreme events ranged from 7.4E-5 m/s to 4.9E-6 m/s, as observed from real-time monitoring. The falling rate of groundwater levels after extreme events was found to be consistent with the permeability of the soil layers in the affected areas.

There is a consistent groundwater flow from the crest to the toe of the hillside study site due to gravity. The measured groundwater level was found to be higher than the measured piezometric head in the same borehole during extreme events, as illustrated in Figures 9 and 10. This indicates the existence of groundwater flow after heavy rainfall and suggests that there are no damping effects or low permeability obstacles in the influenced areas. The rate of groundwater level falling was observed to be similar after two black rainstorm events, despite the dropping pattern being disturbed by another amber rainstorm event and red rainstorm event.

The rises of groundwater levels are influenced by various factors, including site topography, geological profile, site geometry, rainfall intensity and duration, and site activities. For instance, a rise of groundwater level was recorded at BP10P on 3rd Sep due to site activities nearby, which slightly modified the groundwater flow in the affected area. However, only some of the measured groundwater levels were affected by the

rainfall dated 14th Sep, suggesting that the rise of groundwater is more likely to be observed near existing natural drainage lines.

Considering spatial variability in rainfall, autonomous monitoring points are advisable to quantify rainfall-groundwater relationships at specific sites. Attention should be paid to site peripheries and interiors to identify drainage lines, which influence potential for sudden groundwater rises. Notably, groundwater level increases do not proportionally correspond to rainfall intensities, as infiltration effects introduce temporal lags before levels change. Continuous monitoring provides insights into the complex interplay between precipitation inputs and subsurface responses over varying conditions.

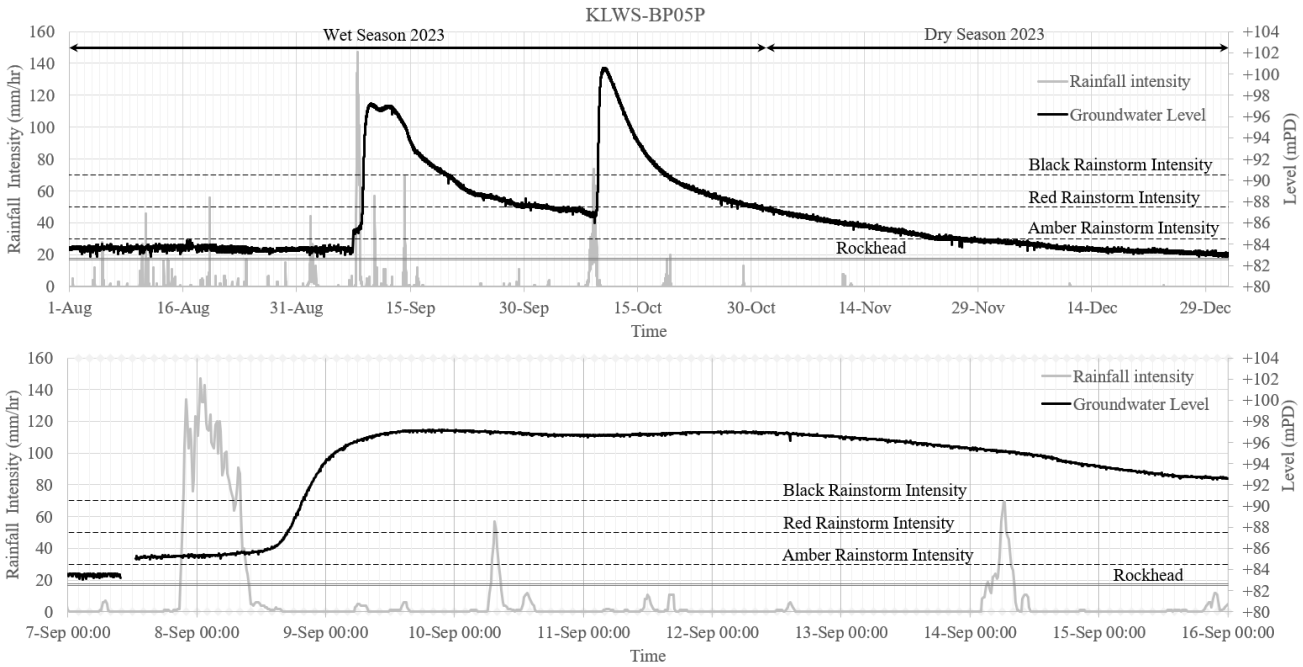


Figure 5: Real time monitoring groundwater level compared with rain gauge information at Southern District at BP05P with ground level at +108.01mPD and piezometer tip level at +82.77mPD

The lead time for the rise of groundwater level from the rainfall varies from 1.6 hours to 28.8 hours in the sloped ground profile in Pok Fu Lam South site with mean of 10.7 hours amongst 15 piezometers or standpipes. Both piezometric head and measured groundwater level rise at the same time at the beginning of extreme rainfall event except the standpipe reading is generally found to be higher than piezometer reading. The piezometric head then will drop to its long-term average together with the measured groundwater level as shown in Figure 9 and Figure 10. In general, the variation of the lead time is believed to be governed by the topography of the site, the permeability of soil profiles, aquifer characteristics, saturation of aquifer and the depth of soil stratum thereat. The soil stratum acted as a de facto water storage tank which the groundwater may rise rapidly provided that the outlet rate (drains) is far less than the inlet rate (infiltrations).

Apart from those piezometers/standpipes located inside the site area, monitoring point DH48 is located on the crest of a fill slope 11SW-C/FR323 on the westbound carriageway of Shek Pai Wan Road. The response of the groundwater is relatively rapid compared with those located on the crest of excavated area of main site which the falling rate of groundwater level after the extreme event is approximately 7.4E-5 m/s. The monitoring record indicates that the groundwater kept steady unless high rainfall intensity with relatively long duration happened. Notwithstanding, 5m rise of groundwater level was observed for some hours which design review for the design groundwater level of the slope feature may be required for those extreme rainfall event.

This observation of measured groundwater level of DH48 raised the concern for a sudden rise of groundwater level which may impact the accuracy of determination of actual design groundwater level for a hillside slope feature involving nature drainage line nearby if no Halcrow bucket are installed at the monitoring points.

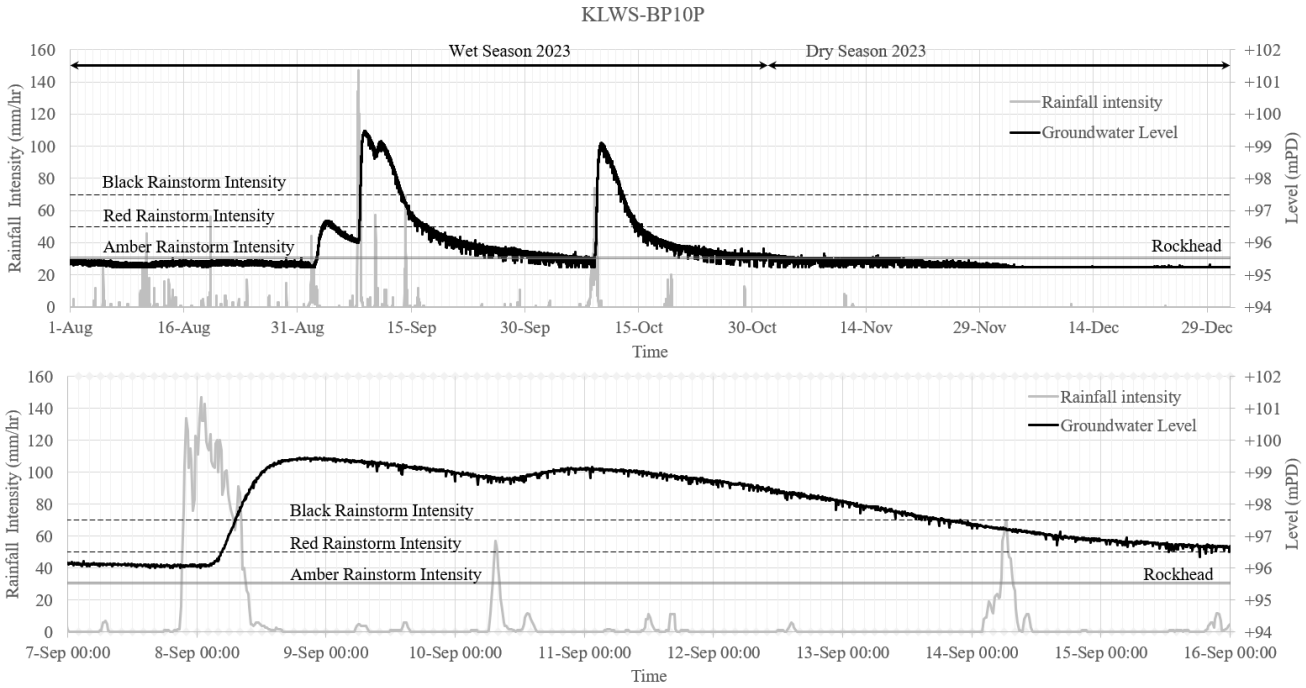


Figure 6: Real time monitoring groundwater level compared with rain gauge information at Southern District at BP10P with ground level at +102.57mPD and piezometer tip level at +95.14mPD

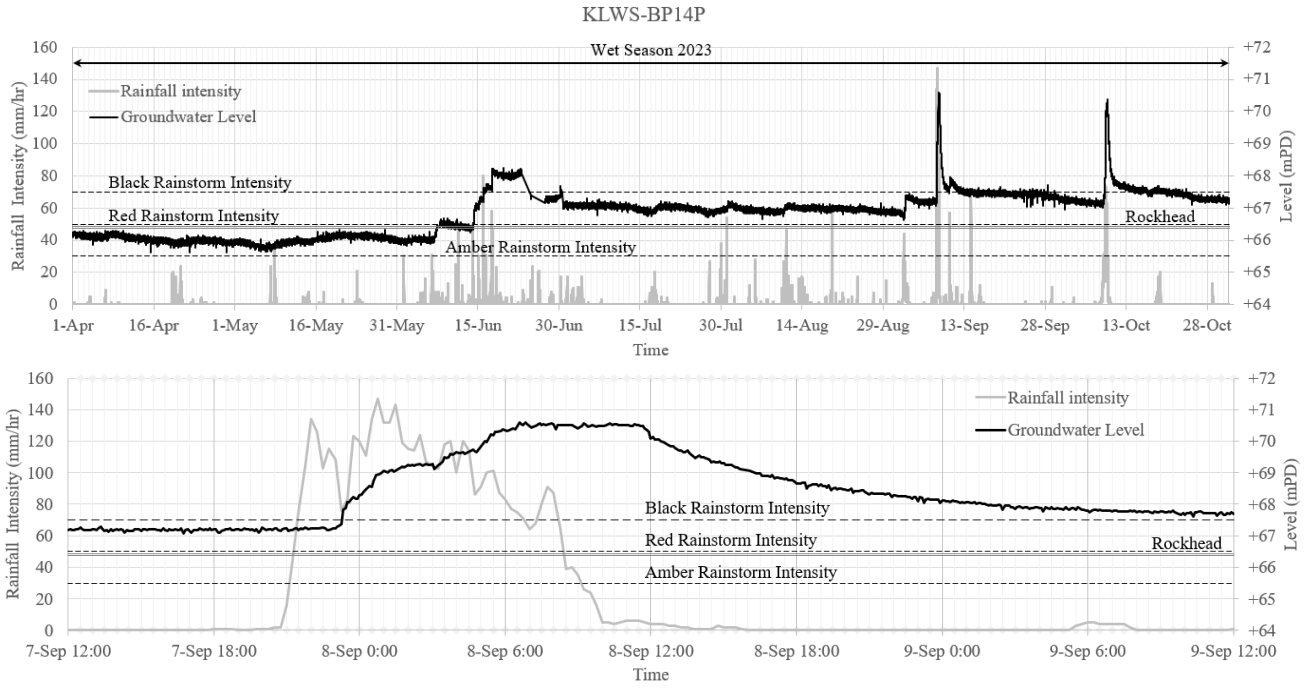


Figure 7: Real time monitoring groundwater level compared with rain gauge information at Southern District at BP14P with ground level at +73.23mPD and piezometer tip level at +65.53mPD

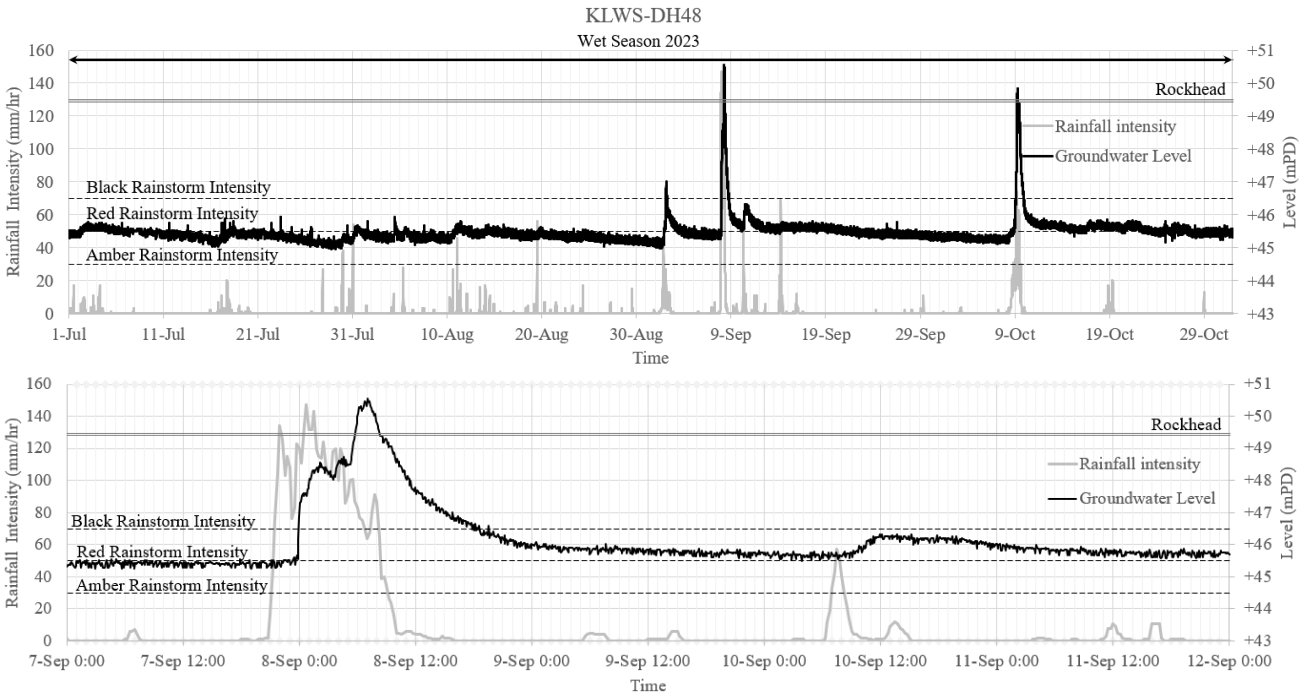


Figure 8: Real time monitoring groundwater level compared with rain gauge information at Southern District at DH48 with ground level at +56.70mPD and piezometer tip level at +43.62mPD

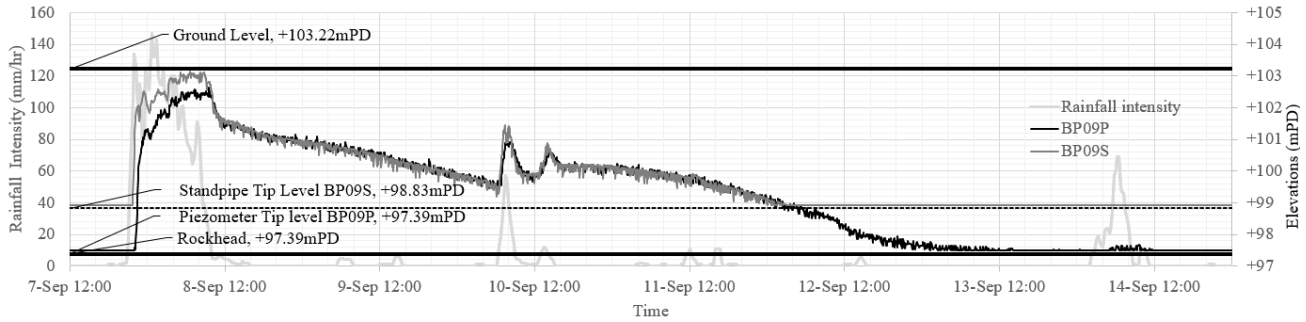


Figure 9: Real time monitoring groundwater level compared with rain gauge information at Southern District at BP09P (Piezometer) and BP09S (Standpipe)

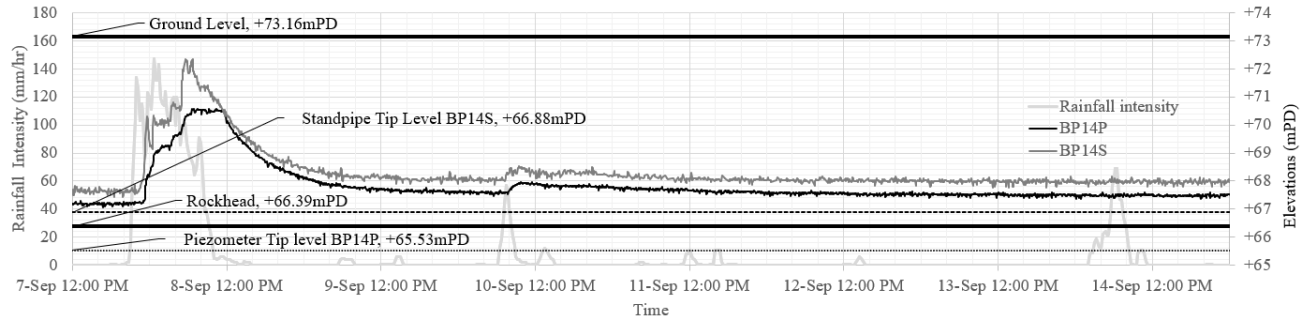


Figure 10: Real time monitoring groundwater level compared with rain gauge information at Southern District at BP14P (Piezometer) and BP14S (Standpipe)

Kaolins was first found in Nov 2023 at the southern portion of the study site during bulk excavation. Further to the following up additional ground investigation fields works for kaolins, it is concluded that kaolins are randomly distributed on the southern corner of the study site. The field works study indicated that up to 7.5m length persistent, shallow dipping, rough undulating rough planar kaolin-rich zone of completely to highly decomposed tuff contains relatively think (55mm to 70mm) veins or stringers of white, firm sandy clay occurs sub-parallel to the surface of Grade II/III rock.

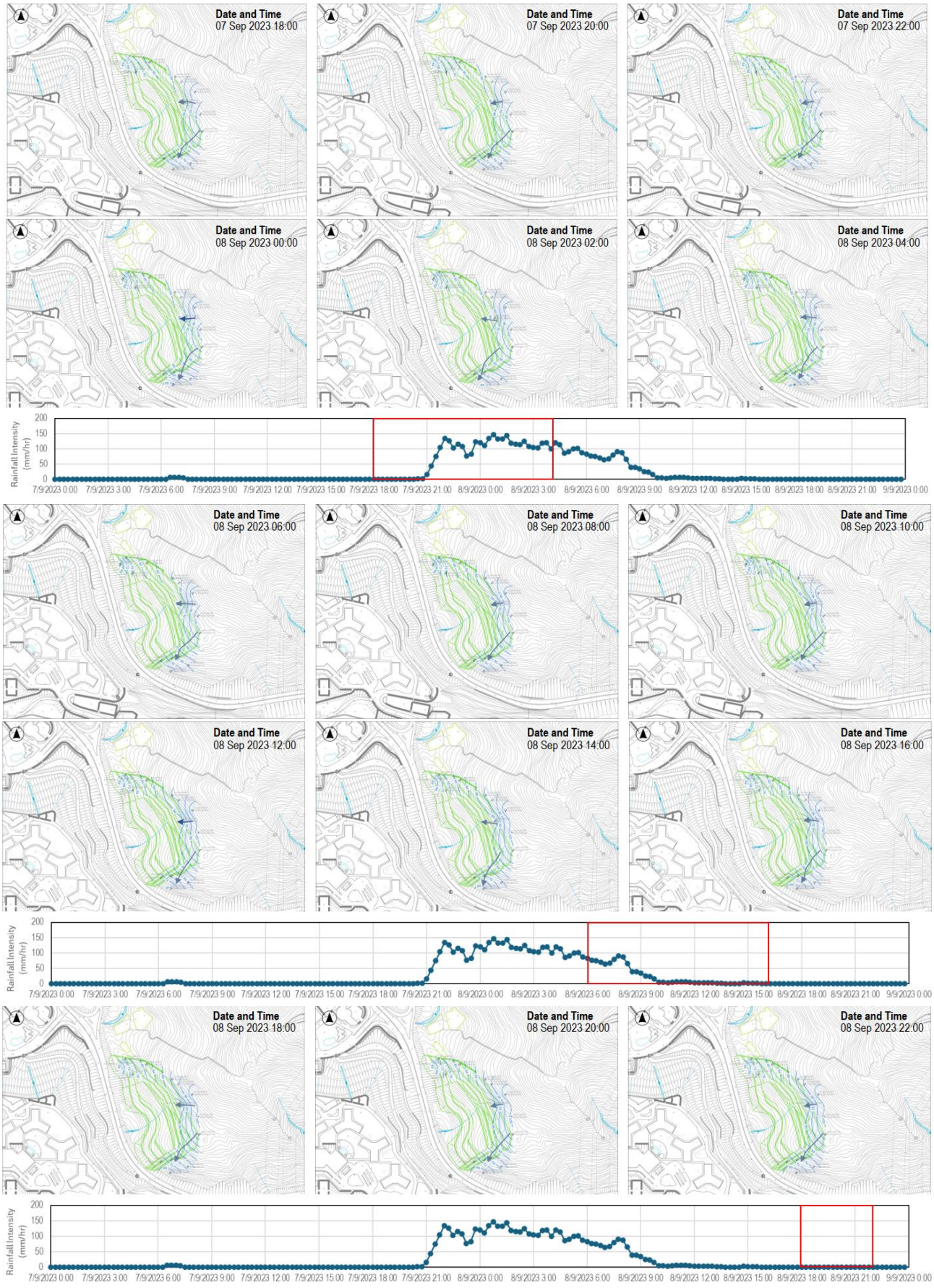


Figure 11: Groundwater contour map and flow direction during the extreme event at 7-8 Sep 2023 with rainfall intensity



Plate 3: Thin veins or stringer of white, firm sandy clay occurs sub-parallel to the surface of grade II/III rock

LiDAR survey was then deployed to identify the existence of potential cavities in the study area to justify the impact to the ground-water hydrology. The LiDAR scanner confirmed that there are three observed voids of size 1.5m wide, 0.5m thick with 4m long identified as natural cavities with same orientation. The field study reveals that the transportation of solutes and fines produced as a by-product of in situ weathering rock masses by intergranular flow of groundwater which may result in formation of those voids. Notwithstanding, the groundwater monitoring record from piezometers and standpipes of BP14 located at southern corner of the site indicated that the damping effect of such cavities are negligible as piezometric head is synchronized with the groundwater level measured by standpipe as shown in Figure 10.

Additionally, the groundwater contour map revealed that the flow directions are quite consistent, as shown in Figure 11. The flow direction changes of groundwater between 18:00 on 7th Sep and 22:00 on 8th Sep were found to be insignificant, even with an observable rapid rise of the groundwater table. These findings suggest that the presence of randomly distributed thin layers of kaolins may not significantly affect ground hydrology in this study area.

3 RECOMMENDATIONS

It is recommended to consider the Factor of Safety (FOS) for slope stability design by introducing the concept of the "Extreme Highest Groundwater," with a defined return period of rainfall, says 1:1000 years, to eliminate the risk under extreme events. The defined return period of rainfall for the “Extreme Highest Groundwater” can be varied up to the satisfaction of geotechnical engineer to suit the needs of different sites especially for those with drainage lines to balance the consideration of economical cost and practicality in civil works design. Meanwhile, the above concept was adopted in the Pok Fu Lam site to demonstrate the stability of retaining structures with FOS at 1.1 for 1000 years rainfall return period to mitigate the risk under the extreme conditions.

Automated monitoring system with intervals of 10 to 15 minutes for measuring rainfall and groundwater changes for geotechnical design is found to be adequate and it provides sufficient information for analysis to verify the design assumption of design groundwater levels and justify the possibility of sudden rise of groundwater level in the subsurface. Nevertheless, it is crucial to thoroughly examine both the periphery and interior of the site to identify the presence of drainage lines including all natural rivers, streams and the former riverbed by aerial photo interpretation study and site survey to mitigate all the potential risks incurred by the sudden rise of groundwater level for sloping terrain. Should real time monitoring be impracticable to be installed, Halcrow buckets may become an alternative solution to record the historical measured highest groundwater level for design concerns. Notwithstanding, technology nowadays such as “Smart Site Safety System” not only record the geotechnical data to the designer for reviewing but also send warning message to frontline staff for if the pre-defined Alert-Action-Alarm values are met.

4 CONCLUSIONS

The extreme event for heavy rainfall becomes more frequent. The average lead time for the rise of groundwater level from the rainfall 10.7 hours in the sloped ground profile in Pok Fu Lam South site. The groundwater levels near natural drainage lines should be handled with care and the superposition effect for extreme rainfall events may lead to catastrophic consequences in design concern. Real time monitoring device or Halcrow bucket is highly recommended to record the historical highest measured groundwater level for those monitoring points located near to the existing natural drainage line for design concern.

ACKNOWLEDGEMENTS

Special thanks to the project team of the CEDD Project CV/2020/01 including but not limited to the Client - Civil Engineering and Development Department, the Consultant - Ove Arup & Partners Hong Kong Limited, the Contractor - China Harbour – China Geo Joint Venture and the Contractor Designer – Asia Infrastructure Solutions Limited for the supports of this study.

REFERENCES

Campbell, S.D.G., Parry, S. 2001. *Report on the Investigation of Kaolin-rich Zones in Weathered Rocks in Hong Kong. GEO Report No. 132.* Geotechnical Engineering Office, HKSARG.

Drainage Services Department. 2018. *Stormwater Drainage Manual 5th Edition*. Hong Kong SARG.

Evans, N.C., Yu, Y.F. 2001. *Regional Variation in Extreme Rainfall Values. GEO Report No. 115,* Geotechnical Engineering Office, HKSARG.

Franks, C.A.M., Campell, S.D.G., Shum, W.W.L. 1997. *Assessment of Geological Features Related to Recent Landslides in Volcanic Rocks of Hong Kong Phase 2B – Aberdeen Study Area. GEO Report No. 67,* Geotechnical Engineering Office, HKSARG.

Fugro Scott Wilson Venture. 2013. *Review of the 3 August 2006 Landslide incident on Slope No. 11SW-C/FR319, No. 131 Pok Fu Lam Road. GEO Report No. 279.* Geotechnical Engineering Office, HKSARG.

Geotechnical Engineering Office. 2004. *GEO Technical Guidance No. 4 (TGN 4) Guidelines on Recognition of Geological Feature Hosting, and Associated with, Silt- and Clay-rich Layers Affecting the Stability of Cut Slopes in Volcanic and Granite Rocks*. Geotechnical Engineering Office, HKSARG.

Geotechnical Engineering Office. 2023. *GEO Technical Guidance No. 30 (TGN 30) Updated Intensity-Duration-Frequency Curves with Provision for Climate Change for Slope Drainage Design*. Geotechnical Engineering Office, HKSARG.

HKO. 2024. *Website http://hko.gov.hk/* . Hong Kong Observatory, HKSARG.

i-lens. 2024. *Website https://i-lens.hk/hkweather/*

Knill, J., GEO. 2006. *Report on the Shum Wan Road Landslide of 13 August 1995. GEO Report No. 178.* Geotechnical Engineering Office, HKSARG.

Lee, R.W.H., Law, R.H.C. 2022. *Review of the Practice on Slope Surface Drainage Management. GEO Report No. 359,* Geotechnical Engineering Office, HKSARG.

Lo, F.L.C., Law, R.P.H., Ko, F.W.Y. 2022. *Territory-wide Rainfall-based Landslide Susceptibility Analysis. GEO Report No. 364,* Geotechnical Engineering Office, HKSARG.

Premchitt, J., Lam, T.S.K., Shen, J.M., Lam, H.F. 1992. *Rainstorm Runoff on Slopes. GEO Report No. 12,* Geotechnical Engineering Office, HKSARG.

Tang, C.S.C., Cheung, S.P.Y. 2011. *Frequency Analysis of Extreme Rainfall Values. GEO Report No. 261,* Geotechnical Engineering Office, HKSARG.

Yang, H., Lohmann, G., Lu, J., Gowan, E.J., Shi, X.X., Liu, J.P., Wang, Q.A. 2020. Tropical Expansion Driven by Poleward Advancing Midlatitude Meridional Temperature Gradients. *Journal of Geophysical Research*: *Atmospheres.* 125:16.

Digital twin visualization of distributed fibre optic strain data for a high-performance early warning system

R.G. Laver
Varadise Limited, Hong Kong
Y.F. Leung
Hong Kong Polytechnic University, Hong Kong

ABSTRACT

Unexpected collapse of civil assets can be mitigated by implementing structural health monitoring. Distributed Fibre Optic Strain Sensing (DFOSS) is a favoured monitoring solution comprising a fibre optic cable installed on the structure, connected to a special analyser to return accurate real-time strains along the entire cable. DFOSS is particularly suited for uninterrupted asset monitoring because it can detect events that discrete sensors would fail to register. The cable is also inexpensive and durable. Despite this, DFOSS has yet to be employed commercially in Hong Kong. A key barrier to commercial adoption is the lack of an accessible platform to assist in making informed timely decisions based upon streamed DFOSS data. This paper presents a design to integrate DFOSS data into a digital twin platform to satisfy this need. Specific features of the integration deliver value to the user, including 4D visualization, BIM model superposition, dashboard charts, alert management, and functions to aggregate data and filter noise. Application of the DFOSS integration is showcased by visualizing data from a DFOSS installation at a deep excavation in Hong Kong, demonstrating that construction-induced strains can be visualized to facilitate responsive decision-making. The integration represents a critical step towards industry procurement of DFOSS.

1 INTRODUCTION

This paper describes the integration of two technologies: Distributed Fibre-Optic Strain Sensing (DFOSS) and digital twins.

1.1 DFOSS Systems

A DFOSS system is a sensor used to measure strain. The sensor comprises a fibre optic cable attached to the structure of interest. A continuous profile of strain is obtained by shining a laser down the cable and interpreting the backscatter. DFOSS is particularly suited for long-term safety-critical strain measurements, such as structural health monitoring of aging infrastructure and slope failure. Continuity of measurement opens the possibility of detecting localized strain development anywhere along the cable, which can extend for tens of kilometres. Measurements can also be made in real time, and the cable is long-lasting.

1.2 Digital Twins

A digital twin is a virtual representation of a real-life counterpart. A twin typically connects to real-time sensors and other data sources to maintain synchrony with reality, making Internet-of-Things (IoT) connectivity a key component.

In simulating the physical world, a digital twin enables prediction and optimization. They also assist decision-making by combining data from multiple sources. Digital twins are used widely in many industries, including manufacturing, healthcare, aerospace and energy. In civil engineering, digital twins are made of both the built and natural environments. Inputs typically include data from Building Information Modelling (BIM), ground investigations, photogrammetry, 3-D scans, site records and sensors.

1.3 Digital Twin Integration of DFOSS

DFOSS has yet to be adopted by the Hong Kong construction industry, despite demonstrating clear benefits for structural health monitoring. Adoption can be accelerated by showing the value of DFOSS data in informing key decisions. Integrating DFOSS into a digital twin contextualizes the data so that it can deliver value; construction progress might highlight cause-and-effect, whilst data from other sensors may validate observations.

This paper describes a design for integrating DFOSS data into a digital twin and showcases the integration on an on-site DFOSS installation in Hong Kong.

Table 1: Key elements of DFOSS procurement

1	Installation design and interpretation methodology	Typically requires an experienced civil engineer with DFOSS expertise
2	Cable installation	Can be performed by a trained in-house team or a subcontractor
3	Interrogator procurement	May be rented or purchased depending upon the application
4	Data visualization	Integrated into a digital twin platform

Table 1 summarizes the four key elements of DFOSS procurement. The application constitutes one of the elements and therefore represents a significant contribution to making DFOSS systems readily available to the engineering industry.

2 WHAT IS DFOSS?

2.1 Overview

A DFOSS system essentially comprises a single-mode fibre optic cable attached to the structure, connected to an optoelectronic instrument called an interrogator. The set-up is pictured in Figure 1. The interrogator pulses laser light which interacts with molecules within the fibre, causing backscattering from each point along the fibre. The frequency shift and magnitude of the backscattered spectrum depend upon the strain and temperature at each point. The interrogator analyses the spectrum to determine strain and temperature profiles along the cable. Most interrogators can attain a repeatability better than 2 με for strain and 0.1°C for temperature.

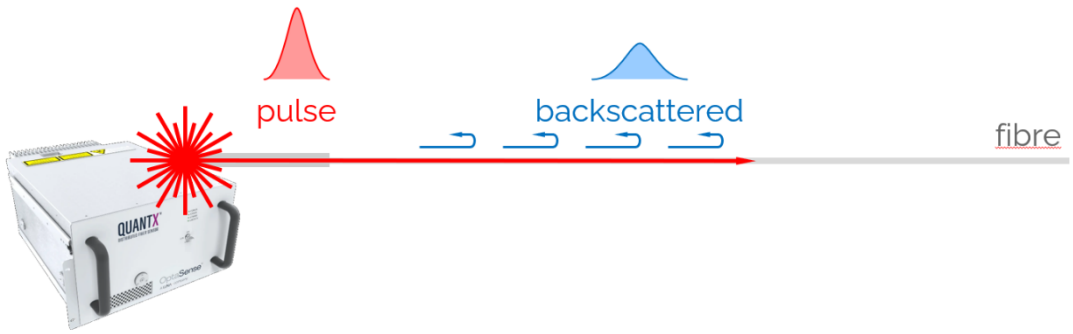


Figure 1: An interrogator interprets fibre conditions from backscattered laser light

The backscattered spectrum comprises the three components shown in Figure 2: Rayleigh, Brillouin and Raman. Raman scattering is not influenced by strain, so interrogators used for structural health monitoring examine either the Rayleigh or the Brillouin components.

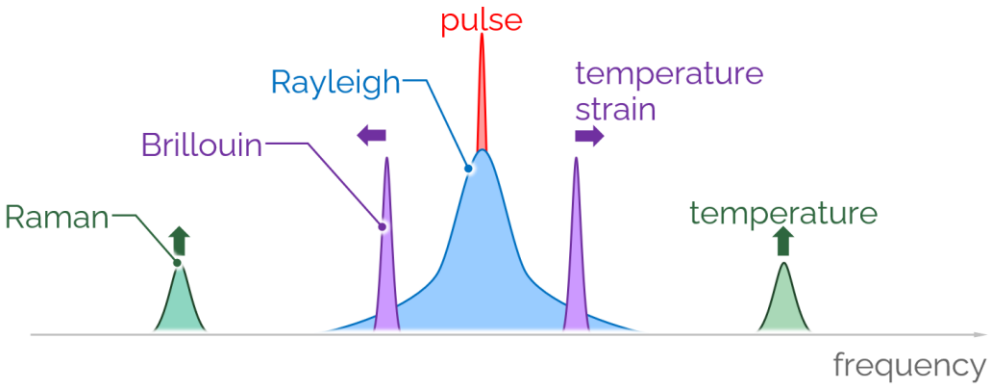


Figure 2: Temperature and strain are interpreted from different backscattered components

2.2 Temperature Compensation

Both Rayleigh and Brillouin components depend upon both strain and temperature, so measurements must be temperature-compensated to derive accurate strains. Temperature compensation is typically achieved by attaching an additional cable to the structure whose optical fibre is de-bonded from its cladding to render it strain-free. This temperature-compensation cable enables temperature effects to be eliminated from strain measurements.

2.3 Spatial Resolution

The transmitted laser pulse has a finite width, and backscattering from the leading and trailing edges of the pulse will superpose. This results in an averaging effect whereby each measurement is a moving average taken over a length of cable called the spatial resolution.

In theory, spatial resolution could be improved by shortening the pulse, but since a laser pulse disperses as it travels down a fibre, this would also limit the sensing range. Selecting an interrogator therefore involves striking the right compromise between spatial resolution and sensing range.

2.4 BODTR and BOTDA

The spatial resolution can be improved by looping the cable back to the interrogator and sending laser pulses down the other end as well. This stimulates Brillouin scattering and improves the spatial resolution. This technique is called Brillouin Optical Time Domain Analysis (BOTDA). Without stimulation, measurement is called Brillouin Optical Time Domain Reflectometry (BOTDR).

2.5 Rayleigh OFDR

The phrase “Time Domain” means that the location of measurements is calculated from the time delay between the transmitted and backscattered light. The accuracy is sufficient for Brillouin analysis, but when the Rayleigh component is used for measurement, Optical Frequency Domain Reflectometry (OFDR) is typically adopted to maximize the spatial resolution. OFDR relies upon the interference between transmitted and returned pulses; the frequency components of the resulting interference correspond to different locations along the fibre.

Interrogators utilizing Rayleigh scattering are capable of high spatial resolution. The scattering profile is unique to a particular fibre since Rayleigh scattering is generated by local defects. The interrogator detects changes in strain or temperature by the corresponding stretch or contraction of this profile. The superior performance of Rayleigh-based interrogators makes them a prime choice for Distributed Acoustic Sensing (DAS), where vibrations are recorded as high-frequency strain fluctuations.

Table 2 compares typical parameters for common interrogator types.

Table 2: A comparison of common interrogators (Barrias, Casas, & Villalba, 2016)

Interrogator Type	Sensing Range	Spatial Resolution	Measurands
Raman OTDR	1–37 km	0.01–17 m	Temperature
Brillouin BOTDR	20–50 km	≈1 m	Temperature, Strain
Brillouin BOTDA	150–200 km	2 cm (at 2 km range) to 2 m (at 150 km range)	Temperature, Strain
Rayleigh OFDR / DAS	50–70 km	≈1 mm	Temperature, Strain, Vibration

3 DFOSS IN STRUCTURAL HEALTH MONITORING

Infrastructure deteriorates with time, with the risk of failure increasing with age. In Hong Kong, slopes susceptible to landslides present a hazard to nearby habitations and transport routes. Failure can be sudden and catastrophic, but it need not occur without warning. If executed effectively, structural health monitoring can trigger pre-emptive action, saving lives and costly reinstatement.

DFOSS is a favoured solution for structural health monitoring worldwide. Table 3 highlights how DFOSS can outperform current monitoring solutions in Hong Kong in ensuring that crucial observations are identified in time to allow mitigation.

Table 3: How DFOSS compares with the performance of conventional structural health monitoring solutions

Monitoring Solution	Can Failure Occur Between Observation Times?	Can Failure Occur Between Observation Locations?
Manual Surveying*	Yes	Yes†
Visual Inspection	Yes	No
Crack Gauges	No, if the right cracks are monitored in real-time	Yes
Slope Inclinometer	No	Yes‡
DFOSS	No, if the cable intersects regions of strain localization. Measurements are real-time.	No. Measurements are distributed along the cable.

* Automatic surveying is unlikely for operational infrastructure due to service disruption and expense.
† Surveying points would need to be impractically close to register cross-crack displacement reliably.
‡ There is a significant chance that inclinometer placement is incompatible with detecting a tilt trend commensurate with landslide development.

DFOSS also boasts other notable advantages:

- The cable allows uninterrupted operation: it is small, requires connection only at its ends and does not interact with electromagnetic fields.
- Although interrogator cost is typically a deciding factor on whether to adopt DFOSS, the cable is relatively inexpensive, and once installed, the system can take advantage of future advances in interrogator technology.
- Since the measuring fibre typically comprises silica, the cable is inert even under aggressive chemical conditions and extreme temperatures. Indeed, it is likely that the cable will outlive the very structure it is monitoring.

DFOSS has delivered value in a diverse range of structural health monitoring applications worldwide for over two decades. Common applications are listed in Table 4.

Table 4: Common structural health monitoring applications for DFOSS

Application	Notes
Bridges	On rebar or retrofitted. Detects spalling, cracking, yielding and joint movement.
Tunnels	Can be aligned longitudinally and circumferentially. Detects spalling, cracking, yielding and joint movement.
Buildings	On rebar of slabs, columns and beams or retrofitted.
Piles	On rebar of bored piles and inside tubular steel piles. Also installed offshore. Outperforms inclinometers for measuring lateral deflection.
Dams	Gives early warning of dam breach.
Slopes	Embedded in a trench for overburden. Reinforced cladding protects fibre.

In Hong Kong, DFOSS has yet to be used commercially to monitor structures and slopes. Notwithstanding, in 2021 a DFOSS system was successfully installed on a construction site as the first full-scale demonstration of DFOSS in Hong Kong (Lin, et al., 2023). This installation is used in this paper to showcase the design of the integration of the DFOSS data into a digital twin of the construction site and is described later in Section 5. The anticipated outcome of the integration is to make DFOSS technology readily usable for Hong Kong practitioners.

4 INTEGRATION DESIGN

4.1 Overview

This paper presents the design of an integration of DFOSS data into a digital twin platform. Currently, software for visualizing DFOSS data is typically developed and sold by the interrogator manufacturer. The software typically lacks the ability to integrate with a digital twin of the monitored structure. In the context of a digital twin—with its associated data such as BIM geometry, site events and sensor data—decisions can be made in a more informed, timely and convenient manner. The digital twin serves as a single portal and hence is readily accessible to stakeholders. Integration of the DFOSS data into a digital twin platform will enable informed, timely and convenient decision-making, namely in respect to:

1 Pre-empting failure by detecting pre-failure movements such as cracking or excessive strain development and taking preventive remedial measures.
2 Measuring performance during construction and operation to understand more about the structural or geotechnical behaviour of the asset under loading, so that designs, construction methods and operational modalities can be optimized.

The DFOSS integration is manifested in a dedicated application in the platform. The application was designed by a probable end user—a qualified civil engineer with experience designing DFOSS systems and familiar with the peculiarities of DFOSS data and its interpretation. The digital twin is rendered using Unreal Engine. Unreal Engine is one of the leading graphics simulators on the market and is widely used for producing ultra-realistic games, movies and simulations. When DFOSS data is being viewed in the platform, the digital twin is ghosted to enable the data to be unobscured, particularly in the case of underground installations or those cast in concrete.

The application requires the inputs and produces the outputs illustrated in Figure 3.

4.2 Geo-Referencing

The interrogator locates each DFOSS measurement by cable chainage. For presentation in the platform however, each measurement must have associated Cartesian coordinates. Attributing coordinates to each DFOSS measurement is referred to as geo-referencing. During set-up for a particular project, the cable alignment is used to geo-reference a set of baseline readings. The resulting coordinates are then applied to all subsequent DFOSS readings, enabling subsequent DFOSS measurements to be displayed at the correct 3-D location.

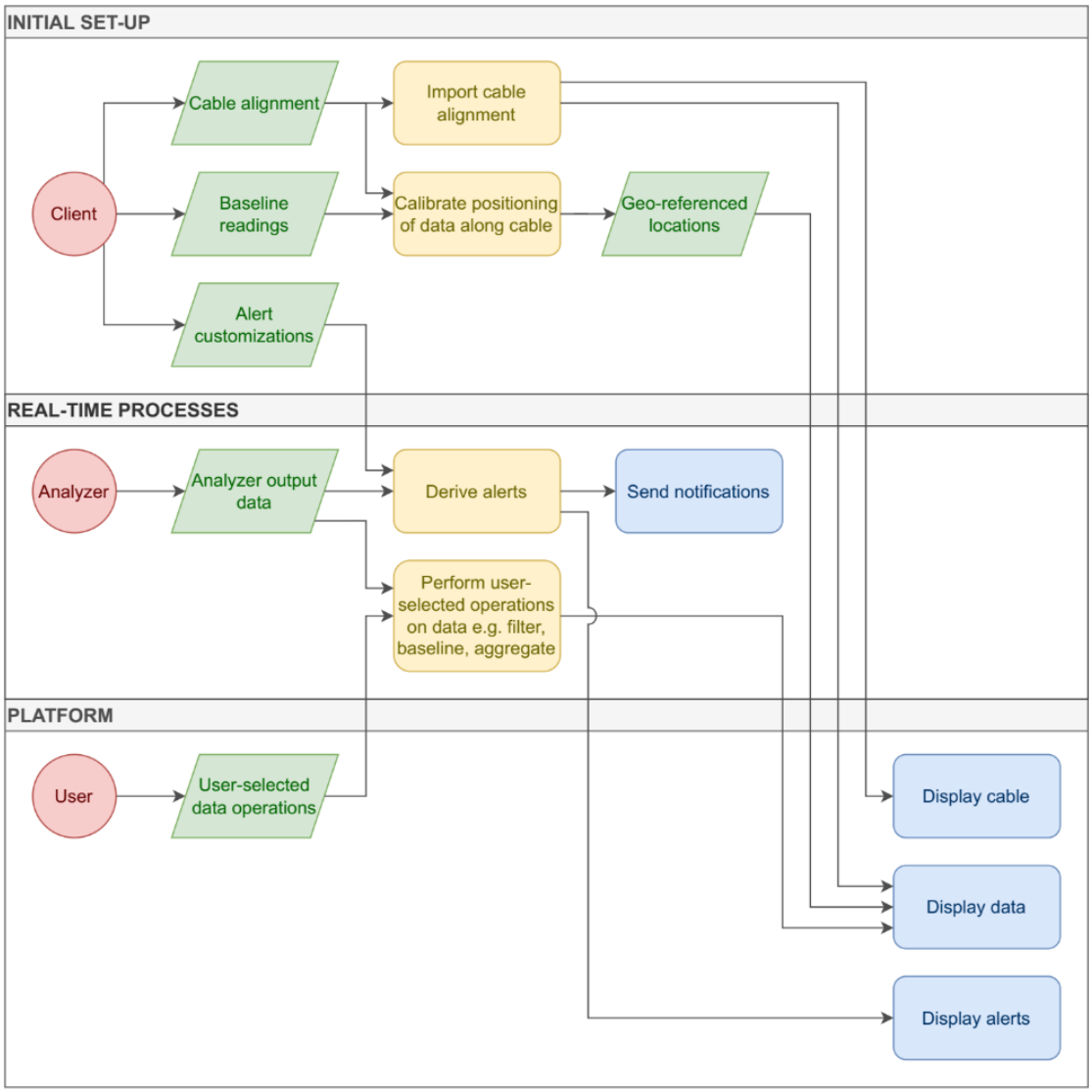


Figure 3: Inputs and outputs for the DFOSS application

4.3 Alerts

Alerts inform the user when DFOSS measurements fall outside predefined limits and enable the user to respond quickly to sudden and hazardous events. An alert can trigger sending of a notification to the user's email, mobile device messaging app or to an in-app notification centre.

Alerts are pre-configured during initial set-up. The configuration comprises defining an envelope outside of which measurements will trigger an alert. The envelope is defined by dividing the cable into sections. For each section, a high and a low threshold can be defined for each measurand as a linear function of chainage. The thresholds can be configured to trigger for readings with or without a baseline dataset subtracted from them.

4.4 Chart Views

Chart views supplement the visualization of DFOSS data in the digital twin, as illustrated in Figure 4. Two charts may be displayed; one chart plots variation against chainage at a selected time, whilst the other plots against time at a selected chainage. The chainage and time for display are selectable interactively on the chart, and synchronize across the digital twin and time bar to maintain a consistent context. The charts enable the user to more readily quantify differences between data and to compare values against design profiles and thresholds. Each chart offers an export option allowing the user to capture data for use in other applications.

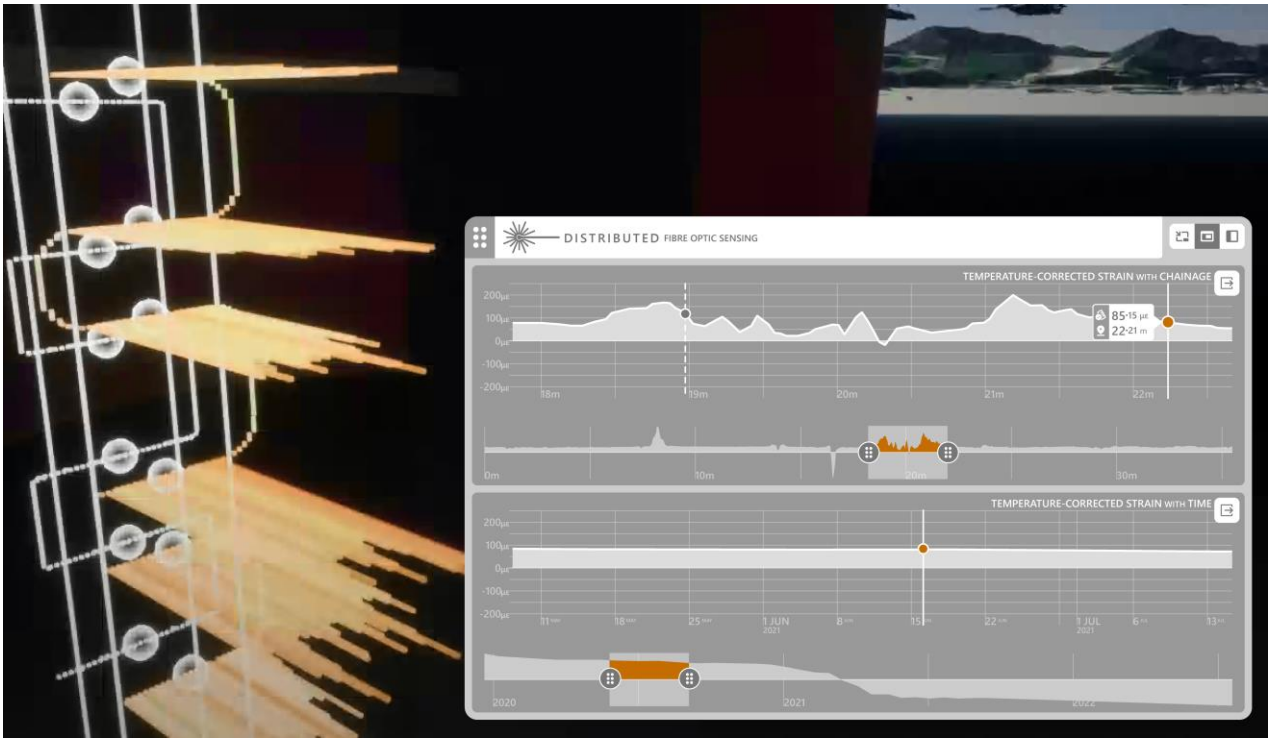


Figure 4: Chart display complements the digital twin view by facilitating more quantitative comparison of values

4.5 Display Measurand

Most interrogators can output temperature, directly-measured strain and temperature-compensated strain. For assessment of structural health, temperature-compensated strain would be most frequently viewed.

The platform displays one measurand at a time. As pictured in Figure 5, the user can either select which measurand they would like to view, or choose to view alerts. The alert view allows users to quickly investigate and follow-up on alert notifications.

The user can select the measurement time to view using a time slider. The entire digital twin is synchronized with the time slider, including the Building Information Modelling (BIM) model and the data from other sensors. In this way, the user can readily identify what caused particular DFOSS observations.

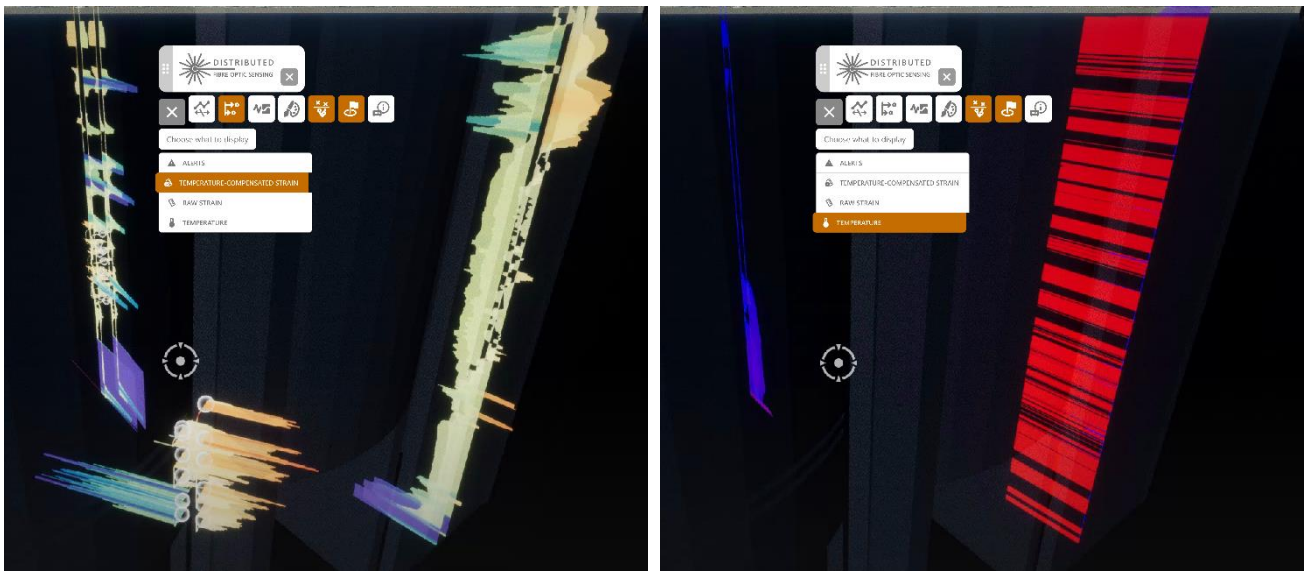


Figure 5: The DFOSS application supports display of both strains (left) and temperatures (right)

4.6 Aggregation with Time

The user can quickly draw insights by aggregating the data over time period at each measurement point, as shown in Figure 6. The period of aggregation is selected via the time slider.

The maximum, minimum and maximum absolute value aggregation functions help identify extreme-value measurements. The maximum absolute value is applicable to strain rather than temperature since strain can be both tensile and compressive. The averaging functions—arithmetic mean and median—are useful for removing noise and determining a representative profile relevant to steady-state conditions.

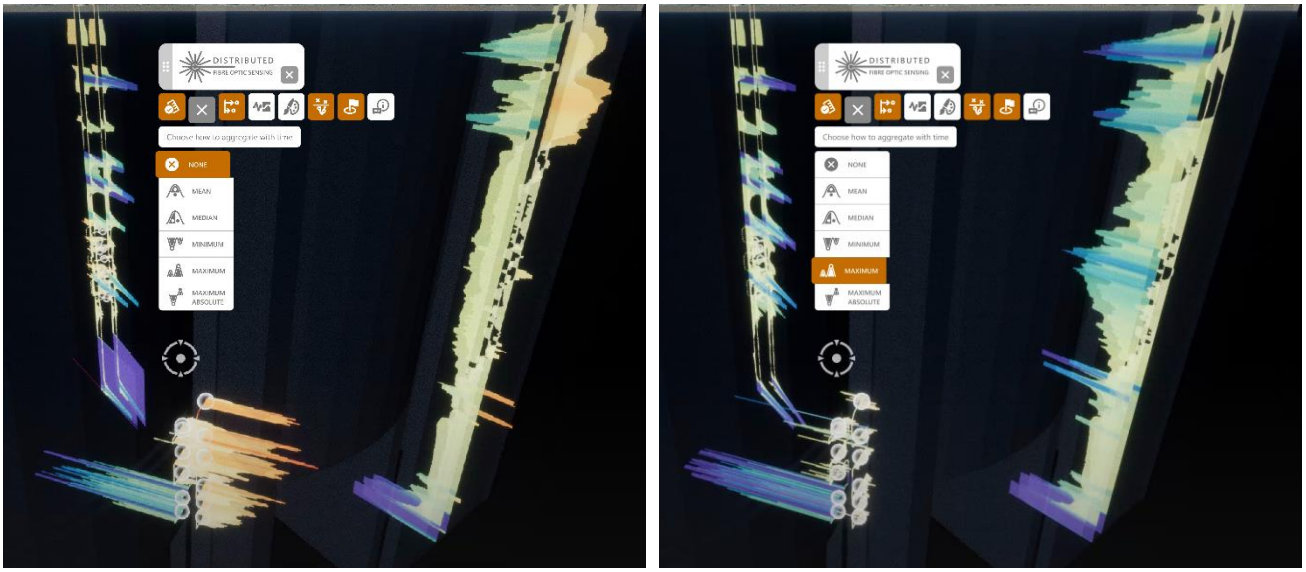


Figure 6: Viewing an envelope of the maximum values over a period (right) helps identify highest recorded values. Non-aggregated data is portrayed on the left for comparison

4.7 Baseline Dataset

The user will typically wish to calibrate strain readings with respect to a baseline dataset:

- The strain at installation of the cable is typically non-zero, particularly if the cable is pre-tensioned to extend the registerable range of compressive strain. It is the strain incurred since installation that is relevant to structural damage, particularly if the cable is cast into concrete.
- Understanding of structural behaviour is crucial for the observational method or design optimization. In this case, observed strains will be compared with design predictions over a distinct construction phase.

The baseline dataset is defined as an average of consecutive readings, offering the opportunity to eliminate noise and spurious data. This process is simplified by automatically identifying the readings to average. As pictured in Figure 7, the user specifies the latest date for these readings via a time bar. A zoom function on the time bar helps the user determine a date by making all available readings readily discoverable. The user can also select the number of baseline readings for averaging, and whether to average by arithmetic mean or by median.

4.8 Data Rendering Options

Both colour and height bars can be used to display variations in DFOSS measurements. Where an installation comprises multiple cables, each individual cable may be rendered differently. This enables the user to focus on data from a cable of interest—particularly useful when cables are closely spaced.

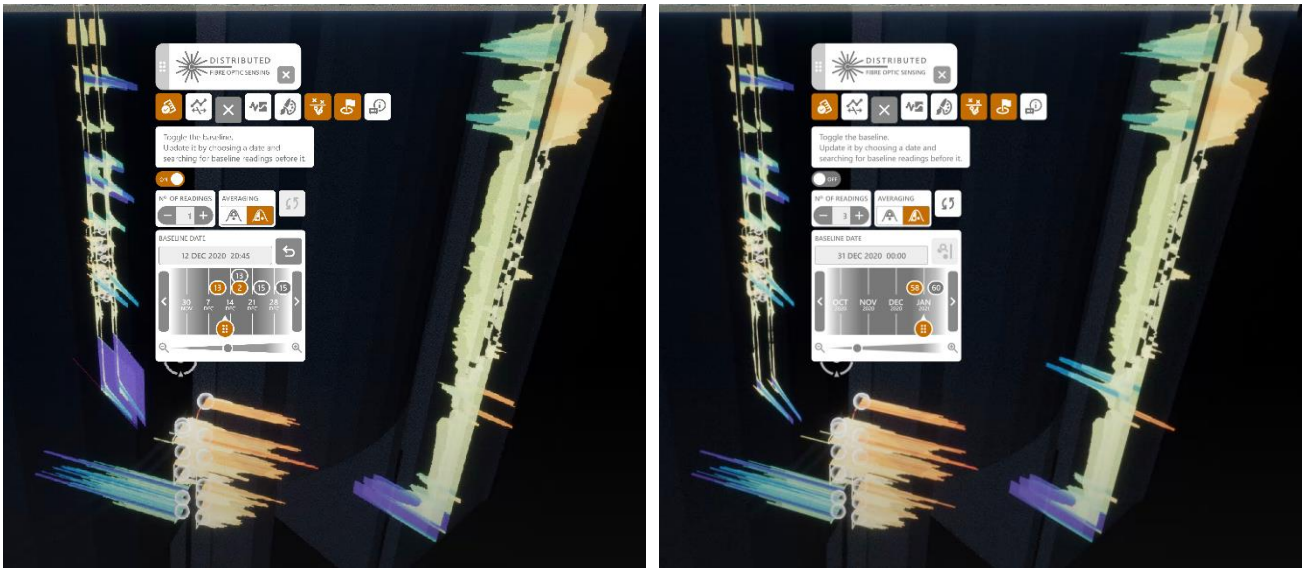


Figure 7: Changes in strain can be visualized by applying a baseline (left). Without a baseline, initial strains will frustrate interpretation of changes (right)

Height bars are plotted normal to the cable alignment to account for situations where the cable is sub-vertical. The user can choose the scale of the height bars relative to the screen. The user can choose from a selection of divergent colour scales to render strain measurements, and a variety of sequential scales are offered for temperature.

4.9 Spurious Values

It not uncommon for DFOSS data to contain spurious values which exceed genuine measurements by orders of magnitude. The maximum and minimum of the colour and height display scales are defined with respect to the extreme available values. Consequently, the spurious values would lead to genuine measurements being displayed across a limited range of colour and height, and variations being indiscernible. It is therefore essential that users are given the ability to identify and remove spurious values. As shown in Figure 8, the application allows the user to effectively ignore data exceeding a desired magnitude for the purposes of both data manipulation and display.

4.10 Reference Markers

The application allows the user to pinpoint precise locations along the cable. This facility can be used to segment the cable or to highlight a sensitive location such as a known crack or stress concentration. During initial set-up, the user can specify these locations as reference markers. These markers can be superposed on the cable alignment, as illustrated in Figure 10.

4.11 Interrogator Settings

Certain interrogator settings such as spatial resolution or measurement rate are helpful to assist in interpreting DFOSS data. The application makes this information available to the user, as shown in Figure 9.



Figure 8: Spuriously large values distort data display (right). The application allows omission of such values so that the profile of genuine data may be viewed (left)



Figure 10: White reference markers help focus on locations of interest

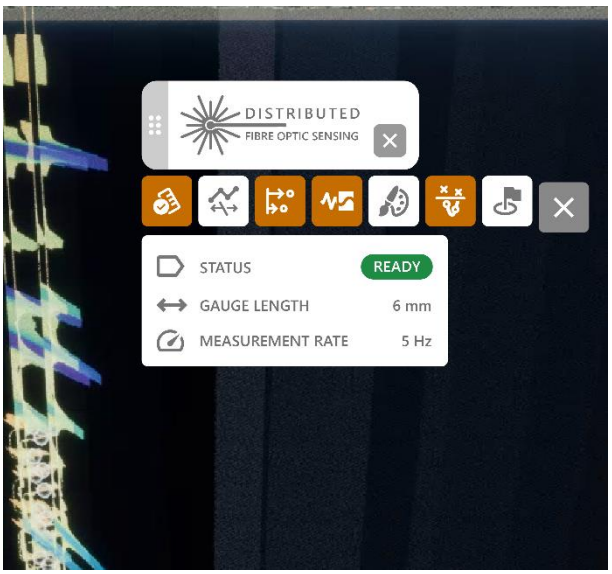


Figure 9: Information on interrogator settings can assist with data interpretation

5 PROJECT APPLICATION

The DFOSS integration was evaluated by applying it to a real on-site DFOSS installation. The government of the Hong Kong Special Administrative Region (HKSAR) is keen to promulgate DFOSS in the industry, and enlisted the DFOSS expertise and equipment of Hong Kong Polytechnic University (HKPU) to execute the installation in 2021. Details of the trial are documented in a paper (Lin, et al., 2023). The fibre optic cables are installed within three of the diaphragm wall panels of a launch shaft for a tunnel boring machine (TBM) used to advance the tunnels for the Trunk Road T2 project. The launch shaft is situated in Kai Tak, Hong Kong. The cables were attached directly to the steel bars of the reinforcement cages before concreting.

A key purpose of the installation was to evaluate hoop stresses developing during excavation within the unique circular peanut-shaped cofferdam of the launch shaft. The results verified the effectiveness of DFOSS in monitoring hoop strains compared with more conventional instruments such as inclinometers, movement markers or vibrating wire strain gauges.

A digital twin was constructed in Unreal Engine by referencing the geometry and construction staging described in the paper. The DFOSS data from fifteen cables was georeferenced from the installation details given in the paper. The zigzag configurations of the two cables measuring hoop strain were deduced by noting development in their strain profiles. Height bars to display the DFOSS data were orientated intuitively—perpendicular to both the diaphragm wall alignment and the cable.

Figure 11 illustrates that DFOSS measurements can be readily explored in the context of construction progress.

6 CONCLUSION

An application has been designed to integrate DFOSS data into a digital twin. The integration is the first of its kind in Hong Kong. In the context of structural health monitoring, the integration helps identify impending failure so that pre-emptive mitigation can be made. DFOSS data can be viewed and manipulated alongside a 4-D BIM model and data from other sensors to correlate observations with site events, and so establish causation.

The readiness of the application for industry use has been demonstrated through a real on-site DFOSS installation in Hong Kong during the construction phase. The demonstration showed that the application can clearly visualize strain evolution as construction progressed. The proven strain visualization capability of the application suggests that anomalous strains during the operational phase can also readily be recognized.

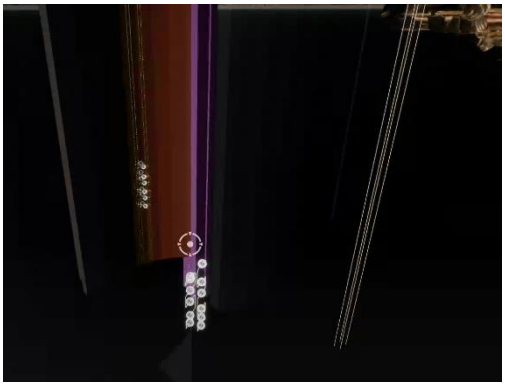
7 ACKNOWLEDGEMENTS

Hong Kong Polytechnic University kindly provided the previously published DFOSS data (Lin, et al., 2023).

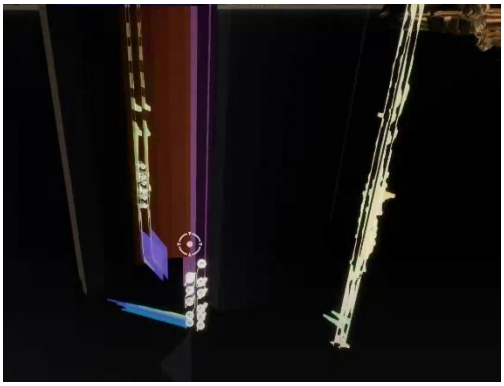
8 REFERENCES

Barrias, A., Casas, J. R., & Villalba, S. (2016). A review of distributed optical fiber sensors for civil engineering applications. *Sensors, 16*(5). doi:https://doi.org/10.3390/s16050748

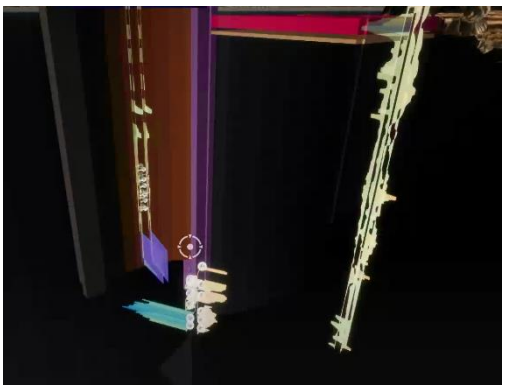
Lin, S.-Q., Tan, D.-Y., Leung, Y. F., Yin, J.-H., Li, I., Sze, E. H., . . . Chan, E. Y. (2023). Fiber-optic monitoring of a twin circular shaft excavation: development of circumferential forces and bending moments in diaphragm walls. *Journal of Geotechnical and Geoenvironmental Engineering, 149*(12).



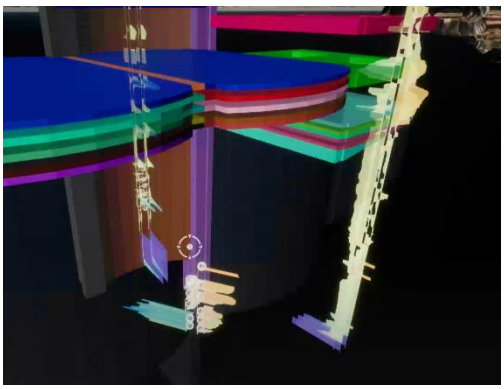
(a) 15 Dec 2020



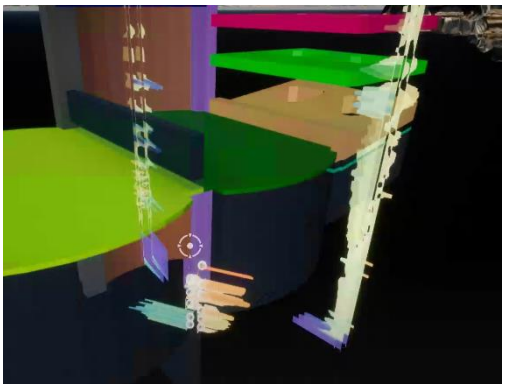
(b) 6 Jan 2021



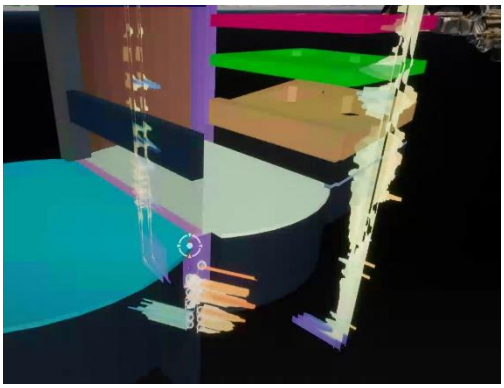
(c) 11 Feb 2021



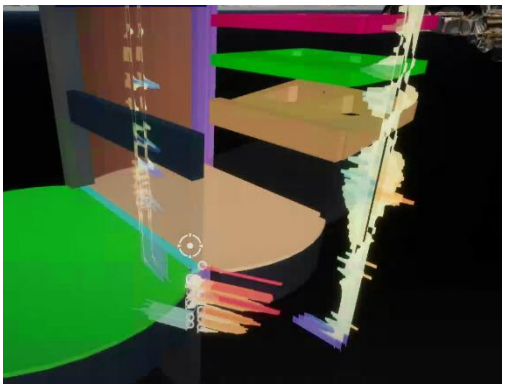
(d) 24 Mar 2021



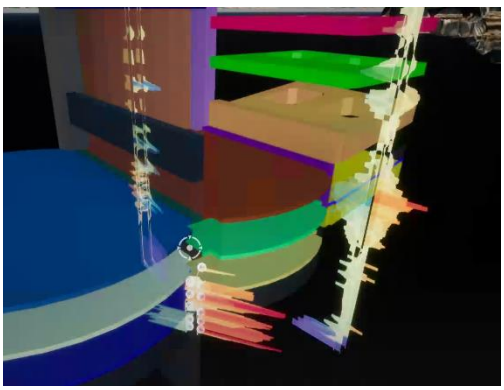
(e) 3 May 2020



(f) 26 May 2021



(g) 17 Jun 2021



(h) 29 Jul 2021

Figure 11: Synchronization of digital twin and DFOSS data can readily reveal insights into structural behaviour as construction progresses

The Establishment of a Safe Method of Offshore Pile Driving in Hong Kong

Daman Lee
Previously CLP Power Hong Kong Ltd., Hong Kong
K.T. Hung
The Hongkong Electric Co. Ltd., Hong Kong
Victor Li
Victor Li & Associates Ltd., Hong Kong

ABSTRACT

Large diameter driven steel tubular piles have been used as the foundations for the recently completed Hong Kong Offshore LNG Terminal located in the southern waters of Hong Kong to the east of Soko Islands. A large number of PDA tests have been conducted for assessing the pile capacity of the offshore piles and gauging the development of pile resistance with time. This has provided a good opportunity to better understand the behaviour of offshore piles in Hong Kong. Analyses of the PDA test data are presented to explore the relationship of pile capacity predicted by the Case method and CAPWAP method and also variation of energy transfer and development of pile resistance over time after the end of initial driving. A simpler approach for describing the set-up curve of pile capacity is also proposed.

1 INTRODUCTION

CLP Power Hong Kong Limited (CLP) and The Hongkong Electric Co., Ltd. (HKE) have jointly developed the Hong Kong Offshore LNG Terminal (hereafter called HKOLNGT or the Terminal) which is an offshore liquefied natural gas (LNG) facility to receive and convert LNG into gas for supply to the gas receiving stations at CLP's power station at Black Point and HKE's power station at Lamma Island for power generation.

The foundations for the Terminal comprise 6 pile groups of mooring dolphins, MD1 to MD6, each with 4 raking piles; 3 pile groups of breasting dolphins, BD1 to BD3, each with 8 vertical piles; and two pile groups of fireboat mooring dolphins, FD1 and FD2, located adjacent to MD1 and each with 3 vertical piles. The piles for MD1 to MD6 and BD1 to BD3 are 1.83m outer diameter open-end driven steel tubular piles and those of the FD1 and FD2 are similar piles but with a smaller outer diameter of 1.26m. There are a total of 54 piles for the Terminal. The project was completed in 2023. Figure 1 shows a photograph of the completed foundation of the Terminal and Figure 2 the completed facility. Some backgrounds of the HKOLNGT project have already been presented in Lee et al (2022) and Shea et al (2022).

Pile Dynamic Analyzer (PDA) tests based on equipment developed by Pile Dynamics Inc (PDI) had been conducted to measure the pile capacity and to gauge the increase in capacity of the piles over time (i.e. the set-up effect which is also known as the aging effect). An agreement was reached with the Building Authority that no full-scale loading tests were to be used to verify the pile capacities and the factors of safety, due to safety reason, as per international practice. Instead, to meet the statutory requirements of Hong Kong for proof testing of completed piles, the number of PDA tests conducted for this project were unusually large as compared with a similar project in other parts of the world. The testing requirements did cause some difficulties to the project team in the planning, construction and testing of pile foundations within a very tight construction programme which was severely constrained by the need to avoid the peak calving season of the Finless Porpoise in the area that would last a total of 6 months within the year between January and June. On

the positive side, the project has provided a wealth of data on PDA testing of offshore piles for understanding the behaviour of driven offshore tubular piles and such knowledge will be useful for similar foundation projects in future in Hong Kong.



Figure 1: Photograph of the completed foundations of HKOLNGT (Lee et al, 2022)

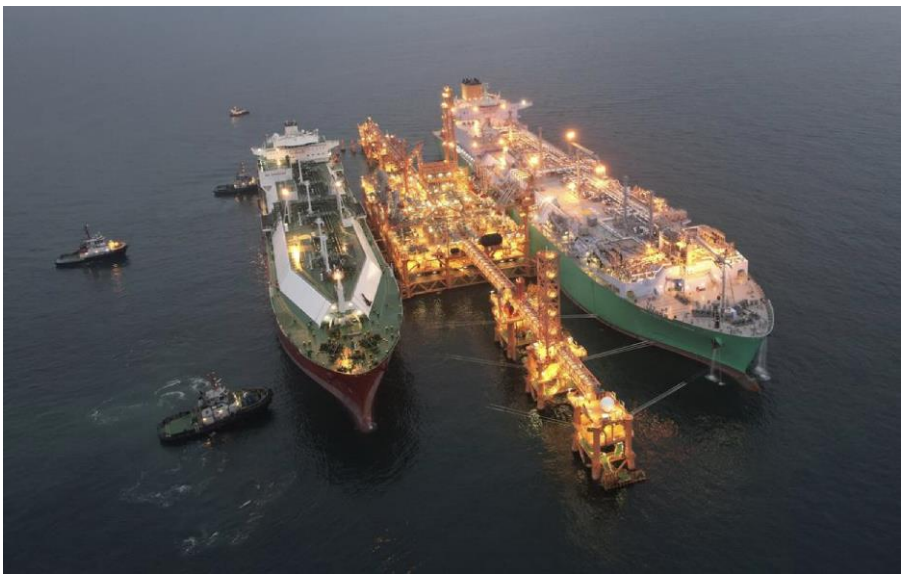


Figure 2: Photograph of the completed HKOLNGT in operation

Some discussions on PDA testing of the piles for the Terminal have been presented earlier in Lee et al (2022) and Shea et al (2002). This paper aims to supplement these two earlier papers by presenting further analyses of the PDA test data in an attempt to gain better insight into the behaviours of driven tubular offshore piles. Only the results of PDA testing of the piles for the mooring and breasting dolphins will be presented in this paper.

2 PILE FOUNDATION AND PDA TESTING

The soil profile along the Terminal consists of marine deposit, underlain in sequence by upper alluvium (clay/silt), interbedded alluvium (plastic clay/sand and silts), alluvial sand (thick dense sand) and lower alluvium (comprising clays, silts and sands). Residual soils and the bedrock were encountered at depths of approximately 85m and deeper than 95m below the seabed respectively. Figure 3 shows the soil profile along the Terminal.

The piles for MD1 to MD6 and BD1 to BD3 are all tubular piles with an outer diameter of 1.83m, with typical thicknesses of 45mm and locally thickened to 50mm as necessary at areas with higher predicted

bending moment. The piles were all driven with hydraulic hammers to found at the target founding levels located within the soil layer of dense to very dense alluvial sand denoted by ALs in Figure 3.

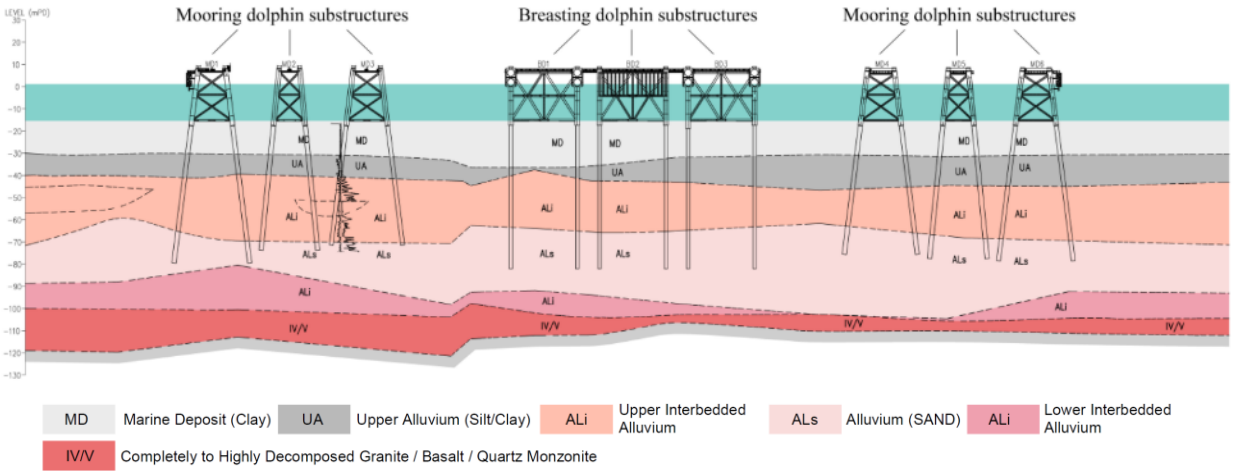


Figure 3: Soil profile along the Terminal

Two sizes of hydraulic hammers were used for the project, namely, MHU800S and MHU1200S. The MHU800S hammer had a nominal ram weight W of 444.51 kN and a drop height h of 1.84m, giving a rated energy of $W \times h$ = 820 kJ. The larger MHU1200S hammer had a nominal ram weight of 648.4 kN and a drop height of 1.85m, giving a rated energy of 1200 kJ. Figure 4 shows the offshore pile of a mooring dolphin being driven with a hydraulic hammer.



Figure 4: Driving of steel tubular pile by hydraulic hammer

The PDA tests were carried out for each pile at end-of-driving (EOD) and on selected piles at restrike to monitor the increase in pile capacity over time after EOD. In PDA testing, the restrike test is given the

abbreviation of BOR to denote beginning-of-restrike. The PDA tests at BOR can help to establish the set-up effect of the piles. The smaller hammer MHU800S was used for initial PDA testing at EOD for MD2 to MD6. For the remaining PDA tests, the larger MHU1200S hammer was used at EOD or BOR.

There are two commonly used methods developed by researchers at the Case Institute of Technology (now Case Western Reserve University) including the Case method and the Case Pile Wave Analysis Program (CAPWAP) (Hussein & Goble 2004) for predicting the capacity of a driven pile. Further discussions of these two methods can be obtained from Turner (1997). The two pile capacities predicted by PDA testing will hereafter be referred as the Case capacity and CAPWAP capacity respectively. The CAPWAP method involves a more complicated soil-pile interaction model. The CAPWAP capacity so obtained is usually regarded as more accurate than the Case capacity.

The predicted Case capacity is dependent on a parameter called the damping factor, J_c. In Hong Kong, the Case capacity is usually presented for a range of J_c values from 0 to 0.9 in increments of 0.1 in a PDA test report. The appropriate value of J_c depends on the soil types and other factors. The designer/contractor should adopt a suitable value of J_c based on local experience, judgement or calibration with CAPWAP capacity on selected piles when predicting the pile capacity using the Case method.

The PDA tests for this project were conducted in a conventional way by a foundation testing company accredited under the Hong Kong Laboratory Accreditation Scheme using PDI test equipment. The information contained in the PDA test reports for this project is similar to that of land piling in Hong Kong.

Measured parameters or predicted pile capacities obtained from a PDA test can be classified as “quick” or “late” results for ease of discussion. Quick results are quantities that are produced by on-board processing of the data measured by the PDA equipment. The quick results can be obtained immediately after the PDA test by reading off the output shown on the monitor of the PDA equipment or its printout. Examples of the quick results include the maximum energy transferred from the hammer to the pile after impact and the Case capacity for different damping factors.

Late results are quantities which require further post-processing of the PDA test data and cannot be made available immediately on site after PDA testing. An example of late results is the CAPWAP capacity obtained by a running a software developed by PDI using the field data obtained from PDA testing.

PDI uses special notations for the quick results obtained from the PDA equipment, including the following that will be discussed in this paper.

Quantity	Abbreviation
Maximum compressive stress	*CSX*
Maximum energy transferred from the hammer to the pile	*EMX*
The maximum driving force measured at pile top	*FMX*
Pile capacity predicted by the Case method	*RMX*

Very often, only the results of *CSX* but not *FMX* are presented in the formal PDA test result. The result of *FMX* can easily be obtained by the product of $CSX \times A$ where A is the cross-sectional area of the pile. PDI does not use any special notation for the pile capacity predicted by CAPWAP method. In this paper, the CAPWAP capacity will be denoted by *RCW* for ease of reference. Another parameter that is commonly used in PDA testing is the energy transfer ratio, X, defined as $X = EMX$ /rated energy. The energy transfer ratio X can be interpreted as the energy transferred to the pile after impact expressed as a proportion of the rated energy.

3 THE IMPORTANCE OF EARLY PREDICTION OF PILE CAPACITY

As discussed by Lee et al (2020), the sea state due to weather conditions often dictates the method of construction and hence the foundation design. Idling is extremely costly and a major safety hazard for offshore foundation works. The capacity of an offshore pile is usually assessed by the CAPWAP method and the results of CAPWAP analysis are often only available a few days after PDA testing. To reduce the idling time, it will be extremely useful to the piling contractor if tools are available for rapidly assessing whether the installed piles are likely to achieve the required capacity such that they can make an earlier decision of relocating the piling equipment for installation of another offshore pile.

For land piling, there are published correlations between the CAPWAP capacity (*RCW*) and the peak/maximum driving force (*FMX*) in the literature. Chow et al (1989) observed a linear relationship between the *RCW* and *FMX* and their data covers a range of pile types including precast reinforced concrete piles, prestressed concrete piles, steel H-piles and steel pipe piles driven to a small set value of less than 25mm per 10 blows by diesel, hydraulic or drop hammers. The scattering of data reported by Chow et al (1989) is fairly large, with the ratio of *RCW*/*FMX* falling generally between 0.8 and 1.3 and having a mean value of 1.04. For steel H-piles driven with hydraulic hammers in Hong Kong, Fung et al (2013) observed that the mean value of the ratio *RCW*/*FMX* decreases from 1.2 for friction piles to 1.0 for end-bearing piles.

It is worth investigating whether *FMX* will be a useful predictor for *RCW* for offshore piles. Figure 5 shows the data of *RCW* plotted against *FMX* for the offshore piles of the HKOLNGT project. The data points in Figure 5 lie entirely below the equality line. Given the large scattering of results, *FMX* is therefore not a useful predictor for the CAPWAP capacity.

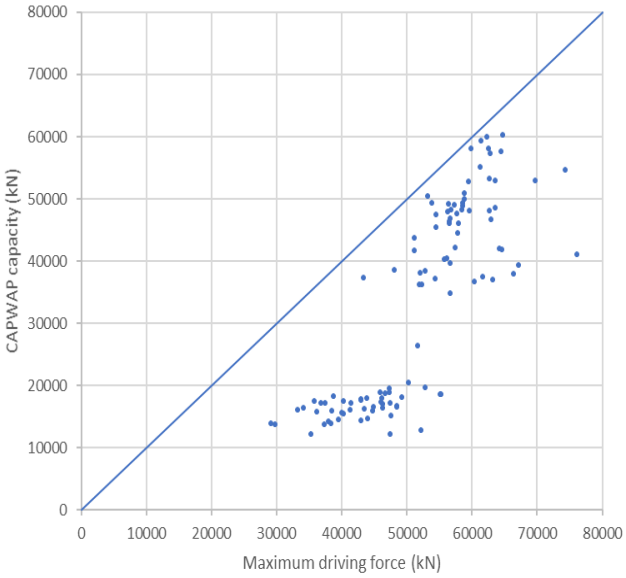


Figure 5: Correlations of CAPWAP capacity (*RCW*) with maximum driving force (*FMX*)

Although the Case method is generally regarded to be less accurate than CAPWAP analysis for estimation of pile capacity, one may explore whether there is a good correlation that can be established between the pile capacities obtained with the two methods. If a good correlation does exist between *RCW* and *RMX*, the correlation can be established initially using early results and then constantly updated using subsequent results for progressively more accurate prediction of the CAPWAP capacity. The value of J_c to be selected for establishing the correlation can be easily obtained by calibration with the early results of CAPWAP analysis. In doing so, the *RCW*-*RMX* correlation can be used for early prediction of the *RCW* based on the quick results of *RMX*.

For land piling, a good correlation can often be established between *RCW* and *RMX* based on a suitably selected value of J_c. Figure 6 shows an example of a very good linear correlation between *RCW* and *RMX* observed for steel H-piles driven with hydraulic hammers to final set for a project in Hong Kong based on the commonly used value of 0.6 for J_c. The R^2 value, which is a measure of goodness-of-fit for a linear regression, is as high as 0.9962 which signifies an extremely good linear correlation for the land piling project.

A review of the PDA test data indicates that a good linear correlation also exists for the offshore piles of the HKOLNGT project when J_c is within the range of 0 to 0.3 with R^2 value exceeding 0.978 as illustrated in Figure 7(a) & (b) for the correlations corresponding to J_c = 0 and 0.2. The value of R^2 begins to drop and the scattering of data points becomes larger as J_c further increases from 0.4 to 0.9 as depicted by Figure 7(c) & (d). In view of these observations, the correlation between *RCW* and *RMX* can be used as a tool for quick prediction of the pile capacity when a value of J_c within a suitable range is adopted for the Case method.

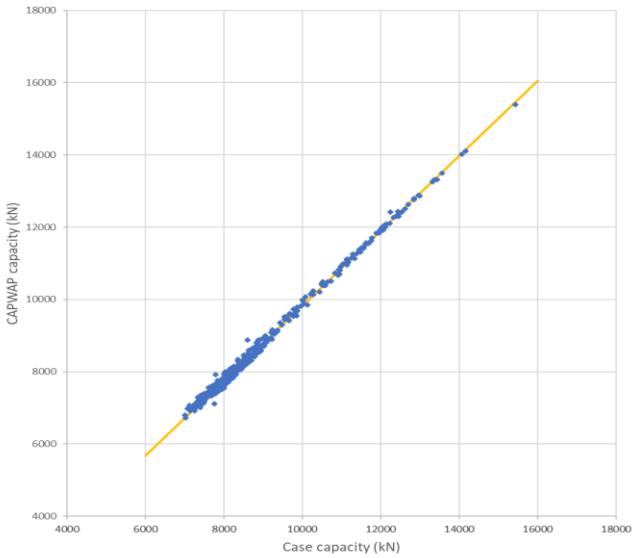
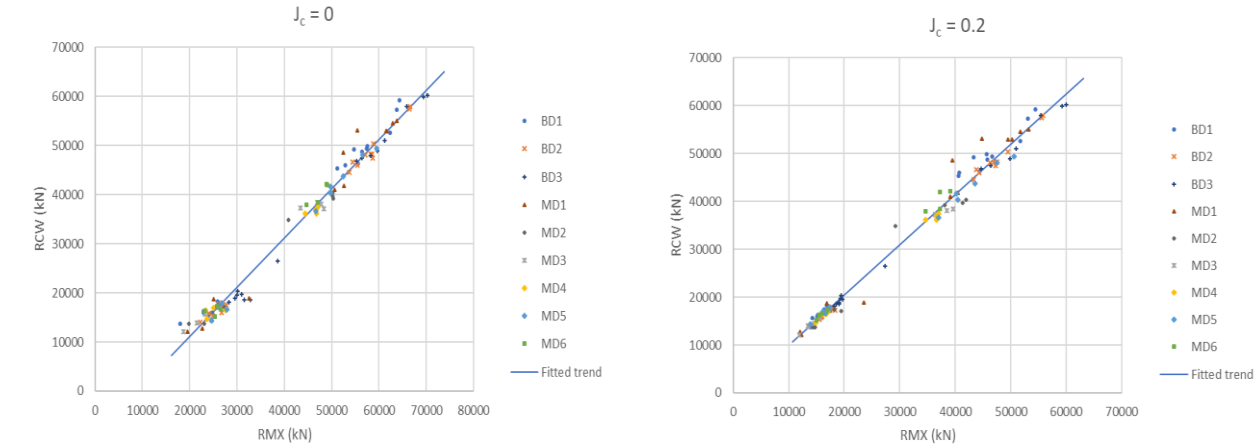
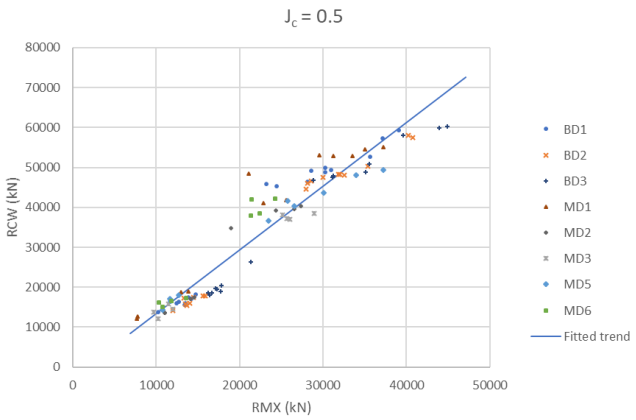


Figure 6: Example of a correlation between *RCW* and *RMX* (based on J_c = 0.6) for H-piles

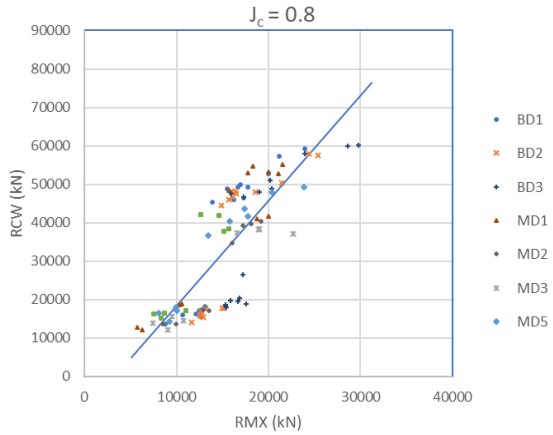


(a)

(b)



(c)



(d)

Figure 7: Correlation between *RCW* and *RMX* for HKOLNGT project

4 TRANSFER OF ENERGY TO PILE DURING DRIVING

For driven steel H-piles in Hong Kong driven to final set, Li (2003) and Li et al (2003a, 2003b) observed that the energy transfer ratio tends to be relatively constant and independent of pile length. The observations of energy transfer to the offshore piles for the HKOLNGT project are quite different, however.

Figure 8 shows the energy transfer ratio X and CAPWAP capacity RCW plotted against time after pile driving for a particular offshore pile for this project. It can be observed that both quantities tend to increase with time after EOD.

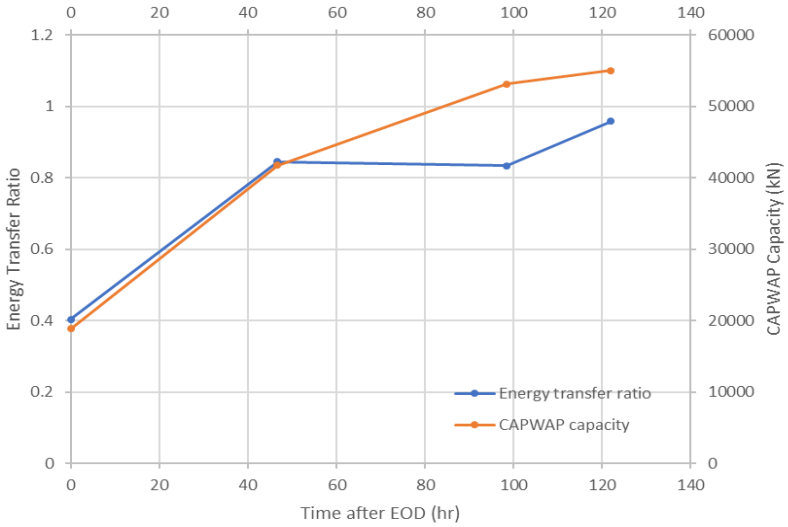


Figure 8: Energy transfer ratio and CAPWAP capacity versus time after EOD for a pile in MD1

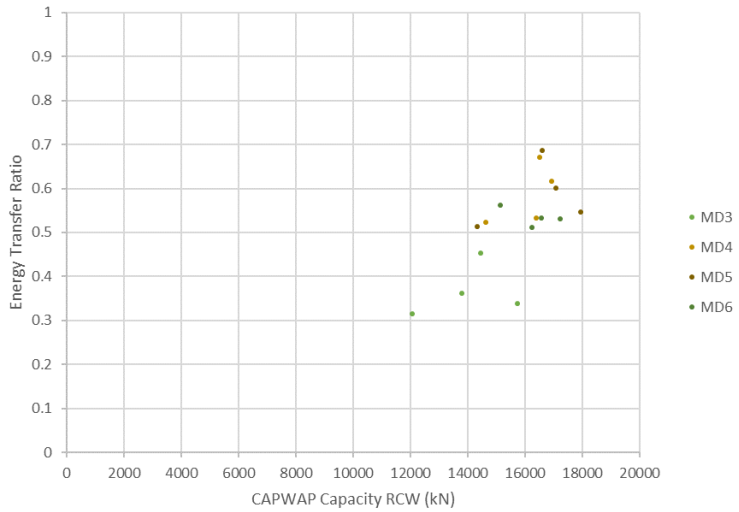
Based on the observation in Figure 8, one would expect a positive correlation between X and RCW as confirmed by the graphical plot in Figure 9 for all piles of MD1 to MD6 and BD1 to BD3.

As discussed in Lee et al (2022), the Hiley formula which is commonly used for land piling in Hong Kong and enshrined in the current Code of Practice for Foundations 2017 published by the Buildings Department is not suitable for offshore piling works. The results of Figures 9 and 10 can be used to further explain this point.

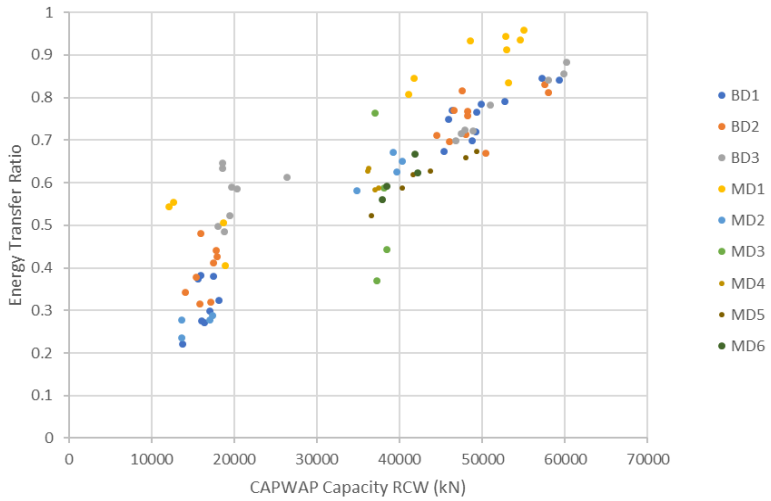
According to the derivations presented in Li et al (2003a, 2003b), the energy transfer ratio based on the Hiley formula can be approximated closely by the product of hammer efficiency α and the efficiency of hammer blow η. α is a measure of the energy loss in the hammer before impacting the pile and it is usually relatively constant for a given hammer type. The quantity η is a function of the weight of pile cushion W_c, the pile weight and hence the pile length L, and the coefficient of restitution e which governs the velocity of the hammer and the pile after impact.

In the current foundation practice, the parameter e is often assumed constant for a given hammer type and pile type. During restrike test, the change of pile length is small and the pile length can therefore be assumed constant for practical purposes. If α, e, L and W_c are all constant or approximately constant based on the above observations, one should expect the energy transfer ratio X to be constant with time. This conclusion is not supported by the observations in Figures 8 and 9 for the offshore piles of the HKOLNGT project. The change of X with time or pile capacity clearly imply that the parameter e in the Hiley formula is not a constant and it changes with time or pile capacity.

For an offshore foundation project, it is difficult to know *a-priori* a suitable value of e to be used for the site and even more difficult to establish its variation with pile capacity. The recording of the pile movement versus hammer blow using the conventional method of sticking a piece of paper on the pile and tracing the record using a pencil is a practically impossible task and outright dangerous when operating in rough sea environments. In summary, the Hiley formula and likely other pile driving formulas are not a practical tool for assessing the pile capacity of offshore piles.



(a)



(b)

Figure 9: Energy transfer ratio versus CAPWAP capacity for piles driven with hammer with rated energy of (a) 1200 kJ and (b) 800 kJ

5 DEVELOPMENT OF PILE RESISTANCE OVER TIME

It is well established that large diameter driven tubular piles will exhibit the set-up effect. Different mechanisms which attempt to explain the set-up effect have been put forward by various researchers. Schmertmann (1991) discussed aging of soils as a contributing factor for the set-up effect and proposed that drained creep movements associated with aging would lead to the increase in soil resistance and stiffness with time. Jardin et al (2006) believe that the dominant process is relaxation of the circumferential arching effect with time caused by creep movement, resulting in progressive increase in radial effective stress and shaft resisance acting on the pile. Bowman & Soga (2003, 2005) attribute the set-up effect to kinematically restrained dilation of soils close to the pile shaft and soil aging.

The real mechanisum for set-up is likely to be complex process affected by a multitude of factors. This, coupled with variability of soil properties along the pile and variation of soil profiles across the site, will often give rise to scattering of data for the set-up curve. Despite the data scatter, significant and rapid set-up effects

had been evidently observed for the offshore piles for the HKOLNGT project as discussed by Shea et al. (2022). The discussions will be augmented by additional data presented in this paper.

While there is an increase in total pile capacity with time, the rates of increase of shaft resistance and toe resistance are different as typified by the pile resistance predicted by CAPWAP analysis for pile P4 in MD1 presented in Figure 10. The shaft resistance tends to be developed more rapidly and over time the shaft resistance occupies a dominant proportion of the total capacity. More data to show the variation of portion of toe resistance relative to the total pile capacity over time (all predicted by CAPWAP analysis) are presented in Figure 11 for individual groups of BDs and MDs.

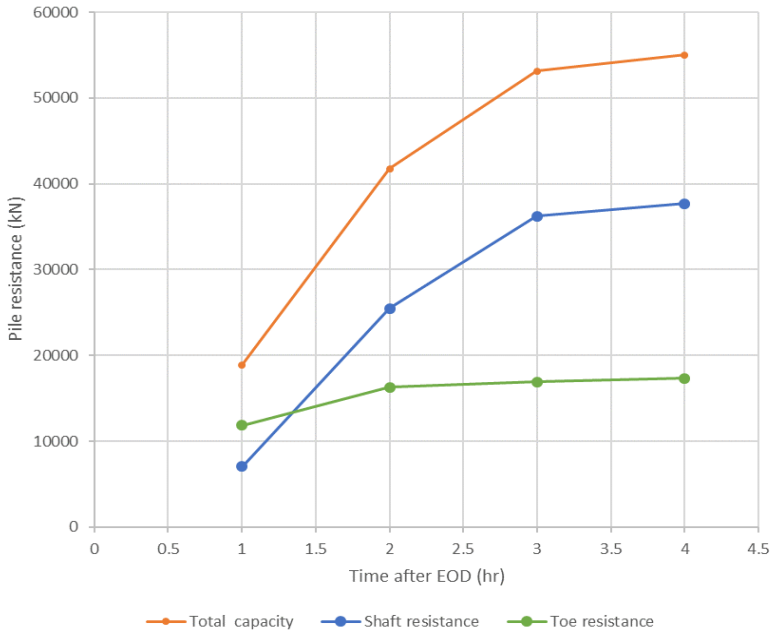


Figure 10: Change with pile resistance with time for pile P4 of MD1

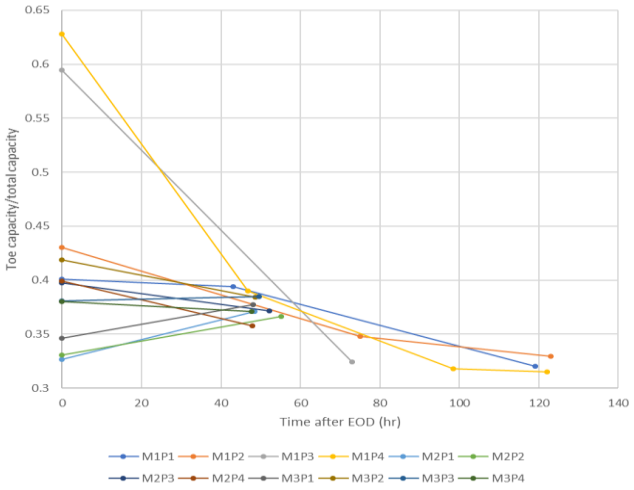
The offshore piles for the HKOLNGP project are founded on alluvial sands. As the shaft resistance increases with time due to set-up effect, the energy that can be transferred to the pile toe by the hammer impact with the same energy is expected to be progressively smaller. The displacement of the pile toe may not be sufficient to mobilize the full resistance of the toe. This may perhaps explain why the proportion of toe resistance tends to decrease with time as indicated in Figure 11 for many of the piles.

The change of pile resistance or pile capacity with time is called the set-up curve. The ratio of pile capacity increase is defined by $r = R/R_o$ where R is the pile capacity at time t and R_o the pile capacity at EOD. It is common in the literature to describe the set-up curve for r using a logarithm relationship, but it has an inherent limitation because the logarithm function gives no upper limit on r. This implies that the pile capacity can continue to increase with time, something which is physically impossible. In a recent paper by Shea et al. (2022), an alternative approach is suggested in which a hyperbolic function has been adopted for describing the set-up curve of the average shaft resistance, but the set-up effect of the toe resistance is ignored when predicting r.

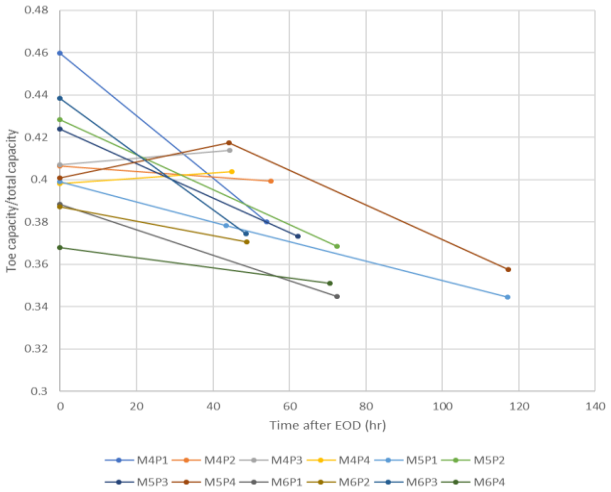
A simpler approach, which is a variation to the methodology by Shea et al. (2022), is to use the hyperbolic function to directly describe the set-up curve for r. Theoretically, $r = 1$ at EOD. A suitable hyperbolic function for describing the set-up curve of r will then be as follows.

$$r = 1 + t/(a + b \times t) \quad (1)$$

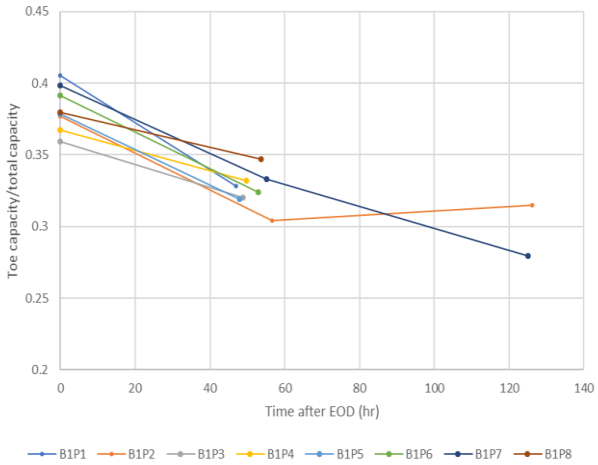
a and b are constants.



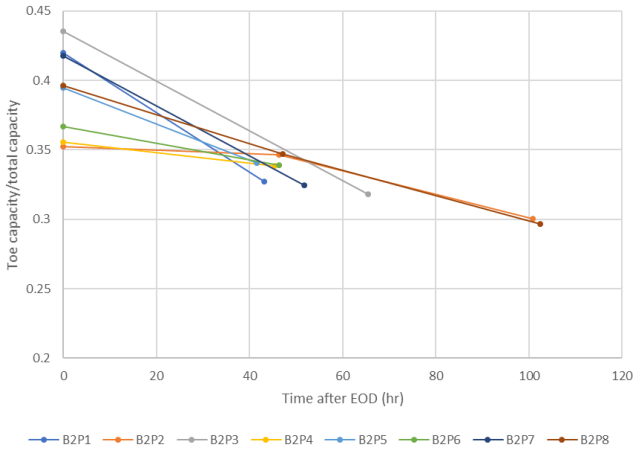
(a)



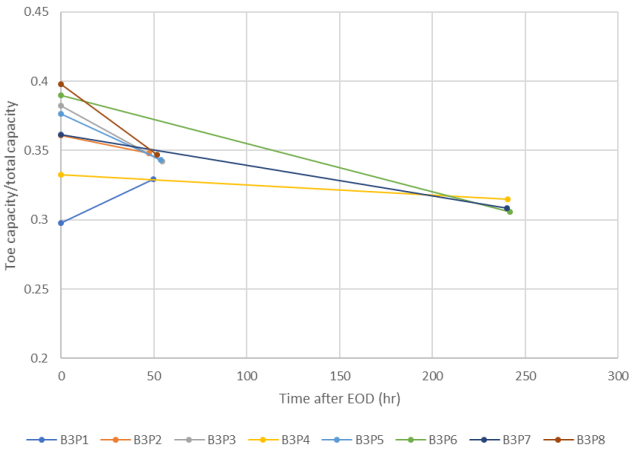
(b)



(c)



(d)



(e)

Figure 11: Ratio of toe capacity / total capacity versus time after EOD for (a) MD1 to MD3, (b) MD4 to MD6, (c) BD1, (d) BD2 and (e) BD3

Eq.1 gives an asymptotic upper limit of 1 + 1/*b* for the value of *r* and it can be re-arranged to give:

$$t/(r-1) = a + b \times t \quad (2)$$

By plotting $t/(r-1)$ against t, one should expect a linear relationship. The constants a and b can be obtained easily by least-squared fitting. It should be noted that the exercise of least-squared fitting used here is different from the conventional linear regression analysis of two variables x and y related by $y = a + b\,x$ in which y is not be a further function of x. In Eq.2, the expression in the left-hand side is itself a function of t and regression analysis will lose its statistical meaning when used to obtain the coefficients a and b. The method of least-squared fitting is only used as a numerical tool for fitting a curve to the data by estimating a and b. Further discussion on this point is given in Li (2007). The left-hand side of Eq.2 contains the multiplier of $1/(r-1)$ to the time t. This multiplier is larger when r is smaller. This implies that the exercise of least-squared fitting gives a larger weighting to smaller values of r. The fitted curve will therefore be biased towards the data points with lower values of r, a result which is conservative. Figure 12 shows the results of least-squared fitting using Eq.2 for the HKOLNGT project, with R^2 value equal to 0.8.

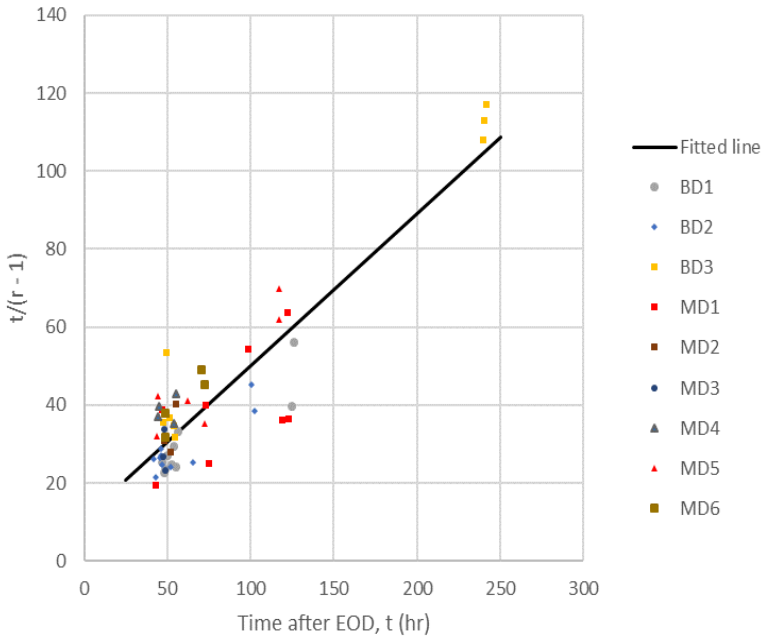


Figure 12: Plotting of $t/(r-1)$ versus time t after EOD

Figure 13 shows the data points of r and the fitted curve plotted against time. It can be observed that the fitted curve does tend to be biased towards data points with lower values of r as discussed above.

If a more conservative design line is preferred, the linear relationship in Figure 12 may be obtained manually by fitting a straight line closer to the upper envelop of the observed data. This will yield a more conservative set-up curve closer to the lower envelop of observed data in the r vs t plot in Figure 13.

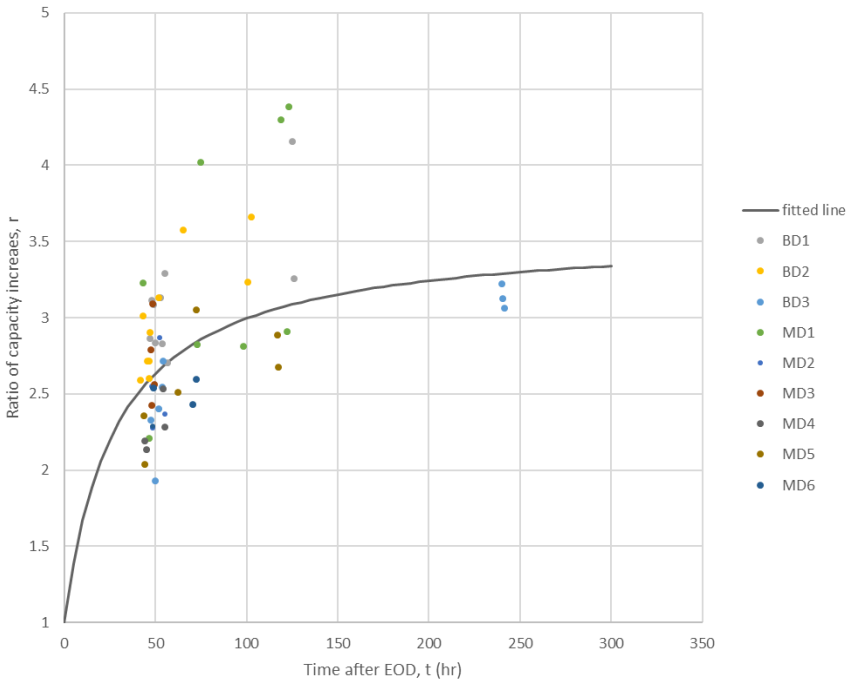


Figure 13: Ratio of capacity increase versus time after EOD (based on CAPWAP capacity)

As discussed earlier in Section 3, there exists a linear relationship between the pile capacity estimated using the Case method and the CAPWAP method with a suitable value of J_c. Based on this observation, the set-up curve can be obtained directly using the Case capacity. Figure 14 compares the set-up curves of r obtained using the CAPWAP capacity and Case capacity based on J_c = 0.2 and the same procedures discussed earlier based on the least-square method.

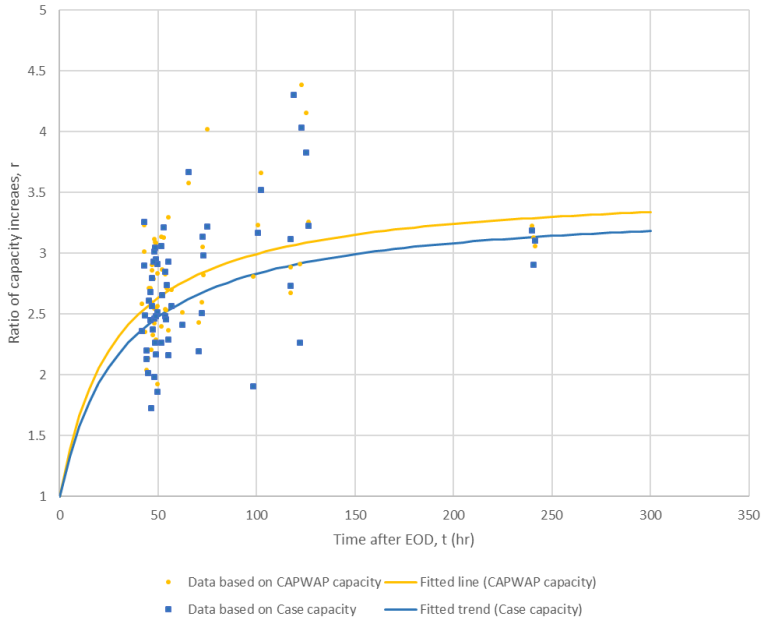


Figure 14: Comparison of set-up curves of r based on CAPWAP capacity and Case capacity

Figure 14 indicates that the set-up curves obtained from results of CAPWAP capacity and Case capacity are quite similar to each other. Based on this observation, a simpler approach for assessing the pile can be

proposed in which the pile capacity at EOD is estimated using the CAPWAP capacity for calibratin of the J_c value and the prediction of subsequent pile capacity over time can be made with the help of the set-up curve obtained using the results of Case capacity corresponding to a suitable value of J_c.

To implement the simplified proecdure, CAPWAP analyses at EOD are carried out for a small percentage of piles completed early in the project. A suitable value of J_c for the Case method can then be obtained by calibration with the CAPWAP analysis based on results of these early PDA tests. As described earlier, a linear relationship exists between the pile capacity predicted by the Case method and CAPWAP analysis for a range of J_c value. As long as the selected value of J_c is within this suitable range, the Case method can be used in lieu of CAPWAP analysis for obtaining a reasonably good prediction of the pile capacity. The subsequent estimation of pile capacity with time and the determination of set-up curve can then be based on the Case method. Figure 15 summarizes details of the proposed simplified procedures.

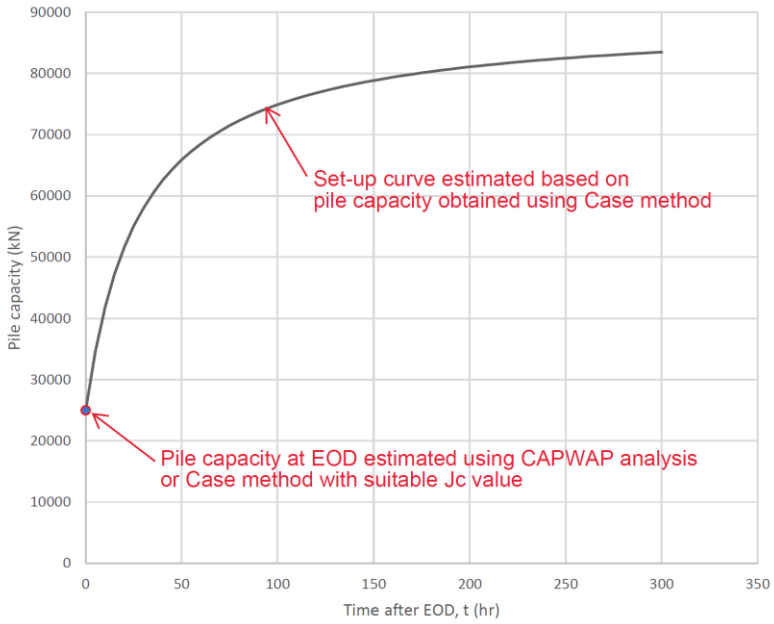


Figure 15: The estimation of pile capacity with time based on the simplified procedures

6 CONCLUSIONS

The HKOLNGT project has provided a wealth of valuable data for understanding the performance of large diameter offshore piles in Hong Kong. More results of PDA testing for the project are presented in this paper to supplement the discussions presented earlier by Shea et al. (2022) and Lee et al. (2022).

It is observed that there exists a good correlation between the pile capacity predicted by the Case method and the CAPWAP method if a value of J_c within the suitable range is used in obtaining the Case capacity. Such a relationship may be used as a quick tool for early predicting the CAPWAP capacity.

The data on energy transfer ratio re-affirms that the Hiley formula is not a viable tool for assessing the capacity of offshore driven piles. The PDA test method have been established as an accurate and practical tool for assessment of offshore pile capacity.

The PDA test data reveals that the development rates of shaft resistance and toe resistance are different and this should be considered when evaluating the static capacity of the piles.

A simpler approach based on the hyperbolic function is proposed for describing the set-up curves of the ratio of pile capacity increase, r. It is further observed that the set-up curves for r obtained from the results of CAPWAP capacity and Case capacity are reasonably close to each other. When planning the installation of offshore piles, one can use of the set-up curve based on the results of Case capacity directly without having to wait for the results of CAPWAP analysis.

ACKNOWLEDGEMENTS

This paper is published with the permission of CLP Power Hong Kong Ltd. and The Hongkong Electric Co. Ltd.

REFERENCES

Bowman, E.T. and Soga, K. 2003. Creep, ageing and microstructural change in dense granular materials. *Soils and Foundations*, 43(4), 107-117.

Bowman, E.T. and Soga, K. 2005. Mechanisms of setup of displacement piles in sand: laboratory creep tests. *Canadian Geotechnical Journal*, 42, 1391-1407.

Chow, Y.K., Yu, C.L., Wong, K.S. and Lee, S.L. 1989. Relation between peak driving force and the bearing capacity of driven pile. *Geotechnical Engineering*, 20: 103-109.

Fung, W.K., Wong, C.T. and Wong, M.K. 2013. A study on capacity predictions for driven piles. *HKIE Transactions*, 11(3): 10-16.

Hussein, M. & Goble G. G., 2004. A brief history of the application of stress-wave theory to piles. *Current practices and future trends in deep foundations*, Geotechnical Special Publication No. 125, ASCE, 186-201.

Jardine, R.J., Standing, J.R. and Chow, F.C. 2006. Some observations of the effects of time on the capacity of piles driven in sand. *Geotechnique*, 56(4): 227-244.

Lee, D., Hung, K.T., Lee, S. and Li, V. 2022. A critical review of the current practice of design and construction of offshore foundations in Hong Kong. *Proc. HKIE Geotechnical Division Annual Seminar*. 38-53.

Li, K.S. 2003. Discussion on "On the application of Hiley formula in driving long piles". *Geotechnique*, 53(3): 373-374.

Li, V. 2007. Analysis of geotechnical data. *Bridging Research and Practice – the VLA Experience*, 121-156.

Li, K.S., Lam, J. and Ho, N.C.L. 2003a. Chapter 3 - driven piles. *Design and construction of driven and jacked Piles*, Centre for Research & Professional Development, 51-71.

Li, K.S., Chan, S.T. and Lam, J. 2003b. An alternative pile driving formula – a preliminary study. *Proc. HKIE Geotechnical Division Annual Seminar*, 179-189.

Schmertmann, J.H. 1991. The mechanical aging of soils. *J. of Geotechnical Engineering*, ASCE, 117(9): 1288-1330.

Shea, V. Li, D., Shum, D. and Chu, F. 2022. Large diameter open-end steel piled foundations for the Hong Kong Offshore LNG Terminal – design and installation. *Proc. HKIE Geotechnical Division Annual Seminar*. 175-187.

Turner, M.J. 1997. *Integrity testing in piling practice*, CIRIA.

Use of Compressible Layer for Raft Footing Design with Winkler Method

Ted Tse, Ka-Ming Lee & Ted Lan
Binnies Hong Kong Limited, Hong Kong

ABSTRACT

Raft footing is a commonly used shallow foundation system, which is largely contingent upon the founding condition. The primary challenges encountered in footing design often revolve around managing maximum settlement and differential settlement. The Winkler method is commonly employed to analyze a raft footing by modelling the founding soil as discrete elements characterized with soil subgrade modulus (k_s). The stiffness of the subgrade modulus is largely influenced by the Young's modulus of founding material (E_s), the Poisson's ratio of soil (υ), and the width of the footing (B). An innovative approach of employing compressible layers beneath a raft footing to reduce its effective footing width for design. These compressible layers, strategically positioned under low-loaded concentrated areas or the middle portion of the raft, enable control over the effective width of the footing, leading to an increased soil subgrade modulus (k_s). The outcomes include significant improvement on calculated values for maximum settlement and differential settlement.

1 INTRODUCTION

Structures supported by raft footings are commonly employed to address bearing capacity and settlement challenges. The pivotal aspect of raft footing analysis lies in determining the distribution of contact pressure and associated settlement beneath the structure. The analysis of raft footings involves the Winkler method, implemented through computer-software (SAFE), in terms of the effect of soil subgrade modulus (k_s), i.e. the interaction between founding soil and foundation represented by a series of linear elastic springs for discrete founding soil elements. This parameter, crucial in raft footing design, is intricately linked to the Young's modulus of founding material (E_s), the Poisson's ratio of soil (υ), and the width of the footing (B).

In the design of raft footings, the bearing capacity is typically high due to the substantial width of the raft footing. This is particularly evident when raft footings are adopted for deep basements, as the overburden pressure at the base of the raft footing and in the surrounding ground can significantly enhance the bearing capacity. As a result, the bearing capacity check is generally less crucial than the settlement assessment in raft footing design.

Settlement assessment in raft footing design is conducted through deformation analysis using SAFE modeling under Serviceability Limit State (SLS) loading combinations. The deformation results are influenced by the soil subgrade modulus (k_s) and the stiffness of the footing. The soil subgrade modulus (k_s) is inversely proportional to the width of the footing, resulting in lower k_s values for wider a raft footing. Consequently, geotechnical design to achieve settlement and differential settlement criteria can be challenging in raft footing design.

The above design findings also mentioned in GEO Publication No. 1/2006 that raft foundation are relatively large in size. Hence, the bearing capacity is generally not the controlling factor in design. Differential and total settlements usually govern the design. A common approach for the raft foundation design is to model the ground support as spring using the subgrade reaction (i.e. Winkler) method.

The function of compressible layer beneath a raft footing is similar to the sleeving for pile foundation or basement wall isolation layer, as they both serve to mitigate load transfer. By installing compressible layers beneath a raft footing, the width of the effective bearing area of the footing can be reduced. Therefore, the soil subgrade modulus (k_s) can be significantly increased, and this results in a reduction of the settlement and differential settlement under the footing. The following sections will discuss on theory behind and recommend the practices of application of a compressible layer beneath a raft footing.

2 DETERMINATION OF SOIL SUBGRADE MODULUS

The soil subgrade modulus (k_s) represents the relationship between soil pressure and displacement, commonly employed in structural analysis of footing foundations. It is important to note that the value of the soil subgrade modulus is not a fixed constant for a given soil; rather, it varies based on factors including the properties of the founding material, the dimensions of the footing (length and width), and the depth of embedment.

A comprehensive study by Terzaghi (1955) of the parameters affecting the soil subgrade modulus indicated that the value decreases with the width of the footing. To illustrate the influence of the width of the footing on k_s, the concept of the bulb of pressure can be used. While the footing widths increase from *B* to *n x B*, the depths of the stress bulb would increase from *D* to *n x D*, respectively. The influence of the depth of the pressure bulb on the settlement of the loaded area depends on the soil deformation characteristics of the subgrade. If the soil deformation characteristics remain relatively consistent across the depths, it can be assumed that settlement increases in direct proportion to the depth of the stress bulb. As the settlement of a footing increases, resulting in a larger width, the subgrade modulus would consequently decrease.

Terzaghi proposed that k_s for full-sized footings could be obtained from a plate-load test using the following equations:

For footings on sand,

$$k_s = k_1 \left(\frac{B+B_1}{2B}\right)^2 \quad (1)$$

For footings on clay,

$$k_s = k_1 \left(\frac{B_1}{B}\right) \quad (2)$$

where B_1 = side dimension of the square base used in the plate-load tests to produce k_1 and B = width of footing. However, the above equations deteriorate when B/B_1 is greater than 3.

2.1 Current Design Practice for Subgrade Modulus

Even though there are many different equations to determine soil subgrade modulus for footing design, the most commonly adopted equation was proposed by Vesic (1961) that the subgrade modulus could be computed using the stress-strain modulus E_s as

$$k_s = \frac{E_S}{B(1-\upsilon^2)} \quad (3)$$

where E_S = Young's modulus of soil, B = width of footing and υ = Poisson's ratio of soil.

The estimated soil subgrade modulus (k_s), calculated by Vesic's equation, serves as input for SAFE modeling in the footing design. The model generates outputs including structural forces such as bending moments and shear forces of footing elements under Ultimate Limit State (ULS) loading combinations, as well as deformation profiles and design bearing pressures under Serviceability Limit State (SLS) loading combinations.

However, there are certain design scenarios where Vesic's equation may be proved too simplistic and insufficient to address, such as footings founding on,

- multi-layer of founding materials;
- soil overlain on shallow bedrock; and
- certain depth below ground with excavated in-situ overburden.

2.2 Suggested Modified Method for Subgrade Modulus

To address the aforementioned complex design scenarios, a modified method is proposed for estimating the subgrade modulus (k_s) from first principles. As previously discussed, the soil subgrade modulus represents the conceptual relationship between soil pressure and deformation. The fundamental equation is defined as follows:

$$k_s = \frac{q}{s} \quad (4)$$

where q = applied pressure and s = induced settlement when q is applied.

For estimation of the soil subgrade modulus, it is suggested to work the other way around to calculate the induced settlement by applying a certain design pressure and considering multi-layer of founding materials with varies depth or with shallow bedrock, i.e. Step 4 to Step 7 below, instead of homogeneous soil stratum by Vesic's equation (Eq 3). The excavated in-situ overburden effect can also be considered under Step 2 and Step 3 to work out the net pressure of the footing. Then, the basic equation (Eq. 4) can be applied to obtain the soil subgrade modulus. The procedures are presented in Figure 1 and listed as follows:

Step 1: Assume a design pressure that can be derived with (Dead Load + Live Load) / Footing Area multiplied by 1.25.

Step 2: Calculate the effective overburden pressure of the excavated soil if the footing is underneath a deep basement. For the calculation of effective overburden pressure, the groundwater level can be taken at the lowest measured groundwater table which the founding materials have experienced such loading.

Step 3: Work out the net pressure for the estimation of settlement, which is equal to the design pressure subtracting the effective overburden pressure.

Step 4: Classify the founding materials underneath the footing into different strata based on the soil types and their deformation properties, i.e. Young's modulus of the soil.

Step 5: Determine the load spread influence factors, based on stress bulb graph (refer to Figure 2 and description below), load spread influence factors (i.e., q/q_o = ratio of applied pressure to induced stress at the certain depth below the footing) at the mid-depth for each soil strata.

Step 6: Estimate the individual settlement for each soil strata by the product of the thickness of each layer, stress at mid-depth and coefficient of volume compressibility (m_v).

Step 7: Calculate the total settlement by summing up the individual settlement for each soil strata.

Step 8: Apply the basic equation (Eq. 4) to obtain the soil subgrade modulus in the 1st iteration.

Step 9: Run the SAFE model with the estimated soil subgrade modulus (Step 8) and find the bearing pressure from the SAFE output under the Dead + Live loading combination.

Step 10: Compare the calculated bearing pressure outputs (Step 9) with the assumed design pressure (Step 1). If the difference between the two values is greater than 10%, adopt the calculated design pressure output (Step 9) to repeat the Step (1) to Step (8).

Step 11: Carry out the iteration until the difference to be within 10%.

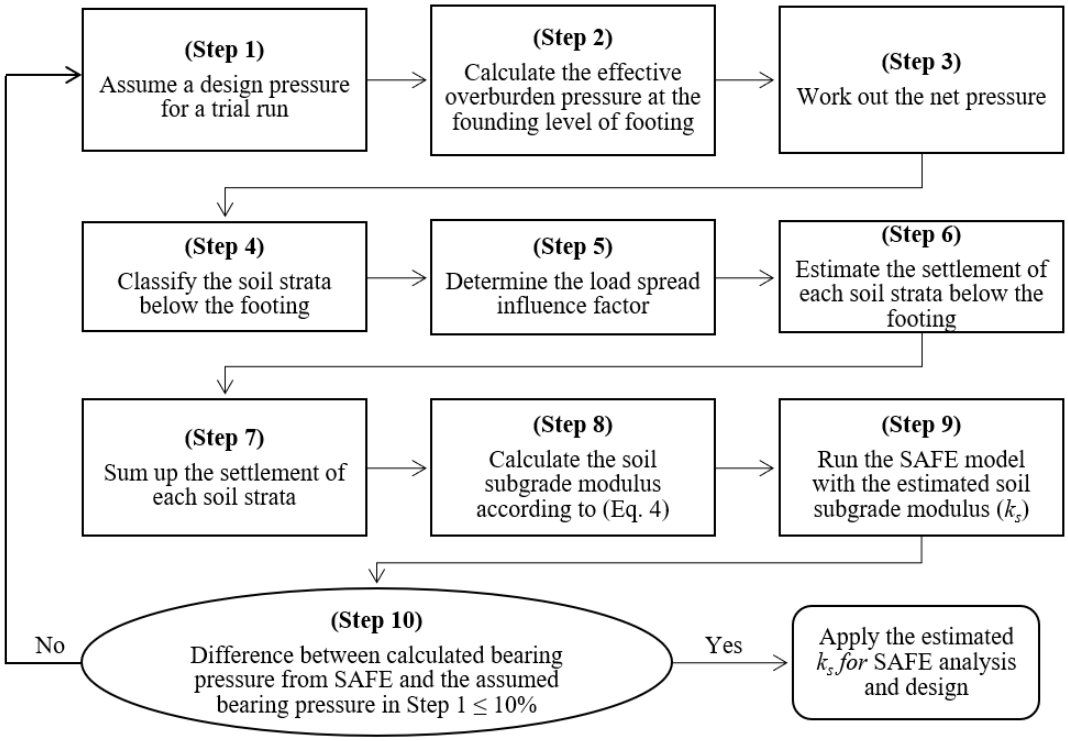


Figure 1: Flow Chart for Modified Method for Subgrade Modulus

A vertical pressure profile, also known as pressure bulb was proposed by Bowles (1974) based on Boussinesq equation. The pressure bulb (Figure 2) shows the relationship between the pressure bulbs and depth below the footing.

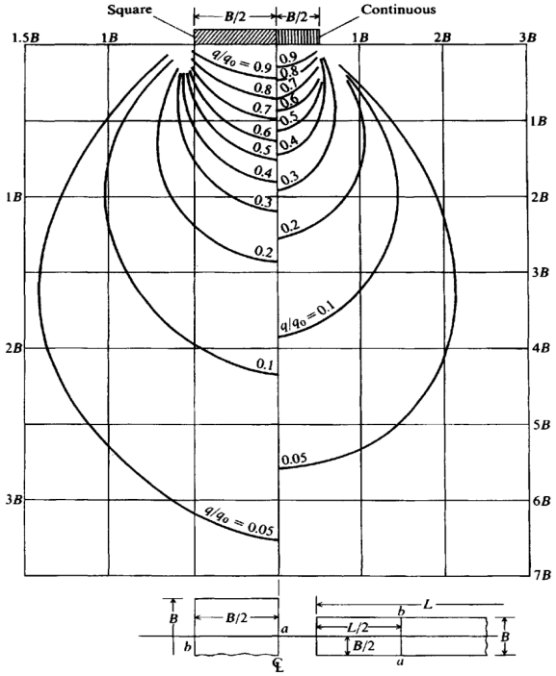


Figure 2: Pressure Bulbs based on the Boussinesq Equation for Square and Strip Footing

In consideration of the uncertainties in subgrade modulus estimation, it is advisable to conduct sensitivity analyses for Ultimate Limit State (ULS) structural and bearing design to enhance the robustness of the design. In certain scenarios, a higher subgrade modulus stiffness may result in significant bending moments and shear forces in a raft footing. This phenomenon can be explained by the relative stiffness factor proposed by Meyerhof (1953), which categorizes footings as either flexible or rigid bodies based on the ratio of footing structural stiffness to founding material stiffness. A smaller relative stiffness factor, indicative of a larger subgrade modulus of the founding material, may render the footing more 'flexible', increase of the design forces. It is recommended that sensitivity analyses cover a range of 50% to 150% of the estimated subgrade modulus for bearing capacity and structural checking.

2.3 Plate Load Test to Verify the Subgrade Modulus of Founding Material

The Plate load test is introduced in the Code of Practice for Foundations 2017 which specified the procedure and acceptance criteria for the test. The main purpose of plate load test is to verify the bearing capacity of the founding soil, as well as the Young's Modulus (E_s) of the founding materials. The two acceptance criteria are listed below:

- To verify the bearing capacity of the founding soil, the maximum settlement of the test plate shall not exceed 0.15B, where *B* is the width or diameter of the test plate; and
- To verify the Young's modulus of founding soil, the settlement of the plate after the completion of the first cycle of the load test shall not exceed the settlement calculated from Eq. (4) or Eq. (5) below.

$$S = \frac{W_t(1-\upsilon^2)}{1.13\,E_s\,B} \quad \text{for square test plate} \tag{4}$$

$$S = \frac{W_t(1-\upsilon^2)}{E_s\,B} \quad \text{for circular test plate} \tag{5}$$

where S = the settlement of the test plate measured at test load, W_t = test load of, E_s = Young's modulus of soil, B = width or diameter of test plate and υ = Poisson's ratio of soil.

The settlement from the plate load test will be adopted to back-calculate the Young's modulus (E_s) using Eq. (4) or Eq. (5). If the back-calculated E_s value is smaller than the design value of E_s, a design review shall be carried out based on the back-calculated E_s values. Subsequently, the soil subgrade modulus shall be updated to reflect the actual Es from the plate load test, and the SAFE design models shall undergo re-analysis to verify both the Ultimate Limit State (ULS) structural and bearing design, as well as the Serviceability Limit State (SLS) deformation assessment to be satisfied.

3 DESIGN CONCEPT OF COMPRESSIBLE LAYER APPLICATION

In light of the preceding discussion, it is evident that the width of the footing (B) plays a crucial role in determining the soil subgrade modulus (k_s). A reduction in the effective footing width results in an increment of the soil subgrade modulus (k_s). To reduce the effective footing width, compressible layers by means of non-bearing zone are employed to be placed beneath the footing at areas of low-load concentration. By implementing the compressible layers, the effective width of the footing can be efficiently limited and managed, thereby enhance the soil subgrade modulus beneath the footing.

On the other hand, placement of compressible layers underneath a portion of the footing would reduce the bearing area and so may cause higher bearing pressure. It is suggested that the proposed compressible layers should be placed in low-loaded areas which can minimize the adverse effect on increment of the design bearing pressure. As mentioned above, the pressure capacity check is normally less critical for the design of raft footing with certain depth of soil embedment.

Conversely, improving the soil subgrade modulus can greatly enhance the settlement and differential settlement outcomes of the raft footing, which are particularly important in raft footing design.

There would be some concessions between the bearing capacity checking and the settlement assessment for the application of compressible layers underneath portions of the raft footing. This typically involves several rounds of trial iteration to determine the optimal location / portion as well as the size of the compressible layers to be required.

4 PARAMETRIC STUDY FOR THE IMPLEMENTATION OF COMPRESSIBLE LAYER

A simple parametric study was carried out to test the effect on a footing design with or without compressible layer (i.e. non-bearing zone) by using the computer software (SAFE). The results of maximum bearing pressure and maximum settlement as well as differential settlement of the footings were compared. A typical raft footing of 10m(width) x 10m(length) x 0.5m(thick) was modeled with and without the implementation of compressible layer beneath the footing. To emphasize the differential settlement effect, a line load of 175 kN/m was applied with a 0.5 m offset from each of the four edges of the footing.

- For Case 1, no compressible layer was applied. The whole footing was fully founded on the bearing material.
- For Case 2, a 4m(width) x 4m(length) compressible layer was positioned at the center of the footing, creating a non-bearing zone beneath the footing.

The SAFE model settings for the two cases are shown in Figure 3 and the results are presented in Figure 4 and summarized in Table 1 below.

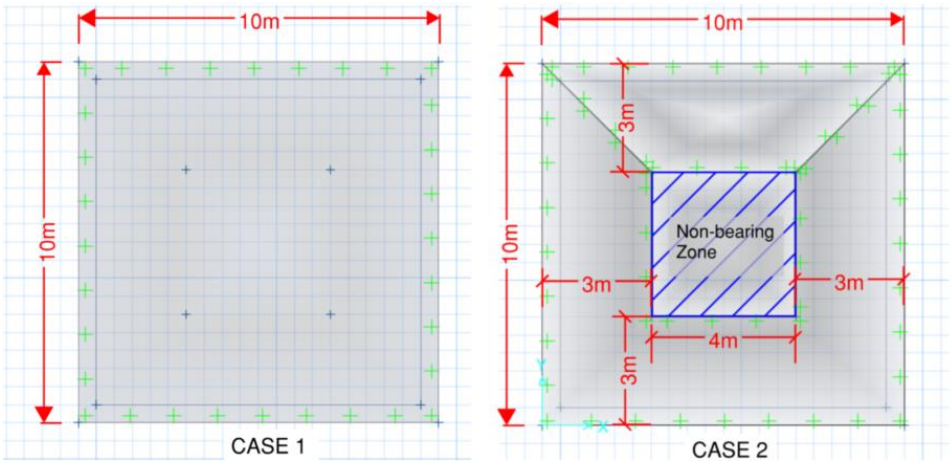


Figure 3: SAFE Models Settings for the Parametric Study

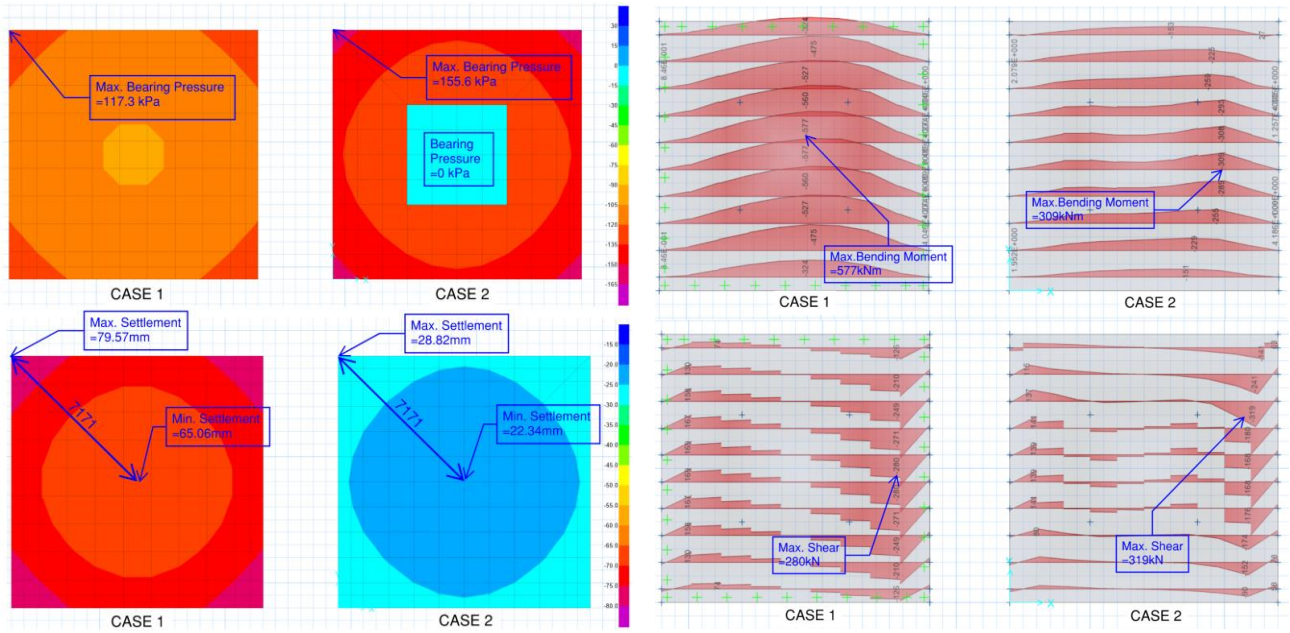


Figure 4: SAFE Analysis Results for the Parametric Study

Table 1: Summary of Inputs and Outputs of Parametric Study

Case	Inputs			Outputs				
	Width of Compressible Layer (m)	**Effective Width of Footing, B (m)**	**Subgrade reaction modulus, k_s* (kN/m^3)**	**Max. bearing pressure (kPa)**	**Max. Bending Moment (kNm)**	**Max. Shear Force (kN)**	**Max. Settlement (mm)**	**Max. Angular Rotation**
1	0	10	1600	127	577	280	80	1:487
2	4	3	5400	156	309	319	29	1:1091

*Remark: * Subgrade reaction modulus were calculated according to Eq. (3), where Es = 15MPa and v = 0.3 were assumed.*

Based on the results of the parametric study, it is noticed that the maximum settlement and angular rotation of footing (also reflecting on the differential settlement) of Case 2 is much smaller than those of Case 1, whereas the maximum bearing pressure of Case 1 is slightly larger than that of Case 2. According to the above parametric study, the benefits resulting from the application of compressible layer is remarkable for the settlement and differential settlement assessment, which is normally critical for raft footing design.

A sensitivity analysis was also carried out for Case 2, which reviewed the analysis results from 50% and 150% of the subgrade modulus. The results of these two sensitivity analyses, namely Case 2A with 50% subgrade modulus and Case 2B with 150% subgrade modulus, are presented in Figure 5 and Table 2.

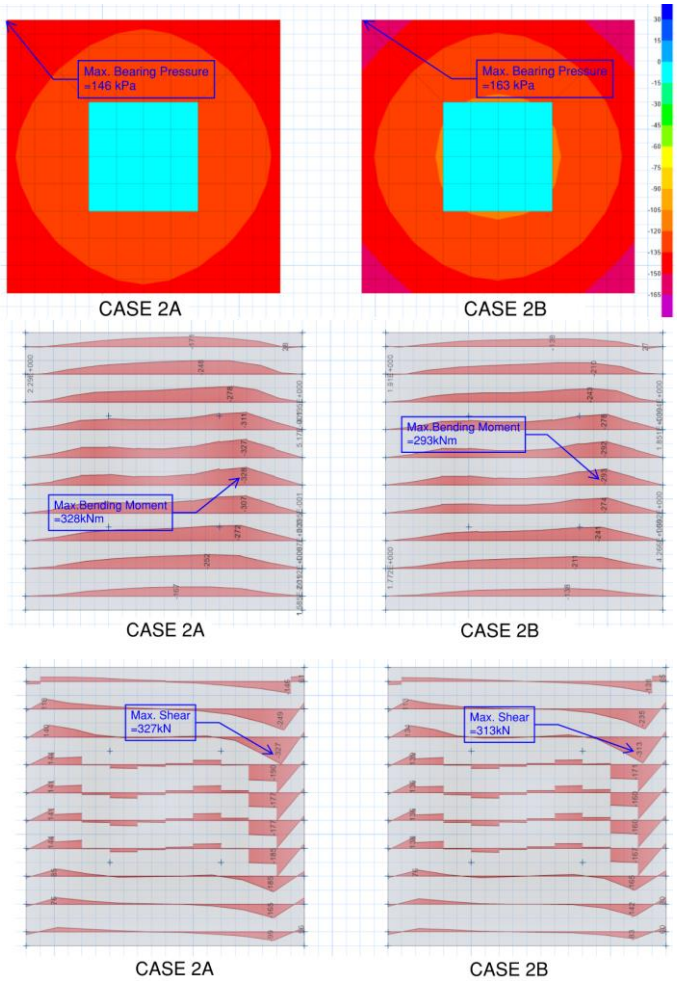


Figure 5: SAFE Analysis Results for Sensitivity Analysis

Table 2: Summary of Input and Output of Sensitivity Analysis

Case	Subgrade Modulus, k_s (kN/m^3)	Max. Bearing Pressure (kPa)	Max. Bending Moment (kNm)	Max. Shear Force (kN)
Case 2A	2700 (50%)	146	328	327
Case 2	5400 (100%)	156	309	319
Case 2B	8100 (150%)	163	293	313

From the sensitivity analysis, it can be noticed that the maximum bearing pressure under the footing is larger when adopting a larger soil subgrade modulus, while the settlement is much smaller in Case 2B (i.e. 150% of the estimated soil subgrade modulus). On the other hand, the bending moment and shear force in the footing are smaller in Case 2B since the deformation of footing is smaller. For this parametric study conditions, the results from the upper bound of the sensitivity analysis (Case 2B) shall be used for the ULS bearing design and the results from the lower bound of the sensitivity analysis (Case 2A) shall be used for the ULS structural design.

5 CASE STUDIES FOR APPLICATION OF COMPRESSIBLE LAYER

The applications of compressible layer have been proposed to a few local projects in Hong Kong. The main purpose was to increase the soil subgrade modulus beneath footing and therefore to reduce the total settlement

and differential settlement of the footing. In Case Study 1, the wide footprint of the raft footing led to a reduced value of the soil subgrade modulus for SAFE analysis. As a consequence, this exacerbated challenge associated with settlement in the footing design, posing significant issues that need to be addressed.

On the other hand, when there are some sensitive structures or geological features underneath the footing, the design of the footing shall minimize the induced stresses to those structures / geological features. By limiting the design (contactable) width of a footing, the depth of the stress bulbs can be managed and so to reduce the impact on those structures / geological features. The footing of Case Study 2 was located at the marble areas where cavities were found in depth. The implementation of compressible material could limit the load spreading on the marble surface within acceptable limit.

5.1 Case Study 1- Large Raft Footing for Deep Basement

Case Study 1 was a large raft footing for a deep basement founding on Completely Decomposed Tuff (CDT). In the initial design, Vesic's equation (Eq. 3) was applied to estimate the subgrade modulus for SAFE analysis. Even though the Young's modulus of the founding CDT material was not low which the SPT'N values were around 40 blows, the estimated subgrade modulus was small due to the large footing width (B). After applying the small subgrade modulus in the SAFE analysis, it was revealed that both the maximum settlement and differential settlement were significantly over the design limits, which inevitably became a major challenge to for the raft footing design.

Table 3: Summary of Inputs and Outputs of Initial Design without Compressible Layer

Case	**Effective Width of Footing, *B* (m)**	**Subgrade reaction modulus, k_s (kN/m^3)**	**Max. Bearing Pressure (kPa)**	**Max. Settlement (mm)**	**Max. Angular Rotation**
Initial Design	51	1724	456	264	1:426

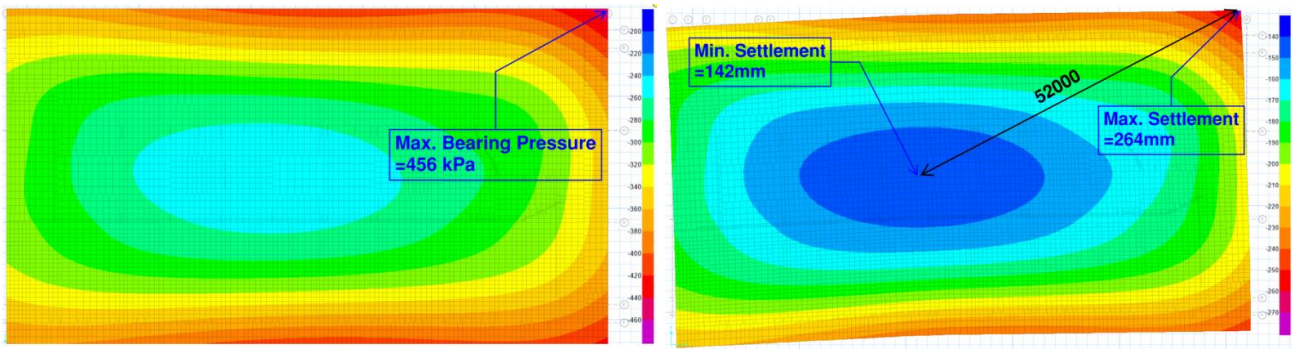


Figure 6: SAFE Analysis Results for Initial Design without Compressible Layer

The initial design showed that both settlement and angular of rotation (i.e., differential settlement) significantly exceeded the recommended acceptance criteria in CoP Foundations 2017 which are 30mm and 1 in 500, respectively. In order to control the design settlement, two measures were considered to improve the subgrade modulus value:

- Apply compressible layer for portions of footing under the low-loaded areas. This would reduce the effective footing width for subgrade modulus calculations.
- Adopt the modified method for estimation of the subgrade modulus as described in Section 2.3. The modified method would take into account for the effect of existing overburden (i.e. depth factor of basement) as well as the increment of soil stiffness with depth.

By applying of the two measures, the subgrade modulus and so the settlement and differential settlement results from SAFE analysis had been significantly improved which were then within the design acceptance limits.

Table 4: Summary of Inputs and Outputs of Improved Design with Compressible Layer

Case	Effective Width of Footing, *B* (m)	Subgrade reaction modulus, k_s* (kN/m^3)	Max. Bearing Pressure (kPa)	Max. Settlement (mm)	Max. Angular Rotation
Improved Design	8	25,000	614	24.6	1:1203

Remark:

** Subgrade reaction modulus were calculated based on the reduced footing width as well as the considerations of multi-layer of founding materials and 14m overburden effect as per the modified method mentioned in Section 2.2 of this paper.*

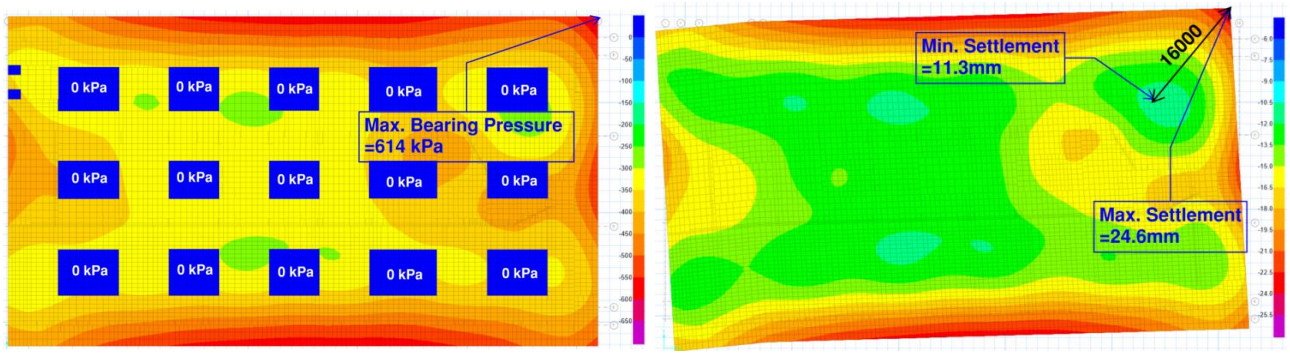


Figure 7: SAFE Models Results for Improved Design with Compressible Layer

As shown in Figure 7 above, the proposed compressible layers were laid beneath the footing to minimize the load transferring from the footing to the founding soil, to create some non-bearing zones and reduce the effective width of the footing thereby increased the soil subgrade modulus. The estimated settlement was effectively reduced without the need of any complicated ground treatment works.

On the other hand, the maximum bearing pressure had increased by 45%. Even though there was quite large percentage increase of the design bearing pressure, it was still well within the design bearing capacity of CDT, i.e. 800kPa for 8m width of footing with overburden.

The design approach remained consistence with the current practice, but some trials were carried out to fine-tune the area of non-bearing zone and soil subgrade modulus. No major change to the method of footing construction is envisaged and also similar to the general construction method, just place the compressible material is required to be placed the footing/soil stratum interface strategically prior to the reinforcement fixing.

5.2 Case Study 2 - Footing above the Underground Structure / Adverse Geological Feature

A common challenge in footing design arises when the load spreading from the footing adversely impacting existing structures or sensitive geological features below. The implementation of compressible layer beneath the footing can also help to mitigate this problem by reducing the load spreading influence zone.

Case Study 2 was a footing proposed for areas with presence of marble geology containing cavities. As a result of proposed raft footing, there would be additional pressure exerted on the underlying soil, which would then be spread to the marble rock surface underneath.

In view of the above-mentioned design concern, compressible layers were proposed to be place beneath the footing with the following considerations:

- The proposed compressible layer could significantly limit the influence depth of the additional pressure caused by the proposed structure;
- A certain clearance between the proposed compressible layer shall be kept so as to mitigate the overlapping effect of the pressure bulbs introduced in Section 2.3;
- The design bearing pressure applying to the founding soil would increase due to the reduced bearing area, the bearing capacity of founding soil shall be checked and satisfied.

With these considerations, the optimal locations and widths of the compressible layer may require some iterations to maximize its effectiveness.

Refer to Figure 8, the arrangement of compressible layer was installed below the walls of the proposed structure with designed width and spacing, which intended to minimize the overlapping effect between pressure

bulbs. The compressible layers were installed at low-loaded areas so that the bending moment and shear force in footing could be controlled accordingly.

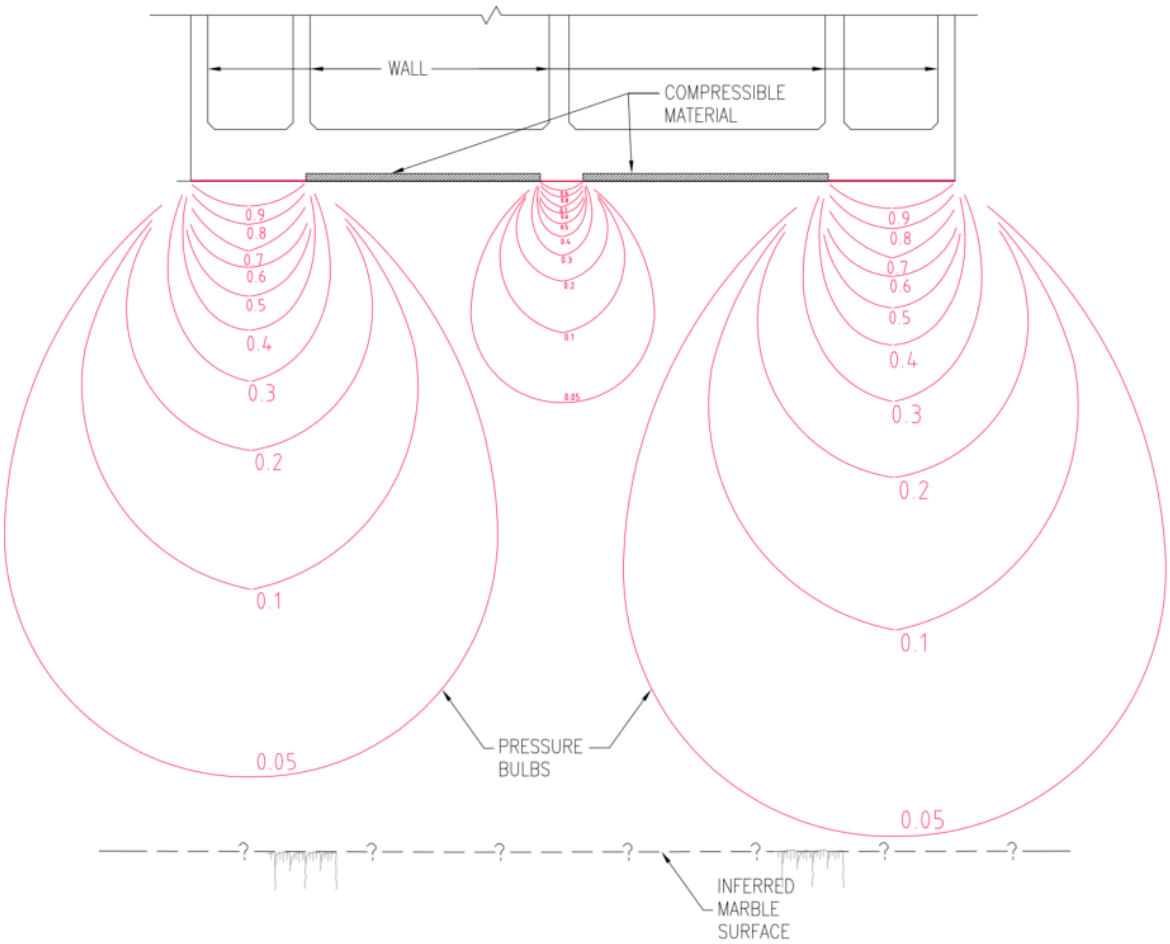


Figure 8: Pressure Bulbs with Application of Compressible Layer

6 SUITABLE MATERIAL FOR COMPRESSIBLE LAYER

Expanded Polystyrene (EPS), shown in Plate 1, which has a long history of application for construction which can be a suitable type of material for compressible layer to be placed under footing. The proposed compressible layer should be soft enough to minimize the load transferring from the footing to founding materials. The lowest grades of EPS can be considered, and their elastic modulus varies from 1,450kPa to 2,200kPa, while the density varies from 11kg/m^3 to 13.5kg/m^3. The material properties of the EPS are presented in Table 5 below for reference. The advantage of EPS is easy handling and easy installation due to its light weight, and it is not reactive with concrete. Similar usages of EPS were commonly applied for construction, such as joint filler for movement joints and horizontal sleeving layer along pile shaft and basement walls.

Table 5: Material Properties of Expanded Polystyrene

Grade	Density (kg/m^3)	Min. Flexural Strength (kPa)	Min. Elastic Modulus (kPa)	Compressive Stress at 1% deformation (kPa)	Compressive Stress at 10% deformation (kPa)
L	11	60	1,450	14	50
SL	13.5	150	2,200	23	70



Plate 1: Compressible Layer beneath Footing

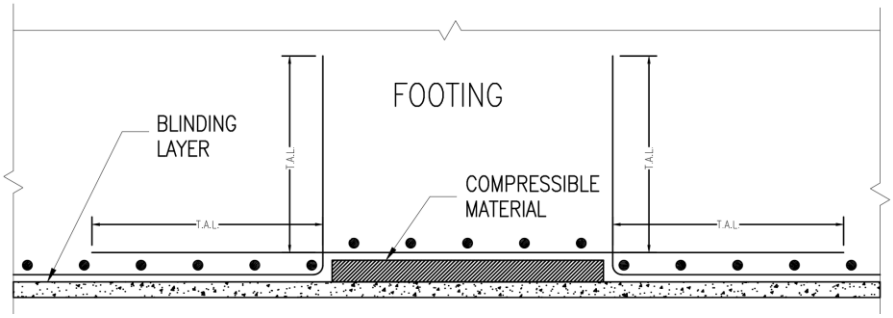


Figure 9: Typical Installation Detail of Compressible Layer

Referring to Plate 1 and Figure 9, the compressible materials were placed on top of the blinding layer and were embedded into the footing. The structural design of the footing should take into account of the relative thinner design depth, along with the structural detailing required for lapping the reinforcement.

Expanded Polystyrene (EPS) possesses several advantageous properties that make it as an ideal construction material. Firstly, EPS is an inert and organic material, meaning it will not decay over time. This property ensures its longevity and durability, making it suitable for long-term use without the risk of rotting. Additionally, EPS is resistant to pests such as ants, termites, and rodents, as it lacks any nutritional value for these organisms. This further enhances its durability and makes it widely used for construction and insulation purposes. Moreover, EPS is not susceptible to damage from the normal range of climate conditions, including temperature fluctuations and moisture exposure. This resilience ensures its stability and performance under various environmental conditions. When specified and installed correctly, EPS can be relied upon as a durable and long-lasting material, providing lasting benefits as compressible layer.

The required thickness of compressible layer shall be determined based on the following:

- The expected deformation of the compressible layer under construction load during the curing of wet concrete, s_1;
- The expected deformation of the compressible layer under working load, s_2;
- The residual thickness of compressible layer deducting the above-mentioned deformation(s_1+s_2);

To estimate the deformation induced by the wet concrete during construction (s_1), it can be calculated by dividing the wet concrete self-weight pressure by the elastic modulus of the compressible layer as shown in Table 5. The stress within the compressible layer under anticipated working conditions can be determined using a Finite Element model, such as Plaxis, facilitating the estimation of the deformation of the compressible layer (s_2).

To ensure the proper performance of the compressible layer, it is recommended that the proposed thickness of the compressible layer should be a least two time of the estimated accumulated deformation (s_1 + s_2).

7 CONCLUSIONS

The compressible layer has a long history of application in construction industry, mainly for movement joints, horizontal sleeving for piles and basement walls to control load transfer and spreading. This paper proposed the use of compressible layer underneath portion of raft footing in order to control the loaded width of the footing. By reducing the loaded width of the footing, the subgrade reaction modulus of the footing would be increased. This yields several advantages, including the reduction of settlement and differential settlement, which in turn has significant implications for the overall performance of the foundation.

In addition, this paper suggested a modified method for the estimation of the subgrade modulus. The modified method allows for the considerations of diverse geological and depth conditions as well as excavation of the overburden soil. Utilizing the modified subgrade modulus in SAFE analysis results in more realistic and accurate Serviceability Limit State (SLS) outcomes, particularly in settlement and differential settlement assessment.

This paper presents a parametric study and two case studies to elucidate the calculation procedures and practical applications of the compressible layer in footing design. These examples showcase the effectiveness of the proposed approach in real-world construction projects.

REFERENCES

[1] Cheng, Yung-ming, 1989. *Finite Element Analysis of Soil-structure Interaction Problems, with Application to Basement Construction Problems*: The University of Hong Kong

[2] Joseph E. Bowles, P.E., S.E.1996. Chapter 9.6, *Foundation Analysis and Design*: McGraw-Hill Book Co

[3] Geotechnical Engineering Office. *GEO Publication No. 1/2006 Foundation Design and Construction:* Civil Engineering and Development Department, HKSAR

[4] Karl Terzaghi, 1955. *Evaluation of Coefficients of Subgrade Reaction*

[5] Meyerhof, G. G., 1953. *Some Recent Foundation Research and its Application to Design*, Struct. Eng., 31(6) 151–167.

[6] The Buildings Department, 2017. *Code of Practice for Foundations 2017:* The Buildings Department, HKSAR

[7] The Hong Kong Institution of Engineers, 2019. *An Explanatory Handbook to the Code of Practice for Foundations 2017:* The Hong Kong Institution of Engineers

[8] Vesic, A.B. [1961]. *Beams on elastic subgrade and Winkler's Hypothesis*, Proc. 5 th. Int. Conf. on Soil Mech. Found. Engrg., Paris, p.p. 845-50.

[9] Ali Khosravifardshirazi, Akbar A. Javadi, Mohammad Hassan Khanjanpour, Behnaz Khosravifardshirazi and Mohammad Akrami, 2022. Role of Subgrade Reaction Modulus in Soil-Foundation-Structure Interaction in Concrete Buildings: Buildings 2022, 12, 540

The Use of Removable Ground Anchors in Deep Basement Excavation in Hong Kong

Brian K.L. Ieong
AECOM Asia Company Limited
Rupert K.Y. Leung
Halcrow China Limited

ABSTRACT

Deep excavation is a critical aspect of construction projects that involve building foundations, tunnels, basements, or other below-grade structures. Ground anchors are a load transfer system designed to transfer the forces applied to it to a competent stratum, commonly used to support temporary excavation support system for deep basement excavation. By using ground anchors, the need for installing temporary struts can be eliminated and so congestion in basement construction can be significantly reduced. Ground anchors are also very suitable for sites on which flying/corner struts system are difficult to be installed. For ground anchors used in private development projects in Hong Kong, the temporary perimeter piles wall are usually constructed along the lot boundaries and so unavoidably the temporary anchors are required to be installed beyond the lot boundaries and encroached upon government land. In the past, the ground anchors were unavoidable to be left-in-place below ground upon completion of basement construction. Advancements in the ground anchor technology include the development of a load distributive compression type removable anchor which offers a complete solution where anchorage systems can be easily removed once they become redundant. The use of removable ground anchors has been gaining popularity gradually because they are not required to be left-in-place below ground. This paper presents the technology behind and shares the experience of using a proprietary product of load distributive compression removable anchors in a deep basement excavation project in urban area of Hong Kong. Apart from that, the details and experience of using another type of single bore multiple anchors, which are also load distributive compression removable anchors, used in previous deep basement projects are shared.

1INTRODUCTION

Ground anchors are active structural reinforcements that optimise safety and ground stability, for both temporary and permanent structures. Anchors are often used in temporary retaining walls to stabilise excavation during the construction phase, or they can even be used as a permanent solution for retaining walls – especially when building in unstable or sloping ground. The anchor ensures that the ground remains stable and allows for deep, wide excavations. It is often temporary, because the long-term stability of the ground is maintained by the structure built in the excavation (car parks, basements, etc.).

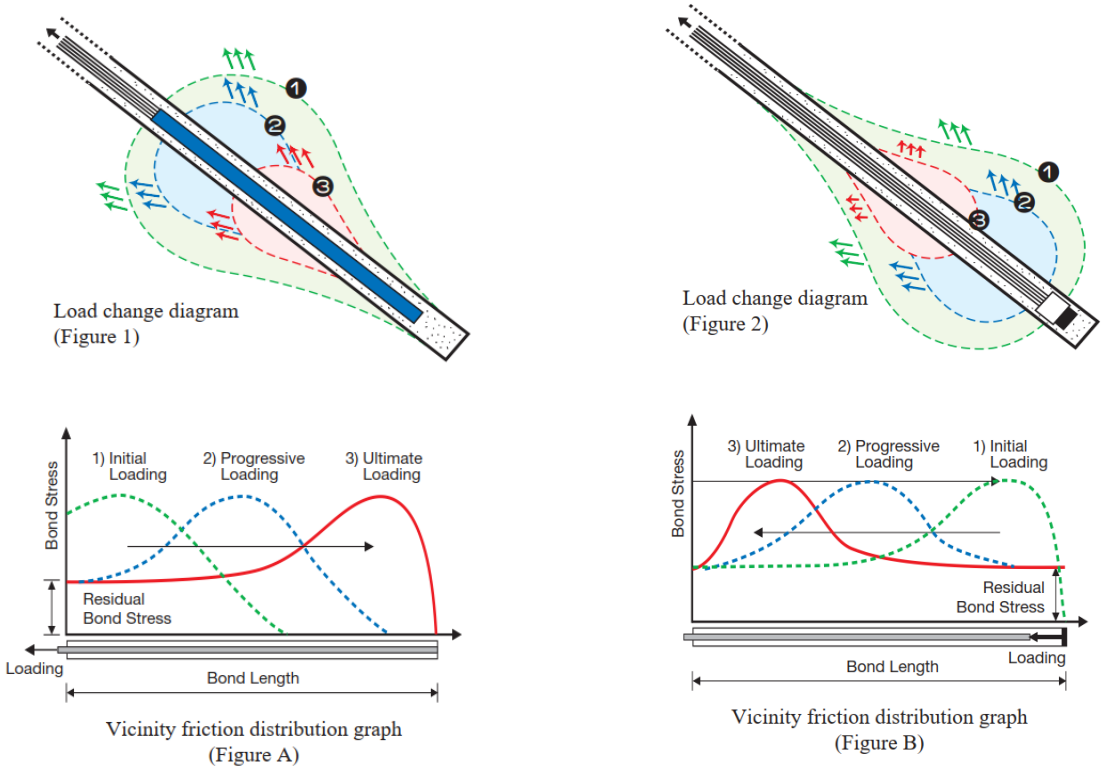
In Hong Kong, installation of temporary ground anchors in government land outside the private lot boundaries were not common as part of the excavation and lateral support (ELS) works for basement construction in the past. Government departments including Lands Department and Highways Department have the view that ground anchors, whether permanent or temporary, are not desirable and applications for permission to install ground anchors must fully justify the need for their use as against alternative methods available.

Temporary anchors, although not permanently sterilising land, are similarly undesirable and in particular can give rise to problems when detensioned.

For temporary ground anchors, in the past, after destressing operation by removing the anchor head and wedges through flame cutting of the strands, they were unavoidable to be left-in and this would sterilize the government land. Rows of temporary anchor tendons left in place can inhibit future construction especially in densely-populated urban areas. The use of removable ground anchors has been developed overseas since the mid 1970s. In Hong Kong, the use of removable ground anchors has been gaining popularity gradually because they are not required to be left-in-place below ground. Load distributive compression removable anchors is a type of removable ground anchors commonly-used in Hong Kong nowadays. In this paper, the load transfer mechanism and removal procedure of 2 types of removable ground anchors, namely, SW-RCD (Samwoo - Removable, Compressive and load Distributive) and SBMA (Single Bore Multiple Anchor) are introduced. Also, the experience of using these 2 types of ground anchors in recent projects is shared.

2 LOAD DISTRIBUTIVE COMPRESSION REMOVABLE ANCHORS

In the conventional type of anchors for which the pre-stressing strands cannot be removed, they are of load concentrative type. Low efficiency of load transfer in conventional anchors is due in part to non-uniform load distribution along the bond length. However, it is fully acknowledged by researchers who have investigated grout/ground load transfer that the distribution of load transfer along the fixed anchor is non-uniform due to general incompatibility between elastic moduli of the anchor tendon, anchor grout and the ground. In the vast majority of conventional anchors, after initial stressing, the bond stress is concentrated over the proximal end of the fixed anchor, while the distal end of the fixed length remains unstressed. As the prestressing load is increased, the ultimate bond stress at the proximal end of the fixed length along either (or both) the steel/grout interface or the grout/ground interface is exceeded. Figure 1 depicts this load transfer phenomenon, referred to as “progressive debonding”. The area under the bond stress distribution line in red represents the ultimate load in the anchor. It can be seen that the load does not increase uniformly with increasing length, causing progressive debonding which can lead to the anchor becoming over-stressed, resulting in failure of the anchor.



Load Concentrative Tension Type Anchor *Load Concentrative Compression Type Anchor*

Figure 1: Load Distribution of Conventional Anchors (SAMWOO)

To eliminate the problem of progressive debonding, load distributive compression type anchors, which can uniformly distribute the anchor load to the grout body and soil/rock along the theoretical length of the bond zone, are gaining its popularity. The load transfer mechanism of load distributive compression type anchors is illustrated in Figure 2.

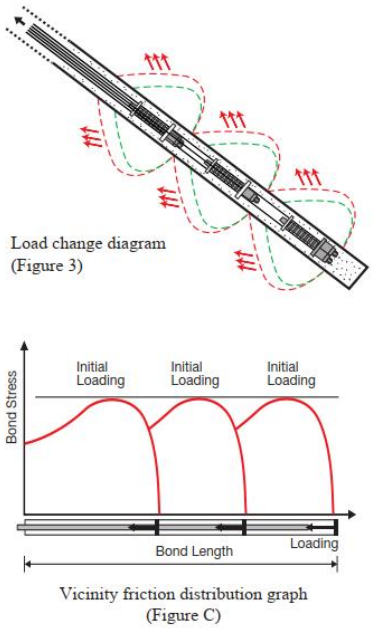


Figure 2: Load Transfer of Load Distributive Compression Type Anchors (SAMWOO)

In Hong Kong, at least 2 types of load distributive compression type anchors had been used so far. One is SBMA anchors and the other is SW-RCD anchors, both are removable ground anchors.

3 SBMA Anchor System

The SBMA system (see Figure 3) involves the installation of multiple units of anchors into a single borehole and the fixed length of each unit anchor being staggered within the borehole length to mobilize its own capacity independent of other unit anchors. Each unit anchor has its own individual tendon and its own unit fixed length in the borehole, and is loaded by its own unit stressing jack. The loading of all the unit anchors is carried out simultaneously by multiple hydraulically synchronized jacks which ensure that the loads in all unit anchors are always identical. The strands are contained in the strand tubes, each tube bends around a metal/aluminum saddle connected to a short steel reinforcement/GFRP stabilizing bar. This multiple SBMA anchors system is also called "U-loop" anchors system.

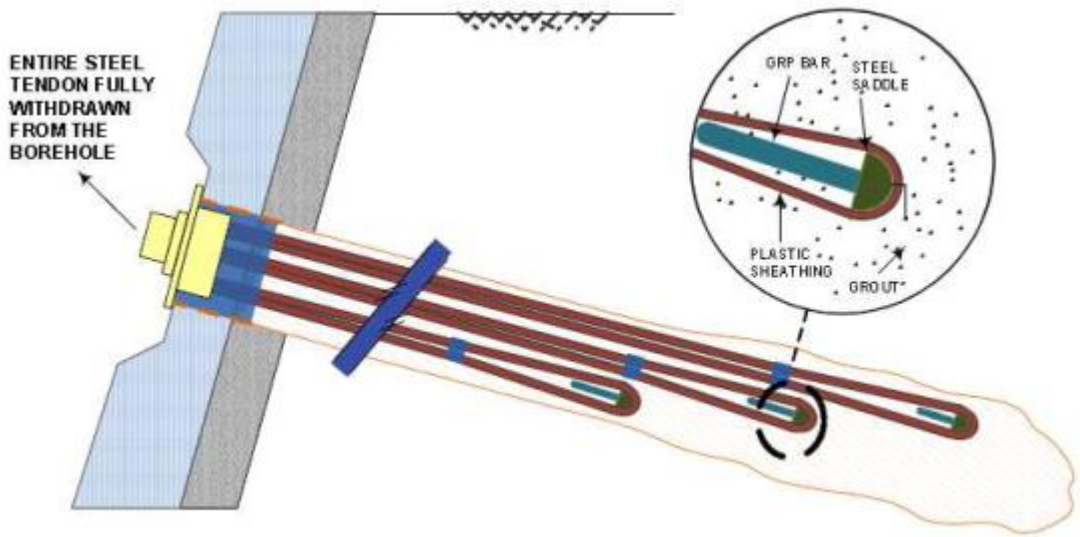


Figure 2: Removable SBMA System

Figure 3: Typical Detail of SBMA Anchors (M. R. Sentry (2012))

The general procedure for destressing and removing the prestressing strands of SBMA anchors by means of a U-loop system is illustrated in Figure 4.

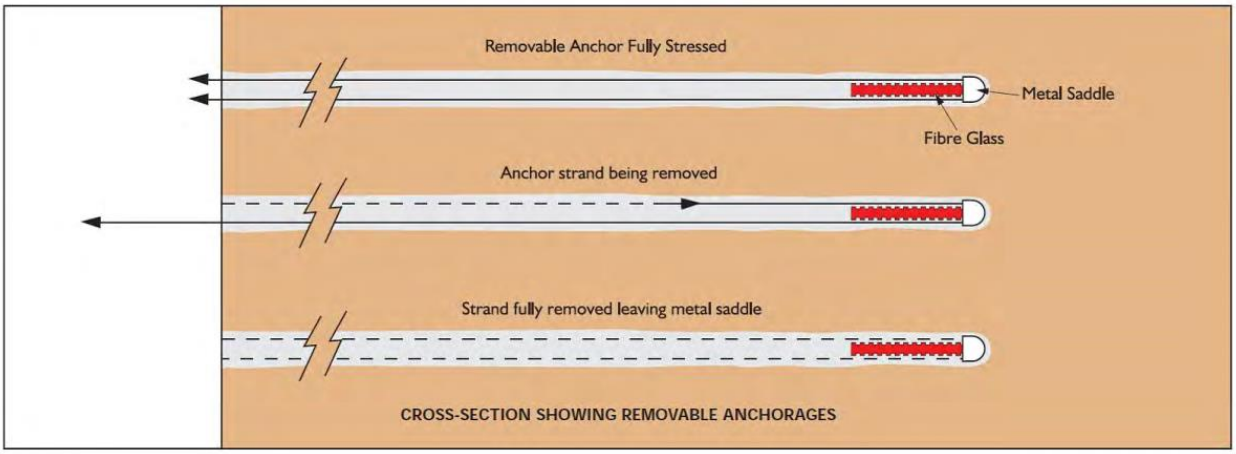


Figure 4: Removal of Strands of SBMA Anchors

SBMA anchors with capacity of 2000 kN were firstly used in Hong Kong for excavation of MTRC Central Station (see Plate 1).



Photograph 3. 200-tonne working capacity multiple anchors at Central Station in Hong Kong.

Plate 1: SBMA Anchors used in MTRC Central Station

4 SW-RCD Anchors

In SW-RCD removable anchors, the prestressing strands are contained in Polyethylene PE sheath (black colour) and the sheath is connected to an aluminum anchor body, see detail in Figure 5.

Classification	● Removable Anchor (SW-RCD Anchor) 
Material	Corrosion-resistant aluminum anchor body
Manufacturing Method	Aluminum die-casting technique
Anchor Body Structure	• Steel strand built-in structure protects PE sheath and steel strand. • Precision combined method and structure created by die-casting technique prevent grout infiltration.
Performance	• Due to decrease in grout debonding, removal performance increases. • Due to high precision and steel strand built-in technique, removal performance increases.

Figure 5: Aluminum Anchor Body of SW-RCD Anchors (SAMWOO)

Typical anchor bodies for multiple strands are shown in Figure 6. The greater is the number of PE sheaths, the larger is the anchor capacity. As shown in Figure 7, a typical section showing SW-RCD anchor bodies in different locations of a drilled hole is illustrated.



Figure 6: Aluminum Anchor Body of SW-RCD Anchors with Different Nos. of Strands (SAMWOO)



Figure 7: SW-RCD Anchor Bodies at Different Locations along the Anchor Length (SAMWOO)

The removal principle of SW-RCD anchors is illustrated in Figure 8. The strands are first destressed by flame cutting to separate them from the waler. After removing the waler, by rotating the steel strands in clockwise direction, the wedges are released. The strands can then be removed manually to separate them from the wedges.

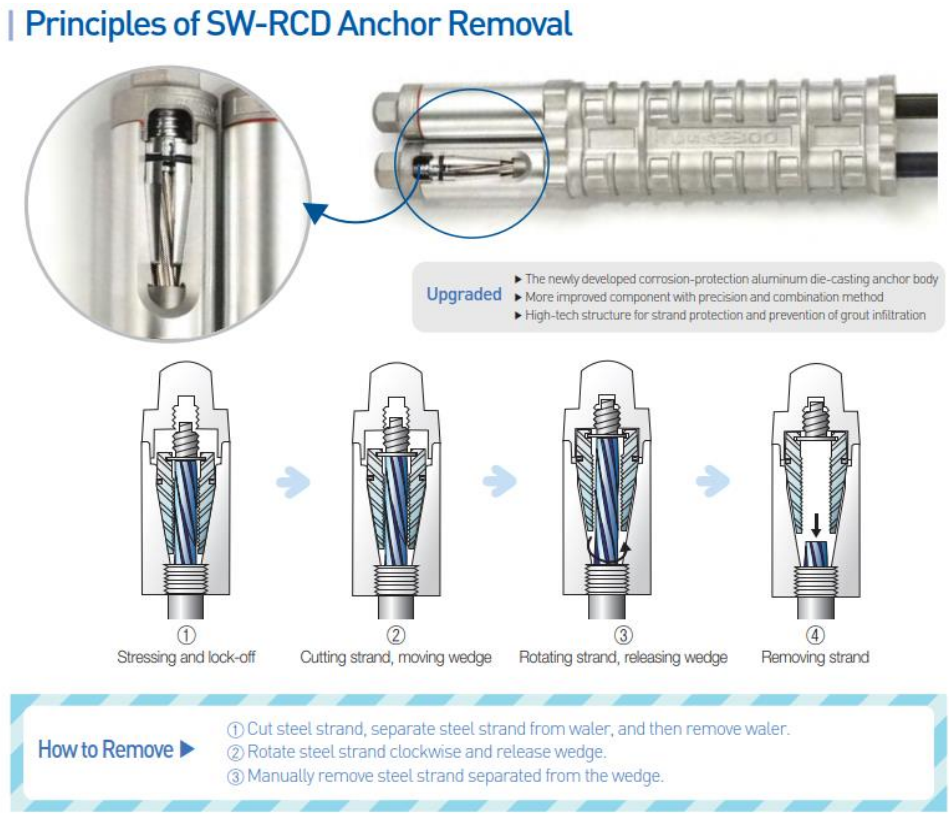


Figure 8: Principles of Removing SW-RCD Anchors (SAMWOO)

The following link provides a video of the strand removal process:

https://www.youtube.com/watch?v=wut8LVNsuNY

5 PROJECT EXPERIENCE SHARING IN USING SBMA AND SW-RCD ANCHORS

5.1 Project A (Using SMBA Anchors)

A large natural terrain on government land is located at the back of the project site. Bulk excavation (maximum depth was about 20 m) along the toe line of the natural terrain was carried out for construction of a semi-basement structure supported by bored piles foundations. The temporary ground anchors were unavoidably required to be installed below government land and Lands Department had imposed a condition that the anchors should be removed upon completion of the building. So removable ground anchors were the only option for implementing the basement excavation works.

The first author adopted 6 layers of SBMA anchors to provide lateral support system to the temporary soldier piles (303x305x223 kg/m UC at 1 m c/c) given that conventional flying/raking struts were not feasible

to be installed. The length of anchors varied from 15 m to 29 m and inclined at 30 degrees from the horizontal. Each anchor consisted of 12 strands with 15.7-mm diameter super grade low relaxation wires (with capacity of 1,750 kN). The anchors were designed to be bonded in Grade III rock. FLAC analysis was adopted for the ELS analysis. The close-up views of U-loop saddle and fabricated anchors units used are shown in Plates 2 and 3 respectively.



Plate 2: Saddle at the end of U-loop System



Plate 3: Fabricated Anchor Units

Close-up and bird's-eye views of the completed ELS works are shown in Plates 4 and 5 respectively.


Fig. 8 Ground anchor system can provide clear site for subsequent construction works

.

Plate 4: 6 layers of SBMA anchors

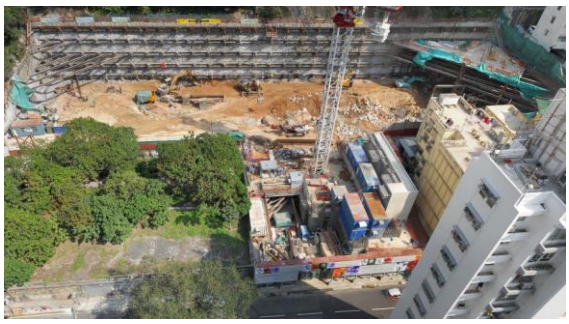


Plate 5: Bird's-eye View of the Completed ELS Works

5.2 Project B (Using SW-RCD Anchors)

The project site was located in urban area. Deep excavation with depth of 48 m was carried out for construction of a semi-basement structure. A public road, which is a single 2-lane carriageway is located on the crest platform at the top of the excavation. The vertical elements of the ELS system comprised 610-mm dia. pipe piles (inserted with 305 x 305 x 223 kg/m UC) at 1.8 m c/c. Similar to the site condition of Project A, conventional flying/raking/corner struts were not feasible to be installed. The temporary ground anchors were unavoidably required to be installed below the public road, and Highways Department and Lands Department had imposed a condition that the anchors should be removed upon completion of the building. So removable ground anchors were an economic option for implementing the basement excavation works and the two authors

proposed to adopt 12 layers of SW-RCD anchors (302 nos., 22 strands in each anchor with capacity of 3,260 kN). The strand diameter was 15.7 mm complying with BS-5896 Super Grade and Low Relaxation.

Due to the constraint of the adjacent lot boundary (i.e. private lots are located adjoining the public road), the anchors with lengths varying from 14 m to 33.5 m were designed to be inclined at 45-degrees to the horizontal and bonded in Grade III rock (see the PLAXIS model in Figure 9). The actual site monitoring readings of ground settlement and pile wall deflection were smaller than those as predicted by PLAXIS. General view of the completed ELS works is shown in Plate 6.

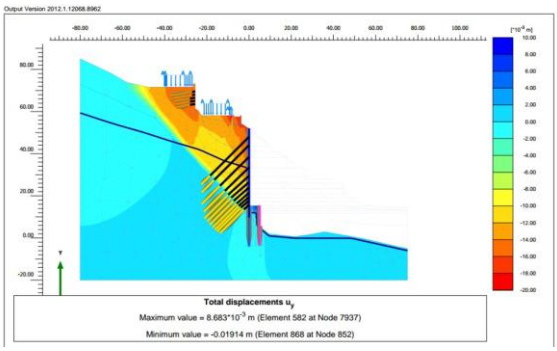


Figure 9: PLAXIS Model for ELS Analysis



Plate 6: General View of Completed ELS Works

Close-up view showing anchor body before inserting into the drilled hole and jacking of the anchors in progress are shown in Plates 7 and 8 respectively.



Plate 7: Anchor Body before inserting into Drillhole



Plate 8: Jacking of Anchors in Progress

Plate 9 shows rotation of the strands in clockwise direction for releasing the wedges.



Plate 9: Removal of strands in Progress

6 CONCLUSION

Two successful projects of using soldier/pipe piles laterally supported by removable ground anchors to facilitate deep basement excavation are presented in this paper.

7 REFERENCES

M. R. Sentry & D. Mothersille (2012) – Removable Single Bore Multiple Anchors (SBMA) – Advancement in Temporary Ground Anchor System, *Proceedings of the 11th Australia New Zealand Conference on Geomechanics*, 221-226

“SAMWOO ANCHOR TECHNOLOGY”

A New Era of Underground Construction in Hong Kong – From Ground Investigation to Construction

Simon C. M. Leung, Bridges Guy D.C. & Franklin K. L. To
AECOM Asia Company Ltd., Hong Kong, China

Michael W.K. Choi
Drainage Services Department, HKSARG, Hong Kong, China

ABSTRACT

In order to support the sustainable development in Hong Kong, the Drainage Services Department (DSD) commenced the project 'Relocation of Sha Tin Sewage Treatment Works to Caverns'. The first stage of construction for Main Access Tunnel was commenced in February 2019 and completed in April 2022 under Contract No. DC/2018/05. The excavation of main caverns to accommodate the sewage treatment facilities is on-going under Contract No. DC/2020/05.

The paper first highlights the comprehensive ground investigation in planning stage. Advanced ground investigation techniques, including horizontal directional coring, surface geophysics tests, downhole geophysical logging, over-coring and hydraulic fracturing tests were carried out. The paper also briefly mentions the rock support design of MAT using rock reinforcement approach.

The construction phase involves the installation of permanent rock bolts and shotcrete lining, implementation and utilisation of innovative and advanced technologies in drill-and-blast excavation with advanced sensors, surveying data with 3D laser scanner, and real-time monitoring via 5G network. These have allowed the team to conduct study on ground parameters, review of blasting design, continuous monitoring on excavation progress and quality control on site.

The MAT construction under Contract No. DC/2018/05 represents a significant milestone in tunnel construction in Hong Kong. It showcases the integration of geotechnical expertise, innovative engineering, and meticulous construction practices. This paper provides an overview and valuable insights in shaping the future and usher in a new era of underground construction in Hong Kong.

1 INTRODUCTION

1.1 The Project and Main Access Tunnel (MAT) completed under Contract No. DC/2018/05

To support sustainable development in Hong Kong, the Development Bureau (DEVB) put forward the initiative to launch strategic planning and technical studies aiming at promoting the enhanced use of rock caverns. The Drainage Services Department (DSD) commenced the project 'Relocation of Sha Tin Sewage Treatment Works to Caverns' as shown in Figure 1. The primary objective of this relocation is to greatly improve the environment of the existing Sha Tin Sewage Treatment Works (STSTW) site and its surroundings. After the relocation, the existing STSTW plants will be demolished to release approximately 28 hectares of land for various beneficial purposes. The relocation plan is being implemented by phases with due consideration of practicality, cost-effectiveness, contract interfacing, and timely delivery of project.

The major geotechnical works include the site formation works at portals, access tunnels and main caverns construction. The stage 1 works (Contract No.: DC/2018/05) for site preparation and MAT construction as demonstrated in Figure 2 was commenced on 28 February 2019 and completed on 10 April 2022. The stage 2 works (Contract No.: DC/2020/05) for main caverns, secondary access tunnel, ventilation adit and ventilation shaft construction commenced on 5 July 2021 and the extensive blasting works on site is currently on-going.

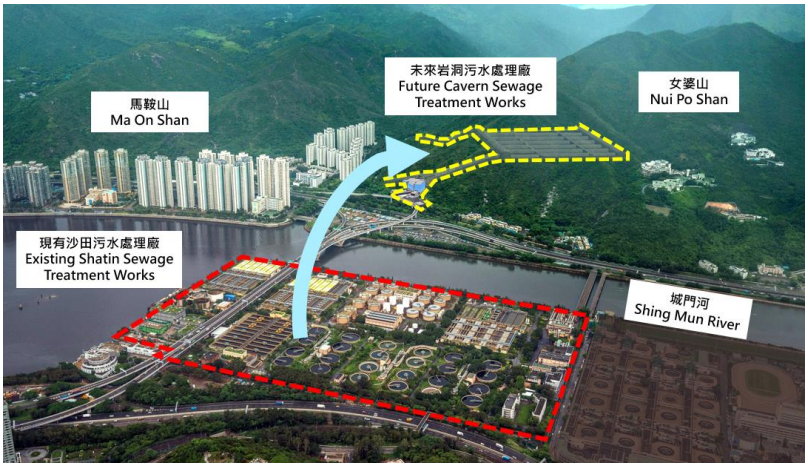


Figure 1: Relocation of Sha Tin Sewage Treatment Works to Caverns

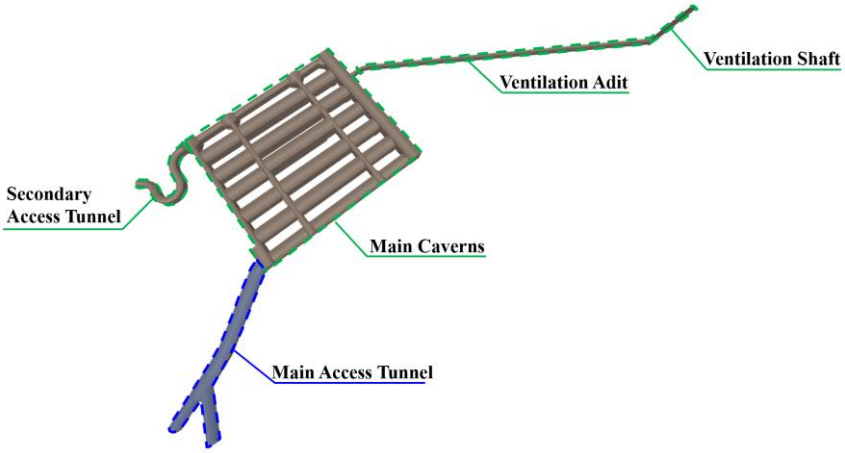


Figure 2: Main Access Tunnel (MAT) and main caverns

2 GROUND INVESTIGATION WITH ADVANCED METHODS

2.1 Horizontal Directional Coring (HDC)

HDC is used to obtain targeted core samples and field testing at specific locations of interest. It allows crossing sub-vertical geological features/faults and provide improved information compared to conventional vertical inclined boreholes. The technique involves "steerable" drilling and continuous core sampling along a planned trajectory. The drilling trajectory including the direction and curvature are controlled by rolling and bending angles. The coring survey is continuously conducted using a miniature electronic multishot (EMS) instrument to ensure the as-built borehole trajectory aligns within the tolerance envelope as per proposed coring alignment.

A total 2 nos. of HDC with approximately total length of 1.85 km were drilled for the project. The drill rig was set up at the base of the hillside with a large working area to accommodate rods of 1 km length. Photos for core barrels and drill rig for HDC are shown in Figure 3 and Figure 4.



Figure 3: Core barrels for HDC

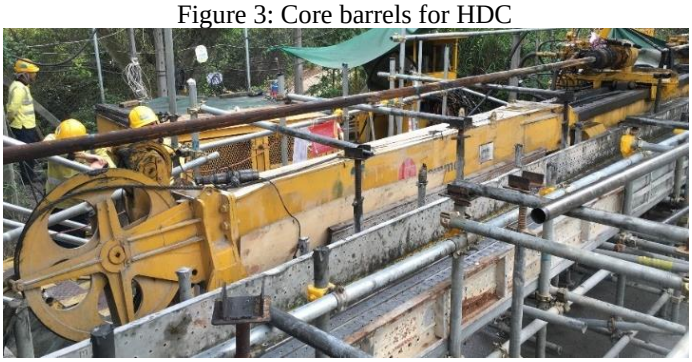


Figure 4: Drill rig set up for HDC

An example of collected information from HDC along MAT is shown in Figure 5, including the Total Core Recovery (TCR) and Rock Quality Designation (RQD). There is a great flexibility in longitudinal gradient to suit the MAT alignment and allows the collection of continuous geological information.

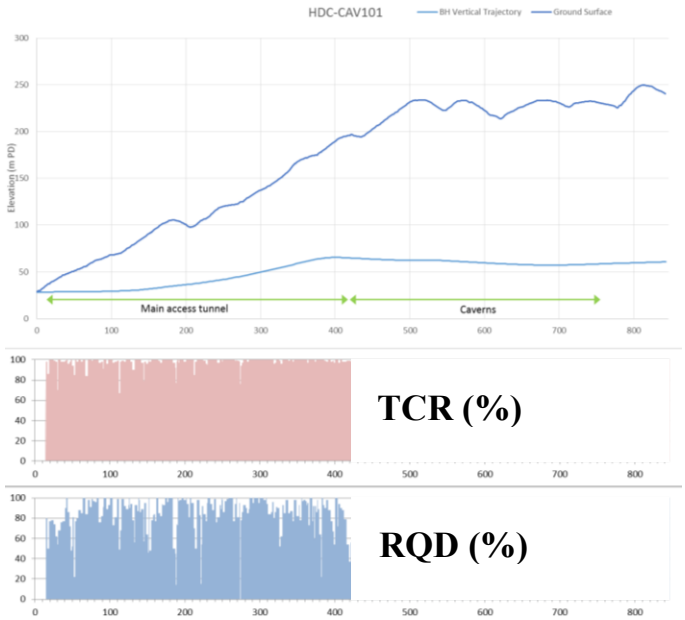


Figure 5: Alignment of HDC-CAV101 along MAT

When cores are retrieved from boreholes, it is difficult to determine the rock joint planes orientation. This project is the very first one in Hong Kong to conduct televiewer tests in HDC. Special equipment with overseas specialist geophysical contractor was employed. Optical televiewer (OTV) was used in upwards inclined hole which cannot retain water; while acoustic televiewer (ATV) was used in downwards inclined hole.




Figure 6a & 6b: OTV tool in end of drill string (left) and cable threaded through 1km long drill rod (right) for HDC

2.2 Surface Geophysics Tests

Seismic refraction tests were conducted to identify rockhead and rock quality at portal areas. It measures the time for seismic waves to travel through different subsurface layers. By analysing the travel times and waves velocities, the subsurface layers and their properties were determined. Geophones were set up along the seismic lines on ground surface and connected to computer. The trained workers then hit the ground with a hammer to induce a seismic wave (Figure 7a). Signals from the geophones were then recorded by the data logger. Analysis of signals for multiple hammer blows can determine seismic velocity through the ground (Figure 7b).




Figure 7a & 7b: Hammar hitting along the seismic lines (left) and signals analysis (right)

In general, the elevated ridges are commonly underlain by thicker layer of soil; whereas the stream cut channels showed a higher bedrock profile according to the tomographic seismic velocities from the refractive waves. The layout plan for the interpreted rockhead depth is presented in Figure 8.

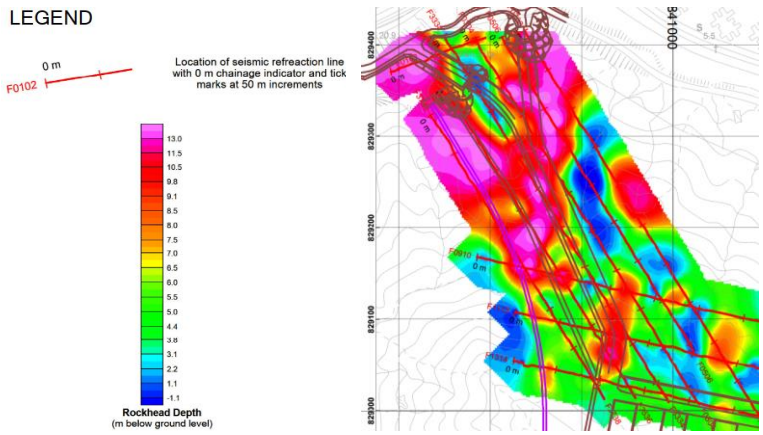


Figure 8: Layout plan for interpreted rockhead depth along MAT by seismic refraction traverses

Surface gravity surveys were conducted to identify any potential deep geological features. The strength of Earth's gravitational field, affected by the density of ground, was measured on a grid across the site to detect

areas of differing densities, such as variations in rockhead levels in Figure 9, which may be indicative of faults or structural features, as well as man-made or natural cavities or the compaction of soil at ground surface.

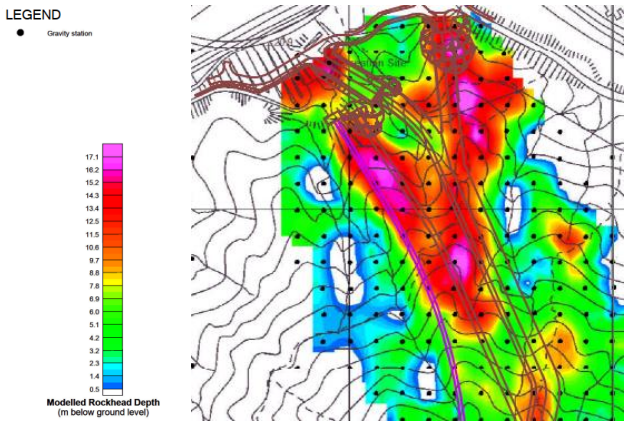


Figure 9: Microgravity survey modelled rockhead depth

2.1.3 Downhole Geophysical Logging

Downhole geophysical logging aims to obtain quantitative data from a drilled borehole, such as the mineralogy and geotechnical properties. It is relatively cheap and fast to obtain information on the borehole conditions. Surveys can cover up to 150m of hole in less than 1 day, with instant availability of the findings. In vertical / inclined boreholes and HDC, uncommon tests in Hong Kong were carried out for the project, including ultrasonic P and S wave velocity measurement, resistivity measurements and gamma logging.

The measurement of P and S wave velocity was able to evaluate the quality of rock. An example is extracted in Figure 10b. With the wave velocities and measured rock density, the elastic modulus and rock mass quality were evaluated based on empirical relationships.

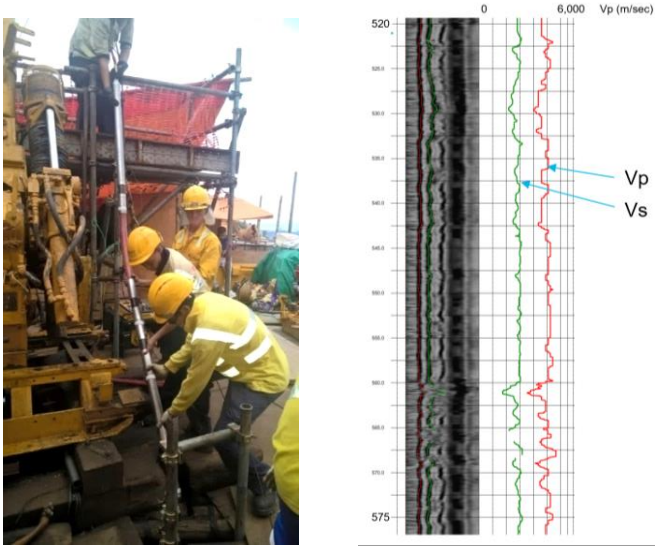


Figure 10a & 10b: Downhole geophysical logging (left) with ultrasonic wave velocity measurement (right)

Downhole resistivity (ohm-m) measures the inverse of the conductivity of the rock between a receiver and a transmitter as the tool was being raised through the borehole, which is mostly affected by water content of rock mass. Therefore, the resistivity appears to be highlighting the more fractured and weathered rock mass with a slightly higher water content (i.e. higher conductivity and lower resistivity). The resistivity could also be correlated to the logged weathering decomposition grade of granite as shown in Figure 11.

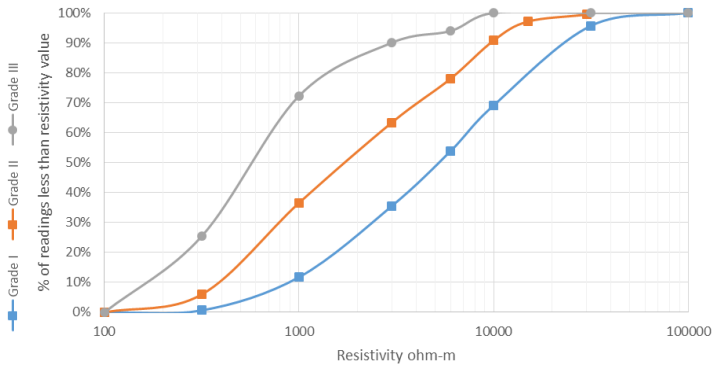


Figure 11: Correlation of resistivity and logged decomposition grade

Granite is known to emit relatively high levels of gamma rays due to the potassium (K) in the feldspars and trace amounts of elements such as uranium (U) and thorium (Th) typically found in granite. The gamma logging tool (Figure 12) was used to measure the natural radiation emitted by rocks down a borehole to determine the chemical and physical properties. The number of gamma rays striking the instrument per second was measured and converted into API (American Petroleum Institute) units.



Figure 12: Gamma tool being extracted from drill rods after testing in a borehole

For Shui Chuen O Granite, the K content is approximately 5%, uranium is only 7ppm and thorium is 43ppm. Unlike measurement for resistivity, there is no difference in gamma count between grade I / II granite, but a possible increase for grade III granite. In general, basalt dykes have a significantly lower gamma count due to lower K, U and Th content. For faulted rock, it had a wide range of gamma count based on minerals redistribution during faulting in related to hydrothermal alteration. An example is presented in Figure 13b.

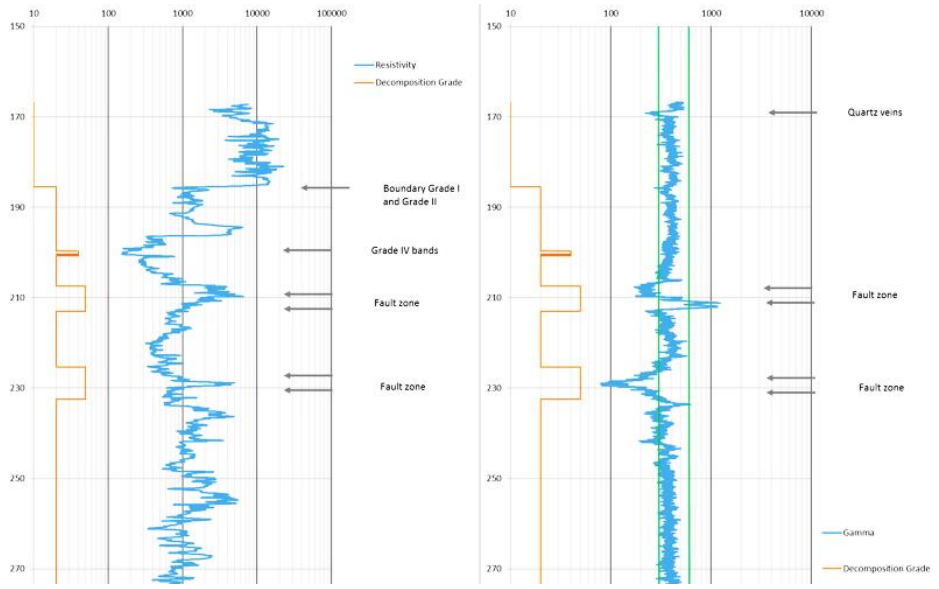


Figure 13a & 13b: Results of resistivity (left) and gamma count (right) along a borehole

2.1.4 In-situ Stress Measurement

Stress-controlled failure is one of the main failure modes for rock tunnels/caverns stability. In order to study the in-situ stress conditions, two field tests named over-coring and hydraulic fracturing were conducted.

Over-coring involved drilling of a borehole (101mm diameter) to a designated depth with a flattened hole bottom by a special drill bit, and further drilled a 38mm dia. smaller pilot concentric hole as shown in Figure 14a. A triaxial measuring cell (Figure 14b) was then inserted and fixed inside the smaller concentric hole.



Figure 14a & 14b: Pilot concentric hole (left) and triaxial measuring cell (right)

The small hole with cell and data logger fixed inside was then slowly overcored by the larger diameter bit and retrieve from borehole as demonstrated in Figure 15a. The stress acting on the rock core is relieved and the corresponding strains before, during, and after overcoring were recorded by the strain gauge rosettes. The in-situ stress states can then be evaluated based on the strain difference elastic properties of the rock.

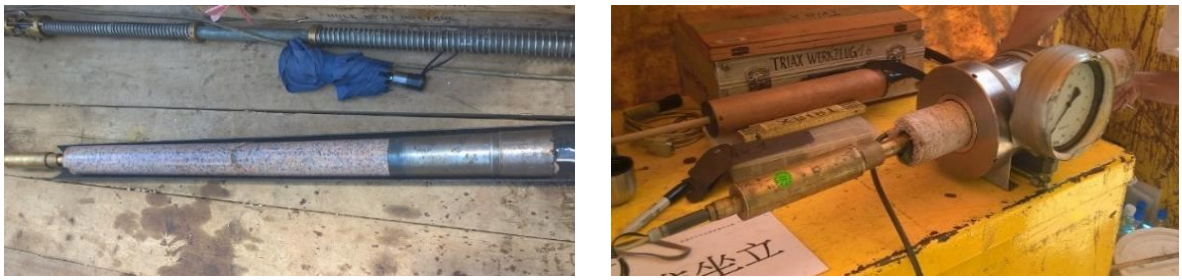


Figure 15a & 15b: Overcored rock with measuring cell (left) and field measurement for elastic properties (right)

Hydraulic fracturing test as presented in Figure 16 involved injecting water or other fluid at high pressures into a test section isolated by packers in a borehole, until the rock failed in tension and induced controlled fractures. The fluid pressure for inducing, propagating, sustaining and re-opening the tensile fractures were constantly recorded as a function of time. The orientation of the hydraulically induced fracture plane coinciding with the orientation of the maximum horizontal principal stress was then determined by the impression packer test; while the orientation of the minimum horizontal principal stress is perpendicular to the fracture plane.



Figure 16: Site establishment for hydraulic fracturing test

2.1.5 Rock Core Samples Logging as Grade I – Fresh Granite

As a conservative approach, local GI contractors have been avoiding to assign grade I – fresh granite to core samples. Therefore, there is a high chance that some excellent rock cores were conservatively classified as grade II rock. For this project, the AECOM team has carefully checked and logged grade I for granite as shown in Figure 17. Differentiating grade I from grade II granite (Figure 18) has not been a usual practice in Hong Kong.



Figure 17: Core samples logged as grade I granite (i.e. fresh)



Grade I granite **Grade II (almost grade I) granite**

Figure 18: Differentiating Grade I from Grade II granite

3 ROCK SUPPORT DESIGN

3.1 Geological Model and Rock Mass Quality

The solid geology is predominantly Shui Chuen O Granite. Based on the extensive GI data, a three-dimensional geological model (Figure 19) was developed. No major faults were identified crossing the MAT. The identified geological features/photolineaments could result in slightly lowered rockhead and fractured altered rocks.

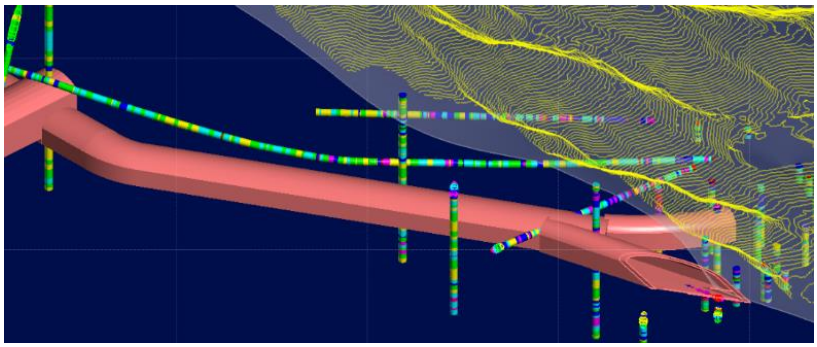


Figure 19: Three-dimensional geological model for MAT

The NGI Q-system first developed by Barton et al. (1974) and updated by Grimstad & Barton (1993) was used for rock mass classification. It describes the stability of an underground opening in jointed rock masses. The Q-value is formulated by the multiplier of six different rock mass parameters as presented in Equation 1:

$$Q = \frac{RQD}{J_n} \times \frac{J_r}{J_a} \times \frac{J_w}{SRF} \qquad (1)$$

A high Q-value indicates good stability, and vice versa. It has been commonly used in Hong Kong to assess the rock mass quality and determine support classes for hard rock tunnels. For a given combination of Q-value and cavern configurations, the shotcrete and rock bolt support requirements for a given rock support class can be obtained. However, the limitations include the appropriateness for large-span and multiple parallel caverns.

The strength of a jointed rock mass depends on the behavior of both intact rock and rock blocks. For rock mass properties in finite element modelling, the Generalized Hoek-Brown (GHB) failure criterion by Hoek et al. (2022) was adopted. It estimates the deformation and strength characteristic of rock mass based on the

interlocking effect and discontinuity conditions. The rock support class defined by the Q-value was correlated to Geological Strength Index (GSI), which is a input parameter for GHB failure criterion, using Equation 2:

$$GSI = 9 \ln Q' + 44 \quad (2)$$

3.2 Permanent Support System with Rock Reinforcement Approach (RRA)

The span of MAT is ~26m underlain by strong granite with uniaxial compressive strength of 65 to 165 MPa, which is much greater than structural concrete. With an arched roof to utilize the arching-effect/hoop stress, the rock support design using RRA as sketched in Figure 20 offered a practical method to consider the hard rock as a structural material to self-support itself. The inherent strength of rock mass is utilised by applying confining pressure from bolts. Permanent rock bolts were installed as primary supports for forming the reinforced rock arch, while permanent shotcrete is the secondary support for the smaller rock wedges between adjacent bolts.

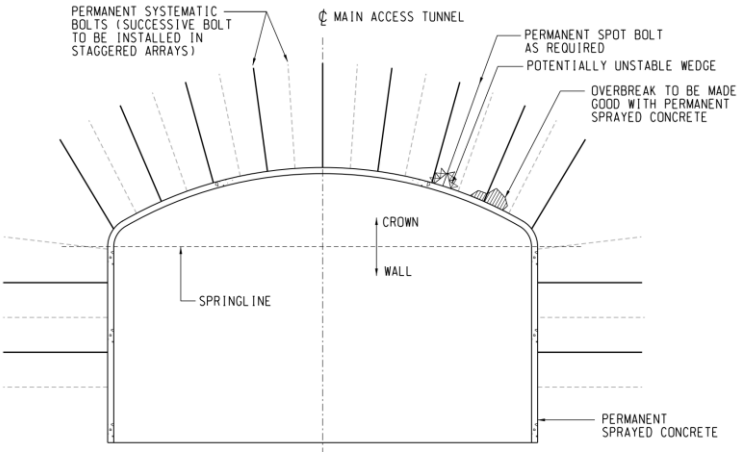


Figure 20: Excavation Profile and Permanent Rock Reinforcement of MAT

Design verification of permanent rock reinforcements estimated by empirical methods and RRA was carried out using numerical analysis, including 2D and 3D finite element modelling (FEM) as shown in Figure 21 and Figure 22, as well as discrete element modelling. The systematic rock bolts and shotcrete lining were designed to withstand the induced rock supporting pressure re-distributed from the surrounding ground after excavation; while permanent spot bolts to support individual rock wedges were determined by the geologist on site.

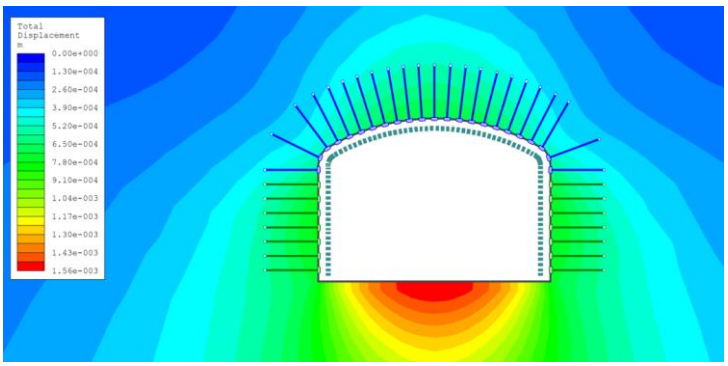


Figure 21: 2D FEM Analysis for Permanent Rock Reinforecment at MAT

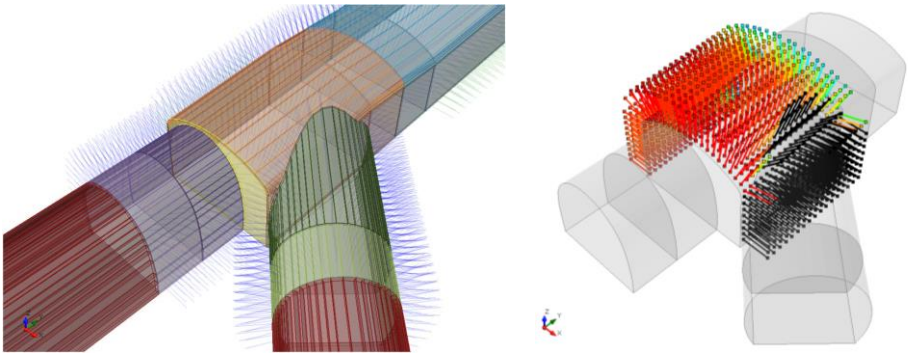


Figure 22: 3D FEM Analysis for Permanent Rock Reinforecment at MAT Junction

4 CONSTRUCTION

4.1 Installation of Permanent Rock Bolts and Shotcrete Lining

Rock bolts and with temporary shotcrete provides immediate support to the excavated rock, which allowed safe and efficient continuation of MAT blasting activities. The proprietary rock bolts with specific corrosion protection measures (Figure 23a) and expansion shell at far end (Figure 23b) provided immediate support through mechanical anchorage and were fully grouted to ensure bond strength and durability prior to next blast. The permanent shotcrete lining was applied in later stage to facilitate blasting and excavation activities. Without the need of heavy steel shutter for cast-in-situ lining, the rapid installation significantly saved time and cost.



Figure 23a & 23b: Permanent rock bolts with specific corrosion protection (left) and expansion shell at end (right)

4.2 Drilling Jumbo with Advanced Sensors

Computerized drilling jumbo was used to carry out probing ahead, drilling blast holes and drilling rock bolt holes. With the use of advanced Measure-While-Drilling (MWD) system which comprised sets of sensors on the jumbo booms, real-time monitoring of the drilling performance data was recorded. The as-built blast holes with actual drilled locations and depth were controlled and checked as demonstrated in Figure 24. The MWD system also provided a complementary tool for rock mass characterization which enabled further optimization of blast design for tunnel and cavern excavation works. Examples are indicated in Figure 25a and Figure 25b.

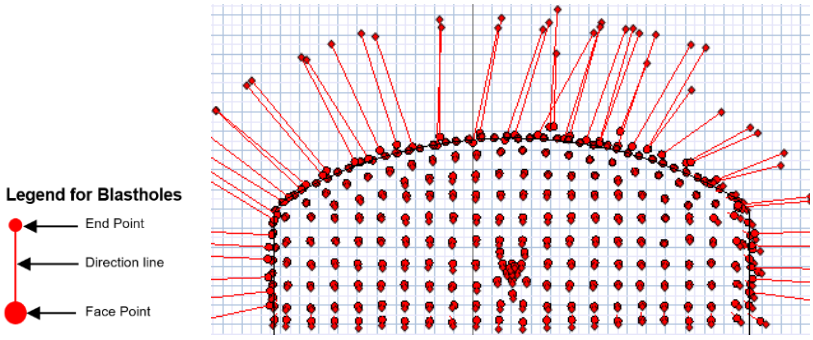


Figure 24: As-built blast holes with actual drilled locations and depth

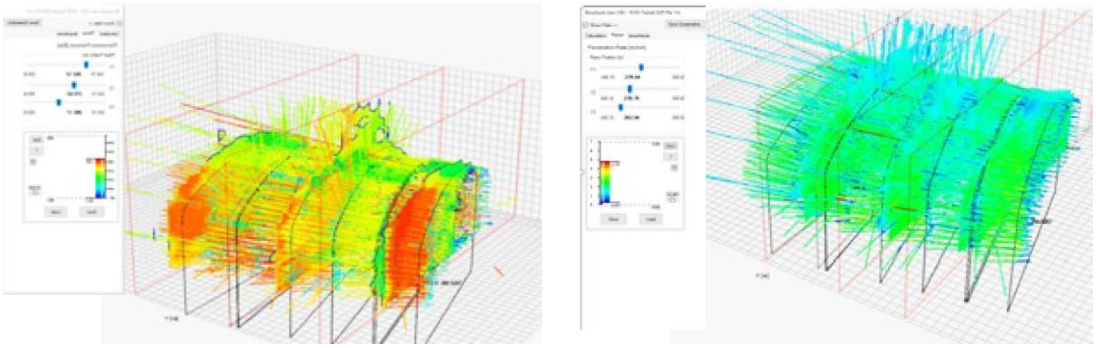


Figure 25a & 25b: Real-time monitoring of percussion pressure (left) and penetration rate (right) using the MWD system

4.3 Surveying of Excavated Profile with 3D Laser Scanner

The three-dimensional tunnel profile after excavation, as shown in Figure 26, was surveyed using a 3D laser scanner with LIDAR technology to generate point cloud data. This data was used to estimate the volume of rock excavation, identify underbreak/overbreak, and immediately assess the thickness of temporary shotcrete after each round of excavation, as demonstrated in Figure 27. The high data intensity significantly improved the precision of surveying data compared to conventional method using total stations. It ensured faster and more efficient checking and monitoring of construction progress, site safety and quality control in tunnel excavations.



Figure 26: Three-dimensional excavtaed profile formed by point cloud data

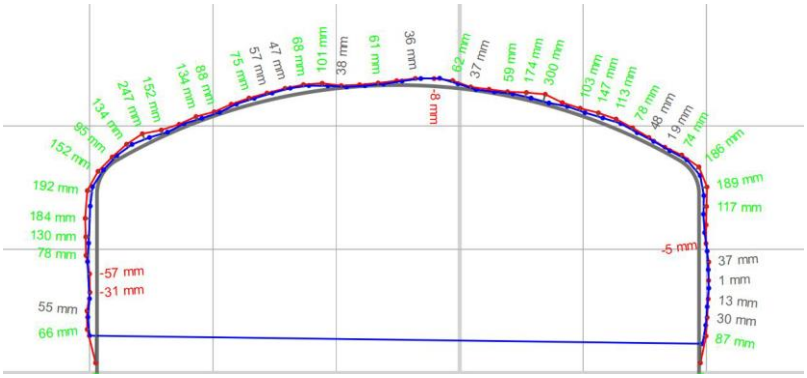


Figure 27: Checking of temporary shotcrete thickness and overbreak/underbreak

4.4 Rock Mass Quality Encountered at MAT

During the MAT excavation, grade II/III granite was encountered. The summary of mapped Q-value along the MAT tunnel is plotted in Figure 28. The Q-value within the shallow rock cover section ranged from 0.06 to 0.65 due to unfavorable conditions for RQD, J_n, J_a and SRF. For hard rock portion, only localised weak seam and intrusion were encountered with Q-value ranged from 3.25 to 5. The mapped Q-value indicated that the rock quality was generally good. Site photos were extracted in Figure 29a and Figure 29b.

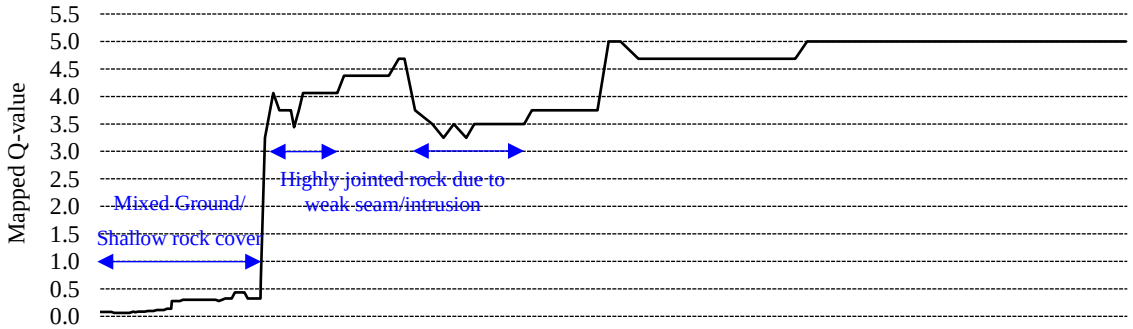


Figure 28: Mapped Q-value along MAT (Top-heading)

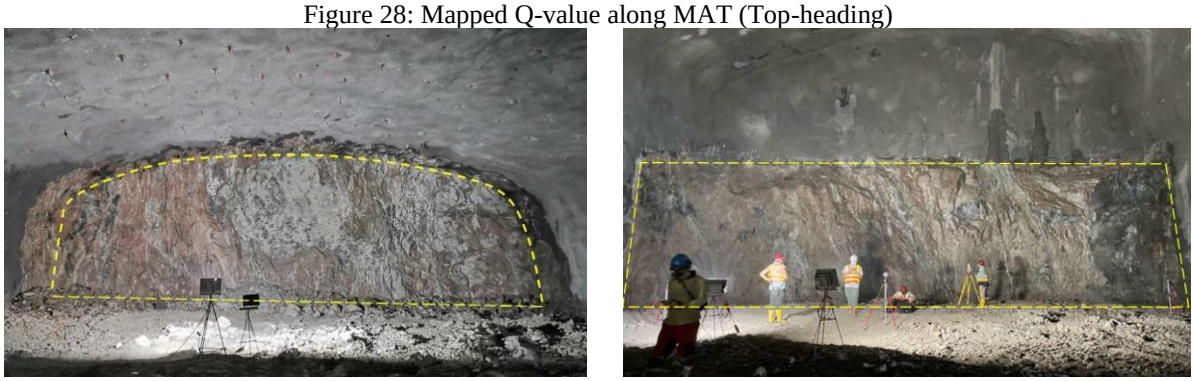


Figure 29a & 29b: Example of top-heading (left) and bench (right) at MAT both with mapped Q=5

4.5 First Site Specific 5G Network for Tunnel Construction in Hong Kong

The project is the first construction site in Hong Kong to establish a site specific 5G network in tunnel as indicated in Figure 30. With the advantages from 5G network of low latency, high-speed transmission and high device capacity, together with the development and implementation of various innovative technologies, the efficiency of project management, construction safety and site progress monitoring were significantly improved. With the 5G network, real-time air monitoring and UWB positioning watch were used to monitor the air, temperature, gas and health status of all site staffs and workers in the confined space environment.



Figure 30: First site-specific 5G base stations in Hong Kong construction site

4 CONCLUSION

The paper has discussed the comprehensive ground investigation in planning stage, as well as briefly mentioned the rock support design of MAT using rock reinforcement approach. Also, the construction stage of MAT involved the implementation and utilisation of advanced technologies, which showcases the integration of geotechnical expertise, innovative engineering, and meticulous construction practices. This paper provided valuable insights in shaping the future and usher in a new era of underground construction in Hong Kong.

ACKNOWLEDGEMENT

The authors gratefully acknowledge the Drainage Services Department, the Government of the Hong Kong Special Administrative Region, for permission to publish this paper.

REFERENCES

Barton N., Lien R. and Lunde J. 1974. *Engineering Classification of Rock Masses for the Design of Tunnel Support*. Rock Mechanics, vol. 6, pp 189-236.

Grimstad E., and Barton N. 1993. *Updating of the Q-system for NMT*. Proceedings of the International Symposium on Sprayed Concrete, Fagernes, Oslo. pp46-66.

Hoek, E., Carranza-Torres, C. & Corkum, B. 2002. *Hoek-Brown Failure Criterion – 2002 Edition*. Rocscience.

AECOM. 2017. *Ground Investigation Report (Final), Geotechnical Engineering Report*, Relocation of Sha Tin Sewage Treatment Works to Caverns – Investigation, Design and Construction.

Leung S. C. M. & Ko E. M. Y. 2022. Active Site Supervision to Enhance Drilling & Blasting. Proceedings of The HKIE Geotechnical Division 42nd Annual Seminar 2022, Hong Kong.

Data-driven Site Supervision on Micro Tunnel Boring Machine (MTBM) on Hard Rock Performance - Objective, Analysis and a Case of Effluent Pipeline in a Caverns Project

Simon C. M. Leung,
AECOM Asia Company Ltd., Hong Kong, China

Elton M.Y. Ko
Drainage Services Department, HKSARG, Hong Kong, China

ABSTRACT

The Relocation of Shatin Sewage Treatment Works (STSTW) to Caverns involves the construction of twin effluent pipelines for conveying treated effluent to the existing inlet chamber via the Tolo Harbour Effluent Export Scheme (THEES) Tunnel.

The paper emphasizes lessons learned from past projects with MTBM jamming underground, leading to project delays, increased costs, safety concerns, and social impacts. This specific case study focuses on a twin pipe driving through a rock mountain. The catastrophic nature of such jamming problem embarks meticulous site supervision, with a 100% successful breakthrough of the MTBM as a paramount objective. Traditional rescue methods, such as vertical shafts, may be impractical and infeasible in our case, further highlighting the importance of comprehensive site supervision by Resident Site Supervisor (RSS).

The first part of the paper delves into a detailed case study of one of the twin pipes, and its performance with insights. The second part explores the fundamental aspects of profound site supervision, discussing the rationale for employing site data to achieve project objectives with aims to mitigating the escalating risks associated with MTBM failures. Moreover, it lays the groundwork for further analysis and utilization of operational data for the second effluent pipeline and tunneling industry.

Keywords: Micro Tunnel Boring Machine, Hard Rock, Cutterhead, Profound Site Supervision, Operational Data

1. INTRODUCTION

Throughout the history of MTBM projects, there has never used to be a standard practice for RSS to place emphasis on reviewing the Geotechnical Investigation and cutter head evaluation in terms of cutter disc configuration and opening ratio etc. when approving the Contractor's proposal. However, it has become increasingly clear that thorough scrutiny of these aspects is essential for ensuring the success of MTBM projects. RSS, as the overseeing authority, plays a pivotal role in diligently supervising the entire process – from verifying contractor submissions to on-site supervision. To effectively carry out these responsibilities, RSS must possess a deep understanding of MTBM technology. By actively engaging in the determination of appropriate MTBM cutter head evaluation, RSS can contribute significantly to the overall success of the project. This proactive approach not only enhances the quality and efficiency of MTBM operations but also minimizes the risks associated with tunneling activities.

1.1 Case Study – The Relocation of Shatin Sewage Treatment Works to Caverns

In Relocation of STSTW, a twin effluent pipe, approximately 330m long with a slight gradient and 2.2m internal dimeter, were installed using MTBM, which was manufactured by China Railway Construction Heavy Industry Corporation Limited. The pipes are located underneath Niu Po Shan with depth ranging between 10m and 140m. Figure 1 show the general view of the project and the twin effluent pipes.

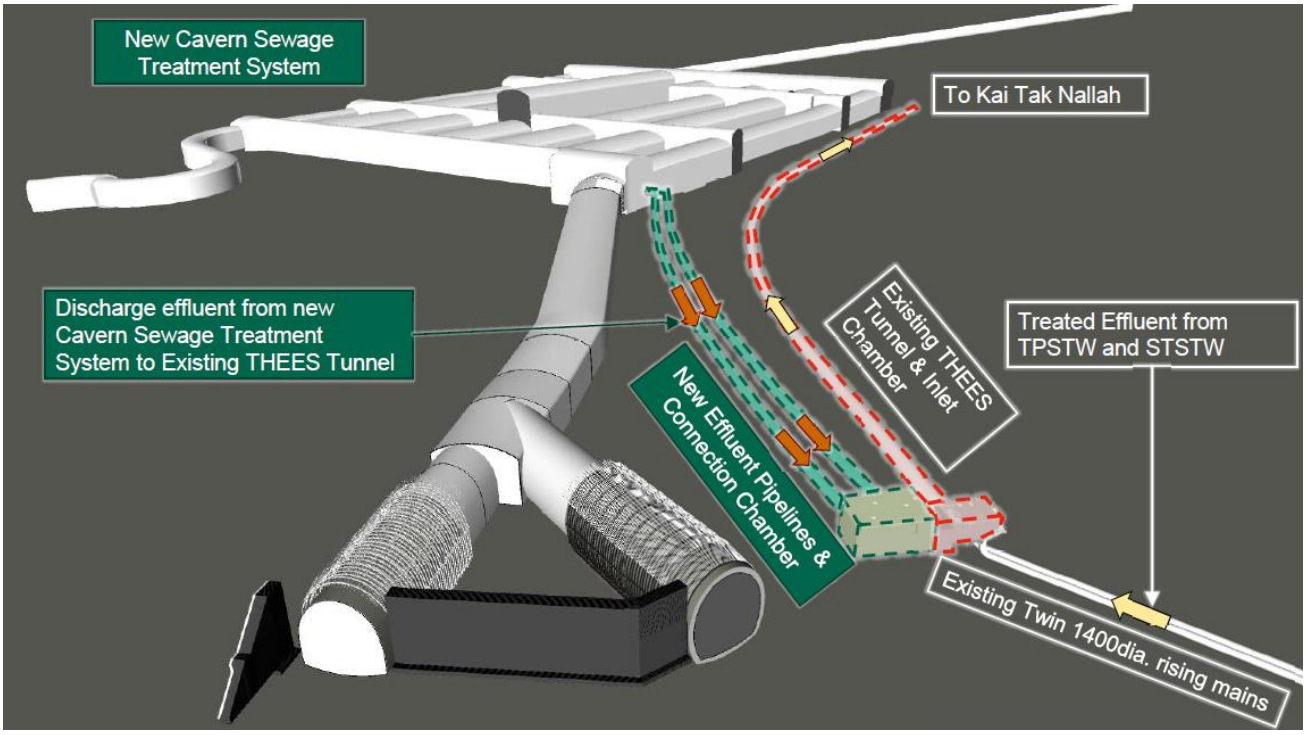


Figure 1 – General view of project and the twin effluent pipes

We are faced with the challenge of beginning the jacking process at a mountain. This unique starting point necessitates the construction of a specific up-stand thrust wall, along with a piling system, to facilitate the jacking process, as shown in Photo 1. This deviation from the norm presents a first-time challenge for our project since, under normal circumstances, an underground jacking pit could be constructed for this purpose. STSTW is Hong Kong's largest secondary sewage treatment works, serving approximately 630,000 residents in Shatin and Ma On Shan. These districts generate a daily sewage volume of 250,000m³. The existing STSTW pumps effluent to the adjacent THEES tunnel, which then flows through a dedicated tunnel to Diamond Hill and discharges into Kai Tak Nullah. The proposed twin effluent tunnels will connect the relocated STSTW with the THEES tunnel, ensuring a continuous discharge route in the future.



Photo 1 – General view of jacking thrust structure and lifting gantry

1.2 Specific Site Constraints

1.2.1 No Turning Back

In the deep bedrock beneath Niu Po Shan, the MTBM faces challenges without the option of a turnaround or rescue shaft. If a cutterhead jam or breakdown occurs, retrieving the machine is unlikely. This limited solution poses a risk of significant disasters, leading to increased costs and delays.

1.2.2 Hard Rock Drilling

Drilling in hard rock presents challenges, especially when continuously drilling over a long distance of 660m in Hong Kong. The extreme hardness of the rock causes rapid wear on the disc cutters, requiring frequent replacements. This process takes place within the confined space of the MTBM, involving the use of hand-held percussion machines and heavy lifting operations, as shown in Photo 2. The frequent disc cutter replacements increase risks, costs, and disruptions to the tunnelling process, raising the likelihood of MTBM failure.

1.2.3 Interference with Nearby Drill-and-Blast Excavation

The receiving pit for the MTBM in the main cavern was excavated using the drill-and-blast method, raising concerns about vibrations causing damage to the surrounding rock. Seismic waves and loads from blasts can harm weak surfaces like joints and fissures, impacting overall stability. Careful planning and monitoring are crucial for the MTBM-blasting interface to minimize risks. Maintaining a safe distance between the MTBM and blasting works is essential to mitigate potential damage.

1.2.4 Sensitive Receiver THEES Tunnels

The proposed effluent pipelines are close to the existing THEES tunnel with minimum separation distance of 7.9m, raising concerns about potential impacts on THEES, such as pressure changes, vibrations, and settlement. To mitigate these impacts, the slurry pressure balance method is used during MTBM operations.

1.3 Tunneling Method and MTBM

The slurry-operated MTBM was adopted. Two intermediate jacks were installed to help pushing the pipeline forward, as shown in Photo 2 and Photo 3 respectively.



Photo 2 – Main jack



Photo 3 – Intermediate jack

1.4 Cutterhead Configuration

In this project, a domed cutterhead was utilized, consisting of various types of cutters, as shown in Photo 5.

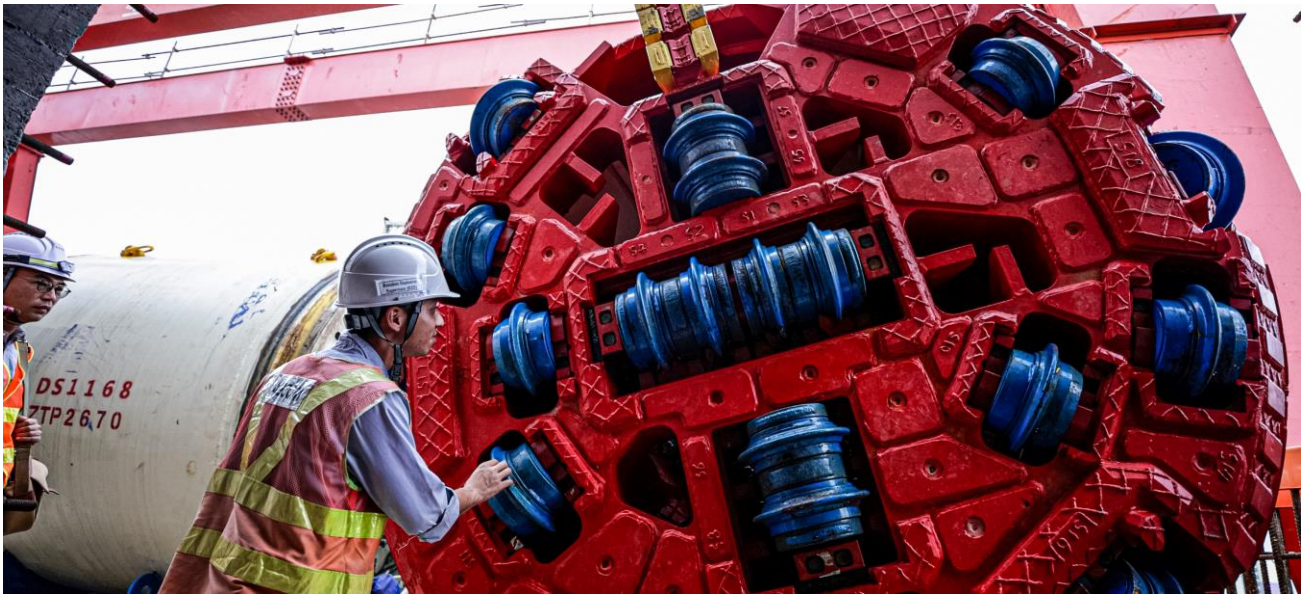


Photo 4 – Adopted cutter head for hard rock MTBM

The center area of the cutterhead featured 4 double-disc cutters with a diameter of 305 mm. The face area had 6 single-disc cutters of the same diameter, while the gauge area also had 6 single-disc cutters. Additionally, a scrapper was incorporated to transport rock fragments out of the excavation face. The spacing between the cutters was set at 80 mm. The single-disc cutters, which played a crucial role in rock breaking, were replaced by double-disc cutters at the center due to space limitations. All the cutters were made of wear-resistant tungsten carbide inserts. The opening ratio of the cutterhead, representing the ratio of the total area of the cutter openings to the total area of the cutterhead, was measured at 16%. Photo 4 show the details of the cutterhead.

1.5 Key Performance Data of MTBM Recorded

Key Performance Indicators during tunnelling were recorded and monitored closely by our RSS to gain an insight into the performance, efficiency and potential issues of MTBM. The indicators include MTBM utilization, jacking force and friction resistance, penetration rate, advancement rate, disc cutter replacement analysis, tolerance of alignment and induced ground settlement. The information helps in making informed decisions and optimizing the tunnelling process.

1.5.1 MTBM Utilization (U)

U refers to the percentage of available shift time during which excavation activities are performed using the MTBM (Gong Qiuming, 2006). It is a comprehensive factor influenced by various operating procedures. The overall U of the MTBM used for the installation of the 1st effluent pipes achieved 39%, as indicated in allocation time chart shown in Figure 2. The U is the result of enhanced site supervision and could be serve as a bench mark for the second effluent pipeline operation in hard rocks. Throughout the tunnelling process, our RSS continuously reviewed U at fixed driving distance of 10m equivalent to the length of 4 nos. concrete pipes, as shown in Figure 3. If exceptionally low U is recorded, a detailed review of the root cause and corresponding corrective measure could be implemented.

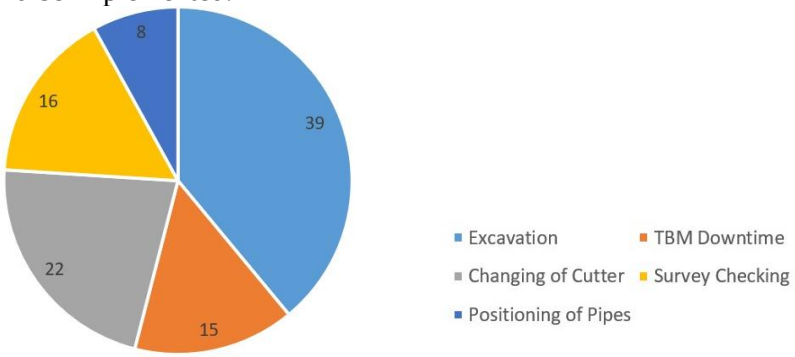


Figure 2 – Allocation time chart for MTBM during installation of 1st effluent pipe

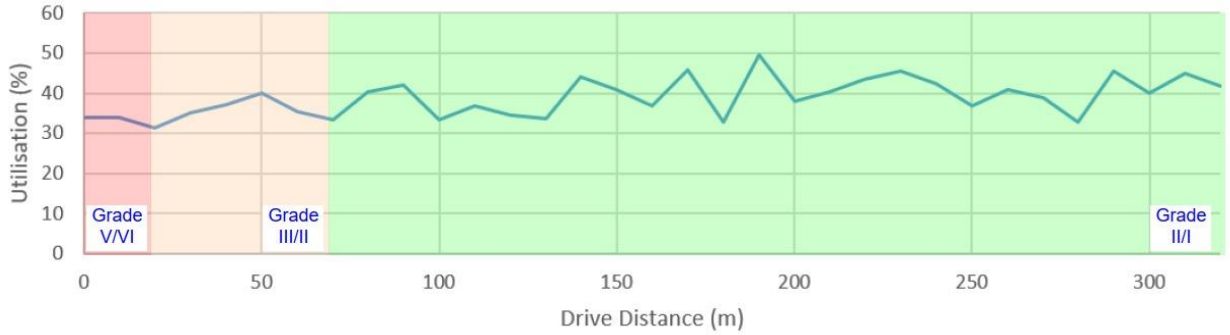


Figure 3 – Utilization along the driving distance of MTBM

1.5.2 Jacking Force and Friction Resistance

In MTBM, the jacking force is necessary to estimate and facilitate the sliding of the pipe through the ground. It involves several factors that complicate the assessment and necessitate close monitoring of the jack force recorded in the field. Figure 4 illustrates the various components contributing to the overall thrust required for an MTBM project. The face pressure component is needed to support the face, balance groundwater pressure, and facilitate excavation by exerting force on cutters. This remains relatively constant along the alignment unless there are significant geological changes. While it becomes a smaller percentage of the total jacking force as the drive progresses, it is generally not a critical factor in estimating the jacking force for long drives. The frictional component increases as the drive length increase and is dominated in long drive. Figure 5 shows the comparison of actual jacking force, design jacking force and the jacking force capacity provided by the main jacks and intermediate jacks along the drive length.

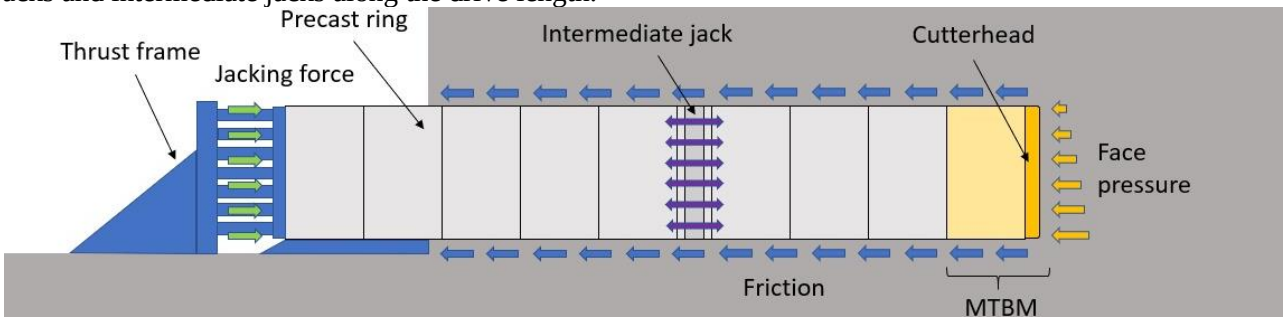


Figure 4 – Contributing components of required thrust force

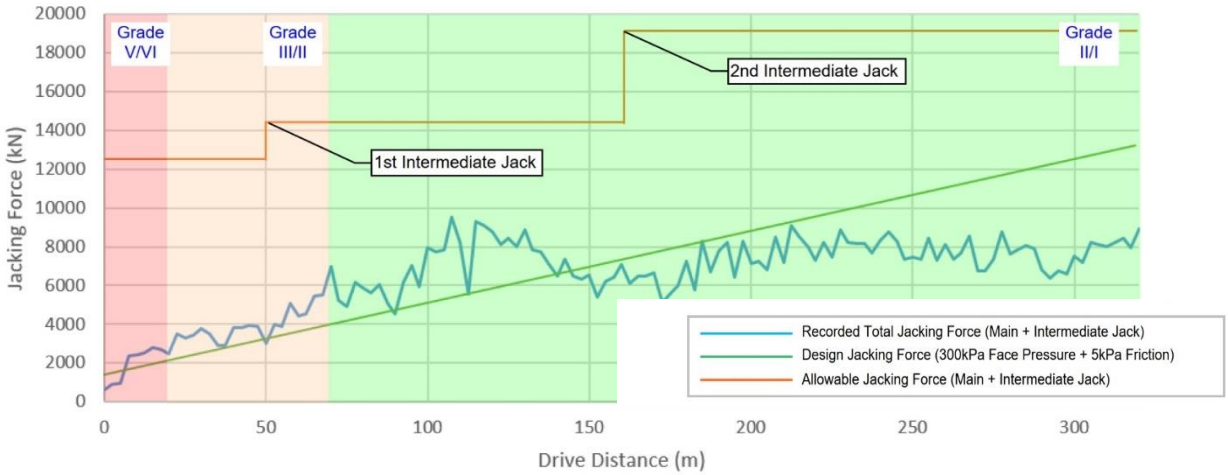


Figure 5 – Comparison between design jack force and actual jacking force

1.5.3 Penetration Rate (PR)

Average PR refers to the excavation distance covered by a TBM per unit of time, usually expressed as meters per hour (Gong Qiuming, 2006). PR is affected by both objective factors, which are geology and MTBM capacity, and subjective factor, which is human operating factor. The Penetration per Revolution (PRev) is a

key indicator of excavation efficiency, representing the distance excavated per revolution of the TBM's cutterhead. The average PR ranges from 0.5 to 7 m/h, (Grandori et al., 1990). In the first effluent pipe, the average PR was 1.9 m/h. Figure 6 illustrates the variation of PR along the MTBM drive.

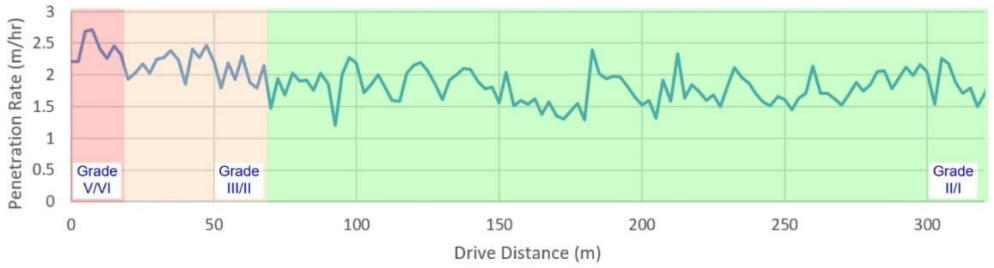


Figure 6 – Variation of PR along MTBM drive

1.5.4 Advance Rate (AR)

Advance rate (AR) is the actual distance mined or supported divided by the total time of the operations and includes downtimes for TBM maintenance (Gong Qiuming, 2006). It equals to the product of U and PR. Based on statistical data suggested by Laughton, 1998, AR ranges from 0.3 to 3.3m/h (Grandori et al., 1990). AR 0.8m/h was achieved in the first effluent pipe as shown in Figure 7.

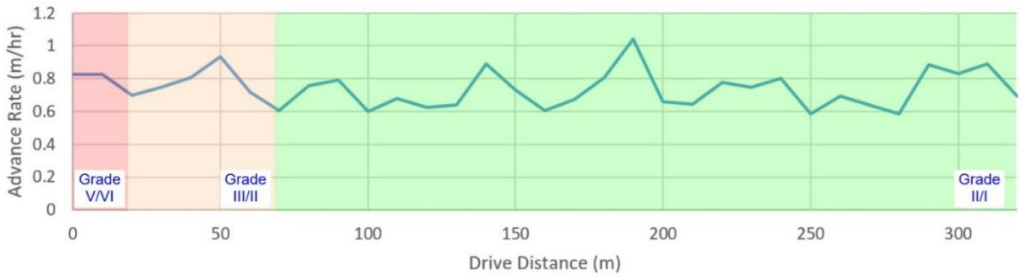


Figure 7 – Variation of AR along MTBM drive

1.5.5 Cutter Wear

Cutter wear is recorded based on the rolling distance of each cutter (Gong Qiuming, 2006), as shown in Figure 8. Due to the outer disc cutter traveling a longer distance than the inner disc cutter for one rotation of the cutterhead, the outer disc cutter should experience more frequent wear compared to the inner disc cutter. Theoretically, a cutter is replaced when its radius loss reaches around 20 mm due to abrasion (Grandori et al., 1990). During MTBM for the first effluent pipe, no centre cutters (S1-S8) were required to be replaced. The average service time were 146m and 114m for face cutters (S9-S14) and gauge cutters (S15-S20) respectively.

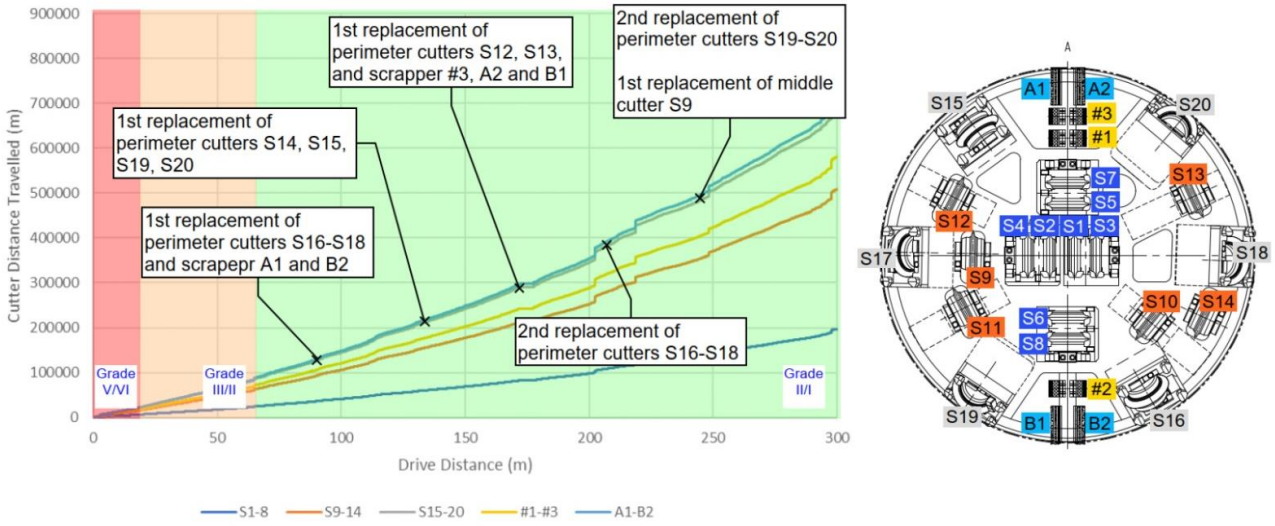


Figure 8 – Records of disc cutter travelling distance

2. ENHANCED SITE SUPERVISION

2.1 Emphasis on reviewing the Geotechnical Investigation for cutter head evaluation

The unique geological conditions at the site, with over 96% of Grade III or above hard rock, present significant challenges for the MTBM. Issues such as penetration rate, cutterhead maintenance, and cutter disc replacement, as shown in Photo 5, are directly impacted by the properties of the rock mass. It is essential to carefully select a MTBM that is specifically designed to handle hard rock conditions, ensuring efficient excavation and minimizing risks and delays.

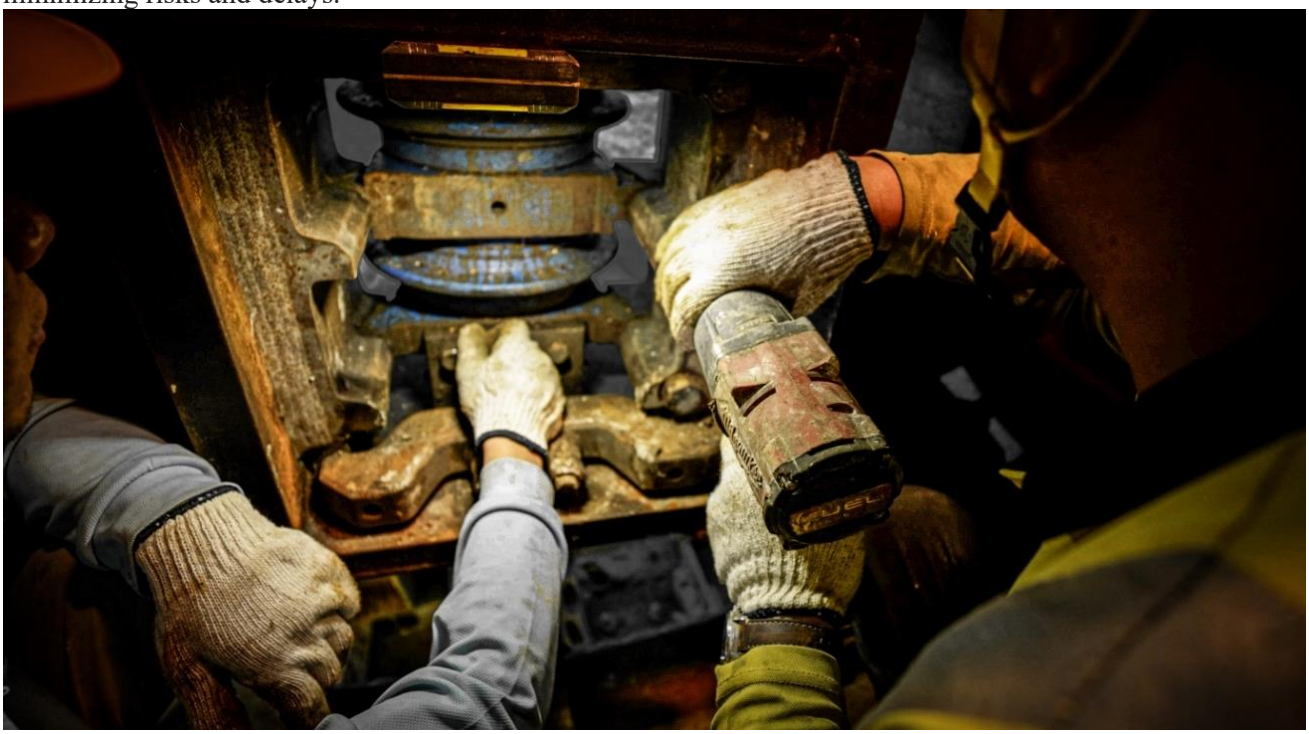


Photo 5 – Replacement of cutter disc

2.1.1 Key Geotechnical Parameters for MTBM in Hard Rock

Considering over 96% of total MTBM drive length was in hard rock under this project, RSS critically reviewed all the governing rock parameters in evaluating a suitable MTBM for hard rock excavation, as summarized in Table 1. The density, abrasiveness, cohesion values, permeability, friction angle, unconfined compressive strength, tensile splitting strength, and triaxial strength of rock all impact the cutting power, tools, durability, torque, thrust, waterproofing measures, and cutter design of MTBMs.

Parameters	Grade I	Grade II	Grade III	Grade IV/V
Density (kg/m3)	2540 to 2610	2420 to 2690	2540 to 2560	1550 to 2400
Abrasiveness	2.85 to 5.2	4.01 to 5.67	3.92 to 5.38	-
Cohesion (kPa)	-	-	71.83	3
Permeability (m/s)	1E-9 to 1.13E-6	1.58E-06	2.3E-9 to 2.48E-6	1.52E-8 to 9.42E-6
Friction Angle (°)	13.4 to 66.3	11.8 to 53.6	29 to 54	37
Unconfined Compressive Strength (MPa)	72.3 to 245.4	15.4 to 225	16.4 to 82.3	-
Tensile Splitting Strength (MPa)	5.01 to 11.64	3.54 to 12.55	3.87 to 7.59	-
Triaxial Strength (MPa)	120.27	106.48 to 193.08	-	-

Table 1 – Summary of key geological parameters

2.2 Enhancing Efficiency and Safety through Evaluation of Cutterhead Design

Currently, the design and evaluation of the MTBM cutterhead are primarily led by the contractor and MTBM manufacturer, with limited involvement from the RSS during the supervision of MTBM works. In response to

this, our RSS has developed a cutterhead evaluation protocol (CEP) to systematically evaluate the suitability of a cutterhead design for specific ground conditions. The CEP includes a checking flowchart, as illustrated in Figure 9, which outlines the steps to be followed. Through the implementation of CEP, the RSS aims to actively contribute to the decision-making process regarding the evaluation of the MTBM cutterhead design.

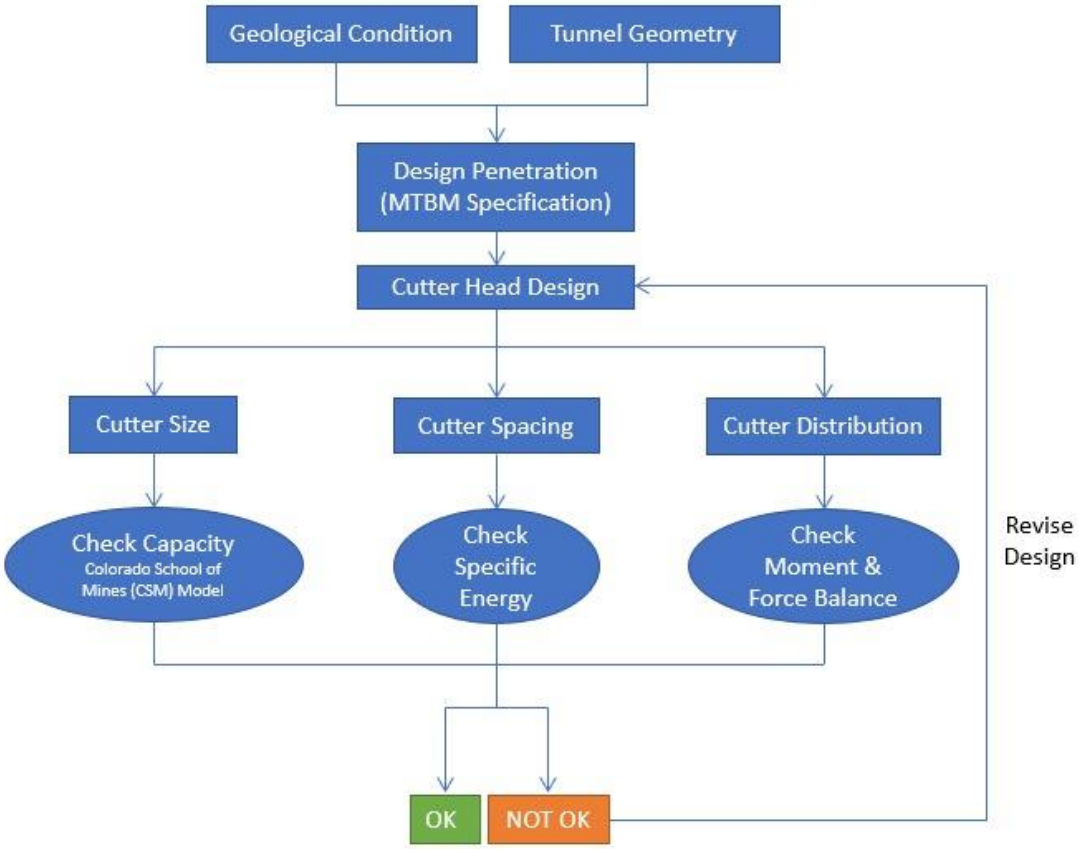


Figure 9 – Flowchart to evaluate the cutterhead in CEP

2.2.1 Basics of Cutterhead Design for Different Geology

MTBMs are adaptable machines that can operate in various ground conditions. Different cutterheads, such as spoke or fan for soft ground and domed with disc cutters for hard rock, are tailored to the specific needs of the project.

2.2.2 Opening Ratio

The opening ratio is the ratio between the open area on the cutterhead and the total face area. The main considerations are (1) the required cutterhead stiffness to support the cutting tools during excavation; (2) the required support to the excavation face; and (3) the efficiency of the mucking process. According to our CEP, the suitable opening ratio is >35% for soft ground, 20%-35% for mixed ground and <20% for rock. The cutter head in hard rock needs to be stronger and more robust to handle the higher cutter forces required and the chips generated are smaller due to slower advancement.

2.2.3 Cutter Disc Size

The main design considerations when selecting the suitable disc cutter sizes are (1) the required cutter load bearing capacity; (2) the cutter velocity; and (3) the space constraint on the cutterhead. In general, the larger the cutter the higher is its load bearing capacity. Larger cutters have higher load capacity, deeper penetration and higher velocity limit. For 2-3m diameter MTBMs, the recommended cutter ring size is typically 305mm in diameter. For 3-5m diameter MTBMs, the recommended cutter ring size is generally 394mm in diameter. In our CEP, the maximum cutter force was estimated using the Colorado School of Mines (CSM) prediction model based on the expected geology, cutter spacing, and design penetration (Guo et. al. 2016). The CEP is designed

to facilitate the evaluation of the proposed cutter head design, ensuring that the cutter force remains within acceptable operational limits and effectively prevents cutter overloading.

2.2.4 Cutter Spacing

The spacing between cutters is an important factor on the rock breaking efficiency of the cutterhead. Too large of a spacing impedes the formation of cracks between subsequent cuts while too small of a spacing would lead to excessive crushing and overbreak. A general guideline is that the optimum cutter spacing/penetration ratio shall be between 10 and 20 (Jamal et. al. 2017). The individual spacings between subsequent cutters could potentially be optimized using the principle of minimizing the specific energy of the cutterhead. The specific energy is the amount of energy required for the MTBM cutterhead to break a unit volume of rock and it is calculated based on the cutting force and torque contribution from individual cutters (Guo et. al. 2016). In the CEP, the specific energy of the proposed cutterhead was evaluated with the spacing of the cutters such that we could make a more informed judgement on whether there is room for optimization given the other cutterhead design constraints.

2.2.5 Cutter Distribution

The spatial distribution of disc cutters on the cutterhead is directly related to the balance of the cutterhead in terms of force and moment (Jamal et. al. 2017). A well-balanced cutterhead would reduce its distortion during excavation, reduce the burden of the MTBM bearing and improve the steering efficiency . However, in reality the cutters are often not distributed perfectly in terms of balance due to the other design constraints such as the need to maintain optimum spacing between cutters and the need to provide openings for efficient mucking. The CEP allows us to evaluate the balance of the proposed cutterhead.

2.3 RSS's Commitment to Innovation

In the ever-evolving construction industry, the use of Common Data Environments (CDE) has become increasingly prevalent for streamlining project management and enhancing collaboration among stakeholders. While there are numerous CDE platforms available in the market, RSS has taken a proactive approach by developing a tailor-made solution specifically for the Shatin Caverns project, as shown in Figure 10.

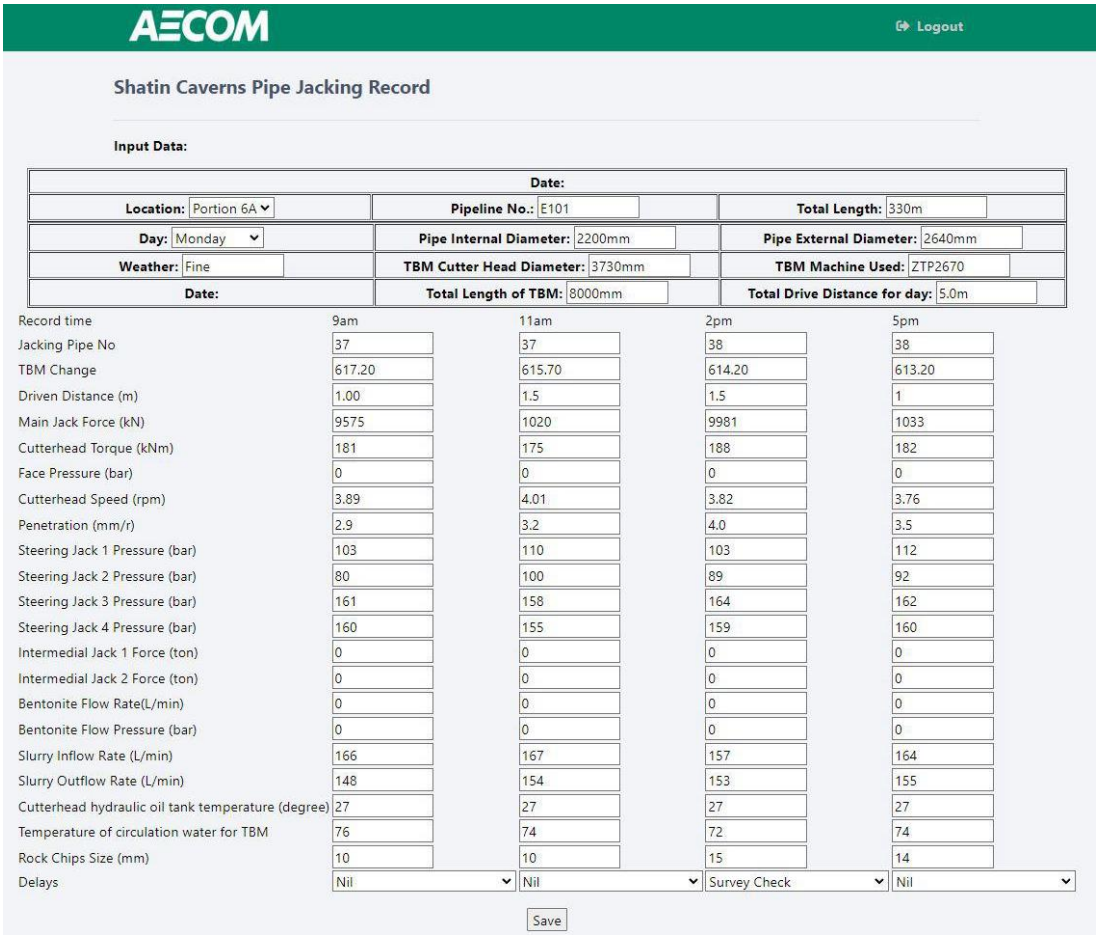


Figure 10 – Tailor-made platform for pipe jacking supervision

This bespoke CDE not only caters to the unique requirements of the project, such as blasting cycle monitoring and pipe jacking supervision, but also allows RSS and the contractor to actively contribute ideas for improving the supervision regime. This collaborative effort enables real-time adjustments and enhancements to be made to the program, ensuring that it remains relevant and effective throughout the project lifecycle. Under the Construction 2.0 framework, RSS has utilized PHP and MySQL for data input and database management, setting the groundwork for future integration of Python for data analysis and prediction. This forward-thinking approach not only enhances the efficiency and effectiveness of the CDE but also demonstrates RSS's commitment to innovation and continuous improvement in construction project management.

2.4 Verification of Jacking Force by BIM

The use of BIM and Robot Structural Analysis (RSA) by RSS, as shown in Figure 11, has transformed their design review process for pipe jacking systems. Previously, RSS had to rely on contractor designs for determining jacking force, but now they use BIM to create analytical models in Revit and import them into RSA for detailed analysis. This allows for accurate determination of thrust force, face pressure, and structural behavior, ensuring project requirements are met. The adoption of BIM and RSA has increased efficiency, accuracy, and confidence in project planning and execution, ultimately delivering projects with greater precision and quality. This technological advancement benefits this project and the construction industry as a whole.

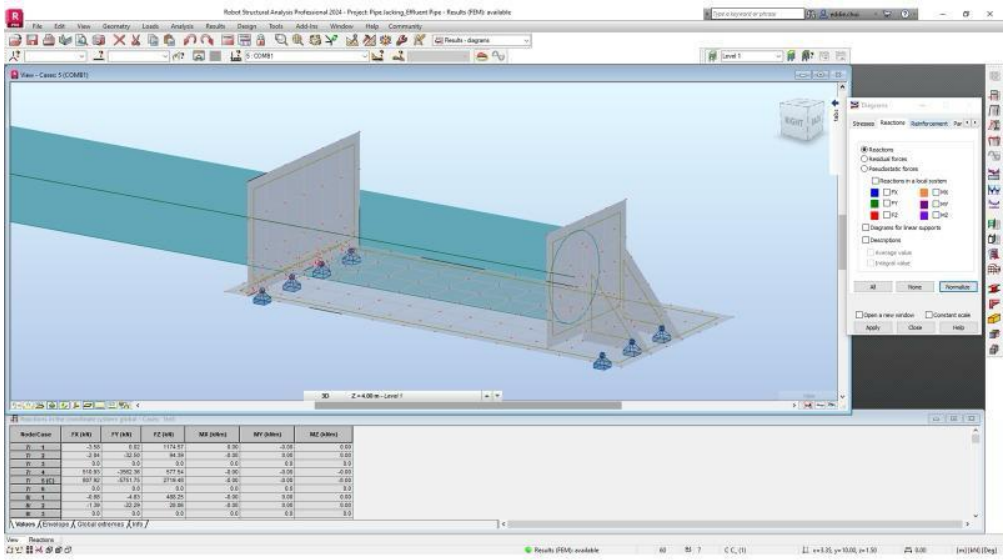


Figure 11 – Robot Structure Analysis to review the pipe jacking system

2.5 RSS Supervision Insights

In practice, MTBM operators rely on experience to operate the machine, but dynamic operating conditions present challenges. Maximizing penetration rate and prolonging worn cutter discs are common practices to reduce costs and replacement time. However, this can lead to decreased cutting efficiency, increased wear, and potential damage to the cutterhead.

2.5.1 Slurry inflow/outflow rate and slurry pressure

The inflow and outflow rate and pressure of the slurry should be balanced under normal working conditions. RSS should pay attention if the situation of "Small-In-Large-Out" occurs, where the inflow rate and pressure are lower than the outflow rate and pressure. This observation suggests the possibility of cutter disk damage and the formation of larger-than-optimum-size chips, which can lead to blockages in the slurry pipe.

2.5.2 Cutterhead pressure and hydraulic oil tank temperature

The cutterhead pressure and the hydraulic oil tank temperature should be within a specified range, depend on the MTBM specification. If the pressure exceeds or falls outside these ranges, it indicates that the cutterhead is experiencing an additional load. In such cases, it is possible that the encountered rock has become harder or that the cutter disks have worn down significantly, leading to the inability to maintain normal values. Under such condition, our RSS would request an inspection of the cooling system, cutter disks, and oil tank to gradually identify the underlying causes of the problem, thereby avoiding a situation where the MTBM becomes inoperable and cannot be repaired.

2.5.3 Total thrust and cutterhead torque

RSS should monitor the total thrust and cutterhead torque to ensure they stay within the design value and optimum range. In one instance, an abnormal thrust and torque were recorded, accompanied by unusual sounds from the MTBM. The operator considered it a normal situation resulting from encountering large boulders and insisted on continuing the excavation. However, our RSS suggested a thorough inspection of MTBM should be taken. It turned out to be found that one of the fastening screws for the cutter disk was damaged. If the damaged cutter disk had not been detected early, it could have fallen between the MTBM and the rock face, making it challenging to address the situation effectively.

2.5.4 Rock fragment inspection

RSS should carry out regular inspections and records the stone fragments brought out by the slurry pipe on a regular basis. Image analysis, as shown in figure 12, was carried out to determine the size distribution curve of the rock fragments. In case that abnormal large size of rock fragment is observed, RSS would stop the MTBM operation and would request a detailed inspection of the cutter disk. It is important to promptly replace excessively worn cutter discs in order to prevent unnecessary adverse impacts on other components of the

MTBM.

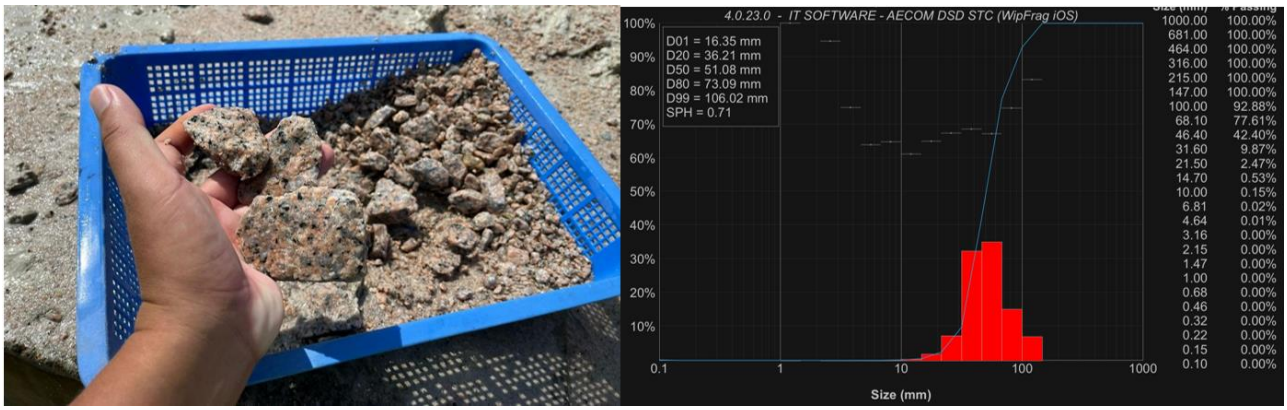


Figure 12 – Periodic inspection of rock fragment by RSS

2.5.5 MTBM advancement rate

The RSS should closely monitor the advancement rate of the MTBM. It is crucial to take note of prolonged stops of the MTBM at the same location during normal working conditions. Such extended pauses raise concerns about excessive ground settlement in adjacent areas, particularly when encountering materials with varying hardness at the excavation face. The softer portion of the material may undergo excessive drilling, resulting in significant ground loss as the MTBM overcomes the harder section of the material. It is important to address these issues promptly to mitigate potential adverse effects on the surrounding ground.

2.5.6 Usage of slurry and bentonite

The RSS also needs to monitor the usage of slurry and bentonite. Operators typically prioritize progress without considering the excessive use of slurry and bentonite, which indicates potential underground leakage, caused by damaged underground pipes or the presence of sinkholes, etc. RSS should also inspect the surrounding area adjacent to MTBM operations to see if there is any excessive settlement.

2.5.7 Prediction of cutter disc replacement

The detrimental effects of exceeding the critical wear of cutters, which not only reduce the cutting efficiency, but also increase stress and potentially leads to bearing damages and overall failure of MTBM. Our RSS realized the importance of timely replacement of the worn cutters and adopted 3-steps cutter wear supervision. First, the average lift time of the cutters were recorded and used as benchmark for estimation of wear levels. Secondly, we monitor the size of chips collected from desilting tanks, identifying any progressively increase in chip size as a warning sign of increasing cutter wear. Lastly, we closely observe applied torque, specifically abnormal high torque that persists over time, indicating potential wear issues, as shown in Figure 13.

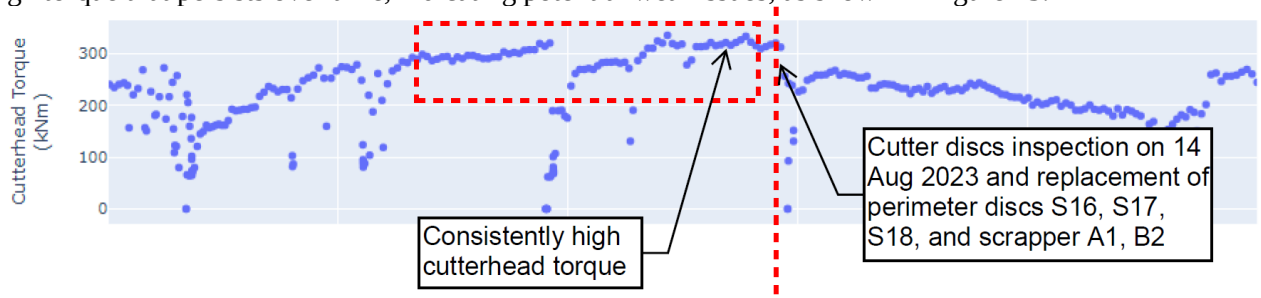


Figure 13 – Evaluation of drilling parameters for disc cutter replacement

3.0 CONCLUSION

The proper selection of the MTBM cutter head is crucial for the successful and efficient tunneling in hard rock conditions. RSS plays a critical role in ensuring that the right cutter discs and configurations are chosen, as it can have far-reaching impacts on the progress, safety, quality, environmental sustainability, and cost effectiveness of the tunneling project. A thorough review and supervision of the MTBM cutter head selection process is essential to mitigate risks and maximize the success of the project. The successful breakthrough of

the MTBM for the 1st effluent pipeline, as shown in Photo 6, stands as a confirmation to importance of meticulous site supervision and the careful evaluation of cutterheads. This achievement highlights the significance of data-driven decision making and utilization of operational data to inform future tunneling project.



Photo 6 – Successful completion of 1st effluent pipe

REFERENCES

1. Grandori R., Lembo-Fazio A. and Ribacchi R. 1990. Excavation of the Ridracoli Hydraulic Tunnels Using a Double-Shield TBM. *Rock Mechanics and Rock Engineering*, 23:141-165. Springer.
2. Guo Wei, Liu Xiao-qing, Liu Jian-qin, Sun Hong-yan, 2018. Optimized Layout Design for Cutterhead's Disc Cutters Based on Rock-Breaking Specific Energy, *Journal of Northeastern University (Natural Science)*, Vol. 39, No.2.
3. Gong Qiuming, 2006. Development of a Rock Mass Characteristics Model for TBM Penetration Rate Prediction, Doctorial Thesis, Nanyang Technology University, Singapore.
4. Jamal Rostami, Soo-Ho Chang, 2017. A Closer Look at the Design of Cutterheads for Hard Rock Tunnel-Boring Machines. Engineering, Vol. 3, Issue 6, P.892-904. doi.org/10.1016/j.eng.2017.12.009.

Energy geostructures for reducing energy consumption in Hong Kong: an example of energy diaphragm wall

Leung, A. K.[1*], Wang, Y. H.[1], Yang, H. X.[2], Zhou, H.[2], and Zhou, C.[3]
[1]*Department of Civil and Environmental Engineering, The Hong Kong University of Science and Technology, Hong Kong SAR, China*
[2]*Department of Building Environment and Energy Engineering, The Hong Kong Polytechnic University, Hong Kong SAR, China*
[3]*Department of Civil and Environmental Engineering, The Hong Kong Polytechnic University, Hong Kong SAR, China*
*Corresponding author: ceanthony@ust.hk

ABSTRACT

Energy geostructure is a green construction technology that turns geostructures such as piles, walls and tunnels to underground heat exchangers; by embedding polyethylene pipes in the concrete body of these geostructures, they could be used to inject heat into the ground in summer for space cooling and extract heat from the ground in winter for space heating, through the control of ground-source heat pump (GSHP). By exchanging ground energy, energy geostructures represent an advantageous technology to reduce energy consumption of air-conditioning nearby buildings sustainably. However, adoption of this technology in Hong Kong is slow primarily because of high cooling load and declining energy efficiency caused by ground thermal imbalances. This study presents a series of finite-element simulations to demonstrate the energy and structural performance of hypothetical, GSHP-coupled, reinforced concrete energy diaphragm wall panels, when operated under long-term extreme and realistic energy use scenarios in Hong Kong for an underground shopping mall. Changes in heat exchange efficiency due to continuous heat injection to the ground are presented. Implications in the engineering design of the diaphragm wall due to the additional thermal functioning through detailed analysis of soil-structure interaction are discussed.

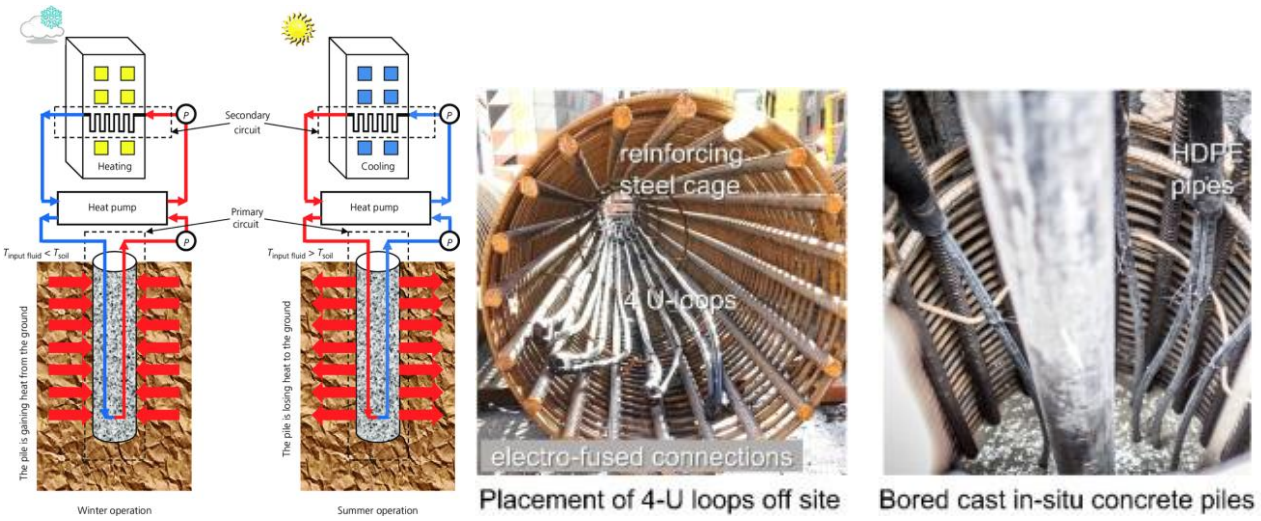
1 INTRODUCTION

In the next decades, vast infrastructure development is needed to support the Hong Kong (HK) Government's '*Hong Kong 2030+*' spatial development strategy, which includes mega projects such as *Lantau Tomorrow Vision* and *Northern Metropolis development strategy*. Underground construction is indispensable to the success and sustainability of all these development plans, but it is also one of the major contributors to carbon emissions. In 2021, about 90% of energy consumption (159,100 TJ) in HK was electricity (EMSD, 2022), more than 30% of which had been used for air conditioning in both residential and commercial sectors. Electricity generation constitutes more than 60% of greenhouse gas emissions in the year. Due to the impending urbanisation plans, future energy demand is expected to increase. It is thus vital to develop green construction technologies that can effectively reduce the energy consumption of infrastructures, especially for air-conditioning.

Energy geostructures are innovative, green construction technologies, by transforming geostructures such as piles, tunnels and diaphragm walls into underground heat exchangers (Fig. 1). The concrete body of these geostructures are embedded with high-density polyethylene (HDPE) pipes. Through ground-source heat pumps (GSHPs), the energy geostructures can inject heat into the ground (heat sink) in summer for space cooling and extract heat from the ground (heat source) in winter for space heating. By exchanging ground energy, energy geostructures represent an advantageous technology to meet the energy requirements of nearby buildings sustainably, helping Hong Kong to accomplish '*net-zero carbon emission for electricity generation*'.

This kind of construction technology has been used in Europe, the UK and North America, and the energy efficiency and structural and geotechnical behaviour of energy geostructures in different forms (especially piles) when operated in these regions have been investigated. However, the uptake of this technology in Hong Kong

and other cities located in the tropical to subtropical regions is slow. This is primarily because the cooling load dominates the energy demands in these regions, and the heat transfer efficiency between energy geostructures and the surrounding soil is *thought* to be low as the efficiency reduces with time due to the thermal imbalance issues in the ground under long-term GSHP operation. How the additional thermal functionality may affect the soil–structure interaction and the structural performance of the energy geostructures, especially when operated under the Hong Kong environment, is unknown.



(a) (b)

Figure 1: (a) Schematic of GSHP-coupled energy pile system (after Abuel-Nage et al., 2013); and (b) two images showing the U-shaped HDPE pipe loop attached on the reinforcement cage of a RC bored pile (after Zhong et al. 2022).

The objective of this study is to investigate the potential of the application of energy geostructure in the form of diaphragm wall (i.e. energy wall) in Hong Kong. A series of finite-element (FE) simulations was carried out to determine the energy and structural performance of hypothetical, GSHP-coupled, reinforced concrete (RC) energy wall panels when operated under extreme and realistic energy consumption scenarios in Hong Kong for an underground shopping mall. Through FE thermal analysis which took into account the heat-and-mass transport process in the soil-wall system, temporal variations of the coefficient of performance (COP) of long-term GSHP operation were determined to aid the evaluation of the significance of performance degradation and energy consumption over time due to thermal imbalance. FE soil–structure thermomechanical interaction analysis was also conducted to determine the wall responses during staged excavation and the subsequent GSHP operation stage. Any additional wall movement and bending due to the thermal functioning were evaluated.

2 METHODOLOGY

2.1 Hypothetical case study and modelling approach

The deep excavation work of the Dragon Centre, Hong Kong, presented by Lui & Yau (1995), was selected as the reference case study for the analysis in this study. The plane area of excavation was 107 m × 67 m and the excavation depth was 27 m. The work adopted the top-down construction method, and the excavation and lateral system (ELS) included multiple panels of 50 m-deep reinforced concrete (RC) diaphragm wall propped with five levels of RC slabs. Each wall panel has a width of 1.2 m, a length of 2.14 m and a depth of 50 m. In this study, the diaphragm wall along the long side of the excavation was hypothetically considered as the energy wall, i.e. with a heat exchange function by integrating a U-shaped heat exchange loop in each wall panel.

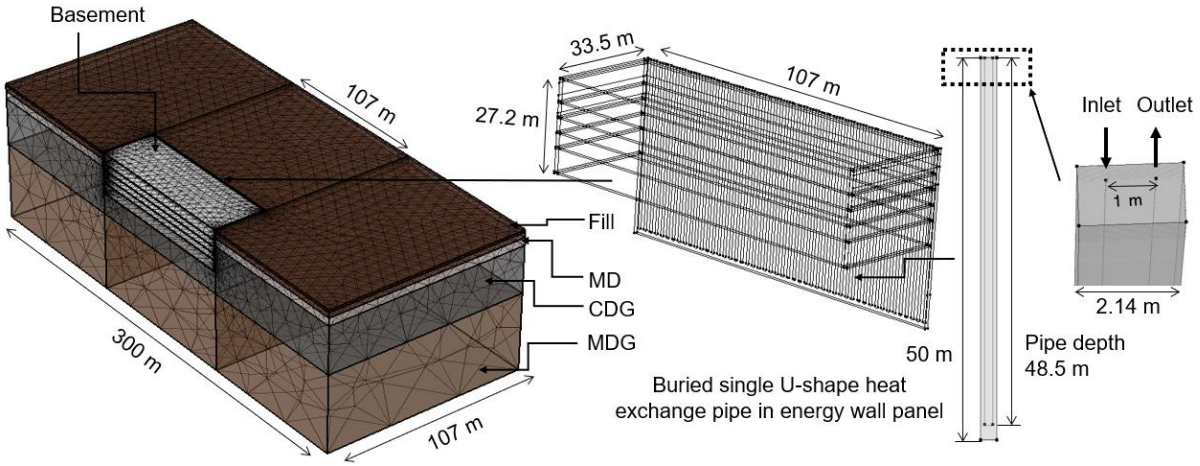
Energy efficiency and structural responses of the energy walls due to thermomechanical soil–structure interaction were analysed. Two types of analysis were conducted. The first analysis focused on heat-and-mass transport processes, with an aim to assess the COP (i.e. a measure of energy efficiency of the whole system). The second analysis focused on the thermomechanical behaviour of the energy wall when subjected to thermal loadings during the operation phase, aiming to determine additional mechanical stress and strain introduced by the thermal function.

2.2 Thermal analysis

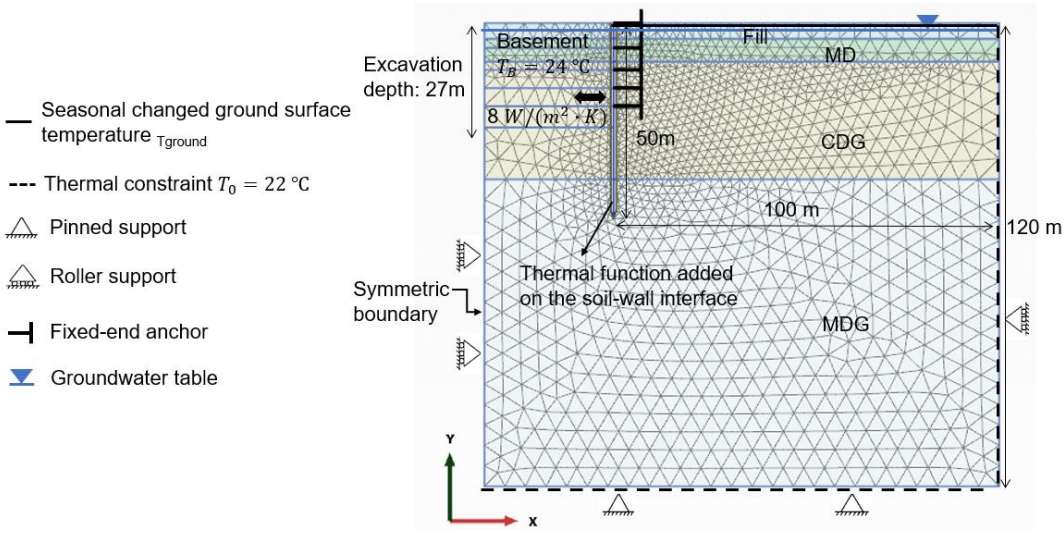
The three-dimensional (3-D) FE platform, COMSOL Multiphysics (version 6.2), was used to evaluate the heat transfer processes within the soil–energy wall system and the heat transfer efficiency of the energy wall. Detailed model setup, boundary and initial conditions, governing equations, input parameters and analysis plan are explained in the following sections.

2.2.1 Model setup, initial conditions and boundary conditions

Figures 2(a) and (b) show a 3-D and cross-section view of the FE mesh of the deep excavation. Due to symmetry, only half of the excavation was modelled, totaling 506,116 elements. Following the site investigation reported by Lui & Yau (1995), four uniform soil layers were considered in the model, comprising of a 5 m-thick loose fill layer overlain a 5 m-thick loose marine deposit (MD) layer, a 30.5 m-thick dense to very dense completely decomposed granite (CDG) layer and finally a 50 m-thick moderate decomposed granite (MDG) stratum. The diaphragm wall along the long-side of the excavation (i.e. 107 m) were hypothetically modified to be the energy wall, whereas those along the short side were non-thermal walls. The energy wall was composed of 50 wall panels that were thermomechanically connected, each of which has a cross-section area of 2.14 m (length) × 1.2 m (thick). In each panel, a single U-shaped heat exchange loop was embedded and modelled (Fig. 2(a)). The distance between the inlet and outlet tubes (both with an inner diameter of 25 mm) was 1 m. The presence of a U-shaped loop in each wall panel meant a reduction of cross-section area of 1.5×10^{-5}%. Pipe flow was modelled in the loop to simulate the heat transfer process. The flow rate of the circulating fluid (i.e. water, in



(a)



(b)

Figure 2: Numerical model geometry and FE mesh; (a) 3D layout of the COMSOL model; (b) section view of the PLAXIS model.

this case) was set to 0.25 m/s, which was sufficient to generate turbulent flow within the U-shaped pipes required for efficient heat exchange (Ground Source Heat Pump Association, 2012). The lateral support system consisted of five levels of identical 450 mm-thick RC slabs (except the bottommost slab that was 700 mm thick) located at 6.4, 12.1, 16.8, 21.5 and 27.2 m below the ground surface, forming a basement.

All the non-thermal and thermal wall panels were modelled by solid elements, whilst the surrounding soils were modelled by porous media. The heat transfer between the circulating fluid of the U-shaped pipes (i.e. water) and the pipe wall was modelled through the dimensionless Nusselt number (Nu), which describes the relative importance between the convective to conductive heat transfer rate within fluid flow. In this study, Nu was set to be 3.66 for heat transfer in fully developed turbulent pipe flow based on the Dittus-Boelter correlation.

Based on the borehole survey conducted by Cui et al. (2008), the underground temperature in Hong Kong was approximately constant at 22 ºC at depths below 10 m, which was thus set as the initial ground temperature uniformly for all soil layers and remained constant at the far sides and bottom boundaries of the model. A 25-year seasonal variation in ground surface temperature with time was applied, according to an equation model validated against the observation records at two meteorological stations: (i) the Hong Kong Observatory Headquarters (HKO) from 1996-2005 and (ii) the King's Park Meteorological Station (KP) from 2008-2009 ((Chow et al., 2011). The ground surface temperature was considered to vary between 18.7 and 29.9 ºC annually following a sinusoidal pattern and this pattern was repeated for 25 times. On the symmetrical side, the adiabatic boundary was imposed. For other sides, the Dirichlet's boundary condition was applied. Moreover, the indoor temperature of the basement was set as a constant value of 24˚C, which is the desired space temperature for human comfort, according to the ASHRAE Standard 55 – 2010. The heat transfer coefficients for the indoor walls and floor surfaces were taken to be 8 W/(m^{2}K) (Shinoda et al., 2019), according to the values provided in existing standards and guidelines (e.g., REHVA, EN1264-5 and ISO 11855-2).

2.2.2 Governing equations and input parameters

In COMSOL, the heat transfer process in all the soil layers was mainly through conduction and can be modelled by considering the energy conservation equation, as follows:

$$\left(\rho C_\rho\right)_{eff,s} \frac{\partial T_s}{\partial t} = \frac{\partial}{\partial x}\left(k_{eff,s} \frac{\partial T_s}{\partial x}\right) + \frac{\partial}{\partial y}\left(k_{eff,s} \frac{\partial T_s}{\partial y}\right) + \frac{\partial}{\partial z}\left(k_{eff,s} \frac{\partial T_s}{\partial z}\right) \quad (1)$$

where x, y and z are the spatial coordinates of the entire modelling domain; T_s is the soil temperature (ºC) and t is the elapsed time; ρ is the density of saturated soil (kg/m^3); C_ρ is the specific heat capacity (J/(kg K)), collectively referring $(\rho C_\rho)_{eff,s}$ to be the effective volumetric heat capacity of the soil; and $k_{eff,s}$ is the effective thermal conductivity of soil (W/(m K)) (Jayachandran & Reddy, 2019), which can be expressed, as follows:

$$\left(\rho C_\rho\right)_{eff,s} = \theta_s \rho_s C_s + (1-\theta_s)\rho_p C_p \tag{2}$$

$$k_{eff,s} = k_s^{\theta_s} \times k_p^{(1-\theta_s)} \tag{3}$$

where θ_s is the volume fraction of soil particles; C_s and ρ_s are the specific heat capacity (J/(kg K)) and density (kg/m^3) of dry soil, respectively; C_p and ρ_p are the specific heat capacity and density of pore water, respectively.

Similarly, the heat transfer process in the structural components, including the walls and floor slabs, was mainly through conduction. The energy conservation equation for the wall, for instance, can be expressed as:

$$\rho_w C_w \frac{\partial T_w}{\partial t} = \frac{\partial}{\partial x}\left(k_w \frac{\partial T_w}{\partial x}\right) + \frac{\partial}{\partial y}\left(k_w \frac{\partial T_w}{\partial y}\right) + \frac{\partial}{\partial z}\left(k_w \frac{\partial T_w}{\partial z}\right) \tag{4}$$

where ρ_w, C_w and k_w are the density (kg/m^3), specific heat capacity (J/(kg K)) and thermal conductivity (W/(m K)) of the wall, respectively. The same governing equation applies to the slab. The material properties of the RC slabs were considered to be the same as the RC wall panels.

To model the heat transfer process by the U-shaped heat exchange pipes, nonisothermal pipe water flow was used to simultaneously simulate the variations in flow, pressure, and temperature. The corresponding energy conservation equation can be expressed as follows:

$$\rho_p A_p C_p \frac{\partial T}{\partial t} + \rho_p A_p C_p u e_t \cdot \nabla_t^{T^2} = \nabla_t \cdot \left(A_p k_p \nabla_t T\right) + \frac{1}{2} f_D \frac{\rho_p A_p}{d_h} |u|u^2 + Q_p + Q_{wall} \tag{5}$$

where A_p is the cross-section area of the pipe (m^2) available for flow; T is the fluid temperature in the U-shaped pipe (˚C), u is the fluid velocity (m/s); k_p is the thermal conductivity of the pipe material (W/(m K)), which is made of high-density polyvinyl chloride in this study. The second term on the right-hand side of the equation represents the friction heat dissipated due to viscous shear, where f_D is the friction factor; d_h is the hydraulic diameter (m); and Q_p is the heat generation (heat source) in the fluid (W); and Q_{wall} is the power loss through the pipe wall (W/m), expressed as follows:

$$Q_{wall} = (hZ)_{eff}(T_{ext} - T)\nabla \cdot \left(\rho_p \nu\right) \tag{6}$$

where h is the heat transfer coefficient (W/m^{2}K); Z is the pipe wall perimeter (m); T_{ext} is the external temperature outside the pipe (°C), which is the soil-wall interface temperature obtained from the heat conduction; ν is the kinematic viscosity of fluid (m^2/s); and $(hZ)_{eff}$ is the effective heat transfer coefficient, as follows:

$$(hZ)_{eff} = \frac{2\pi}{\frac{1}{r_0 h_{int}} \sum_{n=1}^{N} \left(\frac{ln\left(\frac{r_n}{r_{n-1}}\right)}{\lambda_n}\right)} + \nabla \cdot \left(\rho_p \nu\right) \tag{7}$$

where r_n is the outer radius of the U-shaped pipe wall (m); and h_{int} is the internal film resistance (W/mK).

Tables 1, 2 and 3 summarise the input parameters of the soil, heat exchange pipe and the RC wall and floor slabs required for the thermal analysis, after Cui et al. (2023), Cui & Zhou (2022) and Ng et al. (2014).

Table1: Summary of the properties of different soil types used in the thermal analysis

Property	Fill	MD	CDG	MDG
Porosity	0.45	0.45	0.38	0.37
Thermal conductivity of solid phase (k_s) (W/ (m· K))	3.26	2.0	3.26	3.26
Saturated soil density (ρ) (kg/m^3)	1937	1937	1937	2243
Heat capacity at constant pressure (C_s) (J/(kg·K))	2239	1200	1500	1500

Table 2: Summary of the input parameters of the heat exchange pipes

Pipe tubes	Value
Thermal conductivity (k_p) (W/ (m· K))	0.42
Inner diameter (mm)	25
Pipe thickness (mm)	5
Distance between the inlet and outlet (m)	1

Table 3: Summary of the input parameters of RC walls and floor slabs

Concrete	Value
Thermal conductivity (W/(m·K))	1.5
Density (kg/m^3)	2400
Specific heat capacity (J/Kg·K)	880
Wall Depth (m)	50
Wall Length (m)	107
Wall Width (m)	1.2

2.2.3 Analysis plan

A series of parametric thermal analyses were carried out to investigate the heat exchange process and efficiency of the energy wall (Table 4). A primary factor that has been recognised to affect the efficiency is the inlet fluid temperature (T_{in}) in the heat exchange pipe. According to a practical reference geothermal heat pump system in Bangkok, Thailand (Takashima et al., 2011), T_{in} typically varies from 35 to 39 ºC in tropical climate. In this study, the values of T_{in} of 37 and 40 ºC were considered. The initial soil temperature (T_s) and basement temperature (T_B) also play significant roles in the heat transfer process because they directly affect the thermal gradient between the energy geostructure and the surrounding soil. Although an average T_s of 22 ºC were reported by Cui et al. (2008), on some occasions the average T_s could vary up to 26.6 ºC spatially across Hong Kong (Chow et al., 2011). Thus, warmer ground conditions, say T_s of 24 and 26 ºC, were considered, representing worser or more conservative scenarios in terms of heat exchange efficiency. The basement would sometimes be used as a car park. According to survey data collected from an investigation of 22 car parks in Hong Kong, T_B ranges from 24 to 33 ºC (Chan et al., 1998). Therefore, different values of T_B of 24, 30 and 33 ºC were used to study its impact on the thermal performance of the system. Another variable was the number of wall panels being thermally activated. As depicted in Fig. 2, the long side of the excavation area was retained by 50 wall panels. Three cases were modelled, (1) one energy wall panel (1U; located at the middle of the 50 wall panels); (2) 20 wall panels (20U; located every alternative wall panel) and (3) 50 wall panels (50U).

In all the analyses, the so-called continuous operation mode of the GSHP was simulated; under this mode, the energy wall panels operate for 24 hr a day and without stopping for 25 years. This mode of operation means that the heat was continuously injected to the ground throughout all years and the thermal gradient between the energy wall and the surrounding soil would be reduced as the ground was continuously warmed up, representing a worst-case scenario in terms of heat transfer efficiency. A more realistic GSHP operation mode was also considered, known as intermittent operation; under this mode, the energy wall panels operated for 10 hr in one day, i.e. the normal working hours of an office in each day followed by a 14-hour break in a day. Instead of considering 25 years, the simulation of the intermittent mode was limited to about 200 days, due to the significant constraint of computational power required. The 200-day simulation took 13 days of calculation time; as will be shown later, the simulation results up to this duration were adequate to support the conclusion drawn.

Table 4: Parametric analysis plan

Analysis ID	Inlet fluid temperature T_{in} (˚C)	Initial soil temperature T_s (˚C)	Basement temperature T_B (˚C)	No. wall panel activated (N)
$T_{in37\text{-}1u}$	37	22	24	1
$T_{in37\text{-}20u}$				20
$T_{in37\text{-}50u}$				50
$T_{in40\text{-}1u}$	40			1
$T_{in40\text{-}20u}$				20
$T_{in40\text{-}50u}$				50
$T_{in40\text{-}int}$				1
T_{s26}		26		50
T_{s24}		24		
T_{B30}		22	30	
T_{B33}			33	

*All cases considered continuous operation, except the case $T_{in40\text{-}int}$ which considered intermittent operation. N denotes the number wall panels being thermally activated and used as the energy wall panels.

The key simulation output was the outlet fluid temperature (T_{out}). Based on this output, the heat exchange rate ($q(t)$ as a function of time t) that was normalised by the surface area of wall panel(s) ($A_{w,s}$) can be determined, as follows:

$$q(t) = mC_p[T_{in}(t) - T_{out}(t)]/A_{w,s} \quad (8)$$

where m is the water mass flow rate (kg^3/s). The value of T_{out} can be used to determine the COP (dimensionless) of the GSHP, considering the heating and cooling loads of a simulated building. For energy geostructures that adopted a U-shaped loop arrangement, previous studies found an empirically linear correlation between COP and T_{out} (Kahraman & Celebi, 2009; Casasso & Sethi, 2014), as follows (Jia et al., 2024):

$$COP_{cooling-GSHP} = -0.12T_{outlet} + 8.6 \quad (9)$$

Based on the calculated COP, the cumulative energy consumption (W) can be determined as long as the cooling load ($Q_{cooling}$) of the infrastructure that an energy geostructure is supporting is known:

$$W = \sum_{1^{st}day}^{25^{th}year} \frac{Q_{cooling}}{COP} \quad (10)$$

Unfortunately, $Q_{cooling}$ is unavailable for the Dragon Centre because of a lack of building parameters. In this study, the calculated $Q_{cooling}$ reported by Fong (1999) for a commercial building (with a total floor area of 26,340 m^2) in Hong Kong was adopted, based on the Typical Meteorological Year (TMY) weather data of Hong Kong. The commercial building envelope consists of a glass curtain wall resembling the Dragon Centre case and was equipped with a central air-conditioning system.

2.3 Thermomechanical soil–structure analysis

The FE package, PLAXIS 2D Thermal (V20), was used to simulate the thermomechanical behaviour of the energy wall from the excavation stage to the subsequent operation stage of GSHP. A plane-strain analysis was conducted, considering all wall panels to be thermally activated (i.e. 50U case). This consideration represents the worst-case scenario in terms of wall structural responses. Detailed model setup, boundary and initial conditions, governing equations, input parameters and analysis plan are explained in the following sections.

2.3.1 Model setup, initial conditions and boundary conditions

Figure 2(b) shows the cross-section view of the deep excavation problem. Similarly, only half of the excavation was modelled, totaling 986 15-node triangular elements. Drained, effective stress analysis was carried out (i.e. no mechanical or thermal consolidation (and their induced excess pore-water pressure) was considered, which is deemed reasonable for modelling sandy materials). According to Lui & Yau (1995), the initial groundwater table was located 1.5 m below the ground surface, establishing a hydrostatic pore-water pressure distribution. Whilst the elevation of the groundwater table on the retained side remained unchanged, the groundwater table was lowered to the ground level after each stage of excavation. The initial soil stress was established under K_0 condition, estimated based on the Jaky's equation. For the mechanical boundary conditions, the ground surface was free to move, whilst the bottom boundary was fixed in both horizontal and vertical directions. No horizontal displacement was allowed on the two side boundaries. Water was allowed to flow out of the two side boundaries with a constant pressure as the hydraulic boundary conditions, whilst no water flow was allowed at other boundaries. For the thermal boundary condition, all side boundaries were set to a constant temperature of 22 ˚C, whilst the soil–wall interface was set to a thermal function to simulate the GSHP operation (see details in Section 2.3.3 below).

2.3.2 Constitutive models and input parameters

The hardening soil small (HSS) model was used to model the mechanical behaviours of the fill and CDG. The Hardening Soil Model (HS) (Schanz et al., 1999) is an elastoplastic model that introduces a yield cap that expands the yield surface upon plastic straining, incorporating a multi-surface yield criterion. The formation of irreversible plastic strains characterises compression and shear hardenings as a result of primary compression and deviatoric loadings. This model has been extended to be capable of capturing the nonlinear strain-dependency of shear modulus (Atkinson, 1990), including the behaviour at the very-small-strain and small-strain ranges, which have been demonstrated to be vital for modelling deep excavation problems. To consider the stiffness nonlinearity, the following hyperbolic equation has been adopted by the HSS model to allow the secant shear modulus G_s to decrease with shear strain (γ) nonlinearly (Santos & Correia, 2001):

$$\frac{G_S}{G_{\max\,(ref)}} = \frac{1}{1+a\left|\frac{\gamma}{\gamma_{0.7}}\right|} \tag{11}$$

where $G_{max(ref)}$ is the reference maximum shear modulus at the very-small-strain at a reference effective minor principal stress, σ'_3; $\gamma_{0.7}$ is the shear strain at which the G_{sec} reduces to 72% of the $G_{max(ref)}$; and a is a fitting parameter, which was typically taken as 0.385 (Santos & Correia (2001)). Due to the lack of experimental data on the stiffness reduction curve for MD, the perfectly-elastic, perfectly-plastic Mohr-Coulomb (MC) model was adopted to describe its mechanical behaviour. The MDG was modelled to behave elastically. All the key input parameters for each type of soil used in the simulation are summarised in Table 4, after Ng et al. (2014).

All soil types were considered to be thermoelastic, meaning that thermally induced changes in soil volume were linearly related to temperature change through the coefficient of thermal expansion (CTE). As most of the soil conditions are sandy and quartz-based materials, the CTE of all the soils was taken be 10με/°C (Agar, 1984).

For the structures, the wall was modelled as a plate element; in this case, the wall was considered to have a unit width and behaved as an elastic beam, which allowed both axial deformation and in-plane bending. The wall was considered 'wished-in-place', meaning that any wall installation effects were ignored. Each of the five RC slabs was modelled as a fixed-end anchor. No heat transfer was permitted from the wall to slabs. Notably, the area reduction due to the presence of the U-shaped loop in each wall panel was 1.5×10^{-5}%; the associated reduction in the wall moment capacity can be neglected. All the input parameters are summarised in Table 5.

Table 4: Summary of the input parameters required for the three different constitutive models (after Ng et al. 2014)

Soil	γ_{sat} (kN/m^3)	E(MPa)	E_{50}^{ref} (MPa)	m	$\gamma_{0.7}$	G_{max}^{ref} (MPa)	p^{ref} (MPa)	V'	C'(kPa)	φ'_{cs} (°)
Fill	19	-	25	0.5	1.2E-3	105	27	0.17	0.1	32
MD	19	13						0.17	0.1	32
CDG	19	-	40	0.5	1.6E-3	98	30	0.17	0.1	35
MDG	22	15000						0.2	-	-

* γ_{sat} denotes the saturated unit weight; E_{50}^{ref} denotes the secant Young's modulus at 50% strength at a reference confining pressure p^{ref} ; and m is a power parameter that determines stress-dependent stiffness.

Table 5. Summary of input parameters to model the thermomechanical behaviours of the diaphragm wall and slabs

Components	Wall properties		Slab properties	Thermal property
	E_wI_w (kN/m^2/m)	E_wA_w (kN/m/m)	EsA_s (kN/m/m)	CTE ($\mu\varepsilon/K$)
Diaphragm wall	4,032,000	33,600,000	-	12
Basement G/F	N/A		293,800	
Basement 1/F				
Basement 2/F				
Basement 3/F			261,200	
Basement 4/F				

Note: The value of CTE of the structural components were obtained from Cui & Zhou (2022). *EI* and *EA* is the flexural stiffness and axial stiffness, respectively, where *E* is the Young's modulus; *A* is the cross-sectional area; and *I* is the moment of inertia of the cross-section. The subscript of the symbols *E* and *A*, *w* and *s*, refers to the wall and slab, respectively.

2.3.3 Modelling procedures

The modelling included two phases, namely construction phase and GSHP operation phase. The construction phase modelled the staged excavation, following the construction sequence reported by Lui & Yau (1995). When all the slabs were installed and the excavation reached the final depth, the modelling of the operation phase was commenced by applying the temporal variation of the average wall surface temperature obtained from COMSOL after considering heat transfer from the U-shaped loop to the RC (Fig. 3). It can be seen from the figure that under the continuous operation mode, the wall surface temperature in the case of T_{in} = 40 ºC was the highest, implying potentially a more significant influence on the wall structural responses. Notably, although this modelling approach (i.e. using an output from the thermal analysis as an input of the mechanical analysis) is a simplified way of modelling thermomechanical soil–structure interaction, it has been extensively employed when analysing energy geostructures in previous studies (e.g. Gawecka et al., 2021; Liu & Zhou, 2022, 2023).

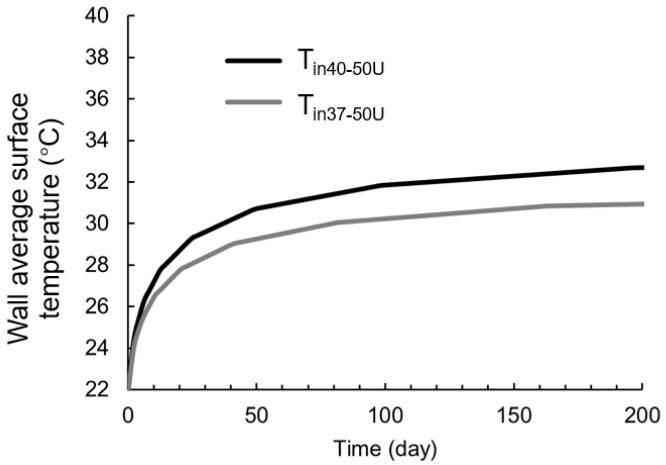
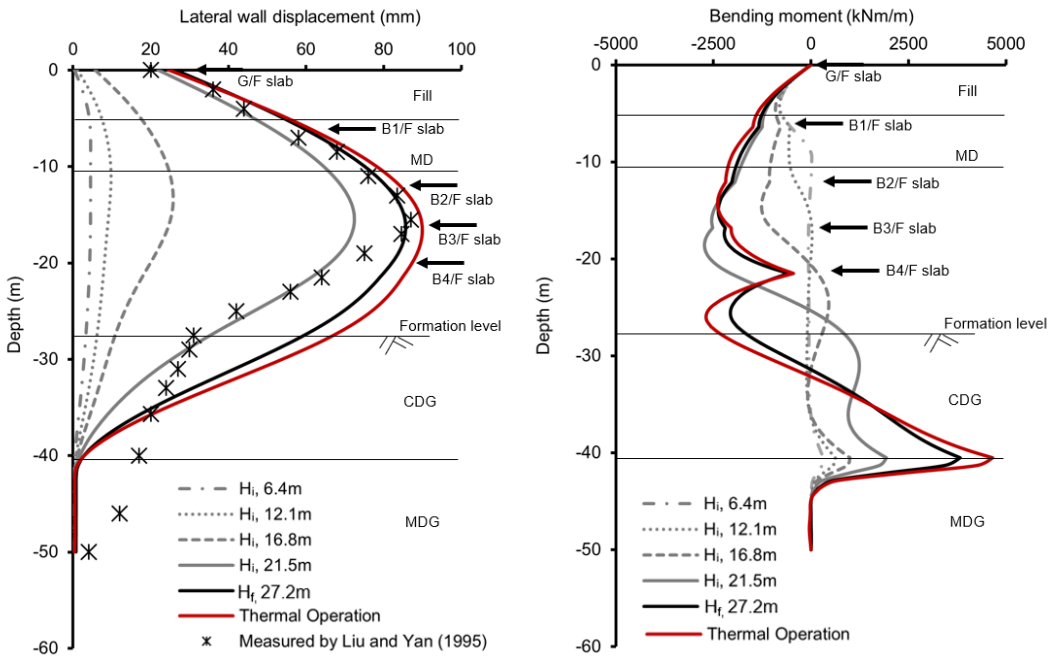


Figure 3: Temporal variations of the average temperature of wall surface output from COMSOL

3. Results and discussion

3.1 Wall behaviour during the construction phase

Figure 4 shows the computed vertical profiles of wall lateral deflection and wall bending moment obtained from PLAXIS. The computed result at the end of the excavation has a reasonable match with the measured results obtained by an inclinometer, validating the effectiveness of the numerical model. The peak wall displacement was 85.7 mm at 16.2 m depth, 10.8 m above the final excavation depth. The maximum normalised wall movement (i.e. y/H_f, where y is the maximum wall lateral displacement; and H_f is the final excavation depth) in this case was 0.0032 (or 0.32%), which is close to the mean value (i.e. 0.23%) for deep excavation works in Hong Kong that have geological conditions similar to this case study (Ng et al. 2014).



(a) (b)

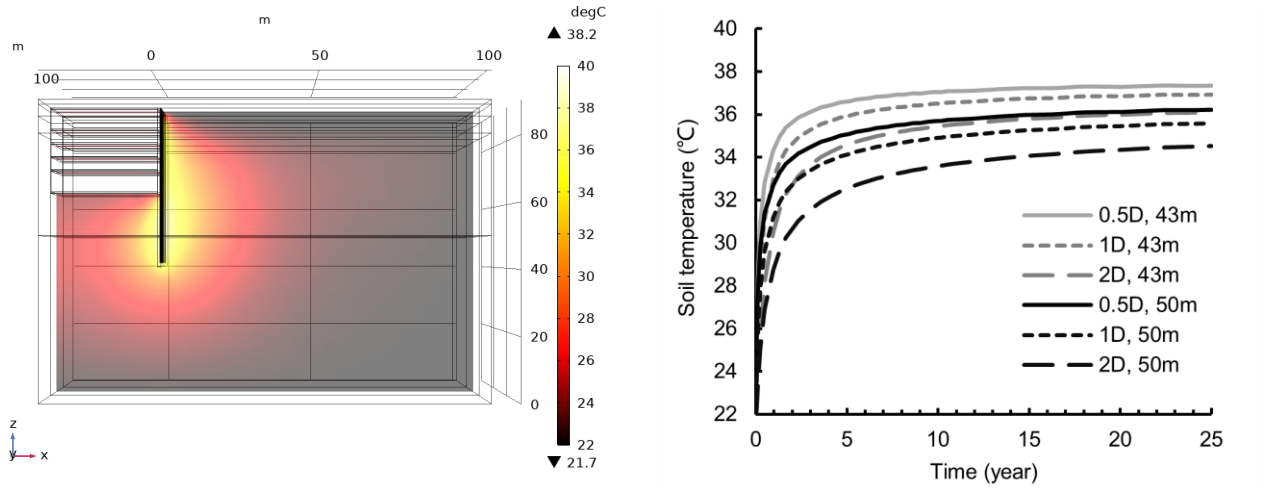
Figure 4: Vertical profiles of (a) lateral wall displacement; and (b) bending moment subjected to multi-stage excavation and post-excavation thermal operation of 25 years continuous heat injection to the ground. Note H_i denotes the intermediate excavation depth.

Unfortunately, field data on wall bending moment is not available from Lui & Yau (1995), and no direct comparison can be made with the simulation results. Nonetheless, the computed profiles of wall bending moment resembled the shapes typically found in multi-propped excavation. The peak bending moment was 3,822 kNm at a depth of approximately 40.5 m, 13.5 m below the final excavation depth (Fig. 4(b)).

3.2 Operation phase

3.2.1 Variations of soil temperature and outlet fluid temperature

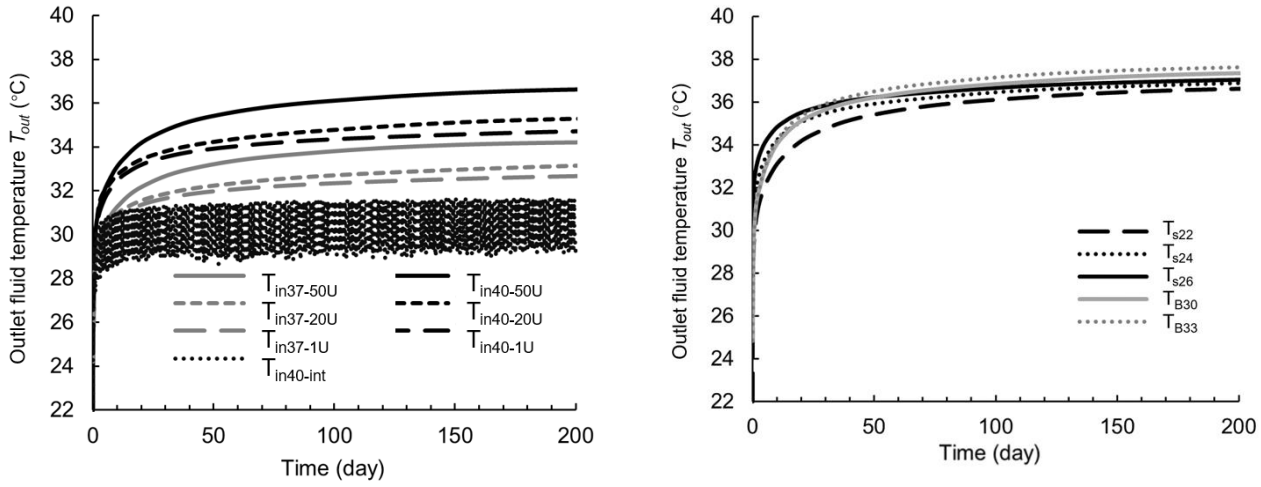
Figure 5(a) shows the computed soil temperature contour at the mid-section of the long-side of the excavation area after 25 years of continuous injection to the ground with T_{in} of 40 °C when all 50 wall panels were thermally activated (i.e. case $T_{in40\text{-}50U}$, again representing the worst-case scenario in terms of heat exchange efficiency). Evidently, the temperature influence zone is approximately 40 m (i.e. 33.*D*, where *D* is the wall width) away from the wall. Figure 5(b) shows the temporal variation of soil temperature of six selected monitoring points. These points were at either 50 m (at the wall toe) or 43 m depth (where the temperature increase was the greatest); in each depth, the points that were 0.5*D*, 1*D*, and 2*D* away from the wall were chosen. The continual injection of heat to the ground (i.e. continuous space cooling) led to an exponential increase in soil temperature at all points, especially for those closer to the wall. After 25 years of continuous operation, a steady state has not been reached and the overall increase in soil temperature from the initial T_s of 22 °C varied from 12.5 to 15.3 °C.



(a) (b)

Figure 5: (a) Soil temperature contour at the mid-section of the long-side of the excavation area after 25 years of operation; and (b) temporary variation in soil temperature at six selected monitoring points around the excavation area under 25 year-continuous operation mode at T_{in} of 40 ºC.

Figure 6(a) shows the temporary variation of T_{out} over about 200 days when considering different T_{in} and the number of energy wall panels. Under the continuous operation mode, exponential increases in T_{out} were identified, following a similar trend of the soil temperature (Fig. 5(b)). At T_{in} of either 37 or 40 ºC, the T_{out} was always higher for greater number of energy wall panels. When only one wall panel (1U) was activated, the heat injected to the ground can be dissipated to not only right behind that energy wall panel but also sideways. As the number of energy wall panels increased, the sideway heat dissipation path became less or even none for the case of 50U. This phenomenon explains the greater increase in soil temperature due to the energy accumulation in the system (Fig. 5(a)) and hence the increase in T_{out} with the number of energy wall panels. After 25 years of operation, the T_{out} approached a steady state value, varying from 34.8 to 37.8 ºC. Accordingly, the normalised heat exchange rate ($q(t)$; Eq. (8)) converged to the range of 10.4 to 12.9 W/m^2. The initial T_s and T_B did play some role in T_{out} (Fig. 6(b)) when considering 50 energy wall panels, yet mainly during the initial stage of operation, and the T_{out} became practically the same after 200 days of operation. The results show that a 9 ºC variation of T_B (i.e. between 24 and 33 ºC) translated to only a 1.2 ºC difference in T_{out} over a period of 200 days.



(a) (b)

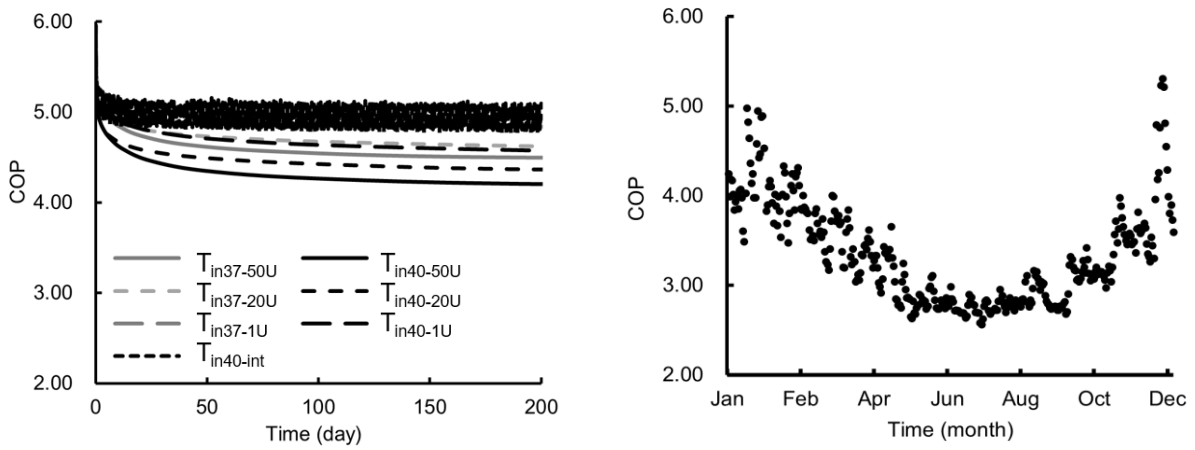
Figure 6: Temporary variation of T_{out} over approximately 200 days considering (a) different T_{in}, number of energy wall panels and GSHP operation mode when considering the same T_s of 22 ºC; and (b) different T_s and T_B when considering 50 energy wall panels.

Figure 6(a) also shows the temporary variation of T_{out} under the intermittent operation mode when T_{in} was set to as 40 ºC (i.e. case $T_{in40\text{-}int}$). As expected, the T_{out} displayed a fluctuation of approximately 1.5 ºC each day

due to the nature of the intermittent operation. Importantly, even the upper bound of the T_{out} was significantly lower than that in the case of $T_{in40\text{-}1U}$. The much lower values of T_{out} translated to a greater range of $q(t)$ from 40.8 to 51.7 W/m^2, meaning a much-improved heat exchange efficiency. Indeed, under the intermittent operation mode, the soil-energy wall system allowed 14 hr of heat dissipation and soil temperature recovery every day before the next cycle of 10 hr-operation began. The major discrepancy of T_{out} between the two operation modes highlights the importance of considering a more realistic pattern of the GSHP operation in order to avoid significant overestimation of T_{out} and inappropriate evaluation of the system efficiency in terms of heat exchange.

3.2.3 COP evaluation

Figure 7(a) shows the temporal variation of COP of the GSHP of different cases over approximately 200 days. Initially, a rather high COP of 5.96 can be achieved. However, accompanying the increase in T_{out} (Fig. 6) due to the accumulation of soil temperature (Fig. 5) upon continuous heat injection, the COP of all cases dropped exponentially. Amongst the cases, the drops for the cases with higher T_{in} and a greater number of energy wall panels were the most significant, approaching a stabilised COP between 4.27 and 4.56. Although not substantial, these drops of COP represent the degradation of the efficiency of heat exchange between the energy wall panels and the soil due to the inevitable thermal imbalance problems associated with the high demand of cooling needs under this particular extreme operation mode. However, when considering a more realistic GSHP intermittent operation mode, the drop of COP was much less for a given T_{in} and the number of energy wall panels. The lower-bound COP approached a stablised value of just slightly below 5.00 (i.e. 4.81).



(a) (b)

Figure 7: (a) COP of the GSHP over 100 days; and (b) the daily COP of the ASHP calculated from the TMY data of T_{air}

The COP of the GSHP was compared with that of the air-source heat pump (ASHP), sometimes referred to as an air-cooler chiller, which is typically used in Hong Kong nowadays for cooling purposes. The COP of ASHP can be determined by the following empirical equation (Congedo et al., 2020) that was assumed to be applicable to the environmental condition of Hong Kong's subtropical climate throughout the year (with a mean annual temperature of 22.6 °C), as follows:

$$COP_{ASHP} = -0.00004T_{air}^3 + 0.005T_{air}^2 - 0.2806T_{air} + 7.7483 \quad (12)$$

where T_{air} is the outdoor air temperature of Hong Kong in °C, which was set to be the value obtained from the Typical Meteorological Year (TMY) weather data of Hong Kong (Fong, 1999). As can be seen in Fig. 7(b), the COP varied from 5.31 during winter (heating demand) to 2.63 during summer (cooling demand), and the yearly average COP was 3.34. This comparison highlights that the GSHP system, even considering the worst-case scenarios, can have a much better energy efficiency than the ASHP system.

3.2.4 Energy consumption and carbon emission

Figure 8 shows the monthly $Q_{cooling}$ of the commercial building reported by Fong (1999). Figure 9(a) shows the corresponding cumulative W of the GSHP of three selected cases and the ASHP, all obtained through Eq. (7). The calculation results show that the GSHP, in any case, had much lower W than the ASHP, primarily because the former always displayed a higher COP (Fig. 7). The amount of energy saving, with respect to the case of ASHP, was 30% to 40% under the continuous operation mode and even more than 50% under the intermittent operation mode. The energy saving translated to a reduction in carbon dioxide emission by 13,132 tons, considering that generating 1 kWh of electricity in Hong Kong corresponds to producing 0.55 kg of carbon dioxide in 2022, according to the report from the "CLP Climate-Related Disclosures Report" (CLP 2022).

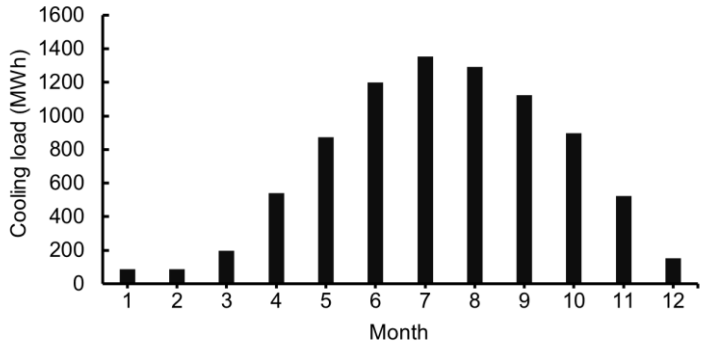
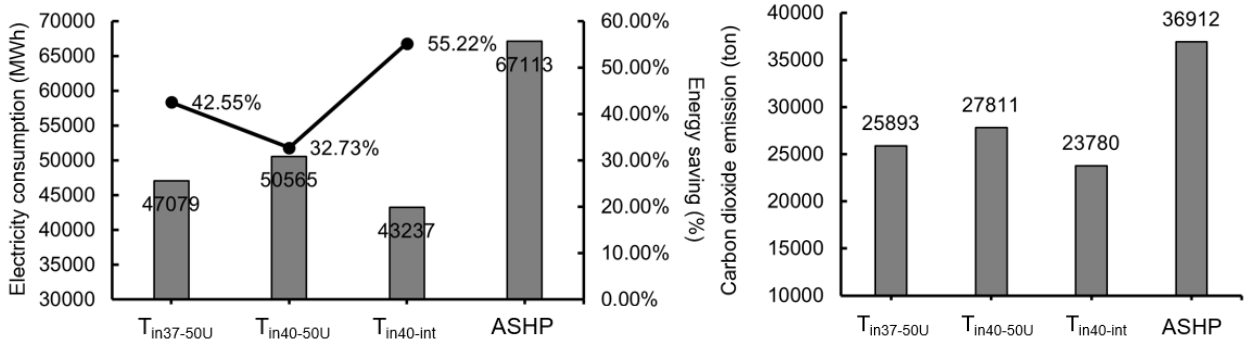


Figure 8: The monthly cooling load of a commercial building in Hong Kong. after Fong (1999).



(a) (b)

Figure 9: (a) Cumulative electricity consumption of three selected cases of GSHP and ASHP over 25-year operation; and (b) cumulative carbon emission for the selected commercial building in 25 years

3.2.5 Thermally-induced wall behaviour

Figure 4(a) depicts the vertical profile of the additional wall lateral deflection after 25 years of continuous operation. The thermal expansion of both the energy wall panels and the surrounding soil as their temperature increase due to continuous heat injection caused additional wall movement. Whilst the heating process did not change the shape of the profile much, the wall lateral displacement was magnified, particularly around the depths where the peak was identified. The maximum wall displacement after both the construction and operation phases was 90.0 mm (i.e. 4.3 mm more than the value of 85.7 mm right after the excavation). Correspondingly, the y/H_f rose from 0.0032 during the excavation phase to 0.0033 after the long-term GSHP operation (i.e. less than 5% increased). Notably, the additional outward wall movement under this extreme operation scenario did not introduce any active failure of the soil being retained.

Figure 4(b) shows the profile of wall deflection. Whilst the shape of the bending moment profile was not altered, the maximum bending moment increased from 3,822 kNm after excavation to 4,652 kNm after operation (i.e. 22% increase), accompanying the additional wall movement seen in Fig. 4(a). Because the case study by Lui & Yau (1995) did not provide any reinforcement details of the wall panels, the yield bending moment (M_{yield}) needs to be deduced for further interpretation. According to the *Code of Practice for Structural Use of Concrete* 2013

(BD, 2020) and *Structures Design Manual for Highways and Railways* (HyD, 2013), the partial factor for the ultimate limit state design-adjusted structural failure in bending was 1.35. Hence, the M_{yield} was deduced to be 1.35 times the peak bending moment after the staged excavation (i.e. 5,160 kNm). With the known M_{yield}, the thermally-induced increase in the wall bending moment from 3,822 to 4,652 kNm meant a drop of the factor of safety from 1.35 to 1.11. Under these extreme worst-case conditions, additional measures will be needed to take into account the effects of thermal functionality in order to satisfy the specific ultimate limit state design.

CONCLUSIONS

The analyses of the energy and structural performance of GSHP-coupled diaphragm wall demonstrated the high feasibility of adopting this construction technology in Hong Kong, addressing the forthcoming challenges of high energy consumption needs due to air-conditioning to support the government's ambitious strategic spatial development plans. The energy wall used for an underground shopping mall displayed a considerably high COP of up to 5.96 even under extreme energy use scenarios in Hong Kong environment. Although the COP reduced with time due to ground heat accumulation when the heat was continuously injected to the ground, it stabilised at about 4.27, which was higher than the yearly average COP of ASHP (i.e. 3.34) that has been typically used for air-conditioning in Hong Kong nowadays. The amount of COP drop of the GSHP would be much reduced by considering more realistic energy use scenarios such as intermittent operation mode when daily heat injection was not continuous for 24 hr but 10 hr with 14 h-break. The higher COP of the GSHP translated to an energy saving of up to 50% and a reduction in carbon dioxide emission of 35%, when compared to the ASHP.

The thermal functionality made the diaphragm wall to experience additional wall lateral displacement and bending moment. The RC wall experienced thermal expansion during continuous heat injection, exerting additional lateral stress and strain to the surrounding soil. Under the extreme 25-year continuous operation mode, the peak wall lateral displacement was increased by less than 5% (i.e. from 85.7 mm after staged excavation to 90.0 mm after thermal operation), yet such increase would not cause any active failure of the retained soil. The increase in the peak bending moment was 22% (i.e. from 3,822 kNm after staged excavation to 4,652 kNm). Although the thermally-induced moment increase did not cause failure against the ultimate limit state, it meant a reduction in the factor of safety (against wall structural failure) from 1.35 to 1.11, and needs of additional measures to account for the effects of thermal functionality of the energy geostructure.

Clearly, validation of the simulation results presented in this study is needed in the future; unfortunately, data concerning the thermal and engineering performance of energy retaining walls is unavailable globally. Ongoing scientific research currently led by the first author focuses on the use of centrifuge modelling technique to study the thermomechanical soil–structure interaction involved in different types of energy geostructures, such as diaphragm walls and tunnels. The new data generated will not only aid the model validation but also provide fundamentals to develop new insights into the design principles of this kind of geostructures due to the additional thermal functionality. The research team is also actively looking for industrial collaboration for any field trials and demonstration of such construction technology to explore the feasibility of adopting energy geostructures in Hong Kong when operating them under the specific environmental conditions in this city.

REFERENCES

Abuel-Naga, H., Lorenzo, G. A., & Bergado, D. T. 2013. Current state of knowledge on thermal consolidation using prefabricated vertical drains. *Geotechnical Engineering*, 44(4), 132-141.

Agar, J. G. 1984. *Geotechnical behaviour of oil sands at elevated temperatures and pressures* [PhD thesis, University of Alberta].

Atkinson, J. H., Richardson, D., & Stallebrass, S. E. 1990. Effect of recent stress history on the stiffness of overconsolidated soil. *Géotechnique*, 40(4), 531–540.

BD. 2020. *Code of Practice for Structural Use of Concrete 2013 (2020 Edition).* Buildings Department, HKSAR Government, 194 p.

Casasso, A., & Sethi, R. 2014. Efficiency of closed loop geothermal heat pumps: A sensitivity analysis. *Renewable Energy*, 62, 737–746.

Chan, M. Y., Burnett, J., & Chow, W. K. 1998. Energy use for ventilation systems in underground car parks. *Building and Environment*, 33(5), 303–314

Chow, T. T., Long, H., Mok, H. Y., & Li, K. W. 2011. Estimation of soil temperature profile in Hong Kong from climatic variables. *Energy and Buildings*, *43*(12), 3568–3575.

CLP Holdings. 2022. CLP Holdings 2022 Sustainability Report.

Congedo, P. M., Baglivo, C., Bonuso, S., & D'Agostino, D. 2020. Numerical and experimental analysis of the energy performance of an air-source heat pump (ASHP) coupled with a horizontal earth-to-air heat exchanger (EAHX) in different climates. *Geothermics*, 87, 101845-.

Cui, P., Yang, H., Spitler, J. D., & Fang, Z. 2008. Simulation of hybrid ground-coupled heat pump with domestic hot water heating systems using HVACSIM+. *Energy and Buildings*, 40(9), 1731-1736.

Cui, S. Q., and Zhou, C. 2022. Coupled effects of stress state and void ratio on thermal conductivity of saturated soils. *Géotechnique Letters*, 12(2), 148–153.

Cui, S.-q., Zhou, C., Liu, J.-q., and Akinniyi, D. B. 2023. Stress effects on thermal soils and heat transfer efficiency of energy piles in the saturated and unsaturated soils. *Computers and Geotechnics*, 160, 105549.

Fong, S.-K. 1999. BLAST: *Building energy simulation in Hong Kon*g [PhD thesis, Hong Kong Polytechnic University].

Gawecka, K. A., Cui, W., Taborda, D. M. G., Potts, D. M., Zdravković, L., & Loukas, A. 2021. Predictive modelling of thermo-active tunnels in London Clay. *Géotechnique*, 71(8), 735–748.

GEO. 2020. *Guide to Retaining Wall Design (Geoguide 1)* (Continuously updated e-version released on 1 June 2020). Geotechnical Engineering Office, Civil Engineering and Development Department, HKSAR Government, 245 p.

GEO. 2023. *Deep Excavation Design and Construction (2023) (GEO Publication No. 1/2023)*. Geotechnical Engineering Office, Civil Engineering and Development Department, HKSAR Government, 144 p.

Electrical and Mechanical Services Department. 2022. Hong Kong Energy End-use Data 2022 [PDF].

Ground Source Heat Pump Association, 2012. *Thermal pile design, installation and materials standard*s. GSHP Association, UK.

Hsiung, B.-C., & Dao, S.-D. 2014. Evaluation of Constitutive Soil Models for Predicting Movements Caused by a Deep Excavation in Sands. *Electronic Journal of Geotechnical Engineering*, 19.

HyD. 2013. *Structures Design Manual for Highways and Railways (2013 Edition)*. Highways Department, HKSAR Government, 216 p.

Jayachandran, S., & Reddy, K. S. 2019. Estimation of effective thermal conductivity of packed beds incorporating effects of primary and secondary parameters. *Thermal Science and Engineering Progress*, 11, 392–408.

Jia, L., Lu, L., Cui, P., Chen, J., & Pan, A. 2024. A novel study on influence of ground surface boundary conditions on thermal performance of vertical U-shaped ground heat exchanger. *Sustainable Cities and Society*, 100, 105022.

Kahraman, A., & Çelebi, A. 2009. Investigation of the Performance of a Heat Pump Using Waste Water as a Heat Source. *Energies*, 2(3), 697-713.

Liu, J. and Zhou, C. 2022. Thermo-hydro-mechanical behaviour of geothermal energy tunnel in different ground conditions. *Computers and Geotechnics*, 151:104954.

Lui, J., & Yau, P. 1995. The Performance of The Deep Basement For Dragon Centre [PDF].

Ng, C. W. W., Leung, A. K., Kwok, S. S. K., & Yip, F. H. T. 2014. Effects of stiffness nonlinearity on E′ standard penetration test N correlations for analysing wall deflections in Hong Kong excavations. *HKIE Transactions*, 21(1), 35–49.

Santos, J. A., & Correia, A. G. 2001. Reference threshold shear strain of soil: its application to obtain a unique strain-dependent shear modulus curve for soil. *In Proceedings of the 15th International Conference on Soil Mechanics and Geotechnical Engineering (Vol. 1, pp. 267-270)*. Istanbul, Turkey.

Schanz, T., Vermeer, P. A., & Bonnier, P. G. 1999. The hardening soil-model: Formulation and verification. In R. B. J. Brinkgreve, *Beyond 2000 in Computational Geotechnics*, 281.

Shinoda, J., Kazanci, O. B., Tanabe, S.-i., and Olesen, B. W. 2019. A review of the surface heat transfer coefficients of radiant heating and cooling systems. *Building and Environment*, 159:106156.

Takashima, I., Yasukawa, K., Uchida, Y., Yoshioka, M., & Won-In, K. 2011. A geothermal heat pump system in Bangkok, Thailand. I*n Proceedings of the 9th Asian Geothermal Symposium. Ibusuki, Japan, 7–9 November 2011*.

Zhong, Y., Narsilio, G. A., Makasis, N., & Scott, C. 2022. Experimental and numerical studies on an energy piled wall: The effect of thermally activated pile spacing. *Geomechanics for Energy and the Environment*, 100726.

A Critical Review of Pile Acceptance Criteria

Victor Li
Victor Li & Associates Ltd., Hong Kong

ABSTRACT

1 Pile acceptance criteria previously or currently used in Hong Kong by the Buildings Department, Housing Department, Architectural Services Department and the Civil Engineering and Development Department are reviewed. It is observed that the pile acceptance criteria are mainly aimed at controlling the settlement of piles. Some of the acceptance criteria used for total settlement or residual settlement are not reasonable and excessively restrictive. A proposal involving simplification of the Davisson criterion and removal of the residual settlement criteria is presented for unifying the current pile acceptance criteria in Hong Kong.

INTRODUCTION

Pile loading tests are commonly used for obtaining or verifying the parameters of pile design or as a means of compliance testing for ascertaining whether a batch of completed piles will meet with the design standard or requirements. A set of pile acceptance criteria is often stipulated to decide whether a test pile will pass the loading test.

Pile acceptance criteria used for loading tests in Hong Kong evolve with time and vary between departments. A review of the past and current acceptance criteria for pile loading tests in Hong Kong is presented and a proposal for simplifying the pile acceptance criteria will also be discussed.

2 HISTORICAL DEVELOPMENT

Over the years, various government departments in Hong Kong, including Buildings Department (BD), Housing Department (HD), Architectural Services Department (ASD) and Civil Engineering and Development Department (CEDD), have developed their own acceptance criteria for assessing whether a test pile would be satisfactory based on the results of a static loading test. The pile acceptance criteria adopted by the BD, ASD and HD are becoming almost identical in recent years. Table 1 summarizes the pile acceptance criteria that have been used by the four departments.

In the following, the evolution of pile acceptance criteria implemented by the above government departments will be briefly reviewed. The review is by no means comprehensive due to difficulties in tracing all the changes that have been made as past information on old pile acceptance criteria is not readily available in the public domain.

Table 1: Summary of pile acceptance criteria adopted by various government departments

Department	Total settlement criterion, δ_{max}	Residual settlement criterion, δ_r	Time	Reference
BD	0.5 inches	-	Prior to 1976	Philcox (1962a, 1962b)
	15mm	-	1976 to late 1980s	HKG (1976), LHK (1985)
	$\delta_{max} = \frac{P \times L}{A \times E} + \frac{D}{120} + 4$	$\delta_r = \frac{D}{120} + 4$	Late 1980s to 2004	Fraser & Ng (1990)
	$\delta_{max} = \frac{P \times L}{A \times E} + \frac{D}{120} + 4$	$\delta_r = \frac{D}{120} + 4$ or $\frac{1}{4}\delta_{max_observed}$ whichever is larger	After 2004	BD (2004, 2017)
ASD	$\delta_{max} = 0.7\frac{P \times L}{A \times E} + \frac{D}{120} + 4$	$\delta_r = \frac{D}{120} + 4$	Between 1993 to 2003	ASD (1993)
	$\delta_{max} = \frac{P \times L}{A \times E} + \frac{D}{120} + 4$	$\delta_r = \frac{D}{120} + 4$	After 2003	ASD (2003)
	$\delta_{max} = \frac{P \times L}{A \times E} + \frac{D}{120} + 4$	$\delta_r = \frac{D}{120} + 4$ or $\frac{1}{4}\delta_{max_observed}$ whichever is larger		ASD (2007)
HD	$\delta_{max} = \frac{P \times L}{A \times E} + \frac{D}{30}$	$\delta_r = \frac{D}{50}$ or 10mm, whichever is less for floating pile $\delta_r = \frac{D}{100}$ or 5mm, whichever is less for end-bearing pile		HKHA (1989), Yiu & Lam (1990)
	$\delta_{max} = \frac{P \times L}{A \times E} + \frac{D}{120} + 4$	$\delta_r = \frac{D}{120} + 4$	Since formation of ICU in 2002 to 2004	
	$\delta_{max} = \frac{P \times L}{A \times E} + \frac{D}{120} + 4$	$\delta_r = \frac{D}{120} + 4$ or $\frac{1}{4}\delta_{max_observed}$ whichever is larger	After release of CoPF in 2004	
CEDD	(a) Brinch Hansen criterion (b) $\delta_{max} \leq$ 20mm for buildings and 15mm for other structures	-	Since 1992	CEDD (1992)

2.1 Buildings Department

The BD originated from the Buildings Ordinance Office (BOO) of the former Public Works Department (PWD). The BOO became the Building Development Department (BDD) from 1982 to 1986, the Buildings and Lands Department (BLD) from 1986 to 1993 before becoming the BD after 1993. In this paper, the BD will also collectively mean the BOO, BDD and BLD.

Up to the late 1970s, the pile acceptance criterion adopted by the BD was simple and based entirely on a total settlement limit of ½ inches when tested under twice the design working load as discussed by Philcox (1962a, 1962b). The total settlement limit was later revised to 15mm and formally incorporated as a legal requirement in the Building (Construction) Regulations (B(C)R) (HKG 1976) and this criterion was still present in the 1985 edition of B(C)R (LHK 1985). There was no residual settlement criterion at the time.

As remarked by Philcox (1962a), if the settlement for a single pile is limited to ½ inches (or about 15mm), the total settlement of a tall building was expected to be within 2 inches (or 50.8mm) and considered to be acceptable. The pile acceptance criterion of a constant settlement limit adopted by the BD up to the late 1980s was simply an indirect tool for ensuring that the building settlement is acceptably smaller, and not a guideline for assessing of the ultimate capacity of the test pile.

In the late 1980s, the simple pile acceptance criterion of a constant total settlement limit was removed from the B(C)R and revised pile acceptance criteria were specified in Practice Note No.66 issued by the BD to building professionals as follows (Fraser & Ng 1990).

$$\delta_{max} = \delta_e + \delta_{tip} = \frac{P \times L}{A \times E} + \frac{D}{120} + 4 \quad (1)$$

$$\delta_r = \delta_{tip} = \frac{D}{120} + 4 \quad (2)$$

where P = maximum test load at design failure load equal to twice the design working capacity in kN; δ_{max} = settlement in mm at maximum test load P; δ_r = residual settlement in mm upon complete release of test load; L, A, E and D are the length in mm, cross-sectional area in mm^2, Young's modulus in kN/mm^2 and D the lateral dimension in mm of the pile respectively. Eq.1 and 2 will hereafter be called the total and residual settlement criterion respectively.

The total settlement criterion of Eq.1 is commonly referred to as the Davisson criterion because it is adapted from the proposal by Davisson (1972). It consists of a component δ_e representing the pile shortening and another term δ_{tip} related to the pile tip movement that will cause yielding of soils at the base. Theoretically, the pile shortening δ_e can be characterized by a coefficient α as follows.

$$\delta_e = \int_0^L \frac{P_A(z)}{A \times E} \, dz = \alpha \frac{P \times L}{A \times E} \quad (3)$$

where $P_A(z)$ is the variation of axial load of pile with depth z. According to Davisson (1972), the component δ_e in the total settlement criterion can be obtained by treating the pile as a free column without shaft resistance. This corresponds to $P_A(z) = P$ and $\alpha = 1$. The expression for δ_{tip} in Eq.1 is suggested by Davisson based on his own experience. There is no data presented by Davisson (1972) or others for confirming the appropriateness of this expression. There was no residual settlement criterion proposed by Davisson (1972).

The residual settlement criterion of Eq.2 was introduced only by the BD and the settlement limit used in equation is the same as the pile tip settlement δ_{tip} in the Davisson criterion. This seems to suggest that the BD would regard the pile shortening to be fully elastic and recoverable and not for the pile tip movement. As it turns out, the residual settlement criterion introduced by the BD is extremely stringent. Test piles would often fail due to inability to satisfy the residual settlement criterion.

In 2004, the BD published the Code of Practice for Foundations (CoPF) (BD 2004) in which the residual settlement criterion was revised as follows, keeping the total settlement criterion unchanged.

$$\delta_r = \frac{D}{120} + 4 \quad \text{or} \quad \frac{1}{4}\delta_{max_observed}\text{, whichever is larger} \quad (4)$$

where $\delta_{max_observed}$ is the observed total settlement at maximum test load. Since then, the BD pile acceptance criteria has remained unchanged in the later edition of CoPF released in 2017 (BD 2017) and subsequent amendments of the code promulgated released between 2021 and 2023.

2.2 Architectural Services Department

The ASD originated from the Architectural Office of the PWD and was formally established as a department in 1986. The pile acceptance criteria adopted by the ASD are promulgated in the General Specification for Building (GSB) published by the Department. Over the years, the acceptance criteria for total and residual settlement adopted by the ASD have the same format as those of the BD as summarized in Table 1, except for the differences mentioned below.

a. In the 1993 edition of GSB (ASD 1993), the total settlement criterion is based on a value of α equal to 0.7, resulting in a significantly more stringent criterion than that of the BD at the time.
b. In the 2003 edition of the GSB (ASD 2003), the coefficient α is revised to 1.0 and the total settlement criterion then became the same as that of the BD at the time.

c. In 2007, the ASD further revised the residual settlement criterion to match with that of the CoPF 2004 Edition (ASD 2007).
d. Over the years, the definitions of the pile dimension *D* used by the ASD are slightly different from those of the BD for certain pile types, although the differences have become smaller with time.

With the above evolution, the pile acceptance criteria currently adopted by the ASD are now identical to those of the BD, except for the definition of *D* for a certain pile type.

2.3 Housing Department

The formats of the pile acceptance criteria adopted by the HD are also similar to those of the BD. In an early version of the HD pile acceptance criteria used in the late 1980s (see Table 1), the pile shortening δ_e in the total settlement criterion was based on $\alpha = 1$ and the pile tip movement δ_{tip} was defined somewhat differently as $D/30$. The residual settlement criterion used by the HD at the time was specified as $\delta_r = D/50$ or 10mm, whichever is less, for normal designs and reduced to $\delta_r = D/100$ or 5mm for piles founding on rock if the group reduction factor is not used for foundation design. The definition of *D* used by the HD at that time also differed from that of the BD for some pile types.

In 2002, the Independent Checking Unit (ICU) was established within the HD to perform independent administrative building control over housing development projects of the Department according to the requirements implemented by the BD (HKHA 2020). Since then, the pile acceptance criteria used by the HD are identical to those of the BD.

2.4 Civil Engineering and Development Department

The pile acceptance criteria adopted by CEDD are described in the General Specification for Civil Engineering Works published by the Department. The Specification was first published in 1992 (CEDD, 1992). The pile acceptance criteria in it have since remained unchanged in subsequent amendments and new editions of the Specification. The pile acceptance criteria are based on the Brinch Hansen criterion, with the pile settlement at working load restricted to no more than 20mm for buildings and 10mm for other structures.

The Brinch Hansen criterion was originally a method developed by Brinch Hansen (1963, 1965) for assessing the failure stress of a soil from its stress-strain curve, not for establishing the failure loads of piles. There are actually two methods proposed by Brinch Hansen, commonly known in the literature as the 90% criterion and the 80% criterion. The former is defined as the stress for which the strain is 2 times the strain at a 10% smaller stress. Brinch Hansen (1965) considers that his two proposed methods should also be applicable to almost any test, including pile loading tests, although there is no data presented in his paper for justifying this assertion. It is perhaps for this remark by Brinch Hansen that the 90% or 80% criterion has now been borrowed by others, including Fellenius (1989), Dotson (2013) and also the CEDD, for estimating the ultimate failure load of a test pile. The Brinch Hansen criterion used by CEDD is actually the 90% criterion.

The pile acceptance criteria adopted by the CEDD are more stringent than just the checking of the ultimate capacity of pile using the Brinch Hansen criterion. For the test pile to pass the acceptance criteria, the pile settlement at working load must also fulfill the additional requirement of a small settlement mentioned above.

3 REVIEW ON PAST AND CURRENT PILE ACCEPTANCE CRITERIA

The acceptance criteria implemented by various government departments in Hong Kong aim at controlling the performance of piles through imposing acceptance criteria for total settlement at maximum test load, residual settlement after full release of test load and/or limiting the settlement at working load. Before discussing possible simplifications to current procedures, it is useful to review the above strategies that have been adopted in formulation of past and current pile acceptance criteria.

3.1 Total settlement criterion based on constant settlement limit

The use of a constant limit for pile settlement under working load or at maximum test load is a very simple strategy for controlling the performance of piles. The use of a constant settlement limit of ½ inches or 15mm by the BD in the past for the total settlement at maximum test load and the limitation of pile settlement by the

CEDD to within 20mm or 10mm at working load are good examples of such a simple approach. Unfortunately, these settlement limits are small and even more stringent than the value of 30mm recommended by the BD in the CoPF (BD 2017) for footings on soils. As remarked very early by Lumb (1962), "most tall buildings in Hong Kong have settled a few inches, unless founded on rock, although such settlements are not very noticeable". Lumb further commented that "probably for tall stiff buildings a total settlement of 2 inches would not be any cause for alarm".

From a technical point of view, it is not rational to adopt a pile acceptance criterion based on a constant settlement limit because pile settlement is larger for piles with a higher strength capable of resisting a higher foundation load and also increases with the pile length due to shortening under loading. For long piles with length exceeding 50m, which are not uncommon in Hong Kong, the pile settlement under working load can easily exceed 20mm according to loading test data presented by Zhang & Yu (2005). Capping the maximum pile settlement at 20mm or less is unreasonably conservative.

A total settlement criterion based on a constant settlement limit may be made more sensible by specifying multiple settlement limits for different ranges of pile lengths or applied load, but this will defeat the very purpose of keeping the approach simple.

3.2 Total settlement criterion based on load-settlement curve

The total settlement criteria currently adopted by the BD, HD, ASD and CEDD all involve assessment of the failure load from the load-settlement curve.

The Brinch Hansen criterion, being originally developed for estimating the failure stress of soils at high strain level, will tend to predict the failure pile load at a point on the load-settlement curve where the settlement starts to plunge. The corresponding settlement at the predicted failure load may be too high to be used as a suitable total settlement criterion. One will have to resort to another means for setting a suitable settlement limit to control pile movement, such as limiting the settlement at the working load as has been adopted by CEDD.

From experience, the Davisson criterion for total settlement is relatively conservative and the failure load of the pile so determined will be not be close to reaching ultimate failure. A similar observation is also made by Fraser & Ng (1990). In a case study reported by Fellenius (1980), the failure load inferred from the Brinch Hansion 90% criterion is found to be 13% higher than that obtained by the Davisson criterion.

When formulating a suitable total settlement criterion, pile shortening should be duly considered. The magnitude of α depends on shaft resistance which is affected by many factors including pile type, details and method of installation, soil profile and others.

For driven and jacked H-piles, voids will be formed on both sides of the web of the H-pile when installed by driving or jacking (Li et al 2003a, 2003b, Tomlinson 1977). Such voids may be as deep as 10m (Li et al 2003b). Even if these voids are backfilled with soils after pile installation, the backfilled materials are likely to be loose resulting in low shaft resistance below the pile head. Friction fatigue of soils can also occur due to repeated cyclic shearing of soils during pile installation (White & Lehane 2004). This will result in higher reduction in shaft resistance at depths nearer to the pile top where the soils will be subjected to more cycles of shearing.

When piles are installed through soft soils, such as marine deposit commonly present in reclamation sites in Hong Kong, the shaft resistance in the soft soil layers will be low. There are also some mind-boggling foundation practices in Hong Kong that can contribute to low shaft resistance. Sleeving of piles is common in Hong Kong to avoid transfer of lateral loads onto adjacent slopes by eliminating shaft resistance in the sleeved zone. Debonding of piles is also common to avoid transfer of vertical loads from spreading onto adjacent sensitive structure, such as Mass Transit Railway structures or tunnels. Debonding is usually by means of sleeving or coating the pile with a bituminous material. The shaft friction in the debonding zone will then be removed.

If the variation of axial load with depth is known, the coefficient α can be computed using Eq.3. For driven piles, such information can be obtained from CAPWAP analysis of the data obtained from a PDA test. Figure 1 shows the variation of axial load obtained by CAPWAP analysis for six driven H-piles installed at a reclamation site in Kowloon. The axial load presented in the figure is normalized by the maximum test load. The soil profile of the site comprises a stratigraphic sequence of fill, a thin layer of marine deposit, alluvial deposit and finally the founding stratum of completely decomposed granite.

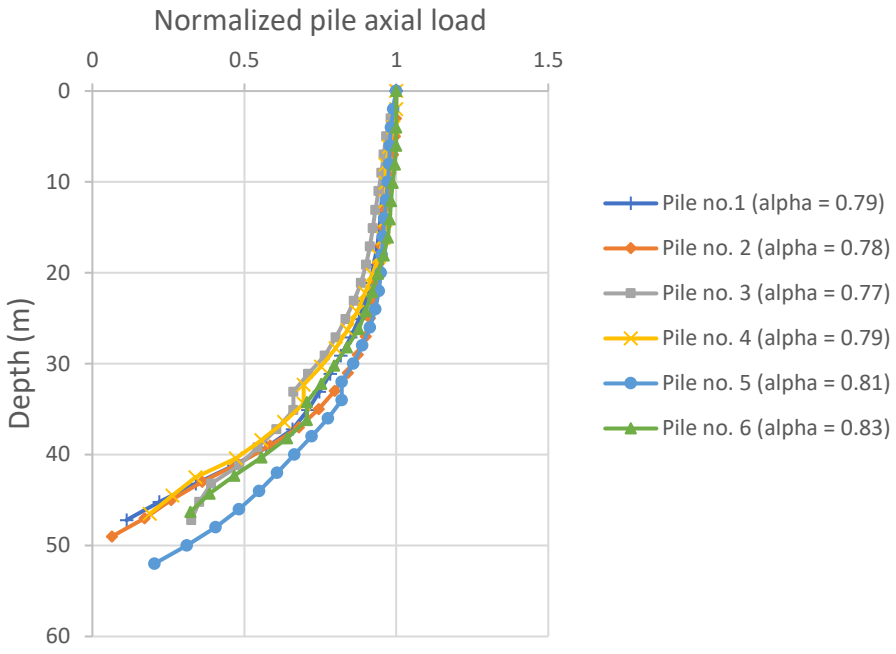


Figure 1: Variation of axial loads of driven piles estimated by CAPWAP analysis

The decrease in axial pile load is slow in the upper portion of the pile, indicating that the shaft resistance is more significant only at the lower part of the pile. The values of α for these 6 piles calculated using Eq.3 range from 0.77 to 0.83. For driven piles installed in a reclamation site with a thick marine deposit, the value of α is expected to be even closer than 1.0. If the 1993 version of the ASD total settlement criterion based on $\alpha = 0.7$ were to be adopted as the acceptance criterion, it will be difficult even for well performing driven piles to pass the loading test.

The total settlement criterion adopted currently by the BD, ASD and HD all contain a component related to the pile tip movement equal to $\delta_{tip} = D/120 + 4$. For the common pile types in Hong Kong, the magnitude of this term is small and generally in the range of about 6.7 to 8mm. According to the CoPF, loading tests are used for proof testing of piles only for piles with lateral dimension not exceeding 750mm. Even for this pile size, the magnitude of δ_{tip} is 10.25mm which is still considered to be small and unlikely to cause plastic failure of soils at the pile tip.

The Davisson criterion currently adopted by BD, HD and ASD is usually dominated by the term δ_e for pile shortening as the magnitude of δ_{tip} is usually small in comparison. As the observed value of α can be close to 1.0 for driven piles, piles installed in profiles with soft soils, and piles with sleeving or debonding provided, the use of $\alpha = 1$ by Davisson in evaluating the pile shortening is regarded to be a very reasonable and practical recommendation.

3.3 Residual settlement criterion

There was no residual settlement criterion used by the BD prior to the late 1980s and by the CEDD throughout. This residual settlement criterion was only introduced by the BD in the late 1980s in the form of Eq.2 and later modified to Eq.4. The residual settlement criterion introduced by the BD has been followed closely by the HD and ASD. The fundamental question to be asked is whether this additional criterion is sensible or necessary. To answer this question, the author will refer to his viewpoints discussed over 20 years ago in Li et al (2003a).

Figure 2 shows schematically the load-settlement response of a pile supporting a structure. The design capacity of the pile under working load is denoted by WL and the design failure load is 2WL based on a factor of safety of 2.0. Loading on the pile will increase from Point O to Point A due to gradual increase in dead loads and superimposed dead loads during construction. When the structure is finished, there will be further variable live loads and transient wind loads acting on the pile with loads varying between the limits between Point A and B. The loads experienced by the pile will fluctuate along the virgin loading curve defined by Point A and

B or the unloading and reloading along the loading curve between A′ and B during the service life of the structure. Full unloading of the pile will not occur like a test pile unless the structure is demolished. It is therefore not meaningful to impose a residual settlement criterion to control the residual movement of an unloaded pile as it has no direct relation to the actual performance of the pile under working condition.

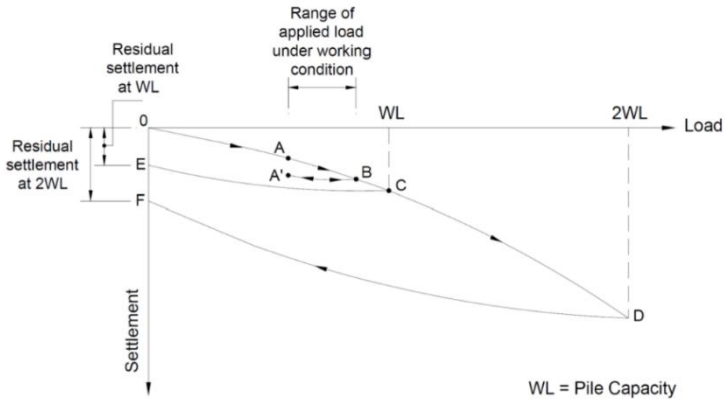


Figure 2 Load-settlement response of a pile foundation supporting a structure (Li et al 2003a)

It may be argued that a small residual settlement criterion is to ensure that the pile will behave elastically for the full range of loading up to 2WL and will therefore serve as an indirect means for ensuring a small pile settlement at working load. If this were indeed the intention of introducing the additional residual settlement criterion, it would be much more meaningful and direct to apply a limit on the settlement of the test pile at working load WL (i.e settlement at Point C) or the residual settlement upon release of test load at WL instead of controlling the residual settlement upon release of maximum test load at the design failure load 2WL.

The BD, HD and ASD had for many years adopted the format of using only the term for the pile tip movement in Eq.2 as the residual settlement criterion, believing that pile shortening should be fully recoverable. This will be demonstrated to be untrue later in the paper.

As the magnitude of δ_{tip} is small and less than 8mm for the common pile types in Hong Kong, the residual settlement criterion is an extremely arduous condition to meet. This is particularly so when the non-recoverable creep settlement which will occur during the 72 hours of maintained loading at maximum test load may itself contribute to a significant percentage of the small residual settlement limit (Lam et al 2021).

The residual settlement criterion has for a long time been the over-riding criterion for pile acceptance, not the total settlement criterion. This has significantly affected the practice of foundation construction in Hong Kong. Driven piles are always driven to a small final set to hopefully produce in a more elastic response of the pile to yield a smaller residual settlement, but this is at the risk of damaging the pile. Jacked piles are preloaded to a load level higher than the design failure load during installation for every pile to ensure that the pile will settle along a loading-reloading path with smaller immediate and creep settlement when load tested (Li 2003b). But preloading of piles will make the foundation design less efficient as the normal full capacity of the pile cannot be used as the design failure load.

Although the residual settlement criterion has been revised to Eq.4 after publication of the CoPF (BD 2004). The revised criterion is only a relaxation compared with Eq.2 for piles with observed total settlement larger than 4 times the magnitude of δ_{tip}. Well performing piles with a smaller total settlement might not be able to benefit from the relaxation and still be unjustifiably rejected. This can be illustrated using a case study in which rock socketed H-piles are used for the foundations. Table 2 summarizes results of loading tests conducted on two piles for the project.

Table 2: Summary of loading test results for two rock socketed H-piles

Pile mark	Pile length (m)	Observed total settlement $\delta_{max\text{-}observed}$ (mm)	Observed residual settlement $\delta_{r\text{-}observed}$ (mm)
Pile A	30.2	40.6	6.3
Pile B	49.4	35.2	10.3

Pile A is shorter but has a larger total settlement at the maximum test load of about 12200 kN. Pile B is significantly longer but exhibits a smaller total settlement at the same maximum test load. From a technical point of view, Pile B has a better performance than Pile A because it has a smaller total settlement despite its longer length. This is a direct indication that there is significant shaft resistance along Pile B to result in a smaller pile shortening (i.e. a smaller α) and total settlement than Pile A. Unfortunately, the total settlement of Pile B is too small to enable the residual settlement limit to be increased. In the end, the pile cannot pass the BD residual settlement criterion.

It has long been recognized that the residual settlement of a test pile is influenced by the residual load in the pile after loading test or pile installation (e.g. Fellenius 2015; Zhang & Wang 2007). Positive shaft resistance (PSF) will be mobilized along the pile when it is loaded during the loading test. When the test load is released, the pile head will rebound and shaft resistance at the top portion of the pile will reverse in direction causing negative shaft friction (NSF) to develop. PSF and NSF will both lead to the development of residual loads along the pile upon full release of test load, resulting in associated residual settlement after the loading test. If shaft resistance along the pile is significant, the residual settlement may be too large to satisfy the residual settlement criterion.

An approach based on simplifying assumptions has been developed in the Appendix for estimating the residual settlement of Pile B due to residual load. The residual settlement is predicted to be 10.3mm which happens to be the same as the observed value. While the analysis presented in the Appendix may be regarded as oversimplified and the good prediction is perhaps a coincidence, it serves to demonstrate that the residual settlement criterion currently used by BD, HD and ASD can cause a well performing pile to be unreasonably rejected.

For rock-socketed H-piles, there is another cause of residual load that is not normally recognized by foundation engineers. The bond resistance between the plain surface of H-pile and cement grout may not be sufficient to prevent bond slip at the steel-cement grout interface during a loading test (Li 2007). If bond slip does occur during loading, a gap may be formed between the cement gap and the H-pile for some distance below the pile head. When the applied load is released, the gap may close up and the cement grout will inhibit rebound of the H-pile. This will also contribute to development of residual load in the pile and therefore residual settlement.

4 DISCUSIONS AND CONCLUSION

The pile acceptance criteria adopted previously or currently by various government departments are largely aimed at controlling the settlement of piles and not so much at obtaining a reliable estimate of the ultimate capacity of piles. From experience, the ultimate capacity of piles is usually far from being reached if they can comply fully all the pile acceptance criteria. When considering the objectives to be fulfilled when setting the pile acceptance criteria, the following factors should be considered.

a. The criteria should be technically sound or reasonable.
b. The criteria are applicable to a wide range of pile types.
c. The criteria are suitably conservative.

To some extent, the three objectives are in conflict with each other. Objective (b) and (c) are always preferable because they can make regulatory control easier, but one must balance the benefit of having a universal set of criteria that are applicable to most pile types with the risk that the same criteria may be inadequate for some particular pile types. Also, it may be difficult to meet objective (a) and (b) concurrently. A set of criteria that are technically sound for one pile type may not be so for another. For driven piles founding in soils, it will be reasonable to include the pile tip movement δ_{tip} as a component of the total settlement criterion. For rock socketed H-piles, the pile load is expected to be resisted predominantly by the shaft friction in soils and the rock socket. There will be hardly any load transferred to the pile tip and it will therefore be unreasonable to include δ_{tip} as a component of the total settlement criterion. If it is intended to adopt a single set of pile acceptance criteria applicable to a wide range of piles, one must lower his expectation in meeting objective (a).

Before exploring suitable simplifications for the current pile acceptance criteria, it is useful to summarize some of the viewpoints already discussed earlier.

a. It is not satisfactory nor technically sound to adopt a constant settlement limit for the total settlement criterion. As the total settlement tends to increase with pile length, a constant settlement limit will not be effective in controlling the performance of piles for different lengths.
b. The total acceptance criterion should take account of settlement due to pile shortening. It is sensible to incorporate the pile shortening δ_e as a component of the total settlement criteria. The calculation of δ_e based on $\alpha = 1$ as suggested by Davisson (1972) is considered to be a reasonable and practical recommendation as the observed value of α is often close to unity.
e. The expression of δ_{tip} in Davisson criterion is small and generally not sufficient to mobilize failure of soils at the pile tip. The end result is that the Davisson criterion is conservative and failure load determined by the criterion is usually not close to reaching the ultimate capacity of the pile.
c. The Brinch Hansen criterion is only a tool for predicting the ultimate capacity of piles. It is less conservative than the Davisson criterion in controlling the design failure load and pile performance in terms of settlement.
d. The residual settlement criterion of Eq.2 or Eq.4 previously or currently used by the BD, HD and ASD is not rational. Eq.4 is a relaxation only for piles with a poorer performance that exhibit a higher total settlement. Such a benefit cannot be enjoyed by well performing piles with a smaller total settlement because they often have a higher observed residual settlement caused by residual loads.
e. The residual settlement bears little direct relation to the settlement of pile under working condition which is more relevant in controlling building settlement.

There are already numerous total settlement criteria available in the literature as described by Fellenius (1980), Fraser & Ng (1990) and many others. The different pile acceptance criteria are developed based on experiences or techniques of curve fitting without a strong theoretical justification. One will doubt whether a technically sound criterion can actually be developed as pile behaviour is too complex to predict and affected by too many factors. There is no point to suggest yet another a set of entirely new pile acceptance criteria. At present, the total settlement criterion used in Hong Kong is either the Davisson criterion or the Brinch Hansen criterion. Foundation engineers in Hong Kong are familiar with both sets of criteria. One can further review the two sets of criteria to examine if possible simplification can be made.

The author is of the view that the Brinch Hansen criterion is a less preferable total settlement criterion from a practical point of view. The Brinch Hansen criterion demands the load-settlement curve to be well defined, including the curve beyond the design failure load often required for interpreting the actual failure load. In the current practice, the test pile will be loaded to the maximum test load in 4 stages according the loading test procedures specified by the BD, HD and ASD and in three stages according to CEDD. There will only be limited data points for defining the full range of load-settlement curve and this will not be sufficiently refined to allow a reliable determination of the ultimate pile capacity using the Brinch Hansen criterion.

In the CEDD pile acceptance criteria, the Brinch Hansen criterion is for assessing the failure load. A stringent limit on the settlement at working load has been specified as an additional criterion by the CEDD for controlling the pile performance. As a result, the determination of failure load using the Brinch Hansen criterion will become a somewhat redundant exercise as it is not the critical condition.

In comparison, the Davisson failure criterion is a considered to be more practical format for formulating the total settlement criterion because:

a. It is now widely accepted by BD, HD and ASD.
b. It is acceptable to a wide range of piles as $\alpha = 1$ is adopted for evaluating the pile shortening δ_e in the criterion.
c. It is relatively conservative mainly because the magnitude of δ_{tip} in the criterion is too small to cause ultimate failure of the pile. Because of this inherent conservatism, the settlement of a pile which passes the Davisson criterion is generally small. If this is the case, the Davisson criterion alone will be sufficient to be used as the single criterion for preventing failure of the pile and controlling its settlement.

As discussed earlier, the magnitude of δ_{tip} is still small, being 10.25mm, even for piles with lateral dimension up to 750mm for which a loading test will be required for proof-testing. Without compromising the conservatism

of the Davisson criterion to any significant degree, it is proposed to simplify the Davisson criterion as follows for all piles no exceeding a dimension of 750mm.

$$\delta_{max} = \frac{P \times L}{A \times E} + 10 \qquad \text{(in mm)} \qquad (5)$$

With this simplification, it is no longer necessary to define the pile dimension *D* and one can avoid the confusion of different definitions of *D* used by different government departments.

Another proposal is to delete the residual settlement criterion for reasons already explained earlier and in line with the suggestions made over 30 years ago by Fraser & Ng (1990). With this, Eq.5 will become the whole and the only criterion for pile acceptance based on the author's proposal.

REFERENCES

ASD 1993. *General Specification for Buildings – 1993 Edition*.

ASD 2003. *General Specification for Buildings – 2003 Edition*.

ASD 2007. *General Specification for Buildings – 2007 Edition*.

BD 2000. *Practice Notes for AP & RSE No. 66 – Pile Foundations*.

BD 2004. *Code of Practice for Foundations – 2004 Edition.*

BD 2017. *Code of Practice for Foundations – 2017 Edition.*

Brinch Hansen, J. 1963. Discussion on "Hyperbolic stress-strain response: cohesive soils". *Journal of Soil Mechanics and Foundation Engineering*, ASCE, 89(4): 241-242.

Brinch Hansen, J. 1965. Some stress-strain relationship for soils. *Proc. 6th ICSMFE,* 231-234.

CEDD 1992. *General Specification for Civil Engineering Works* – 1992 Edition.

Davisson, M.T. 1972. High capacity piles. *Proceedings, Lecture Series, Innovations in Foundation Construction*, ASCE, Illinois Section, Chicago, 81-112.

Dotson, D.W. 2013. Direct solution of the Brinch-Hansen 90% pile ultimate failure load. DFI Journal, 7(1): 18-21.

Fellenius, B.H. 1980. The analysis of results from routine pile load tests. *Ground Engineering*, Sept., 19-31.

Fellenius, B.H. 2015. Static tests on instrumented piles affected by residual force. *Journal of Deep Foundation Institute*, 9(1): 11-20.

Fraser, R.A. & Ng, H.Y. 1990. Pile failure. *Proc. HKIE Geo. Division Annual Seminar*, 75-93.

Hong Kong Government (HKG) 1976. Legal Notice 295/76, Hong Kong Gazette.

Hong Kong Housing Authority (HKHA) 1989. *Specification Library for Building Works*, 1989 Edition.

Hong Kong Housing Authority (HKHA) 2020. *Building Committee Paper No. BC 10/2020 – Quality Control of New Buildings Works for Public Housing Development*.

Lam, J. Pak, K. & Li, V. 2021. Study of creep settlement of driven H-piles in loading test. *Proc. HKIE Geotechnical Division Annual Seminar*, 113-122.

Laws of Hong Kong (LHK) (1985). Building (Construction) Regulation, 1985 version.

Li, K.S., Lee, P.K.K. & Lam, J. 2003a. *Chapter 1 - General principles*, In K.S. Li (ed.), *Design and Construction of Driven and Jacked Piles*, Centre for Research & Professional Development, 1-22.

Li, K.S., Ho, N.C.L, Lee, P.K.K, Tham, L.G. & Lam, J. 2003b. *Chapter 2 – Jacked piles*, In K.S. Li (ed.), *Design and Construction of Driven and Jacked Piles*, Centre for Research & Professional Development, 23-33.

Li, V. 2007. A critical review of the current practice for design of rock socketed H-piles in Hong Kong. In V. Li (ed.), *Bridging Research and Practice – the VLA experience*, 157-177.

Lumb, P. 1962. Discussion. In P. Lumb (ed.), *Proc. Symposium on Hong Kong Soils*, 125-126.

Philcox, K.T. 1962a. Some recent developments in the design of high buildings in Hong Kong. *The Structural Engineer*, 303-323.

Philcox, K.T. 1962b. Foundation problems in Hong Kong. In P. Lumb (ed.), *Proc. Symposium on Hong Kong Soils*, 109-123.

Tomlinson, M.J. 1977. *Pile Design and Construction Practice*.

White, D.J. & Lehane, B.M. 2004. Friction fatigue on displacement piles in sand. *Geotechnique*, 54(10): 645-658.

Yiu, T.M. & Lam. S.C. 1990. Ultimate load testing of driven piles in meta-sedimentary decomposed rocks. *Proc. Conference on Deep Foundation Practice*, 293-300.

Zhang, L. & Xu, Y. 2005. Settlement of building foundations based on field pile load tests, *Proc. 16th ICSMGE*, 2871-2874.

Zhang, L.M. & Wang, H. 2007. Development of residual loads in long driven piles in weathered soils. *J. of Geotechnical and Geoenvironmental Engrg*, ASCE, 113(10): 1216-1228.

APPENDIX

In this Appendix, a simplified approach is used to illustrate how residual settlement can occur after release of loading after a loading test based on the following simplifying assumptions (see Figure 3).

a. The pile head is at the ground surface.
b. The shaft resistance $\tau(z)$ varies linearly with depth z
c. The pile is sufficient long such that total shaft resistance itself is sufficient to resist the maximum test pile before reaching the pile toe.

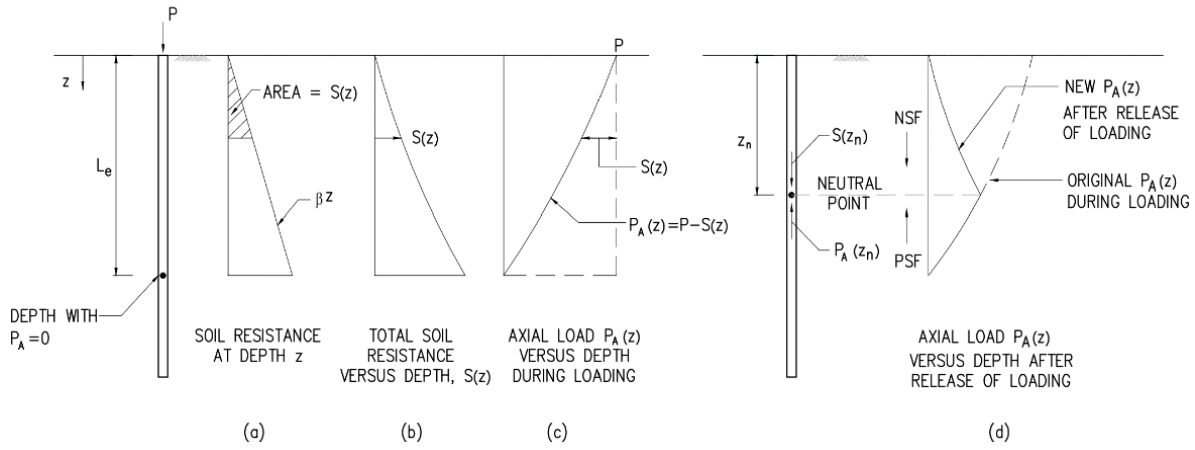


Figure 3: Force distribution along a pile during a loading test

Assumption (b) may be reasonable for a replacement pile installed in a uniform soil profile with the groundwater near the ground surface. Figure 3(a) to (c) show the distributions of shaft friction $\tau(z)$, total shaft resistance $S(z)$ and the axial load $P_A(z)$ at depth z below the pile head respectively according to the above assumptions. L_e is the pile length at which the total shaft resistance is sufficient to balance the applied load test P. The relationships between these quantities can be expressed as:

$$\tau(z) = \beta \times z \tag{6}$$

$$S(z) = \beta \times \frac{z^2}{2} \tag{7}$$

$$P_A(z) = P - S(z) \tag{8}$$

When $z = L_e$, $P_A = 0$ and this gives:

$$P = S(L_e) = \beta \times \frac{{L_e}^2}{2} \tag{9}$$

The total settlement due to pile shortening is given by:

$$\delta_{max-observed} = \int_0^{L_e} \frac{P_A(z)}{A \times E} \, dz = \frac{1}{3} \times \beta \times \frac{{L_e}^3}{A \times E} \tag{10}$$

By solving Eq.9 and 10, we can obtain closed form solutions for β and L_e. When the test load is fully released, the upper portion of the pile will rebound causing reversal of shaft friction (i.e. NSF) to develop. The shaft resistance at the lower portion of pile remains unchanged because the rebound movement cannot reach such depths. There will be a neutral point at which the downdrag caused by the NSF above the neutral point will be equal to the total PSF which has originally developed below the neutral point at full test load, leading to new equilibrium of the pile after full release of test load. By assuming that the magnitude of shaft resistance will remain unchanged after stress reversal, the neutral point can be obtained by solving the following equation.

$$S(z_n) = P_A(z_n) \tag{11}$$

By substituting Eq.7 and 8 into Eq.11, one can obtain the solution for the depth of the neutral point z_n. Based on the solutions for β, L_e and z_n, the following closed-form solution can be obtained for predicting residual settlement $\delta_{r\text{-}predicted}$.

$$\delta_{r-predicted} = \int_0^{z_n} \frac{P_A(z)}{A \times E}\,\mathrm{d}z + \int_{z_n}^{L_e} \frac{P_A(z)}{A \times E}\,\mathrm{d}z = \delta_{max-observed} \times \left(1 - \frac{1}{\sqrt{2}}\right) \tag{12}$$

Using the relevant input parameters for Pile B, the effective length L_e is estimated to be above the rockhead level of pile, thus justifying the above assumption (c) in the analysis. The predicted residual settlement given by Eq.12 is 10.3mm for Pile B, which is close to the observed residual settlement.

Digital Integration for Condition Assessment for Water Tunnels in Hong Kong

S.W. Millis & J.R. Connell
Ove Arup & Partners Hong Kong Limited, Hong Kong
W.F Liu & C.W. Poon
Water Supplies Department of the HKSAR Government, Hong Kong

ABSTRACT

Unbeknown to many, the supply of fresh water in Hong Kong is dependent on water conveyance through almost 200 km of water tunnels in conjunction with other waterworks installations managed and maintained by the Water Supplies Department (WSD). A significant number of these tunnels were constructed during the 1960's and 1980's, with over 50% now being more than 50 years in age and some even dating back to the late-1800's. Given the age and strategic importance of the tunnels, periodic condition and maintenance assessment works are required to enhance the asset management performance continuously so that water supply service of the highest quality is provided to the public. In the last complete round of asset-wide condition assessment for the tunnels, the development and use of digital inspection and data management tools were in the early stages and not ready for digital asset management. To address this and provide an integrated, structured and more usable dataset for asset management and future assessment works, a variety of digital approaches and tools have been explored, developed and implemented during the on-going round of condition assessment works. These have included the use of a central dashboard-based system for data management and access, together with trials of tools such as mobile apps, 360 imagery, laser scanning and UAV photogrammetry to aid with data collection, management and reporting for the tunnel inspection works. An outline of the findings from the trial of these approaches is provided herein, together with recommendations on the preferred solution for digital asset inspection and management as well as possible future developments that could be integrated to these.

1 INTRODUCTION

1.1 WSD Water Supply Network

To ensure the provision of high quality water in meeting the need of the public and economic activities in Hong Kong, the Water Supplies Department (WSD) operates and maintains a total of 17 impounding reservoirs, 20 water treatment works, over 190 pumping stations/houses, over 230 service reservoirs, about 120 km of catchwaters, about 200 km of water tunnels (including associated portals, shafts and shaft towers), and other miscellaneous installations, in addition to over 8,400 km of water mains and various associated valves and civil, mechanical & electrical installations.

1.2 WSD Water Tunnel Network

Integral to the distribution of water amongst WSD's various waterworks facilities is the functionality of their water tunnel network. This includes 168 water tunnels with a combined length of about 200 km, as well as various associated assets including 148 access portals, 44 access shafts and 8 shaft tower structures (Figure 1). The lengths of the individual tunnels vary from 35 m in the case of small connecting tunnels along catchwaters, to over 7,200 m for major fresh water supply tunnels. The average tunnel length is about 1,200 m. Similar variance exists for tunnel diameter, which ranges between 0.9 m and 10.2 m and averages 4.2 m. Most of the tunnels (>70%) were constructed between the 1960s and 1980s, when significant development and enhancement to Hong Kong's water supply system was undertaken. However, assets such as the Pok Fu Lam and Tai Tam Conduits date as far back as the 1880's and even include elements designated as declared monuments due to their historical significance. Some examples of the varying nature and typical condition of the tunnels in the network are shown in Figure 2.

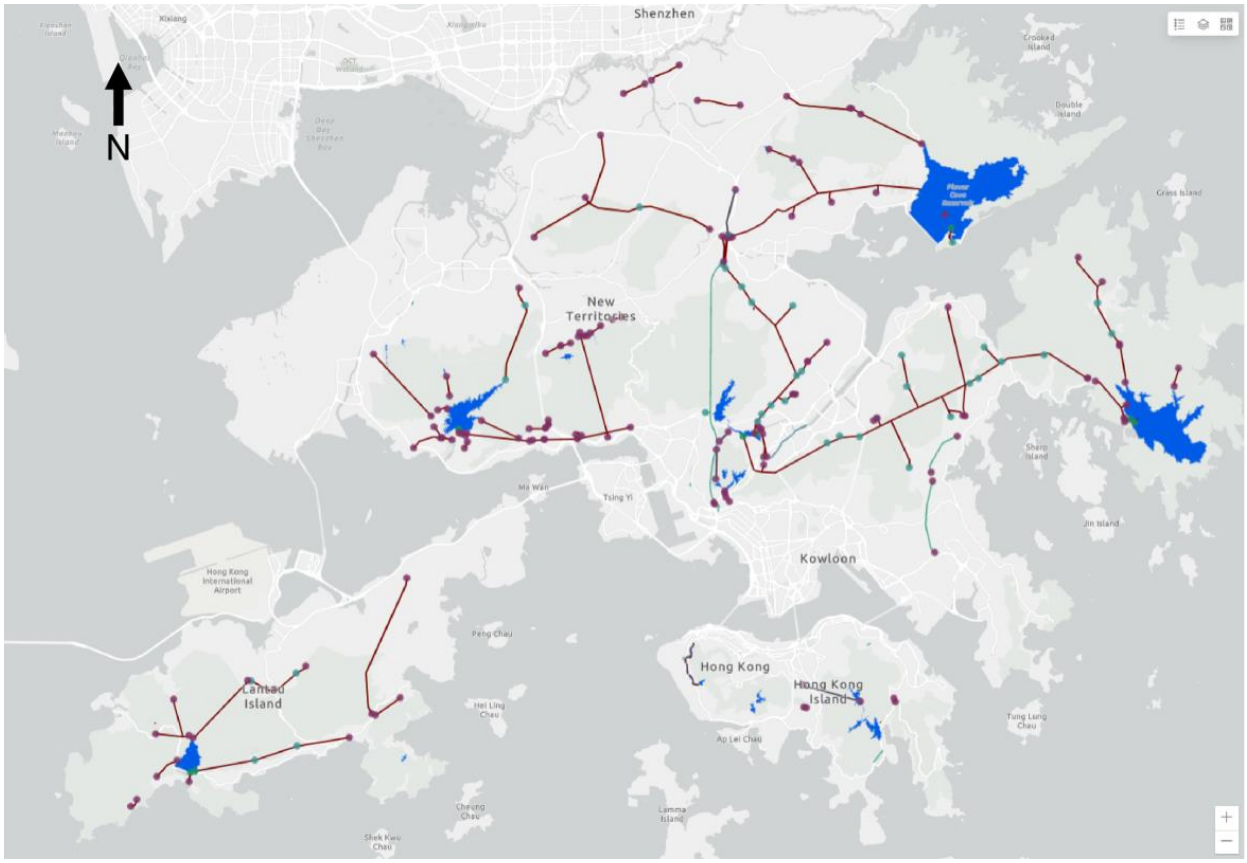
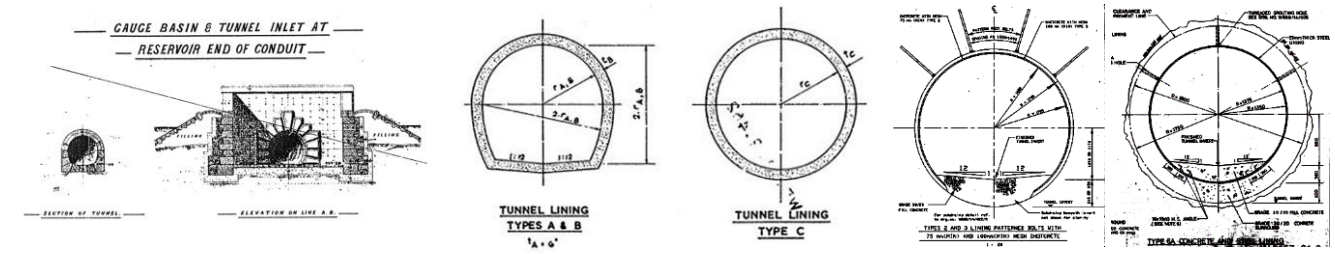


Figure 1: WSD Water Tunnel Network





Historic Water Tunnel (1880s)
- Tai Tam Conduit

Typical Water Tunnel (1960s to 1980s)
- High Island Eastern Tunnel

Recent Water Tunnel (post-1980s)
- Silvermine Bay Aqueduct

Figure 2: Examples of Typical Tunnel Nature and Condition

2 EXISTING DATASETS

2.1 Asset Register

To assist with the asset management of the water tunnels, WSD had established a GIS-based dataset containing the following basic information for the tunnels:

- Asset ID Number
- Tunnel Diameter
- Responsible Region of WSD
- Name (English & Chinese)
- Installation Date
- Asset System (Fresh or Raw Water)
- Length (Tunnels) / Depth (Shafts)
- Drawing No.

2.2 Previous Inspection Records

With a view to conducting detailed condition assessments of water tunnels, consultants commissioned by WSD undertook the first round of on-condition monitoring of their tunnel assets from 2010 to 2012 and collated the following datasets for each asset:

1. As-constructed Records from the original construction contracts;
2. Condition Assessment Forms detailing the overall condition level for key aspects of the asset;
3. Performance Risk Assessments detailing the performance level of assets where physical inspection was not feasible;
4. Asset Improvement Forms outlining the specific maintenance and/or enhancement works requirements identified during the on-condition monitoring; and,
5. Photo and video (in some cases) records from the inspection works.

The data stored for each of the above datasets comprised either a Word or PDF file following the standard proforma layout defined in the Surface Asset Management (SAM) Manual (WSD, 2010) (see Section 3.3) for details, supplemented with the raw image and, where available, video files.

3 CONDITION ASSESSMENT REQUIREMENTS

3.1 Assessment Guidelines

In order to assist with the on-going management and assessment of asset functionality, the WSD has prepared the SAM Manual detailing the overall service delivery strategy, the policies, assumptions, obligations and targets relating to water supply, as well as the detailed methodologies and procedures for the classification, inspection, assessment, maintenance and management of all assets within the water supply network. An overview of the workflow relating to the condition assessment of subsurface tunnel assets (and associated surface facilities) per the SAM Manual requirements is shown in Figure 3. This workflow covers the full spectrum of works from asset selection through criticality assessment, performance risk assessment and on-condition monitoring to the development and prioritisation of any necessary maintenance or asset enhancement works from failure risks, criticality and cost-effectiveness.

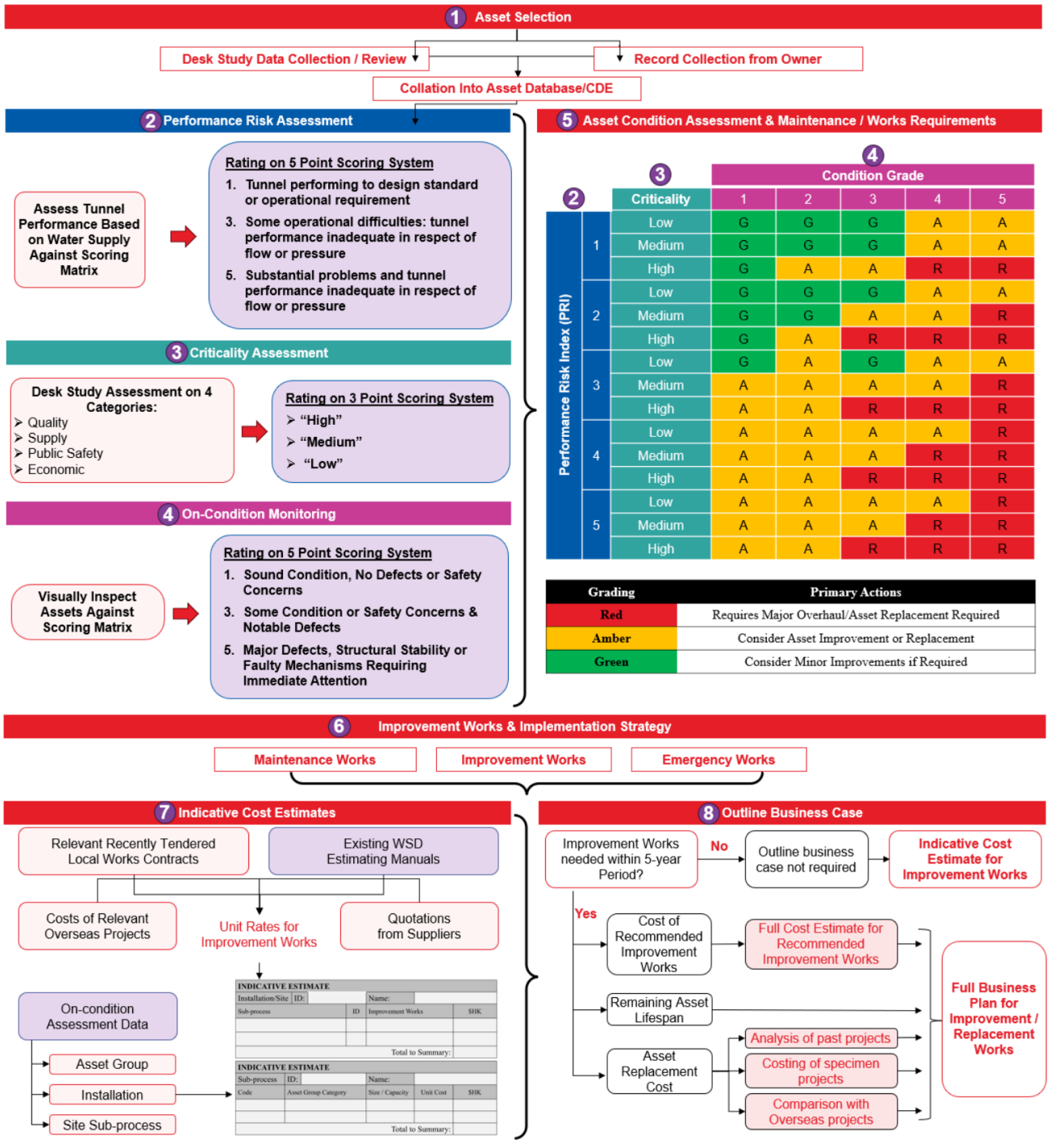


Figure 3: Workflow for Condition Assessment of Subsurface WSD Assets

3.2 Inspection Guidelines for Water Tunnels

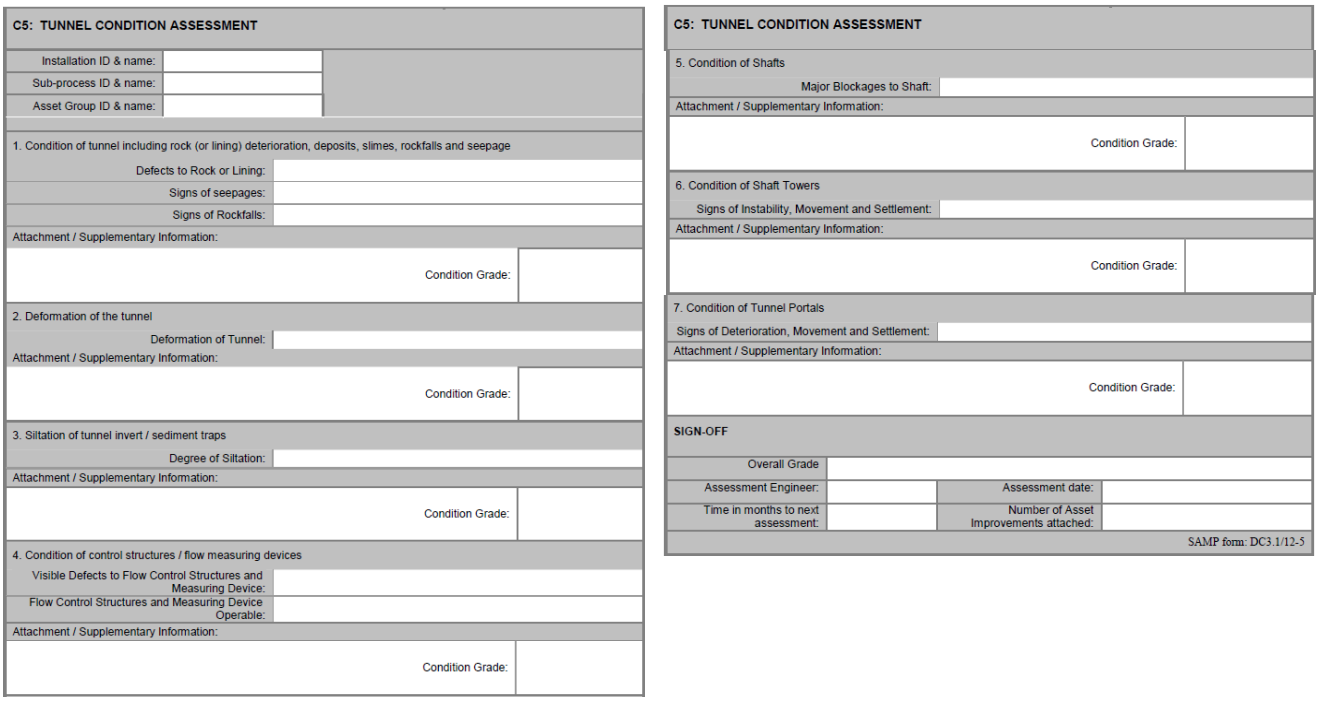
The core part of the condition assessment workflow for the water tunnels (and associated assets) comprises the on-condition assessment of the assets themselves. These primarily comprise physical inspections of the assets to review and assess the condition status according to the various criteria shown in Figure 4.

Task	Information	Assessment Criteria	
Tunnel Condition	Observe damage to the rock face or tunnel lining through walkthrough inspection.	Major damage to rockface or lining	5
		Some damage or deposits	3
		Sound condition	1
Tunnel Deformation	Observe ovalisation or displacements of tunnel lining and/or rock face by walkthrough inspection and measurements.	More than 10% of the surface area deformed	5
		Some deformation	3
		No deformation	1
Tunnel Siltation	Observe siltation build up walkthrough inspection and clear before resuming service.	20% or more of the tunnel depth	5
		< 20% of the tunnel depth	3
		No significant problems	1
Flow Control Structures Condition	Observe mechanism, seals and other aspects by visual inspection.	Seized or missing systems	5
		Significant defects	3
		No significant problems	1
Shaft Condition	Observe damage to the rock face or shaft lining by visual inspection.	Major damage or blockage	5
		Some damage or deposits	3
		Sound condition	1
Shaft Tower Condition	Observe condition and security of towers	Major movement, settlement or security problem	5
		Some signs of movement or settlement	3
		Sound condition	1
Tunnel Portal Condition	Observe condition of the portal and surrounding areas by visual inspection.	Major movement, settlement or deterioration	5
		Some movement, settlement or deterioration	3
		Sound condition	1
Other Issues	Record any significant issues, in particular safety related issues, that may endanger the tunnel or operating flexibility		

Figure 4: On-condition Assessment Criteria for Water Tunnel Assets

3.3 Reporting Standards

The findings of the inspections are documented according to reporting formats defined within the SAM Manual, which includes standard proforma forms for the reporting of on-condition assessment findings, as shown in Figure 5.



C5: TUNNEL CONDITION ASSESSMENT

Installation ID & name:
Sub-process ID & name:
Asset Group ID & name:

1. Condition of tunnel including rock (or lining) deterioration, deposits, slimes, rockfalls and seepage
Defects to Rock or Lining:
Signs of seepages:
Signs of Rockfalls:
Attachment / Supplementary Information:
Condition Grade:

2. Deformation of the tunnel
Deformation of Tunnel:
Attachment / Supplementary Information:
Condition Grade:

3. Siltation of tunnel invert / sediment traps
Degree of Siltation:
Attachment / Supplementary Information:
Condition Grade:

4. Condition of control structures / flow measuring devices
Visible Defects to Flow Control Structures and Measuring Device:
Flow Control Structures and Measuring Device Operable:
Attachment / Supplementary Information:
Condition Grade:

C5: TUNNEL CONDITION ASSESSMENT

5. Condition of Shafts
Major Blockages to Shaft:
Attachment / Supplementary Information:
Condition Grade:

6. Condition of Shaft Towers
Signs of Instability, Movement and Settlement:
Attachment / Supplementary Information:
Condition Grade:

7. Condition of Tunnel Portals
Signs of Deterioration, Movement and Settlement:
Attachment / Supplementary Information:
Condition Grade:

SIGN-OFF
Overall Grade
Assessment Engineer:
Assessment date:
Time in months to next assessment:
Number of Asset Improvements attached:
SAMP form: DC3.1/12-5

Figure 5: On-condition Assessment Report Proforma

4 ENHANCED DIGITAL APPROACH

4.1 Overall Approach

The previous round of on-condition monitoring for the water tunnels in early 2010 was conducted at a time when the development and use of digital inspection and data management tools were in the early stages and not ready for digital asset management. Works at that time were generally conducted in a manual format. Although following a well-established filing structure, the approach meant that the saved data was manually input and extracted from each file, which cannot completely prevent data inconsistencies or errors. The approach also used a tree format data structure, which was less efficient for the user to navigate and trace the output files from the original core data sets.

To address this and provide a more integrated, structured and connected approach to data management and future assessment works, an overarching digital approach was established early in the current round of on-condition monitoring. This approach was developed around the use of centralized secure online servers (e.g. a Common Data Environment or "CDE") that could host the existing datasets collected either directly from the Client or through desk study searches, as well as all new datasets (e.g. inspection data, records and performance calculations) generated by the on-going works. Through the implementation of standardized filing conventions and structures, the datasets could then be used to populate dashboards for easy visualization and progress tracking as well as the semi-automated generation of inspection reports and other deliverables as shown in Figure 6:

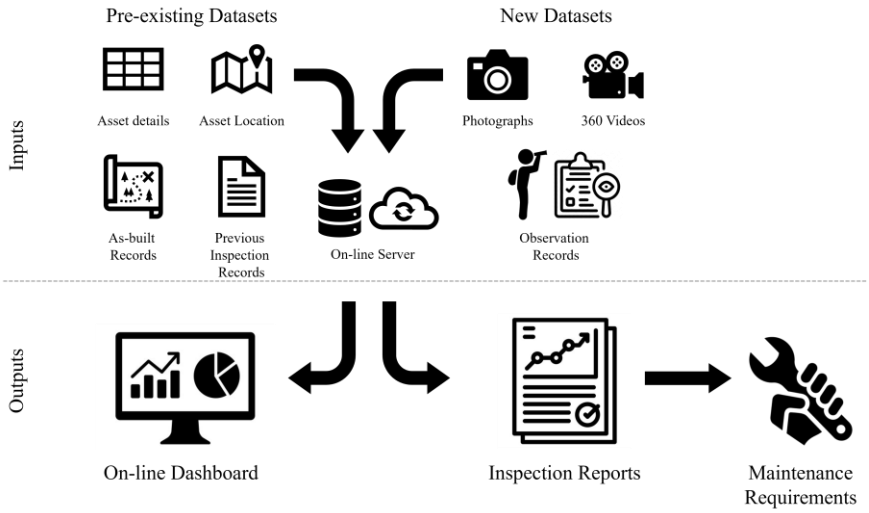


Figure 6: Overall Approach to Data Management and Use

4.2 Centralized Asset Register

To facilitate enhanced management of the available data for each of the assets, key information from the various available asset datasets was collated and input to a single, simple on-line excel spreadsheet (Figure 7) that included the following information.

1. Asset ID;
2. Sub-process ID and Name;
3. Asset Group ID and Name;
4. Asset Name (English / Chinese);
5. WSD Region;
6. WSD Responsible Team;
7. Up/Downstream Assets Reference;
8. Tunnel Length/Shaft Depth;
9. Tunnel/Shaft Diameter;
10. Water Type (Raw/Fresh);
11. Year Asset Constructed;
12. Asset Age;
13. Asset Design Life;
14. Asset Remaining Life;
15. As-built Record Drawing No.(s);
16. P&I Manual Reference;
17. O&M Manual Reference;
18. Date of Last Inspection;
19. Date of Current Inspection;
20. On-condition Grade;
21. Asset Criticality;
22. Performance Risk Assessment;
23. Risk of Failure Score;
24. Replacement Cost;
25. Modern Equivalent Value;
26. Maintenance Strategy;
27. Priority Score;
28. Asset Prioritisation.

Batching	General Data												
Batch (Actual)	Region	Responsible WSD Team	Installation No.	Installation Name	Waterworks Installation Ref. No. 1 (u/s)	Waterworks Installation Ref No. 2 (d/s)	Length (km)	Diameter (m)	Lining Type	Raw/ Fresh/ Catchwater	As-Built Records	Data Sheet Completed?	Tunnel able to be Isolated for Inspection
1	K	HW1	TL020	Tai Po Road WTW Raw Water Inlet Pipe Tunnel	TP058	TP059	0.105	5.4	Concrete	R	W05877_0000	Y	Y
1	NTW	HW3	TL027	Tai Lam Chung Catchwater J Tunnel 05	TP073	TP072	0.148	2.21	Shotcrete	C	W02522_0000	Y	Y
1	NTW	HW3	TL029	Tai Lam Chung Catchwater J Tunnel 06	TP077	TP076	0.339	2.21	Shotcrete	C	W02522_0000	Y	Y
1	NTW	HW3	TL030	Tai Lam Chung Catchwater LMNOTunnel 02	TP079	TP078	0.777	3.2	Shotcrete	C	W06102_0005	Y	Y
1	NTW	HW3	TL031	Tai Lam Chung Catchwater LMNOTunnel 03	TP081	TP080	0.167	3.6	Shotcrete	C	W06102_0005	Y	Y
1	NTW	HW3	TL032	Tai Lam Chung Catchwater LMNOTunnel 04	TP083	TP082	0.221	3.6	Shotcrete	C	W06102_0005	Y	Y

Figure 7: Simple Online Excel-based Asset Register

The asset register was hosted on a secure Microsoft Sharepoint server to allow for integration to various tools within the digital data management system. To effectively integrate GIS map data with the inspection records and Excel database, the "Atlas" tool (Figure 8) was used to facilitate real-time data updates and ensure that the project team were working on the correct and most up-to-date data possible.

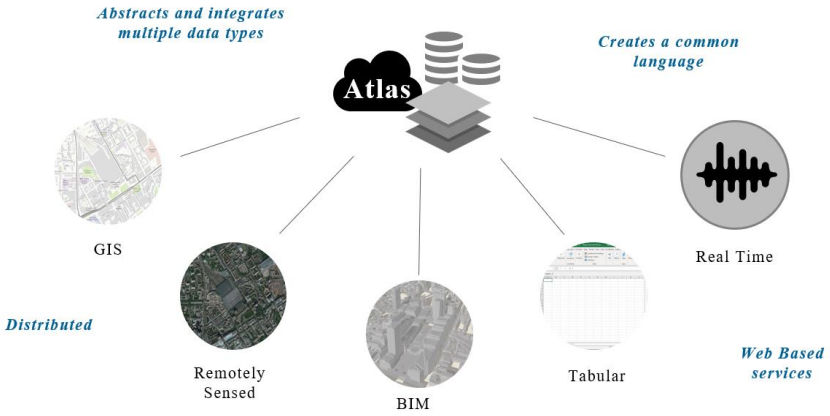


Figure 8: Atlas Database System

4.3 Data Collection App

The on-condition monitoring requires manual inspections to be undertaken for all physically accessible assets. Throughout the course of the inspections, the inspecting personnel would be required to identify, photograph and record the location and details of various different types of maintenance defects including, but not limited to lining damage, cracks/fractures to lining, rockfalls, seepages, and siltation of the invert. They would also need to record the general tunnel condition at regular intervals to capture a complete picture of the tunnel condition along its length. Typically, the inspections would need to be undertaken in confined space settings that were unlit, poorly ventilated, damp and wet, and deep underground thus lacking cellular signal connectivity.

To enhance the ease with which data could be collected, recorded and managed in an integrated, structured and systematic manner, decisions were quickly made to develop a bespoke tunnel inspection application that could be loaded to a mobile phone, could easily be operated one-handed and that would be capable of working in an off-line environment, syncing the collected data back to the central server once network connectivity resumed. To facilitate app development in a cost-effective manner that allows for direct integration with Microsoft Sharepoint, a relatively low-tech approach was adopted using Microsoft PowerApps. This app (Figure 9) allows the user to load a "light database" to their phone handset when connected to the internet before the inspection. The user could then select the desired asset for inspection without signal before and easily collects on-site observations through the simple pre-set interface which includes tunnel chainage, tunnel element (e.g. crown, left/right wall, or invert), the observation type (e.g. fracture, seepage, siltation, rockfall, damage, or other) and then takes a photo through using the app interface. This approach means that all key information for a photo is saved as structured metadata that could be directly shared to the online server and immediately integrated in the online data management platform.

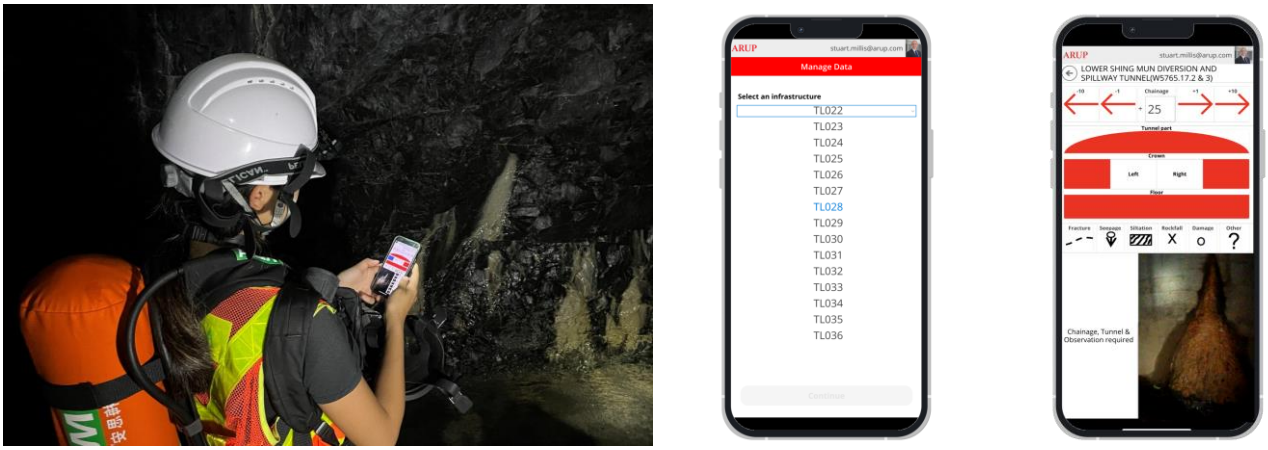
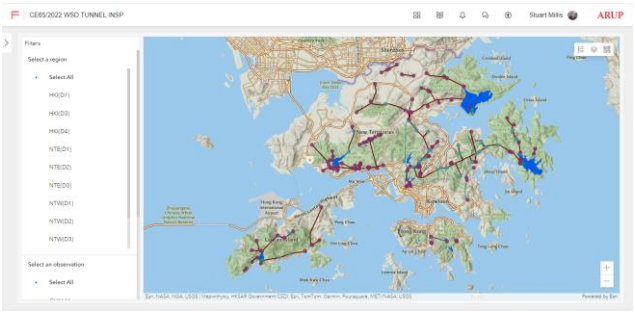


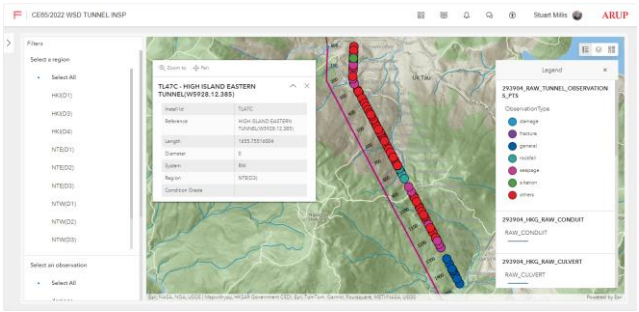
Figure 9: Data Collection App

4.4 Data Management Platform

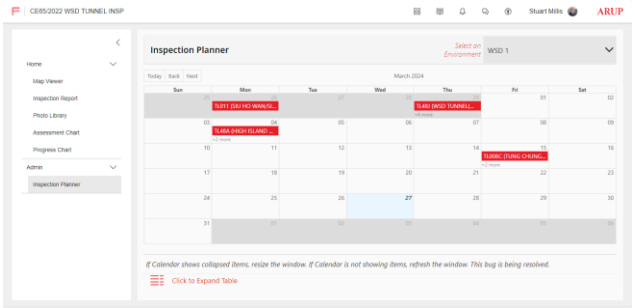
Central to the effective use of both the existing available digital datasets and the additional datasets generated during the on-condition inspections was the development of an online dashboard to facilitate data management, access and visualization (Figure 10). This was achieved using Arup's in-house "Fuse" platform, which will be interfaced with the WSD Asset Management Information System (AMIS) via the Application Programming Interface and the relevant information will be stored in the WSD AMIS repository accordingly.



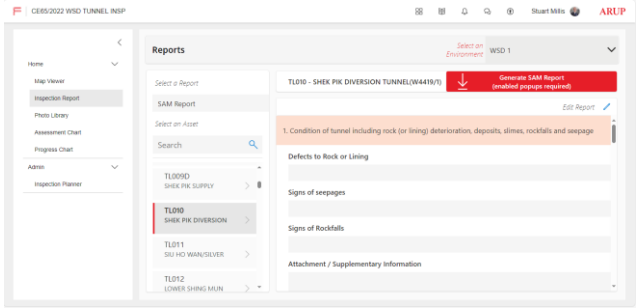
Dashboard Overview for Assets



Inspection Record Integration



Inspection Planning Module



Inspection Report Generation Module

Figure 10: Data Management Dashboard

4.5 Semi-automated Reporting

In addition to standard data management, the Fuse platform also enables the inspector to rapidly populate and generate inspection reports. This is completed using simple entry prompts in the dashboard environment that allows the inspector to select and annotate the appropriate images to be included in the report, provide inspection summaries and descriptions and easily report observation locations before generating the report. The tool automatically creates the required reports according to the proformas in the SAM Manual, including all necessary written text fields, summary documents, photo records and drawings as appendices.

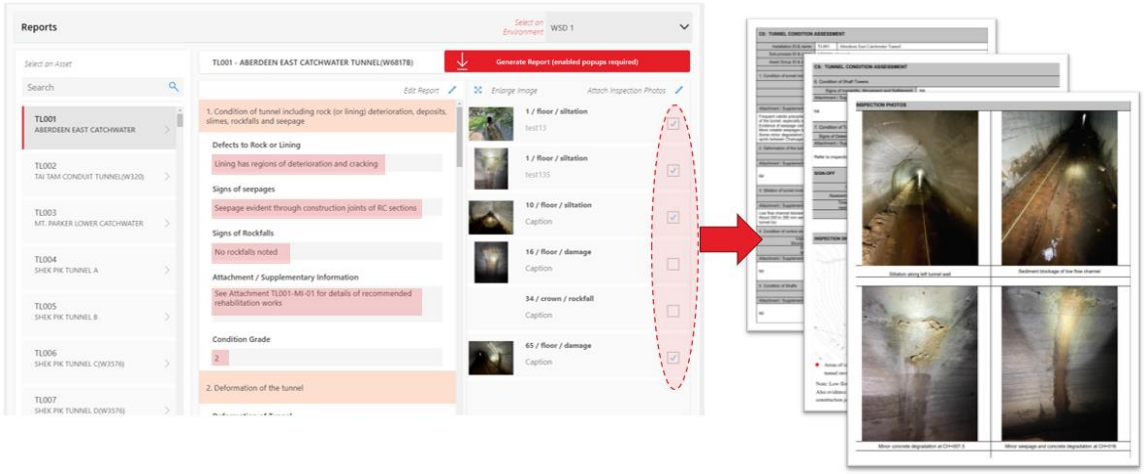


Figure 10: Semi-Automated Report Generation

5 SUPPLEMENTAL DIGITAL APPROACHES

5.1 360º Imagery and Videos

The photographs collected by the bespoke Mobile PowerApp are supplemented through the collection of additional 360º videos and images. These are captured using an Insta360 X3 camera mounted to a custom-made lighting rig that provides full 360º illumination of the main camera field of view (Figure 11). The collection of continuous and narrated 360º video footage enable the inspecting engineers to conduct virtual re-inspections of the assets to review and refine the findings documented using the Mobile PowerApp, whilst also allowing project participants not present during the physical inspections the chance to clearly observe and review the actual asset condition. This process acts both as a quality control measure and allows full internal audit capability to ensure that each inspection team is consistent with condition grading.

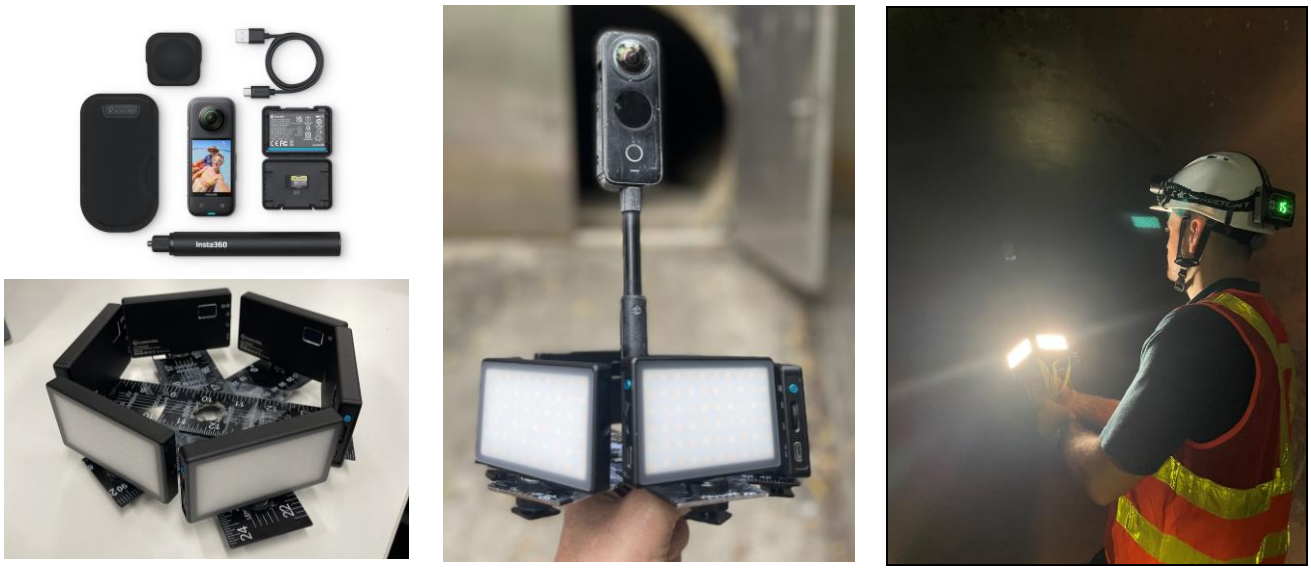


Figure 11: 360º Video & Image Capture Equipment

The 360º equipment has also been used to facilitate the inspection and defect identification/logging for vertical shafts in which no physical access is possible. This is achieved by lowering the equipment down the shaft from a tripod set up across the shaft top, with depth-time logs used to correlate the images captured to the location within the shaft, similar to the concept used by tethered CCTV crawler rigs (Figure 12).



Figure 12: Inspection of Inaccessible Shafts

5.2 UAV Surveys

To investigate the potential for unmanned inspection of water tunnels, a trial Unmanned Aerial Vehicle (UAV) survey was undertaken at the Lower Shing Mun Spillway Tunnel, a 326 m long, 5.5 m diameter concrete lined tunnel. The trial was undertaken by WSD's Term Contractor, Ming Hing Waterworks Engineering Co. Ltd., using an Elios 3 UAV to conduct 3D-scanning by LiDAR, and collect 4k video footage and photographs of the tunnel condition as shown in Figure 13.

The inspection took less than 20 minutes to complete and yielded high quality photographs and videos in which all key defects identified during the physical survey of the same tunnel were clearly visible. To maintain sufficient signal to the pilot, the maximum line-of-sight distance for indoor UAV systems deployed in tunnels is effective over approximately 400-500m. This length would be considerably reduced if the tunnel has some curvature (breaking line-of-sight). Currently, the flight time is also not an uncommon challenge to the use of indoor UAVs, including the maximum flight time of approximately 20 minutes for Elios 3 UAV in this trial, which also acts as a constraint to the length of survey.

It should also be noted that in Hong Kong, the deployment of UAV systems for is subject to Civil Aviation Department law and when utilized for commercial settings, relevant flight restrictions must be adhered to.



Figure 13: UAV Survey Equipment and Data

On-going research on the use of indoor UAV devices for tunnel surveys identified some isolated examples of autonomous 'unpiloted' UAVs being used to conduct video and 3D scanning surveys of water tunnels up to 7 km in length. Should these devices become more readily available in Hong Kong, they would provide a highly effective tool for the collection of detailed tunnel survey datasets.

5.3 Laser Scanning Surveys

Similarly, trials were undertaken in the consultancy to explore the potential to collect detailed point cloud data of the tunnel geometry and condition using laser scanning technology. The trial included the use of both terrestrial tripod mounted scanners (Faro Focus Core Laser Scanner) as well as handheld scanning devices (FJD Trion S1 Portable Scanner) as shown in Figure 14.



Figure 14: Terrestrial and Mobile Laser Scanning

Data capture with the static (mounted) system was undertaken at intervals of 50 m to generate a series of continually overlapping point clouds that, due to the placement of survey spheres along the tunnel length, could be merged to cover the entire asset length. Data capture with the mobile system was undertaken using a 'there and back' loop for portions of an asset that could be covered in a 25-minute time interval, limiting the scanning distance of a single dataset to about 500 m. For assets exceeding this length, survey spheres were used with overlapping portions of adjacent scans to enable merging of the survey datasets.

Although only trialed on a limited number of assets, it is worthwhile to highlight the following findings of note about the suitability and effectiveness of laser scanning for water tunnels (Figure 15):

1. *Terrestrial Scanners:* Provided the survey is well-planned and adequate survey spheres provided across overlapping scan areas, tripod mounted scanners can yield very high-quality point cloud datasets for all tunnel lining types. However, such surveys can require considerable time to complete, in the case of the 326 m Shing Mun Spillway Tunnel this equated to about 30 minutes per 100 m of tunnel.
2. *Mobile Scanner:* Scanning of similar tunnel lengths using handheld mobile laser scanners required only about 10% of the time needed for tripod-mounted scans. However, the SLAM technology used by such devices means they are not capable of collecting data within tunnels of uniform and consistent profiles where insufficient variance exists for the device to distinguish between different locations within the tunnel. This provides a severe constraint for use within cast in-situ or segmentally lined concrete tunnels, in which scans typically fail within about 10 m from the last distinguishable geometric change or feature. However, reasonable quality datasets could be rapidly obtained from scans within shotcrete lined tunnels with irregular profiles and unlined rock tunnels.

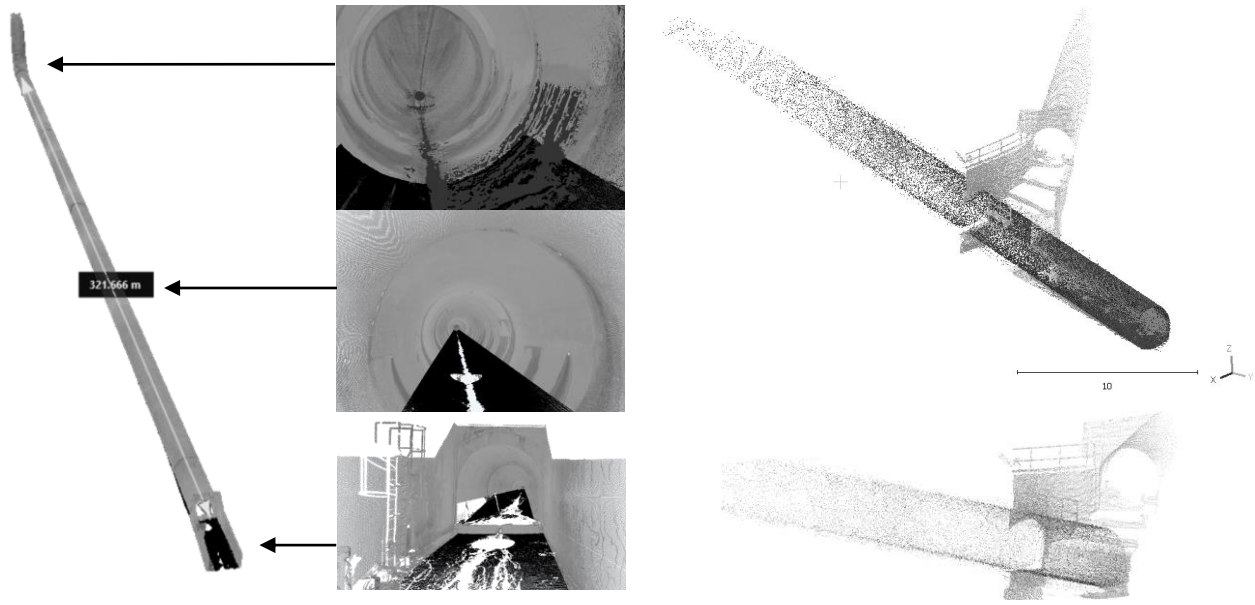


Figure 15: Examples of Point Cloud Datasets from Terrestrial (left) and Mobile (right) Laser Scanning

5.4 Arup Loupe 360 Tool

Arup Loupe 360 (Figure 16) is a tunnel inspection visualization and analytics platform that leverages 360º imagery and computer vision to enable visualization and asset analysis, supported by machine learning (ML) and artificial intelligence (AI) for defect detection, inventorying and condition rating analytics. Initially developed in the UK to facilitate the rapid and semi-automated inspection of segmentally lined railway tunnels, the platform is customizable and can integrate high-quality 360-data for any tunnel asset. Trial integration of regularly spaced 360 images from several of the WSD tunnels was therefore undertaken. The trials showed that the tool provided an ideal platform for conducting 'Google Street View' style walkthrough inspections, allowing the user to navigate their way quickly and easily through the available images for an asset. Regarding the use of AI for defect detection, the trial revealed that additional training of the ML algorithms would be required as the lining types and defect condition/classification used for the WSD tunnels differed notably from those in the segmentally lined tunnels on which the tool was originally trained. Such ML-training is considered entirely feasible and the trial provided a good proof-of-concept for further exploration when opportunity arises.

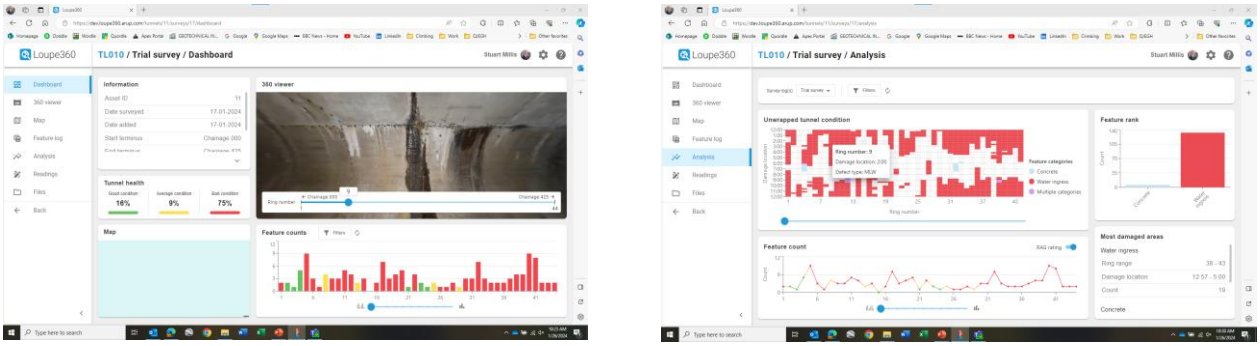


Figure 16: Data Integration within the Arup Loupe 360

6 SUMMARY

The Water Supplies Department (WSD) of Hong Kong owns, operates and maintains about 200 km of water tunnels, some of which are over 100 years old, as part of an extensive water supply network that must operate at considerable capacity, year-round, in order to facilitate the consistent supply of high-quality water to Hong Kong residents. As part of routine maintenance, condition assessments of these critical tunnels must be undertaken to ensure supply continuity. On behalf of WSD, Arup have completed these inspections utilising the latest technology and novel data collection and management methods to enhance every stage of the assessments including data management, on site data collection, condition assessment, dashboarding and reporting using the "single source of truth" approach.

Extensive testing of various data collection methods and inspection tools and techniques was completed as part of the project to determine the most optimum condition assessment method for existing water tunnels. The conclusion of these trials is directly applicable to other, similar maintainers in the industry (e.g. drainage, electricity supply or gas networks). This approach is also being adopted by the WSD in which the data of the tunnel assessment could be retrieved in the WSD AMIS to facilitate future asset management under the WSD asset management policy.

ACKNOWLEDGEMENTS

This paper is published with the kind permission of the Director of the Water Supplies Department of the Government of the Hong Kong Special Administrative Regions.

REFERENCES

Water Supplies Department. 2010. Surface Asset Management Manual (Volumes 1 & 2).

Analytical Chloride Diffusion Model for Durability Assessment of Concrete-Lined Tunnels

P.L. Ng
The University of Hong Kong, Hong Kong, China
S.J. Zhou
BAE Australia, Queensland, Australia
J. Wang
Sun Yat-Sen University, Guangdong Province, China

ABSTRACT

The presence of chloride ion de-passivates reinforcing steel, thereby accelerating the corrosion of reinforcement and deterioration of reinforced concrete elements. Chloride ion diffusion constitutes the major deleterious factor undermining the durability of concrete-lined tunnels, especially tunnels through aquifers with high salinity. Hence, the service life prediction of concrete-lined tunnels should reliably take into account the chloride diffusivity in the concrete lining. Conventional serviceability design of reinforced concrete considers the exposure conditions in a categorical manner, with corresponding prescribed measures such as cover thickness and strength grade applied to the design. However, as a basis for quantitative assessment of durability, the chloride diffusion is generally dependent on the diffusivity of concrete, chloride ion concentration, environmental condition and the age. This paper devises an analytical chloride diffusion model with explicit formulation, which provides practical reference for adoption by design engineers. The application of the model is illustrated by examples of durability assessment of reinforced concrete tunnel lining.

1 INTRODUCTION

The corrosion of steel reinforcement in concrete is an electro-chemical reaction. Under the normal service conditions of reinforced concrete, the alkalinity of hydrated cement provides passivation for the embedded reinforcing steel, i.e. a passivating layer of oxide forms at the surface of reinforcing steel, thereby protecting the steel from corrosion (Mehta & Monteiro 2014). However, when chloride ion is present, the chloride ion activates the surface of steel to become the anode, whereas the passivated surface becomes the cathode. Such de-passivation by chloride ion sets up the electro-chemical cell and drastically accelerates the corrosion of reinforcing steel (Gjørv 2014). This in turn deteriorates the structural health and undermines the durability of reinforced concrete elements.

A variety of tunnels constitutes the lifeline infrastructure in urban settings. For concrete-lined tunnels, especially the tunnels through aquifers with high salinity, the deleterious effect of chloride ion on the durability and service life should be duly considered. In general, chloride ions could ingress into concrete by way of different transport mechanisms (Hooton 2014), including: a) diffusion of chloride through the pore water due to a chloride concentration gradient; b) permeation under a differential hydraulic pressure; c) absorption (sorption or convection) into unsaturated concrete due to a differential moisture concentration; and d) wick action with evaporation leaving high salt concentration at the drying front.

Among the aforementioned transport mechanisms, diffusion of chloride ions is the dominating mechanism practically (Wang et al. 2017). Thus, the durability assessment and service life prediction of concrete-lined tunnels should reliably take into account the chloride diffusion process in the concrete lining or concrete tunnel box structure. In conventional service life design of reinforced concrete, the exposure conditions are considered in a categorical manner, as exemplified by the exposure conditions of mild, moderate, severe, very

severe, and abrasive (Buildings Department 2013). The European Standard adopts a more refined categorization. In EN 206 (CEN 2013) and Eurocode 2 (CEN 2023), the exposure classes related to chloride induced corrosion are further designated into X0 (no risk of corrosion or attack), XD1 (moderate humidity), XD2 (wet, rarely dry), XD3 (cyclic wet and dry), XS1 (exposed to airborne salt but not in direct contact with seawater), XS2 (permanently submerged in seawater), and XS3 (tidal, splash and spray zones). With respect to the exposure classes, corresponding prescribed measures such as cover thickness, water to cement ratio and strength grade are applicable to the reinforced concrete design.

To more realistically and quantitatively assess the durability and service life of concrete construction, mathematical modelling of chloride diffusion has been formulated and applied (Shi et al. 2020). The chloride diffusion is generally dependent on the diffusivity of concrete and its rate of change, surface chloride ion concentration and its rate of change, environmental condition and the age. This paper devises an analytical chloride diffusion model with explicit formulation, which provides practical reference for adoption by design engineers. The application of the model is illustrated by examples of durability assessment of reinforced concrete tunnels.

2 CHLORIDE ION DIFFUSION MODELS

2.1 Fick's First Law

As a result of the physical phenomenon of Brownian motion, chloride ions in aqueous solution move randomly due to their frequent collisions with water molecules. Statistically, the random Brownian motion drives the chloride ions from high concentration zones to low concentration zones, eventually increasing the uniformity of the system (Freedman 1983). Such mass transfer of chloride ions from high to low concentration zones is referred to as chloride diffusion (Mauro 2021). The diffusion flux of chloride ions in aqueous solution is governed by Fick's First Law, as described in Equation (1) for typical one-dimensional diffusion process in a steady-state system (i.e. there is no change of chloride concentration at any point along the diffusion path).

$$J = -D\frac{\partial C}{\partial X} \tag{1}$$

where J = diffusion flux (or rate of mass transfer) through unit area in unit time (mol/m^{2}s), D = diffusion coefficient or diffusivity of chloride ions in aqueous solution (m^2/s), C = concentration of chloride ions (mol/m^3), and X = distance (m).

Fick's First Law determines that the diffusion flux has a linear relationship with the concentration gradient. Equation (1) is valid for concrete with a capillary pore water system. It is because the diffusion of chloride ions in solid cement paste is negligible, whereas diffusion of chloride ions does not occur in dry air or dry concrete without a connected capillary system of pore water.

2.2 Fick's Second Law

The change of chloride concentration in aqueous solution with time in the one-dimensional diffusion process is described by Fick's Second Law, as described in Equation (2) which reflects that the rate of chloride concentration change has a linear relationship with the second derivative of concentration function with respect to distance (Mauro 2021; Spiechowicz et al. 2023).

$$\frac{\partial C}{\partial t} = D\frac{\partial^2 C}{\partial X^2} \tag{2}$$

where t = time (s). It can be seen that time is related with Fick's Second Law but not with Fick's First Law.

Consider a semi-infinite homogenous medium with the finite face exposed to constant concentration of chloride source. Denote the initial chloride ion concentration in the medium to be C_0 as the initial condition, the solution of the above differential equation, i.e. Equation (2), is given by:

$$\frac{C-C_0}{C_s-C_0}=erfc\left(\frac{X}{2\sqrt{Dt}}\right) \tag{3}$$

where C_0 = initial chloride concentration, C_s = surface chloride concentration, and *erfc* = complementary error function. More information about the complementary error function is contained in the Appendix. Equation (3) can determine the change of chloride ion concentration with time at various distances from the exposed surface (Crank 1975). It should be noted that in the durability assessment of concrete elements, to predict the time to corrosion initiation and to evaluate the residual service life, the apparent chloride diffusivity estimated from the chloride profile is significantly influenced by the initial chloride concentration. A higher C_0 could yield a lower diffusivity, and consequently a longer time to corrosion initiation.

2.3 Time-variation of chloride diffusivity

Equation (3) is suitable for concrete with constant chloride diffusivity. In reality, the continual chemical reactions in concrete would gradually decrease the diffusivity and decelerate the rate of chloride ion ingress (Tang & Nilsson 1992). The decreasing chloride diffusivity could be accounted for via two approaches: a) to vary the instantaneous chloride diffusivity with time; and b) to adopt an apparent chloride diffusivity.

Regarding the first approach, the instantaneous chloride diffusivity is the diffusivity value obtained for concrete at a particular age and thus is valid only for that age (Wang et al. 2020). An empirical relationship between the diffusivity and age was put forward by Tang & Nilsson (1992), as expressed in Equation (4):

$$D_a=D_r\left(\frac{t_r}{t_a}\right)^m \tag{4}$$

where t_a = age of concrete (year), D_a = instantaneous chloride diffusivity at age t_a (m^2/s), t_r = reference concrete age at test or measurement (year), D_r = reference instantaneous chloride diffusivity at reference age t_r (m^2/s), and m = instantaneous age factor. The value of factor m is empirically dependent on the type of binder materials in the concrete mix and the mix proportioning. For example, for a concrete mix containing 25% pulverized fuel ash by mass as cement replacement, the corresponding value of m could be taken as 0.4; whereas for a concrete mix containing 25% pulverized fuel ash and 35% ground granulated blastfurnace slag by mass as cement replacement, the corresponding value of m could be taken as 0.6. Tang & Gulikers (2007) put forward a mathematical model based on decreasing chloride diffusivity, as formulated in the following:

$$\frac{C-C_0}{C_s-C_0}=erfc\left(\frac{X-\Delta X}{2\sqrt{\frac{D_c}{1-m}\left[\left(1+\frac{t_{e0}}{t_e}\right)^{1-m}-\left(\frac{t_{e0}}{t_e}\right)^{1-m}\right]\left(\frac{t_r}{t_e}\right)^m t_e}}\right) \tag{5}$$

where t_{e0} = age of concrete when exposure starts (year), t_e = duration of exposure (year), and ΔX = depth of convection zone (mm). It should be noted that $t_a = t_{e0} + t_e$. Regarding the depth of convection zone, it is to account for the case that the chloride concentration at concrete surface is not the highest but lower than that at a deeper zone, namely the surface convection zone whose depth is ΔX. Such phenomenon may occur when the chloride solution is repeatedly absorbed into the surface, followed by drying and evaporation of water leaving an increased chloride concentration which is not diffusion based, or when free chloride at surface is washed away by tide, splash or rain, or when carbonation of the near-surface concrete releases some bound or absorbed chloride. For concrete tunnels, the above circumstances are inapplicable or unlikely, so that ΔX could be nullified.

Regarding the second approach, the apparent chloride diffusivity is an approximate approach to determine an averaged or integrated diffusivity for a certain exposure period (Wang et al. 2019). It is evaluated based on

chloride profiles obtained after the exposure period by assuming a constant diffusivity for the period before the test (Bamforth 2004). Due to the sustained chemical reactions in concrete, the apparent chloride diffusivity would also decrease with age. Equation (6) denotes the mathematical expression.

$$D'_a = D'_r\left(\frac{t_r}{t_a}\right)^n \tag{6}$$

where D'_a = apparent chloride diffusivity at age t_a (m^2/s), D'_r = reference apparent chloride diffusivity at reference age t_r (m^2/s), and n = apparent age factor. The value of factor n is estimated from actual chloride profiles at various ages in the exposed concrete. The mathematical formulation of the apparent diffusivity model is given in the following:

$$\frac{C-C_0}{C_s-C_0} = erfc\left(\frac{X-\Delta X}{2\sqrt{D'_a t_e}}\right) = erfc\left(\frac{X-\Delta X}{2\sqrt{D'_r\left(\frac{t_r}{t_a}\right)^n t_e}}\right) \tag{7}$$

Typically, the decrease of chloride diffusivity of mature concrete is a gradual and long-term process that could sustain decades. By regression analysis of chloride profiles, the following relationships between D_a, D'_a, m and n have been yielded (Zhou 2018):

$$\frac{D_a}{D'_a} = m_4(\log t_a)^4 + m_3(\log t_a)^3 + m_2(\log t_a)^2 + m_1 \log t_a + m_0 \tag{8a}$$

$$\begin{pmatrix} m_0 \\ m_1 \\ m_2 \\ m_3 \\ m_4 \end{pmatrix} = \begin{pmatrix} -0.6895 \\ -0.2976 \\ 0.1717 \\ -0.0668 \\ 0.0118 \end{pmatrix} m + \begin{pmatrix} 0.9830 \\ -0.0081 \\ 0.0091 \\ -0.0013 \\ -0.0002 \end{pmatrix} \tag{8b}$$

$$\frac{D_a}{D'_a} = n_4(\log t_a)^4 + n_3(\log t_a)^3 + n_2(\log t_a)^2 + n_1 \log t_a + n_0 \tag{9a}$$

$$\begin{pmatrix} n_0 \\ n_1 \\ n_2 \\ n_3 \\ n_4 \end{pmatrix} = \begin{pmatrix} -0.7589 \\ -0.3295 \\ 0.1901 \\ -0.0738 \\ 0.0130 \end{pmatrix} n + \begin{pmatrix} 0.9943 \\ -0.0032 \\ 0.0062 \\ -0.0002 \\ -0.0004 \end{pmatrix} \tag{9b}$$

$$n = -0.1669m^2 + 1.0375m - 0.0052 \tag{10}$$

$$m = 0.2253n^2 + 0.9387n + 0.0073 \tag{11}$$

2.4 Time-variation of surface chloride concentration

The chloride ion concentration at the concrete surface, namely the extrados of lining or external side of tunnel box structure, is not constant but undergoes an accumulation or building-up process. Generally, two patterns

of surface chloride concentration variations with time could be found. They include the linear increase and square root increase patterns, as expounded hereunder.

With regard to the linear pattern, the relationship between surface chloride concentration and time in exposure is given by:

$$C_s - C_0 = k_1 t_e \tag{12}$$

where k_1 = gradient of linearly increasing surface chloride concentration (s^{-1}). The analytical model for chloride concentration *C'* at various depth and time follows Equation (13) and Equation (14), applicable when the chloride diffusivity is simultaneously decreasing (Zhou 2014):

$$C' = C_0 + k_1 t_e \left[(1+A) erfc\left(\sqrt{\frac{A}{2}}\right) - \sqrt{\frac{2}{\pi} A} \exp\left(\frac{-A}{2}\right) \right] \tag{13}$$

$$A = \frac{(X - \Delta X)^2 (1-m)}{2 D_r t_r^m \left[(t_e + t_{e0})^{1-m} - t_{e0}^{1-m} \right]} \tag{14}$$

With regard to the square root pattern, the relationship between surface chloride concentration and time in exposure is given by:

$$C_s - C_0 = k_2 t_e^{0.5} \tag{15}$$

where k_2 = gradient of square root increasing surface chloride concentration ($s^{-0.5}$). The analytical model for chloride concentration *C''* at various depth and time follows Equation (14) and Equation (16), applicable when the chloride diffusivity is simultaneously decreasing (Zhou 2016):

$$C'' = C_0 + k_2 t_e^{0.5} \left[\exp\left(\frac{-A}{2}\right) - \sqrt{\frac{A}{2}} erfc\left(\sqrt{\frac{A}{2}}\right) \right] \tag{16}$$

Dependent on the surrounding geo-environmental condition, the building-up of surface chloride concentration may resemble a linear, square root, or other pattern with variable gradients in general. From past experience, the accumulation of airborne chloride is relatively close to linear pattern, while the accumulation of chloride in wet-dry cycles and submerged conditions is relatively close to square root pattern. When the surface chloride concentration has built-up to a steady level, then C_s becomes constant and the mathematical model given by Equation (5) can be employed, with the exposure time substituted by an equivalent exposure time to account for the chloride profile attained during the surface chloride building-up process.

2.5 Effect of temperature

Since heat provides activation energy for diffusion, the temperature affects the chloride ion diffusion through altering the diffusivity. The effect of temperature on chloride diffusivity can be estimated according to the Arrhenius equation as follows (Laidler 1984):

$$D_T = D_{Tr} \exp\left[\frac{E_a}{R} \left(\frac{1}{T_r} - \frac{1}{T} \right) \right] \tag{17}$$

where T = temperature (K), D_T = chloride diffusion coefficient at temperature T, D_{Tr} = chloride diffusion coefficient at reference temperature T_r, E_a = activation energy of diffusion process (J/mol), and R = universal

gas constant which is equal to 8.314 JK^{-1}/mol. Taking the logarithm of both sides of Equation (17), it can be seen that the logarithm of chloride diffusion coefficient has a linear relation with the inverse of temperature.

$$\log D_T - \frac{E_a}{RT_r} = \log D_{Tr} - \frac{E_a}{RT} \tag{18}$$

Considering the diffusion near the cover zone of lining extrados or external side is of concern, the temperature of concrete thereat should be referred to. The value of E_a/R could be computed from Equation (19), with dependence on the water to cement ratio (W/C) of concrete (Page et al. 1981):

$$\frac{E_a}{R} = 1000\left[-52.5(W/C)^2 + 41.75(W/C) - 2.3\right] \tag{19}$$

3 EXPERIMENTAL MEASUREMENT OF CHLORIDE DIFFUSIVITY

In applying the chloride ion diffusion models, it is of prime importance to establish the chloride diffusivity of concrete. While concrete samples extraction from tunnels in service would be destructive and/or arise practicality concerns, representative samples could be prepared by casting specimens from the same concrete mixes as the tunnel lining or structure. Batch-by-batch differences from constituent materials could be eliminated by pre-planning the specimen preparation and testing during trial mixing, or minimized by replica sourcing of each ingredient for specimen preparation during post-construction or operation stage of the tunnel. There are different experimental methods to measure the chloride diffusivity of concrete, as outlined below.

3.1 Migration cell experiment

The testing methodology and procedures are specified in NT Build 355 (Nordtest 1997). Concrete cylinder of 100 mm diameter is cast and cured in water tank until 90 days of age. After curing, the cylinder is wiped with dry cloth and wait to attain surface-dry condition. The curved surface of the cylinder is coated with epoxy to achieve water impermeability. Concrete slices of 100 mm diameter and 50 mm thickness are cut from cylinder (during cutting, the top 10 mm portion of cylinder is discarded). The concrete slice is then placed into the migration cell, where one face of the slice is in contact with 5 wt.% NaCl solution (compartment 1 of the cell) whereas the opposite face of the slice is in contact with 1.2 wt.% NaOH solution (compartment 2 of the cell). A rubber sealant ring is fitted onto the epoxy-coated side (curved) surface to separate the two compartments.

The two half-cells are connected to a 12V fixed voltage D.C. (direct current) and an ammeter. The voltage drop ΔE across the slice specimen is measured with two reference electrodes each inserted into a compartment. The chloride concentration in compartment 2 is measured daily over one week to obtain the rate of change of chloride concentration. The chloride diffusivity is then obtained as:

$$D = \frac{RTh}{Fz\Delta EA}\left(\frac{V_2}{C_1}\right)\left(\frac{\Delta C_2}{\Delta t}\right) \tag{20}$$

where h = slice thickness (m), F = Faraday constant which is equal to 96485 C/mol, z = absolute value of valence of chloride ion (z = 1), ΔE = voltage drop across slice specimen (V), A = area of concrete slice (m^2), C_1 = chloride concentration in compartment 1, V_2 = volume of compartment 2 (m^3), and $\Delta C_2/\Delta t$ = rate of change of chloride concentration in compartment 2.

3.2 Accelerated chloride penetration

The methodology and procedures of accelerated chloride penetration test are described in NT Build 443 (Nordtest 1995). Concrete cylinder of 75 mm or 100 mm diameter is cast and water cured until 28 days of age. The cylinder is then cut into halves. Upon dried to surface-dry condition, all surfaces of half-cylinder except the cut face is coated with 1 mm thick epoxy or polyurethane coating. After the coating has hardened, the half-

cylinder specimen is immersed in 14 wt.% NaCl solution at 23°C ± 2°C for a period of 35 days with stirring of the chloride solution once per week. Subsequent to exposure to chloride solution, grinding is performed at the face of slice within a diameter of approximately 10 mm less than the diameter of cylinder (in order to avoid the influence of edge effect). At least 8 layers are to be ground off, with the outermost layer having a thickness of minimum 1.0 mm and each remaining layer sufficiently thick to yield at least 5 g of dry concrete dust. The depth of each layer from the exposed surface is re-measured at 5 points using caliper and averaged.

The acid-soluble chloride content of concrete dust sample from each layer is measured using Volhard titration method (Nordtest 1996) as detailed in the Appendix. This enables the determination of chloride concentration $C(X,t)$ at various depth X and time t. From the other half-cylinder, concrete slice of 20 mm is cut, and circa 20 g of concrete fragment sample is obtained by crushing. The acid-soluble chloride content of concrete fragment sample is measured using Volhard titration method as the initial chloride concentration C_0. By fitting of Equation (21) based on regression analysis, the values of C_s and D_e can be obtained:

$$C(X,t) = C_s - \frac{C_s - C_0}{erf\left(\frac{X}{2\sqrt{D_e t}}\right)} \tag{21}$$

where D_e = effective chloride diffusion coefficient (m^2/s). Given a selected value of reference chloride concentration C_r, say 0.05% by mass of concrete, the chloride penetration parameter K_{Cr} ($m/s^{0.5}$ or $mm/s^{0.5}$) corresponding to the selected C_r value can be evaluated in accordance with Equation (22):

$$K_{Cr} = \frac{2\sqrt{D_e}}{erf\left(\frac{C_s - C_r}{C_s - C_0}\right)} \tag{22}$$

3.3 Non-steady-state migration experiment

The methodology and procedures of the experiment are detailed in NT Build 492 (Nordtest 1999). Concrete cylinder of 100 mm diameter is cast, from which slice specimen of the same diameter and 50 mm thickness is cut. A silicone rubber sleeve is fitted onto the curved surface of slice specimen and secured with stainless steel ring clamp. The rubber sleeve is of 150 mm length and extends above the slice specimen. The assembly is placed on an inclined plastic support with plastic stud spacers, altogether put at the base of catholyte reservoir filled with 10 wt.% NaCl solution. The plastic spacers provide a gap for direct contact between the bottom face of concrete slice and NaCl solution. The rubber sleeve above the slice is filled with 1.2 wt.% NaOH solution, which becomes the anolyte solution in direct contact with the top face of concrete slice. A regulated voltage D.C. power supply is set up with the negative pole connected to a 0.5 mm thick stainless steel plate cathode and positive pole connected to a 0.5 mm thick stainless steel perforated plate or mesh anode.

The voltage is initially set as 30V and the initial current through the specimen is recorded upon turning on the power. Then, the voltage is adjusted within the range of 10V to 60V with respect to the initial current and the test is sustained for a duration ranging from 6 hours to 96 hours according to NT Build 492 (Nordtest 1999). After the test, the slice specimen is rinsed and split into two halves. Silver nitrate ($AgNO_3$) solution of 0.1 M concentration is sprayed onto the split surface of one half-slice and wait for circa 15 minutes until white silver chloride precipitation appears on the split surface. The chloride penetration depth is measured using caliper at 10 mm intervals (to avoid the influence of edge effect, measurement is not made within 10 mm from the edge) and averaged. The chloride diffusivity can be evaluated from Equation (23):

$$D_n = \frac{RTh}{Fz(U-2)t}\left[x_d - \sqrt{\frac{RTh x_d}{Fz(U-2)}}\frac{2}{erf(1-2r_C)}\right] \tag{23}$$

where D_n = non-steady-state migration coefficient (m^2/s), U = absolute value of applied voltage (V), x_d = average value of chloride penetration depth (m), r_C = ratio of chloride concentration at which the colour changes to chloride concentration in the catholyte solution (r_C is approximately equal to 0.07/2 = 0.035).

3.4 Rapid chloride permeability test

The methodology and procedures of rapid chloride permeability test (RCPT) are specified in American Standard AASHTO T 277 (AASHTO 2007). Concrete cylinder of 100 mm diameter is cast and cured until 56 days of age. Slice specimen of 100 mm diameter and 50 mm thickness is cut from the cylinder. A potential difference of 60V D.C. from a constant voltage power supply is maintained across the ends of slice specimen, one of which is immersed in 3.0 wt.% NaCl solution, and the other is immersed in 1.2 wt.% NaOH solution. The amount of electric current passing through the slice specimen during a 6-hour period is monitored using a voltmeter. The total charge passed is related to the resistance of the slice specimen to chloride ion penetration. Empirical relationship between the total charge passed and chloride diffusivity was recommended by Hooton et al. (1997), as given by Equation (24):

$$D = 0.3\times10^{-6}Q^2 + 0.6\times10^{-3}Q + 0.9375 \tag{24}$$

where Q = total charge passed (C).

3.5 Threshold chloride concentration

When the chloride concentration at the reinforcement surface reaches the threshold level, corrosion of reinforcing steel accelerates and is considered to enter into the corrosion propagation period. The values of threshold chloride concentration vary widely as reported in the literature (Angst and Vennesland 2009), and attention has to be paid regarding the expression of chloride component (free chloride or total chloride) and proportional basis (by mass of concrete or by mass of binder). According to Japanese Standard (Japan Society of Civil Engineers 1999), before the availability of a more reliable value, a threshold chloride concentration of 0.06% total chloride by mass of concrete may be used.

4 APPLICATIONS TO DURABILITY ASSESSMENT

4.1 Delineation of exposure period

To demonstrate the applications of chloride ion diffusion model, examples of durability assessment are presented hereunder. At the outset, to duly consider the time-variations of chloride diffusivity of concrete and surface chloride concentration in the analysis, the entire duration of chloride exposure is delineated into distinct time periods with different diffusion conditions. Figure 1 illustrates the delineation of exposure period, namely: a) period 1 (up to time t_I) during which the surface chloride concentration increases and diffusivity decreases; b) period 2 (up to time t_{II}) during which the surface chloride concentration is constant and diffusivity decreases; and c) period 3 during which the surface chloride concentration and diffusivity are both constant.

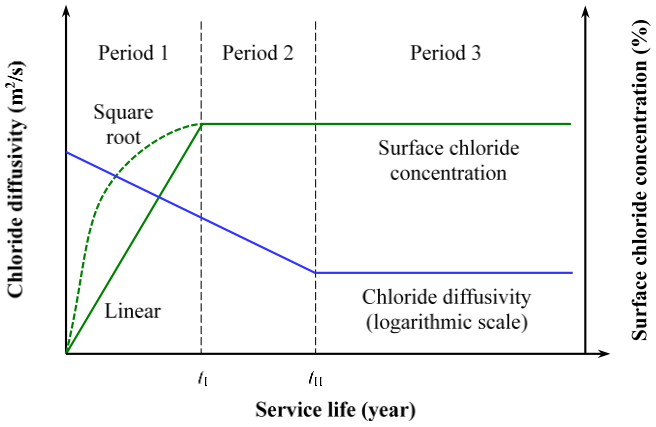


Figure 1: Delineation of exposure period

Equations (13) and (16) are applicable to period 1 but not to subsequent periods. Instead, in period 2, an equivalent exposure time for period 2 ($t_{eq\wedge I}$) having a similar profile at the joint time with Period 1 is introduced: $t_{eq\wedge I} = t_e - \Delta t_{eq\wedge I}$, where $\Delta t_{eq\wedge I}$ is the time difference between period 2 and period 1 with matching chloride profiles (year). With a linearly increasing surface chloride concentration during period 1, the chloride concentration in period 2 is given by:

$$C'_{II} = C_0 + k_1 t_I erfc\left[\frac{(X-\Delta X)\sqrt{1-m}}{2\sqrt{D_r t_r^m\left[(t_e+t_{e0})^{1-m}-(\Delta t_{eq\wedge I}+t_{e0})^{1-m}\right]}}\right] \tag{25}$$

On the other hand, with a square root increasing surface chloride concentration during period 1, the chloride concentration in period 2 is given by:

$$C''_{II} = C_0 + k_2 t_I^{0.5} erfc\left[\frac{(X-\Delta X)\sqrt{1-m}}{2\sqrt{D_r t_r^m\left[(t_e+t_{e0})^{1-m}-(\Delta t_{eq\wedge I}+t_{e0})^{1-m}\right]}}\right] \tag{26}$$

Likewise, in period 3, an equivalent exposure time for period 3 ($t_{eq\wedge II}$) having a similar profile at the joint time with period 2 is introduced: $t_{eq\wedge II} = t_e - \Delta t_{eq\wedge II}$, where $\Delta t_{eq\wedge II}$ is the time difference between period 3 and period 2 with matching chloride profiles (year). With a linearly increasing surface chloride concentration during period 1, the chloride concentration in period 3 is given by:

$$C'_{III} = C_0 + k_1 t_I erfc\left[\frac{(X-\Delta X)\sqrt{(t_{II}+t_{e0})^m}}{2\sqrt{D_r t_r^m\left(t_e-\Delta t_{eq\wedge II}\right)}}\right] \tag{27}$$

On the other hand, with a square root increasing surface chloride concentration during period 1, the chloride concentration in period 3 is given by:

$$C'_{III} = C_0 + k_2 t_I^{0.5} erfc\left[\frac{(X-\Delta X)\sqrt{(t_{II}+t_{e0})^m}}{2\sqrt{D_r t_r^m\left(t_e-\Delta t_{eq\wedge II}\right)}}\right] \tag{28}$$

4.2 Service life design of highway tunnel

The first example is the service life design of a highway tunnel with reinforced concrete box structure. The concrete has design strength grade of C40. Two mix compositions are considered in the design stage: Mix A which contains 20% pulverized fuel ash by mass as cement replacement; and Mix B which contains 30% ground granulated blastfurnace slag by mass as cement replacement. The slabs and walls have thickness of 400 mm and the cover to reinforcement is 50 mm except for particular sections of the top slab where the cover is 40 mm. The threshold chloride concentration is taken as 0.06%. The following assumptions are made: a) the surface chloride concentration increases linearly from initial value of 0.01% at start of exposure with 0.018% gradient throughout a build-up period of 3 years; b) the chloride diffusivity decreases with time from value of 5.6×10^{-12} m^2/s for Mix A and 3.7×10^{-12} m^2/s for Mix B at age of 28-day up to an age of 25 years; and c) the instantaneous age factor *m* for Mix A and Mix B are respectively 0.360/s and 0.371/s. The design life of the tunnel is 100 years and the model predicts the chloride diffusion at 90-year of age, i.e. a corrosion propagation period of 10 years is considered. Figure 2 depicts the assessment results. Both concrete mixes are satisfactory in terms of durability performance. It can be seen that at 90-year age, the threshold chloride concentration reaches only circa 5 to 6 mm and there is no risk of corrosion with a concrete cover of 40 or 50 mm.

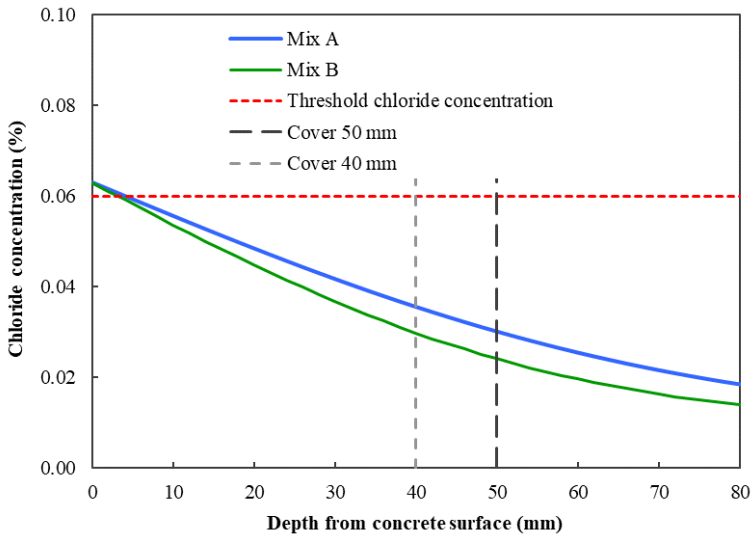


Figure 2: Chloride modelling for different concrete mixes

4.3 Service life checking of temporary haul tunnel

The second example is a temporary haul tunnel of reinforced concrete box structure. The concrete is an ordinary Portland cement concrete mix of grade C40 and the value of *m* is taken as 0.2. The cover to reinforcement is 45 mm. The threshold chloride concentration is taken as 0.06%. The following assumptions are made: a) the surface chloride concentration increases in square root manner from initial value of 0.005% at start of exposure throughout a build-up period of 7.5 years; b) the gradient of square root increasing surface chloride concentration k_2 is 104.46×10^{-6} $/s^{0.5}$; and c) the chloride diffusivity decreases with time from value of 3×10^{-12} m^2/s at age of 56-day up to an age of 25 years. The design life of the temporary tunnel is 30 years and the age of modelling is 24 years to check and identify any risk of corrosion in the remaining years of usage. Figure 3 depicts the assessment results. It can be seen that the depth of threshold chloride concentration reaches circa 28 mm and there is no risk of corrosion with a concrete cover of 45 mm.

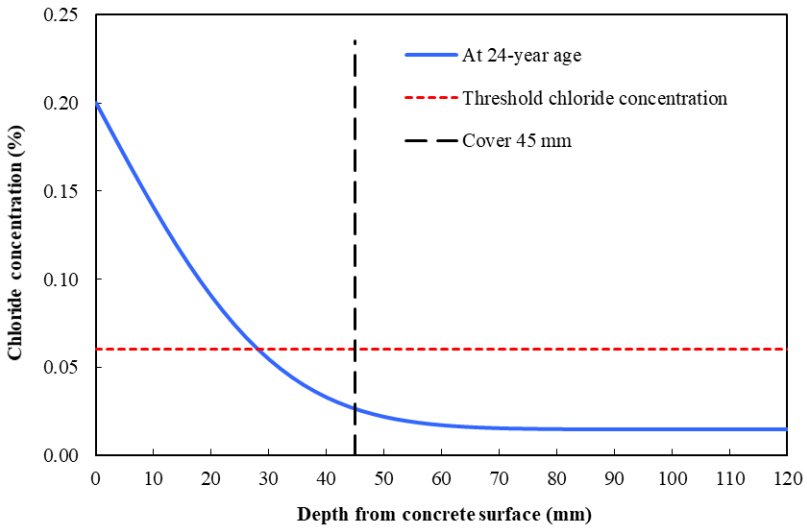


Figure 3: Chloride modelling for temporary haul tunnel

5 CONCLUSIONS

In this paper, analytical models of chloride ion diffusion have been devised, with explicit formulations to account for the effects of time-variation of chloride diffusivity of concrete, time-variation of surface chloride concentration, and temperature. The accuracy of the analytical models is highly dependent on the model input. Experimental measurements to establish the chloride diffusivity of concrete by way of migration cell experiment, accelerated chloride penetration, non-steady-state migration experiment, and rapid chloride permeability test have been outlined. Examples of durability assessment of reinforced concrete tunnels are presented to demonstrate the applications of the chloride diffusion model.

APPENDIX

A.1 Error function

The error function, denoted by *erf*, is defined as:

$$erf(z) = \frac{2}{\sqrt{\pi}} \int_0^z e^{-t^2} dt \qquad \text{(A1)}$$

Mathematically, the error function represents the area under the Gaussian probability density function $2e^{-t\wedge 2}/(n)^{0.5}$ for $t \in [0, z]$, where $erf(\infty) = 1$. The complementary error function, denoted by *erfc*, is defined as:

$$erfc(z) = 1 - erf(z) = \frac{2}{\sqrt{\pi}} \int_z^\infty e^{-t^2} dt \qquad \text{(A2)}$$

There exist various numerical approximations of the error function, for example:

$$erf(z) \approx 1 - \frac{1}{\sqrt{\pi} z} e^{-z^2} \qquad \text{(A3)}$$

A.2 Volhard titration

The methodology and procedures of Volhard titration are detailed in NT Build 208 (Nordtest 1996). To start with, the concrete sample is ground to < 0.1 mm particle size. Approximately 5 g of ground sample is placed

into a glass bottle and dried at 105°C and weighed. Distilled water and concentrated nitric acid are added respectively to the bottle and shaken. The solution is then filtered and rinsed twice with 1% nitric acid. Silver nitrate ($AgNO_3$) solution is added in excess from the burette, followed by 2 to 3 ml of benzyl alcohol (C_7H_8O) or nonanol ($C_9H_{20}O$) and 1 ml of saturated ammonium ferri-sulphate solution ($NH_4Fe(SO_4)_2 \times 12H_2O$). A stopper is then inserted to the bottle followed by vigorous shaking to separate the silver nitrate. The remaining amount of silver nitrate is titrated with ammonium thiocyanate solution (NH_4SCN) with intensive mixing until the solution attains a permanent weakly red colour (formation of $FeSCN^{2+}$). The chloride ion content is determined from the silver ion content minus the thiocyanate ion content.

REFERENCES

AASHTO 2007. *Standard Method of Test for Electrical Indication of Concrete's Ability to Resist Chloride Ion Penetration*. *AASHTO T 277*, American Association of State Highway and Transportation Officials, Washington DC, USA.

Angst, U. & Vennesland, Ø. 2009. Critical chloride content in reinforced concrete – state of the art. In M.G. Alexander, H.-D. Beushausen, F. Dehn & P. Moyo (ed.), *Concrete Repair, Rehabilitation and Retrofitting II: Proceedings, 2nd International Conference on Concrete Repair, Rehabilitation and Retrofitting*. *Cape Town, 24-26 November 2008*. Taylor & Francis Group: 311-317.

Bamforth, P. 2004. *Enhancing Reinforced Concrete Durability*. *Technical Report 61*, Concrete Society, Surrey, UK.

Buildings Department 2013. *Code of Practice for Structural Use of Concrete*. Buildings Department, Hong Kong.

CEN (European Committee for Standardization) 2013. *EN 206: Concrete - Specification, Performance, Production and Conformity*. European Committee for Standardization, Brussels.

CEN (European Committee for Standardization) 2023. *EN 1992: Eurocode 2 - Design of Concrete Structures: Part 1-1: General Rules and Rules for Buildings, Bridges and Civil Engineering Structures*. European Committee for Standardization, Brussels.

Crank, J. 1975. *The Mathematics of Diffusion*. Clarendon Press, London, UK.

Freedman, D. 1983. *Brownian Motion and Diffusion*. Springer-Verlag, New York, USA.

Gjørv, O.E. 2014. *Durability Design of Concrete Structures in Severe Environments*. Second edition. CRC Press, Boca Raton, USA.

Hooton, R.D. 2014. Achieving concrete durability for specified service-life in chloride exposures. In S.O. Ekolu, M. Dundu & X. Gao (ed.), *Construction Materials and Structures: Proceedings of the First International Conference on Construction Materials and Structures*. *Johannesburg, 24-26 November 2014*. IOS Press: 3-15.

Hooton, R.D., Pun, P., Kojundic, T. & Fidjestol, P. 1997. Influence of silica fume on chloride resistance of concrete. In L.S. Johal (ed.), *Proceedings of International Symposium on High-Performance Concrete*. *New Orleans, 20-22 October 1997*. Precast/Prestressed Concrete Institute: 245-249.

Japan Society of Civil Engineers 1999. *Standard Specification for Design and Construction of Concrete Structures*. Japan Society of Civil Engineers, Tokyo.

Laidler, K.J. 1984. The development of the Arrhenius equation. *Journal of Chemical Education*, 61(6): 494-498.

Mauro, J.C. 2021. *Materials Kinetics: Transport and Rate Phenomena*. Elsevier, Amsterdam, Netherlands.

Mehta, P.K. & Monteiro, P.J.M. 2014. *Concrete: Microstructure, Properties, and Materials*. Fourth edition. McGraw-Hill Education, New York, USA.

Nordtest 1996. *NT Build 208: Concrete, Hardened: Chloride Content by Volhard Titration*. Nordic Council of Ministers, Espoo.

Nordtest 1997. *NT Build 355: Concrete, Mortar and Cement-based Repair Materials: Chloride Diffusion Coefficient from Migration Cell Experiments*. Nordic Council of Ministers, Espoo.

Nordtest 1995. *NT Build 443: Concrete, Hardened: Accelerated Chloride Penetration*. Nordic Council of Ministers, Espoo.

Nordtest 1999. *NT Build 492: Concrete, Mortar and Cement-based Repair Materials: Chloride Migration Coefficient from Non-steady-state Migration Experiments*. Nordic Council of Ministers, Espoo.

Page, C.L., Shott, N.R. & El Tarras, A. 1981. Diffusion of chloride ions in hardened cement pastes. *Cement and Concrete Research*, 11(3): 395-406.

Shi, C.J., Yuan, Q., He, F.Q. & Hu, X. 2020. *Transport and Interactions of Chlorides in Cement-based Materials*. CRC Press, New York, USA.

Spiechowicz, J., Marchenko, I.G., Hänggi, P. & Łuczka, J. 2023. Diffusion coefficient of a Brownian particle in equilibrium and nonequilibrium: Einstein model and beyond. *Entropy*, 25(1): 42.

Tang, L. & Gulikers, J. 2007. On the mathematics of time-dependent apparent chloride diffusion coefficient in concrete. *Cement and Concrete Research*, 37(4): 589-595.

Tang, L. & Nilsson, L.-O. 1992. Chloride diffusivity in high strength concrete at different ages. *Nordic Concrete Research*, 11(1): 162-171.

Wang, J., Ng, P.L., Wang, W.S., Du. J.S. & Song, J.Y. 2017. Modelling chloride diffusion in concrete with influence of concrete stress state. *Journal of Civil Engineering and Management*, 23(7): 955-965.

Wang, J., Ng, P.L., Su. H. & Du, J.S. 2019. Meso-scale modelling of stress effect on chloride diffusion in concrete using three-phase composite sphere model. *Materials and Structures*, 52(3): 55.

Wang, J., Ng, P.L., Su, H. & Du, J.S. 2020. Influence of the coupled time and concrete stress effects on instantaneous chloride diffusion coefficient. *Construction and Building Materials*, 237: 117645.

Zhou, S. 2014. Modelling of chloride diffusion with linear increase of surface chloride concentration. *ACI Materials Journal*, 111(5): 483-490.

Zhou, S. 2016. Analytical model for square root increase of surface chloride concentration and decrease of chloride diffusivity. *Journal of Materials in Civil Engineering, ASCE*, 28(4): 04015181.

Zhou, S. 2018. Relationships of diffusivities and age factors between analytical and empirical chloride models for decreasing diffusivities. In T.B. Sui, T.C. Holland, Z.M. Wang & X.L. Zhao (ed.), *Proceedings of 14th Conference on Recent Advances in Concrete Technology and Sustainability Issues*. *Beijing, 28 October-2 November 2018*. *ACI Special Publication, SP-330*, American Concrete Institute: 55-66.

Effects of Vibration due to Piling in Proximity of MTR Structure and Mitigation Measures

Shawn Y.T. Shang
Ove Arup & Partners Hong Kong Ltd, Hong Kong
Y. Chen
China State Construction International Holdings Ltd.

ABSTRACT

Excavation and Lateral Support (ELS) techniques have been widely adopted in Hong Kong, where limited space and high population density necessitate innovative construction methods. Pile wall installation along the perimeter or within the site area for ELS works serves as common construction practice but invariably generates vibrations. Energy originates from the pile driver would cause the vibration of piles during the driving or installation process. Due to the interaction between pile and the surrounding soils, vibrations are transferred at the interface between pile and soil, and finally propagates through the ground, leading to vibration of ground and existing structures.

The primary objective of this technical paper is to present vibration measurements during pile installation for temporary ELS retaining structure as well as permanent foundation and discuss the measures of mitigation for its influence on nearby buildings and MTR structures. It focuses on a specific case of ELS in Hong Kong, providing a detailed study based on actual site records, field experiments, and in-situ documentation of works.

Additionally, the paper will draw upon other projects with vibration measurements to summarize the relationship between vibration and distance from the pile installation with consideration of various factors including ground conditions, pile type, ring bit size and piling methods, contributing to a deeper understanding of vibration-induced piling works. The study aims to offer valuable insights and precedents to engineering practitioners and researchers regarding vibration effects and corresponding mitigation measures.

Key words: Vibration; Peak Particle Velocity; Pile Installation; Excavation and Lateral Support; Underground Structure; Mitigation Measures

1 INTRODUCTION

The proposed development is located at Central, Hong Kong, which comprises a 34-storey building with a single-level basement, reaching a height of approximately 153m. The site has approximate dimensions of 54m × 18m, with a total excavation depth of around 7.8m. The foundation works consists of 11 numbers of large dimeter bored piles. The site was previously occupied by Tak Shing House, which had an existing basement and was supported by pile foundation. The presence of the existing basement and foundation posed a significant challenge for the construction of the temporary retaining wall, permanent foundation, and basement of the new development. This site was also surrounded by One Chinachem Central building to the north, Des Voeux Road to the east, Wheelock House to the south, and Pedder Building to the west. The Pedder Building is a Grade I Historical Building. Additionally, the site falls within Scheduled Area No. 3 under the Building Ordinance. MTR Central Station Exits C and D, along with the island line tunnel, are in close proximity to the south and east of the site. The site location plan, including adjacent buildings and the MTR station, is displayed in Figure 1.

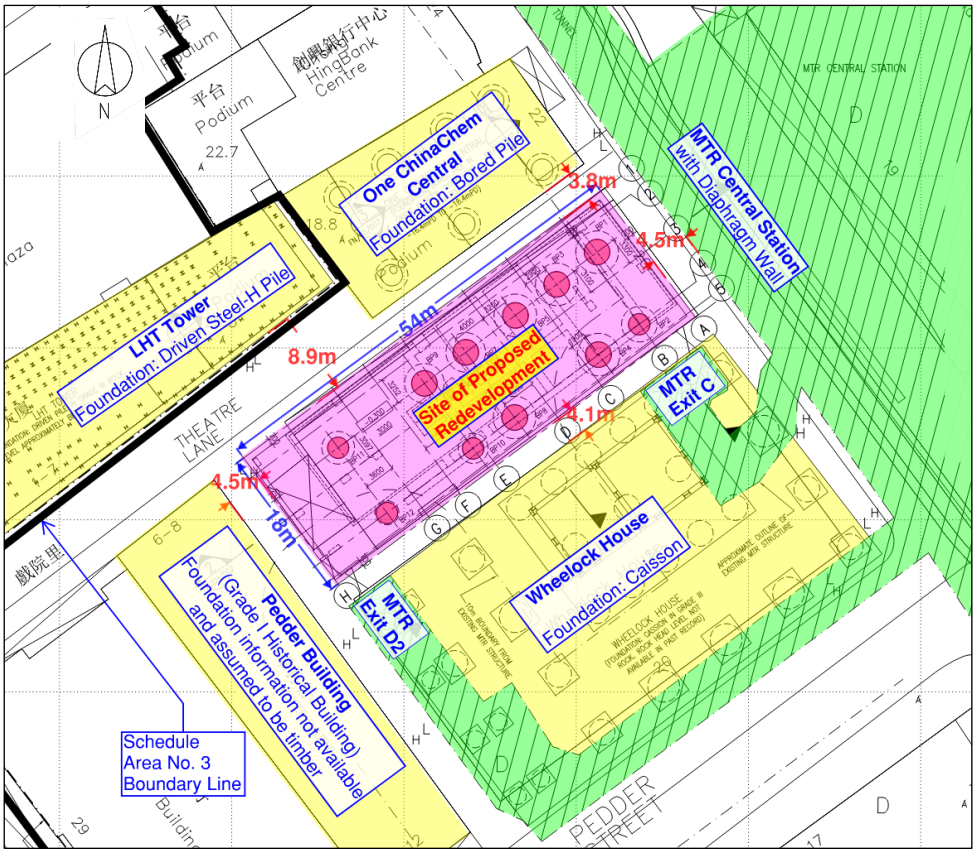


Figure 1: Site Location Plan

2 GROUND CONDITIONS

The ground investigation (GI) revealed that the geology of the site comprises fill, marine deposit, alluvium, completely/highly decomposed granite, and moderately/slightly decomposed granite. The geological condition is summarized in Table 1.

Table 1: Summary of Soil and Rock at Different Depths

Soil Material	Thickness (m)
Fill	4.0 to 6.1
Marine Deposit	2.0 to 8.0
Alluvium	2.0 to 8.0
Completely/Highly Decomposed Granite	3.1 to 9.0

The rockhead level of grade III or better rock generally varies from approximately -19.4mPD in the Northeast of the site to approximately -14.8mPD at the Southwest side. According to the groundwater monitoring record, the highest measured groundwater level is +2.940mPD.

3 DESIGN CONISDERATIONS

Laboratory tests were conducted on soil samples which were obtained from the GI works to determine the cohesion (c') and friction angle (φ'). The SPT N-values extracted from the vertical drillholes were utilized to estimate the elastic soil modulus. The effective soil stiffness, E (kPa), was calculated based on $E = f \times N \times 1000$, where the factor f ranges from 1.0 to 2.0 based on the soil type (Chan, 2003). In this project, f was conservatively assumed to be 1.0. A summary of the geological design parameters is presented in Table 2.

Table 2: Summary of Geotechnical Design Parameters

Soil	Unit Weight (kN/m^3)	Cohesion, c' (kPa)	Friction Angle, φ' (°)	SPT N Value Range	Adopted E (kPa)	Incremental E (kPa/m)
Fill	18	0	34	13-15	11,000	-
Marine Deposit	18	0	33	10-21	14,000	-
Alluvium (Sand)	19	0	36	10-53	18,000	-
CDG/HDG	19	5	36	20-200	27000 / 45000	7200 / 15400

The major constraints of the site were summarized as follows:
(1) The presence of weathered rock, corestones, and the existing basement wall near complicates the pile installation within the site;
(2) The requirements of the maximum pressure change (<20 kPa according to PNAP-APP24) and the maximum displacement for nearby historic building (with shallow foundation) and MTR structure pose additional challenges during pile installation works.

4 PROPOSED FOUNDATION AND ELS SCHEME

4.1 Foundation of Proposed Development

The proposed foundation system consisted of 11 numbers of large diameter bored piles varying from 2.5m to 3m in diameter, with founding level at Category 1(c) rock according to the Code of Practice for Foundations 2017.

4.2 Peripheral Wall and Construction Sequence of Basement

The proposed ELS works was to facilitate the construction of the pile cap, basement and superstructure. The general excavation level at Zone A, B and C was -3.5mPD, -2.5mPD and -5.2mPD respectively.

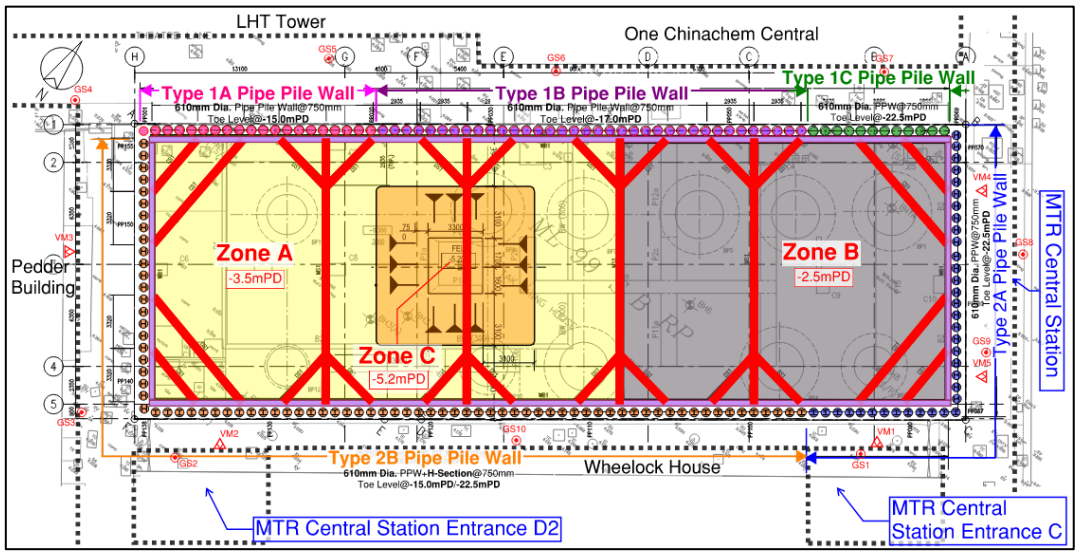


Figure 2: Proposed ELS Scheme – 610mm dia. Pipe Pile Wall and Three Layers of Struts

The excavation was supported by a CHS 610 x 30 pipe pile wall with a 305x305x283 UC at 750mm centres along the perimeter facing the MTR station, Wheelock House and Pedder Building whereas a CHS 610mm x 15.9mm pipe pile wall was proposed abutting the One Chinachem Central and LHT Tower. Grout curtain was proposed to provide the hydraulic cut-off. A total of three layers of steel shoring at levels +3.7mPD, +1.85mPD and -0.7mPD were proposed. A 200mm thick concrete propping slab was formed at the bottom of excavation for lateral support during removal of shoring and before cast of pile cap/basement.

5 VIBRATION ASSESSMENT IN DESIGN

Ground vibrations resulting from pile installation is a process of complex soil-structure interaction. Energy originates from the down-the-hole hammer during the drilling process would cause the vibration of piles during

the installation process. Due to interaction between pile and surrounding soils, vibrations are transferred at the interface between pile and soil, and finally propagates through the ground, leading to vibration of the ground and the existing structures.

Wiss (1967) suggested that the magnitude of vibration was affected by the amount of energy, energy loss, soil properties and distance between source of vibration and the receiver. He suggested that the peak particle velocity (PPV) was a function of the square root of the hammer energy. Attewell and Farmer (1973) proposed the first empirical equation and suggested that the PPV was given according to the following equation. From filed measurements, they claimed that the results correlate quite well if k=1 and x=1. However, they suggested that k=1.5 should be used for practical conservative prediction of ground vibrations due to pile driving. The parameter k and x were discussed by many researchers to address the application of the empirical equation considering the effect of soil properties, pile types, source type, geometrical and material damping (Wiss, 1981; Attewell et al., 1992a; Wiss 1967; Hiller and Crabb, 1998).

$$PPV = k\left(\frac{\sqrt{W}}{r}\right)^{x} \quad (1)$$

where

PPV	Peak particle velocity
k	Empirically determined constant
W	Input energy
x	Empirically determined index

In this study, the PPV is estimated based on BS 5228-2:2009, TRL Report 429 (ASD SEB - PL 13, Section 5.2), and UK Transport Research Laboratory. Hiller et al. (2000) conducted specific ground vibration measurements for different construction equipment and process at a wide range of distances, and different types of ground conditions. The proposed empirical equation is widely used as the basis of construction vibration prediction. The following empirical equation as extracted from BS 5228-2 can be adopted to analyze the PPV due to pipe pile wall installation in Hong Kong according to Code of Practice for Foundation 2017:

$$PPV = k_p\left(\frac{\sqrt{W}}{r^{1.3}}\right) \quad (2)$$

$$W = W_h \times H \times \beta \quad (3)$$

$$\beta = K \times n \quad (4)$$

where

PPV	Peak particle velocity (mm/s)
k_p	Ground borne vibration coefficient
W	Hammer energy to pile, in joules (J)
r	Distance between source of vibration and the receiver (m)
W_h	Weight of hammer
H	Drop height (m)
β	Overall energy transfer
K	Hammer efficiency
n	Energy transfer from hammer head to pile

According to BS 5228-2: 2009, Hiller et al. (2000) proposed several empirical equations to predict the resultant peak particle velocities (PPV). Among several empirical predictors for ground-borne vibration arising from mechanized construction works, Equation (2) would be suitable for piling operation in this study. For other mechanized construction works such as vibratory compaction (steady state), vibratory compaction (start up and rundown), vibratory piling, dynamic compaction and tunnelling, other empirical equations would be more suitable. In this study, the pipe pile is installed by concentric ring bit drilling system, which reduces disturbance due to better air-flow and minimizes overbreak with specification of minimum advancement rates. The down-the-hole (DTH) hammer makes strokes within driver bit to have ring and casing penetrate through ground and

it indicates that the mechanized construction works undergoes a process of percussive piling and the empirical equation is only affected by scaling factor k_p, nominal hammer energy W, distance between the vibration source and the receiver.

The scaling factor k_p is affected by the pile toe location, pile length, and ground conditions. Specifically, if piles are driven to refusal, the suggested value of k_p is 5. For piles not at refusal, the value of k_p is 3 if pile toe is driven through very stiff cohesive soils, dense granular soils, fill containing obstructions which are large relative to the pile cross-section. The value of k_p is 1 if pile toe is driven through soft cohesive soils, loose granular soils, loose fills, and organic soils (Hiller *et al*., 2000; BS 5228-2:2009). In this study, the scaling factor k_p is to be compared between values specified in table from Hiller *et al.*, 2000 and those calculated from back-analysis.

The exponent of 1.3 in the equation represents the power-law attenuation term for estimating peak particle velocity (PPV) as vibrations propagate from the source to the measurement point. This exponent is specific to the TRL (Transport Research Laboratory) reported by Hiller and Crabb (2000) and was derived based on empirical observations and measurements. The choice of the exponent value in the attenuation term depends on the nature of the source, the characteristics of the propagation medium (such as soil or rock), and the distance between the source and the measurement point. The exponent value is typically determined through field measurements and analysis of vibration data collected from different projects. The specific value of 1.3 in this equation indicates that the vibrations attenuate with distance in a manner where the amplitude decreases faster than a linear relationship (exponent of 1.0). In other words, as the distance (r) increases, the effect of the vibrations diminishes more rapidly due to factors such as energy dissipation and scattering in the propagation medium. It's important to note that the choice of the exponent can vary depending on the specific conditions and characteristics of the vibration sources and propagation paths. Different studies or reports may adopt different exponent values based on their specific observations and analysis.

While it is widely accepted that the vibration magnitude due to impact piling increases with increasing driving energy, there are insufficient database of different types of hammers to verify the relation in Hong Kong local practice. It is suggested to improve the database by analyzing the correlation between PPV and $\sqrt{W}/r^{1.3}$ considering the effect of ground conditions, levels of vibration, pile types, hammer types, etc.

In this study, two pipe piles (PP073 and PP090) were used to analyze vibration due to pile installation. Table 3 outlines the detailed calculation of the Peak Particle Velocity (PPV) for the proposed project for PP073 and PP090. The distance (r) between the vibration source and the receiver was approximately 4.6 meters. The scaling factor (k_p) was influenced by the depth of the pipe pile and was linked to the Standard Penetration Test (SPT) N value. Specifically, k_p was set at 1.0 for SPT N values below 80, at 1.5 for values above 80, and at 3.0 when the pipe pile reached the rock head level. Regarding the hammer efficiency coefficient (K), a value of 0.7 is assumed for the power machine being used (Poulos and Davis, 1980). The Hammer weight (W_h) was specified at 0.998 tons as per the manufacturer's catalogue and the maximum drop height was 0.2 meters according to piston stroke (≤ 200mm) in specification of DTH. The energy transfer factor was taken to be 0.7 (McCabe and Flynn, 2017) as well as typical value from 0.7 to 1 in GEO Publication No.1/2006 based on general Hong Kong experience. With these parameters in place, peak particle velocities at different receiver levels were computed.

Table 3: Vibration Assessment for Pipe Pile Construction

Critical Case	Sensitive Receiver ntified building/ structure/ utility)	Plan distance between pipe pile and sensitive receiver (m)	Reciever Level (mPD)	r, slope distance between source and sensitive receiver (m)	Kp	Hammer type	Hammer weight, W_h (ton)	Max. drop height, H (m)	Hammer efficiency K	energy transfer factor η (efficiency of hammer blow)	Overall Energy Transfer (K x η)	W, hammer energy (KJ)	ppv (mms^{-1})
	MTR Central Station											<Modified Alarm Level 10 mm/s	
A1	Concentric ring bit drilling	4.550	+3.95	4.6	1.0	Piston	**0.998**	0.20	0.7	0.700	0.49	1.0	4.3
A2	Concentric ring bit drilling	4.550	+0.00	4.6	1.0	Piston	**0.998**	0.20	0.7	0.700	0.49	1.0	4.3
A3	Concentric ring bit drilling	4.550	-6.80	4.6	1.5	Piston	**0.998**	0.20	0.7	0.700	0.49	1.0	6.5
A4	Concentric ring bit drilling	4.550	-12.60	4.6	1.5	Piston	**0.998**	0.20	0.7	0.700	0.49	1.0	6.5
A5	Concentric ring bit drilling	4.550	-18.00	4.6	1.5	Piston	**0.998**	0.20	0.7	0.700	0.49	1.0	6.5
A6	Concentric ring bit drilling	4.550	-18.00	5.0	3.0	Piston	**0.998**	0.20	0.7	0.700	0.49	1.0	11.6

Pile installation in soil | Pile installation in corestone | Pile installation in rock

Refer to Piston Weight/Stroke in manufacturer's catalogue

<Modified Action Level 12.0 mm/s

6 IN-SITU MEASUREMENTS

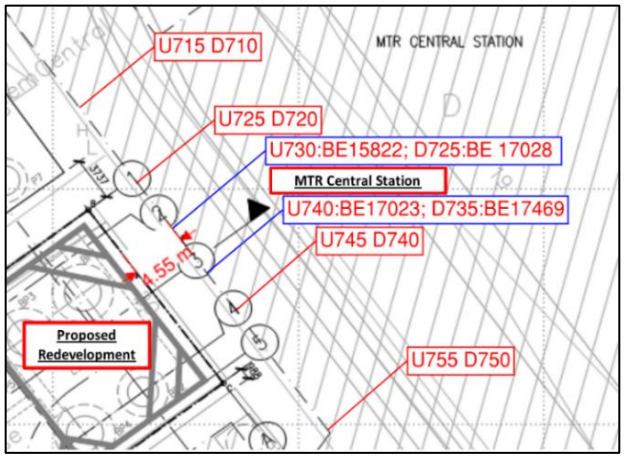


Figure 3: Vibration Monitoring along MTR Chainage



Plate 1: Vibration Sensor with Automatic Remote Data Transmission

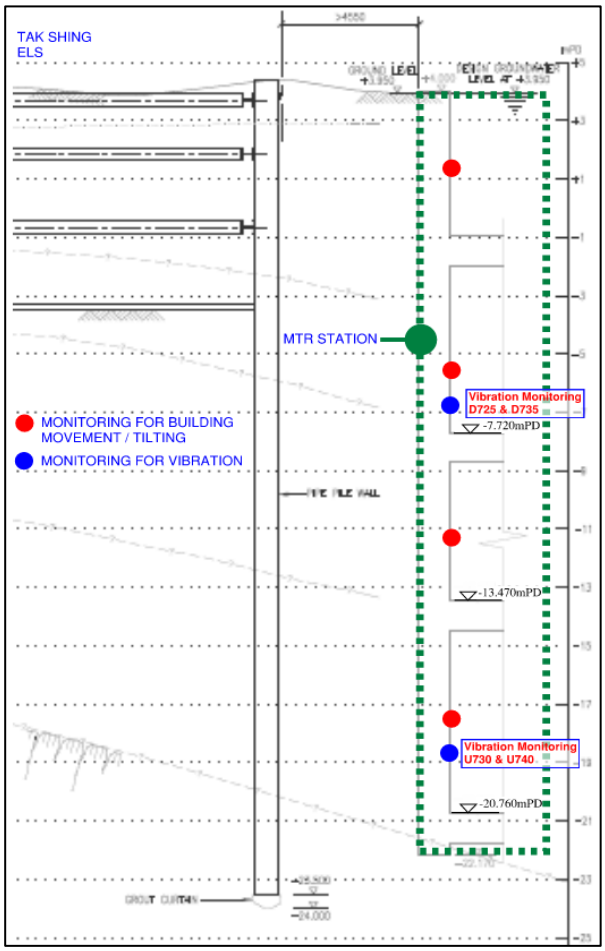


Figure 4: Location of Monitoring Checkpoints within MTR

Figure 3 illustrates the layout plan of the vibration monitoring points positioned along the MTR chainage. Figure 4 is a section plot showing the monitoring points' locations within the MTR station. For data analysis purposes, the vibration monitoring points D725, D730, D735, and D740 were used in this study. The elevations of points D725 and D735 were at -6.80mPD, while D730 and D740 were situated at -18.00 mPD. Additional information regarding the vibration sensors equipped with automatic remote data transmission can be found in Plate 1 for reference. It is worth noting that the pipe pile was embedded deeply into ground with toe level below Category 1(c) rockhead (~-22mPD), which is on purpose of preventing seepage resulted from high groundwater table (+2.94mPD) as well as controlling stress change during piling and excavation works within 20kPa (as required in PNAP APP-24).

6.1 Measured Vibration due to Foundation Installation

Due to the traditional methods and machinery adopted for installing large diameter bored pile (i.e. Hammer grabbing, Oscillator, RCD drillbit, Bell-out drillbit, etc), the vibration generated during foundation construction, according to vibration monitoring points on ground and within underground structure, was within tolerance and no larger than background vibration generated by pass-by vehicles and MTR train.

6.2 Measured Vibration due to Temporary Retaining Structure

Vibration during pile installation was closely monitored with different pile size, toe level, distance and ground conditions.

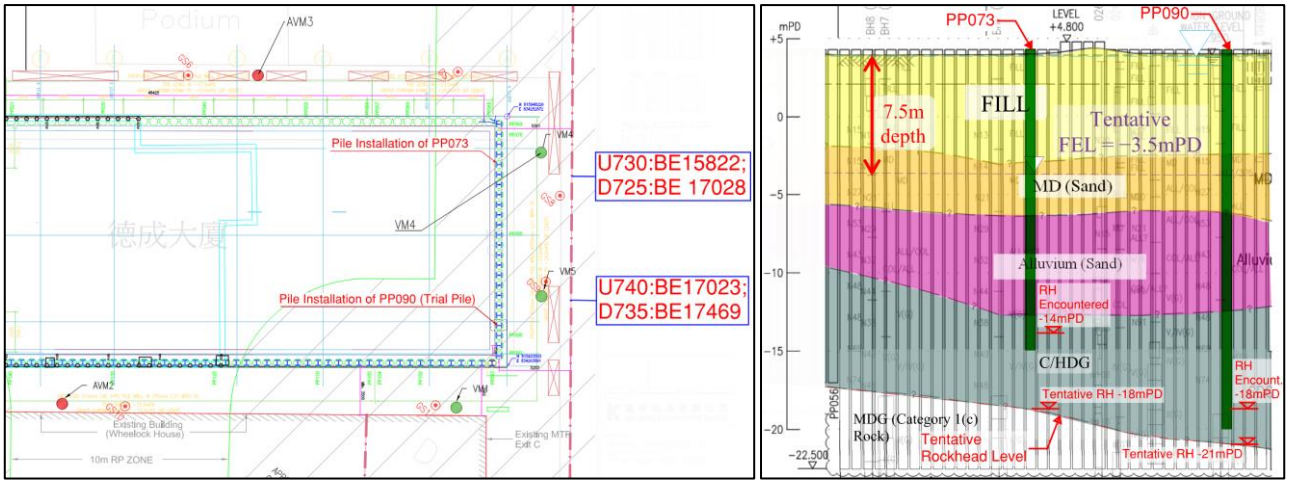


Figure 5: Location (Left) and Ground Conditions (Right) of PP073&090 for Vibration & Piling Level Relationship

Figure 5 shows the location of the pipe pile walls (PP073 and PP090) and the vibration monitoring points (VB-U730, VB-D725, VB-U740 and VB-D735). The receivers at VB-D725 and VB-D735 were situated at approximately -6.8mPD, while those at VB-U730 and VB-U740 were around -18.0mPD.

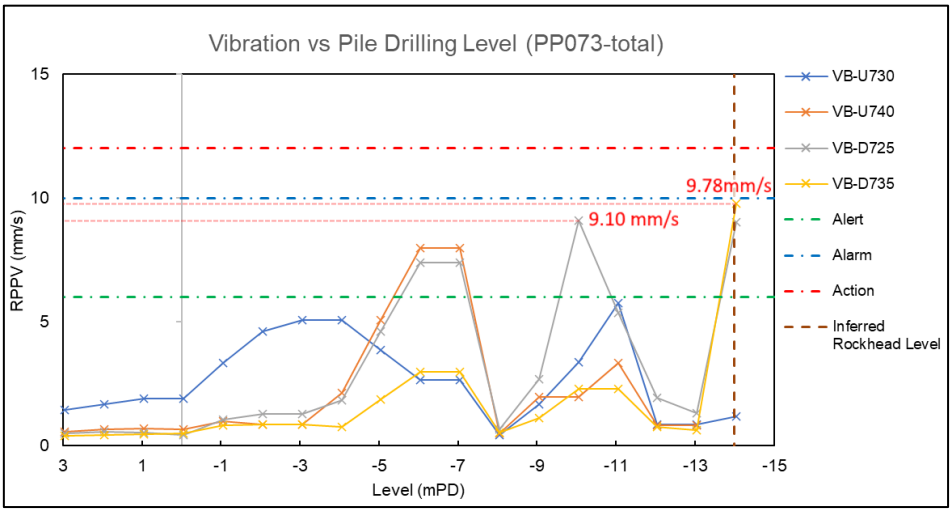


Figure 6: Vibration vs Piling Level for 610mm dia. PP073

Figure 6 illustrates the variation of PPV with the installation level during the piling works of PP073. The peak particle velocity for VB-D725 initially hit the alert level when the pipe pile was installed to around -6mPD, subsequently dropping to 0.5mm/s as the pipe pile was further driven to -8mPD. This could be attributed to the presence of hard materials (i.e. weathered rock, corestone, etc.) from -4.8mPD to -7mPD followed by a weak ground layer between -7.5mPD and -9.0mPD, with another potential weak layer between -12mPD and -13mPD following weathered rock/corestone near -10mPD. By referring to Figure 5 (Right) ground conditions and logging of nearby GI, it is found that soil stratum transits from MD composed of fine to coarse sand to Alluvium consisting coarse sand with subrounded fine gravel sized rock fragment at around -6mPD, which coincided abrupt increase of vibration measurement around same level. And similar case was obtained near -11mPD when geological layer changes from Alluvium to completely decomposed medium grained Granite. The peak particle velocities obtained from VB-D735 and VB-D725 as the pile approached rockhead near its founding level. It is worth noting that VB-U740 which is far away from PP073 also record drastic change of PPV during piling around -6mPD and the reason is likely due to vibration transmission within layer of corestone and between rock and MTR structure. Although the discrepancy is unavoidable, the plot is still valuable to provide a rough idea between the vibration and piling works and shall further our understanding regarding soil-pile interaction.

Figure 7 showcases the variation of peak particle velocity with the piling level during the piling activities of PP090, where a trial was carried out for evaluating the pile performance and vibration generated to nearby MTR

structure. The peak particle velocity for VB-U740 triggered the alert level as the pipe pile was driven to -9.0mPD, decreasing as the pile reached -13mPD. Meanwhile, the peak particle velocity for VB-D735 (12.45mm/s) reached and exceeded the action level at -18mPD, which was close to the tentative Category 1(c) rockhead level. The pile installation was ceased immediately.

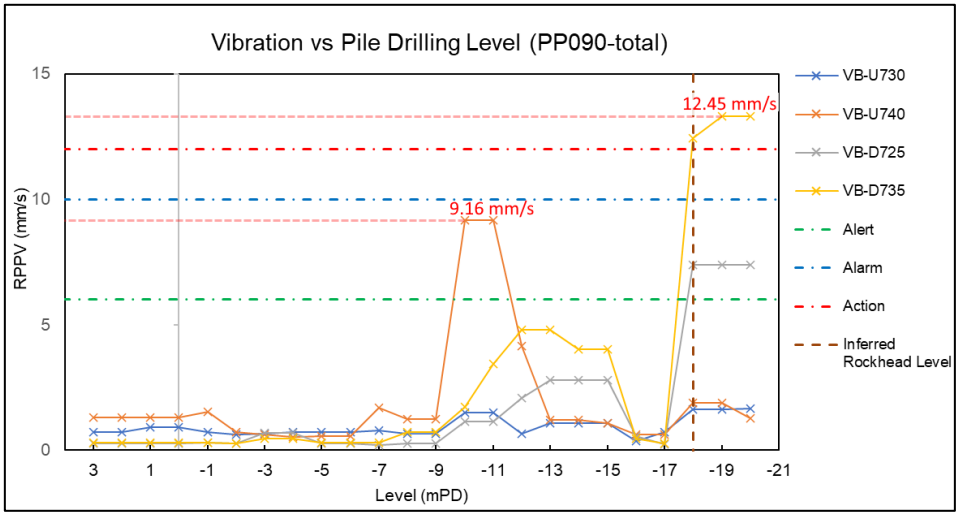


Figure 7: Vibration vs Piling Level for 610mm dia. PP090 (Trial Pile)

From Figure 6 and Figure 7, it can be observed that the Peak Particle Velocity (PPV) of receivers located far away from the pile remains more stable compared to those in close proximity to the vibration monitoring points. The increased fluctuation in PPV near the pile can be attributed to the presence of surface waves at the interface between the pile and the soils. The damping characteristics of the soils play a significant role in regulating energy transmission during piling activities, resulting in more uniform vibrations as the distance between the pile and monitoring receivers increases. Essentially, higher PPV levels near the pile are a result of surface waves interacting with the pile-soil interface. As the distance from the pile to the monitoring receivers increases, soil damping contributes to energy dissipation, leading to more stable vibration levels. This phenomenon stabilizes the magnitude and intensity of vibrations, as energy dissipates due to material damping and wave reflections across different ground layers.

Table 4: Correlation between Estimated Vibration and Actual Measurments

	ppv (mm/s)			Average Diff.	k_p (original)	k_p (back-calculated)
	Estimated	Actual (PP073)	Actual (PP090)			
vibration during pile installation in soil	4.3	4.62	3.45	-6%	1.0	1.0
vibration during pile installation in corestone	6.5	9.10	9.16	+41%	1.5	2.0
vibration during pile installation at rock	11.6	9.78	12.45	-4%	3.0	3.0

6.3 Assessment of effectiveness of Vibration Equation in Predicting in-situ Vibration

By comparing the estimated vibration with the in-situ measurements as shown in Table 4, the Equation (2) can be quite effective in predicting the vibration. However, effort needs to be further made in assuming appropriate values of W (with reference to manufacturer's catalogue, product specifications and project database) and k_p which would underestimate vibration level without appropriate verification by back analysis.

7 MITIGATION MEASURES

In response to the vibration monitoring point VB-D735 reaching the action level, mitigation measures were implemented to manage the vibration stemming from pile installation activities. From practical experience, adjustments were made to the dimensions of the pipe pile wall and the founding level to minimize vibration during the construction of the wall. Specifically, for PP057 to PP068, the pipe sizes were altered with CHS 610x30.0 (outer) + CHS 323x16.0 (inner) in replacement of the initial size CHS 610x15.9, with the toe levels of outer 610mm pile terminating at -15.0mPD and inner 323mm pile extending to -22.5mPD, where the bending moment was smaller than portion above, to mitigate vibration concerns. For PP069 to PP104, similar tube-in-tube pile wall was proposed to replace the CHS 610x30.0 with H-section, with the 610mm pile tentative founding levels at -15.0mPD and 323mm pile founded at -22.5mPD.

Figure 8 displays the vibration monitoring data of PP088 after taking mitigation measures, showcasing the effects of the modified pipe pile sizes and founding levels. Notably, VB-U740, VB-D725, and VB-U730 did not reaches the alert levels. However, VB-D735 did trigger an alert with a maximum peak particle velocity reaching up to approximately 7.6mm/s, possibly due to local hard materials. Comparing the PPV for VB-U740, VB-D735, and VB-D725 with those in Figure 7, the proposed mitigation measures are effective to control the ground vibration. It should be mentioned that the reduction of the pipe pile wall size could reduce the cross-section area of the interface between the soil and the pipe pile wall, contributing to reduction of the vibration.

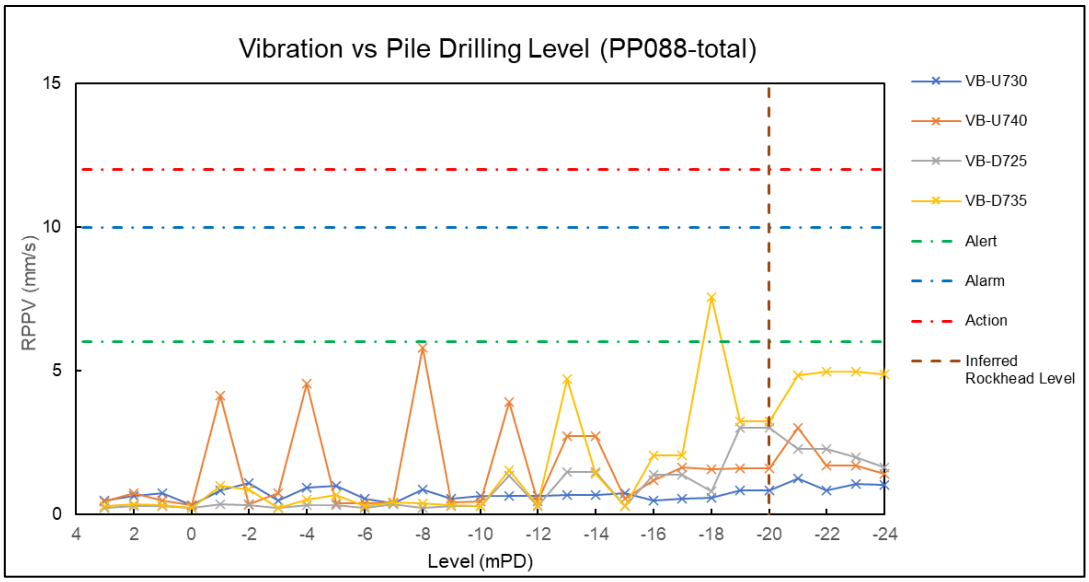


Figure 8: Vibration vs Piling Level for 323mm dia. PP088 (Trial Pile)

The pipe pile wall size and tentative founding level before and after taking mitigation measures are presented in Figure 9.

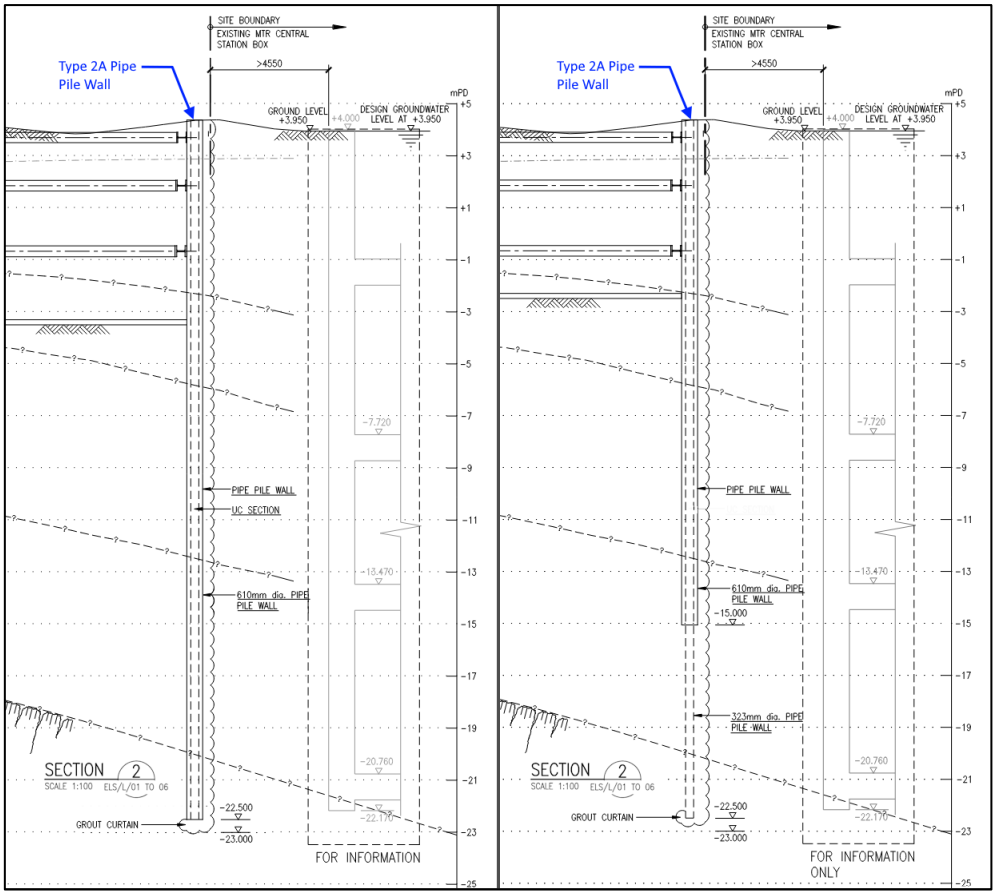


Figure 9: Change of Pile Wall from Casing with H-section (Left) to Tube-in-tube (Right)

8 REFERENCE TO OTHER PROJECTS WITH VIBRATION MEASUREMENTS

8.1 Case 1 – Project at Northwestern Hong Kong in adjacent to MTR

One project which can be referred to for the relationship between piling works and vibration is at northwestern area of Hong Kong. With sheetpiling works being carried out about 10m away from MTR rail track, the PPV of vibration monitoring is at 2.94 mm/s.

$$PPV = k_p \left(\frac{\sqrt{W}}{r^{1.3}} \right) \quad (2)$$

$$W = W_h \times H \times \beta \quad (3)$$

$$\beta = K \times n \quad (4)$$

where

PPV	Peak particle velocity (mm/s)
k_p	Ground borne vibration coefficient
W	Hammer energy to pile, in joules (J)
r	Distance between source of vibration and the receiver (m)

By assuming k_p at 1.0 for soil at ground (SPT N < 80) with hammer weight of 1 ton (W_h) to be dropped from 0.5m height (H),

Overall energy transfer:
$\beta = K \times n = 0.7 \times 0.7 = 0.49$

Hammer energy to pile, in joules (J):
$W = W_h \times H \times \beta = (1000 \times 9.81) \times 0.5 \times 0.49 = 2403$ J

Peak particle velocity (assumed $k_p = 1.0$):

$$PPV = k_p \left(\frac{\sqrt{W}}{r^{1.3}}\right) = 1.0 \times \left(\frac{\sqrt{2403}}{10^{1.3}}\right) = 2.46\, mm/s$$

The estimated PPV basing on Energy Equation is 16% smaller than the actual measurement (2.94 mm/s). And that is likely due to our adopting k_p lower than actual coefficient. Therefore, by re-adjusting k_p to 1.2 in comparing estimated results with field measurements,

Peak particle velocity (back-calculated $k_p = 1.2$):

$$PPV = k_p \left(\frac{\sqrt{W}}{r^{1.3}}\right) = 1.2 \times \left(\frac{\sqrt{2403}}{10^{1.3}}\right) = 2.95\, mm/s$$

The difference between actual measurement and estimated one basing on back analysis (0.2%) is considered satisfactory. Hence, the k_p value equal to 1.2 shall be adopted for vibration estimation under such ground conditions and construction arrangements of sheetpiling works.

8.2 Case 2 – Redevelopment at Mong Kok, Kowloon

The other project with vibration measurement is presented with predicted vibration (**Error! Reference source not found.**) and piling layout (Figure 10) below.

Table 5: Energy and Distance Estimation for Piling Construction

Vibration Receiver	Plan distance btw. pipe pile and vibration receiver (m)	r, slope distance between source and sensitive receiver (m)	k_p	Hammer weight, W_h (ton)	Max. drop height, H (m)	Overall Energy Transfer (K x η)	W, hammer energy (KJ)	ppv (mm/s)		Diff.
								Est.	Act.	
V1	14.90	17.4	1.5	0.998	0.2	0.49	1	1.1	1.17	+6%
V2	4.60	10.1	1.5	0.998	0.2	0.49	1	2.3	1.08	-53%

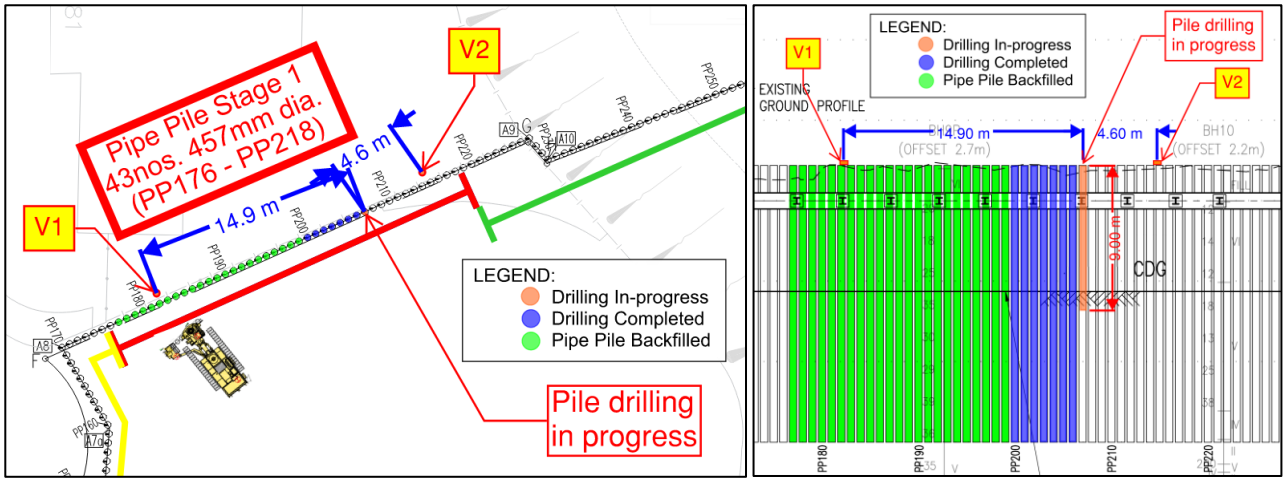


Figure 10: Location of V1 & V2 Relative to Piling Work in Progress

By comparing the vibration prediction with actual measurement in **Error! Reference source not found.**, the E quation (2) is effective in predicting V1 vibration. For V2, there are several possible reasons for discrepancy, including but not limited to instrument error, measurement gap and disturbance by other site works.

9 CONCLUSION

The vibration generated during pile drilling works is inevitable and target of engineering practice is to reduce its adverse effects. To have a sound estimation of vibration induced by piling works, reference has been made to empirical equation widely used which generates result reasonably predicting the actual vibration. The efforts made in assuming appropriate parameters, especially k_p varying from 1.0 to 1.5 for soil, 2.0 for corestone and 3.0 for rock obtained in our study, shall contribute to the professional's prediction in similar settings.

To minimize the effects of vibration on the MTR structure, modified pile wall size with differential toe levels has been adopted basing on practical experience and sensitivity test. The outcomes are satisfactory with vibration within AAA limits. The mitigation results, along with reference to other projects with vibration measurements, provide engineering industry and academia further understanding of vibration-induced piling works and form basis for potential application of the measures.

ACKNOWLEDGEMENT

The authors are grateful to the Tak Shing Investment Co., Ltd. for approval of reference to project record in this paper. Great gratitude is given to Alvin Lam and Andrew Sun for comments and liaison during the preparation of publication. Sincere thanks to Arup colleague for sharing project data to gain further insights.

REFERENCE

Attewell, P.B. & Farmer, I.W. (1973). Attenuation of ground vibrations from pile driving. Ground Engineering, Vol. 3, No. 7, pp. 26 - 29.

Attewell, P.B., Selby, A.R., O' Donnell, L. (1992a). Estimation of ground vibration from driven piling based on statistical analyses of recorded data. *Geotechnical and Geological Engineering*, Vol. 10, pp. 41-59.

Chan, A.K.C. 2003. Observations from Excavations – A Reflection. *The HKIE Geotechnical Division Annual Seminar 2003.*

Deckner, K. (2013). Ground vibrations due to pile and sheet pile driving: influencing factors, predictions and measurements. *KTH Royal Institute of Technology*.

Hiller, D.M., Hope, V.S. (1998). Groundborne vibration generated by mechanized construction activities. *Proceedings of the ICE-Geotechnical Engineering*, Vol. 131, No. 4, pp. 223-232.

Hiller, D.M., Crabb, G.I. (2000). Groundborne Vibration Caused by Mechanised Construction Works, *Transportation Research Laboratory*.

McCabe, B.A., Flynn, K.N. (2017). *Proceeding of the 19th Intl. Conf. on Soil Mechanics and Geotechnical Engineering*, Seoul, pp. 2817-2820.

Poulos H.G. and Davis E.H. Pile (1980). *Foundation Analysis and Design*. John Wiley & Sons.

Saher, H. S., Al-Jubair, H. S. and Ali, J. K. (2024). Measurements of induced vibrations due to steel pipe pile driving in Al-Fao soil: Effect of partial end closure. *Open Engineering*, vol. 14, no. 1, 2024, pp. 20220550.

White, D., Finlay, T., Bolton, M. and Bearss, G. (2002) Press-in Piling: Ground Vibration and Noise during Installation. *Proceeding of the International Deep Foundations Congress*, Orlando, USA. ASCE Special Publication 116, 363-371.

Wiss, J.F. (1967). Damage Effects of Pile Driving Vibration. *Highway Research Board Record 155*, pp.14-20.

Wiss, J.F. (1981). Construction Vibrations: State of the Art. *Journal of Geotechnical Engineering Division*, Vol. 107, No. GT2, pp. 167-181.

Evolution of Three-Dimensional Geotechnical Information Infrastructure

Lawrence KW SHUM, Sammy PY CHEUNG, Chris SC TANG, Richard CM HO and Raymond CH KOO

Geotechnical Engineering Office, Civil Engineering and Development Department, The Government of the HKSAR, Hong Kong, China

ABSTRACT

Innovation has always been the priority of the Geotechnical Engineering Office (GEO) to unlock new possibilities and drive advancement in the engineering practice. In 2009, the GEO commenced the operation of the Geotechnical Information Infrastructure (GInfo), which is a digital infrastructure framework for developing and launching geotechnical applications for practitioners and the public. It has since become the authoritative source of geotechnical information in Hong Kong. In recent years, there are remarkable advancements in 3D visualisation and data capturing technologies that revolutionise and transform the way that 3D objects and spatial data are created, analysed and communicated in an immersive and realistic visual representation. Riding on these advancements, the GInfo was migrated to 3DGInfo that creates a new horizon for smarter applications. More 3D objects and spatial data are generated using novel technologies, such as pulsed-laser scanning, photogrammetry and BIM modelling. GEO is also capturing photorealistic 3D mesh models, such as man-made features, landslides, tunnels, etc., to enhance the user experience. In parallel, a 3D geotechnical model (3DGM) is being assembled with existing GI records kept by GEO. The 3DGM will assist planners and engineers with a quick reference of the geology and ground conditions of their development site. The 3DGInfo also acts as the backbone of the GEO digital twin platform that connects the physical and digital world, where predictive analysis can provide simulated scenarios with greater sophistication in visualisation and immersive environment. This paper discusses the smart technologies and innovative solutions provided in the 3DGInfo, that aim to enhance the GEO services and benefit the practitioners.

1 INTRODUCTION

GEO is always taking a steering role in development of innovation and technology (I&T) for slope safety in Hong Kong. Some successful engineering applications are presented in Cheung (2006) and Cheung (2021). Recently, GEO has completed the project of enhancing the Geotechnical Information Infrastructure (GInfo). One of the main enhancements is the strengthening the three-dimensional (3D) visualisation capability of GInfo, such that the 3D spatial data and objects are organised and presented in a truly 3D representation with greater sophistication on their details and spatial correlations. The three-dimension GInfo (3DGInfo) comes into operation in September 2023.

As part of the enhancement works, the 3DGInfo is migrated to a cloud platform which improves the resilient and reliability of this infrastructure framework. This is important for the critical systems that support GEO emergency services, such as Slope Information System, Landslide Information System, Mobile GInfo Application, GEO Rain Gauge System and Landslip Warning System. In addition, computing resources in the cloud platform are highly scalable and can be upscaled easily to meet any sudden surge in the demand of computing resources where situations warrant. The interface mapping capability is also improved by using the cloud rendering technology, where parsing and rendering highly sophisticated and detailed 3D models are done in the remote servers. The levels of detail and data size of 3D objects and models have increased significantly for better visualisation and representation, such as the LandsD 3D spatial data model, BIM as-built model, ground feature and digital terrain model captured by Light Detection and Ranging (LiDAR) scanning and photogrammetry technology, etc. Cloud computing provides the efficient rendering solution

which is a prerequisite for enhancing the user experience when browsing and analysing the 3D models and spatial data in the 3DGInfo.

Besides improving the infrastructure and computing capability of the 3DGInfo, it is also essential to create 3D object and spatial data that can simulate the real-world environment and provide contextual information, spatial relationships and real-time monitoring capabilities. Traditionally, 3D spatial data in GIS are captured and presented in a two-dimensional coordinated mapping space and the third dimensional values is then represented by cartographic symbols. In recent years, advancements in remote sensing technology, such as LiDAR scanning and photogrammetry, and retrieval algorithms have significantly improved the data quality with real world textures and photorealistic impression. GEO has invested on these technologies and developed affordable solutions that can capture and build highly sophisticated 3D objects, e.g. photorealistic mesh models of man-made feature, landslide, etc. The display of these models in 3DGInfo requires substantial rendering power for effective uses. In addition to capturing and managing 3D objects and spatial data above the ground surface, GEO is also developing a 3D Geotechnical Model (3DGM) to represent the subsurface conditions of Hong Kong, with emphasis on their implications to the engineering works (e.g. founding levels of pile). The 3DGM in some pilot study areas has already been incorporated in the 3DGInfo.

It has been one of the GEO strategic developments to establish a digital twin platform for enhancing the GEO services and improving decision process with better understanding of the unfolding severe weather event. The 3DGInfo also serves as the backbone of the digital twin platform which provides the connection between physical and digital world. When GEO data are managed and maintained centrally in the 3DGInfo and on a cloud platform, it provides the opportunity to make use of cloud computing and artificial intelligence technology to carry out big data analytic to uncover insights from structured and unstructured data of GEO to advance the engineering practice, improve the services and enhance the operation efficiency.

2 3D SPATIAL DATA IN THE CENTRAL REPOSITARY OF 3DGINFO

It is well acknowledged that data is the main ingredient of any successful digital solution. GEO is capturing and creating lots of 3D spatial data to support the 3DGInfo. Existing 2D spatial data (e.g. slope feature boundary, land lot, country park boundary, railway protection zone) can be incorporated into the 3DGInfo by projecting their planar boundary into the digital elevation model (DEM) or converting them into 3D models based on available as-constructed drawings (e.g. existing tunnels and caverns). However, such conversion may not satisfy and meet the needs of the user, when it comes to the positional accuracy and levels of detail of the converted 3D model. The methodologies of capturing 3D data and creating models are continuously modernised and enhanced. Nowadays, 3D models are routinely created by high-resolution satellite imaging, UAV-based laser scanning and photogrammetry and extraction from as-constructed BIM of the engineering works. The GEO also works with relevant parties in expanding the contents of the 3D spatial data in the central repository of the 3DGInfo.

2.1 3D models of the cityscape by the Lands Department

The success of the 3DGInfo rides on the comprehensive 3D spatial data developed by the Lands Department (LandsD), which is a key milestone to transform Hong Kong to a smart city. The land features include buildings and infrastructures for the entire Hong Kong and the levels of detail can provide highly photorealistic city models for visualisation. The base map of the 3DGInfo is built on the 3D spatial data that are completed timely by LandsD in 2023 (Figure 1). By superimposing the available 3D spatial data onto the digital elevation model (DEM) constructed with the 2020 airborne LiDAR survey, the 3DGInfo is capable to replicate the entire Hong Kong city in a virtual 3D environment. The visualisation map will help facilitate the execution of works projects, slope engineering studies, town planning, spatial analysis, simulation, application for smart mobility and other feasibility studies.

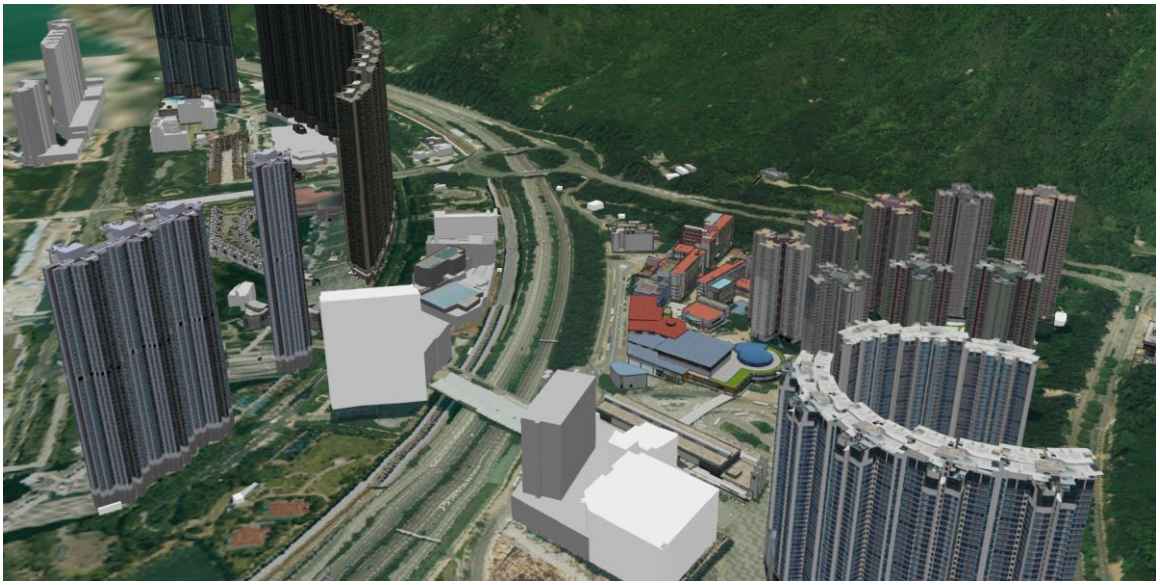


Figure 1: The base map of 3DGInfo assembled using the spatial 3D objects produced by the Lands Department

2.2 BIM models of engineering work

It has been the Government strategy to adopt Building Information Modelling (BIM) to enhance the productivity of the construction industry in Hong Kong. Over the years, various policies and measures have been rolled out to support the use of BIM in public works and private projects. Since 2018, GEO has incorporated the BIM technology in the design and construction of major slope works (e.g. soil nailing, flexible and rigid barriers) under the Landslip Prevention and Mitigation Programme (LPMitP). Apart from on-going projects which BIM has already been adopted for design and construction, GEO has initiated the exercise of gradually digitising and creating BIM models of natural terrain hazard mitigation measures (NTHMM) that were completed years ago. Under this exercise, the GEO has utilised the as-constructed records and additional LiDAR survey data to create BIM models for NTHMM (e.g. debris-resisting barriers). In digitising the as-constructed NTHMM, contextual information such as project details, material properties, key data (e.g. energy rating, brake element model) of the defensive measures are also embedded in the BIM model. Figure 2 shows the high-level details of the flexible barrier that could facilitate future maintenance.

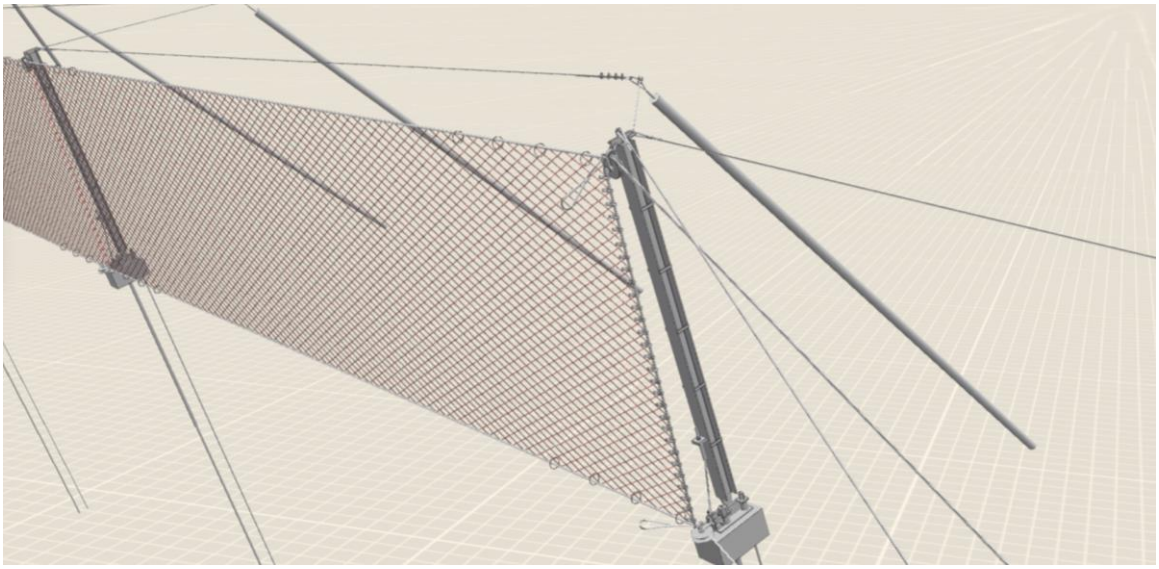


Figure 2: Flexible barrier with high levels of detail converted and embedded in 3DGInfo

In recent years, there has been significant progress in the integration of BIM models into GIS environment and it becomes easier to turn design and construction data embedded in the BIM model into GIS assets. Available as-constructed BIM models of the geotechnical works carried out under the LPMitP are also uploaded to the 3DGInfo (Figure 3). There are ample potentials to make use of these BIM models to facilitate the maintenance agents to maintain the NTHMM or to turn them to digital twins with real-time IoT sensors.



Figure 3: BIM models of as-constructed NTHMM in 3DGInfo

2.3 Point cloud and photorealistic mesh model using LiDAR survey and photogrammetry

The Survey Division of CEDD has been supporting GEO with taking LiDAR survey on unmanned aerial vehicle (UAV) of area of interest from time to time. The deliverables include high quality photorealistic 3D mesh models, point clouds and loads of aerial photographs. These are important assets that provide the snapshot of the ground features at the time of inspection and they are systematically uploaded to the 3DGInfo for proper management and temporal change analysis at later stage. The Survey Division always accords high priority of capturing landslide features whenever requested by GEO. It was timely that the 3DGInfo was available in early September 2023 ahead of the extreme rainstorm event that followed. Photorealistic 3D mesh models of many significant landslide were captured and uploaded to 3DGInfo. These 3D models provided a quick overview of the landslide source uphill, which was otherwise difficult to be inspected from downslope. The landslide source volume could also be estimated by comparing the 3D model of the landslide scar with the digital terrain model based on 2020 LiDAR survey. The information greatly facilitated GEO officers in assessing the residual risk, together with a better representation of the spatial distance between remaining debris and threatened facilities. Some examples of landslide photogrammetry models created during the extreme rainstorm events in September and October 2023 using UAV survey are illustrated in Figure 4.

The drone flight paths are also stored and presented in the 3DGInfo. This facilitates users to retrieve any aerial photograph taken during the flight (Figure 5). The flight path can also be used as reference for the repeated drone inspection to create the latest ground feature model for temporal change analysis. Figure 6 shows the latest conditions of the landslide at Yiu Hing Road in February 2024, which is useful to assess the residual risk after the implementation of the emergency works.



(a) Kam Shue Road



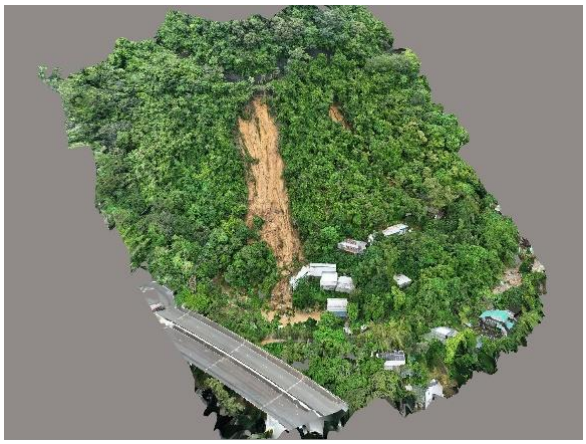
(b) Shek O Road



(c) Ping Chi Street



(d) Red Hill Peninsula



(e) Pak Tin Village



(f) Yiu Hing Road

Figure 4: Photogrammetry models of landslide event in September and October 2023

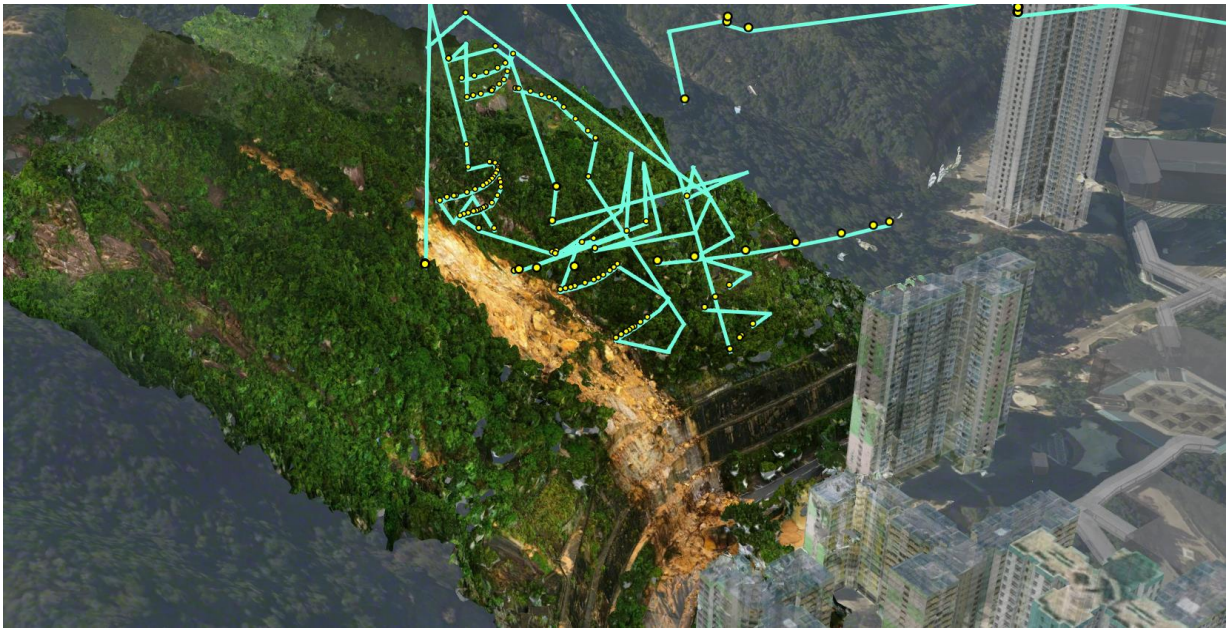


Figure 5: Site specific LiDAR data and drone flight path of Yiu Hing Road landslide site in 2023



Figure 6: Condition of the landslide site at Yiu Hing Road in February 2024

2.4 Highly detailed photorealistic mesh model by handheld remote sensing device (Pano360)

GEO has collaborated with the Mechatronics and Robotic System (MaRS) Laboratory of the University of Hong Kong and a local IT firm to develop an affordable handheld remote sensing device (Pano360) for capturing and creating highly detailed photorealistic 3D models. The application of the Pano360 is widespread, which can be used in capturing the details of failure scar before surface protection are applied; or taking snapshots of the ground feature during site inspection and preparing the slope inventory during routine or engineer maintenance inspection of features. Figure 7 shows the site inspecting personnel carrying the Pano360 and traversing the area of interest in normal walking manner. Figure 8 shows the levels of detail of the 3D spatial model of slope feature No. 11SE-C/C717 at Tai Tam Reservoir Road that were created with Pano360. It could upend the conventional way of compiling slope inventory record with a few discrete aerial photographs. It is planned to promote the usage of Pano360 amongst geotechnical consultants.

The quality of the slope inventory in the 3DGInfo will gradually be enhanced when more 3D spatial models of man-made slope feature are created.



Figure 7: Inspecting personnel holding Pano360 for capturing pictures to form the photorealistic mesh model of the landslide site at Yiu Hing Road



Figure 8: Photorealistic 3D mesh model of 11SE-C/C717 at Tai Tam Reservoir Road that is superimposed to the terrain based on aerial photographs

2.5 3D Geotechnical Model

The Geotechnical Information Unit (GIU) currently holds more than 370,000 GI records collected over the years. The GI records are mainly managed and disseminated in the GInfo as scanned records, which are ineffective for the users to quickly understand the geology and ground conditions at depths. In recent years, voxel-based modelling has gained popularity in representing the space complex and discrete volumetric objects. Voxels are small cubed shaped units of volume that can be arranged in a 3D space to form objects of any size and shape. They are particularly suitable to represent irregular and discrete objects, such as terrain and geology. With the advancement in this modelling technique, it is feasible to build the 3DGM of Hong

Kong that could facilitate planners, practitioners and the public to appreciate the subsurface geology and ground conditions pertinent to different engineering applications.

Unlike a geological map, the 3DGM would emphasize on their relevance in engineering applications based on the interpretation of the engineering properties of the material encountered at depths. For example, delineation of stratigraphic interfaces is based on the tentative levels of different type of foundation (e.g. driven steel H piles usually are driven to refusal at soil stratum with SPT 'N' value greater than 200; deep piles founded on Cat. 1(d) and Cat. 1(c) rock profiles that have different presumed bearing capacity in accordance with current practice for foundation works). Certainly, there will be unavoidable limits arising from the completeness and adequacy of GI records within a study area, which can affect the accuracy of the delineated stratigraphic interfaces. Nevertheless, it should not defeat the purpose of 3DGM to provide quick and preliminary information to users of the ground conditions within the boundary of their project. On the other hand, the 3DGM is not a replacement to site-specific ground investigation works, which are important to provide sufficient site-specific details for the design of any geotechnical works and avoid unacceptable construction risks. The 3DGM could be further refined when additional and site-specific ground investigation are available at the subsequent stages of the project.

Completing the 3DGM for the entire Hong Kong will be a substantial task and it is intended to start the 3DGM with blocks of small area based on map sheet delineation (e.g. 1:5,000 map sheet no. 11SW-14B with a dimension of 750m × 600m). The first pilot study examined about 1,000 GI boreholes within and around the map sheet and Figure 9 illustrates the 3DGM under part of Wan Chai area. Besides visualising in 3DGInfo, all the interpreted data that are used to create the voxel models (e.g. the textual data and TIN surface representing the interfaces) can be downloaded for further engineering analysis by users. Using map sheet delineation allows flexibility in selecting the priority areas for developing 3DGM. For example, the regional geotechnical study for the Northern Metropolis Region will also produce a 3DGM for the study areas and be incorporated into 3DGInfo when available.

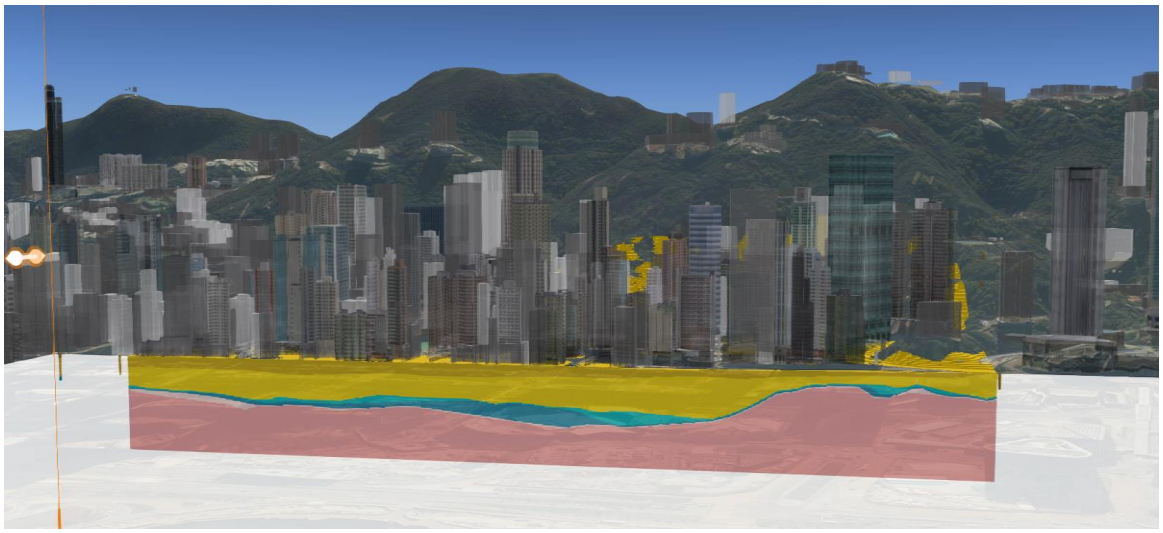


Figure 9: 3DGM in Wan Chai (Map Sheet No. 11SW-14B

A different approach has to be adopted when it comes to representing the ground conditions of marble rock formation for foundation design. It is very common to find the marble rock formation in Hong Kong to be severely affected by dissolution process, resulting in many karstic features (e.g. presence of overhang, underground channels and cavities, highly undulating rock surfaces, etc.) that pose significant difficulty for deep foundation works. It is the practice to develop site-specific karst geomorphological model that is based on stratifying the site into multiple strata of fixed thickness (e.g. 5 m) and then delineating competent and non-competent marble within each stratum. By overlying the strata together, the 3D karstic features within the marble rock formation can be visualised. The voxel-based modelling is excellent for representing the highly irregular karstic features in a 3D space. A separate workflow has been developed where different marble

zones are assembled by cubes, such as stacking Legos. Figure 10 shows the 3DGM for a Yuen Long site with zones of different marble class. The 3DGM allows users to quickly identify competent marble mass zone (i.e. Classes I and II) and provide preliminary information for placing high-rise building away from weak marble mass zone (i.e. Classes III, IV and V).

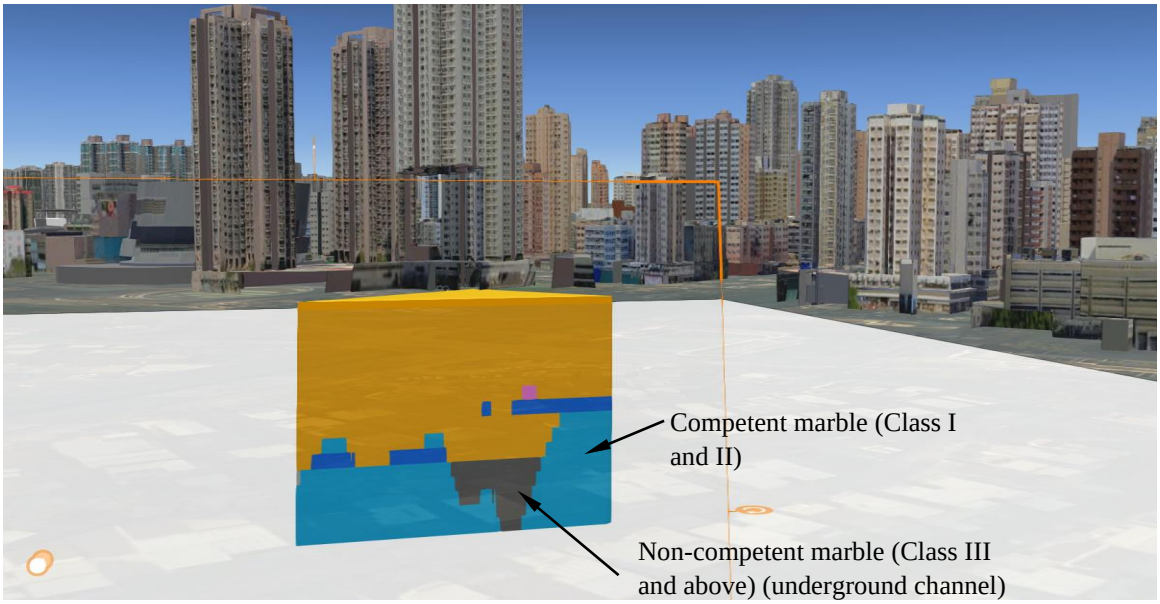


Figure 10: 3DGM showing the karst geomorphology in a Yuen Long site

3 NEW IMPETUS OF THE 3DGInfo

3.1 Development of GEO Digital Twin Platform

Digital twin is a dynamic and responsive system connecting the physical and digital world, where predictive analysis provides simulated scenarios with greater sophistication in virtual reality visualisation and immersive environments. A well-designed digital twin can transform many organisations in their ways of managing the complex and dynamic real-world environment. In recent years, the digitalisation of the built environment has been greatly enabled by the advancement in digital technologies, notably in the fields of remote sensing, real-time monitoring sensors and Internet of Things (IoT) and virtual reality simulation engine. Establishing a digital twin platform under the 3DGInfo is one of the GEO strategic developments to enhance the services and improve the decision process with better understanding of unfolding scenarios.

There is no lack of such systems in GEO that integrate real-time data in the physical environment and provide predictive scenarios for decision making. An early example is the GEO Landslip Warning System that was first deployed in 1980s, with rainfall data collected in every five minutes at rain gauges installed in different parts of Hong Kong. The rainfall data are fed into predictive models for analysing the increase of landslide risk during severe rainstorm event. The results of the prediction often provide the basis of deciding the necessity of issuing Landslip Warning to the public.

Another example is the Po Shan Drainage Tunnels that are constructed at Po Shan, Mid-levels in 2009. The stability of the hillside was affected by high groundwater level and the drainage tunnels, comprising a network of 172 sub-vertical drains, were constructed to regulate the groundwater level in the soil mass and reduce the landslide risk in the region. The groundwater level is continuously monitored by the pressure gauges installed on the sub-vertical drains and the piezometers in the slope above. A pressure relief valve is mounted at the end of the sub-vertical drains and it will automatically open and close to keep the groundwater level within pre-defined ranges. The monitored data are transmitted to a central interface in every 15-minute with modern pressure sensor equipped with IoT devices. These are used for interpreting the location of the groundwater level and comparing the rainfall reading from the nearby rain gauge stations.

Barrier are commonly constructed to mitigate the landslide hazard arising from natural hillside. However, they are very often erected at the foot slopes of hillside and stream courses where accumulation of landslide debris behind the barriers may easily go unnoticed. GEO has developed the Smart Barrier System (SBS) with the installation of state-of-the-art IoT and detection sensors. When the barriers are hit by landslide debris, instant alert will be sent to responsible officer, who will then assess the need for inspections and follow-up actions to ensure public safety. The detection sensors include impact switches for detecting debris impacts, depth gauges for measuring thickness of debris accumulated behind the barriers, and cameras for confirming field condition and screening out false alarms. Currently, smart barriers are installed at strategic locations protecting important facilities and residential dwellings, including Braemar Hill, Sham Tseng, Queen Mary Hospital, Shatin Hospital and Tate's Cairn Highway.

The enhancement of the 3DGInfo provides the opportunity of centrally managing different GEO IT systems in the digital twin platform and bringing in better visualisation of the site setting environment with real-time monitoring data and predictive scenarios. This enables prompt review of the performance of facility and their surrounding environmental conditions. Digital twin has already been set up under the 3DGInfo for the SBS (Figure 11) and the Po Shan Drainage Tunnels (Figure 12). This greatly enhance the effectiveness of information dissemination among the different action parties during severe rainstorm events and will be detrimental to making informed decision by respective officers.

3.2 Other Potential Development

The potential of digital twin technology in building management is enormous and diverse. GEO is currently implementing the projects of reprovisioning the Public Works Central Laboratory and building a new Archive Centre in the caverns at Anderson Road ex-quarry site, which will be completed in 2026. It is planned to create a digital twin for representing the entire buildings and the assets inside, including the laboratory equipment, structural elements, HVAC systems, lighting, and even occupancy patterns. The digital twin will integrate real-time data from IoT sensors and mirror the state of a building and equipment, simulates future scenarios, and provide actionable insights for efficient operation and management.

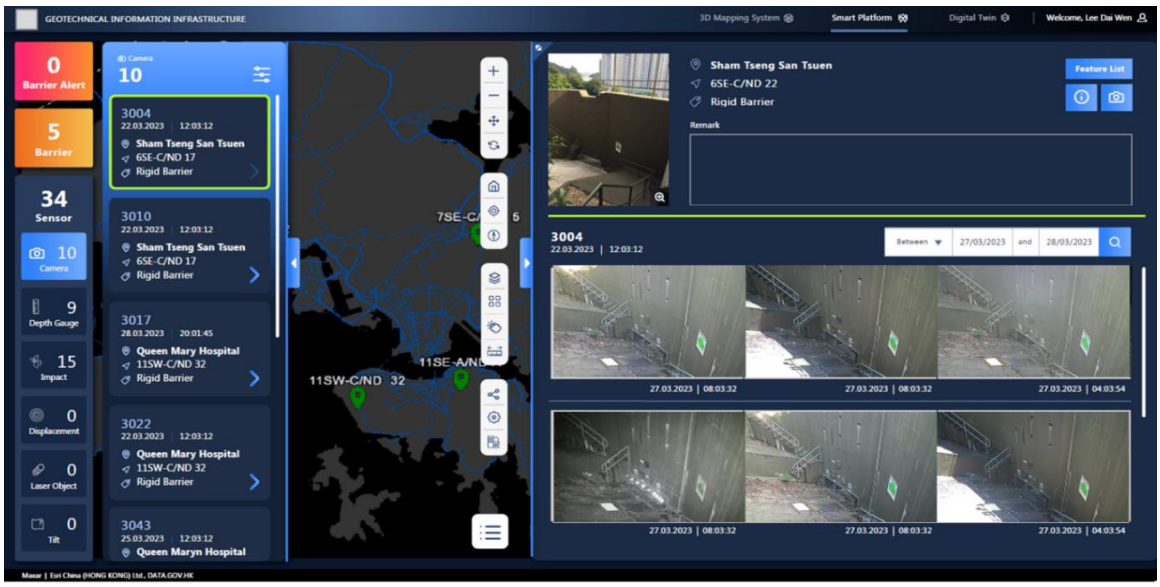


Figure 11: Digital twin of Smart Barrier System

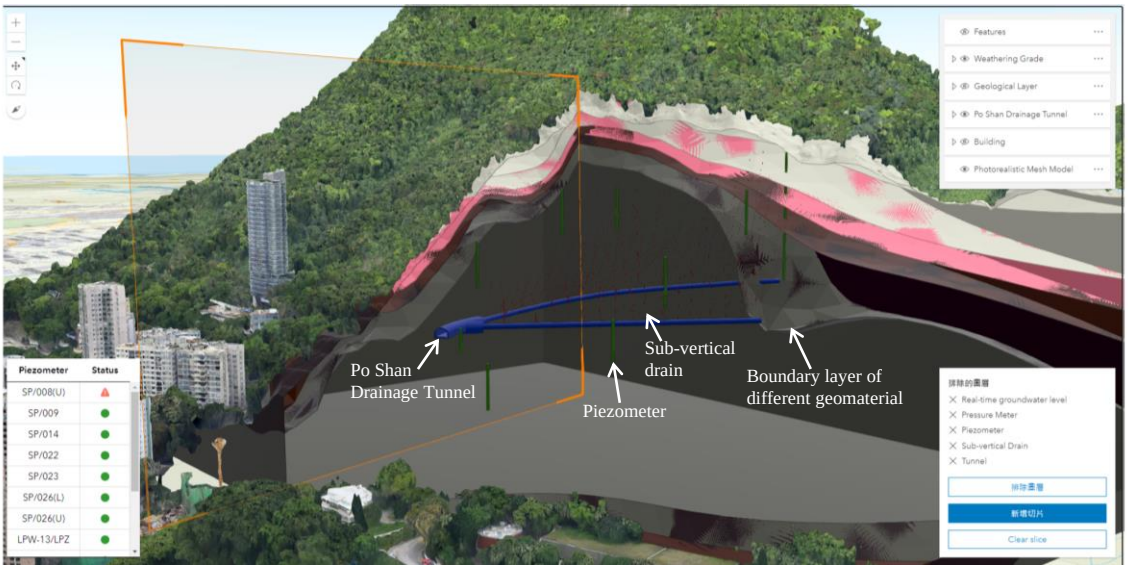


Figure 12: Digital twin of Po Shan Drainage Tunnel Monitoring and Operation System

4 WAY FORWARD

The development of the 3DGInfo provides the necessary infrastructure for managing and processing large amount of 3D spatial data that could replicate the real-world environment. As a centralised platform operating on cloud, the opportunities of further digitising the slope inventory and land features using the modern data collection techniques are ample. Spatial data is inherently 3D, such as the land topography, the built environment of the city, and even subsurface geology, and these can now be displayed not only intuitively and visually in the 3DGInfo, but also in a quantifiably and measurably representation. Data analytic based on all 3D attributes and even temporal change can now be carried out and further developed. GEO has been working on using machine learning techniques to improve the prediction in different areas of interest (e.g. rainfall and landslide correlation). As a logical step, the dataset in the cloud platform and the versatility of the cloud computing could set the scene for developing AI-based solutions in the 3DGInfo in future to facilitate more smart applications for slope safety management in the GEO.

ACKNOWLEDGEMENTS

This paper is published with the permission of the Head of Geotechnical Engineering Office and the Director of Civil Engineering and Development, Government of the Hong Kong Special Administrative Region, China.

REFERENCES

BD 2017. *Code of Practice for Foundation*. Buildings Department, Hong Kong Government, Hong Kong, 104 p.

Chan, Y.C. 1994. *Classification and Zoning of Marble Sites. GEO Report No. 29*. Geotechnical Engineering Office, Civil Engineering and Development Department, Hong Kong Government, Hong Kong, 37 p.

Chan, Y.C. & Pun, W.K. 2004. *Karst Morphology for Foundation Design. GEO Report No. 32 (Second Edition)*. Geotechnical Engineering Office, Civil Engineering and Development Department, Hong Kong Government, Hong Kong, 90 p.

Cheung, R.W.M. 2021. Landslide risk management in Hong Kong. *Landslides*, 18 (10), 3457-3473.

Cheung, S.P.Y. 2006. The application of information technology in managing landslide risk. *Symposium of the Science in Public Services*, Hong Kong, 12 p.

GEO 2006. GEO Publication No. 1/2006. *Foundation Design and Construction*. Geotechnical Engineering Office, Civil Engineering and Development Department, Hong Kong Government, Hong Kong, 376 p.

Advancements in Design and Construction Practice for Deep Excavation

Lawrence K.W. SHUM, Sammy P.Y. CHEUNG,
Raymond C.H. KOO, Ivan LI and J.C. LIU

Geotechnical Engineering Office, Civil Engineering and Development Department,
The Government of Hong Kong SAR, Hong Kong, China

ABSTRACT

The building of basement or placing infrastructure underground has gained popularity in developed city, as it can maximise the development potential and optimise the planning of useable surface area. However, construction costs in Hong Kong could be prohibitively expensive and practitioners have to optimise the design to achieve a better return on the investment. In 1990, the Geotechnical Engineering Office (GEO) published GCO Publication No. 1/90 – Review of Design Methods for Excavation, which has since become the *de-facto* standard for design of excavation and lateral support (ELS) works. Over the years, significant advancements and novel solutions have emerged in the execution of ELS works. GEO has the undisputable role of shaping the geotechnical practice and certainly sees the need to partner with practitioners in producing practical and cost-effective solutions. Since 2021, GEO has worked with practitioners and regulatory authorities to prepare a new GEO Publication No. 1/2023 – Deep Excavation Design and Construction, which aims to provide guidance on ELS works with a right balance between safety and cost-effectiveness. Attempts were made to address the problems that had troubled many in the execution of excavation works for years. This paper discusses the rationale behind the technical advancements and improvements made in the new publication.

1 INTRODUCTION

Developments in Hong Kong have, in many instances, necessitated the building of basement or placing infrastructure underground. Such arrangement has the advantage of maximising the development potential of the site and allowing better planning and utilisation of the usable surface land. However, the costs of deep excavation for underground structures can be substantial and therefore, it is important to optimise the design in order to balance the benefits and the investment of building structures underground. Local practice of deep excavation started with the construction of the first Mass Transit Railway (MTR) Line in the mid-1970s. Over the years, guidance documents were issued by the Government regulatory authorities that put emphasis on the safe execution of the deep excavation works, as there are always nearby buildings, structures and services to be protected and the consequences of any collapse could be serious and costly. Unavoidably and understandably, conservatism has been allowed in the rules promogulated in the guidance documents.

In recent years, construction cost has increased significantly and there are calls for achieving better economy in the construction industry, especially as excavation gets deeper and more complex in congested urban environment. The practice, that was found to be acceptable in the past, become questionable and the conservatism given in the guidance documents is also under stringent scrutiny to confirm its appropriateness. There were quite a few examples that were open to criticism by practitioners. It is common consent that over-design or overly stringent requirements may not make the construction works any safer. For instance, the construction risk associated with installing piles to a much deeper depth or erecting heavy sections for cross-lot strutting and preloading them will surely be increased. Prolonged suspension of excavation works due to exceedance of unrealistic ground settlement control limit may worsen the impact on adjoining ground, as active dewatering has to be in place during the period of suspension. The overdesign not only increases the construction cost and time, but can also lead to buildability and safety issues.

The GEO published the GCO Publication No. 1/90 – Review of Design Methods for Excavation in 1990 (GEO, 1990), which has since been used as the *de-facto* standard in the design of excavation and lateral support (ELS) works. In the past thirty years, there are many advancements in the design and construction methods of ELS works, particularly in the field of digital construction, numerical modelling, novel construction methods, limit state partial factors analysis. In view of these developments and the call for higher cost-effectiveness on construction works, the GEO sees that maintaining normalcy in geotechnical practice is not sustainable to satisfy the expectation of society and the productivity gains necessitated for the huge infrastructural investment. Pragmatic enhancement to the practice in deep excavation is warranted. It has been opportune that the GEO has been working with practitioners, academia and other Government authorities in recent years, and made advancements in the geotechnical practice that provide practical and cost-effective solutions in the execution of deep excavations.

A Working Group on Revision of GCO Publication No. 1/90 (denoted as the WG) was set up to update the publication (i.e. GEO, 1990), with members coming from Buildings Department (BD), Architectural Services Department (ArchSD), the Hong Kong Institution of Engineers (HKIE) and the Piling Contractors Committee of the Hong Kong Construction Association. The new version of the publication is entitled as GEO Publication No. 1/2023 "Deep Excavation Design and Construction" (GEO, 2023) (referred as the New Publication hereafter) and was published in end of 2023. The New Publication aims to give guidance that improves the cost-effectiveness of executing ELS works in Hong Kong while ensuring adequate safety to protect the public. It also consolidates local practice and experience in the construction of ELS works and provides recommendations for mitigating the geotechnical risks associated with deep excavation.

Cheung et al. (2023) presented some debated issues and rationale on the improvements that have been incorporated in the New Publication. In the following sections, the consideration and rationale behind some of the changes and improvements to the practice, as promulgated in the New Publication, are presented.

2 RECENT ADVANCEMENT IN DESIGN PRACTICE

2.1 Limit state design approach

Limit state design approach is commonly adopted in the design of ELS works, which should satisfy the fundamental requirements of stability and serviceability (i.e. Ultimate Limit State (ULS) and Serviceability Limit State (SLS)). In the New Publication, it has clarified that either the Global Factor Method (GFM) or the Partial Factor Method (PFM) can be used to check the limit states of the ELS works. The GFM is more widely adopted in local practice for checking of ULS because it allows simple stability checks based on a single factor of safety (FOS) to cater for all uncertainties. On the other hand, the PFM permits uncertainties to be considered for individual loadings and material characteristics and provides a more rational basis for design. The New Publication documented advancements in the design practice using GFM and PFM, particularly on the elaboration of the recommended minimum safety factors to be applied under GFM and PFM.

2.2 Global factor method

The New Publication harmonised the global factor requirements specified in different guidance documents for overturning and toe stability checks. Global factor of 1.5 is commonly adopted in the design of ELS works of public works projects, which follows the recommendations given in GCO Publication No. 1/90 using GFM. For private projects, the Practice Notes No. PNAP APP-57 (BD, 2012) stipulates that the stability checks should comply with the Building (Construction) Regulation 15, which required that the FOS against overturning stability should not be less than 2 for loadings other than transient wind loads. The Buildings Ordinance and the relevant subsidiary legislations were amended in 2020, which was redrafted to implement the performance-based principles on building control to facilitate innovation in building technology and provide flexibility in design. The Building (Construction) Regulation (2020) no longer prescribes the requirements on the FOS for stability checks. As such, the New Publication took the opportunity to unify the technical requirements for public and private projects and retained the same set of recommended minimum FOS in the New Publication as shown in Table 1. In collaboration with GEO, BD is making the corresponding amendments to the relevant PNAPs for adoptions of recommendations given in the New Publication.

Table 1 : Recommended minimum global factors of safety

Limit States		Minimum Global Factor of Safety
Ultimate Limit State	Overturning / Toe instability	1.5 for effective stress analysis 2.0 for total stress analysis
	Hydraulic failure	1.5
	Base heave	1.5
Serviceability Limit State		1.0

2.3 Partial factor method

Geotechnical design based on PFM has been adopted in the design of retaining wall and reinforced fill and slopes since 1990s. In addition, GEO is also in the process of revising the Geotechnical Manual for Slopes, which will incorporate the use of partial factor method in slope design. In preparing the guidelines for using PFM in the New Publication, it is determined that the recommended values of partial factors given in the New Publication should be based on those from Geoguide 1 (2nd Edition) (GEO, 2020), in order to ensure consistency on the partial factors amongst various guidance documents. Notwithstanding that, there are still rooms for reviewing and rationalising some partial factors in the New Publication with consideration of the temporary nature of deep excavation and the recent advancements in field testing techniques in Hong Kong.

The shear strength (s_u) value for clayey material can be quite variable and is influenced by many factors, e.g. soil minerals, the initial moisture content, the degree of saturation, the over-consolidation ratio, the initial void ratio, the porosity, the loading conditions, etc. Hence, a partial factor of 2.0 on s_u is recommended in Geoguide 1. In recent years, site-specific Cone Penetration Tests (CPT) have gained popularity amongst practitioners when designing geotechnical works in reclaimed land. It is well documented that CPT can provide a continuous profile of the ground and assessment of soil behaviour based on CPT values. CPT test has been widely adopted in a number of major infrastructure projects in reclaimed land, including Three-runway System, Shatin to Central Link, Tuen Mun-Chek Lap Kok Link, Central-Wanchai Bypass, Central Kowloon Route. With the advancement in knowledge of applying field tests and correlation with laboratory tests, it is considered that there is room to review the recommended partial factor on s_u. A conducive arrangement has been adopted in the New Publication such that where sufficient site-specific CPTs are carried out and calibrated with representative laboratory test results, the minimum partial factor of s_u could be reduced from 2.0 to 1.5. It is intended that the experience gained on using and calibrating CPT with laboratory triaxial strength tests would further rationalise the design of ELS works in future and enhance the cost-effectiveness.

Another deviation from the Geoguide 1 is the partial load factor on surcharge load. CIRIA C760 (Gaba et al. 2017) recommended values of 1.0 and 1.3 for permanent load and variable load, respectively, for design of ELS works. These are less than the partial load factor of 1.5 as recommended in Geoguide 1. In Hong Kong, a quality supervision system is a requisite for deep excavation projects and only qualified professionals and contractors, are responsible for supervising and executing the excavation works in accordance with the approved drawings and design assumptions. Therefore, the surcharge load imposed on the ELS works is generally more controllable and any irregularity of overloading should be prevented on site or rectified promptly. Therefore, it is considered reasonable to adopt 1.3 as the partial factor on surcharge load, similar to the recommended value given in CIRIA C760. The recommended minimum partial factors in the New Publication are given in Table 2.

Table 2: Recommended minimum partial factors

	Strength Properties and Load Conditions	Ultimate Limit States	Serviceability Limit States
Partial material factor (γ_m)	Unit weight	1.0(1)	1.0
	Drained shear strength(2)	1.2	1.0
	Undrained shear strength	2.0(3)	1.0
	Shear strength of rock joint	1.2	1.0
	Soil and rock stiffness parameters	1.0	1.0
Partial load factor (γ_l)	Dead load	1.0	1.0
	Surcharge(4)	1.3	1.0
	Water pressure	1.0	1.0
Notes:	(1) γ_m = 0.67 should be applied to the effective vertical stress which provides a stability effect for the hydraulic failure checks (i.e. piping and uplifting). (2) γ_m should be applied to soil shear strength parameters of c' and tan ϕ'. (3) γ_m may be reduced to 1.5 where sufficient site-specific representative field tests are carried out (e.g. CPT calibrated with representative laboratory test results). (4) γ_l should be set to zero for surcharge which provides a stabilising effect.		

A benchmarking exercise was carried out to review the implication on wall embedment depth due to the new factors in GFM and PFM. Six cases of different geological conditions and excavation depths are analysed and Figure 1 shows the configuration of the ELS works and the stratigraphy of the ground. Three cases are excavations with depths ranging from 8 m to 20 m at typical geology of colluvium overlain by Completely Decomposed Granite (CDG). The other three cases are excavations in the reclaimed land with typical succession layers of marine deposits and alluvium. Typical soil parameters, which largely followed the recommendations from Geoguide 1, were used in this benchmarking exercise.

Table 3 summarises the required toe penetrations of the temporary embedded retaining wall based on the New Publication and the PNAP APP-57 for the six cases. For GFM, 10% to 25% saving on the wall embedment depth can be achieved by changing the global factor for toe stability checking (effective stress analysis) from 2.0 to 1.5, which has already been adopted in public works projects for long time. Besides, after the update of recommendations on the factors, the outcomes of GFM and PFM become more comparable with each other.

Table 3: Required toe penetrations under recommendations in the New Publication as compared with the current practice

Assumptions			Required wall embedment depth by overturning checking			
			New Publication		Current Practice (PNAP APP-57)	
Case	Surcharge (kPa)	Excavation depth (m)	GFM with global factor of 1.5	PFM with partial factors on (1) surcharge = 1.3 and (2) s_u = 1.5	GFM with global factor of 2.0	PFM with partial factors on (1) surcharge = 1.5 and (2) s_u = 2.0
1	20	8	3.8	3.8	5.0	4.7
2	20	15	6.7	6.6	9.3	7.9
3	20	20	9.3	9.1	12.9	10.5
4	20	11	13.4	13.0	15.1	13.2
5	20	17	9.2	8.9	12.2	9.9
6	20	12	11.7	12.0	12.8	12.4

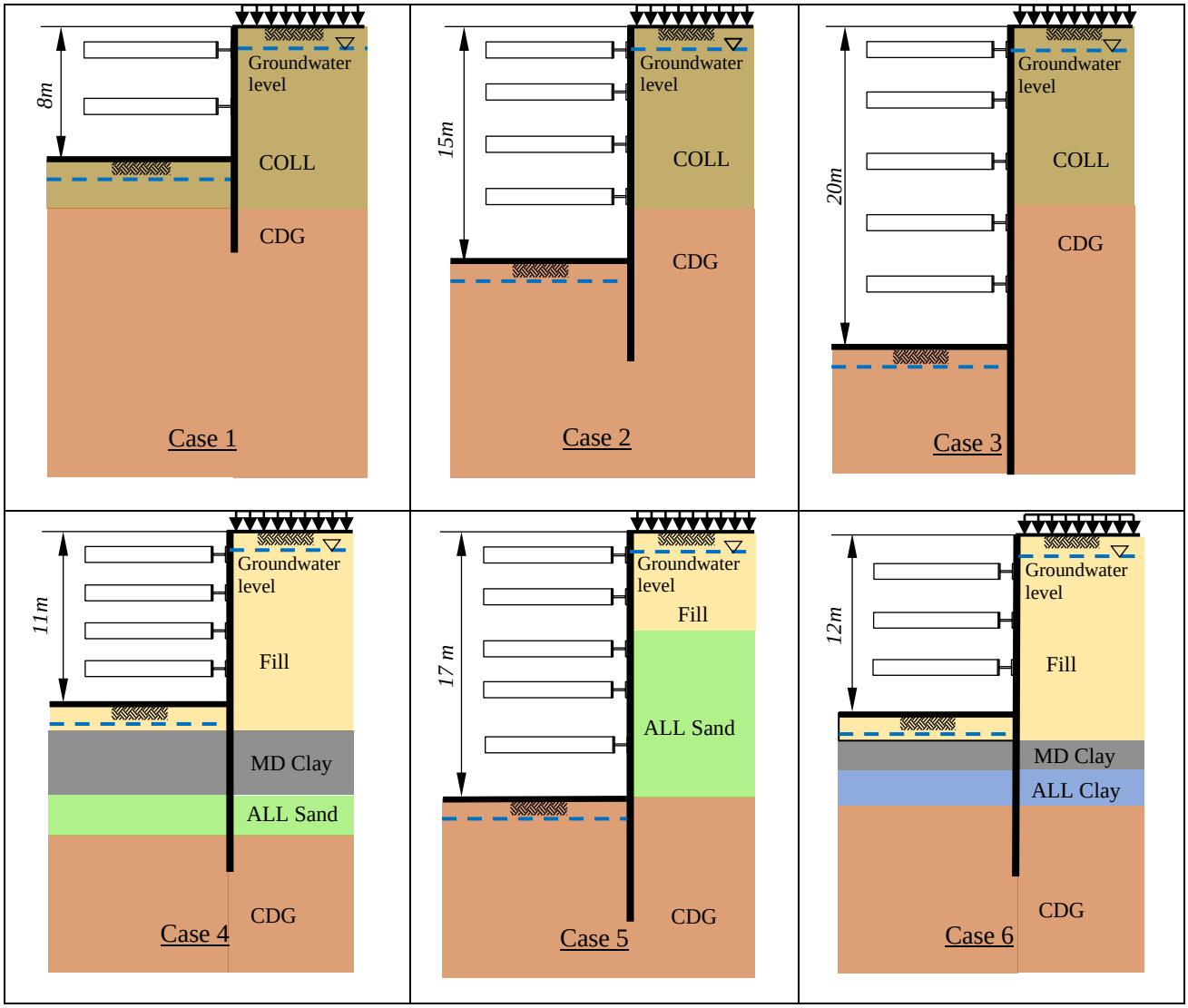


Figure 1: Six cases of excavations for benchmarking exercise

2.4 Serviceability limit state

2.4.1 Estimation of groundwater level

The groundwater on the retained side of the excavation has a marked influence on the design of ELS works and there was much debate on the appropriate groundwater levels to be used in the design amongst practitioners and the regulators. It is, therefore, one of the focuses when preparing the New Publication to give enhanced guidelines on how to estimate the groundwater levels and their uses in ULS and SLS. However, it must be emphasised that monitoring of the groundwater levels and proper assessment of the results should be conducted anyway, particular for sites where the groundwater regime can be affected by surrounding environments and seepage flow. The damming effect of the temporary embedded retaining wall can be substantial, particularly when it intercepts buried underground water flow channel.

Practitioners may sometimes prefer to adopt a conservative assumption on the groundwater level. However, this is not necessary a safer assumption. For instance, in a multi-level strutted excavation, the soil-structure interaction between the installed struts and the embedded retaining wall is dependent on the soil and water pressure and can be varied at each stage of excavation. The soil pressure acting on the embedded retaining wall can be assessed with good certainty given the availability of numerical modelling tool. However, this is not the case for groundwater pressure, if a conservative level is assumed in the SLS design. The actual loads in struts and deflection profile of the wall may deviate from the design significantly. Therefore, the New

Publication advocates to adopt a realistic and reasonably assumed groundwater level in the SLS check and does not encourage using a single groundwater level for both ULS and SLS design.

Given the temporary nature of ELS works, the design groundwater level (DGWL) for a ULS design should represent the highest groundwater level anticipated during the ELS works. GEO has reviewed past designs of ELS works and noted that it has become the common practice by practitioners to adopt the DGWL for ULS by adding a rise of 1 to 2 m to the monitored highest groundwater level; and in circumstances where the monitored groundwater level is found to be lower than the excavation level, the DGWL for ULS is assumed to be at one-third of the excavated depth. These assumptions are found to be satisfactory for performance of most excavation works taking into consideration of their limited duration, unless the works will affect particularly sensitive structures or the environmental setting have great influence on the underground seepage flow. It should be borne in mind that there are usually still additional safety margins on the overall ELS system, although the design water pressure is usually unfactored. Nevertheless, sensitivity check of the design using a range of DGWLs could be carried out to demonstrate the robustness of the ELS works.

2.4.2 Estimation of ground settlement

CIRIA C760 tabulated the case studies of excavation projects in different countries. The database covers quite comprehensively different types of soil stratigraphy, strutting system, and excavated depths of up to about 30 m. The experience indicated that maximum ground settlement due to excavation in loose to medium dense sand was about 0.3% times maximum excavation depth (H_e) immediately adjacent to the wall, and decreasing to zero at a lateral distance of about $2H_e$. This is comparable to the experience as documented in GCO Publication No. 1/90. However, the excavation data given in CIRIA C760 covered mostly overseas projects. It was determined that the New Publication should also consolidate the performance of the local excavation projects. For this reason, a comprehensive review of the deep excavation projects was carried out, as this would better reflect the performance of the design and construction practice in Hong Kong. Twenty-seven excavation projects with quality field monitoring data were selected for the review and they are tabulated in Appendix A of the New Publication.

Figure 2 shows the correlation between maximum ground settlement (δ_v) and maximum excavated depth, H_e, based on the review. The general range of δ_v varies from about $0.05\%H_e$ to $0.45\%H_e$ but most of the measurements are less than $0.25\%H_e$, which is largely comparable with overseas experience. Observations were given in the New Publication of the isolated cases where the correlation exceeded $0.3\%H_e$. As expected, there is a large scatter in the data, which is due to different ground conditions (e.g. reclaimed land with varying ground conditions), wall types (e.g. circular shaft, diaphragm wall and pipe pile wall) and construction methods (e.g. top-down or bottom-up construction sequence). The $0.3\%H_e$ to $0.5\%H_e$ appears to be a reasonable ground settlement range when devising a suitable ELS system, unless particularly sensitive receivers are present (e.g. historical or dilapidated building, MTR rail track, etc.). If the estimated settlement is higher than this range, the design of the ELS works should be critically reviewed and revised. Additional measures, such as ground improvement, preloading, etc. may be needed, so as to bring the estimated ground settlement to below the maximum range. On the contrary, a lighter ELS system may be preferred, if the estimated settlement is well below the common range of ground settlement. However, it should be noted that ground settlement associated with excavation using circular shafts and tied-back walls should be relatively small (e.g. ground settlements of less than $0.1\%H_e$) based on past local projects.

2.5 Implementation of pumping test – Recent enhanced practice

The need for conducting full-scale pumping test prior to bulk excavation should be carefully considered. The difference in water levels across the embedded wall could induce significant deformation, as the lateral support to the embedded retaining wall is not in place. Some practitioners consider that the pumping tests could be used to validate the soil mass permeability as assumed in the groundwater seepage analysis. However, this is seldom the case, as the geology of the site can be highly variable and heterogeneous in nature. In fact, it is much preferable to allow dewatering to be carried out in tandem with the excavation, when the lateral supports are installed as excavation goes on. This would give a better control to the deformation of the embedded retaining wall and ground settlement. The safety of the excavation system is, indeed, safeguarded by the

monitoring of the groundwater levels and the deformation of adjoining building, services and ground to be within acceptable range. Hence, in the New Publication, some examples are given for situations that pumping tests are generally considered unnecessary. These include site with (a) mass permeability of the soils that is low or the anticipated groundwater level at the site is below the final excavation level, (b) water cut-off barrier that is installed down to soil strata with low permeability or to a rock formation with suitable rock fissure grouting, or (c) there are no nearby sensitive receivers that could be affected by groundwater drawdown.

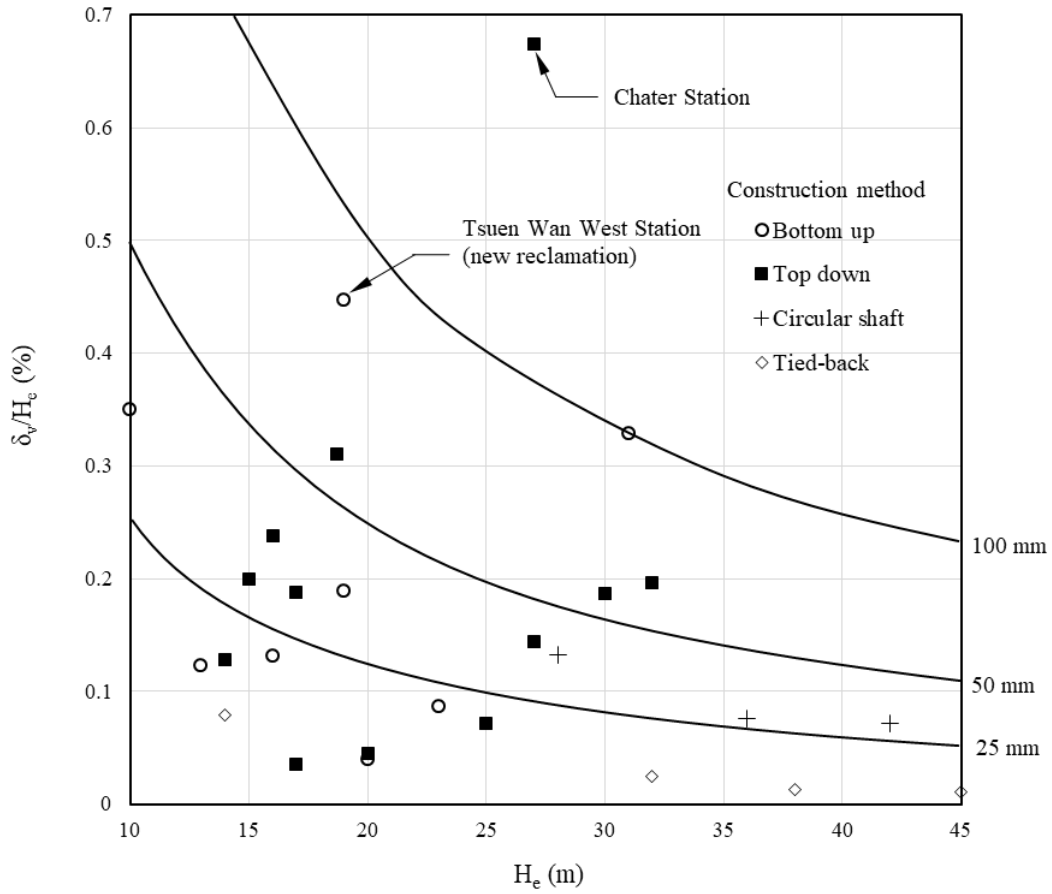


Figure 2: Total ground settlement against maximum excavation depth (H_e) from case study data for projects in Hong Kong

In the event that a full-scale pumping test is deemed necessary, it is also proposed in the New Publication that the duration of active pumping during the pumping test should be minimised as much as possible. Active pumping inside the excavation would promote underground water flow and inevitably cause the loss of fine-grained soils within the soil matrix. There are many reported incidents of ground settlement or subsidence as a consequence of underground water flow. Cheung et al. (2023) reported a review of 24 pumping tests conducted in recent deep excavation projects in Hong Kong. All the tests indicated that whenever steady-state conditions were achieved, there was practically no change to the water level in the subsequent 72-hour period. Therefore, it is recommended in the New Publication that, for a full-scale pumping test in excavation project, maintaining the dewatering for a minimum of 24 hours after achieving steady state seepage is considered adequate and the recovery stage can be commenced thereafter.

3 INNOVATIVE CONSTRUCTION METHODS

Significant advancements and novel solutions have emerged in the construction industry in recent years. There have been a number of projects using multi-cell shaft excavation method and tied-back wall system for excavation exceeding 30 m in depth and they were successfully completed with minimum ground deformation (Figure 2). The New Publication consolidated the examples of these novel construction projects (Plates 1 and

2), as a reference and evidence that these systems are acceptable to the authorities when situations are considered favourable.

In fact, tied-back wall system may actually be more preferable in some circumstances. For example, where excavation is to be carried out on a steep sloping site, there would be a large unbalanced excavation across the site and inadequate space for constructing cross-lot strutting to support the embedded retaining wall on the higher ground. Some practitioners consider impracticable to install tied-back into unexcavated ground, as permission from the land administration is difficult to obtain. GEO has worked with relevant authority, including the Lands Department (LandsD) and Highways Department (HyD), to workout streamlined procedures for considering application of installing tied-back or soil nails in unallocated government land (UGL). As a pre-requisite, the affected UGL should not have any upcoming proposed developments or land disposal proposal. Upon receiving application for installing tied-back and soil nails in UGL, LandsD would consider positively on such proposal based on the advice of GEO regarding whether the construction work is geotechnically desirable. Such arrangement is currently applicable to public works projects or slope remedial works conducted by private owners for reason of public safety. In parallel, suitable land clauses have also been drafted to facilitate the application process.



Plate 1: Permanent tied-back wall support system for the excavation works at Stubbs Road



Plate 2: Retractable prestressed ground anchor support system at the redevelopment of Grantham Hospital

4 ENHANCED MECHANISM ON GROUND DEFORMATION CONTROL

It is inevitable that some degree of ground deformation would occur in association with excavation, no matter how sophisticated the design was and stringent the excavation works were carried out. It must be borne in mind that geotechnical design is often made with some degree of simplifications and assumptions and the inherent characteristic of the soil can be very variable. Therefore, it has been the standard practice in the design of ELS works of devising a comprehensive instrumentation and monitoring plan, together with a ground control mechanism to predetermine the response actions when the monitored deformation exceeds the predetermined limits. Practitioners usually adopt the three-tier triggering control mechanism (i.e. Alert-Alarm-Action (AAA) Levels) as stipulated in the PNAP APP-137 (BD, 2018) for safeguarding the sensitive receivers during excavation. At Action Level, the ground deformation control mechanism usually calls for suspension of all site works.

There has been much debate on the ground deformation control mechanism in recent years, particularly there were quite a number of noticeable projects that were suspended due to exceedance of the ground settlement limits. Cheung et al. (2023) discussed the undesirability of adopting the empirical limit of 25 mm for all depths of excavation. The indiscriminate use of 25 mm has resulted in either adopting unnecessary heavy excavation systems or speculating on whether the limit would be breached during construction. Based on past records, many excavations were suspended due to the exceedance of the Action Level for ground settlement, rather than

the building structures which are commonly supported on deep foundations. Works suspension is very disruptive on the construction programme and always produces a negative impression to the public. There were many cases that it took months, if not years, to get approval to recommence the project and regardless of the justifications, the public will see the Government and the project proponents moving the goalpost in the interest of construction programme. Also, it is also highly undesirable to have an excavation with active dewatering maintained during suspension, which prolongs the risk of affecting the nearby facilities. Therefore, pragmatic enhancement in ground deformation control mechanism of ELS works is warranted and it has been a major issue to be tackled with by the WG when drafting the New Publication.

The New Publication recommended to enhance the current Alert-Alarm-Action system into a five-level system (5A) by further refining the Action Level into 3 levels with ascending scope of response actions for different monitoring markers. This was the results of months of deliberations and persuasion amongst relevant Government departments (including project office and maintenance office), regulators and utility undertakings. The New Publication provides comprehensive rationale and justifications for adopting the respective empirical limits in the action levels and the corresponding response actions at each action level. Nevertheless, mutual trust between the project team and the stakeholders of the affected sensitive receivers is the most essential element to ensure the 5A approach becoming a practicable control mechanism that is acceptable to all parties, including the owners of the affected sensitive receivers and the regulatory authorities.

4.1 Action Level 1 to address serviceability concern

When it comes to the question on devising an enhanced ground control mechanism, it is important to delineate the magnitude of ground deformation that would raise serviceability concerns from deformation that cause safety issues. Serviceability concerns would normally occur at the early stage of settlement and the problem can be tackled easily. It is absolutely important to understand the concerns of the affected stakeholders, so as to devise a plausible scheme that would be acceptable to them.

Irregularities were reported in the construction of the Shatin-Central Link project and the Government appointed an Expert Advisor Team (EAT) to provide advice to follow up on the alleged irregularities. The EAT recommended the Government to improve the formulation and implementation of the monitoring and control system. In this regard, a realistic Action Level (i.e. the threshold limit for suspension of works) which tallies with the predicted ground response, subject to proper justification of the acceptability of this limit, should be set. It was timely that a task force under the Development Bureau was set up to implement the recommendations of the EAT, which included representatives of HyD, BD, ArchSD, Water Supplies Department (WSD), Drainage Services Department (DSD), Housing Department, Electrical and Mechanical Services Department. The WG members of the New Publication had been actively involved in the task force and undertook a comprehensive review for enhancing the control mechanism of ground deformation. Besides the Government departments, the Joint Utilities Policy Group (JUPG) was also consulted to understand their concerns on the adverse impact to their managed utilities due to excavation works. Members of the JUPG include the undertakings of private and public underground utility, such as gas company, power companies, cables and internet service providers, etc., whom they have laid enormous amount of underground utility.

In the consultation, the grievance of the utility undertakings mainly focused on not being notified promptly and consulted on the necessity of remedial works for their affected utility, until the Action Level was reached or damaged was done. Also, the project team and contractor often argued that the damage or leakage of underground utility was due to the impoverished condition of their utilities, or presence of existing cavities on the ground prior to their excavation. Utility undertakings did not have the time to dispute with the project team, as they had tremendous pressure of reinstating their services. As such, many repairs were carried out by the utility undertakings and the project team often took a hands-off attitude.

When devising the enhanced ground control mechanism and response actions, emphasis have been placed to ensure proper consultation and communication are made between relevant stakeholders, including the project proponents, contractors, consultants and maintenance parties and utility undertakings, when ground deformation reaches different action levels. In fact, serviceability of road, pavement and utility could be promptly rectified, such as sealing cracked in road pavement, relevelling paving blocks, repairing damaged

subgrade, realigning or supporting deformed pipelines. The essence of rapidly resolving serviceability concerns is to obtain prior agreements with the relevant stakeholders on when and what to do, when the ground deformation reaches the pre-determined limit; and to implement them accordingly. It will be less costly and more effective to carry out such repair works, other than suspending the site works and arguing the responsibility and scope of the remedial actions.

In some cases, the causation of damages to the utility may not be positively determined after the incident, but early confirmation of the conditions of the ground and underground utility will help eliminate the uncertainty. In the enhanced ground control mechanism, the New Publication highlighted the importance of carrying out the precondition survey of the surroundings and the underground utility, prior to the commencement of the construction works. Relevant government departments, including the WSD, DSD and HyD, would assist project proponents by providing pertinent information of their maintained utilities, such as allowable maximum movements, records of any pipe burst or leakage incident within the affected area, causes of the incidents and remedial actions taken by the responsible departments. The information should assist the project team in assessing the condition of the utility and take necessary precautionary measures to minimise the adverse impact to them. Besides the records provided by the government departments, ground investigation should be carried out to ascertain the condition of the ground and underground utilities, with particular attention paid to any recent incidents of bursting and significant leakage of buried water-carrying services and the possible presence of underground cavities. Ground penetration radar (GPR) and GCO probe may be used to help detect the presence of pre-existing cavities, whereas CCTV survey may be conducted to ascertain the condition of underground drains. Where the results indicate anomaly, additional investigations such as GCO probe or SPT should be conducted to confirm the presence of any cavities at depths. These investigations are usually carried out as part of the precondition survey of the site prior to the commencement of site works. Such pre-condition survey and investigations are usually imposed by GEO when processing the application of building plans or excavation proposal and should be completed before commencement of the construction works (including installation of embedded retaining wall). For project with deep excavation and prolonged period of excavation, the New Publication also recommended repeating the GPR and CCTV inspection when the installation of the embedded wall is completed and at regular intervals (e.g. once every three months) during bulk excavation with active dewatering. Any changes between records of the GPR and CCTV would provide an early warning and indication of possible damages or deterioration of the underground utility.

4.2 Action Levels for Safety Concern

It must be emphasised that the project team should not solely base on the monitoring results of the instruments when determining whether the specified response actions in the ground control mechanism should be triggered. There were many incidents that obvious evidence of damages or undue settlement were ignored and the excavation works were allowed to be continued until more serious consequence occurred. Plate 3 shows a damaged pedestrian pavement adjoining an excavation site. The project team argued that all the measured settlement at the monitoring stations did not exceed the AAA levels and hence they were not in the position to suspend the excavation works. Similarly, there were cases where water was observed to have leaked between individual panels of the embedded retaining wall and the site supervisory staff ignored the potential risk of causing cavities on the ground. In the enhanced control mechanism, more specific actions are prescribed when significant or severe leakage occurs; and whenever obvious damage on the road or pavement is identified.

The enhanced ground control mechanism is developed in consultation with the Government departments. While the magnitude of empirical limits for ground settlement have been increased, it should be noted that these values are agreeable with the maintenance departments (e.g. HyD). In the event that the affected road and pavement belong to private owners, agreement from the relevant private owners should be obtained before the 5A approach given in the New Publication can be used, though the same principle of establishing the limits for ground settlement is still applicable. In such circumstance, it would be beneficial to commence the dialogue with the affected private owners at the earliest possible time, so as to ensure smooth implementation of the excavation works. Otherwise, the control mechanism as given in PNAP APP-137 should be followed.



Plate 3: Damage of the pedestrian pavement adjacent to an excavation site

Under the 5A approach, a set of specific and targeted response actions with respect to exceedance of the corresponding trigger values has been prepared in the New Publication to enhance the effectiveness and efficiency of the control mechanism. The recommended typical response actions in respect to the exceedance of the Action Levels 1 to 3 are given in the New Publication. Other project or site-specific response actions could also be included if necessary and appropriate.

5 APPLICABILITY OF 5A APPROACH TO OTHER GEOTECHNICAL WORKS

The GEO published the Technical Guidance Note No. 54 (GEO, 2024), which expands the ground deformation control mechanism to other types of geotechnical works, including piling and TBM tunnelling. Given the same nature of sensitive receivers being affected, the 5A approach for ELS works can also be applied to other geotechnical works. In this connection, it is necessary to establish the corresponding empirical limits for setting trigger levels for Action Level 2 and Action Level 3 that are realistic and practical for the geotechnical works. For foundation works, piles are usually installed at a distance from the site boundary and the maximum ground settlement induced by the construction of common pile types (e.g. driven steel H piles, pipe pile and bored pile) seldom exceeded 30 mm based on local experience. Settlement caused by diaphragm wall construction is documented in the New Publication, which also falls generally within this limit. Given the settlement limit at Action Level 3 is taken as 30 mm, the corresponding limit for Action Level 2 is set as 25 mm. For soft ground tunnelling works using TBM, review of design standards and case histories of local TBM works indicates that the induced ground settlement is best estimated by correlation with the maximum tunnel excavation Volume Loss (VL). The commonly observed range of VL in TBM works varies between 1% and 2% and the maximum ground settlement is usually less than 100 mm, given the typical size of tunnels in Hong Kong. Hence, it is recommended to set 1% VL and 2% VL as the basis for determining the trigger levels of Action Level 2 and Action Level 3 of ground settlement.

6 CONCLUSIONS

The new GEO Publication No. 1/2023 consolidated the experience and practice in the design and construction of deep excavation in Hong Kong. This New Publication was redrafted with the purpose and aspiration of providing updated guidance to practitioners in design of ELS works, such that a right balance between safety and cost-effectiveness is obtained. Attempts were made to address the problems that had troubled many in the execution of excavation works for years. The New Publication highlighted the harmonization of design approaches, advancements in design and construction practices, and the application of innovation solutions, and more importantly, the enhancement of ground deformation control mechanisms. It also put strong emphasis on the proactive and early collaboration with different stakeholders to develop a mutual trust, which

is considered important in the safe and successful execution of deep excavation projects. Practitioners are encouraged to provide comments on the contents of the publication to GEO at any time, so that improvements can be made in future editions. In addition, a regular review on the effectiveness of the implementation of the enhanced 5A approach for control mechanism of ground deformation and response actions will be carried out. As in normal practice, the technical standards for public and private development should be the same and GEO is collaborating with BD to review and update the relevant PNAPs, such that the recommendations in the New Publication can be consistently applied to Hong Kong projects.

ACKNOWLEDGEMENTS

This paper is published with the permission of the Head of the Geotechnical Engineering Office and the Director of Civil Engineering and Development, the Government of the Hong Kong Special Administrative Region. In addition, the Geotechnical Division of the Hong Kong Institution of Engineers (HKIE) established a Task Force led by Ir Dr Richard Pang to conduct a technical review and recommend updates of the GCO Publication No. 1/90. A Technical Review Report of Design Methods for Excavation was produced by the Task Force in 2021. The Technical Review Report made suggestions on the key updates of the GCO Publication No. 1/90, which greatly facilitate the Working Group in preparing the new GEO Publication No. 1/2023. The effort of the Task Force is gratefully appreciated.

REFERENCES

BD 2012. *Requirements for an Excavation and Lateral Support Plan Building (Administration) Regulation 8(1)(bc) (Practice Note for Authorized Persons, Registered Structural Engineers and Registered Geotechnical Engineers PNAP APP-57)*. Buildings Department, HKSAR Government, 7 p.

BD 2018. *Ground-borne Vibrations and Ground Settlements Arising from Pile Driving and Similar Operations (Practice Note for Authorized Persons, Registered Structural Engineers and Registered Geotechnical Engineers PNAP APP-137)*. Buildings Department, HKSAR Government, 7 p.

Cheung, P.Y.S., Shum, K.W. & Koo, C.H.R. 2023. Advancement in geotechnical practice. *Proceedings of the HKIE Geotechnical Division Annual Seminar*, 2023, HKIE Geotechnical Division, pp 168-187.

Gaba, A., Hardy, S., Doughty, L., Powrie, W. & Selematas, D. 2017. *Guidance on Embedded Retaining Wall Design (CIRIA C760)*. Construction Industry Research & Information Association, London, 285 p.

GEO 1990. *Review of Design Methods for Excavations (1990) (GCO Publication No. 1/90)*. Geotechnical Engineering Office, Civil Engineering and Development Department, HKSAR Government, 187 p.

GEO 2020. *Guide to Retaining Wall Design (Geoguide 1) (2020 Version)*. Geotechnical Engineering Office, Civil Engineering and Development Department, HKSAR Government, 258 p.

GEO 2023. *Deep Excavation Design and Construction (GEO Publication No. 1/2023)*. Geotechnical Engineering Office, Civil Engineering and Development Department, HKSAR Government, 144 p.

GEO 2024. *Guidelines on Ground Deformation Control Mechanism for Geotechnical Works (GEO Technical Guidance Note No. 54 (TGN 54))*. Geotechnical Engineering Office, Civil Engineering and Development Department, HKSAR Government, 5 p.

An Innovative ELS System on Recently Reclaimed Land – Construction and Performance

Gavin S.H. Toh & C.N. Ho
Lambeth Associates Limited, Hong Kong
Jack Yiu, Tom S.K. Chan & Chris C.F. Shum
Ove Arup & Partners Hong Kong Limited, Hong Kong
Oscar Y.N. Tse & Kimberly H.Y. Leung
Gammon Construction Limited, Hong Kong

ABSTRACT

On the recently reclaimed land for the airport three-runway system, deep excavations have been carried out to construct tunnels connecting the terminals. A novel excavation and lateral support (ELS) design comprising a double wall system connected by ties was introduced in one portion to cater for the challenging geotechnical condition with improved constructability at the site adjacent to the shoreline. This paper will briefly discuss the development of the scheme, then focus on the construction and performance of the system. The design was developed through close collaboration between the designers and contractor, based on a thorough site investigation and analyses. It offered a cost-effective construction option allowing clear access to the cofferdam, flexibility for lifting and logistics, and efficient structure construction processes. The robustness of the system could also be enhanced by additional ground improvements across a limited extent. The performance of the system during construction has been reviewed by comparing the predicted deflection of the temporary vertical walls in design analyses with the monitoring data. It is observed with positive results giving confidence in the implementation of deep excavation with a double wall system. Site observations are also shared with recommendations of potential improvements for future implementation.

1 INTRODUCTION

1.1 Project Background

The Airport Authority Hong Kong Contract 3802 project is a part of the Three-Runway System (3RS) to construct tunnels and related works for an automatic people mover (APM) and baggage handling system (BHS) at Hong Kong International Airport connecting the third runway concourse (TRC) building and the system on the existing reclaimed land. The tunnels were mostly to be constructed on the recently reclaimed land by cut-and-cover method. The excavations involved varying depths, different ELS systems were therefore proposed for different portions. This paper will focus on discussing the construction and performance of a double wall ELS system for up to 9.5m deep excavations.

1.2 Ground Conditions

The site is located offshore of the original Chek Lap Kok Island as well as the existing reclaimed land of the airport area in the north. Marine muds underlain by alluvium layers of different characteristics are present, followed by saprolite and solid rock. No dredging had been carried out for the recent reclamation in this area and up to more than ten metres of soft marine clay remains beneath the reclaimed land. Around ten metres of fill materials were placed on top of the marine mud improved by deep cement mixing (DCM) elements. Sand blanket was placed on the seabed followed by ground improvement involving the installation of DCM

elements before reclamation. There were different zones with DCM in different patterns, replacement ratio, required uniaxial compressive strength, installation methods, and embedment into competent stratum.

2 EXCAVATION AND LATERAL SUPPORT (ELS) DESIGN

2.1 Constraints

The tunnel structures to be constructed were in various depths. Conventional multi-strutted cofferdam was used for deeper excavations more than 10m. For shallower excavations, more cost-effective design was pursued. Where space was abundant, open cut excavation could be carried out. While at the subject portion of tunnel, the seaside was close to the shoreline of the new reclamation, being only 10 to 20m away from the seawall. With the landside having enough space for open cut, struts were desired to be avoided not to introduce additional retaining wall on landside and obstructions across the tunnel construction footprint, with the help of a self-sustained retaining system on the seaside. With the limited distance of 10m shortest between the tunnel and the shoreline, it made effective typical tie-back wall into soil and deadman anchor system difficult. A double wall system was therefore introduced for retaining an up to 9.5m deep excavation on the seaside coupling with the open cut on the landside (Figure 1 and Plate 1).

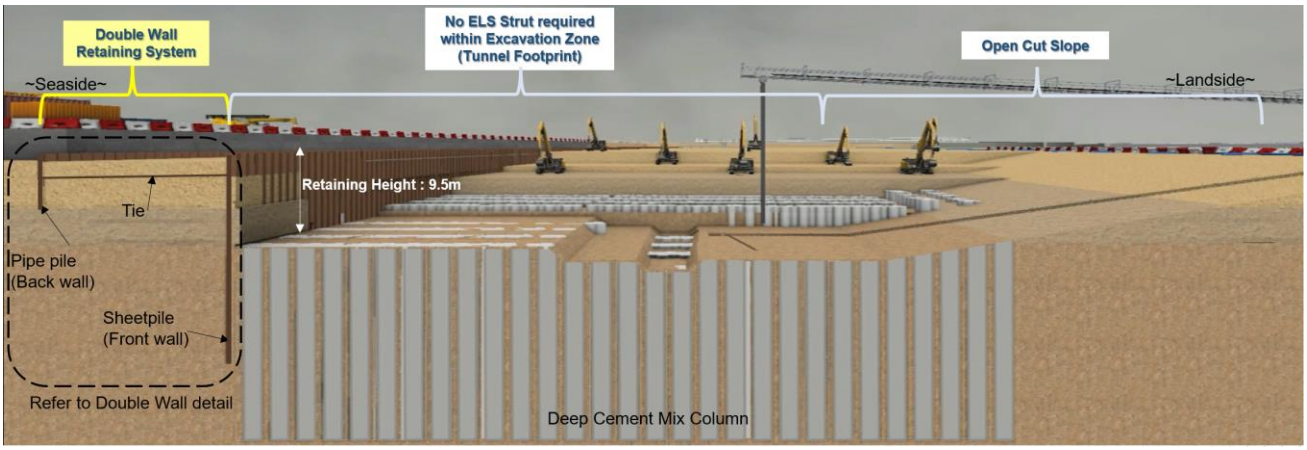


Figure 1: ELS design with double wall and open cut

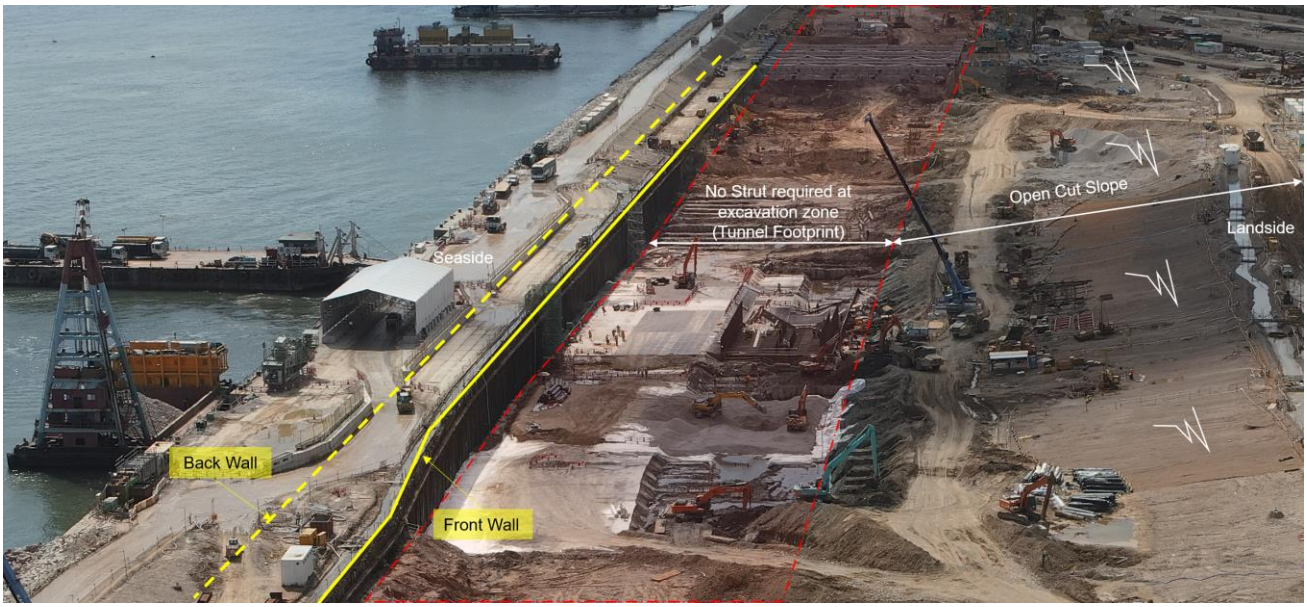


Plate 1: General view of the double wall and open cut ELS

2.2 The ELS system

With the abovementioned constraints, an extra element was designed for tie-back anchorage to form a double wall system. It was composed of a continuous front wall (sheet piles) and discrete back wall (pipe piles) connected by steel ties (Figure 2). The member sizes of sheet piles and pipe piles were various at different design sections, and UB sections were inserted into the pipe piles where necessary. The spacing between the front wall and back walls varied from 9m to 16m. The back wall was designed as a laterally loaded pile row, with enhanced resistance from the existing DCM panels. Additional ground improvement by Deep Jet Mixing (DJM) was also constructed at certain spots to enhance the robustness of the design (Figure 3).

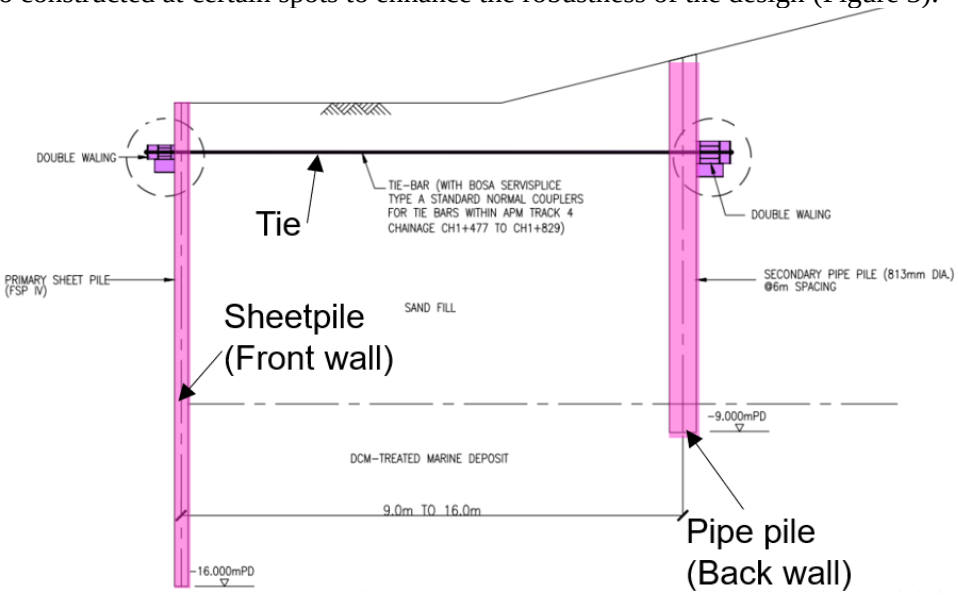


Figure 2: Double wall detail

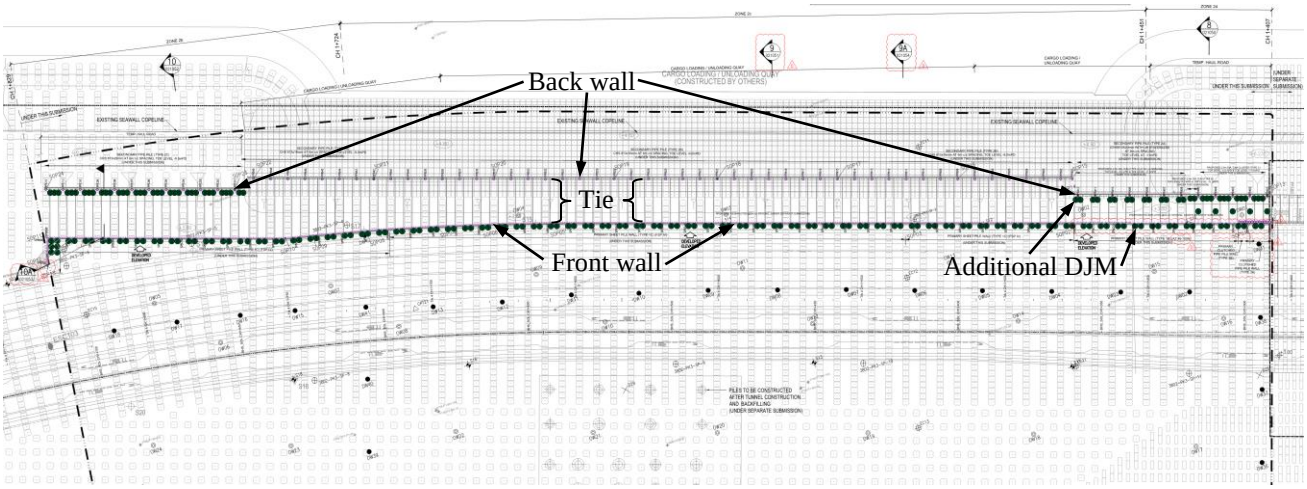


Figure 3: Double wall layout plan

The double wall system is the result of the interaction between the front and back wall as well as the soil in between. Early in 1974, Sawaguchi recommended that a double sheet pile wall structure should be analyzed as a composite structure consisting of both sheet pile walls and the filling so that the interaction between the components could be taken into account. While it was a problem to establish soil constants for more accurate computation by the theory of elasticity, the current design is well facilitated with the help of finite element modelling. Lee et al. (2007) suggests a double piled wall system could be effective in reducing by more than half the surface settlement, horizontal displacement, tilting angle, and the maximum bending moment on the pile compared to the single pile wall. These made the double wall design feasible as a desired self-sustained retaining system.

The ELS system was a result of the close collaboration between the designers and contractor. The communication of the site constraints and design considerations made the scheme satisfy both the site and design requirements. The client also welcomed innovative ideas and was supportive to motivate the development of the solutions and eventually the real construction of the system. When modifications were needed during construction, the team could address the safety concerns and constructability problems upon site conditions effectively.

3 ELS CONSTURCTION

3.1 Construction Sequence

At this site with complicated ground conditions, thorough ground investigation played an important role to facilitate the geotechnical interpretations including delineation of design ground profile and selection of design parameters. Only after the design had been verified with a detailed geotechnical interpretative report based on the ground investigation, the installation of ELS elements on site was carried out. The major steps (Figure 4) of the construction included:

1. Install front wall and back wall
2. Install DJM in front of wall toe where applicable
3. Shallow excavation for tie installation (Plate 2)
4. Backfill with compaction on top of tie (Plate 3)
5. Bulk excavation to final excavation level (FEL) for tunnel construction

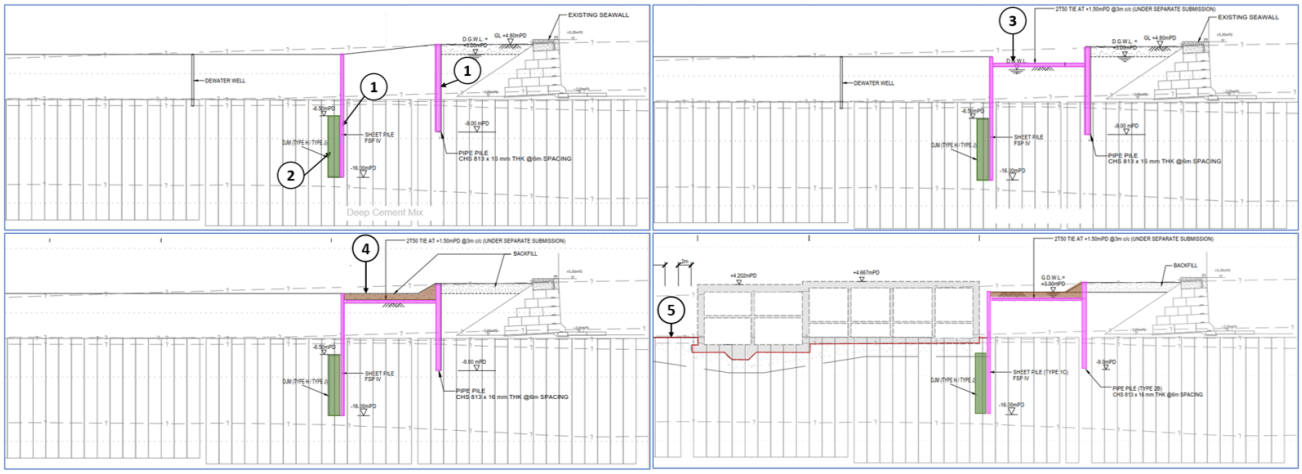


Figure 4: Construction steps

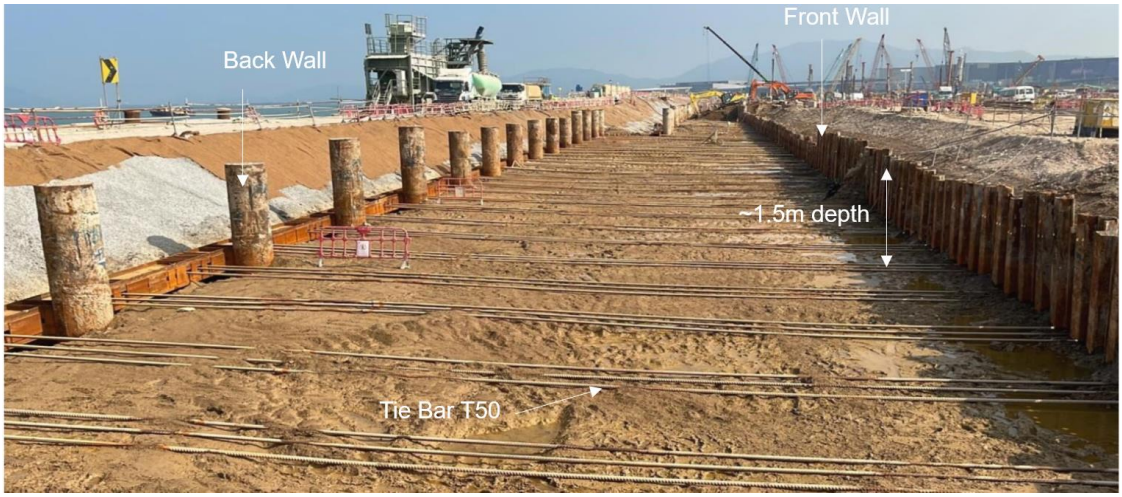


Plate 2: Shallow excavation for tie installation



Plate 3: Backfill with compaction on top of tie

During the construction, there were different considerations in each step of the sequence. For installation of the front wall and back wall, on top of the common problem of potential obstructions to sheet piles which would require pre-boring, the embedment locations of the walls were of importance dependent on the design assumptions. Where the front or back wall was assumed to be embedded in DCM ground improvements, engineering control procedures were implemented to ensure the wall was properly installed at the right positions. The as-built information of the ground improvements would be reviewed, and the site responsible personnel would confirm the pile wall to be located at the centre of the DCM clusters or panels on site. Geotechnical engineers or geologists would inspect the materials when the drilling is sunk to the designated depths, both at the top of the ground improvements and at design wall toe levels, to confirm the materials reached. Installation records would be taken and properly filed. Additional DJM works had to be carefully executed not to damage the adjacent installed walls.

The shallow excavation for tie installation was next to the shoreline. While the back wall was individual pipe piles at spacing without full cutoff, the excavation works had to be planned with consideration of the tidal conditions and proper water management. Special connection details were developed facilitating both the load transfer design and fabrication considerations, and it was also made for easy installation on site (Plate 4). During backfill with compaction on top of tie, attention was paid not to damage the installed tie bars.

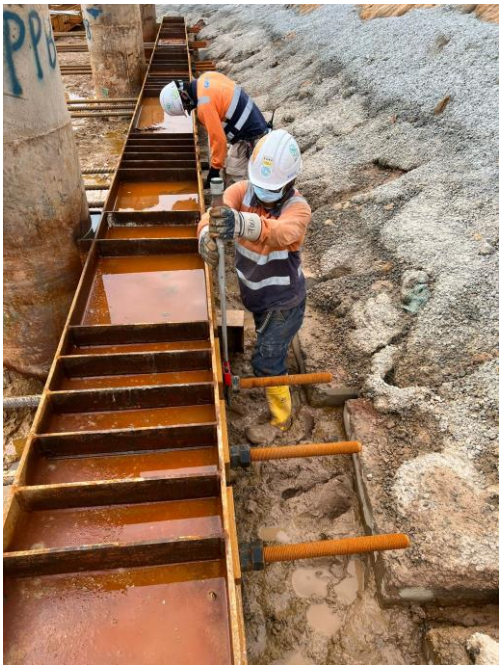


Plate 4: Tie connection installation

The bulk excavation seemed to be straight forward without the level limitation for strut installation or headroom restriction from struts, yet problems could be encountered in the process and close supervision could not be relaxed. For example, where imperfection of wall installation was encountered, water leakage could occur. Well planned bay by bay excavations with sequential level difference were still carried out to ensure problems could be spotted at an early stage and timely remedial measures could be carried out.

3.2 Features

With the double wall system adopted, several obvious benefits were observed. First, heavy lifting works were saved, as no shoring installation layer by layer was required. Plants could be delivered from the open cut side here in one piece. Works at height were also minimized without the shoring segments installation and dismantling. The ties here could be installed or trimmed at the corresponding formation level. The use of mobile elevating work platforms (MEWP) and elevated mucking out were therefore not required. Next, hot works including welding and flame cutting could be minimized with no shoring installation and dismantling. The ties could be designed to allow mainly mechanical installation. Moreover, the site logistics were improved by the open working space (Plate 5), eliminating the congestion and headroom restriction caused by the shoring. Lifting works could be carried out more smoothly, plants could transport across the site freely, and man access to within the excavation could be safer. This also allowed the smooth use of travelling formwork facilitating the tunnel structure construction. All these made the system preferred with enhanced productivity and safety.

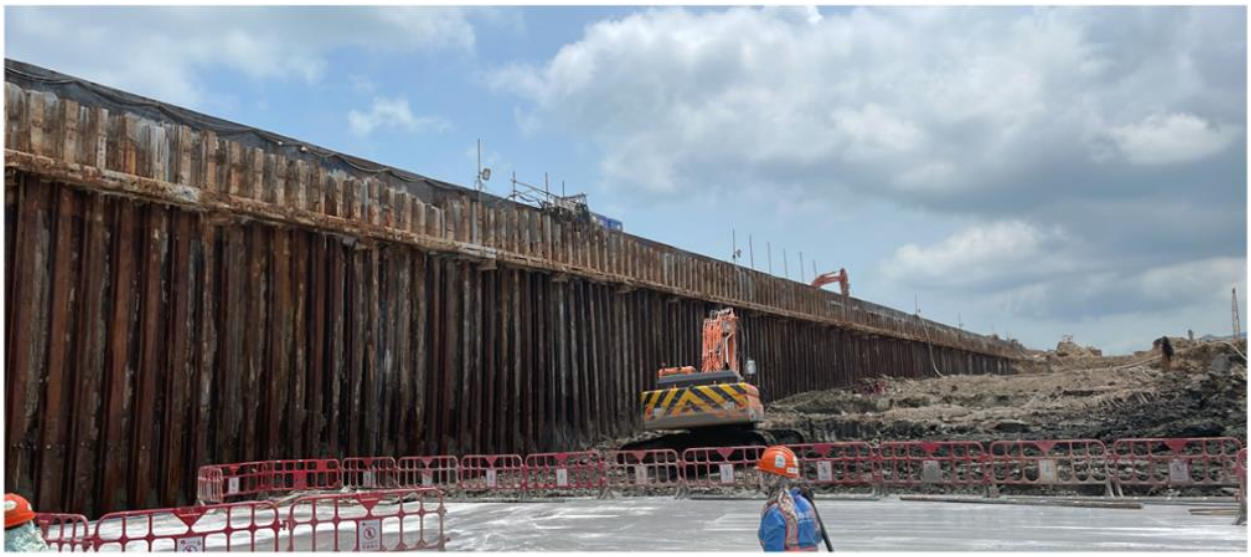


Plate 5: Open working space in excavation

The double wall system was also flexible for variations of design. Different wall types could be used according to different conditions and constraints, for example, different sizes of sheet piles and pipe piles as well as interlocking pipe piles. Transition to adjacent strutted cofferdam was also feasible, where struts could be installed against the front wall.

4 PERFORMANCE OF THE SYSTEM

4.1 Instrumentation and monitoring

The geotechnical instrumentation and monitoring programme had been developed in accordance with the project requirements and predicted zone of influence and included both geotechnical and structure monitoring as a precautionary measure to closely monitor the construction works. The proposed monitoring points were generally within a distance of 1.5 times excavation depth of the subject cofferdam. The instrumentation types

used to monitor the ground movements, structure movements and changes in groundwater levels during the relevant ELS stages included ground settlement markers, building settlement markers (for seawall), tilt plates, standpipes/piezometers, inclinometers (in soil, pipe pile and DCM), and vibrating monitoring points. A monitoring programme with Alert, Alarm and Action (AAA) triggering system was implemented on site to provide a safeguard against any abnormal or rapid change of movement of the adjacent ground and ELS structures during the construction works.

4.2 Comparison between design prediction and monitoring

The inclinometers were particularly useful for comparison with the design analyses to verify the performance. Compared to ground settlement markers, they were less vulnerable to site works disturbance and more continuous readings could be retrieved. They also provided more than a single value for each reading, where both the magnitude and shape of deflections could be investigated. A number of inclinometers were used to compare with the analysis predictions in four design sections (Figure 5).

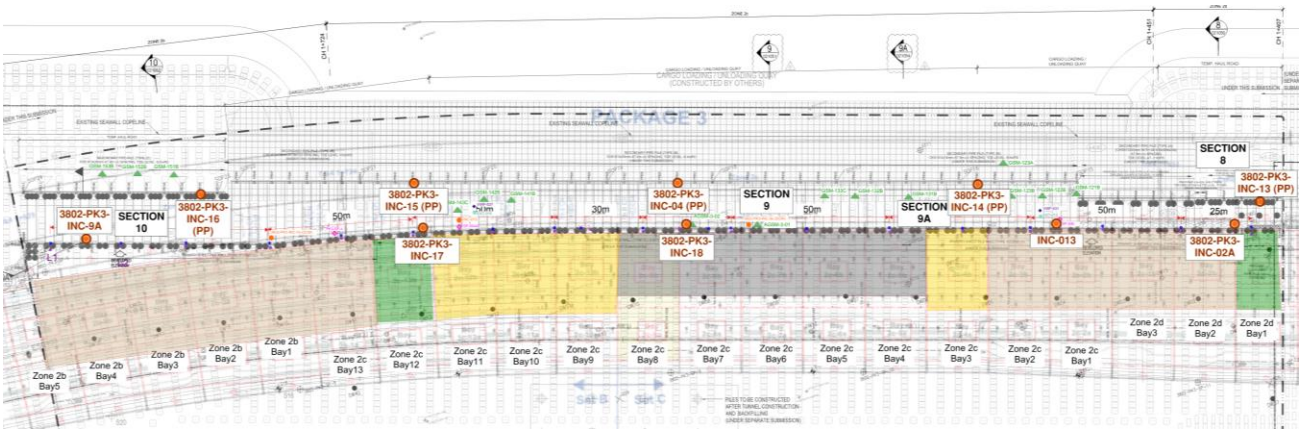


Figure 5: Monitoring layout plan – inclinometers for comparison

The data on the date with maximum magnitude of deflection for each target inclinometer was extracted, and the readings from top level to wall toe level were plotted against the predicted maximum wall displacement profile in the corresponding 2D finite element analysis model under normal loading (Figure 6 and Figure 7). First, most of the deflection shapes from inclinometers were comparable to the predicted ones, verifying the design failure mechanism where the back wall was laterally loaded at the top tie level having maximum deflection, and the front wall was held by the tie and embedment having maximum deflection in between. Second, most of the monitored magnitudes of deflection were well within the predictions except at the front wall of one location. It could have implied that the moderately conservative design approach was justified, where the actual stiffness of soil or ground improvements was higher than that adopted in design. The adoption of reduction factors on the stiffness of sheet pile could also contribute.



Figure 6: Comparison between prediction and monitoring – part 1

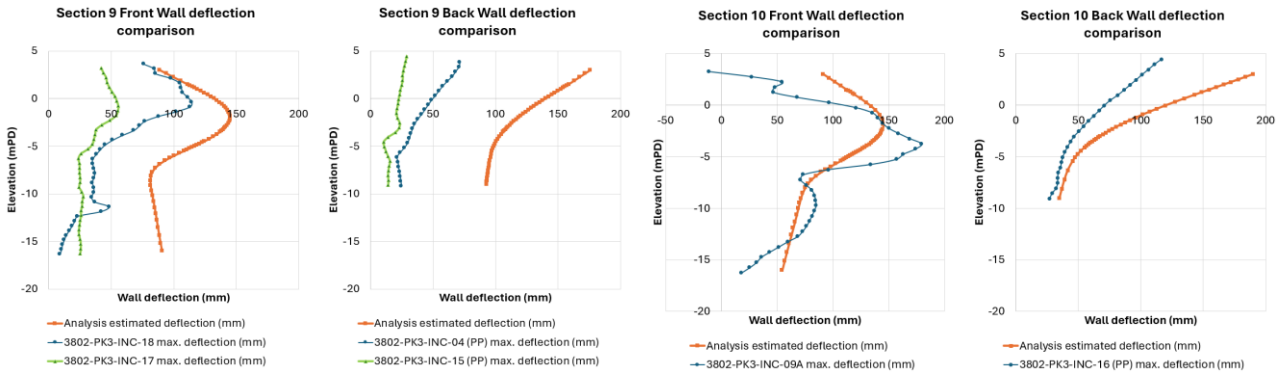


Figure 7: Comparison between prediction and monitoring – part 2

Looking into individual comparisons, variations were observed and the potential contributing factors will be discussed. At Section 8, the deflection shapes of both walls between inclinometer readings and predictions matched well. The magnitudes of deflection were also close from wall toe to around top of existing ground improvement levels, while further towards top level the monitored deflection became smaller and smaller compared to the predicted values. This could imply the wall embedment was working hard as in design while the fill and ELS walls on site could be stiffer than in design. At Section 9A, inclinometers showed much smaller deflection from top to bottom of both walls. The back wall looked mildly loaded while the front wall did not show an obviously larger deflection between the tie and embedment, the mobilizing pressure could be much smaller than as predicted. At Section 9, there was a similar trend to what was observed at Section 9A except the front wall showed a more obvious bulge below tie level. The area was with a temporary bus stop and close to a traversing haul road, which may be subject to a higher surcharge loading condition causing the difference. At Section 10, the shapes of deflection matched well. The maximum deflection reading of the front wall exceeded what was predicted in the analysis with normal loading as shown but still within the prediction with additional loading, and that of the back wall was still within prediction. Other than in a period there was a working barge unloading materials onshore around the area, this could be attributed to a water leakage incident at the location near the subject inclinometer which caused minor soil washout at the front wall sheet pile. Provided the back wall still performed well and the exceedance was local and within the prediction with loading variation, the system was considered still functioning well as designed.

Overall, the monitored deflections were with considerable safety margin from the predictions for Section 9A and 9 where the distance between front and back walls was larger, while those at Section 8 and 10 with closer front and back walls were approaching the corresponding predictions, especially near the wall toe level. It was inferred that the double wall system could work better with larger front and back wall separation distance, benefiting from the resistance of soil in between. As moderately conservative design parameters were adopted in design predictions, a further gap from reality may be observed. When the two walls were closer to each other, more structural capacity of the back wall could have been mobilized and the laterally loaded pile behaviour became more obvious. With the more certain structural stiffness assumption in the design, the predictions could have been more realistic and approached by the monitoring readings.

4.3 Other Observations

Other than the movement readings of the ELS system, there were also some site observations worth noting which may give insights into the understanding of the system. While the wall deflection profile could be inferred from inclinometer monitoring readings, the potential variations along the wall alignment direction were not captured. Upon reaching the final excavation level, an obvious varying wall deflection along wall alignment direction was noted (Plate 6). This suggested that solely 2D analysis may not be thorough for representing the behaviour of the ELS system, especially at this site where DCM ground improvements were present at a spacing with untreated in-situ soft marine clay in between. This, in addition to the tie supports at a spacing, could lead to a complicated behaviour variation in 3 dimensions. Hence, a more representative 3D analysis may help the further understanding of the potential impact on the system performance including the bending along the wall alignment direction.

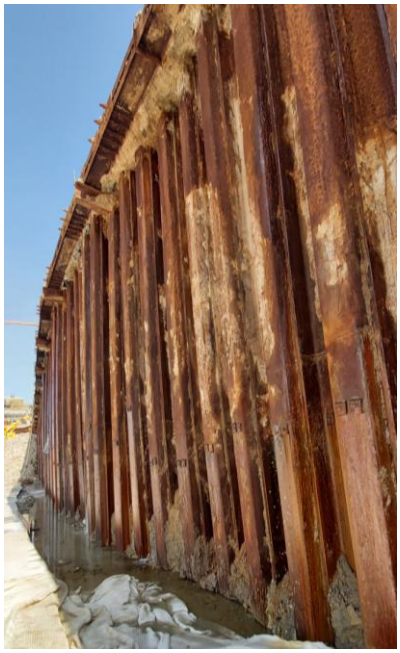


Plate 6: Varying wall deflection along the wall alignment direction

The water tightness of the ELS was not perfect but manageable. Local leakage occurred for a few different reasons. Some minor water inflow came in from the lifting eyes of the sheet piles, this was improved when awareness was raised and covers were welded after lifting. There was also local declutching resulted from the wall installation process, and it cost some efforts for remedial measures when excavation had reached relatively low level. It would be better if any water leakage problems could be spotted at an early stage with timely remedial measures carried out.

5 RECOMMENDATION

With the successful experience of adopting the double wall system for a 9.5m deep excavation (Plate 7), it is recommended the system shall be considered for future projects. It is shown to be well applicable for a site requiring space within the cofferdam, far from sensitive structures while having limited space next to the excavation. Upon reaching the final excavation level, the open working space could facilitate productive structure construction without obstructions (Plate 8).



Plate 7: Maximum 9.5m excavation without strut

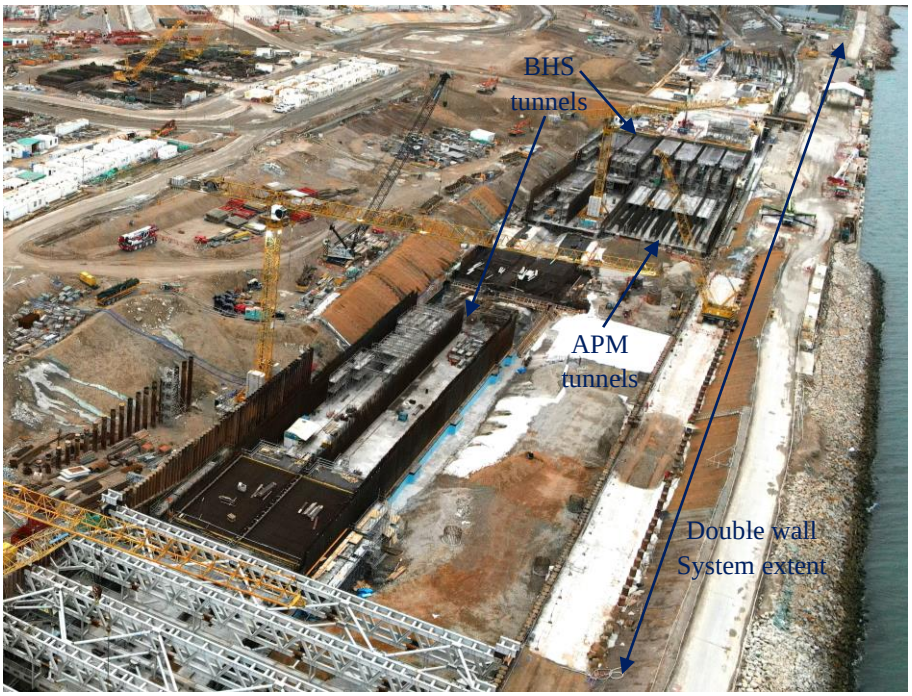


Plate 8: Construction of tunnel structure in spacious area

As suggested by Jiang et al. (2023), the excellent structural stability, strong resistance to deformation and seepage, and adaptability to engineering challenges of double-row steel sheet pile cofferdam is favoured in soft soil areas, with numerous studies having analyzed the structural stability of cofferdams and the safety of the construction process. The system has been shown here suitable for the complicated soft ground conditions with the aid of DCM/DJM ground improvements. The existing ground improvements as well as additional ones were made use of. While non-dredged reclamation with ground improvements has become more common, it may help if their planning such as DCM patterns and strength involves considerations of facilitating future development such as the potential ELS systems for excavations.

It shall however be noted that the design and construction of a double wall system may not always be successful. As recorded by Hsieh et al. (2003), the underestimate of the influence from groundwater, overestimate of soil strength and optimistic design without proper supervision could have led to an excessive displacement and collapse after rainstorm in a case study. Here, incidents were also encountered but thanks to the robust monitoring system, close supervision, good responsive action planning and continuous design review, a safe construction was secured. In the future, improvements to the double wall system are feasible with its flexibility. The choice of wall types, use of additional ground improvements and combinations with other systems could all be worked on according to the specific site conditions. For example, the use of interlocking pipe piles could maintain the water tightness feature while offering stiffer option of pile members, the use of interlocking wall system for both front and back walls may further improve water cutoff performance.

It is also hoped that the successful experience here would give confidence for checkers to be more open for innovative solutions, not only the presented system but also any uncommon systems in Hong Kong supported by theories, overseas experience, and robust monitoring and review processes. With a close collaboration between the designers, contractors and clients, a safe and efficient design and construction can be produced.

6 CONCLUSION

The subject construction and performance review of the application of double wall ELS system hopes to provide a case study for future reference. The site conditions, constraints and the elements of the system have been presented. The construction sequence and benefits of the system to construction process are then investigated. The performance is reviewed by inspecting the inclinometer monitoring results, which are

compared with the design analysis predictions and found generally satisfactory. Discussion is provided for variations at a few different locations. There have also been some site observations and recommendations on the future application of such a double wall ELS system. Facing more and more engineering challenges in a world looking for higher productivity and cost efficiency, the self-sustained strut-free double wall ELS system would provide an option for consideration.

ACKNOWLEDGEMENTS

The authors thank Airport Authority Hong Kong for the permission and kind support to publish this paper. The efforts and participation of the project teams and supervision teams are highly appreciated.

REFERENCES

Hsieh, H.S., Shih, C. and Lin, T.M., 2003. A note on the behavior of double-rail earth retaining system. *Sino-geotechnics,* 97, pp.5-14.

Jiang, Y., Guo, F., Wang, W., Yang, G., Yue, J. and Huang, Y., 2023. Stability Study of a Double-Row Steel Sheet Pile Cofferdam Structure on Soft Ground. *Water,* 15(14), p.2643.

Lee, C.J., Chen, H.T., Wei, Y.C., Lin, Y.C., Huang, W.S. and Chiang, K.H., 2007. Centrifuge modeling of a self-supported double soldier-piled wall in sandy soil. *J. GeoEng,* 2(3), pp.97-109.

Sawaguchi, M., 1974. Lateral behavior of a double sheet pile wall structure. *Soils and foundations,* 14(1), pp.45-59.

Economical Design Approaches for Deep Excavation and Lateral Support (ELS) in Soil with Shallow Bedrock

Ted Tse & Kelvin Ng
Binnies Hong Kong Limited

ABSTRACT

Deep excavation and lateral support (ELS) are integral components of urban development, particularly in the construction of multi-storey basements. The conventional ELS design employs the Mohr-Coulomb (M-C) Failure Criterion for both soil and rock parameters, even when bedrock is encountered at shallow depth. This may lead to over-conservative design by underestimating the rock mass strength and stiffness in the overall rock-structure interaction analysis. This paper explores an alternative design approach by suggesting the application of the Hoek-Brown (H-B) Failure Criterion for ELS design in the presence of shallow bedrock. While the M-C parameters are well-established for soil, the conservative nature of M-C Failure Criterion for rock parameters derived from rock joints or discontinuities defect shear strength properties can lead to avoidable costs. Additionally, the paper addresses common scenarios involving the design of temporary piled walls socketed into bedrock for deep excavation, which involve the design of groundwater seepage in rock. The paper suggests a more nuanced approach, advocating for an assessment of the likelihood of possible rock joint failures to derive sensible and cost-effective solutions. By reconsidering conventional design criteria and incorporating alternative geotechnical principles while highlighting the importance of rock testing and field observation, the proposed methodologies contribute to more efficient and economically viable deep excavation practices in rock.

1 INTRODUCTION

The most economical method for excavation in rock is open pit excavation with steep gradients, generally 60° to 80°. In such cases, rock support measures such as rock dowels / bolts, rock anchors or rock face dentitions would be required if unfavourable rock discontinuities are observed after geological rock face mapping by experienced geologists or geotechnical engineers. However, open rock pit excavation is not practical for deep basement excavation in the urban areas of Hong Kong. This is because the basements typically occupy the entire site to maximize the usable area leaving no space for steep rock cutting batters.

Excavation and lateral support (ELS) for deep basements in urban Hong Kong commonly consists of temporary piled walls with layers of steel strutting. Even though the excavations are carried out in bedrock, the piled wall would still be required to be socketed with a certain embedment into the rock below the excavation levels, and some heavy strutting layers would be propped against the rock face. There seems to be little difference between excavation in “soil” and “rock”, although it is widely accepted that “rock” should have significantly better engineering properties and may even be self-supporting safely.

In other words, the current design practices for ELS works in rock are generally over-conservative. This paper reviews the current design practices and tries to identify the processes leading to conservative outcomes. By understanding the properties, behaviours and potential failure mechanisms of rock, economical design approaches for deep ELS system with shallow bedrock can be applied to offer potential opportunities for cost-effective and safe design.

2 OVERVIEW ON MODELLING APPROACH FOR DEEP EXCAVATION DESIGN

In Hong Kong, limit state design is commonly adopted in the design of ELS works, which must satisfy the fundamental requirements of stability and serviceability (GEO Pub. 1/2023, 2023). To meet both limit state design requirements, especially in complex site setting, it is preferred to utilize numerical modelling to consider soil-structure interaction and excavation sequence. Numerical methods, including the boundary element method introduced in FREW and the finite element method adopted in PLAXIS 2D, are widely used in the design of ELS works.

In both numerical methods, the fundamental Mohr-Coulomb (M-C) Failure Criterion is commonly adopted in local practice to determine the soil shear strength parameters of the principal material types encountered at depth. This criterion is well known as a linear function of shear strength parameters, including cohesion intercept (c') and angle of shearing resistance (ϕ'). The c'-ϕ' values of the soil strata are determined from consolidated undrained (CU) triaxial tests. The typical ranges of c'-ϕ' values for selected Hong Kong soils are given in Table 8 of Geoguide 1 (GEO, 2020).

In addition to shear strength parameters, the stress-strain behaviour, which can be expressed by the modulus of deformation of soil or Young's modulus, needs to be incorporated into the soil stiffness matrix for the calculation of ground movement. In prevailing practice, the Young's modulus is correlated with in-situ test results, such as standard penetration test (SPT) 'N' value (GEO Pub. 1/2023, 2023).

By establishing the fundamental failure criterion and stress-strain relationship in the soil model, we can realistically model the ground conditions, describe soil-structure interaction interfaces in numerical analysis, and obtain subsequent estimations of geotechnical and structural results of the ELS system. These results include soil stress and ground movement from the geotechnical aspect, as well as deflection, shear force and bending moment of structural components such as piled walls and strut members.

The current design practices for ELS systems in rock assume that rock possess physical properties of "soil". In other words, the c'-ϕ' values for the rock are taken as the shear strength of the rock joints, which can be obtained from the results of direct shear box tests. If no direct shear box test is carried out, it may be considered to adopt the upper bound of the typical ranges of completely decomposed rock, such as:

- For granite bedrock: c'= 15kPa and ϕ' = 44°
- For volcanic bedrock: c'= 10kPa and ϕ' = 38°

For Young's modulus (E_s') of rock, it is assumed that SPT'N is greater than 200 blows, and thus the E value is empirically assumed to be twice the SPT'N value, i.e., greater than 400MPa. Typically, E_s' is proposed to be 400MPa for design purpose.

For the design groundwater pressure, hydrostatic pressure is adopted, with groundwater continuing to increase with depth from soil to rock. However, it should be noted that in the majority of rock excavation portions, grout curtain, lagging plates or shotcrete are not required between the piles. Therefore, the groundwater pressure should be relieved by seeping groundwater through persisting rock joints exposed between the piles.

For the design of the required rock socket for the ELS piled wall, two failure modes should be considered. Firstly, the rock socket should be checked against the bearing failure in accordance with Figures 51 to 53 of Geoguide 1 (GEO, 2020) for different directions of bending moment and shear force at the top of rock socket. Secondly, the rock socket should be designed against planar discontinuity-controlled failure based on Figure 54 of Geoguide 1 (GEO, 2020). The variations of rock socket capacity are calculated with various dip angles of discontinuity and thus the calculated minimum ultimate lateral resistance should be greater than the required lateral resistance from numerical models, i.e., ULS bending moment and shear force from FREW or PLAXIS 2D. The latter checking mode often leads to much deeper rock sockets, which would require similar embedment as determined by kickout checking using K_p method.

3 MATERIAL MODELLING OF ROCK MASS

In consideration of the shear strength parameters of rock, it can be classified as discontinuity shear strength or rock mass shear strength based on scale effects and geological conditions, as represented in Figure 1. The relationship between shear stress and effective normal stress varies for rock with different characteristics of discontinuities and rock strength.

As presented in Figure 1, there are shear strength properties for "Discontinuities" and "Rock Masses". The shear strength properties for "Discontinuities" refer to the properties of individual joints / joint sets in the rock mass, which are related to the joint's properties and can be determined from direct shear box tests of rock joint specimens. The shear strength properties for "Rock Masses" refer to the properties of the overall rock structure, which take into account of intact rock strength obtained from the Unconfined Compression Strength (UCS) Test, and Geotechnical Strength Index (GSI), concentrating on the description of two rock characteristics: rock structure and block surface conditions.

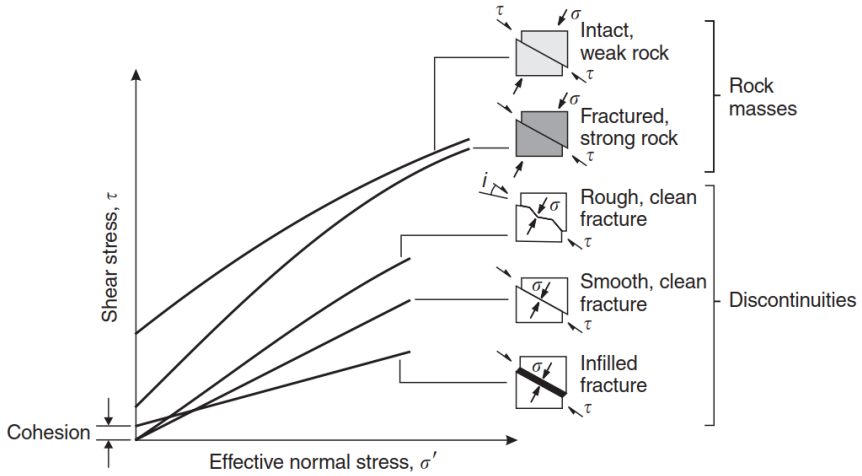


Figure 1: Shear Strength Parameters of Rock (Wyllie and Mah, 2004)

Depending on the different checking scenarios, designers should determine which set of rock shear strength parameters should be adopted for the design. For example, when designing of rock plane or wedge failure at localized areas, the shear strength properties of "Discontinuities" should be used. While working on numerical analysis, the rock strata should be modelled with the shear strength properties of "Rock Masses".

The Hoek-Brown (H-B) Failure Criterion is a widely used rock mass strength criterion that provides a method for estimating the strength of rock masses and predicting their behaviour under various loading conditions. Developed by Evert Hoek and E. T. Brown in the 1980s, this criterion has become a fundamental tool in geotechnical engineering for assessing the stability of rock slopes, tunnels, and mining works globally.

The original H-B Criterion has a major limitation in handling some geotechnical problems, especially for slope stability and underground excavation design, since it is defined in the terms of principal stresses rather than shear and normal stress, as shown in the following equation:

$$\sigma_1' = \sigma_3' + \sigma_{ci}\left(m\frac{\sigma_3'}{\sigma_{ci}} + s\right)^{0.5} \qquad (1)$$

where:

- σ'_1 and σ'_3 are the major and minor effective principal stresses at failure;

- σ'_{ci} is the uniaxial compressive strength of the intact rock material;
- m and s are material constants, where s = 1 for intact rock.

In contemplation of the limitation of H-B Criterion, Hoek endeavoured to provide a comprehensive presentation of the H-B Criterion within the framework of M-C Failure Criterion, and the generalized H-B Criterion was developed. In the generalized H-B Criterion, the shape of the principal stress plot or the Mohr envelope could be adjusted by replacing the square root term in Eq. (1) with a variable coefficient, resulting in the following equation:

$$\sigma_1' = \sigma_3' + \sigma_{ci}\left(m_b \frac{\sigma_3'}{\sigma_{ci}} + s\right)^a \qquad (2)$$

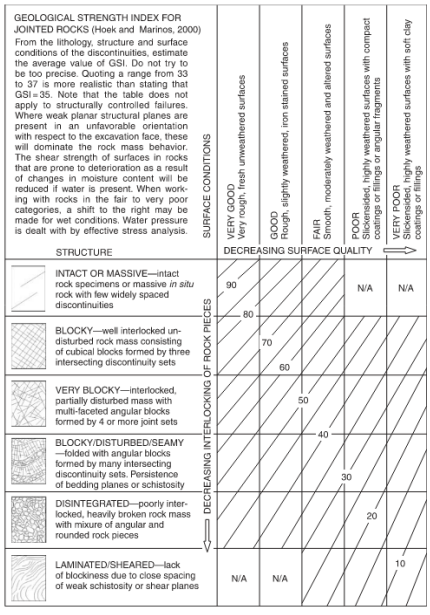
On the other hand, the introduction of the material constant (m_i), Geological Strength Index (GSI) and the degree of Disturbance (D) to which the rock mass subjected by stress change due to any activities such as blast damage and stress relaxation completes the expression of Generalized H-B criterion by quantifying the value of material constants and the variable coefficient (i.e., m_b, s and a) and given by the following relationships:

$$m_b = m_i\, e^{\frac{GSI-100}{28-14D}} \qquad (3)$$

$$s = e^{\frac{GSI-100}{9-3D}} \qquad (4)$$

$$a = \frac{1}{2} + \frac{1}{6}\left(e^{\frac{GSI}{15}} - e^{-\frac{20}{3}}\right) \qquad (5)$$

The values of GSI, m_i and D are generally empirical and subject to the rock particle interlocking condition, types and texture of intact rock, and the disturbance to the rock mass itself due to the nature of geotechnical works involved. The Disturbance Degree Factor (D) for normal ELS rock excavation by mechanical method is 0.7 in according to Hoek, Carranza-Torres & Corkum, 2002. The suggested values for the GSI, m_i and D are shown in the tables of Figure 2. Apart from the GSI chart, several literatures suggest different methodologies for determining the value of GSI based on well-established systems such as the rock mass rating system (RMR) and Q-system (Ágnes, Kovács, Somodi & Vasarhelyi, 2016) and (Hussian et al., 2020).



Rock type	Class	Group	Texture: Coarse	Medium	Fine	Very fine
SEDIMENTARY	Clastic		Conglomerates (21±3) Breccias (19±5)	Sandstones 17±4	Siltstones 7±2 Greywackes (18±3)	Claystones 4±2 Shales (6±2) Marls (7±2)
	Non-Clastic	Carbonates	Crystalline Limestone (12±3)	Sparitic Limestones (10±2)	Micritic Limestones (9±2)	Dolomites (9±3)
		Evaporites		Gypsum 8±2	Anhydrite 12±2	
		Organic				Chalk 7±2
METAMORPHIC	Non foliated		Marble 9±3	Hornfels (19±4) Metasandstone (19±3)	Quartzites 20±3	
	Slightly foliated		Migmatite (29±3)	Amphibolites 26±6	Gneiss 28±5	
	Foliated*			Schists 12±3	Phyllites (7±3)	Slates 7±4
IGNEOUS	Plutonic	Light	Granite 32±3 Granodiorite (29±3)	Diorite 25±5		
		Dark	Gabbro 27±3 Norite 20±5	Dolerite (16±5)		
	Hypabyssal		Porphyries (20±5)		Diabase (15±5)	Peridotite (25±5)
	Volcanic	Lava		Rhyolite (25±5) Andesite 25±5	Dacite (25±3) Basalt (25±5)	Obsidian (19±3)
		Pyroclastic	Agglomerate (19±3)	Breccia (19±5)	Tuff (13±5)	

* These values are for intact rock specimens tested normal to bedding or foliation. The value of m_i will be significantly different if failure occurs along a weakness plane.

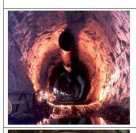
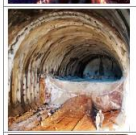
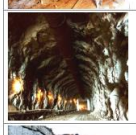
Appearance of rock mass	Description of rock mass	Suggested value of *D*
	Excellent quality controlled blasting or excavation by Tunnel Boring Machine results in minimal disturbance to the confined rock mass surrounding a tunnel.	*D* = 0
	Mechanical or hand excavation in poor quality rock masses (no blasting) results in minimal disturbance to the surrounding rock mass. Where squeezing problems result in significant floor heave, disturbance can be severe unless a temporary invert, as shown in the photograph, is placed.	*D* = 0 *D* = 0.5 No invert
	Very poor quality blasting in a hard rock tunnel results in severe local damage, extending 2 or 3 m, in the surrounding rock mass.	*D* = 0.8
	Small scale blasting in civil engineering slopes results in modest rock mass damage, particularly if controlled blasting is used as shown on the left hand side of the photograph. However, stress relief results in some disturbance.	*D* = 0.7 Good blasting *D* = 1.0 Poor blasting
	Very large open pit mine slopes suffer significant disturbance due to heavy production blasting and also due to stress relief from overburden removal. In some softer rocks excavation can be carried out by ripping and dozing and the degree of damage to the slopes is less.	*D* = 1.0 Production blasting *D* = 0.7 Mechanical excavation

Figure 2: GSI chart for jointed rock (Hoek & Marinos, 2000) (Left), Table of values of constant m_i for intact rock by rock group (Wyllie & Mah, 2004) (Middle), Guiding table for estimating disturbance factor D (Hoek, Carranza-Torres & Corkum, 2002) (Right)

After introducing the Generalized H-B Failure Criterion, the next step is to derive the equivalent friction angle and cohesion of rock mass and stress range. By fitting an average linear relationship with the curve generated by solving Eq. (2) for a range of minor principal stress values defined by $\sigma_t < \sigma_3 < \sigma'_{3max}$, as shown in Figure 3, the value of friction angle can be expressed in the H-B Failure Criterion, and the relationship is presented in the following equations and figure (Hoek, Carranza-Torres & Corkum, 2002):

Substitute the values from Eq (3) to Eq (5) to Eq (6) then Eq (7).

$$\sigma'_{cm} = \frac{\sigma'_{ci}\left(m_b+4s-a(m_b-8s)\right)\left(\frac{m_b}{4}+s\right)^{a-1}}{2(1+a)(2+a)} \quad (6)$$

$$\sigma_{3n} = \sigma'_{3max}/\sigma_{ci} = \sigma'_{cm} \times 0.72\left(\frac{\sigma'_{cm}}{\gamma H}\right)^{-0.91}/\sigma_{ci} \quad (7)$$

Then, substitute the values from Eq (3) to Eq (5) and Eq (7) to Eq (8) and Eq (9).

$$\varphi' = \sin^{-1}\left[\frac{6am_b\left(s+m_b\sigma'_{3n}\right)^{a-1}}{2(1+a)(2+a)+6am_b\left(s+m_b\sigma'_{3n}\right)^{a-1}}\right] \quad (8)$$

$$c' = \frac{\sigma_{ci}\left[(1+2a)s+(1-a)m_b\sigma'_{3n}\right]\left(s+m_b\sigma'_{3n}\right)^{a-1}}{(1+a)(2+a)\sqrt{1+\frac{6am_b\left(s+m_b\sigma'_{3n}\right)^{a-1}}{(1+a)(2+a)}}} \quad (9)$$

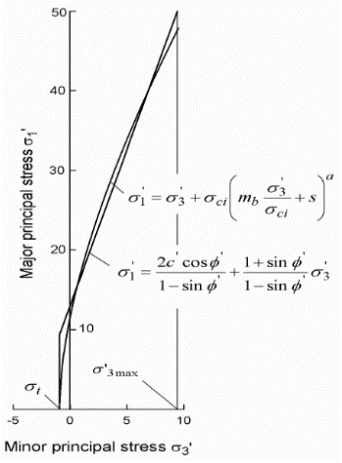


Figure 3: Relationship between major and minor principal stresses for H-B and equivalent M-C criteria

Apart from the rock mass shear strength parameters, the rock mass modulus of deformation, E_m in (GPa) can also be derived from σ'_{ci}, D and GSI. This is given by the following equations when σ'_{ci} is smaller or equal to 100MPa and larger than 100MPa respectively:

$$E_m = \left(1-\frac{D}{2}\right)\sqrt{\frac{\sigma'_{ci}}{100}}\cdot 10^{\frac{GSI-10}{40}} \quad \text{where } \sigma'_{ci} \leq 100\text{MPa} \quad (10)$$

$$E_m = \left(1-\frac{D}{2}\right)\cdot 10^{\frac{GSI-10}{40}} \quad \text{where } \sigma'_{ci} > 100\text{MPa} \quad (11)$$

Alternatively, the rock mass deformation parameter can be determined using either the equations in Section 5.9 of Geoguide 1 (GEO, 2020) or Table 10 (Section 1 for Granite Rocks) and Table 7 (Section 2 for Volcanic Rocks) of GEO Report No. 8 (GEO, 1995).

4 DESIGN GROUNDWATER PRESSURE IN ROCK EXCAVATION

Hong Kong is a wet city with heavy rainstorms in the summer season. The groundwater table is generally high, especially along the shorelines and low-lying areas. Therefore, the design groundwater level is critical for the ELS design. It is essential for geotechnical engineers to confirm the groundwater regime and subsequent effect on groundwater level due to dewatering during the deep excavation.

In common practice, ELS designers would consider rock strata as low permeability materials. Hence, water cut-off barrier such as grout curtains would be embedded a nominal 1m to 2m into the rockhead to cater to rock fracture zones at the soil-rock interface. Then, the groundwater pressure for ELS kickout checking and numerical analysis is assumed as hydrostatic pressure from the design groundwater level to the toe of the piled wall.

However, when there is no impermeable water cut-off throughout the excavated rock face, such as pre-bored sheetpile, interlocking pipe pile or steel / shotcrete lagging, the groundwater would be able to flow through the rock fissures / rock joints, leading to a deviation in the assumed groundwater pressure distribution. Such seepage through rock mass would relieve the groundwater pressure and reduce the loading to the ELS system.

With sufficient ground investigation (G.I.) data, such as in-situ mass permeability parameters for both soil and rock strata, it is suggested to conduct a numerical seepage analysis under steady-state seepage conditions. The groundwater pressure acting at the back the ELS piled wall can be obtained for ultimate limit state (ULS) design and while the changes of groundwater table inducing ground settlement can also be obtained for serviceability limit state (SLS) design.

It is common for ELS designers to assign in-situ soil permeability tests using either the falling head or constant head method. However, rock permeability parameters must also be ascertained to ensure a realistic groundwater pressure distribution under seepage for robust ULS and SLS design of the ELS system. Rock permeability tests like the Lugeon test or Packer test are generally recommended for obtaining the in-situ averaged hydraulic permeability value of rock mass for ELS design.

In the following example, the design groundwater pressure distribution acting on the ELS piled wall was determined by conducting a numerical seepage analysis with the aid of SEEP/W. In this hypothetical seepage analysis, it was assumed that the deep excavation would be 24m below the existing ground with the level of +4mPD and grout curtain, by means of TAM and / or rock fissure grouting, from existing ground level to 5m below rockhead level, was provided as water cut-off barrier. The design groundwater table, mass permeability parameters and geological profile adopted are shown in Figure 4.

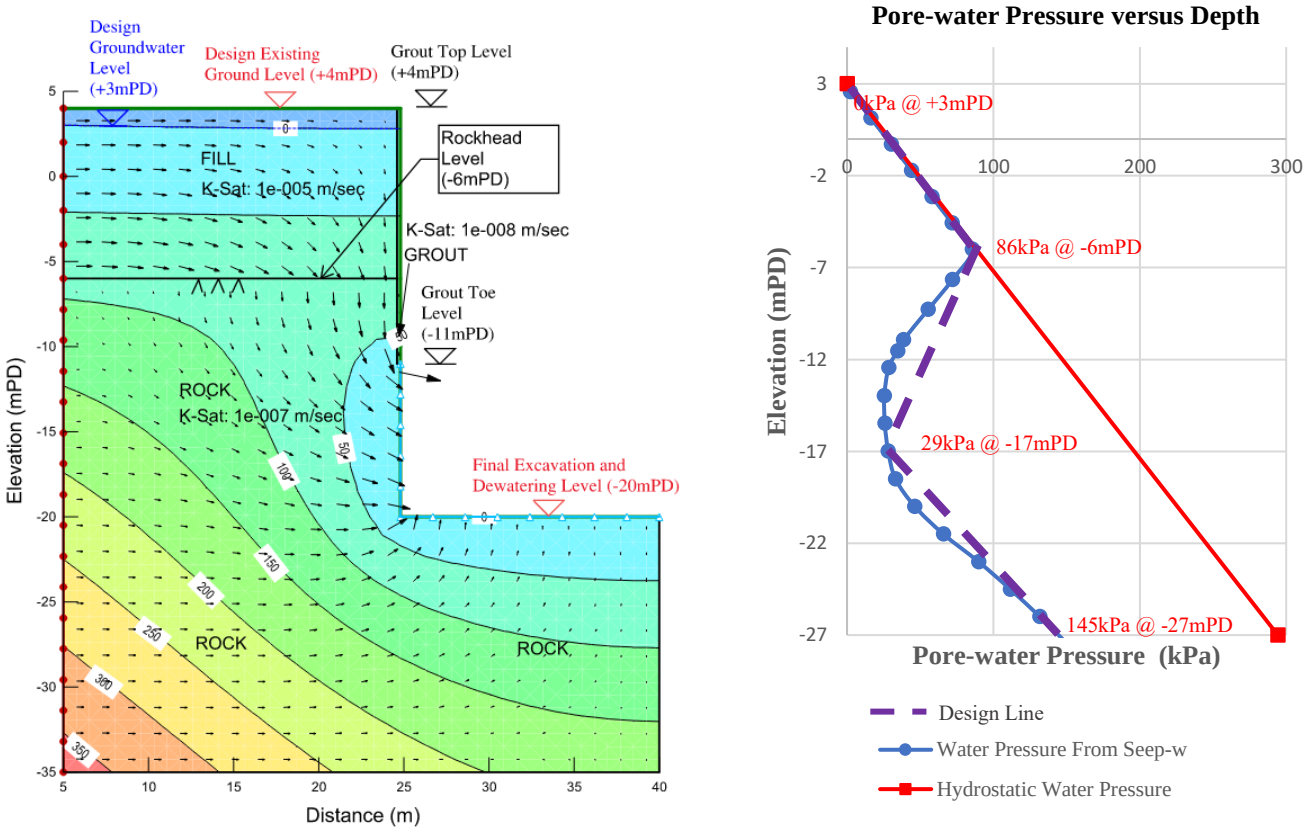


Figure 4: Numerical seepage analysis (Left) and groundwater pressure distribution on the active side (Right)

The results of seepage analysis revealed that the groundwater pressure behind the piled wall on the active side was generally hydrostatic in fill layer from the design groundwater table to the rockhead. Below the rockhead level, the groundwater pressure decreased and was much lower than the hydrostatic pressure profile due to the pressure relief through groundwater seepage. The linear approximation of the design groundwater pressure profile as presented in the purple dotted line in Figure 4 could be applied for stability checking for ULS design such as toe

stability checking and wall structural capacity checking as well as for SLS design of wall deflection and induced ground settlement.

Based on the findings from the above example, there is a significant reduction in the design groundwater pressure in the rock strata if the soil and rock permeability parameters are obtained from the G.I. field tests and then simulated by seepage analysis.

5 ROCK SOCKET DESIGN

For the design of an ELS piled wall system, the overall stability checking against overturning failure is a basic procedure to determine the required pile toe embedment, i.e., rock socket design. As discussed in Section 2 above, there are two possible failure modes for the design of a rock socket which are bearing failure of intact rock and planar discontinuity-controlled failure of rock mass. In the absence of sufficient rock joints data, all rock discontinuity combinations should be checked to obtain the lowest ultimate lateral resistance of the proposed rock socket length. However, assuming that the rock mass has the most adverse joint in the stability checking may lead to over-conservative and unrealistic rock socketed required for the piled wall.

It is suggested that the rock joint data can be measured using borehole acoustic televiewer (ATV) surveys. If there is no potential rock joint planar failure sets against rock socket kickout, the rock socket would then be controlled by the bearing failure mode, resulting in a much shorter length. Even if there are potential rock joint sets causing planar failure of rock socket kickout, the dip angles and dip directions can be identified for checking against the planar discontinuity-controlled failure by applying the equations in Figure 54 of Geoguide 1 (GEO, 2020). In this case, the rock socket length would still be generally shorter by confining the dip angles. Additionally, such potential adverse rock joint set only affects one side of the excavation face and the remaining excavation faces can still undergo the bearing failure mode checking only. Thus, the rock socket design would be more economical and specific based on the site-specified G.I. information. This approach significantly saves time and costs by avoiding the installation of unreasonably deep pile wall into bedrock.

In the following sample of stereo plot analysis, the approach for finding the adversely oriented joint set(s) is demonstrated. Firstly, relevant rock joint data, including dip angle and dip direction at levels within the influence zone of planar failure (i.e., from the final excavation level to the design toe level of the piled wall), are selected. With the aid of computer-aided stereographic projection software (e.g., DIPS developed by Rocscience) a variety of poles representing the plane orientation of each rock joint are plotted in the stereonet as shown in Figure 5. Additionally, the daylight envelope for planar failure against rock socket kickout is plotted with the known dip direction of the piled wall.

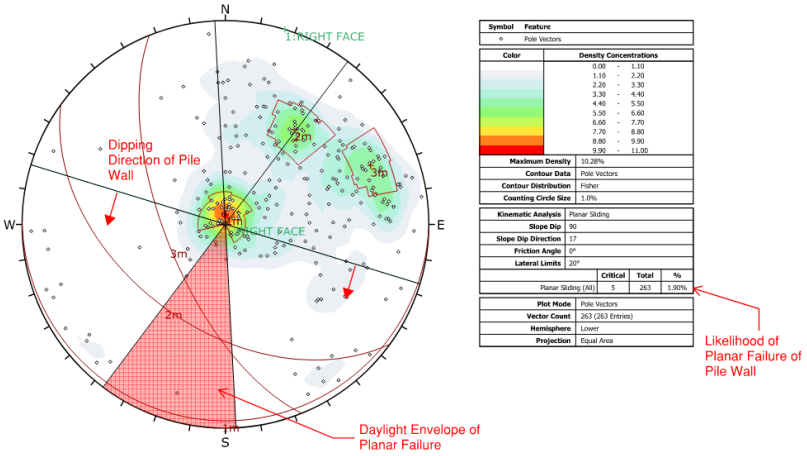


Figure 5: Kinematic analysis of rock discontinuities as rock socket of pile wall

When a high concentration of poles falls within the daylight envelope for planar failure, it indicates that there is a high likelihood of those rock joint sets, with their range of dip angles in their corresponding dip direction, experiencing planar failure under external load. Conversely, if the rock joint sets lay outside the planar failure zone, it is concluded that no planar discontinuity failure will occur under lateral load for the retaining wall. Therefore, we are confident in designing the rock socket checking against the bearing failure of intact rock.

6 CASE STUDIES

6.1 Case Study 1 – ELS design with shallow rockhead under M-C and H-B Failure Criterions

The site was located at the toe of the hillside with existing ground level varying from +5.0mPD to +8.7mPD. The site-specific G.I. results indicated that the site was underlaid with fill followed by moderately/slightly decomposed granite (M/SDG). The engineering rockhead level varied from +2.0mPD to -5.0mPD, while the final excavation level was -23.75mPD, resulting in a 32.5m deep excavation, including approximately 25.8m of deep rock excavation. The groundwater table of the site varied from +1.3mPD at its lowest and +3.0mPD at its highest.

In the initial design, the analyses of ELS for ULS and SLS design were based on a constitutive soil model which relates linear stress to strain relationship controlled by the M-C Failure Criterion of rock joints. The design geotechnical parameters were assumed as follows:

- Fill: c' = 0kPa, ϕ' = 30° and Es =110MPa
- M/SDG: c' = 10kPa, ϕ' = 40° and Es = 250MPa
- Design groundwater pressure adopted from Seep-W results

To satisfy the ULS and SLS design requirements, the ELS system required a 323mm diameter pipe pile wall at 500mm centre-to-centre spacing with 8 layers of steel strut propping and heavy preloading on the bottom 6 layers of shoring support, with at least 4 layers to be installed below the bedrock.

Design optimization was carried out to achieve cost saving design by adopting M-C fit values derived from the H-B Failure Criterion for rock mass. Based on the rock core obtained from the boreholes and laboratory results of unconfined compressive strength (UCS) tests, the adopted values for the inputs are listed out in the Table 1 and with the steps of calculation to obtain the rock strength and stiffness parameters are shown in Figure 6.

Table 1: Summary table of adopted input parameters for H-B Failure Criterion

Input Parameters	Descriptions	Adopted Values
GSI	• Based on GI records, the encountered rock mass was intact with minor fracture • The rock cores were generally fully recovered (i.e. TCR=100% and RQD=100%) • The fracture index was low (i.e. generally less than 1.0) • From Figure 2 (Left), range of GSI was considered from 60 to 90 for intact to blocky rock with good to very good surface conditions	55
σ'_{ci}	• From laboratory testing results, average intact uniaxial compressive strength (UCS) = 100MPa	75MPa
m_i	• From Figure 2 (Middle), the material constant was range from 32 +/-3 for granite rock	32
D	• From Figure 2 (Right), the disturbance factor was 0.7 for mechanical excavation of open pit	0.7
H	• Average excavation depth	30m
γ	• Typical unit weight for granite rock	26kN/m^3

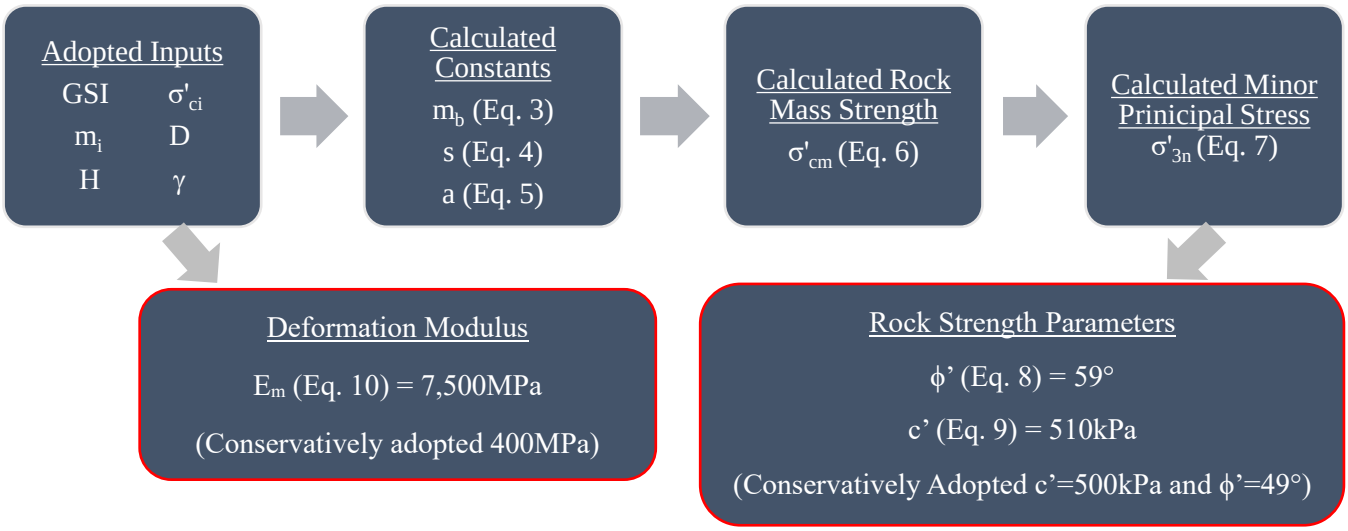


Figure 6: Flow chart for calculation of equivalent M-C parmeters based on H-B failure criterion

Even though conservative design parameters for M/SDG were adopted, significant improvements were achieved in the design, resulting in significant time and cost savings. The number of shoring layers could be reduced to 6 layers and all preloading works were no longer necessary while obtaining a satisfying wall movement. By the time of cost saving design, the pipe pile installation had been completed and so no optimization on the proposed piled wall. The comparison of the initial design and cost saving design is presented in Figure 7.

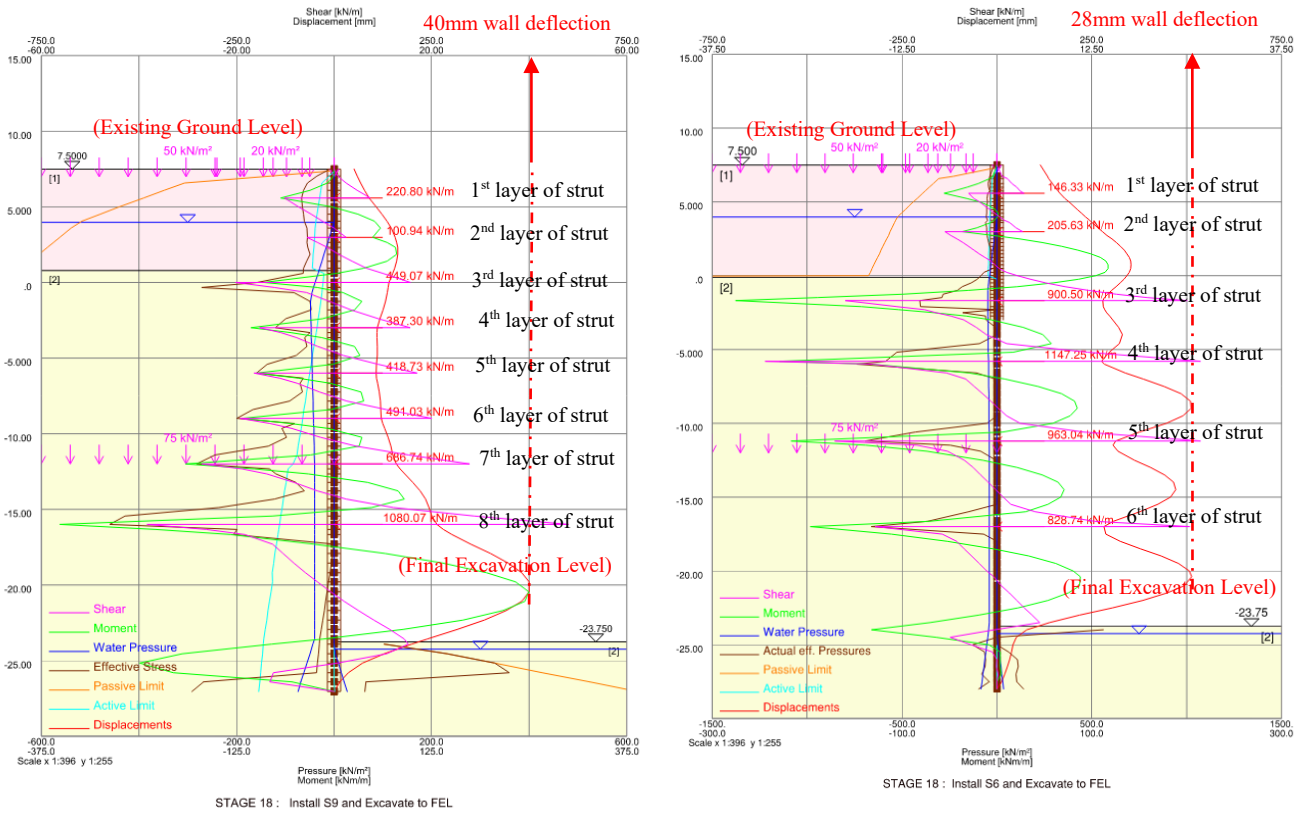


Figure 7: Oasys FREW model of initial design adopted M-C Criterion (Left) and cost saving design adopted H-B Criterion (Right)

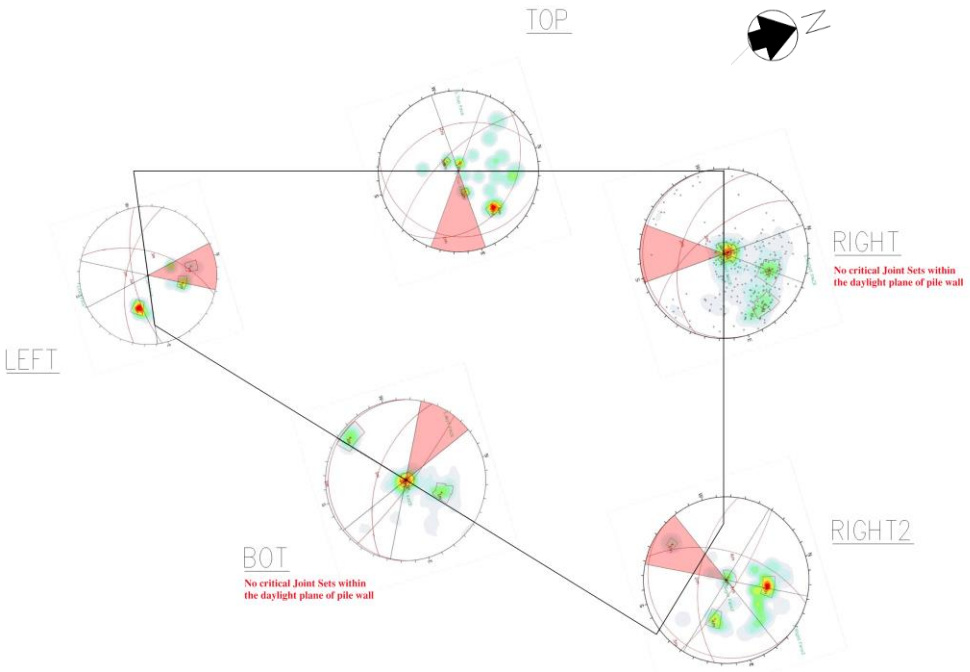
6.2 Case Study 2 – Rock socket design with review of rock joint conditions

The site was located in an urban area at Tsim Sha Tsui, Hong Kong with an existing ground level of approximately +4.5mPD. According to the site-specific G.I. information, the site was underlain by a vertical sequence of fill or alluvium, completely decomposed granite (CDG), highly decomposed granite (HDG) and underlain by moderately/slightly decomposed granite (M/SDG). The engineering rockhead level varied from -18mPD to -25mPD. The proposed final excavation level varied from -22 to -25mPD, with a maximum depth of excavation of 29.5m. A multi-strutted interlock pipe piled wall embedded in rock was adopted as the temporary ELS wall for deep excavation to construct the underground permanent basement structure.

A PLAXIS 2D model using the global safety factor method was employed to model the construction sequences of proposed excavation and lateral support works. The bending moment and shear force of the wall could be extracted from the model for the design of the rock socket. With reference to Figures 51 to 54 of Geoguide 1 (GEO, 2020), the estimated embedment length of piled wall into bedrock was about 5m in general, while the checking of planar discontinuity-controlled failure dominated the overall design of rock socket length.

A comprehensive design review was carried out to minimize the construction cost and time for ELS works. One of the solutions was to reduce length of the rock socket by conducting a detailed study on the discontinuities condition of the rock mass to provide lateral resistance to the pile. By compiling a considerably large sample size of dip angle and direction of rock joints from the acoustic televiewer (ATV) surveys, more confidence could be gained in the rock joint conditions around the site. In general, it is recommended including ATV in 25% of total proposed G.I. boreholes which are assigned evenly along the excavation face near the rock socketed piled wall.

According to Figure 8, the joint sets with high concentration were sorted out into generally five directions of the site. Among these, only joint sets at the top, left and bottom-right of the site fell within the zones of planar failure of the rock socket kickout. The concerned joint sets (highlighted in red in the table below) with specific dip angles and directions were checked against failure due to planar discontinuities. For all three critical joint sets, the dip angles were relatively large, resulting in a high ultimate lateral resistance supporting the piled wall under lateral load. As a result, the design rock socket length was halved to 2.5m, which was controlled by the bearing failure of intact rock.



Face	Right	
Joint Set No.	Dip Angle	Dip Direction
1	4	181
2	48	216
3	66	248
Face	Right 2	
Joint Set No.	Dip Angle	Dip Direction
1	76	50
2	53	205
3	5	147
4	52	303
Face	Bot	
Joint Set No.	Dip Angle	Dip Direction
1	51	216
2	2	197
3	82	54
Face	Left	
Joint Set No.	Dip Angle	Dip Direction
1	65	185
2	55	209
3	52	303
Face	Top	
Joint Set No.	Dip Angle	Dip Direction
1	12	117
2	30	268
3	64	242
4	21	56

Figure 8: Plan showing rock joints at each excavated face of piled wall (Left) and summary table of joint sets (Right)

6.1 Case Study 3 – Deep excavation in Sedimentary Rock

It is uncommon to encounter deep Sedimentary Rock excavation in Hong Kong. The site for this case study was located in Central Business District (CBD) of Sydney which involved deep shaft excavation in Sandstone and adjacent to high-rise buildings. The rock mass shear strength parameters were developed by H-B Failure Criterion as listed in Table 2. The PLAXIS 2D analysis inputs and outputs are presented in Figure 9.

Table 2: Shear strength rock mass parameters for Sandstone

Material	Unit Weight, γ (kN/m^3)	Cohesion, c' (kPa)	Friction Angle, ϕ'(deg)	Young's Modulus, E (kPa)	Poisson's Ratio	Principle Stress (MPa)
Sandstone (Class III)	24	300	36	1,000	0.3	Major: $\sigma_H = 2\sigma_v$ Minor: $\sigma_H = 1.2\sigma_v$
Sandstone (Class II)	24	500	36	2,000	0.2	Major: $\sigma_H = 2\sigma_v + 2.5$ Minor: $\sigma_H = 1.4\sigma_v + 1.75$
Sandstone (Class I)	24	700	36	3,000	0.2	

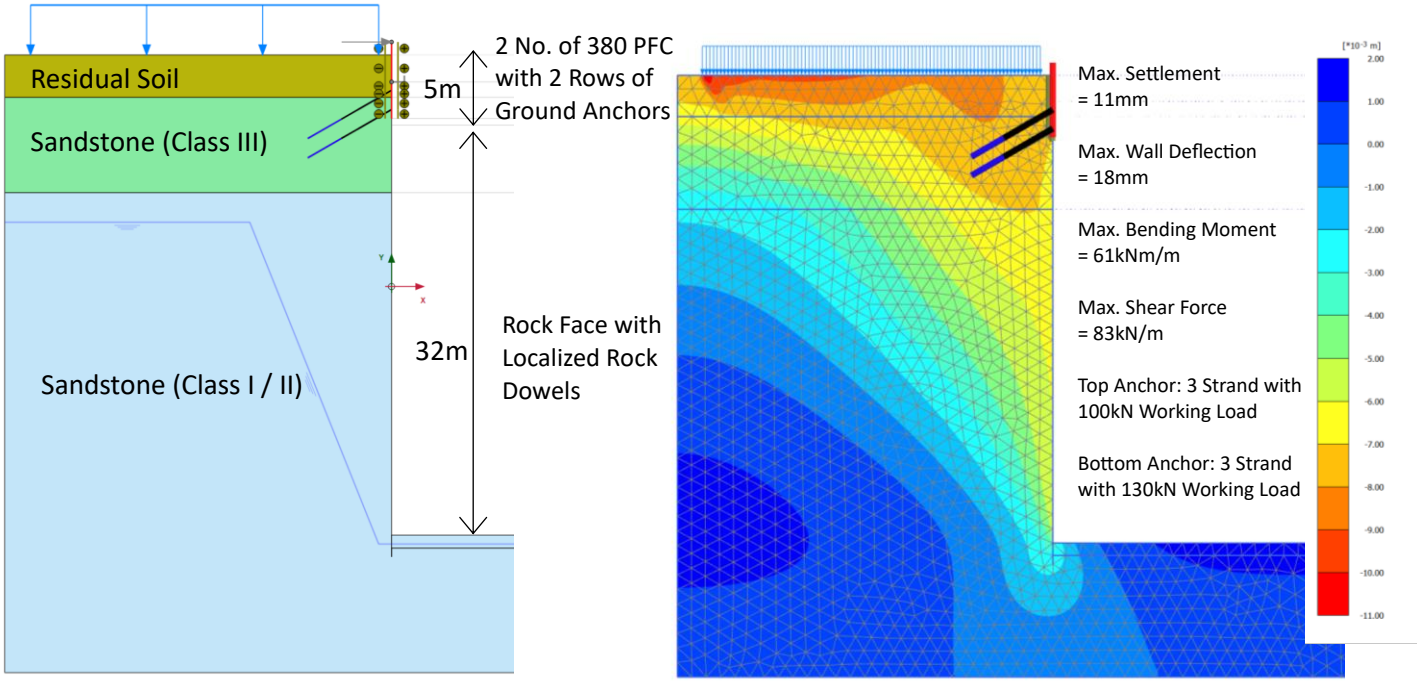


Figure 9: PLAXIS 2D Input of Deep Excavation in Sandstone (Left) and PLAXIS 2D Outputs (Right)

7 CONCLUSION AND RECOMMENDATION

The purpose of this paper is to explore more economical design approaches in the ELS design with deep excavation and shallow bedrock. Three main ideas are discussed in the paper:

1. Determination of fundamental material strength and stiffness parameters of rock mass based on H-B Failure Criterion;
2. Design groundwater pressure in rock excavation by considering the free seepage from excavated rock surface; and
3. Rock socket design with the rock joint survey information

It is emphasized that the implementation of suitable material modelling for rock is crucial in the overall ELS design in terms of safety and project finance. Providing unreasonable stiff and heavy shoring members with large preloading based on over-conservative assumptions of low rock strength parameters can be costly and time-consuming and sometimes dangerous. Moreover, it is revealed that the design of groundwater pressure and rock socket can be optimized by understanding the rock joint conditions in terms of their quantities, dip angles and directions.

However, the design approach heavily relies on field tests and examinations, as well as laboratory tests on the rock samples. It is recommended that sufficient quantities and types of rock tests and surveys shall be assigned for obtaining realistic and proper strength and stiffness parameters, including but not limited to the following:

1. Lugeon test or Packer test in rock mass;
2. Acoustic or optical televiewer survey;
3. Direct shear box test of rock joint samples; and
4. Unconfined compressive strength test and point load test for intact rock samples.

Apart from the field and laboratory testing for the rock mass in the design stage, it is essential to carry out geological mapping, including rock joints, weathering / fracture zones, adverse features and groundwater seepage from rock joints, of the excavated rock faces during the construction stage. All mapping information should be continuously reviewed by the designers to verify and confirm the design assumptions. If required, some remedial measures, such as local rock dowels / bolts, additional strutting, and raking drains, should be applied.

It is strongly believed that when designers progressively pay more attention to the importance of testing and observation of rock mass and discontinuity in the planning stage of G.I. works, it would greatly benefit the design and construction of ELS works when shallow rockhead is encountered. The construction time and project cost could be significantly reduced, allowing a more efficiently use of resources without compromising the robustness and safety of the ELS system.

REFERENCE

[1] GEO (2020). *Guide to Retaining Wall Design (Geoguide 1) (Continuously updated e-version released on 1 June 2020).* Geotechnical Engineering Office, Civil Engineering and Development Department, HKSAR Government

[2] GEO (2023). *Deep Excavation Design and Construction, GEO Publication No. 1/2023.* Geotechnical Engineering Office, Civil Engineering and Development Department, HKSAR Government

[3] Hoek, E., Carranza-Torres, C. & Corkum, B. (2002). *Hoek-Brown Failure Criterion – 2002 Edition*: 267-273. Proc. NARMS-TAC Conference, Toronto

[4] Hoek, E. & Marinos, P. (2000). *GSI - a geologically friendly tool for rock mass strength estimation.* Proc. GeoEng 2000 Conference, Melbourne

[5] Hussian, S., Mohammad, N., Ur Rehman, Z., Khan, N.M., Shahzada, K., Ali, S., Tahir, M., Raza, S. & Sherin, S. (2020) *Review of the Geological Strength Index (GSI) as an Empirical Classification and Rock Mass Property Estimation Tool: Origination, Modifications, Applications, and Limitations*. Advances in Civil Engineering, Vol. 2020

[6] Irfan, T.Y. & Powell, G.E. (1991). *Foundation Design of Caissons on Granitic and Volcanic Rocks*, *GEO Report No. 8*. Geotechnical Engineering Office, Civil Engineering and Development Department, HKSAR Government

[7] Vasarhelyi, B., Somodi, G., Ágnes, K. & Kovács, L. (2016). *Determining the Geological Strength Index (GSI) using different methods*: 1049-1054. In Proceedings of the 2016 ISRM International Symposium, EUROCK 2016, Cappadocia, Turkey

[8] Wyllie, D.C & Mah, C.W. (2004). *Rock Slope Engineering: civil and mining (4th ed.)*: 78 & 98. Taylor & Francis e-Library

Enhancing Pore Water Pressure Monitoring by Fully Grouted Piezometers: A Case Study of Crossrail and Prospects of Application in Hong Kong

M.S.P. Wan & F.L.C. Lo
Geotechnical Consulting Group, London

ABSTRACT

This paper presents a comprehensive case study on pore water pressure measurements using fully grouted piezometers for London Crossrail project, focusing on the insights gained and exploring their potential applications in Hong Kong. Multi-level vibrating wire piezometers, strategically placed in single boreholes fully backfilled with carefully designed cement-bentonite grout, were deployed in a 'greenfield' research site in Hyde Park, London, anticipating the passage of two earth pressure balanced tunnel boring machines (EPBMs) constructing twin-bore Crossrail tunnels through London Clay. The performance of these fully-grouted piezometers are discussed, while presenting the pore water pressure measurements in low-permeability ground before, during and after Crossrail tunnel construction. It is evident from the steady-state measurements that there exists an under-drained steady-state pore water pressure profile within the low-permeability ground separating the upper and lower aquifers, also being influenced by a nearby London Underground tunnel. During the EPBM passage, these fully-grouted piezometers were capable of reliably measuring the rapid response of pore water pressure. The advantages and practical challenges of employing fully-grouted piezometers for pore water pressure monitoring are explored, accompanied by their potential applications in Hong Kong, particularly reclamation and deep excavations in low-permeability ground. This paper shares perspectives on enhancing the reliability and benefits of pore water pressure measurements for civil engineering projects in Hong Kong.

1 INTRODUCTION

Standpipes and piezometers have widely been used for monitoring groundwater levels and pore water pressures for civil and geotechnical engineering projects in Hong Kong and overseas. The most common type of piezometer used in Hong Kong is open-hydraulic standpipe piezometers with a Casagrande-type piezometer tip. Typically, standpipe piezometers are installed in a borehole with the piezometer tip embedded in a granular filter response zone between bentonite seals.

Forming an effective seal to the response zones is crucial to the performance of the piezometer. In practice, the seals are formed by backfilling bentonite balls or bentonite pellets into the borehole with a minimum 500mm thickness beneath and above the response zone (which itself is formed by backfilling a sand pocket around the piezometer tip). To ensure an effective seal, sufficient time should be allowed for the swelling action of the bentonite pellets before bentonite-cement grout is placed in the remaining section of the borehole.

Because of the need for effective seals, it is not normally desirable to install more than two response zones in a single borehole. Geoguide 2 (GEO, 2017) highlights this practical constraint in relation to the typical installation method: "*Poor sealing of the piezometer will permit the migration of water from one level to another, and may render the readings meaningless. The installation of more than one piezometer in a single borehole is not generally recommended. If two piezometers are placed in a single hole, great care must be taken to achieve proper seals.*"

The use of vibrating-wire (VW) piezometers has become increasingly popular thanks to recent advances and improved performance of VW instrumentation. The authors observe that in Hong Kong the current practice of installation of VW piezometers in boreholes appears to mostly involve the traditional method of creating

granular response zones and bentonite seals, with the VW piezometer sensor either simply being lowered within a standpipe (Figure 1a) or directly embedded in the granular response zone (Figure 1b).

For the traditional method of piezometer installation, the restriction of no more than two response zones in a single borehole remains. Furthermore, if a standpipe is used to host the VW sensor, the response time of the pore water pressure measurement is greatly increased, especially in low-permeability ground, as a significant volume of water flow into the standpipe is needed for the sensor to register the pore water pressure in the ground (which is balanced by the hydrostatic pressure in the water column by the raised water level inside the standpipe).

It has been demonstrated through analytical (Vaughan, 1969) and numerical analysis (Contreras et al., 2008) that for the operation of diaphragm (including VW) type piezometer devices, theoretically the presence of a granular filter response zone is not necessary and the piezometer sensors can be installed by grouting the borehole fully with a grout of suitable permeability (Figure 1c). The fully-grouted method, having a major advantage of the straightforward backfilling procedure, eliminates the need for granular filters and bentonite seals and hence all the associated restrictions. This allows multi-level (more than two) VW piezometer sensors to be installed in one single borehole, and makes it possible to obtain a higher-spatial-resolution pore water pressure profile with depth at the same location, significantly reducing the number of boreholes required and hence the costs. In addition, the VW piezometers fully grouted in a borehole have a rapid response time, which means that measured pore water pressure response to the stress changes in the ground is usually near instantaneous, even in low-permeability ground.

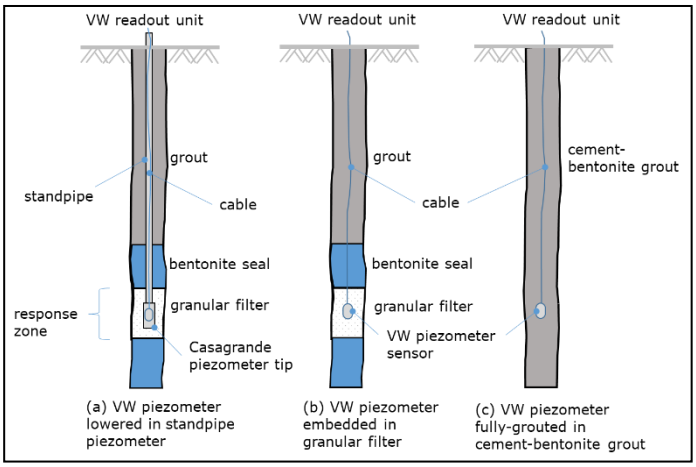


Figure 1: Traditional and fully grouted piezometer installations in boreholes

Despite the benefits, there appear to be only limited applications of the fully-grouted method of VW piezometer installation in Hong Kong. Laver (2020) reported such an application for the cofferdam water drawdown monitoring in the Hong Kong Boundary Crossing Facilities reclamation project, but much wider use of fully grouted piezometers should be welcome and encouraged.

2 FULLY GROUTED INSTALLATION OF VW PIEZOMETERS

The VW piezometers contain a diaphragm sensor which requires only a very small amount of water flow for pressure equalisation and to operate. These devices are therefore suitable for installation in a borehole fully grouted with cement–bentonite grout of suitable permeability, as the grout can transmit this volume of flow over a short distance from the ground to the sensor tip quickly.

2.1 Bentonite cement grout as a filter and a seal

In order for the fully-grouted VW piezometer to measure the pore water pressure in the ground accurately and effectively, the grout in the borehole shall act as both a filter in the radial (horizontal) direction and a seal in the vertical direction. This is so as not to adversely affect the horizontal flow of water to the piezometer and so as to prevent significant vertical flow along the borehole (EN ISO 18674-4:2020), and can be achieved by controlling the relative permeability of the grout to the ground.

Based on the work of Vaughan (1969) and Contreras et al. (2008), the error of pore water pressure measurement induced by the vertical water flow within the grout column is insignificant if the permeability of

the grout is no more than 100 to 1000 times the permeability of the ground. For instance, for a typical silty or clayey soil with a coefficient of permeability in the order of 10^{-10} m/s, a backfill grout with a coefficient of permeability up to 10^{-7} m/s can be used. In practice, this order of grout permeability can be readily achieved by bentonite cement grouts of a typical range of mix ratios that is also pumpable into a borehole through a standard tremie pipe. On the other hand, it should be noted that when the grout is less permeable than the ground, response time of the measurement is increased. However, the delay in response time should not be significant for a small diameter borehole.

2.2 Grout requirements – permeability and viscosity

The grout mix shall be designed before installation, with the grout permeability and viscosity being the key properties to consider. Whilst the former is essential for ensuring the functionality as a filter and a seal, the latter is important to ensure the grout (a) is thin enough to be pumped into the borehole and (b) is thick enough to avoid excessive grout loss into the ground, especially in high-permeability soil/jointed rock. As a starting point, there are guide grout mix ratios published in standards (e.g. EN ISO 18674-4) and case histories (e.g. Mikkelsen & Green, 2003). It is strongly recommended that a site trial of the grout mixes based on the design is undertaken before the installation, because the grout properties are sensitive to the mixing environment (e.g. temperature) and procedure (e.g. mixing sequence and duration). The grout mix trial should use the same materials, mixing equipment, mixing sequence (add water to the cement first, before adding bentonite), and mixing environment (e.g. ambient temperature and humidity). The trial should ideally also test the grout pumpability using the same grout pump to backfill a borehole of similar depth. The grout pump should be powerful enough to pump the grout into the bottom of the borehole by tremie method and rise the wet grout to ground level. A borehole not hosting any instrument within the same ground investigation contract would be most suitable for the grout trial. As a minimum, the grout viscosity shall be measured by marsh funnel test on site. Grout cylinder samples shall be made for testing the permeability at 3, 7 and 28 days in laboratory.

2.3. Benefits and limitations

The most practically significant benefit of fully-grouted VW piezometers is its simple, economical, and rapid installation process, allowing multi-level installations in a single borehole saving significant borehole drilling cost. VW piezometers enables fast response time even in low-permeability ground. Since VW sensors measure the frequency of the vibrating wire instead of the amplitude of the electrical signal, the measurement readings are not affected by cable electrical resistance, making the depth of sensors not a technical limitation. VW piezometers can measure small suction so long as all parts of the piezometer system remains saturated, and the use of bentonite cement grout enhances the suction measurements with its ability to sustain hydraulic tensions without desaturation up to a suction pressure of 100 kPa (Ridley, 2015). In traditional installation method involving granular response zones, the piezometer elements embedded in a clean sand pocket would readily desaturate when in touch with soil even with a small suction.

One drawback of VW piezometers in practice, full-grouted or not, is that they, being a closed system, cannot be de-aired once installed (unless for a special flushable type), and therefore care must be taken in ensuring full saturation of the VW sensor (including the reservoir and porous filter) during and post installation. As with all closed systems, VW piezometers measure absolute pressure including the barometric pressure. This is not entirely a limitation but it means that with independent barometric measurements it is possible to validate and correct the piezometer readings.

3 CROSSRAIL CASE HISTORY

Dunnicliff (2008) and Contreras et al. (2008) reported successful installation and monitoring of VW piezometers installed by the fully-grouted method at various sites around the world. More recently, Wan & Standing (2014) and Wan et al. (2019) reported a comprehensive case history of the installation and monitoring of multi-level fully-grouted VW piezometers for the Crossrail project where twin running tunnels were constructed in over-consolidated stiff clay (London Clay Formation) by two EBPMs.

3.1 Crossrail tunnelling work and research instrumentation site

The research site at Hyde Park, London was set up close to where the Crossrail tunnels pass beneath the existing tunnels of the London Underground Limited (LUL) Central Line. The exact location of the crossing is beneath Bayswater Road, which runs alongside the northern boundary of Hyde Park. The relative position of

the tunnels is shown in Figure 2 and their respective axis depths are about 24 m (Central Line) and 34.5 m (Crossrail) below ground level (mbgl). At the site, the two Crossrail tunnels are about 16 m apart between their tunnel axes. The twin tunnels were constructed by two EPBMs with excavation diameters of approximately 7.1 m. Both the westbound and eastbound tunnels were constructed with 6.2m internal diameters (6.8m external diameters) bolted precast concrete segmental lining. The tunnel lining comprised seven segments plus a small key and had a nominal length of 1.6m.

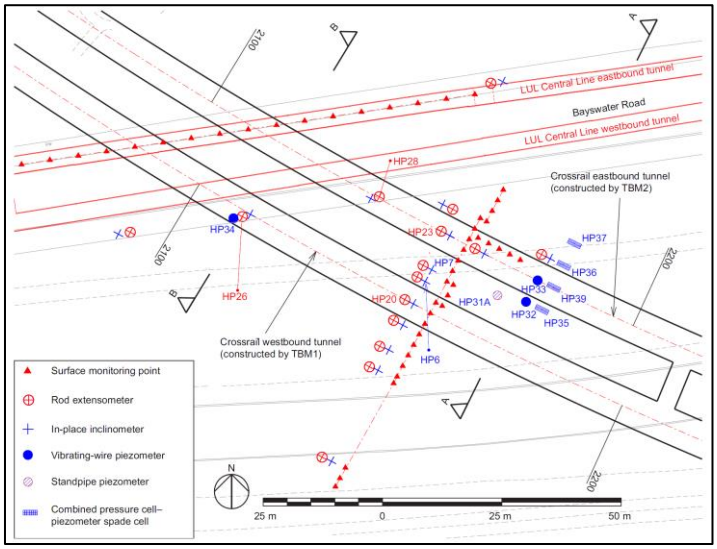


Figure 2: Location plan and instrumentation layout plan of Hyde Park instrumentation site (Wan et al., 2019).

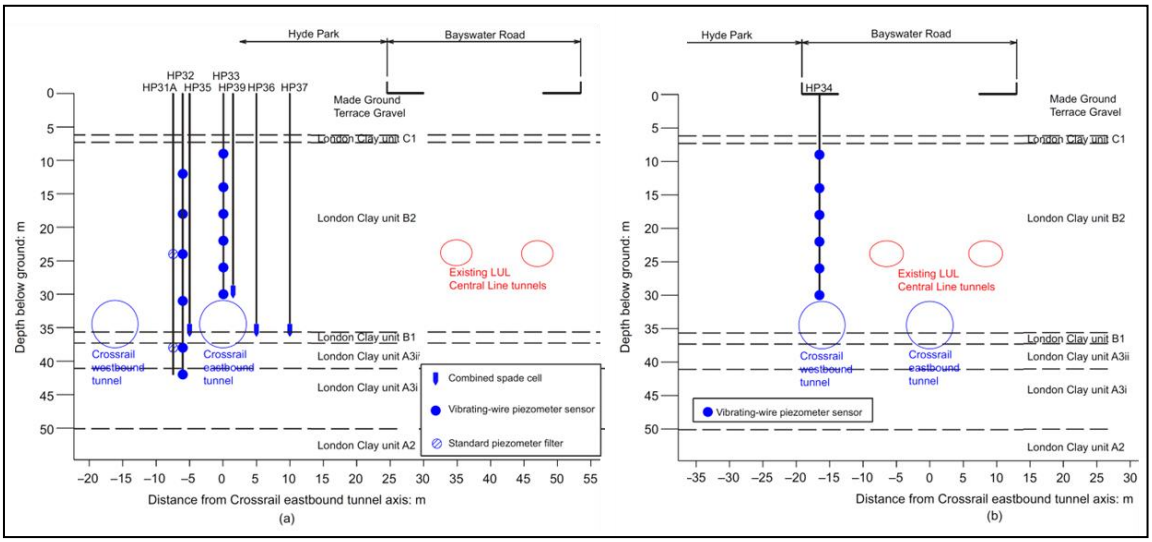


Figure 3: Cross-sections of piezometers installed: (a) cross-section A–A: piezometers in 'greenfield' ground; (b) cross-section B–B: piezometers in the vicinity of the existing LUL running tunnels (after Wan et al., 2019).

The EPBMs for the westbound and eastbound tunnel construction under-passed the instrumentation site in November 2012 and February 2013 respectively. Since then, the instrumentation has been retained and measurements continued. The measured immediate ground response to the EPBM tunnelling have been presented, interpreted and discussed in detail in three papers (Wan et al., 2017a, 2017b, and 2019). The results of the on-going post-construction monitoring of the same instruments are presented and discussed in Wan et al., 2021. The piezometer installations and their pore water pressure measurements are highlighted in this paper.

3.2 Ground conditions

A typical London Basin stratigraphy was found at the Hyde Park site with made ground and Terrace Gravels overlying the descending sequence of the London Clay Formation (LCF), Lambeth Group, Thanet Sand and Chalk bedrock. Two aquifers are present at the instrumented site - the Terrace Gravels constitute the upper

aquifer, and the combined lower granular units of the Lambeth Group (Upnor Formation), the Thanet Sand and Chalk the lower aquifer. These aquifers are separated by the LCF and, if present, the upper and lower mottled beds of the Lambeth Group.

3.3 Types of piezometers installed

As shown in Figure 2, there are in total 38 boreholes with each borehole accommodating one or more instruments for ground movement, total stress and pore water pressure monitoring. Eight of the boreholes were for pore-water pressure measurements. Among other instruments, piezometers and combined total stress-piezometer spade cells were installed around the Crossrail tunnel alignments to measure the pore pressure and total stress response resulting from the new tunnel construction. At locations within Hyde Park, the piezometers and spade cells were installed, as shown in Figure 3(a), with the pressure sensors located at various distances vertically and horizontally around the Crossrail eastbound tunnel. Multiple piezometers were installed within a borehole on Bayswater Road, above the Crossrail westbound tunnel, to investigate the effect of the existing Central Line tunnels on pore-water pressures prior to, during and after tunnel construction (Figure 3(b)).

Figure 4 shows the three types of piezometers in the Hyde Park instrumentation site. Note that fully-grouted multi-level VW piezometers were installed in three boreholes (HP32, HP33 and HP34), each hosting six VW sensors (Figure 4a). A standpipe piezometer with two response zones were installed in a borehole (HP31A) about 10m away from HP32 (Figure 2 and Figure 4c) for the purpose of comparing and verifying the piezometer readings of the multi-level VW piezometers.

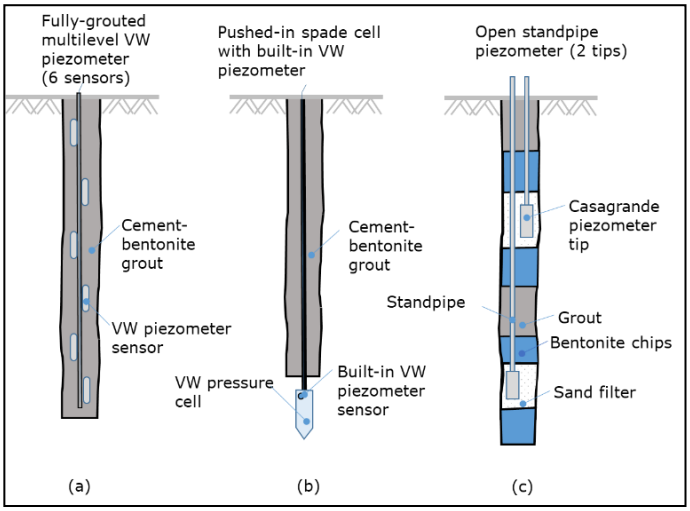


Figure 4: Schematic presentation of three types of piezometers installed at the instrumented site: (a) multi-level VW piezometers in fully grouted borehole (HP32, HP33 and HP34); (b) VW piezometer sensor built in spade-shaped pressure cell (HP35, HP36, HP37 and HP39); (c) conventional standpipe piezometer (HP31A)

3.4 Installation of fully-grouted piezometers

A number of trail grout mixes were undertaken to determine their properties. Four mixes (Mix A to Mix D) were designed with different water/binders ratios aiming to match the permeability of the ground. Laboratory permeability tests were conducted using a triaxial apparatus on cylinder specimens of 100 mm diameter, which were consolidated under different cell pressures before permeability was tested under a constant pressure gradient. The tests were performed in accordance with BS1377, Part 6: 1990, Clauses 5.3, 5.4, 5.5.2.2 to 5.5.2.7 and 6. Table 1 shows the results of the permeability tests on the 4 trial grout mixes.

In the field, falling head tests were performed at the two response zones of the standpipe piezometer HP31A and the results show the coefficients of horizontal permeability at 24.0 mbgl (London Clay unit B2) and 37.0 mbgl (London Clay unit B1/A3ii) of 1.2×10^{-9} m/s and 1.6×10^{-11} m/s respectively.

Grout Mix B has a measured coefficient of permeability of up to 1.5×10^{-9} m/s which is of similar permeability of London Clay unit B2 and about 100 times more permeable than London Clay unit B1/A3ii. Considering the sealing requirement, design grout Mix B was selected for backfilling the fully-grouted piezometers. A trial tremie operation using Mix B was also carried out to backfill a 40m deep borehole at the same site to ensure the pumpability of the grout.

Table 1: Results of permeability test in triaxial apparatus on trial grout mixes

Mix no.	A	B	C	D
Mix proportion by mass (water: cement: fly ash: bentonite)	2.5: 1.0: 0.0: 0.74	2.0: 1.0: 0.0: 0.5	4.0: 1.0: 0.5: 1.0	2.5: 0.8: 0.9: 0.55
Sample void ratio	3.57	2.84	3.72	2.34
(Confining pressure: kPa) Coefficient of permeability: m/s	(200) 6.3×10^{-9}	(200) 1.5×10^{-9}	(100) 9.4×10^{-9}	(200) 1.3×10^{-10}
	(400) 4.4×10^{-9}	(400) 1.2×10^{-9}	(200) 6.0×10^{-10}	(400) 7.0×10^{-11}
	(600) 3.7×10^{-9}	(600) 8.9×10^{-10}	(300) 4.2×10^{-10}	(600) 6.0×10^{-11}

3.5 Pore water pressure measurements - steady state before Crossrail tunnel construction

The steady-state pore water pressures measured by the VW piezometers and standpipe piezometers over one year after the installation and just before the Crossrail tunnel construction (September 2012) are presented in Figure 5. During borehole drilling for the installation of the instrumentation, the upper water table was established to be about 4–5 mbgl within the Thames Gravels. In Figure 5, a hydrostatic pressure line with a water level at 5 mbgl is drawn as a reference line to compare with the pore water pressure measured by the various piezometers.

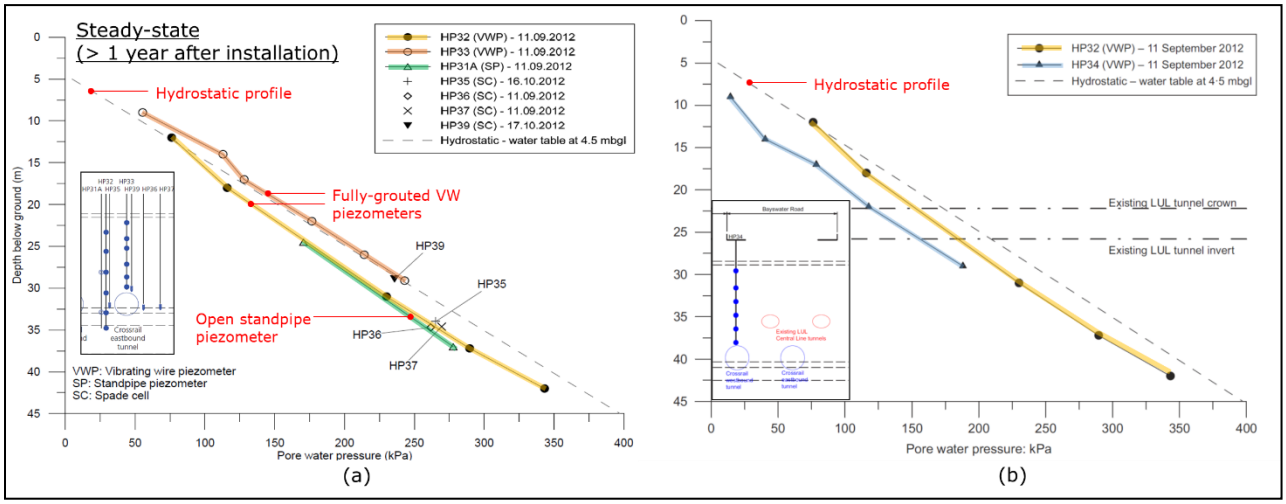


Figure 5: Steady-state pore water pressure profile measured before Crossrail construction (a) 'Greenfield' - Section A-A of Figure 2; (b) Near pre-existing LUL tunnels - Section B-B of Figure 2 (after Wan et al., 2019)

Typically in central London, the LCF is under-drained due to excessive abstraction activities in the early 1900s. In Figure 5a, the pore water pressure profile measured by the 'greenfield' multi-level VW piezometer (HP32) clearly demonstrates the LCF was under-drained. The adjacent standpipe piezometer (HP31A), at two response zone levels, verified the under-drained profile observed by the multi-level VW piezometers HP32.

It is worth noting that the other 'greenfield' VW piezometer (HP33) does not show the same under-drained profile but one that is closer to a hydrostatic profile. This has been interrogated in detail by Wan & Standing (2014) which found that there appears to be interconnectivity between the lower three sensors within the fully-grouted borehole. It is speculated that some grout loss might have occurred during the piezometer installation due to the concentrated presence of claystones in LCF at the horizons of these sensors. As a result, the seal between the lower three sensors may be compromised and therefore they were measuring the same total head.

In Figure 5b, the pre-construction steady-state pore water pressure measured at the multi-level piezometer HP34 located about 5 m from the existing Central Line westbound tunnel was shown to be less than for the nearby 'greenfield' ground. This is a clear indication that these existing tunnels, with cast-iron segmental linings, drain the surrounding London Clay ground after being constructed in early 1900s. (Wan et al., 2019; Wan & Standing, 2014).

3.6 Pore water pressure measurements – immediate response during Crossrail tunnel construction

During Crossrail tunnel construction, all the VW piezometers, including both the fully-grouted sensors (HP32, HP33, HP34) and pushed-in combined cells (HP35, HP36, HP37, HP39), registered immediate response of pore water pressure changes as each of the two EPBMs passed the instrumentation site. All these VW piezometers were connected to a datalogger housed in the headworks of each borehole which read and logged the piezometer readings every hour automatically. The multi-level fully-grouted piezometer installations in HP32 and HP33, being closest from the eastbound tunnel construction, registered the most prominent response as the EPBM approached, passed and left the instruments (Figure 6).

At the instrumentation site, the eastbound EPBM advanced with an average rate of 35-40 m/day, or about 1.4-1.6 m/hr. As can be seen from Figure 6, the measurable pore water pressure changes started at about 40m ahead of the EPBM cutterhead and the measured pore water pressure stabilised after the cutterhead had left and was about 40m away from the instruments. This means the piezometers were within the passing EPBM's zone of influence for about 2 days only.

In general, five stages of pore water pressure changes (3 rising stages and 2 dropping stages) are observed in the ground in close proximity of the passing EPBM. Wan et al. (2019) interpreted and related the observed pattern to the different EPBM operations (including shield overcutting, tail grout application and tail void closure) and a soil arching mechanism that forms around an advancing shield. Due to the overall unloading of the ground by the tunnelling works, net changes of pore water pressure up to -100kPa (unloading) were measured at the VW piezometer sensors in HP32 and HP33 closed to the tunnel construction.

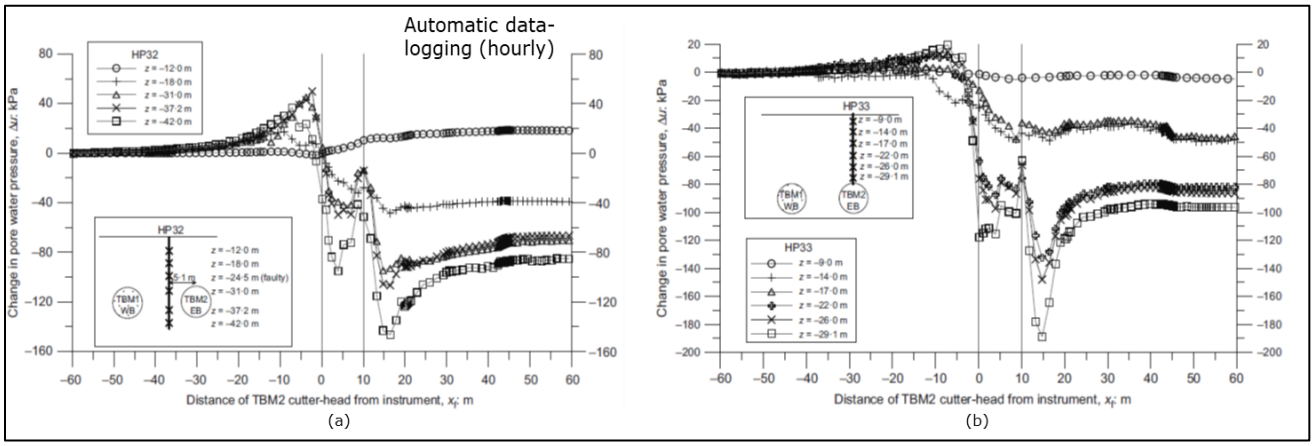


Figure 6: Change in pore water pressure measured in piezometers (a) HP32 and (b) HP33 in response to eastbound tunnel construction (after Wan et al., 2019)

The clear pattern of measurement observed was available only because of the rapid response time of the fully-grouted VW piezometers operating in the low-permeability London Clay. It is also worth noting that for the multi-level VW piezometers HP33, even though the lower three sensors appear to be interconnected as demonstrated in the pre-construction measurements (see section 3.5 above), they were still able to register different immediate responses of pore water pressure at the different sensors.

3.7 Pore water pressure measurements – Long-term response post-construction

Monitoring of the instruments continued after the tunnel construction, with the last round of measurements taken in August 2019, about 6.5 years after the eastbound tunnel construction. Figure 7 shows the full histories of measured pore water pressures by the multi-level VW piezometers HP32 and HP33. The events of the westbound and eastbound tunnel construction can be easily identified by the instantaneous changes in pore water pressures (November 2012 and February 2013). The measured pore water pressures at different depths appear to have almost fully equalised (i.e. approaching steady-state conditions) 6.5 years after the tunnel construction. It can be seen that for the ground between the depth of 22 m and 42 m, the pore water pressures were equalising towards values that are lower than their corresponding pre-construction values. Conversely, they tend to equalise towards higher values than the pre-construction values for depths above 18m. However, at these shallower ground levels the pore water pressure could also be affected by the seasonal variation of water level in the upper aquifer. This suggests that the Crossrail tunnels are draining the surrounding ground influencing the pore water pressure distribution up to 9 m above the tunnel crown.

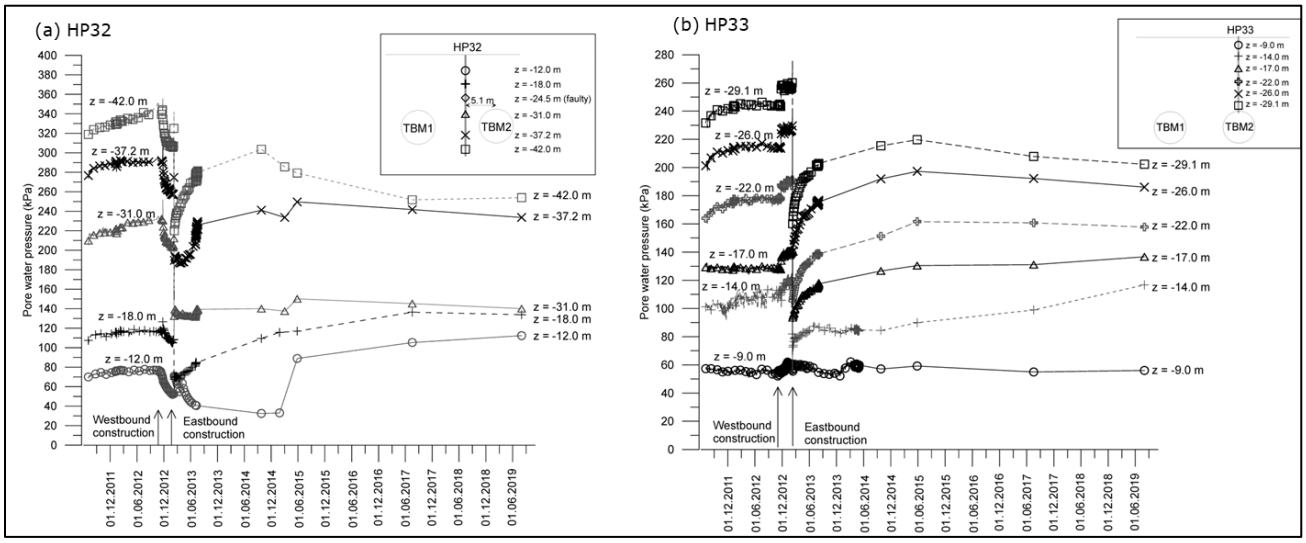


Figure 7: Post-construction pore water pressures measured by multi-level VW piezometers (a) HP32 and (b) HP33 (after Wan et al, 2021)

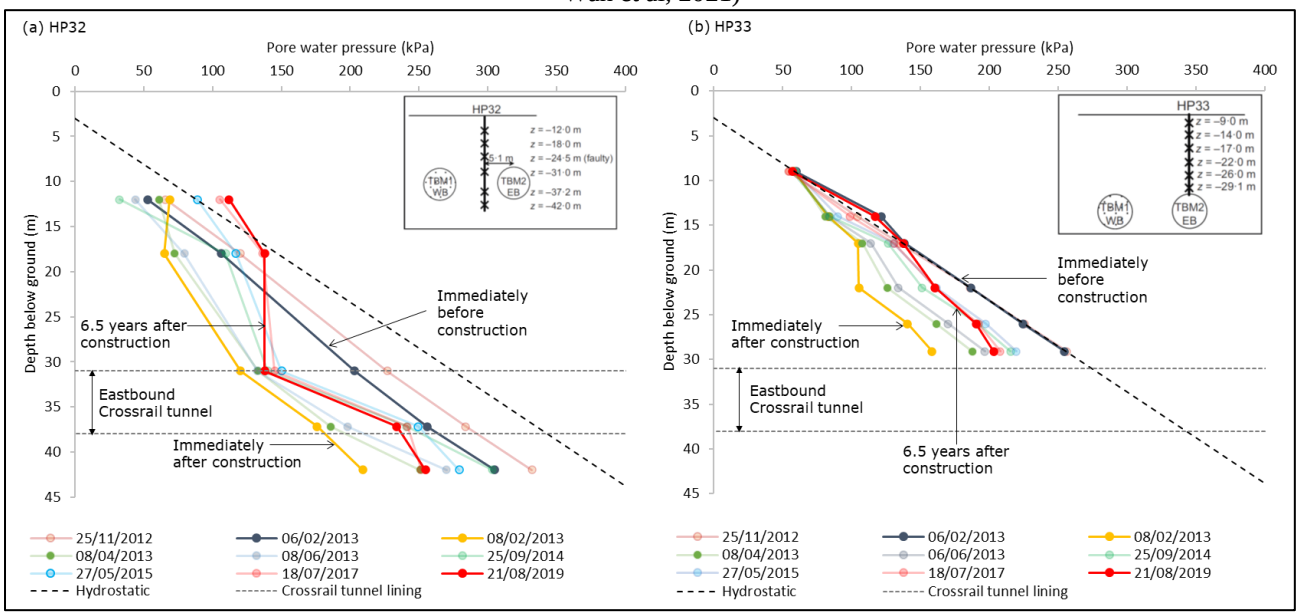


Figure 8: Post-construction pore water pressure profiles measured by VW piezometers (a) HP32 and (b) HP33

The magnitude and extent of the draining effect by the new Crossrail tunnels can be visualised by plotting the development of the measured post-construction pore water pressure profiles in Figure 8. As discussed above, immediately after the tunnel construction up to 100 kPa of negative excess pore water pressure developed due to the overall unloading by the tunnel construction (the difference between the dark blue and the orange profiles). After 6.5 years, the negative excess pore water pressures were measured to have dissipated partially, with the piezometers closest to the tunnel crown level registering the greatest magnitude of residual negative excess pore water pressure. At about 30 m below ground (about 1 m above the tunnel crown), the residual negative excess pore water pressure (difference between the dark blue and red profiles) at 6.5 years after the construction was registered about 80 kPa for both HP32 and HP33.

Because of the waterproof measures especially the presence of the annulus grout around the linings, it seems unrealistic that a significant amount of groundwater is draining into the tunnels. It is possible that groundwater flow could occur via some flow paths longitudinally along the tunnel formed in any gap between the impermeable tunnel lining (including the annulus grout) and the surrounding ground.

In general, the post-construction monitoring demonstrated that the fully-grouted multi-level VW piezometers have performed satisfactorily at least 8 years after installation (n.b. they were installed in the Summer of 2011). Their measurements provided useful insight into the long-term ground response to and the soil-structural

interaction with the constructed tunnels. Interestingly, the lower 3 sensors of HP33 seemed to have restored some ability to measure the pore water pressure independently, as the profiles after May 2015 are no longer seen to be hydrostatic.

4 RELEVANCE TO APPLICATIONS IN HONG KONG

4.1 Limited applications of fully-grouted piezometers in Hong Kong

Despite the benefits, there appear to be only limited applications of the fully grouted method of VW piezometer installation in Hong Kong. The authors consider the main reasons for the fully grouted piezometers not gaining popularity in the local ground investigation and geotechnical instrumentation sectors boil down to two key factors: (i) a lack of confidence in the performance of fully-grouted installation and (ii) a lack of appreciation of the benefits that the fully-grouted piezometers could bring to geotechnical projects. More specifically, the followings may have hindered the application of fully-grouted piezometers in Hong Kong:

- A lack of proven records of their performance through well-documented local case histories.
- A lack of quality research on local applications.
- A lack of trusted local guidelines for installation, which would depend on the availability of local case histories and research results.
- A misconception that the hydrogeology in most development projects is always ‘simple’, with experience suggesting that low-permeability soils or isolated aquifers are not often encountered.
- Pore water pressure not often considered a critical monitoring parameter for construction control.

While the Crossrail research work presented in this paper would contribute to a reference of case study, in this section the authors aim to help realise the benefits and potential of the use of fully-grouted piezometers for civil engineering projects in Hong Kong.

4.2 Excavations in reclaimed lands

Land reclamation has played an important role in providing land to support the development of Hong Kong since as early as the 19th century. With Hong Kong’s strategy of increasing land supply and reserves to meet its housing and development needs, reclamation has been revived as one of the means to create land under a multi-prong approach. Soft marine and/or alluvial deposits are often encountered in reclamation works and subsequent development in the reclaimed land.

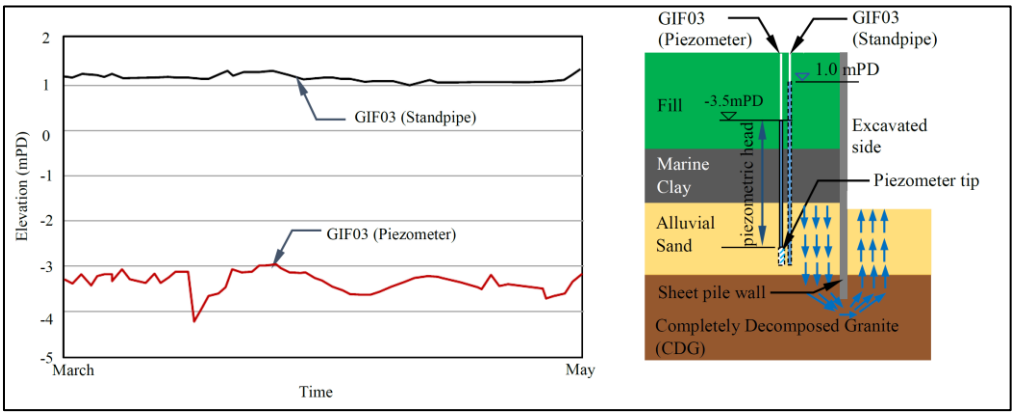


Figure 9: Measured groundwater pressure above and beneath the marine clay layer behind an excavation in reclaimed land in Kai Tak area, east Kowloon, reported in GEO Publication No. 1/2023 (GEO, 2023)

Low-permeability marine mud overlying more permeable alluvial deposits or saprolite is common in both old and recently reclaimed land in Hong Kong. Early reclamations before 1970s were formed mainly by uncontrolled end-tipping of fill placed directly onto the seabed, leaving the marine mud with large mud waves in place (Endicott, 2007; Ng & De Silva, 2007). This low-permeability disturbed marine mud layer with uneven thickness is therefore often encountered and act as an aquiclude in old reclamation areas. Excavations which involve dewatering the confined aquifer (i.e. below the aquiclude) would induce groundwater flow into the excavation around the toe of embedded retaining wall. The groundwater pressure responses behind the retaining wall are separated into two zones by the marine mud: the upper unconfined aquifer without significant seepage; and an underlying confined aquifer with seepage and associated piezometric head drop in the confined aquifer.

The difference in piezometric head across the marine mud layer due to the underdrainage causes consolidation and settlement of the layer, which could in turn cause excessive settlements or damages to structures behind, and even at a far distance from, the excavation.

This is not particularly a new problem unknown to the practitioners and had been seen in the excavation for Chater Station (Davis & Henkel, 1980) and a 90m-deep shaft in Tseung Kwan O (Endicott, 2020). The newly published guidance document GEO Publication No. 1/2023 (GEO, 2023) on deep excavation design and construction has timely reminded and illustrated this mechanism with a recent example seen in an excavation in the Kai Tak area (Figure 9), which resulted in settlements of proximate highway structures. The publication recommends that "*In similar ground and seepage conditions, piezometers should be installed at appropriate depths on the unexcavated sides of the embedded wall (e.g. at a depth below the interface between the permeable and impermeable soils), in order to monitor the changes in groundwater pressure and to facilitate estimation of the potential consolidation settlement.*"

For the traditional piezometer installation method, it is a standard practice that no more than two standpipe/piezometers are to be installed in a single borehole. One of the practical choices that designers have to make is the balance between spatial resolution of piezometers on plan and across depths/strata with a given number of boreholes. For sites with non-uniform stratigraphy, these decisions are not always easy.

In addition, it is not uncommon to find that the piezometric head data obtained with a network of piezometers of low spatial resolution (both vertically and horizontally) difficult to interpret in non-uniform, inhomogeneous ground conditions in a way that could offer meaningful explanations to the observed responses. Sometimes, these measurements that cannot be explained would be treated as 'outliers' and prematurely discarded. This could potentially lead to observations of untoward ground response being overlooked. The value of the monitoring of piezometers is often limited to that for the purpose of directly comparing the measurements with pre-set trigger levels in the instrumentation and monitoring plan.

With the fully-grouted technique, the designers would be able to choose to install multiple piezometers in a single borehole, where necessary. This would greatly enhance the versatility in formulating the instrumentation and monitoring scheme with the aim to collect more extensive data for understanding the site hydrogeology, in particular for sites with complex stratigraphy.

4.3 New reclamations

Non-dredged method has become the de-facto standard practice for reclamations in Hong Kong in light of sustainability considerations. This involves leaving the low-permeability marine mud in place, and improving their mechanical properties to meet the performance requirements of the reclaimed land through various ground improvement techniques. Conventional techniques include perforated vertical drains (PVD) and stone columns. More recently the deep cement mixing (DCM) technique has been successfully introduced in Hong Kong. There are also examples of using low-permeability sediments as the fill materials for reclamation in both local and overseas studies and projects (e.g. Yin et al., 2023; Kitazume, 2016; Karthikeyan et al., 2004 & 2007).

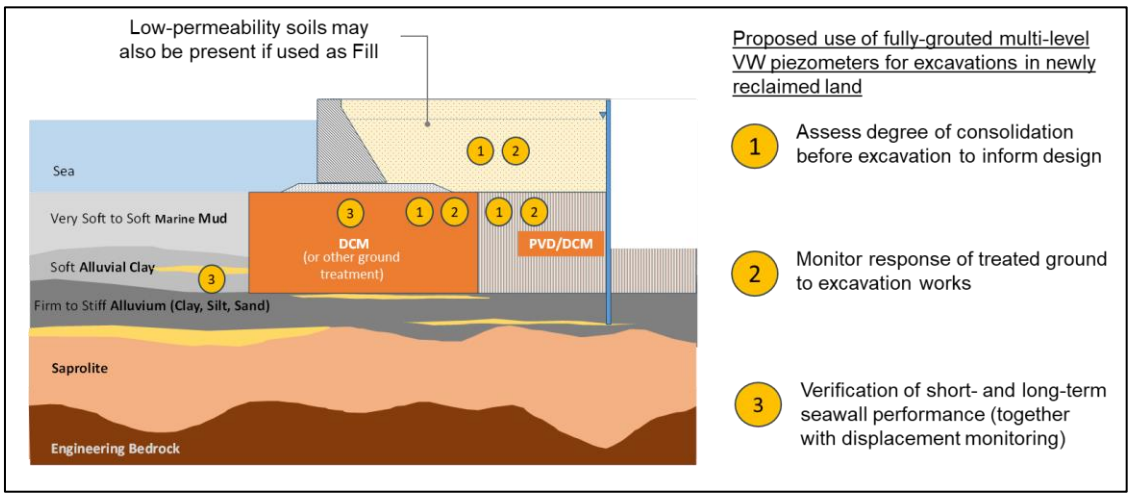


Figure 10: Proposed use of fully-grouted multi-level VW piezometers for construction in newly reclaimed land

The ground improvement and filling works for land formation, as well as any subsequent excavation and foundation works on such land formed, introduce changes to the stress state of these soils. In low-permeability soils, these changes often occur under undrained and subsequently partial-drained conditions, depending on the ground improvement technique used for land formation and the time period concerned for the engineering structures. For instance, the properties and responses to stress changes of soft marine mud improved by conventional PVD with surcharge through consolidation with shortened drainage paths would be very different from those of the same mud between areas replaced by stiff DCM columns, with the latter taking up significant amount of the overburden stress through arching.

Figure 10 presents schematically the typical ground conditions encountered by new (usually non-dredged) reclamations and subsequent excavation works within the reclaimed land. The proposed use of full-grouted multi-level VW piezometers for construction works in newly reclaimed land is also illustrated.

Understanding of the stress state of the treated soft marine mud for the design and construction of excavation and foundations works on the reclaimed land would require knowledge of the actual pore water pressure distribution at the site. For reclamation with PVD, experience has shown that while the overall degree of consolidation might be satisfactorily achieved as indicated by the ground settlements, the dissipation of excess pore water pressures throughout a site could vary, both vertically with depth and horizontally across the site. Slower than expected dissipation of excess pore water pressure or even 'stagnant' pore pressures are not uncommon in previous reclamation projects in Hong Kong (Ng & De Silva, 2007). In such cases, simply assuming the marine mud to have fully consolidated could result in an underestimation of the excess pore water pressure and hence an overestimation of its shear strength and stiffness, which could result in geotechnical design not on the conservative side. However, in light of the above-mentioned variabilities, it is often difficult for a designer constrained by the low density of piezometers across the site to fully appreciate the pore water pressure distribution.

Much of the above-mentioned information of pore water pressure distribution may also be obtained by piezometers installed conventionally with granular filter response zones. However, the multi-level, fast-responding fully grouted VW piezometers certainly offer a more versatile and cost-effective tool in the designer's tool kit. As multiple piezometers can be placed in a single borehole, a higher density of sensors across depths can be achieved with the same number of boreholes. This can provide more complete information to facilitate interpretation of the initial stress state of the soils and their actual responses to the construction works.

4.4 Other applications

Apart from applications in reclaimed land where low-permeability sediments are often encountered, the versatility of installing multiple piezometers in a single borehole could also be useful for measuring groundwater pressure in slopes, in particular where the hydrogeology is complex and/or site access is limited.

5 CONCLUSIONS

This paper has presented a detailed case history of the installation and application of fully-grouted VW piezometers for monitoring the immediate and long-term response of pore water pressure changes to the construction of Crossrail tunnels by EPBMs in London Clay. It has demonstrated the satisfactory performance of these instruments, highlighting the key benefits of the fully-grouted installation in (a) allowing fast, straightforward installation of multi-level VW piezometers in a single borehole, and (b) providing high spatial resolution of fast-responding pore water pressure measurement points in the ground. Because of these benefits, the fully-grouted piezometers offer a cost-effective and reliable tool that is versatile and enables almost-instant measurements of pore water pressure, which is useful for gaining important insights into the responses of the ground with low-permeability soils or complex stratigraphy/hydrogeology to construction works.

In particular, for design and construction of reclamations and deep excavations in reclaimed land, to more holistically investigate the field behaviour of low-permeability soils of substantial thickness during and after reclamation, there is a huge potential of making use of multi-level, fast-responding fully-grouted VW piezometers as part of the instrumentation and monitoring scheme. It would greatly complement other instrumentation such as those for displacement monitoring to enhance both construction control and understanding/verification of the performance of geotechnical structures. Comprehensive and reliable instrumentation and monitoring results are essential when developing and optimising innovative solutions of geotechnical works.

More well-documented local and overseas case histories would help promote confidence and wider use of fully grouted piezometers in Hong Kong. Guidance on the installation of fully grouted piezometers has now been included in the European Standard EN ISO 18674-4:2020. It is suggested that technical research and development on the use of fully-grouted VW piezometers in local conditions are pursued to support development of specific guidelines for Hong Kong practice.

REFERENCES

Contreras, I.A., Grosser, A.T. & Ver Strate, R.H. 2008. The use of the fully-grouted method for piezometer installation, Part 1 and Part 2. *Geotechnical News*, 26(2): 30–37.

Dunnicliff, J. 2008. Discussion of 'The use of the fully-grouted method for piezometer installation' by Contreras et al. (2008). *Geotechnical News*, 26(2): 38–40.

EN ISO 18674-4:2020 *Geotechnical investigation and testing - Geotechnical monitoring by field instrumentation. Part 4: Measurements of pore water pressure: Piezometers.* European Committee for Standardization (CEN). Brussels.

Endicott, L.J. 2007. Review of last 30 years of geotechnical engineering in Hong Kong 1976 to 2006. *Proceedings of the HKIE Geotechnical Annual Seminar 2007 - Geotechnical Advancements in Hong Kong since 1970s, Hong Kong, 14 May 2007*, pp. 99-108.

Endicott, J. 2020. *Deep Excavations in Soil*, 258 p. CRC Press.

Geotechnical Engineering Office. 2017. *Geoguide 2 - Guide to site investigation*. Hong Kong: The Government of the Hong Kong Special Administrative Region.

Geotechnical Engineering Office. 2023. *GEO Publication No. 1/2023 - Deep Excavation Design and Construction*, 144 p. Hong Kong: The Government of the Hong Kong Special Administrative Region.

Karthikeyan, M., Dasari, G.R. and Tan, T.S. 2004. In situ characterization of land reclaimed using big clay lumps. *Canadian Geotechnical Journal*, 41(2): 242-256.

Karthikeyan, M., Tan, T.S., Chia, W.S. & Tee, C.P. 2007. Use of dredged clay lumps as fill materials for land reclamation. *Proceedings of the Second International Maritime-Port Technology and Development Conference, Singapore, 26 -28 September 2007*, MTEC 2007, pp.640-646.

Kitazume, M. 2016. *The Pneumatic Flow Mixing Method*, 250 p. CRC Press.

Laver, R., 2021. Construction dewatering in reclaimed land in Hong Kong - a review of best practices. *The HKIE Transactions*, 28(3): 130-138.

Mikkelsen P.E. & Green G.E. 2003. Piezometers in fully grouted boreholes. *Proceedings of 6th International Symposium on Field Measurements in Geomechanics, Oslo*, pp. 545-554, Lisse (Swets & Zeitlinger).

Ng, F. & De Silva, S. 2007. Geotechnical practice of reclamation in Hong Kong. *Proceedings of the HKIE Geotechnical Annual Seminar 2007 - Geotechnical Advancements in Hong Kong since 1970s, Hong Kong, 14 May 2007*, pp. 69-83.

Ridley A.M. 2015. Soil suction – what it is and how to successfully measure it. *Proceedings of 9th International Symposium on Field Measurements in Geomechanics*, Sydney, pp. 27-46, Perth, Western Australia.

Vaughan P.R. 1969. A note on sealing piezometers in boreholes. *Géotechnique*, 19(3): 405–413.

Wan, M.S.P. & Standing, J.R. 2014. Field measurement by fully grouted vibrating wire piezometers. *Proceedings of the Institution of Civil Engineers – Geotechnical Engineering*, 167(6): 547–564.

Wan, M.S.P., Standing, J.R., Potts, D.M. & Burland, J.B. 2017a. Measured short-term ground surface response to EPBM tunnelling in London Clay. *Géotechnique*, 67(5):420–445.

Wan, M.S.P., Standing, J.R., Potts, D.M. & Burland, J.B. 2017b. Measured short-term subsurface ground response to EPBM tunnelling in London Clay. *Géotechnique* 67(9), 748–779.

Wan, M.S.P., Standing, J.R., Potts, D.M. & Burland, J.B. 2019. Pore water pressure and total horizontal stress response to EPBM tunnelling in London Clay. *Géotechnique*, 69(5): 434–457.

Wan, M.S.P., Standing, J.R., Potts, D.M. & Burland, J.B. 2021. Measured post-construction ground response to EPBM tunnelling in London Clay. *Proceedings of the Tenth International Symposium on Geotechnical Aspects of Underground Construction in Soft Ground, IS-Cambridge 2022, Cambridge, United Kingdom, 27-29 June 2022.* CRC Press.

Yin J.H., Chen W.B., Tan D.Y. & Wu P.C. 2022. A Sustainable Approach to Marine Reclamations Using Local Dredged Marine Soils and Wastes: Soft Soil Improvement, Physical Modelling Study, and Settlement Prediction-Control. *Proceedings of The HKIE Geotechnical Division 43rd Annual Seminar: Towards a Smart-Green-Resilient Geo-Future for World-class City, Hong Kong, 19 May 2023.* AIJR Books.

Innovative Synergy between Slope Upgrading and Ecological Conservation in Preventive Maintenance Programme

Jay P. H. Wan, W. K. Yeung & Dr. C. C. Pang
Coalition for Research on Ecology and Wildlife Ltd., Hong Kong, China

Lawrence C. F. Leung, Ronald P. M. Li & Stanley K. M. Chung
Jacobs China Ltd. Hong Kong, China

ABSTRACT

In order to preserve the natural woodland and vegetation under Preventive Maintenance Programme of Highways Department of HKSAR (HyD), tree preservation and species conservation are of important factors to be considered during the construction phase. However, drawbacks such as degraded micro-habitats, diminished both bio- & genetic diversities from non-native sources, and the challenges of maintenance works against invasive plants persist. Traditional post-construction soft landscape plantation is often insufficient in addressing such complex ecological issues, especially in exposed / ecologically sensitive slopes.

This paper shares a practical, collaborative case study between Ecologists / Plant Specialists and Geotechnical Engineers in preserving a natural floral community during slope upgrading works. Challenges and lessons learnt in this case contribute to an insight for sustainable management of both ecological preservation and slope engineering project.

1 INTRODUCTION

The Prevention Maintenance Programme of Highways Department of HKSAR (HyD) has evolved not only to stabilize substandard roadside man-made features from an engineering aspect; but also puts significant efforts to ensure that upgraded features are well blended with the surrounding natural environment as far as practical.

Other than visual amenity, ecological considerations has been taken an increasing role in slope vegetation cover in recent years, especially in man-made features adjacent to ecologically sensitive areas (e.g. conservation areas/ Country Parks). Such ecological consideration aims at maintaining the original habitat or enhancing habitat quality and floral diversity as a resource for various local wildlife.

Feature No. 15NE-B/C273 located at Shek O Road was a selected roadside man-made slope feature to be upgraded under Prevention Maintenance Programme of HyD. The feature is an approximately 125m long soil and rock cut slope. The cut slope has a maximum height of 18m and an average slope angle of 45^{o}. The southern end and the crest of the middle portion of the feature was covered in vegetation (30%) while the rest of the feature was covered in shotcrete (70%). During the course of the slope upgrading works, Landscape Division of HyD expressed important concern on the high amenity value of the existing woodland at the southern end of the feature (Figure 1, Plates 1 and 2). The preservation includes the existing trees and species of conservation value and also the natural vegetation was of importance during construction phase.

This paper shares a practical, collaborative case study between Ecologists / Plant Specialists and Geotechnical Engineers in preserving a natural floral community during the planning stage and implementation stage of the slope upgrading works. Meanwhile, discussions on the challenges encountered and lessons learnt in this case provide insight for sustainable management of both ecological preservation and slope engineering.

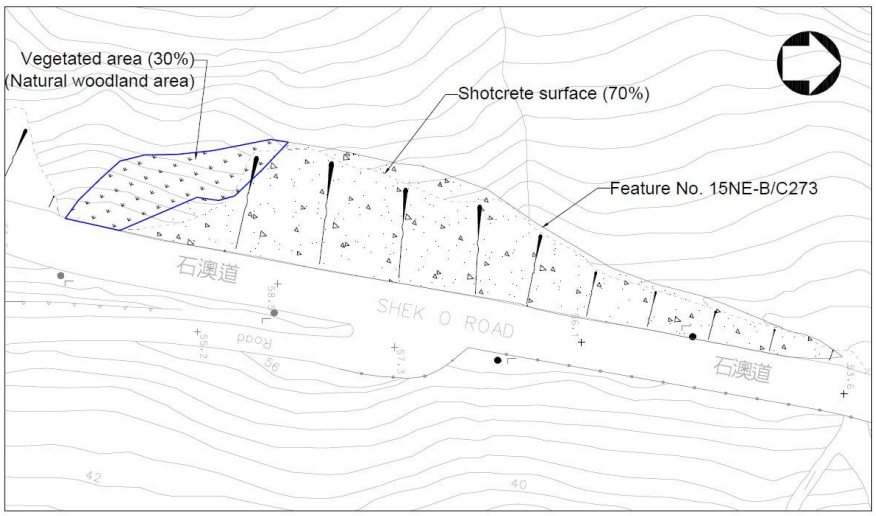


Figure 1: Location Plan of Concerned Natural Woodland Area at Feature No. 15NE-B/C273

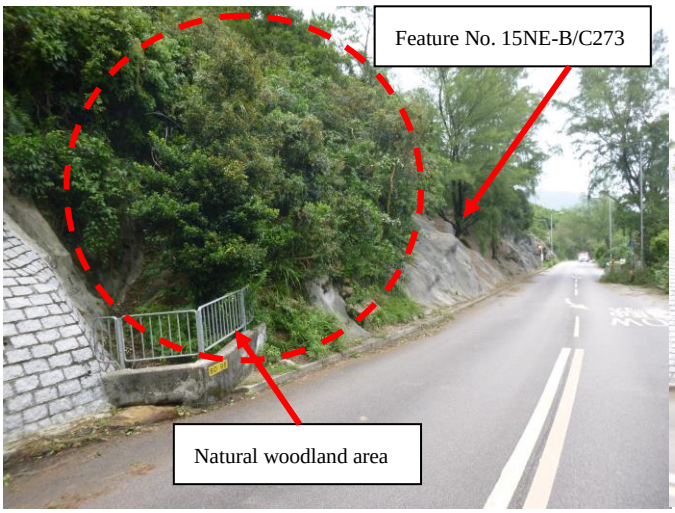


Plate 1: Existing condition of natural woodland area prior to commencement of works (View from South-eastern direction) (Date: 24/08/2017)



Plate 2: Existing condition of natural woodland area prior to commencement of works (View from Eastern direction) (Date: 24/08/2017)

2 SEQUENECE OF WORKS

2.1 Ecological Condition Survey

The Government has implemented a comprehensive range of administrative requirements for tree preservation such as the submission of Engineering and Landscape Plans, Tree Preservation and Removal Proposals (TPRP) and Arboricultural Assessment Reports (AAR) for all government project as stipulated in DEVB TC(W) No. 7/2015 (Development Bureau, 2015). On top of the above, an Ecological Condition Survey in woodland area (ECS) was suggested in Jan 2020 to obtain up-to-date baseline information on habitat type, vegetation communities, and presence of any species of conservation importance within the concerned woodland area (Plates 3 and 4). Information presented by a tree survey / tree risk assessment was not included in the scope of the ECS. An ecologist / Plant Specialist was assigned to identify target species of vegetation to be retained before site clearance works commenced at the Southern portion of the slope.

A methodology of ECS was submitted to HyD for comment prior to the commencement of the physical survey. The field surveys covered not only flora but also animal groups. In case important feeding / breeding habitat and fauna species of conservation importance were revealed, corresponding mitigation measures should also be proposed. However, the ECS results found that there were no conservation concerns for fauna but only the floral community baseline with some plant species of conservation importance.



Plate 3: Ecological Condition Survey in woodland area (ECS) conducted by Landscape Contractor and Ecologist / Plant Specialist with Geotechnical Engineer



Plate 4: Locating Species of Conservation Importance by Ecologist / Plant Specialist

The floral community consisted of various plants forming a complex structure of shaded woodland area (Table 1). Over 92% of the recorded species are native which are locally common in Hong Kong (Corlett et al., 2000; Hong Kong Herbarium, 2024) and would be very likely prone to site clearance during the construction phase. Three species of conservation importance were recorded within the survey extent (Figure 2).

Table 1: Plant Species Recorded during the Ecological Condition Survey in Natural Woodland Area (ECS)

Type	Plant groups (Dominated species); Species of conservation importance*		No. of species recorded
Tree	• *Celtis timorensis* (假玉桂) • *Schefflera heptaphylla* (鴨腳木)	• *Pinus massoniana* (馬尾松) • *Styrax suberifolius* (栓葉安息香)	14
Shrub	• *Carallia brachiata* (竹節樹) • *Litsea rotundifolia var. oblongifolia* (豺皮樟) • *Pavetta hongkongensis* (香港大沙葉)*	• *Gardenia jasminoides* (梔子) • *Diospyros vaccinioides* (小果柿)*	18
Herbaceous plant	• *Liriope spicata* (山麥冬)	• *Asparagus cochinchinensis* (天門冬)	5
Climber	• *Smilax* spp. (菝葜屬) • *Gnetum luofuense* (羅浮買麻藤)*	• *Strychnos* sp. (馬錢屬)	15
		TOTAL	**52**

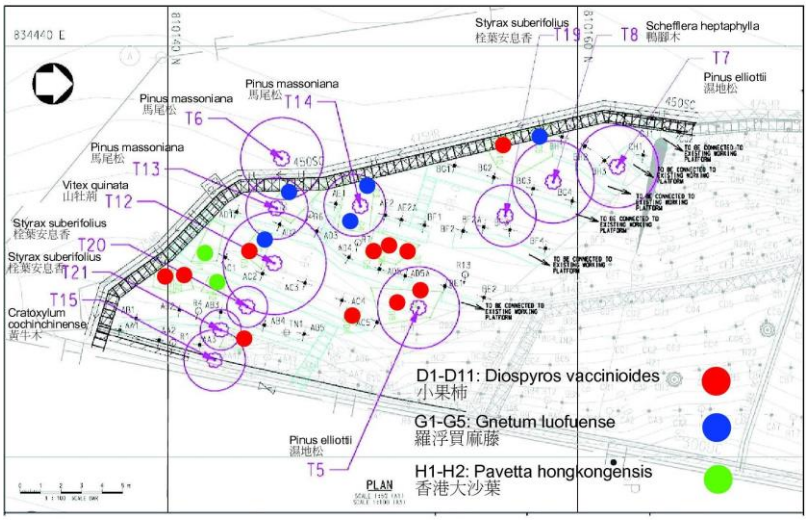


Figure 2: Recorded Trees and Plant Species of Conservation Importance with Corresponding Protection Zones

2.2 Design Revision to Preserve the Existing Vegetation

Noting there were dense vegetation growing on the natural slope on the southern end of slope with species of conservation importance, design amendment was required to preserve the existing vegetation as much as possible. The design revision was submitted for approval as detailed in Table 2 below.

Table 2: Summary of Design Revision to Preserve Vegetation

No.	Item	Revision	Beneficial Effects to Woodland Area
1.	Soil Nails	• The spacing of soil nails was changed from 1.5m centre-to-centre to 2.0m centre-to-centre in horizontal direction.	• To reduce the soil nail density in the woodland area so that total extent of excavation of soil nail head could be reduced in the woodland area.
		• Diameter of 10 nos. of soil nails had been increased from 100mm to 150mm; and the spacing of 3 nos. soil nails at the crest of the woodland area has been changed from 1.5m to 1.3m.	• To compensate of reduction of soil nail density in order to meet the design requirement of slope stability.
2.	Surface Protection	• Biodegradable erosion control mat of natural jute fibre type with minimum average weight 500 g/m^2 was applied.	• To preserve and retain the existing species within the woodland area, as the application of non-biodegradable erosion control mat with hydroseeding may hinder the growth of existing species to be retained.
3.	Surface Drainage System and Maintenance Access	• A new alignment of the stepped channel was counter-proposed as the position of the original proposed 300mm U-channel with concrete apron and 300mm high upstand is in conflict with the vegetation growing on the natural slope.	• To minimize the impact on the woodland area so that natural rainwater will not be completely diverted away from the vegetation and to lessen the visual impact of the stepped channel leading to the slope toe.
		• The portion of 300mm U-channel with concrete apron in the vegetated slope portion was deleted accordingly. A 300mm diameter downpipe was proposed to convey the surface runoff rather than a stepped channel.	• To suit the actual site conditions and reduce the extent of excavation and concrete works on the slope surface in woodland area (Plates 5 and 6).
		• The alignment of the steel maintenance staircase was further adjusted to the centre of the slope and the mid-berm access with U-channel were deleted within natural woodland area.	• To preserve trees and natural slope vegetations as much as possible (Figures 3 and 4).



Plate 5: A new stepped channel alignment was counter-proposed to preserve the flora species of conservation importance fenced off by an orange net

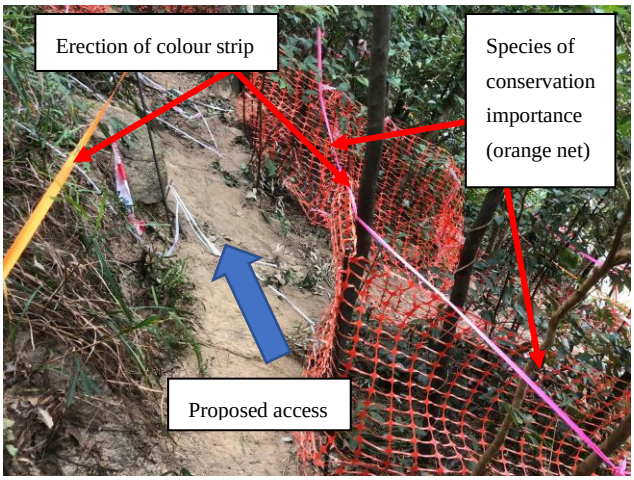


Plate 6: Condition of natural woodland area when assigning erection of access

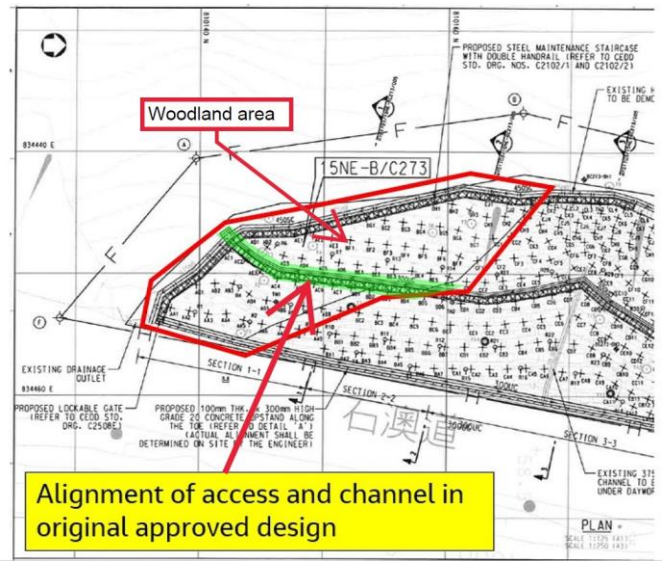


Figure 3: Alignment of access and channel in Original Approved Design

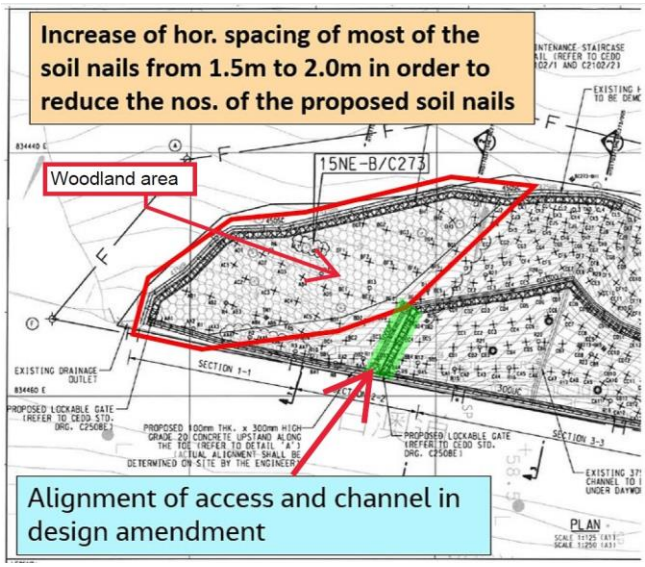


Figure 4: Alignment of access and channel in Design Revision

2.3 Erection of Temporary Access and Protection Measures

After conducting the ECS, the draft works alignment was marked temporarily using the colour strips by fitting the mosaics of dense vegetation. All existing trees, species of conservation importance and woody vegetation were appropriately cordoned off by orange net (Plates 7 and 8). For secure protection, all the area outside the colour strips of lands reserved for soil nail head / temporary access and working platform were also cordoned off properly (Plate 7). Photo records upon completion of fencing was submitted to HyD for obtaining their consent for erection of physical temporary access and working platform.

Having experienced the practicability of erecting the temporary access and working platform for equipment mobilization and construction activities at the first two uppermost rows of soil nails, further on-site adjustment was made for the remaining rows of soil nails as required when deemed necessary.

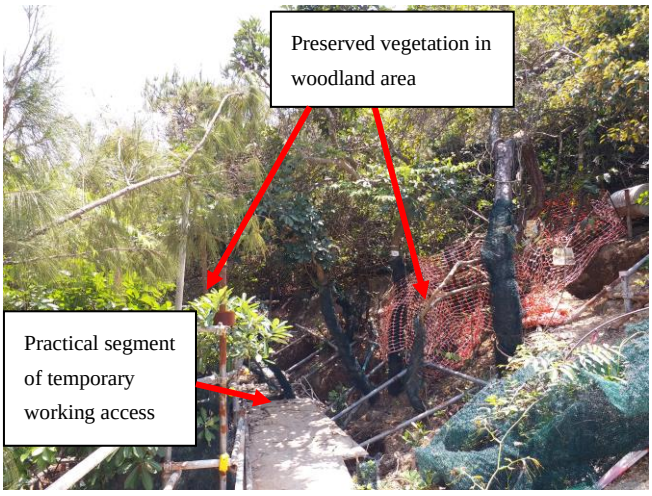


Plate 7: A practical segment of temporary working access among preserved vegetation

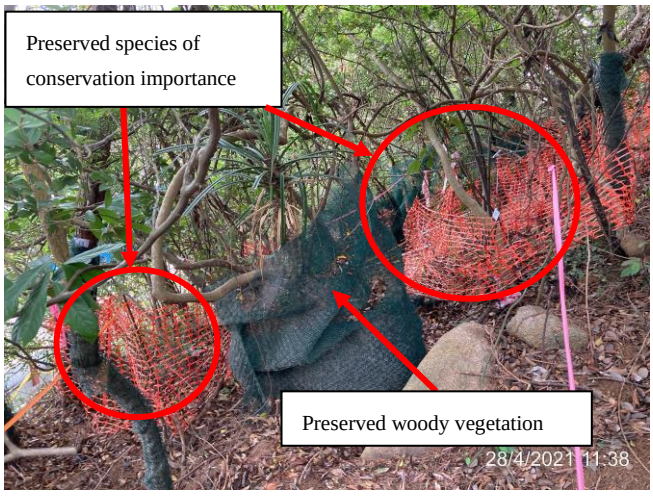


Plate 8: Woody vegetation was preserved by a green fence while orange fence was used for species of conservation importance. Preserved woody climber provided a shaded canopy layer to sustain the microhabitat.

2.4 Limited Site Clearance with Selective Trimming of Vegetation

To minimize disturbance to the natural woodland area, site clearance was minimal and restricted to areas only for erection of temporary access and working platforms under the supervision of the Landscape Contractor with landscape softworks or establishment works experience and Ecologist / Plant Specialist. To further minimize the impact from the engineering works, a specialist team was engaged to conduct site clearance and vegetation preservation works.

When a localized clearance was unavoidably, the selective trimming of woody plants would be carried out under the supervision of the Ecologist / Plant Specialist and the Geotechnical Engineer. Non-woody herbaceous plants and grass was not limited for site clearance. If the common plant species without conservation importance was affecting the erection of the working platform, the authorized Landscape Contractor (but not other site workers) conducted the selective trimming (Plates 9 to 12) and pruning of the hanger and overhanging branches affecting headroom as identified on site during inspection also had to be carried out.



Plate 9: Before selective trimming during erection of scaffolding and working platform for soil nail Row BH in woodland area

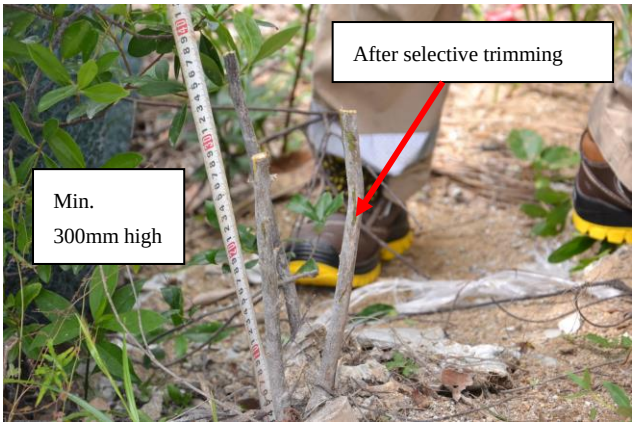


Plate 10: After selective trimming, erection of working platform will avoid soil compaction and risk of stepping on the remaining stems by the workers



Plate 11: Only hand-held tools were allowed for selective trimming. Plant identification and extent of trimming was confirmed by the Ecologist before trimming.



Plate 12: Adventitious root system of *Pandanus* sp. (露兜樹屬) allows a quicker recovery against selective trimming of its spiky leaves that obscuring the work path. The clutch was preserved as a good coverage at the boulder zone.

2.5 Inspection Pits Excavation with Relocation of Soil Nails

The aim of an Arboricultural Assessment Report (AAR) is to assess the impact of the proposed construction work through inspection pit excavation in the proposed soil nail location and to review the method statement

of the engineering and tree protection works including the Methodology of Soil Nailing Works in Woodland Area.

Inspection pit excavation in the proposed soil nail location (i.e. 400mm x 400mm x 250mm) was carried out prior to installation of soil nails to ascertain whether the proposed soil nailing work including installation of soil nail head (i.e. 600mm x 600mm x 250mm) would be in conflict with the tree roots and make adjustment as appropriate to avoid the conflict and recorded in the AAR.

A Certified Arborist of the International Society of Arboriculture (ISA) was assigned to supervise and inspect the inspection pit excavation on-site in order to prevent major tree roots damage during excavation. Manual excavation of inspection pit at each soil nail location within a tree protection zone (TPZ) was adopted to confirm any tree roots at the proposed soil nail location (Plates 13 and 14).

If significant tree roots were encountered in the inspection pit, the soil nail had to be re-adjusted to minimize adverse impact to the existing trees (Plates 15 and 16). No major tree roots were observed in the excavated inspection pits for this site.

Photographic records of each of the inspection pit were provided and the amount of root loss was recorded. The exact location of the adjusted soil nail head was confirmed on-site and recorded in the revised working drawings.

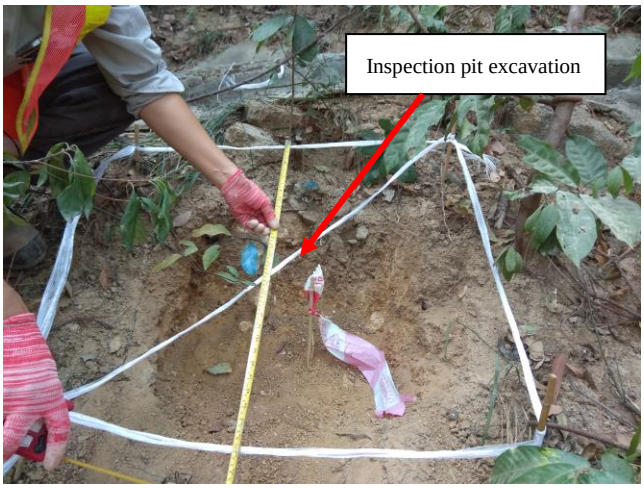


Plate 13: Inspection pit excavation for Row BG Soil Nails

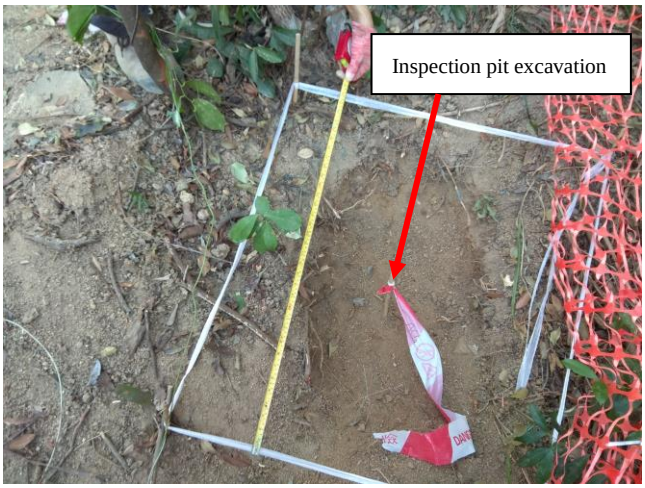


Plate 14: Inspection pit excavation for Row BF Soil Nails



Plate 15: Original soil nail head locations at Row BG

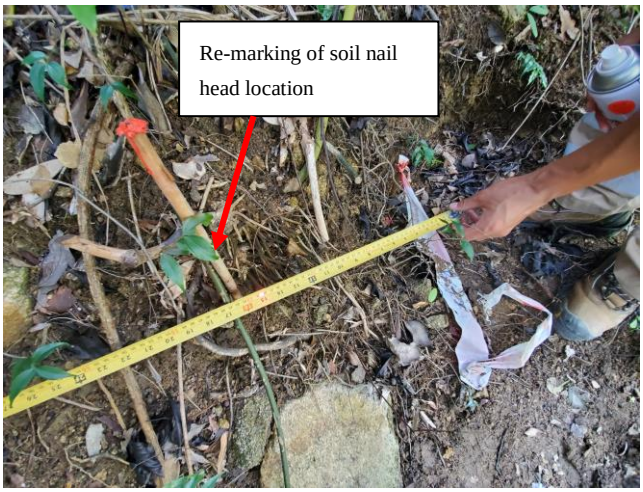


Plate 16: Re-marking of soil nail head locations at Row BG

2.6 Erection of Temporary Scaffolding and Working Platform for Soil Nailing Works

Erection of temporary scaffolding and working platforms was considered unavoidable for soil nailing works. 600mm wide temporary access and 1m wide working platform were originally proposed. It was considered that the tiebacks / metal poles of stabilizing the scaffolding of temporary access and working platform outside the soil nail head ("SNH") area had to be minimized to reduce the damage to the preserved vegetation. Hence, 900mm wide temporary access and working platform was counter-proposed to allow the workers to carry out the soil nailing works which is considered the optimized platform design with the least number of tiebacks / metal poles outside the 800mm x 800mm SNH area (Figures 5A and 5B). In the meantime, sufficient temporary working space could be provided to safeguard the workers safety.

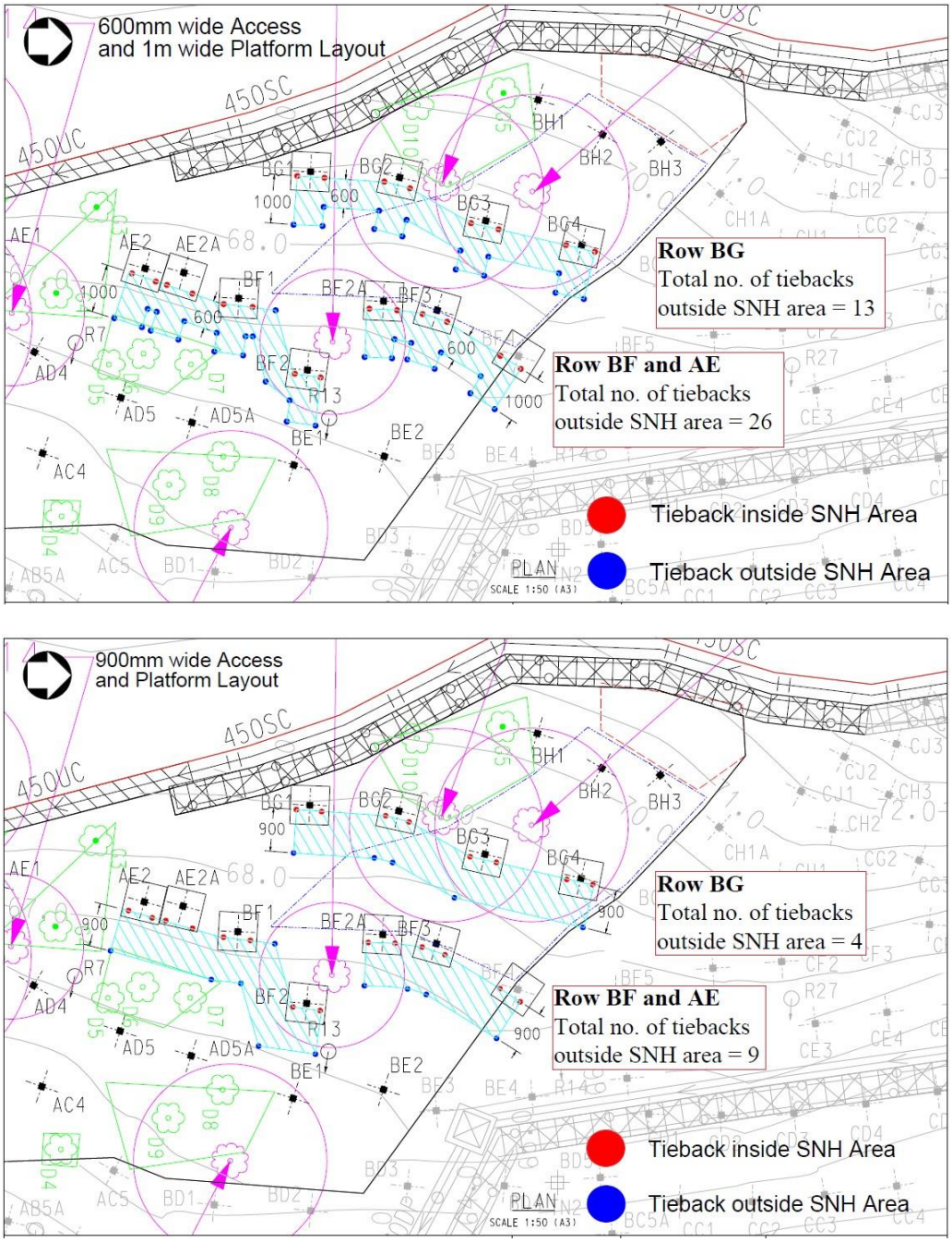


Figure 5A (upper) and Figure 5B (lower): Fewer tie backs were needed for soil nailing works at Row BG, BF and AE when the width of the access and working platform layout changed from 600mm and 1m respectively into 900mm

2.7 Soil Nailing Works in Woodland Area

A "method statement for soil nailing works in woodland area" ("MS") appending the sequence of works had to be submitted for approval prior to commencement of soil nailing works within the woodland area. According to the MS, shorter steel bar combination was adopted for easier transportation among preserved vegetation.

A steel effluent collecting tray was tailor-made by the Contractor and placed in the excavated soil nail head for water collection during the coring works (Plate 17). Adequate sand bags were also provided at the bottom of the tray as contingency measure. Effluent was then pumped to a sedimentation tank located outside the existing woodland. The route for effluent diversion was shown in the method statement for approval. Based on the experience of grouting for first two rows soil nails in woodland area, it was observed that longer construction time was required as only two nos. of effluent collecting trays could be placed for better control. After that, the Contractor proposed an alternative effluent collecting tray by using cement sand mortar and plastic sheet (Plate 18). This alternative tray not only could be placed in greater numbers within the woodland area for shortening the construction time, but also provided a good collection of effluent during coring works.



Plate 17: Tailor made effluent collecting tray using steel plate



Plate 18: Alternative effluent collecting tray using cement sand mortar and plastic sheet

2.8 Monthly Ecological Monitoring

Overall condition of preserved trees, species of conservation importance and woody vegetation; as well as the implementation of mitigation measures of plant preservation were monitored monthly by the Ecologist / Plant Specialist throughout the 32-month construction phase (January 2020 to August 2022) (Plates 19 to 28).

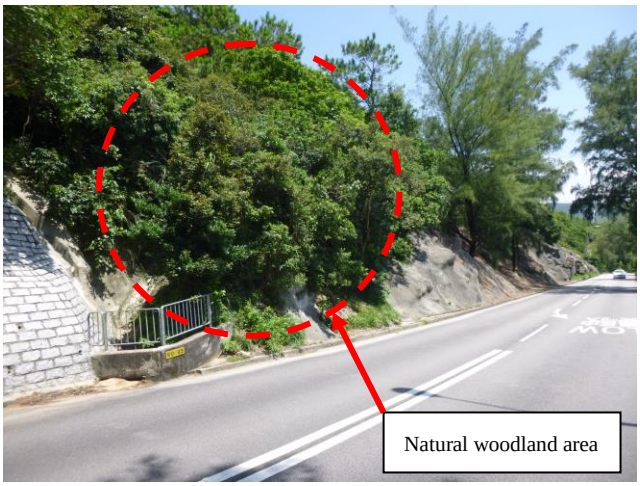


Plate 19: The woodland patch before slope upgrading works (Date: 26/07/2017)



Plate 20: The woodland patch after ECS before site clearance at dry season (Date: 16/01/2021)



Plate 21: The woodland patch three months after ECS (Date: 28/04/2021)



Plate 22: The woodland patch six months after ECS (Date: 29/07/2021)

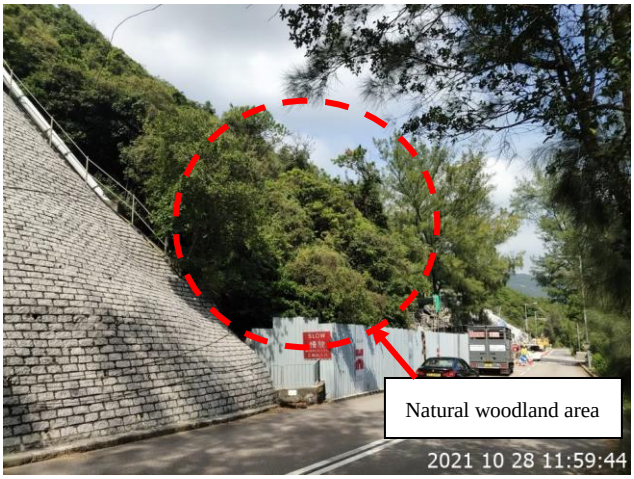


Plate 23: The woodland patch nine months after ECS (Date: 28/10/2021)



Plate 24: The woodland patch twelve months after ECS (Date: 11/01/2022)



Plate 25: The woodland patch fifteen months after ECS (Date: 30/04/2022)



Plate 26: The woodland patch eighteen months after ECS (Date: 26/07/2022)



Plate 27: Preserved woodland patch after completion of construction phase in late wet season. (Date: 29/09/2022) Note that native parasitic climber *Cuscuta chinensis* (菟絲子) has been depressed by the recovering floral community. No invasive plants compete in a rather intact community of native species in various forms.



Plate 28: General view of preserved woodland patch 1 year after completion of construction phase. (Date: 19/08/2023)

3 CHALLENGES AND LESSONS LEARNT

This task provided the dynamic communications among Ecologists / Plant Specialists, Geotechnical Engineers and Contractors (construction and soft landscape) throughout the whole construction phase; rather than a top-down construction based on approved survey reports, design drawings and typical common practices.

3.1 Plant Preservation Priority

The biggest challenge was to provide works space for engineering structures in a dense woodland, which had no guarantee on its condition with such an intense works disturbance. The ECS aimed at advising what type of vegetation or plant species can be cleared, at what extent; such that core floral community could sustain a recovery to the same habitat type in a reasonable timeframe (i.e. woodland would not degrade into exposed shrubland or grassland during / after construction phase).

From this case, the lesson learnt was that on top of species of conservation importance and existing trees that have to be preserved, protection priority would be given for the undersized trees (Diameter at breast height (DBH) < 95mm), tall shrubs, then woody climbers and lastly herbaceous plants. Among each plant forms, uncommon / species with restricted distribution but yet without any conservation status would be preserved with a higher priority. This requires highly experienced and qualified Ecologists / Plant Specialists with a sense of habitat quality and ecological value from site to site.

3.2 Drawbacks of Traditional Post-construction Soft Landscaping Works

Another challenge was that the drawbacks of traditional post-construction soft landscape plantation in terms of degraded micro-habitats, diminished bio- and genetic diversity from non-native nursery stocks, and challenges of maintenance works against invasive plants can be improved through a works design preserving the native vegetation.

Whole natural floral community or diversity is hard to replicate, as reflected by 52 species observed in just 300m^2 of the works site. Post-construction soft landscape planting on slope feature seldom adopted more than 15 native species due to site constraints. This means there is always a degradation of the original habitat quality (at least at micro-habitat level) after slope upgrading works even if the survival rate of soft landscaping is assumed as 100%. In this case, Landscape Contractor has put greater efforts in protecting and selective trimming existing vegetation but a minimal soft landscaping only at highly eroded areas and around soil nail heads.

Given relatively high costs for land and the labour force in the local industry, Landscape Contractors often import from a few nursery stocks of commonly used native species with better survival and at lower cost, resulting in a non-native sources and diminished genetic diversity in plants used for soft landscape planting. However, a temporary holding nursery can be set up when works area is available for various woody shrubs and saplings before they could be transplanted back to the site construction activities. This encourages the Landscape Contractor to locally stock native plants that are still uncommonly available on the market.

3.3 Green Slopes without Invasive Plant Species

The last challenge is that construction sites are always vulnerable to invasive species, which further suppresses the recovery or even outcompetes soft landscape plantation on man-made slopes. As a result, maintenance work becomes a burden of challenge, a waste of planting efforts, poor recolonization of native floral community, and always ends up with a 'green' slope surface dominated by weeds and invasive species.

A self-sustained native vegetation encourages recolonization of other natural plants if surrounding areas are in high ecological value; while it depresses the invasion of invasive species and weeds (e.g. *Bidens alba* (白花鬼針草), *Lantana camara* (馬纓丹), *Leucaena leucocephala* (銀合歡), *Mikania micrantha* (薇甘菊) and *Melinis repens* (紅毛草) for the case in Hong Kong) when adjacent areas has been disturbed or low habitat quality.

Selective trimming of smaller woody plants preserved an intact root system to facilitate regeneration. These plants, despite being small in size, may already be of a mature stage compared to newly planted shrubs and groundcover. New root systems of soft landscape planting could be hard to establish in a harsh environment on slope features. In contrast, an intact root system of original vegetation maintains a suitable microhabitat, organic matters (top soil) and microbial communities for resilience of the protected plant species of conservation importance; and a better resistance to invasive species.

4 CONCLUSION

To summarize, a new ecological approach to minimize and mitigate impacts of slope upgrading works in woodland / natural habitat has been demonstrated by this task. Although working in a segmented working platform with a minimum working space among dense vegetation and canopy would result in a higher cost and longer work programme; such well-preserved habitat quality would enhance a minimal and more adaptive soft landscape planting. The higher habitat preservation cost at the beginning helps to lower maintenance effort and cost in long-term without degrading the habitat quality / ecological value of the upgraded slope. A reallocation of budget and construction programme should be considered when such practice will be adopted for natural terrain, or man-made slopes located within / in close vicinity of Conservation Areas / Sites of Special Scientific Interest (SSSI) / Country Parks.

ACKNOWLEDGEMENTS

This paper is published with the permission of the Director of Highways Department, the Government of the Hong Kong Special Administrative Region.

REFERENCES

Corlett, R.T., Xing, F.W., Ng, S.C., Chau, L.K.C. & Wong, L.M.Y.. 2000. *Hong Kong vascular plants: Distribution and status. Memoirs of the Hong Kong Natural History Society*, 23: 1-157.

DEVB. 2015. *Development Bureau Technical Circular (Works) No. 7/2015. Tree Preservation.* The Government of the Hong Kong Special Administrative Region. This Circular was superseded by DEVB TC(W) No. 4/2020 after 26 February 2020.

GEO. 2009. *GEO Publication No. 1/2009. Prescriptive Measures for Man-made Slopes and Retaining Walls.* The Government of the Hong Kong Special Administrative Region.

Hong Kong Herbarium. 2024. *HK Plant Databasae*. https://www.herbarium.gov.hk/en/hk-plant-database/index.html. Accessed on 20th March 2024.

Adopting Underslab Drainage System to Tackle Groundwater Uplift Force: A Holistic Overview and Experience Consolidation

Andrew T F Wong, Alvin K M Lam & Tony K S Mak
Ove Arup & Partners Hong Kong Limited, Hong Kong

ABSTRACT

Groundwater uplift is one of the key factors affecting the foundation design of building works, especially for deep basements with limited building self-weight. In Hong Kong, it is common to use tension piles to resist groundwater uplift for building projects or provide additional counterweight to overcome the uplift with adequate safety factor. However, tension pile can be costly, which renders the initiatives to devise a more cost-effective and sustainable alternative. This paper presents a comprehensive review of the novel strategies for uplift control, aiming for producing a more economic foundation solution through a synthesis of theoretical frameworks, case studies, and practical experiences. The review focuses on the application of underslab drainage system beneath the basement slab in Hong Kong. The design principles of the system, the construction control and considerations, and the routine maintenance are discussed. Through a meticulous consolidation of experiences, the paper showcases a few successful applications of underslab drainage system from design prediction, through site verification and finally to implementation stage. In one of the case examples, prolonged groundwater monitoring has been carried out to demonstrate the reliability and the effectiveness of the system.

1 INTRODUCTION

Owing to the limited land supply in urban area, the use of underground space for car parking or shopping arcade has become more common in Hong Kong over the last decade. For sites with high groundwater table and deep basement, when the groundwater uplift pressure beneath the structure exceeds the pressure exerted by its own self-weight, the foundation system needs to account for net buoyancy. If the groundwater uplift is not properly considered, it can lead to various stability and serviceability issues such as structural instability, excessive movement, and water ingress at basement. In Hong Kong, the traditional approach to mitigating high groundwater uplift force usually involves the use of deep foundations to acquire sufficient anchorage from deeper and more stable layers of soil or rock. Despite constructing piles to resist uplift forces are on most occasions technically feasible, deep foundations in some cases can be costly and require extensive site preparation and construction efforts. Moreover, constructing piles may not be always suitable for sites with complicated geological conditions or space constraints. Therefore, this paper aims to explore alternative strategies for uplift control, with a focus on achieving more economic and sustainable foundation solutions.

The use of underslab drainage system is one of the alternatives. Such system is designed to effectively lower the groundwater table inside the basement, reducing the uplift pressure and thereby the need for extensive tension pile. In Hong Kong, the application of underslab drainage system can be traced back to the 1970s. The New World Centre in Tsim Sha Tsui East, constructed in 1974, was the first project adopting such system to reduce uplift pressure according to Chan et al. (2007). Subsequently, the system was implemented in other commercial and residential developments such as Dragon Centre, Festival Walk, Imperial Cullinan, Century Link, Park Yoho, etc.

2 APPLICATION OF UNDERSLAB DRAINAGE SYSTEM

2.1 Principle of Underslab Drainage System

The principle of the underslab drainage system is to release the groundwater pressure by introducing a drainage layer comprising crushed rock-fill or no-fines concrete with high permeability beneath the basement slab. The groundwater is collected through a network of perforated piping systems inside the drainage layer, junction pits and sump pits and discharged through submersible pumps to the existing ground and finally diverted to the public drainage system. The uplift pressure exerting on the basement slab can hence be eliminated. To ensure the effectiveness of the system, a permanent groundwater cut-off wall along the perimeter of the basement is required.

The success of the system relies on the prompt evacuation of the groundwater underneath the basement slab from the in-situ ground via the drainage layer. Therefore in the case of future basement soffit being underlain by clayey deposits such as marine clay or alluvial clay, this layer of clayey deposit may act as a low-permeability barrier to obstruct the groundwater flow. In such cases, groundwater may not be effectively diverted away from the soil mass beneath the basement. The uplift pressure may continue to act on the basement structure, undermining the underslab drainage system's purpose.

2.2 Major Components

One of the key elements in an underslab drainage system is the drainage layer intalled beneath the basement slab. It facilitates groundwater flow through its highly permeable material in horizontal, inclined, or vertical manner to suit the basement design. The drainage material inside the drainage layer consists of clean and durable aggregates or no-fines concrete. In order to ensure that no excessive groundwater pressure is developed at areas with no drainage layer such as beneath the footings, pile caps or sucken pits, the drainage layer shall be designed to cover the majority of the basement footprint. Though there is no available guideline to determine the thickness of the underslab drainage layer, it shall be thick enough to house the perforated pipe with a fall gradient to facilitate the groundwater flow to the junction or sump pits. From past projects, the thickness of the drainage layer typically ranges between 500mm and 800mm. The typical detail of drainage layer is shown in Figure 1. Comparing to Geoguide 1, a nominal granular drainage blanket with thickness of 300mm is considered acceptable behind the earth retaining wall. However for an underslab drainage system, sufficient provision shall be made to cover the risk of blockage in the long-term causing economic loss, the difficulty of repairing and extreme weather resulting in rise of groundwater table in assessing the thickness of the drainage layer.

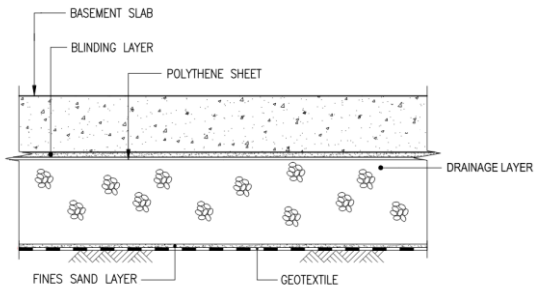


Figure 1: Typical detail of drainage layer installed underneath the basement slab

To prevent the infiltration of soil fines into the drainage layer, a geotextile filter fabric is essential and shall be positioned at the interface with the in-situ soil. This filter layer acts as a barrier, preventing the ingress of fine-grained soil particles into the drainage system. The design specifications for the filter, including criteria for retention and permeability in relation to the opening size of the geotextile, can be referenced to Table 11 of GEO Publication No. 1/93.

In addition, a polythene sheet shall be laid atop the drainage layer to act as a protective barrier against the infiltration of concrete during the concreting process of the basement slab. This precaution ensures the integrity and functionality of the drainage system by preventing concrete from encroaching into the drainage layer. However, to safeguard the polythene sheet from damage during the rebar fixing phase of the basement slab, a blinding layer shall be provided above the polythene sheet. This blinding layer serves as an additional protective measure, shielding the polythene sheet from potential punctures or tears caused by the rebars. The typical joint detail for geotextile filter and polythene sheet shall refer to Figure 2.

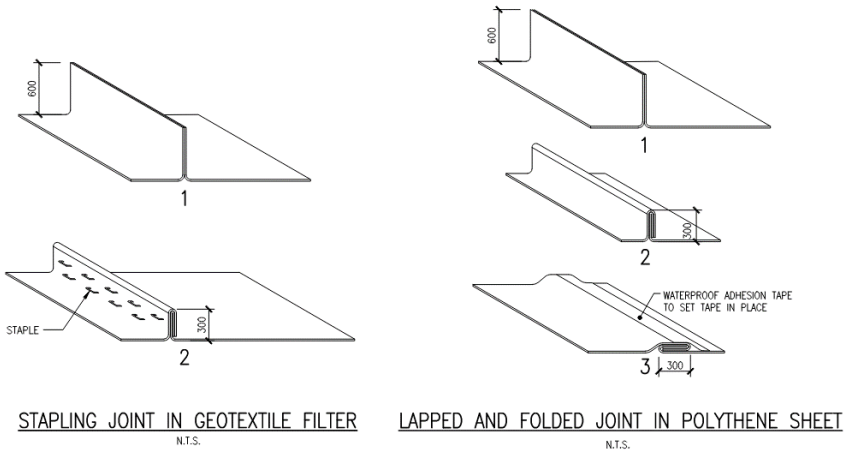


Figure 2: Typical joint detail for geotextile filter and polythene sheet

The embedded perforated drainage pipes inside the drainage layer serves to efficiently transport the collected groundwater to the discharge point via the pipe network. In general, the perforated pipes are crafted from unplasticized polyvinyl chloride (uPVC), corrugated high-density polyethylene (HDPE) or similar material. The material shall be durable and capable to sustain the design life of the system. The perforated pipes are recommended to be laid as low as practicable within the drainage layer while maintaining the fall gradient to maintain a low groundwater table within the drainage layer. The spacing between these perforated pipes shall be carefully planned to ensure there would be no excessive uplift pressure built up at areas with no drainage layer. In most past projects, the perforated pipes adhere to a minimum fall gradient of 1:200 to avoid ponding inside the pipe. Despite the relatively gentle pipe gradient, a 150mm diameter pipe is usually sufficient to meet the capacity requirements. To facilitate long-term maintenance of the perforated pipes, rodding eyes are typically installed to the upstream end of the pipe (see Figure 3 and Plate 1). Rodding eyes allow maintenance personnel to easily insert cleaning tools or apply pressurized water to remove blockages and flush away debris, ensuring the drainage pipes remain clear and functional.

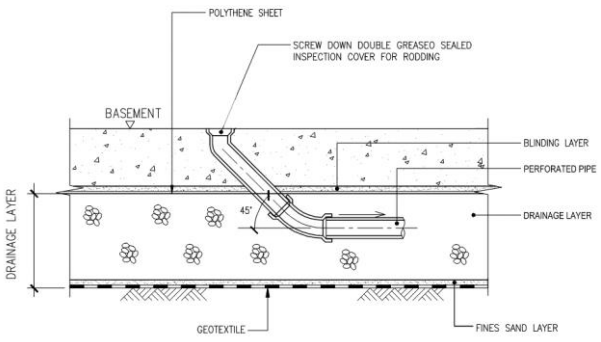


Figure 3: Typical detail of rodding eye connecting to perforated pipe



Plate 1: Rodding eye connected to horizontal perforated pipe inside drainage layer

When perforated pipes are redirected to accommodate other structural components like footings, pile caps, and tie-beams, junction pits are typically provided at the turns to facilitate future maintenance. These junction pits serve as the access points for inspection and collection for debris or sediment flushed from the perforated pipes. Eventually the pipe network terminates at the sump pits and the groundwater collected will be discharged to the public drainage system located at the ground level via the submersible pumps in the sump pits. Apart from housing the submersible pumps, the sump pits can also serve a similar role as junction pits by collecting debris or sediment flushed from the drainage system. The schematic drainage routing layout and section are shown in Figures 4a & 4b. Flowmeters are usually installed to monitor the groundwater discharge rate throughout the design life cycle of the underslab drainage system. To minimize the risk of blockage of the perforated pipes at critical junction pits and sump pits, double pipes may be considered. For example, if a sump pit connects to only one inlet perforated pipe, the sole blockage of this single inlet could already lead to a complete failure of groundwater discharge from the system. In such cases, adopting double inlet perforate pipes may be considered a better arrangement.

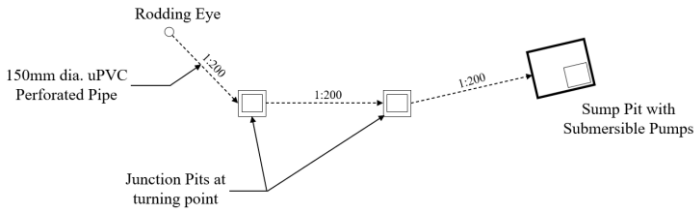


Figure 4a: Schematic underslab drainage routing layout

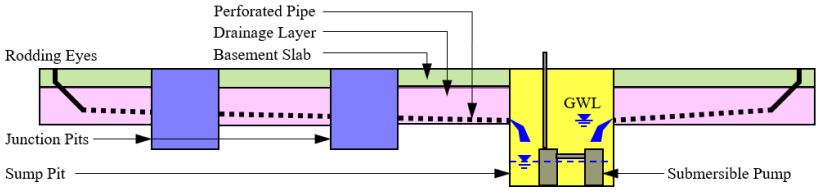


Figure 4b: Schematic underslab drainage routing section

Apart from the aforementioned components, an underslab drainage system typically includes provisions for pressure relief wells, which not only allows discharge of water to relief water pressure beneath the basement slab due to blockage or malfunction of the drainage system but also allows a deep well submersible pump to be installed to enable emergency repairment or replacement of the underslab drainage system when required. These wells are usually distributed evenly throughout the basement area. Normally, the pressure relief wells are sealed at the top to prevent unpleasant odors from entering the basement. An alternative arrangement is to raise the

outlet of the well above the basement slab (say, 1m) to allow direct discharge of groundwater in case of emergency or sudden raise in pressure head. The raised pipes can be constructed at column location to minimize the operational impact to the basement. Figure 5 and Plate 2 show an example of the raised pressure relief wells.

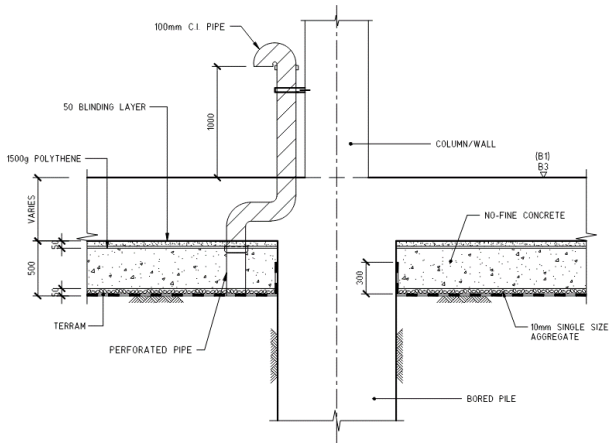


Figure 5: Detail of pressure relief well rising above the top of basement slab



Plate 2: Pressure relief well rising above the basement slab

2.3 Provision of Permanent Groundwater Cut-off Wall

A permanent groundwater cut-off wall is required for underslab drainage system. The depth of the cut-off wall is not only designed to meet the requirement of hydraulic stability but also control the drawdown outside the site and the amount of groundwater influx. In Hong Kong, the drawdown for temporary excavation and lateral support works is normally controlled within 1m aiming to control the induced ground settlement due to the increase in effective stress. The drawdown is usually monitored by open standpipe. In fact, the seepage flow also triggers drop in piezometric head. In some situations where clayey deposits such as marine clay or alluvial clay exist, the piezometric head drop outside the site may trigger excessive consolidation settlement in the long term, which may render the use of underslab drainage system becoming infeasible. Nevertheless, for site not sensitive to ground settlement or more settlement buffer is allowed, the control of drawdown is of less concern.

The groundwater influx is also a key consideration of the underslab drainage system design. In case all submersible pumps were failed due to electricity breakdown, sufficient time shall be allowed to restore the power to minimize the economical loss. Based on the experience from past projects, when the groundwater drawdown is controlled within 1m, the groundwater raise is generally not exceeding 300mm per day. In Hong

Kong, the reliability rate of electricity supply is greater than 99.999% and the duration of any unplanned power interruption is generally less than an hour except a serious power outage incident happened in Northwest New Territories in 2022, where the full recovery was achieved in 13 hours after the incident. In addition, according to the record of the Hong Kong Observatory, the longest hoisting of Hurricane Signal No. 10 lasted for 11 hours in 1999. With the interruption from these extreme incidents, it is therefore considered reasonable to accept the groundwater raise of not more than 200 to 300mm per day.

Since the underslab drainage system relies heavily on the groundwater cut-off performance, an interlocking-natured wall providing reliable and persistent watertightness throughout the operation cycle of the building is essential. The choices often lie among diaphragm wall with water stops between panels or cutter joint, interlocking sheet pile wall or interlocking pipe pile wall. Meanwhile, if contiguous pipe pile wall with grout curtain is adopted for the purpose of permanent cut-off, the long-term performance of the grout curtain shall be considered.

2.4 Design for Contingency

Incorporating reasonable safety factor into the design of underslab drainage systems can ensure their reliability and resilience against unforeseen conditions. Drawing from experience gleaned from past projects, a safety factor of 3 to 5 was usually applied to the predicted water influx from the seepage analysis to cover the uncertainty due the variation of geological profile and ground permeability, any deficiency of the groundwater cut-off wall, the differential groundwater flow due to various drainage layer levels and other unexpected flow under normal groundwater condition. Extreme weathers or events shall also be considered in order to ensure that the underslab drainage system can cope with those situations with factor of safety greater than unity.

Additionally, the performance of pumping test either full-scale or partial prior to the excavation provides valuable data to review the ground permeability through back-analysis, the effectiveness of the groundwater cut-off wall as well as the predicted groundwater influx when the target dewatering level to the future drainage layer is reached under steady condition. This data available at the early stage of the project enables further refinement of the underslab drainage design, potentially allowing a more accurate prediction of groundwater flow and a lower safety factor to be adopted whereas appropriate.

2.5 Design for Minimum Provisional Uplift

Despite an underslab drainage system is designed with considerations encompassing uncertainties and contingencies and thereby aims to promote negligible uplift on the structures, it is always a good practice to reserve a minimum provisional uplift in the basement slab design to cater for unexpected blockage resulting in building up of groundwater pressure beneath the basement slab between the window of the routine maintenances, monitoring and inspections. According to past projects, the typical practice for such minimum provisional uplift is 15kPa. This can minimize risk of any structural damage in case of system failure and enhance the robustness and resilience of the system.

2.6 Pre-occupancy Performance Review

After the completion of the basement and its associated underslab drainage system, conducting a performance review to verify the actual performance of the system is imperative. In past projects, the performance review typically lasts for 3 to 6 months. At the beginning of the review period, the dewatering pumps originally deployed to maintain a dry excavation is switched off to allow recovery of groundwater table within the basement cofferdam. The performance review involves monitoring the groundwater pressure inside the basement by piezometers and the flow rates at discharge outlets by flow meters. Whereas possible, the monitoring covering one wet season is preferable to the assessment of the system's performance under seasonal high groundwater table and intense precipitation events. The groundwater table outside the site should also be monitored to obtain the groundwater level fluctuations over the review period.

Based on the performance review's monitoring data, it is advisable to carry out a final review of the design flow rate to back-calculate the ground permeability in order to project the groundwater influx under design

condition with due consideration of the seasonal fluctuation and other design contingency and extreme weather condition which may not be encountered during the period of the performance review. It is recommended to estimate the flow rate by seepage analysis with the back-calculated ground permeability based on two groundwater table conditions – the routine groundwater table condition, and the extreme groundwater table condition. The design flow rate should then be determined by adopting the greater value from 1) the flow rate estimated under routine condition multiplied by two, and 2) the flow rate estimated under extreme condition. Submersible pumps of sufficient discharge capacity to meet the design flow rates shall be provided to the corresponding sump pits. This will ensure that the underslab drainage system is capable to handle regular influx while also reserves a sufficient buffer to account for potential surges during extreme weather events.

2.7 Post-occupancy Long-term Monitoring and Maintenance

The implementation of an underslab drainage system necessitates long-term monitoring and routine maintenance protocols. Upon the completion and satisfaction of the pre-occupancy performance review, a maintenance manual will be prepared for the owners to facilitate their future long-term monitoring and maintenance.

Long-term monitoring is typically directed towards two key aspects: monitoring the pressure levels at piezometers inside the basement and measuring the flow rates at drainage outlets. By tracking the groundwater pressure and flow rates, the performance of the system can be evaluated. The typical routine monitoring works and the corresponding frequency are summarized in Table 1. This ongoing surveillance ensures no sign of blockage or malfunction of the underslab drainage system.

Table 1: Typical routine monitoring works

Typical Routine Monitoring Works	Typical Frequency
Measure flow rate from submersible pumps	Once per week
Measure piezometric head in piezometers	Once per week

Additionally, triggering levels such as alert and action levels are usually established to notify the maintenance personnel when groundwater pressure or flow rates reach the predetermined limits. Generally speaking, reaching alert levels provide a signal of potential issues requiring closer monitoring, while reaching action levels trigger immediate corrective measures to prevent any performance degradation. For groundwater monitoring, since the groundwater level is anticipated to be well within the drainage layer, the alert level can generally be set at the soffit level of the basement slab to indicate a full flow condition within the drainage layer. Meanwhile, the action level can be set at 50 – 100mm below the top level of basement slab to prompt suitable actions to prevent groundwater overflow into the basement area. For flow rate monitoring, the action level can be set at the design flow rate or the limiting capacity of the provided submersible pumps, while the alert level could be set at 70 – 80% of the total submersible pump capacity. This early warning can prompt the preparation of additional pumps before the limiting capacity is reached.

It is reminded that the primary purpose of setting an alert level is to provide an early warning to the maintenance personnel, enabling them to prepare for potential worsening conditions before serious incidents occur. The specific alert level adopted should take into account of the estimated response time needed for basement users to take necessary actions before being significantly impacted by groundwater influx. This includes considering how quickly the situation might escalate to the action level and ensuring that there is adequate time for preparation. Depending on the estimated rate of water rise, it might be necessary to set a more stringent alert level to allow earlier warning signals. It should be ensured that there is enough time to address the issue effectively, thereby preventing severe consequences.

Table 2 and Table 3 present the typical activities to be undertaken when these two triggering levels are reached. By adhering to these practices, the maintenance personnel can proactively manage and maintain the effectiveness of the underslab drainage system over time. It should be aware that if the flow rates or piezometric head exceed the action level for a substantial period, a holistic review on the underslab drainage system shall be carried out.

Table 2: Typical follow up activities for alert level

Triggering Level	Follow up Activities
Alert Level	Flow rates by flow meters: • Inform the management office and the engineer. • Increase monitoring frequency. • Ensure extra submersible pumps suitable for placing in the sump pits are available and in good order. Piezometric head in piezometers: • Inform the management office and the engineer. • Increase monitoring frequency. • Ensure deep well submersible pumps suitable for inserting into the pressure relief wells are available and in good order. • Carry out rodding of perforated pipes around the area where the alert level is recorded. • Inspect the conditions of submersible pumps, sump pits and junction pits. • Carry out response tests on nearby piezometers. If the permeability of the material around the piezometer has significantly reduced, the engineer shall be informed and the piezometer may need to be replaced.

Table 3: Typical follow up activities for action level

Triggering Level	Follow up Activities
Action Level	Flow rates by flow meters: • Inform the management office and the engineer. • Place sufficient extra submersible pumps in the sump pits to enhance the groundwater discharge capacity. The groundwater collected by the extra submersible pumps should be pumped to nearby sump pit for discharge. Piezometric head in piezometers: • Inform the management office and the engineer. • Place sufficient number of deep well submersible pumps into the pressure relief wells around the area where the action level is recorded. The groundwater collected by the deep well submersible pumps should be pumped to nearby sump pit for discharge.

Routine maintenance procedures commonly involve directing pressurized water through the rodding eyes or various pits to flush the accumulated debris or sediment within the pipes, and ensuring the proper functioning of pressure relief wells. Regular response test on piezometers shall be performed to ensure they are properly functioning and are truly reflecting the groundwater pressure beneath the basement slab. These monitoring and maintenance practices are essential for ensuring the continued effectiveness and reliability of the drainage system in managing groundwater uplift forces over time. The typical routine maintenance works and the corresponding frequency are summarized in Table 4.

Table 4: Typical Routine Maintenance Works

Typical Routine Maintenance Works	Typical Frequency
Clean sump pits and junction pits	Once per 6 months
Clean perforated pipes from rodding eyes	Once per 6 months
Clean flowmeter strainers	Once per month
Response tests for piezometers	Once per 6 months
Check conditions of submersible pumps	Once per 6 months
Check conditions of flowmeters	Once per 3 months

It is considered that long-term monitoring outside the basement cofferdam is unnecessary, owing to the argument that the most extreme hydraulic difference conditions have already been experienced by the ground at the former basement excavation phase. During the bulk excavation, the groundwater table inside the cofferdam has already been lowered to the final excavation level, which is deeper than the permanent underslab

drainage level. In addition, with the shut-down of dewatering pumps during the pre-occupancy performance review period, monitoring on the external ground response due to the underslab drainage system has already carried out over a substantial period. Therefore, it is confident that the external ground conditions have already been stabilized and any significant future settlement is unlikely, eliminating the need for long-term monitoring outside the basement cofferdam unless continuous settlement potentially due to consolidation of the ground is still observed.

2.8 Reliance on Submersible Pumps and Recommended Arrangements

Failure of submersible pump is possible, which could result from mechanical malfunctions, short-term power outages, or other operational issues. Pump failures can lead to the accumulation of groundwater within the sump pits, causing flooding at the basement and compromising the effectiveness of the underslab drainage system. Additionally, reliance on submersible pump introduces maintenance requirements and associated costs, including regular inspections, repairs, and replacements. With the consideration of the potential interruption from the extreme incidents as discussed earlier on, the dependency on external power sources for pump operation leaves the system vulnerable to disruptions in electricity supply. To mitigate the risk of short-term power outage, it is crucial to ensure that the building has incorporated a backup power system, which is capable of providing sufficient electricity to the submersible pumps for at least 24 hours.

Regarding the submersible pump arrangement, opting for a dual-pump strategy to split the required discharge capacity between two separate smaller pumps instead of one single pump can effectively mitigate the risk of malfunctions. This practice ensures that if one submersible pump malfunctions or fails, there will still be another submersible pump within the same sump pit to continue operating, thereby maintaining the system's basic functionality. Additionally, this arrangement allows for maintenance or replacement of one pump without entirely suspending the drainage system's operation.



Plate 3: Operation of submersible pumps inside a sump pit

2.9 Risk of Flooding

In view of the frequent extreme precipitation events occurring over the recent years, the risk of flooding caused by unexpected stormwater ingress becomes higher. In such instances, the capacity of the pumps may be overwhelmed as they need to handle both the subsoil groundwater collected in the sump pits and the sudden inflow of stormwater into the building basement. This increased workload can strain the pumps and diminish their effectiveness in managing the subsoil groundwater discharge. In extreme cases where the stormwater ingress is particularly severe, the pumps may even reach their operational limits for solely discharging the stormwater, leaving no spare capacity to discharge the subsoil groundwater from the underslab drainage system. In addition, the public drainage system may also be saturated under extreme weather. This highlights the importance of incorporating robust and reliable flood prevention measures such as raised basement entrances, automated or self-closing flood gates or demountable flood barriers for projects using subsoil drainage systems.

3 CASE STUDY OF SUCCESSFUL APPLICATION

One notable past project demonstrating the successful implementation of underslab drainage systems for uplift control is a commercial development located in Mong Kok. The development features a 5-level deep basement involving an excavation depth of 25m below ground. To support the deep excavation, the development adopted a 1.2m thickness diaphragm wall and a 1.2m diameter secant bored pile wall extending down to the bedrock. To cope with the high regional groundwater table, additional toe grouting was employed in rock to enhance the effectiveness of the groundwater cut-off. The development utilized a comprehensive underslab drainage system to effectively manage groundwater uplift forces since its completion in 2004.

The underslab drainage system consisted of a layer of drainage layer with perforated pipes beneath the basement slab. The drainage layer was filled with 10mm single sized aggregate of 800mm thick. The perforated pipes were 150mm diameter laid at a minimum gradient of 1:200. These pipe segments were connected via junction pits, which were in turn connected to four sump pits equipped with submersible pumps. Additionally, the system included a total of 16 numbers of pressure relief wells, 35 numbers of rodding eyes, and 6 numbers of piezometers, all constructed to facilitate routine maintenance and monitoring. The design flow rate of the system was 40m^3/hour. The alert and action levels for the flow rate in long-term monitoring were set at 30 and 38m^3/hour respectively.

The project undertook a full-scale pumping test after completing the perimeter diaphragm wall and bored pile wall prior to excavation. After the completion of the underslab drainage system and basement structure, a 3-month performance review on the system was carried out. Subsequently along with the occupation of the development, long-term monitoring was carried out at weekly intervals.

In February 2002, a full-scale pumping test was conducted, involving 27 numbers of dewatering wells installed to lower the groundwater table within the cofferdam. The steady state was reached after 8 days of dewatering. Given the distributed arrangement and locations of the dewatering wells across the basement area and the enclosed perimeter wall cut-off extending to bedrock, it was believed that the groundwater table within the cofferdam was successfully drawn down to a level slightly deeper than the final excavation level. According to the pumping test records, the total discharge over the 72-hour steady state period was approximately 1,900m^3, with a generally consistent discharge rate averaging around 26.8m^3/hour.

When the underslab drainage system was completed, a performance review was conducted between December 2003 and March 2004. The average discharge rate throughout the 3-month monitoring period was around 20m^3/hour. A higher pumping rate is observed during the pumping test may be attributed to the deeper level of submersible pumps inside the dewatering wells during the test while the groundwater level during the performance review is close to the soffit of the basement slab. Nevertheless, the pumping test result provides approximate and conservative discharge rates for comparison with the design prediction.

Based on the available long-term monitoring records between 2009 and 2023, the piezometers revealed that the groundwater table was well maintained below the design level. All six piezometers showed that the groundwater table remained within or below the drainage layer without reaching the soffit of the basement slab, demonstrating the effective performance of the underslab drainage system in collecting and diverting groundwater. The weekly monitored piezometric head at various piezometers is illustrated in Figure 6. For the flow rate, the monitoring in the four sump pits was carried out in daily interval. The annual average flow rate summing up all the sump pits ranged between 10.4 to 20.0m^3/hour as illustrated in Figure 7.

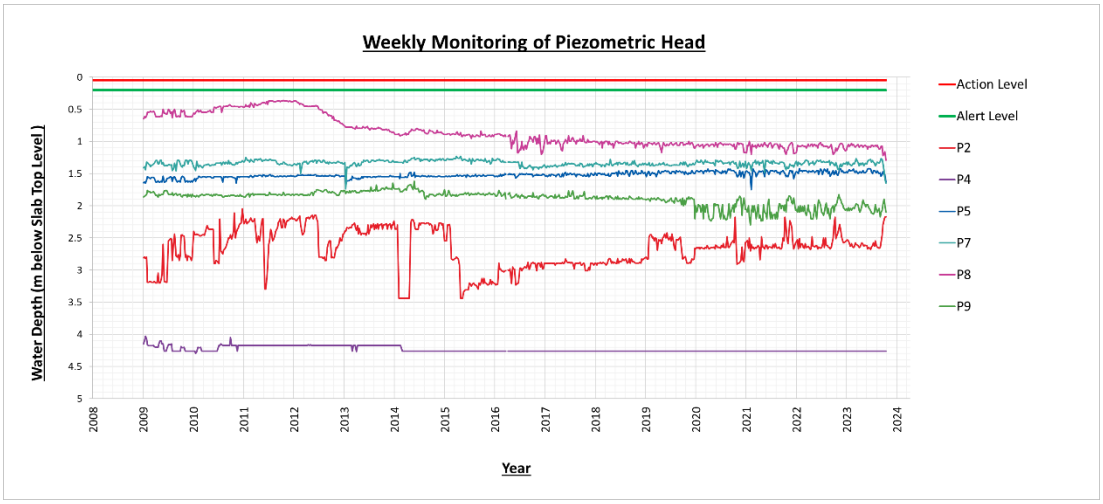


Figure 6: Weekly monitoring of piezometric head between 2009 and 2023

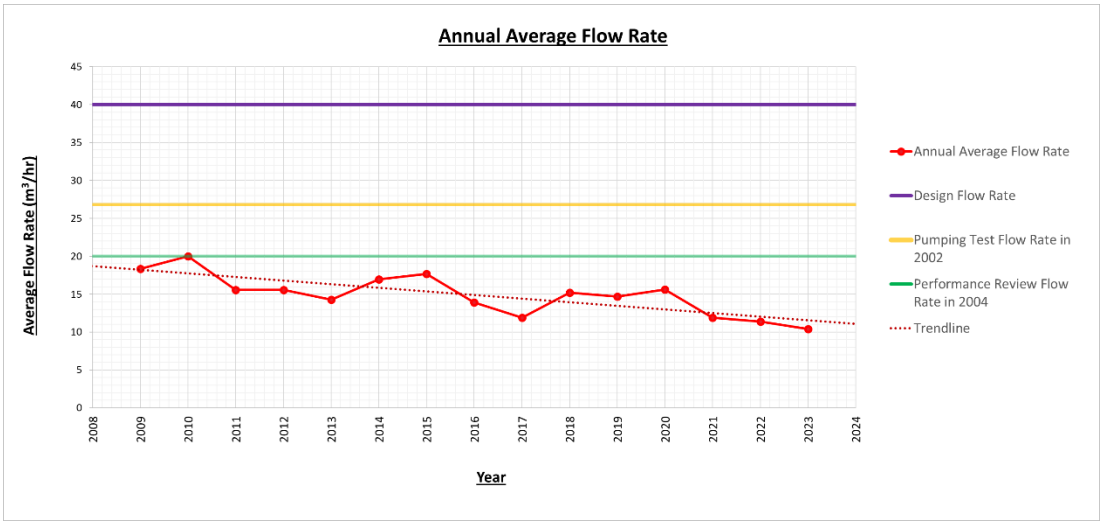


Figure 7: Annual monitoring record of flow rate between 2009 and 2023

The trend in piezometric heads was relatively steady and all levels were well below the basement slab. The range of piezometric head difference in each piezometer was within 1 to 1.5m. There was no substantial variation in the piezometric heads over the past years, reflecting a well-maintained and unimpeded underslab drainage network. Meanwhile, a downtrend in the average flow rate is observed. At the earlier years, the average flow rate is close to that monitored during the performance review period at around 18 – 20m^3/hour. Afterwards, a decreasing flow rate can be observed between 2011 and 2013, followed by a slight recovery in 2014 and 2015. Although similar up and down can be observed in the subsequent years, the average flow rate is generally diminishing. Considering that no significant underground development has been noticed in the vicinity of the site after this development, the surrounding subsoil condition and underground regime is expected to be similar. One possible reason for the downtrend of groundwater flow may be owing to the continuous seepage flow beneath the permanent groundwater cut-off wall which carried the fine particles to gradually fill up the voids and thereby enhanced the groundwater cut-off performance.

The satisfactory performance indicates a judicious application of underslab drainage system in the project. Ongoing monitoring and assessments of uplift pressure and flow rates would be continued to ensure the effectiveness of the system.

4 CONCLUSION

The application of an underslab drainage system is particularly beneficial in situations where the magnitude of compression forces from the structure is relatively low compared to the uplift forces exerted on the foundation. In such cases, the conventional approach of relying solely on tension piles to counteract uplift can be excessively costly. By strategically incorporating an underslab drainage system into the foundation design, engineers can effectively mitigate uplift pressures and reduce the reliance on tension piles. This not only helps to optimize the structural performance of the foundation but also contributes to significant cost savings by minimizing the number of piles required for uplift control. Therefore, the application of underslab drainage systems offers a practical and cost-effective solution for addressing uplift challenges in geotechnical engineering projects. With the increasing adoption of underslab drainage systems and the accumulation of successful experiences in the industry, the reliability of the systems is expected to grow. As more projects incorporate these innovative solutions to tackle uplift and engineers gain familiarity with their design and implementation, confidence in the effectiveness will strengthen.

REFERENCES

BD 2017. *Code of Practice for Foundations 2017*. Buildings Department, Hong Kong.

GEO 2020. *Geoguide 1 – Guide to Retaining Wall Design (2020 Version)*. Geotechnical Engineering Office, Civil Engineering and Development Department, The Government of the Hong Kong Special Administrative Region, Hong Kong.

GEO 1993. *GEO Publication No. 1/93 – Review of Granular and Geotextile Filters*. Geotechnical Engineering Office, Civil Engineering Department, Hong Kong.

Andrew K. C. Chan, James Y. H. Lui & L. M. Mak. 2007, *Development of Deep Excavation Practice in Hong Kong*, Proceedings of the HKIE Geotechnical Division Annual Seminar 2007, HKIE, 109-118.

James W.C. Sze & Henry C.F. Lau. 2010, *A Special Cofferdam in a Reclaimed Site at West Kowloon*, Proceedings of the HKIE Geotechnical Division Annual Seminar 2010, HKIE, 87-92.

Ground Movements Caused by Diaphragm Wall Installation

L.W. Wong
SMEC Asia Limited, Hong Kong

ABSTRACT

Two-dimensional numerical analysis has been conducted on a case history on ground movements caused by installation of diaphragm walls in soft ground. The trenching was supported with bentonite slurry. Inward ground movements occurs due to the horizontal earth pressures imbalance. The approach of replacing the unit weights of the soil in the trench with that of the bentonite slurry has been adopted. While the slurry supporting the trench has virtually no stiffness, the trench was mainly resisted by the adjacent ground between the primary panels, the concrete wall and gravel infill. This study provides an approximation on the 2-Dimensional analysis on wall trenching. The analysis shows that the surcharge load and the groundwater pressures would affect the ground movements induced by diaphragm wall installation.

Keywords: Slurry trenching, Hardening-Soil Model, Small Strain, Ground Movements

INTRODUCTION

Ground movements estimation has been the prime concern of deep excavations. In addition to the main excavation, diaphragm wall installation would also generate some ground movements. Cowland & Thorley (1985), Morton et al. (1980) reported that ground movements induced by diaphragm wall installation could account for 30 % to 50 % of the total settlements induced by the entire excavation activities. The contribution of the ground movements induced by wall installation should, therefore, not be overlooked.

There are studies on the ground movements induced by diaphragm wall installation. Ng et al. (1995) conducted 2-Dimensional (2-D) numerical analysis on 3 wall panels. The analysis results were however not compared with the field observations. Ou and Yang (2011) reported the observed ground movements for a 5-panel test conducted in a Taipei MRT Contract. Based on the observed settlements for the wall construction for the entire station excavation, settlements envelopes were established to evaluate the ground settlements induced by diaphragm wall construction.

In this paper the ground movements induced by diaphragm wall installation for City Hall Station of the Nankang Line of the Taipei Rapid Transit Systems are collected for the study. The Hardening-Soil with Small Strain stiffness (HSS) model have been adopted for the numerical analysis. The stiffness parameters of the soft clay have been established previously by a well-documented excavation case history (Wong, 2023). An innovative approach of replacing the unit weights of the soil in the trench with that of the bentonite slurry has been adopted. Based on the field observations on the case histories of diaphragm wall installation, the virtual stiffnesses of the slurry supporting the trench have been assessed in this study.

2 DIAPHRAGM WALL INSTALLATION

Diaphragm walls are line structures, therefore 2-D analyses will be appropriate to evaluate the effects of diaphragm wall installation to ground movements. However, as depicted in Figure 1, each diaphragm wall is installed panel by panel. Primary panels will be dug first and the cavities made would rely on the pressures of slurry for stability. The middle section of these primary panels will be filled up by reinforced concrete with the

remaining two end sections infilled with gravels to provide spaces to join with the secondary panels to form a continuous wall. Therefore, the trench of a diaphragm wall, as the installation proceeds, is supported by the slurry pressures, the reinforced concrete sections, the sections with gravels and the soils yet to be dug. As the sequence of digging of primary panels and secondary panels is to be decided by site managers with considerations given to many constraints, the simulation of the effects of trenching is an extremely difficult issue. To simplify the problem to the extent that it becomes manageable, it is proposed to replace the materials in the trench with slurry with a virtual stiffness to be established by back-analyses.

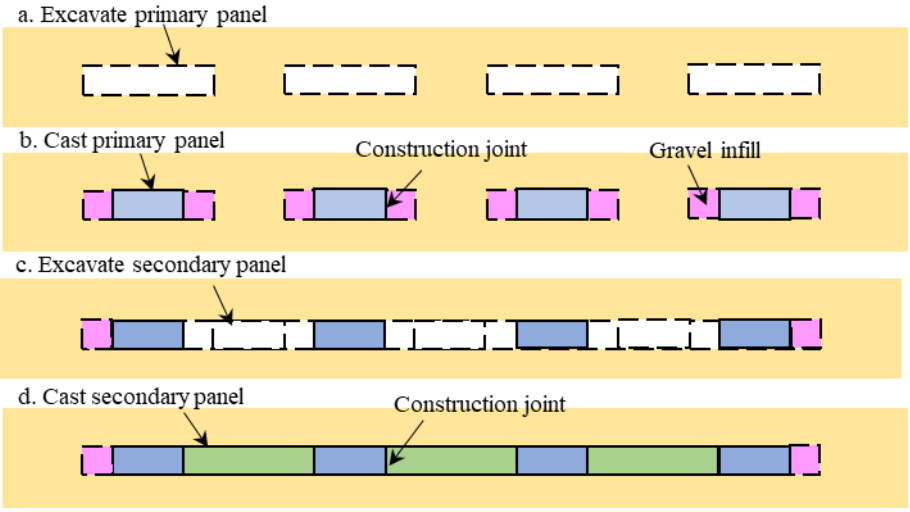


Figure 1: Plan view of the typical sequence for installation of diaphragm wall panels

3 CASE STUDIED

3.1 City Hall Station

City Hall Station of the Nankang Line is located in the K1 Geological Zone at the eastern portion of the Taipei Basin. The excavation case history was presented by Chen et al. (1997). As depicted in Figure 2, the station was 278 m in length and 24 m in width. Inclinometers in ground, SIS2 and SIS3, were deployed on the north and the south sides of the station. The diaphragm wall was 1.2 m in thickness and 44.5 m in depth. The perimeter diaphragm walls for the station and for the ancillary entrances were installed in a 13-month period, starting from November 1992 and with the completion in December 1993.

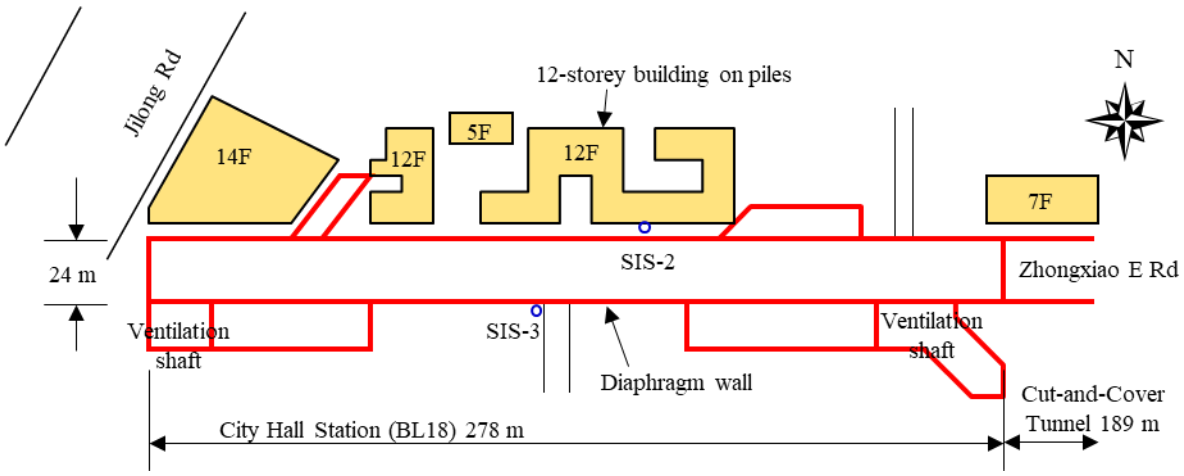


Figure 2: Instrumentation layout of City Hall Station

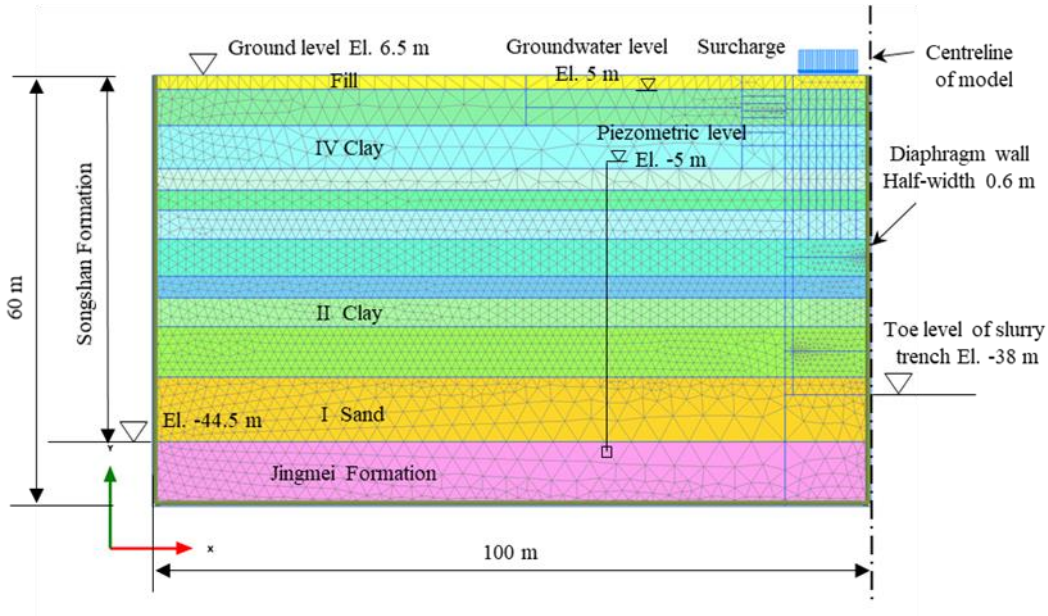


Figure 3: The soil profile and the finite element mesh for the analytical model for City Hall Station

As depicted in the soil profile shown in Figure 3, the total thickness for the clayey Sublayers IV and II of the Songshan Formation is 40 m. The properties of the sublayers in the Songshan Formation have been well discussed in literature (Moh and Ou 1979; MAA 1987; Moh et al. 1989). Underlying the Songshan Formation is a water-rich gravelly (GM) Jingmei Formation, which is a competent formation with very high stiffness.

3.2 Observed ground movements due to wall installation

Monitoring on the inclinometers SIS2 and SIS3 commenced prior to the diaphragm wall installation in November 1992. Figure 4 presents the horizontal ground movements observed in the inclinometers SIS2 and SIS3, which were installed at 2 m behind the diaphragm walls on the north and the south sides of the station respectively. The observation shows that the horizontal ground movements, the δ_h values, gradually developed during the wall installation period. Installation of the first wall panel induced the maximum δ_h values of 17.1 mm and 5.8 mm at inclinometers SIS2 and SIS3 respectively. In the completion stage of wall installation at the end of 1993, installation the full length of diaphragm wall induced the maximum δ_h values of 23.9 mm and 35.6 mm at SIS2 and at SIS3 respectively.

Inclinometer SIS3 is located on the south side of the station, which was an open space utilized as the working area for constructing the southern diaphragm wall of City Hall station. The occurrence of larger δ_h values at SIS3 could be due to surcharge loads imposed from the construction plants.

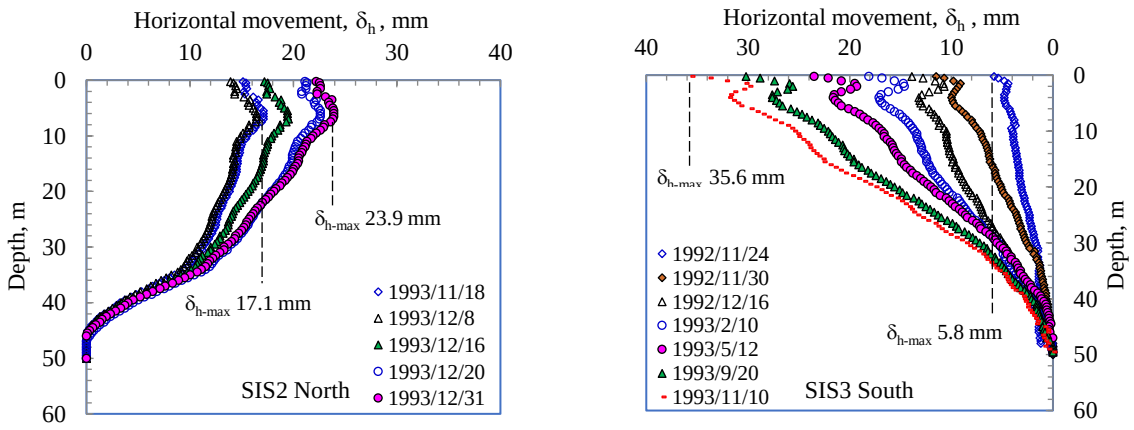


Figure 4: Observed horizontal ground movements on the north and the south sides of City Hall Station

Figure 4 shows the gradual development of the lateral ground movements. After installing the first wall panel in November 1992, the maximum δ_h value of 5.8 mm occurred at SIS3. Installation for the adjacent 24 panels, 12 numbers on the west and 12 on the east sides of the first panel, took 6 months. The maximum δ_h value at SIS3 increased to 23.5 mm in May 1993. Probably due to consolidation, the ground movements continued in the following 6 months with the maximum δ_h value reached 35.6 mm in November 1993.

3.3 Undrained shearing strengths for clay sublayers

An advanced study was conducted by Geotechnical Engineering Specialty Consultant engaged by the Department of Rapid Transit Systems of Taipei City Government in the very early stage of the metro construction. This Designated Task studied the characteristics of the soils in the Taipei Basin to provide the basic information required for the design and construction of metro facilities (Chin et al. 1994 and 2007; Chin & Liu 1997; Hu et al. 1996). This was a research project so it was carried out under stringent supervision. Soil samples of high quality were obtained and tested with great care. The test results are therefore more reliable than those normally obtained. Figure 5 presents the results of the CK_0UC tests conducted on the specimens recovered from borehole R-1 that Chin et al. (1994) reported. Borehole R-1 was located at approximately 50 m to the south of City Hall Station.

Kung et al. (2009) and Ou et al. (2000) also presented the results of undrained shear strength, s_u, for the K1 Geological Zone in the Taipei Basin. The s_u values were determined from consolidated triaxial undrained compression and extension tests conducted on specimens recovered from the clayey Sublayer IV. The specimens were saturated and K_0-consolidated to the in-situ effective stress states. The undrained shear strengths to the vertical effective stresses, the s_u/σ'_v ratio, for the compression tests is 0.29. For the extension tests, the s_u/σ'_v ratio is 0.21. The variation in undrained shear strengths for the compression tests that Ou et al. (2000) and Kung et al. (2009) also reported are presented in Figure 5 for comparison. Compared with the CK_0UC tests reported by Chin et al. (1994), the s_u values obtained by Ou et al. (2000) and by Kung et al. (2009) are somewhat lower. The lower s_u values would likely be attributable to sampling disturbance. Although the specimens were consolidated to the in-situ horizontal stress, such process could not fully compensate the effect due to sample disturbance.

In this study, as depicted in Figure 5, the Author has proposed that the undrained shear strengths of the sublayers IV and II clayey soils of the Songshan Formation in the K1 Geological Zone be expressed by the empirical equation:

$$s_u = 60 + 4.8\ (D - 15) \text{ in kPa} \qquad (1)$$

where D is the depth in metre and s_u is the undrained shear strength in kPa. Moh et al. (1989) reported that the sublayer IV clay of the Songshan Formation have the over-consolidation ratios (OCR) ranging from 4 to 1.25 at the depths between 3 m and 15 m. Oedometer tests conducted by Kung et al. (2009) confirmed that OCR profile. The Author has proposed the s_u value ranging from 50 kPa to 60 kPa at the depths within 15 m.

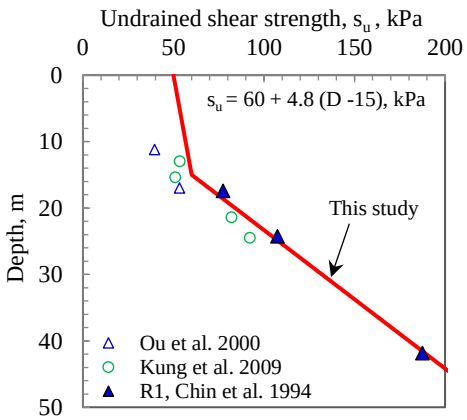


Figure 5: Undrained shear strengths of clays obtained by CK_0UC triaxial tests

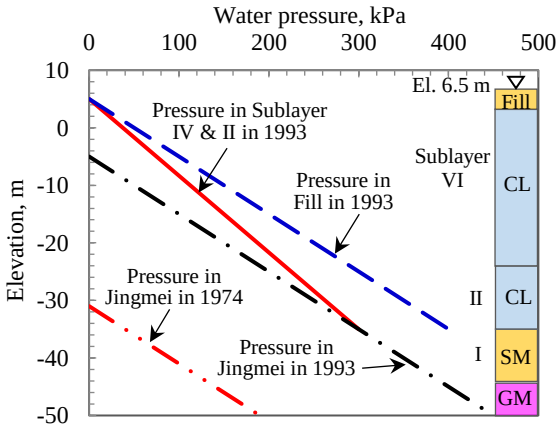


Figure 6: Groundwater pressures distribution in the soil strata at City Hall Station

3.4 Groundwater conditions

The piezometric level in the Jingmei Formation was lowered to a level near the bottom of the Songshan Formation in the 1970s due to excessive extraction of groundwater to supply water to the city, leading to significant reductions in water pressures in the Songshan Formation and substantial ground settlements as a result. The piezometric level in the Jingmei Formation did not recover till 1974 although pumping had been banned since 1968. The subsoils in the Songshan Formation in the Taipei Basin are thus substantially over-consolidated as the groundwater table rose. This is particularly true for the clayey Sublayer II because the underlying sandy Sublayer I is so permeable that the piezometric level in Sublayer I essentially dropped by the same magnitudes as those in the Jingmei Formation.

Based on monitoring records at the deep well at Sun Yet Sin Memorial Hall, located at 0.5 km east of City Hall Station, Hwang and Moh (2022) reported that the piezometric level in the Jingmei Formation in the eastern portion of the Taipei Basin was around El. -5 m in 1993. In the central portion of the Taipei Basin, the piezometric level in Jingmei Formation recovered to El. 0 m in 2017. The distributions of the water pressures outside the diaphragm wall at City Hall Station in 1993 are presented in Figure 6. For sublayer I and the Jingmei Formation, the piezometric level of El. -5 m in 1993 is adopted. The water pressures for sublayers II to IV are interpolated between the fill layer and sublayer I.

4 NUMERICAL SIMULATION

4.1 Finite element mesh

The section for the 2-D numerical analysis is depicted in Figure 3. The half-width of the excavation trench is 0.6 m. Because of symmetry in geometry, only half of the section is analyzed. The slurry supported trench is assumed to reach a depth of 44.5 m in the analysis. The lateral extent of the finite element model reaches a distance of 100 m from the central axis of the excavation trench. The ground model is 60 m in depth and the diaphragm wall is located along the axis of the trench.

The Jingmei Formation is a competent formation with very high stiffness and is frequently assumed to be the base of the numerical models. However, the base of the finite element model in this study is placed at a depth of 60 m to include a 9 m layer of the Jingmei Formation to ensure that the contribution of this formation to ground movements is accounted for.

4.2 Nonlinearity of soil behavior - Hardening-soil with small-strain stiffness model

The PLAXIS-2D finite element software developed by PLAXIS BV (2013) has become a very popular tool in geotechnical analysis and design. The Hardening-Soil with Small-strain stiffness (HSS) constitutive soil model is an extension of the Hardening-Soil model (Benz 2006, Schanz & Vermeer 1998; Schanz et al. 1999) introduced in the PLAXIS program and is adopted herein to simulate the non-linear stress-strain relationship of soils under loading and unloading conditions. In the HSS model, the parameters adopted to define the hyperbolic stress-strain relationship are as follows:

- E^{ref}_{50} is the reference secant stiffness from standard triaxial drained test,
- E^{ref}_{oed} is the reference tangent stiffness for oedometer primary loading,
- E^{ref}_{ur} is the reference unloading-reloading stiffness from standard triaxial drained test,
- m is the exponential factor for stress-level dependency of stiffness,
- R_f is the failure ratio, $R_f = q_f / q_a$,
- q_a is the asymptotic value of the shear strength and q_f is the failure strength,
- G^{ref}_0 is the reference shear modulus at the level of very small strains,
- $\gamma_{0.7}$ is the reference shearing strain to define the behavior of degradation of moduli when G^{ref}_0 is reduced to 0.7 G^{ref}_0.

In this study, the stiffness values of soils are related to the undrained shear strengths for clays and the N values for sands as expressed in the empirical Equations 2 to 6:

$E^{ref}_{50} = 150\ s_u$ (for clayey soils) (2)

$E^{ref}_{50} = 2\ N$ (in MPa for sandy soils) (3)

$E^{ref}_{oed} = E^{ref}_{50}$ (4)

$E^{ref}_{ur} = 5\ E^{ref}_{50}$ (5)

$G^{ref}_0 = E^{ref}_{ur}$ (6)

in which s_u is the undrained shear strengths of clayey soils (CL) and N is the blow-counts obtained in standard penetration tests for sandy soils (SM). The parameters adopted in this study are summarized in Table 1. The effective shear strength parameters, i.e., the c' and the ϕ' values, for the silty sand strata, are determined from laboratory tests conducted on specimens trimmed from thin-wall tube samples. For the clayey layers, $c' = s_u$ and $\phi' = 0^o$ are assumed in the analyses. The dilation angle, ψ', of 2^o, 0^o, and 3^o are adopted for the sandy, the clayey and the gravelly soils (GM) respectively. The R_f equals 0.9 is adopted. The unload-reload Poisson's ratio, υ_{ur}, of 0.2 is used as suggested by Benz (2006) and Schanz et al. (1999).

The set of the stiffness parameters in Equations 2 to 6 has been obtained from the small-strain triaxial tests and bender element tests. Wong (2023) verified that set of parameters by a well-documented excavation case history in the K1 Geological Zone of the Taipei Basin.

The HSS soil model is an effective stress model and adopting the $\phi' = 0^o$ for the clayey soils loses its compression hardening function and stress-dependent stiffness. However, parametric studies using both the effective and the total stress models show that the computed wall deflections and settlements are essentially the same. The total stress model for clay is thus adopted in this study.

Table 1: Soil parameters for the HSS model adopted in the PLAXIS analyses – City Hall Station

Mid depth m	Soil type	Unit weight γ' kN/m^3	N value	Undrained shear strength s_u, kPa	Effective cohesion c' kPa	Effective friction angle ϕ', deg	Dilation angle ψ' deg	Reference stiffness, MPa		Initial shear moduli G^{ref}_0, MPa
								Secant stiffness E^{ref}_{50}	Unload-reload stiffness E^{ref}_{ur}, MPa	
1	SM	18.5	8	-		30	0	16	80	80
4.5	CL	18.4	2	54	0			8.1	41	41
10	CL	18.4	3	57				8.6	43	43
14.5	CL	18.4	4	60				9	45	45
17.5	CL	18.4	5	72				10.7	54	54
20.5	CL	19	6	88				13.2	66	66
25.5	CL	19	7	110				16.5	82	82
29.5	CL	19	9	130				19.5	97	97
33	CL	19.5	10	146	0			22	110	110
38.55	CL	19.5	20	173				26	130	130
46.5	SM	19.5	26	-	0	32	2	52	260	260
55.5	GM	21.9	>100	-	0	35	3	200	1000	1000

4.3 Determination of small-strain stiffness

The parameters for the small-strain stiffness, i.e., the G^{ref}_0 and the $\gamma_{0.7}$, for the Taipei clay have been determined from the laboratory tests. Chin et al. (2007) presents the K_0-consolidated undrained direct simple shear test (CK_0UDSS) results that depicted in Figure 7. Santos & Correia (2001) recommended that the stress-strain curve for small-strains can be described as:

$$G / G_0 = 1 / (1 + 0.385\ \gamma / \gamma_{0.7}) \quad (7)$$

where G_0 is the maximum small-strain shear modulus. The modulus degradation curves with the threshold $\gamma_{0.7}$ values ranging from 0.8×10^{-4} to 10^{-3} are shown in Figure 8. The degradation of the shear moduli with shear strain interpreted from the direct simple shear test is presented Figure 8, showing that the Taipei clay would have the $\gamma_{0.7}$ value of 5×10^{-4}. This $\gamma_{0.7}$ value is adopted for all the soil layers in this study. Since slurry trenching is mostly conducted in the clay layers, that $\gamma_{0.7}$ value of 5×10^{-4} for sand and gravel would not be influential to the analysis results.

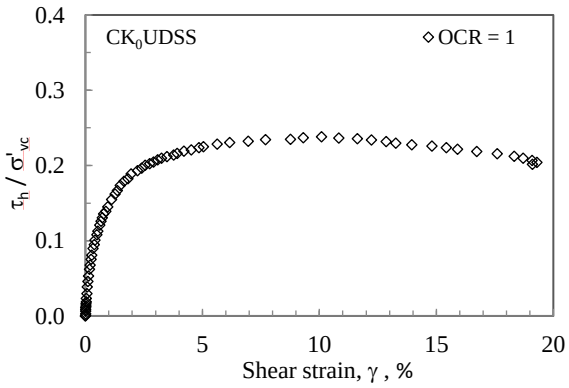


Figure 7: Stress-strain curve of Taipei clay under CK_0UDSS test (after Chin et al. 2007)

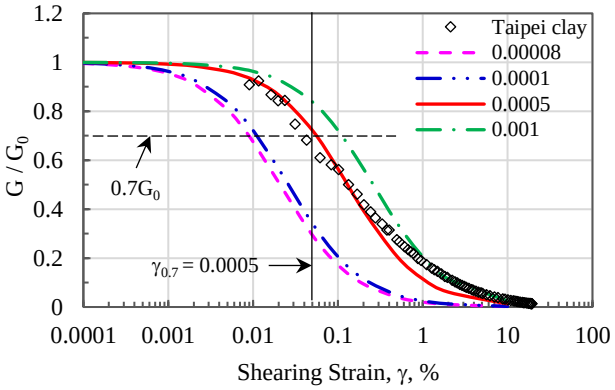


Figure 8: Degradation of shear moduli with shearing strain

4.4 Modeling of the slurry trenching

In the simulation for the trenching, the unit weight of 12 kN/m^3 for the slurry in the trench has been adopted. In reality, the slurry in the trench has no stiffness. However, as depicted in Figure 1, during excavating the primary wall panels, the trench is supported by the soil yet to be dug for installing the secondary panels, the concrete wall and the gravel infill. In the 2-D analysis, it is considered that the stiffnesses of materials supporting the trench, the quasi E_{trench} values, could be the weighted average of the Young's moduli of the slurry and the ground to be dug at the secondary wall panels.

In this study, the materials supporting the trench (ie., the slurry, in a sense) have been taken as the linear elastic materials. Based on the results of test runs, the E_{trench} values have been related to the E^{ref}_{50} values of the adjacent soil strata and the E_{trench} / E^{ref}_{50} ratios would vary from 0.001 to 0.2. The variation of the E_{trench} / E^{ref}_{50} ratios along the depth of the slurry trench are presented in Figure 9. The depths of the soil strata, h, are normalized with the depth of the slurry trench, the H value. It should be noted that this distribution of the E_{trench} / E^{ref}_{50} ratios is obtained from the results of back-analysis from the case history reporting in Section 5.1.

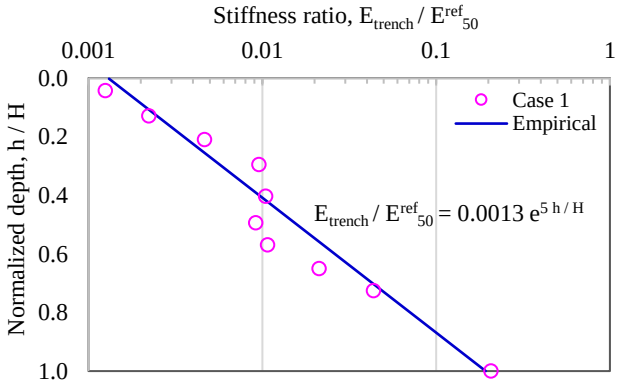


Figure 9: Variation of the stiffness ratios between the slurry trench and the adjacent soil

4.5 Cases analyzed

Three cases with different scenarios have been studied. For Case 1 there is no surcharge load. In Case 2, the surcharge pressure of 10 kPa is adopted to simulate the pressures imposed by the crawler cranes operating the clamshell buckets, lifting the reinforcement cages and for tremie concreting. The lateral extent of the surcharge area of 8 m is adopted. As mentioned in Section 3.4, the piezometric level of El. -5 m, which is the observed piezometric level in Jingmei Formation in 1993, has been adopted in Case 1 and Case 2.

The effect of ground water pressures to the ground movements due to diaphragm wall installation is studied in Case 3. The piezometric level in Jingmei Formation recovering to El. 5 m is adopted in the analysis. The

various conditions adopted for Case 1 to Case 3 are summarized in Table 2. For all the 3 cases the unit weight of the bentonite slurry of 12 kN/m^3 is adopted.

During excavation, the bentonite slurry in the trench is supposed to be maintained to the ground level. However, the clamshell bucket itself displaces part of the slurry in the trench. The top level of the slurry in the trench would drop when the bucket is lifted above the ground level to dispose the spoil. In the analysis, the top level of the slurry 2 m below the ground level is adopted to simulate this slurry displacing condition.

Guide walls were erected on both sides of the trench to prevent the ground from collapsing during slurry trenching. Due to the relatively shallow depth of the guide walls, the effect of installation of guide walls to ground movements is not simulated in this study.

Table 2: Cases studied for diaphragm wall installation

Scenario	Unit weight of slurry, kN/m^3	Piezometric level in Jingmei, El. m	Surcharge q, kPa	Main feature
Case 1	12	-5	0	No surcharge. Benchmark case.
Case 2		-5	10	Surcharge effect.
Case 3		5	0	Recovery in piezometric level with no surcharge.

5 RESULTS OF NUMERICAL ANALYSIS

5.1 Horizontal ground movements

The computed horizontal ground movements, the δ_h values, for Case 1 and Case 2 are presented in Figures 10 and 11. The computed maximum δ_h value at 2 m behind the wall for Case 1 is 26.4 mm. The analysis results are comparable with those observed at inclinometer SIS2, which was located next to a 12-storey building founding on bored piles. The pile toe levels are the same as that for the diaphragm wall. There would be no surcharge load imposing from the building foundation. Figure 10 shows that the computed maximum δ_h value of 26.4 mm is close to the observed value of 23.9 mm with the difference of 2.5 mm.

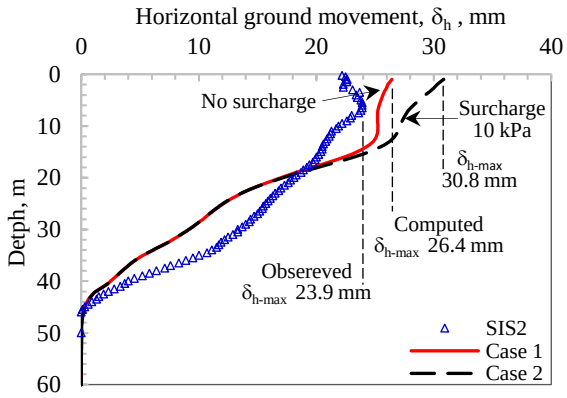


Figure 10: Computed horizontal ground movements at 2 m behind the wall compared with SIS2

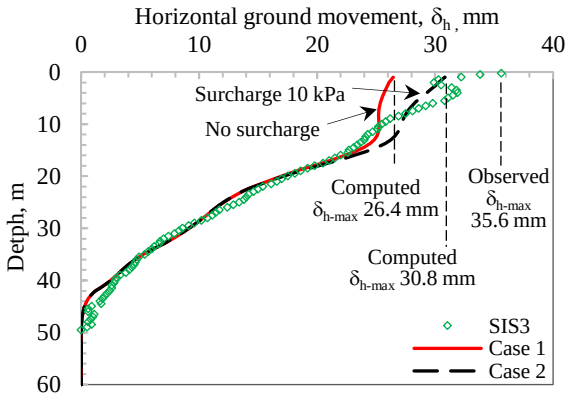


Figure 11: Computed horizontal ground movements at 2 m behind the wall compared with SIS3

5.2 Effect of surcharge

The computed δ_h values for Case 2 are compared in Figure 11 with those observed in inclinometer SIS3, which is located in the works area on the south side of City Hall Station. The crawler cranes operating could impose the surcharge load at the ground level and would affect the ground movements in the vicinity of SIS3. Figure 11 shows that the computed maximum δ_h value with surcharge is 30.8 mm, which is 4.4 mm larger than that of 26.4 mm without surcharge. The computed maximum δ_h value with surcharge of 30.8 mm is close to the 35.6 mm observed at SIS3, with the difference of 4.8 mm.

5.3 Effect of groundwater pressures

The groundwater pressure would have critical effect to ground movements. The computed δ_h values for Case 3 are presented in Figure 12. The numerical analysis shows that with the piezometric levels recovering from El. -5 m to El. +5 m, the maximum δ_h value could increase by 11.3 mm, from 26.4 mm to 37.7 mm.

As described in Section 3.4, the piezometric level in the Jingmei Formation was drawn-down to near the bottom level of the Songshan Formation in the 1970s. The lateral pressure increment acting on the slurry trench would be low and stable trench excavation have been experienced. With the piezometric levels in the Jingmei Formation fully recovering to close to the ground surface in recent years, say in 2024, the horizontal pressures acting on the trench would be larger than those previously experienced. The past stable and minimal ground movements induced by wall trenching would no longer be taken for granted.

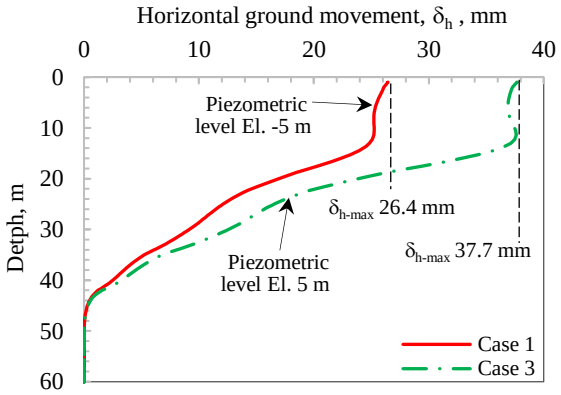


Figure 12: Computed horizontal ground movements with the piezometric level recovered to El. 5 m

5.4 Vertical ground movements

The computed vertical ground movements, the δ_v values, for Case 1 and Case 2 are presented in Figure 13. For Case 1 with no surcharge, the computed maximum δ_v values immediately behind the wall would be 20.8 mm. The maximum δ_v value for Case 2 with 10 kPa surcharge would be 26.9 mm, which is 6.1 mm larger than that without surcharge. As there is no settlements data in the diaphragm wall installation stage for City Hall Station (BL18), the settlements observed at the adjacent metro stations are collected for comparison.

Ou & Yang (2011) reported the settlements observed at Zhongxiao-Fuxing Station (BL16) and at Yongchun Station (BL19). The settlements were observed upon completion of the entire perimeter diaphragm walls of these stations. Station BL16 is located at 2 km west of Station BL18. Station BL19 is located at 1 km east of Station BL18. The diaphragm wall at Station BL16 was 1.0 m in thickness and 41 m in depth. The combined thickness for the clayey sublayers IV and II was 26 m. According to Chen et al. (1997), the diaphragm wall at Station BL19 was 1.2 m in thickness and 38 m in depth and the total thickness for the sublayers IV and II was 34 m. The wall lengths and the soil conditions at Stations BL16 and BL19 are similar to those at Station BL18.

Figure 13 presents the surface settlements, the δ_v values, observed at Station BL16. At the distance around 10 m behind the wall, the observed δ_v values range from 4.4 mm to 36.7 mm, with the mid value of 20.5 mm. At that distance, the computed settlement profile for Case 1 with no surcharge has the δ_v value around 18 mm, which is close to the average settlement observed.

The surcharge adopted in the analysis extends from 2 m to 10 m behind the wall. The 10 kPa surcharge would cause the computed maximum δ_v value of 26.9 mm. Figure 13 shows that the upper bound envelope of the observed settlements would be caused by the surcharge load. Such surcharge would likely be attributable to the operation of the crawler cranes for installation of the wall panels.

Figure 13 shows wide scattering of the settlements observed. One of the probable reasons for the lower bound envelope is that some of the settlement points were installed on pavements. Some of the settlement points were underlain by utilities such as the water mains, stormwater drains, sewer pipes and gas pipes. In future studies, settlements data affected by utilities shall be sorted out for fair comparison. It is very likely that the upper bound envelope of the measurement would be closer to free-field ground response. On the other hand, some settlements

would be induced by consolidation, which is not considered in the analyses. Besides, the possibility that some of the settlement points were disturbed by traffic cannot be ruled out.

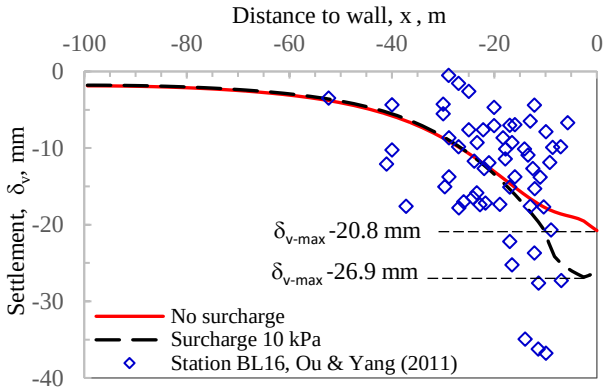


Figure 13: Computed settlements behind the wall with and without surcharge

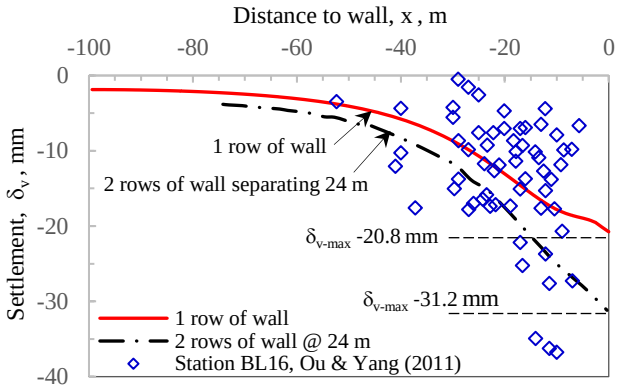


Figure 14: Computed settlements behind the wall induced by 2 rows of slurry trench

5.5 Multi-row of wall installation

Figure 13 shows that the settlements induced by slurry trenching would have wide lateral extent. At the distance of 24 m behind the wall, the computed δ_v value would be around 10 mm, which is about 50 % of the maximum δ_v value of 20.8 mm immediately behind the wall for the case with no surcharge.

As shown in Figure 2, City Hall Station was retained by 2 rows of diaphragm wall separating apart by 24 m. Installation for these 2 rows of wall could have the superimposing effect to the ground movements. The computed result for Case 1 gives the settlements caused by installing the single row of wall located at the near side. Shifting the computed profile to the other side by 24 m gives the settlements caused by installation of the wall located on the far side.

The combined settlements profile for the 2 rows of slurry trenching are presented in Figure 14. The computed maximum δ_v value immediately behind the wall caused by installing the single row would be 20.8 mm. That δ_v value would increase to 31.2 mm by adding the settlements induced by the earlier installation of the wall on the far side, with an increment of 10.4 mm. As the computed settlements profile for installing 2 rows of slurry trench fall into the upper bound envelope of those observed at Station BL16, the superimposing effect is verified by the field observation.

5.6 Normalized settlement profiles

Figure 15 presents the settlements observed at Station BL19. The observed settlements, δ_v, and the distances to the wall, x, are normalized with the depth of the slurry trench, H. The H value for the slurry trench of City Hall Station is 44.5 m.

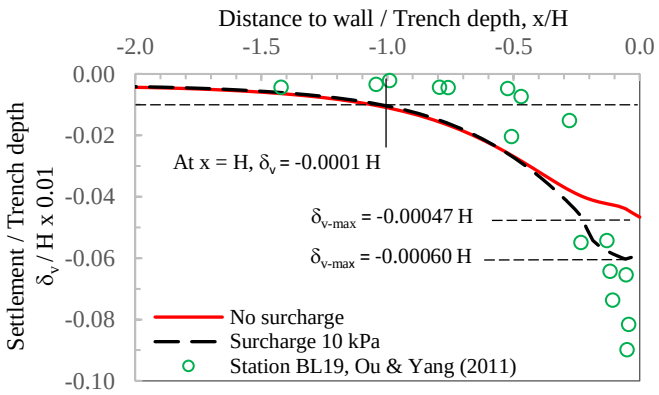


Figure 15: Normalized observed and computed settlements behind the wall

Figure 15 also shows the similar trend that the observed upper bound settlements envelope would be attributable to the surcharge load. Both Figures 13 and 15 show the agreement between the computed and the observed settlements caused by diaphragm wall installation. Figure 15 shows that the settlement trough induced by slurry trenching would have the extent of 1H. At that distance, the δ_v value would be around 20 % of the maximum δ_v value occurring immediately behind the wall for the case with no surcharge. The maximum δ_v value immediately behind the wall would be 0.00047H and 0.0006H for the cases without and with surcharge respectively.

6 CONCLUSIONS

A 2-Dimensional numerical analysis have been conducted for assessing the ground movements caused by diaphragm wall installation. The nonlinear Hardening-soil with Small-strain stiffness (HSS) soil model is adopted for the soil materials. The following conclusions could be drawn:

(1) In the case histories reported in this study, both the observed horizontal and vertical ground movements caused by diaphragm wall installation were as large as 36 mm. Such large magnitude of ground movements should not be over-looked from the buildings protection point of view.
(2) In addition to the unit weight of the bentonite slurry that would affect the performance of the ground movements, the surcharge due to the construction plants for wall installation would have significant effect to ground movements.
(3) The superimposing effect of ground movements due to installation multi-rows of slurry trenches shall be considered, especially where the horizontal distance between 2 rows of slurry trench would be less than 1 time the depth of the trench and at the entrances.
(4) Taking 20 % maximum settlement occurring immediately behind the wall as the criterion, the settlement trough induced by slurry trenching would have the influence of 1 time the depth of the trench.
(5) The groundwater pressure would have critical effects to ground movements. The numerical analysis in this study shows that with the piezometric levels recovering from El. -5 m to El. +5 m, the maximum horizontal ground movements could increase from 26.4 mm to 37.7 mm. With the piezometric levels fully recovering in recent years, the stable and minimal ground movements induced by wall trenching experienced in the past decades would no longer be taken for granted.

The building foundations would affect the magnitude of ground movements. In the next studies, the ground movements due to the surcharge imposing from the nearby shallow foundations shall be considered.

There is an empirical approach that the slurry trench would have some virtual stiffness, which is the weighted average of the stiffness of the surrounding soil along the trench. The empirical stiffness values for the trench have been calibrated against the observed horizontal ground movements. The application of the empirical relationship between the trench stiffness and the soil stiffness to other geological zones shall be verified with more observed case histories.

This study provides the method of replacing the soil unit weights with that of the bentonite slurry in the numerical analysis on the ground movements induced by wall installation. The method would be a simplified approach as an alternative to the more sophisticated 3-Dimensional analysis. With the proposed 2-Dimensional approach, the stress histories due to trenching could be properly assessed. The wish-in-place for wall could no longer be assumed in the analysis on the following construction such as station excavation and jet grouting.

ACKNOWLEDGEMENTS

The Author wishes to express his sincerely thanks to Dr R.N. Hwang of Moh and Associates, Inc. for providing the field observation data on diaphragm wall construction and his valuable advices on this study.

REFERENCES

Benz, T. (2006). Small-strain stiffness of soils and its numerical consequence. *Dissertation of thesis*, the Institute of Geotechnics, University Stuttgart.

Chen, Y. K., Huang, C. C. & Wang, F. G. (1997). Grouted raft for building protection in excavation in soft clay. *Proceedings of 7th Conference on Current Research in Geotechnical Engineering*, Chinshan, Taiwan, August 1997, Vol. 1: 593-600. (in Chinese)

Chin, C.T., Chen, J.R., Hu, I.C., Yao, D.H.C. & Chao, H.C. (2007), Engineering characteristics of Taipei clay. In T.S. Tan, K.K. Phoon, D.W. Hight & S. Leroueil (Eds), entitled*: Characterization and Engineering Properties of Natural Soils,* Taylor & Francis Group, v3: 1755-1803.

Chin, C.T., Crooks, A.J.H. & Moh, Z.C. (1994). Geotechnical properties of the cohesive Sungshan deposits. *Geotechnical Engineering, J. Southeast Asian Geotechnical Society*, Taipei, Taiwan 25(2): 77-103. (in Chinese)

Chin, C.T. & Liu, C-C. (1997). Volumetric and undrained behaviors of Taipei silty clay. *J. Chinese Institute of Civil and Hydraulic Engineering*, Taipei, Taiwan 9(4): 665-678. (in Chinese)

Cowland, J.W. & Thorley, C.B.B. (1985). Ground and building settlement associated with adjacent slurry trench excavation, *Ground Movements and Structures*, Pentech Press, London, UK: 723-738.

Hwang, R. & Moh, Z.C. (2022). Groundwater drawdown and subsidence in the Taipei Basin. *Sino-Geotechnics*, No. 173/2022.9: 99-110. (in Chinese)

Hu. I.C., Chin, C.T. & Liu, C.J. (1996). Review of the geotechnical characteristics of the soil deposits in Taipei, *Sino-Geotechnics*, No. 54: 5-14. (in Chinese)

Kung, G.T.C, Ou, C.Y. & Juang C.H. (2009). Modelling small-strain behavior of Taipei clays for finite element analysis of braced excavations. *Computers and Geotechnics* 36 (2009): 304-319.

MAA (1987) *Engineering properties of the soil deposits in the Taipei Basin*, Report No. 85043, Ret-Ser Engineering Agency and Taipei Public Works Department, Taipei. (in Chinese)

Moh, Z.C. & Ou C.D. (1979). Engineering characteristics of Taipei Silt. *Proc., 6th Asian Regional Conference on Soil Mechanics and Foundation Engineering*, Singapore, 1: 155-158.

Moh, Z.C., Chin, C.T., Liu, C.J. & Woo, S.M. (1989). Engineering correlation for soil deposits in Taipei. *J. Chinese Institution of Engineers*, 124(9): 798-808.

Morton, K., Cater, R.W. & Linney, N. (1980). Observed settlements of buildings adjacent to stations constructed for the modified initial system of the mass transit system, Hong Kong. *Proceedings of the 6th Asian Conference of the Soil Mechanics and Foundation Engineering*, Taipei, Vol. 1: 415-429.

Ng, C.W.W., Lings, M.L., Simpson, B. & Nash, D.F.T. (1995). An approximate analysis of the three-dimensional effects of diaphragm wall installation. *Geotechnique* 45, No.3: 497-507.

Ou, C.Y. & Yang, L.L. (2011). Observed performance of diaphragm wall construction. *Geotechnical Engineering Journal of the SEAGC & AGSSEA*, Vol. 42, No.3, September 2011. ISSN 0046-5828: 41-49.

Ou, C.Y., Liao, J.T. & Cheng, W.L. (2000), Building response and ground movements induced by a deep excavation, *Geotechnique*, Vol. 50, No. 3: 209-220.

PLAXIS B.V. (2013). *PLAXIS Reference Manual*. PLAXIS, BV, Delft, the Netherlands.

Santos J.A. & Correia, A.G. (2001). Reference threshold shear strain of soil. Its application to obtain a unique strain-dependent shear modulus curve for soil. *In 15th Int. Conf. SMGE*, Volume 1, Istanbul, A.A. Balkema. 267-270.

Schanz, T. & Vermeer, P.A. (1998). On the Stiffness of Sands. *Geotechnique*, 46, No. 1: 145-151.

Schanz, T., Vermeer, P.A. & Bonnier, P.G. (1999). The hardening soil model: formulation and verification. *Beyond 2000 in Computational Geotechnics*. Rotterdam, the Netherlands: 281-290.

Wong, L.W. (2023). Effects of soil-structure interaction on wall deflections and surface settlements during deep excavations. *Proceedings, 43rd HKIE Geotechnical Division Annual Seminar*, Hong Kong, May: 70-81.

.

Exploring Computer-based Rock Mass Characterization

Louis N.Y. WONG & K.K. CHAN,

Department of Earth Sciences, The University of Hong Kong

S.N. GOH, Ivan H.H. CHAN & Regis L.G. CHEE

Geotechnical Engineering Office, Civil Engineering and Development Department, HKSAR Government

ABSTRACT

The precision and representativeness of manual rock mass characterization result are often limited by site constraints or practices due to accessibility, safety, time, and unfavourable environmental conditions. In this study, we have formulated a computerized workflow for rock mass characterization by adopting the NGI Q-system, with the aid of laser scanning that could be easily deployed on underground construction sites. This study also explores the application of artificial intelligence, specifically deep learning, in the proposed workflow for rock mass characterization based on the relationship between Rock Quality Designation (RQD) and number of discontinuity sets (J_n) and the block shapes and sizes. In order to effectively train the deep learning model, we propose a novel technique called Synthetic Rock Mass Point Cloud (SRMPC) to generate point clouds model of rock mass with varying RQD and discontinuity sets. SRMPC utilizes an implicit approach with signed distance functions to model rock mass geometry and employs the sphere tracing technique for efficient point cloud generation. A synthetic dataset comprising 35 classes of RQD and J_n combinations was created to train and test a deep learning model, PointNet++ (Qi et al., 2017), for classification. The deep learning model exhibited a certain ability to identify the features of the synthetic rock mass with varying RQD, but faced challenges in distinguishing rock masses with similar RQD and discontinuity sets. To address this problem, a revised 20-class classification model was developed and trained, resulting in improved accuracy.

1 INTRODUCTION

1.1 Background

Rock mass characterization is essential to rock support design of underground openings. However, site constraints, accessibility, unfavorable environmental conditions, and procedures related to safety and time often limit the precision and representativeness of rock mass characterization in conventional practice. For example, measuring joint orientations at a tunnel's crown using a compass is challenging, if not impracticable. This study explored the application of remote sensing techniques and computer vision for rock mass characterization, primarily on digitizing the process of rock mass classification, to enhance safety and cost-effectiveness of underground construction in rock.

One of the most commonly used rock mass classification systems in Hong Kong – the NGI Q-system by Barton et al. (1974), updated by NGI (2015) has five out of six parameters (i.e. Rock Quality Designation, Joint set number, Joint roughness number, Joint alteration number and Joint water reduction factor) characterizing various discontinuity properties in a rock mass. The successful applications of the NGI Q-system in Hong Kong have been recognized by Barton (2015) and play a pivotal role in the local hard rock tunnelling and cavern engineering practices.

Remote sensing techniques such as photogrammetry and laser scanning can capture point clouds of rock mass with sufficient information for interpreting RQD and Joint set number (J_n). Laser scanners, particularly handheld/mobile laser scanners, are found to be more suitable for underground construction. However, capturing other parameters, including Joint roughness number (J_r), Joint alteration number (J_a) and Joint water reduction factor (J_w) from the point clouds data is still challenging due to the resolution and different nature of the measurements.

This study focused on streamlining the process of characterization of RQD and J_n, using point cloud data, since these two parameters are critical to the result of rock mass characterization and could vary greatly within a small space. Moreover, these parameters can be interpreted from point cloud data with relatively high accuracy. The remaining parameters (i.e. J_r, J_a, J_w and stress reduction factor) generally relate to larger-scale geological conditions and vary less when compared to RQD and J_n. Obtaining these parameters through engineering geologists' field observations is considered more efficient and reliable.

1.2 Related work

In recent years, many researchers have investigated extracting discontinuity planes from point clouds (e.g. Chen et al., 2016; Gigli & Casagli, 2011; Riquelme et al., 2014; etc). Theoretically, RQD and J_n can be determined if all discontinuities are perfectly outlined in a point cloud. However, characterizing RQD or J_n using these existing methods is typically not reliable enough for actual construction. For example, wavy discontinuity planes are often split into multiple planes by these algorithms. Moreover, existing analytical methods require users to determine multiple parameters, such as minimum angular difference between two planes. Obtaining the best result necessitates careful calibration and tuning of these parameters to accommodate the site and the geology, which can be time-consuming (So et al., 2021).

One potential solution to overcome the limitations of these existing methods is deep learning. Recent research, such as PointNet++ by Qi et al. (2017), has demonstrated the capability of deep learning to perform tasks including classification and segmentation of point cloud data. We noticed that an experienced mapping personnel can roughly describe rock mass quality based on the overall appearance without delineating every discontinuity. Deep learning has the potential to acquire this capability and expedite rock mass characterization. Since current studies on applying deep learning to rock mass characterization are limited, this study aims to explore the feasibility of applying deep learning to characterize RQD and J_n.

2 METHODOLOGY

2.1 Overall workflow

The characterization of RQD and J_n can be regarded as a "classification" task. NGI (2015) suggests that the quotient RQD/J_n describes the relative block size of a rock mass due to different combination of joint frequency and pattern. The deep learning model's goal is to predict the combination of RQD and J_n from a rock mass's point cloud.

The quotient of RQD/J_n has to be first categorized. NGI (2015) classifies RQD into five categories, namely excellent (>90), good (75 – 90), fair (50 – 75), poor (25 – 50) and very poor (<25), and J_n into nine categories, namely massive, one joint set with/without random joints, two joint sets with/without random joints, three joint sets with/without random joints, four or more joint sets and crushed rocks. In theory, there are 45 RQD/J_n categories. The details of classification scheme will be discussed in Section 2.3.

The first step of training a deep learning model was the preparation of training dataset. However, collecting sufficient training data for each category in the field is time-consuming. It is also uncommon to find rock masses with low rock mass quality since they are typically avoided during the selection of site location in most of underground construction projects. Therefore, this study proposed a novel technique called **synthetic rock mass point cloud (SRMPC)** to generate point clouds with appearances similar to rock masses of different qualities. The details of SRMPC will be presented in section 2.2.

The second step was choosing a suitable deep learning architecture. According to a recent review of deep learning for point cloud by Guo et al. (2020), there are three major categories of deep learning architectures for point cloud classification. The first category recognizes objects by two dimensional images of a point cloud rendered at different angles (Guo et al., 2020). Classic 2D image deep learning techniques, such as convolution neural network (CNN), are applied to these images to perform classification. The main challenge of using this approach for rock mass characterization is that rock masses lack distinct outlines, and meaningful images are difficult to render. The second category converts point clouds into voxels and recognizes objects using 3D convolution (Guo et al., 2020). However, the resolution of the voxelized point cloud is often limited (order of about 64 x 64 x 64 voxels) as computational resources required increase exponentially with the resolution. Given the typical size of rock mass and spacing of discontinuities, the voxelized point cloud requires a very high resolution to capture all discontinuities, which is difficult to handle. The last category directly intakes the

coordinates of a point cloud and performs classification by the spatial relationship of the points (Guo et al., 2020). PointNet++ by Qi et al. (2017) is an example of this category and performed well in various benchmarking datasets for point cloud classification, such as ModelNet40.

After evaluating the strengths and limitations of different deep learning architectures, this study selected PointNet++ since it showed good performance when applied in different fields and could directly utilize point cloud data. The details of PointNet++ will be presented in section 2.3.3.

The last step was assessing the performance of trained deep learning models. Due to limited available real datasets, the performance of the model was evaluated quantitatively using a separated set of SRMPC, which is never seen by the model. The separated set is also used as the testing dataset during the training process. Real datasets were used to assess the performance of the model qualitatively. Details of the real datasets will be discussed in section 2.6.

2.2 Synthetic Rock Mass Point Cloud (SRMPC)

2.2.1 Overall process

The generation of synthetic rock mass point cloud (SRMPC) comprises three stages, namely discontinuity generation, point cloud generation, and attributes computation, as shown in Figure 1.

The first stage aims to create an implicit representation of a rock mass before excavation. The discontinuity generation process of SRMPC was inspired by the creation of synthetic rock mass (SRM) for numerical modelling. SRM refers to explicit jointed rock mass models using discrete fracture network (DFN) to model discontinuities (Ivars et al., 2011). A DFN specifies the location, orientation and other geometric properties of discontinuities, which can be obtained by geological mapping, stochastic generation and/or numerical simulation (Lei et al., 2017). In this study, stochastically generated discontinuities were used.

The second stage exposes the rock mass by mimicking the excavation process, allowing for point cloud generation. The "excavation" process was developed by combining geotechnical engineering experience and techniques in computer constructive solid geometry (Voelcker & Requicha, 1977). To convert the implicit representation of the rock mass into an explicit point cloud, sphere tracing, a computer graphic technique, was used.

The final stage involves computing and appending attributes to the generated point cloud for subsequent applications.

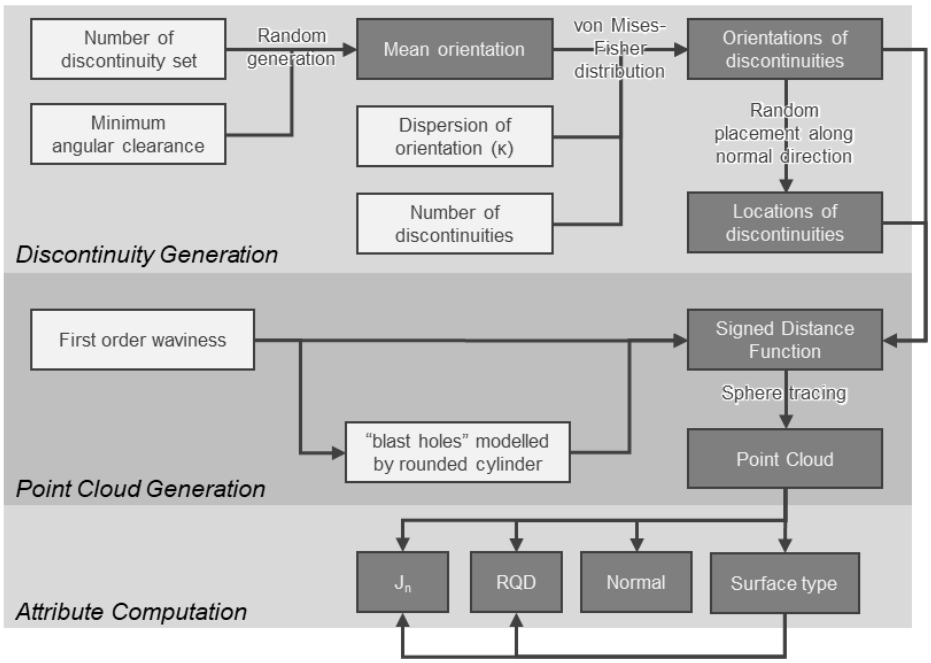


Figure 1: Workflow of generating a synthetic rock mass point cloud

2.2.2 Discontinuity Generation

The first step of generating a SRMPC is to determine the desired discontinuity pattern, including the number of discontinuity sets, number of discontinuities, angular difference between sets and dispersion of orientation within set. The von Mises-Fisher (vMF) distribution was used to generate the orientation of discontinuities, and a Poisson point process was used for determining the location of discontinuities, as the presence and spatial distribution of natural discontinuities were found to fit well with these stochastic processes (Dershowitz, 1984).

Firstly, the mean orientation of each set is picked randomly while keeping a minimum angular clearance. This ensures that different discontinuity sets can be distinguished by their orientation.

Secondly, for each discontinuity set, the orientation of individual discontinuities is generated by assuming their orientations follow the von Mises-Fisher Distribution. The generation algorithm by Hornik & Grün (2014), based on the Wood (1994)'s algorithm, was adopted in this study. To avoid excessive mixing between different discontinuity sets, the parameter of dispersion (i.e. κ) of the orientations within each set is selected randomly from a range of values based on the minimum angular clearance.

Next, as the discontinuities are assumed with infinite persistence, their position can be fixed by their distance from the origin along their normal vector. Discontinuities are randomly positioned within the specified extent. This process can recreate a discontinuity spacing pattern that generally follows the negative exponential distribution, commonly observed in real rock masses (Priest & Hudson, 1981).

2.2.3 Point Cloud Generation

The next step is to "expose" the discontinuities planes and add curved random fractures to the rock mass, simulating a blasting process. The algorithms for various 3D objects and sphere tracing were adopted and modified from Quilez (2023). First, the first order waviness of a rock mass is modelled using a cosine function. Second, rounded cylinders that mimic "blast holes" and the radial cracks generated by "blasting" are placed on the wavy surface created by the cosine function. The discontinuity planes and these cylinders are combined to form a signed distance function for the rock mass. A signed distance function provides information on the distance between the surface and the input coordinates (Quilez, 2023). Next, sphere tracing, which makes use the properties of signed distance functions to effectively render 3D geometry, is applied to produce the point cloud.

2.2.4 Attribute Computation

Lastly, the surface each ray encounters is tracked during the sphere tracing process. Attributes of that surface, including the surface type (random fractures caused by the "blast holes" or discontinuity surface) and the normal vector, are inherited to the point cloud. With these attributes, the RQD and J_n value can be obtained by volumetric joint counting (Palmstrom, 2005).

2.3 Training datasets

2.3.1 35-class classification scheme

The 35-class classification scheme is developed based on the five categories of RQD and nine categories of J_n defined in NGI (2015). In theory, the combinations of RQD and J_n represents different shapes and sizes of blocks in a rock mass, which is represented by the quotient of RQD/J_n (NGI, 2015). However, some combinations of RQD and J_n yield the same value but have different appearances. For instance, a rock mass with one joint set (J_n = 2) and an RQD of 10, and a rock mass with three joint sets and random joints (J_n = 12) and an RQD of 60, both have the same quotient value (5), but their appearances are likely to differ significantly. As the deep learning model characterizes rock mass by its appearance, the direct use of RQD/J_n as the label may confuse the deep learning model. Therefore, a categorical label instead of a numerical value was adopted. As a result, it is necessary to convert RQD into a categorical variable, and the qualitative classification scheme for RQD used by NGI (2015) is adopted.

With five classes of RQD and nine classes of J_n, there are 45 possible RQD/J_n combinations. Upon examining these combinations, it was discovered that some of them are rare or not possible, such as crushed rock mass with excellent RQD, and some combinations have similar appearances, such as crushed rock and rock mass

with four or more joints sets with very poor RQD. As such, some of these 45 classes are removed and grouped, resulting in a 35-class classification scheme. The RQD/J_n of each class is shown in Figure 2 : RQD/J_n value of the 35-class classification scheme.Figure 2.

J_n / RQD	Massive (0.5 – 1.0)	One joint set (2)	One joint set + random (3)	Two joint set (4)	Two joint set + random (6)	Three joint set (9)	Three joint set + random (12)	Four or more joint sets (15)	Crushed rock (20)
Excellent (> 90)	95	48	32	24	16	11	8		
Good (75 – 90)		41	28	21	14	9	7	6	
Fair (50 – 75)		31	21	16	10	7	5	4	
Poor (25 – 50)		19	13	9	6	4	3	3	
Very Poor (<25)		6	4	3	2	1.4	1.0	0.8	0.6

Figure 2 : RQD/J_n value of the 35-class classification scheme.
Very poor rock masses with four or more joint sets and crushed rock (highlighted in orange) are considered as one class in this scheme.

2.3.2 20-class classification scheme

After experimenting the 35-class classification scheme (details will be discussed in 3.1), it was noted some classes in the 35-class classification scheme had similar appearances, in particular rock masses with the same number of major joint sets but with and without random joints. The deep learning model struggled to distinguish between these classes. Since a reasonably high accuracy is essential for practical applications, a simplified 20-class classification scheme was developed to improve accuracy. As random joints are generally limited in number and have a minimal impact on the rock mass's appearance, the J_n classes with and without random joints are combined. For example, a rock mass with one discontinuity set and another with one discontinuity set plus random discontinuity are considered the same in this scheme. In practice, the J_n value can be conservatively taken as that with the random discontinuity sets, as shown in Figure 3. This scheme reduces the task's difficulty while maintaining applicability in practical scenarios.

J_n / RQD	Massive (0.5 – 1.0)	One joint set (2)	One joint set + random (3)	Two joint set (4)	Two joint set + random (6)	Three joint set (9)	Three joint set + random (12)	Four or more joint sets (15)	Crushed rock (20)
Excellent (> 90)	95	32		16		8			
Good (75 – 90)		28		14		7		6	
Fair (50 – 75)		21		10		5		4	
Poor (25 – 50)		13		6		3		3	
Very Poor (<25)		4		2		1.0		0.6	

Figure 3: RQD/J_n value of the 20-class classification scheme

2.3.3 Generation of training dataset

The following process was adopted to produce a balanced dataset with an equal number of instances in each class. For both classification schemes, a total of 300 instances for each class were generated.

First, a large number of point clouds are generated for each J_n class, with a randomly picked number of discontinuities. During point cloud generation, some generated discontinuity planes may not be exposed due to

their locations, orientations, and density and sizes of "blast holes". As a result, the number of discontinuities and discontinuity sets subsequently shown in the SRMPC is usually less than the targeted number. A large number of SRMPCs with ranges of targeted properties were generated, and the actual class that each SRMPC belongs to was determined.

The previous step was repeated for classes with fewer number of instances than the target (i.e. 300). On the other hand, if there were more instances than the target, the desired number of instances were picked randomly.

The training dataset for the 20-class classification scheme was prepared from that for the 35-class classification scheme through random selection. As the classes with and without random joints are combined in the 20-class classification scheme, 150 point clouds with random joints and 150 point clouds without random joints were randomly selected to form the combined class.

2.4 Model architecture

After reviewing some well-known point cloud classification architectures, PointNet++ by Qi et al. (2017) was chosen for this study. The primary reason is that it is capable to cope with point clouds with a large number of points and has many previous studies demonstrating its performance in classification.

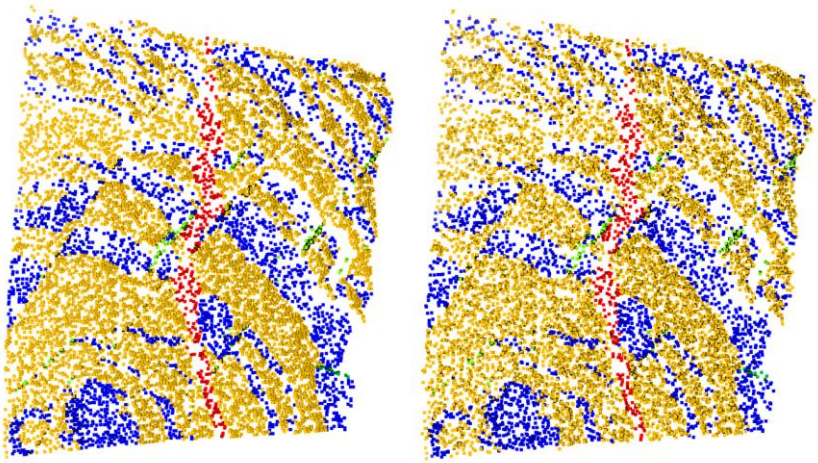
Since most available pre-trained PointNet++ models (e.g. Yan, 2019) were trained for classifying objects with distinct outlines, such as a desk or a chair, and used point clouds with relatively few points (<10,000 points), it was considered that these pre-trained models could not be applied directly to rock mass characterization. Therefore, this study trained the deep learning model from scratch with randomly initialized parameters.

Compared to the original structure of PointNet++, the number of input points was increased to 10,000, and the output class was changed to 35 or 20, depending on the adopted classification scheme. The layers in between remain unmodified.

2.5 Model training

The training dataset was first randomly split into training and testing datasets with an 80:20 ratio (i.e 240 samples for training and 60 samples for testing). The total numbers of training samples and testing samples were 8,400 and 2,100 respectively, for the 35-class classification scheme, and 4,800 and 1,200 respectively for the 20-class classification scheme.

Before feeding the data into the model, pre-processing including subsampling, random rotation, random shift and jittering, was carried out at the beginning of each epoch. Each SRMPC in the training and testing dataset was a 3 m x 3 m x 3 m rock mass with about 40,000 points. Each SRMPC was randomly subsampled to 10,000 in every epoch. The training data was then rotated, shifted and jittered to further augment the data, while the testing data remained unmodified. This process aimed to simulate variations in field data collection to make the synthetic data more realistic. An example of data augmentation is shown in Figure 4.



Subsampled Rotated, Shifted, Jittered

Figure 4: Data augmentation applied on the training data. The colors denote the surface types and are shown for illustration purposes. The information of surface type is not included in the training data.

An implementation of PointNet++ in PyTorch (Paszke et al., 2019) developed by Yan (2019) was adopted for training the deep learning models in this study. A total of 200 epochs of training was performed for both the 35-class and 20-class classification schemes. The hyperparameters adopted for the training of deep learning models in this study are shown in Table 1. Since the initial focus of this study was to explore the feasibility of applying deep learning for rock mass characterization, fine-tuning of these hyperparameters was not carried out. It was anticipated that the difference caused by fine-tuning is likely limited.

Table 1: Hyperparameters adopted for training the deep learning models

Hyperparameters	**Value**
Epoch	200
Batch size	36
Optimizer	Stochastic gradient descent
Learning rate	0.01
Momentum	0.9

2.6 Evaluation

The performance of the deep learning models was evaluated both quantitatively and qualitatively. Due to limited variations of rock mass quality in real datasets, it is difficult to evaluate the model quantitatively with real datasets. Instead, the synthetic testing dataset was used for quantitatively assessing the performance.

The real datasets were retrieved from the Geotechnical Engineering Office, Civil Engineering and Development Department of the Hong Kong Special Administrative Region Government (GEO, 2021), which were released under the benchmarking exercise for rock mass discontinuity survey. These datasets include the point cloud of an abandoned quarry face (Feature No. 11SE-B/C249**Error! Reference source not found.**) located at Lei Yue Mun Point and the point cloud of a rock slope (Feature No. 11NW-D/C80**Error! Reference source not found.**) located at Shun Yung Street, Ho Man Tin.

These real datasets contain noises, such as vegetation, since they were acquired on the surface rather than underground. Portions with little vegetation and rock mass with clear exposures were extracted for evaluation to minimize the impact caused by these noises.

Furthermore, real point clouds, including those used for verification, are usually larger than that of the training data (i.e. 3 m x 3 m x 3 m). As such, a sliding window approach was adopted (Figure 5). The input point cloud is first dissected into 1 m x 1 m x 1 m cells. For each cell, the surrounding neighbouring cells (i.e. 26 cells) are selected together to form a 3 m x 3 m x 3 m window. The prediction result of the deep learning model is written to the points in that 1 m x 1 m x 1 m cell at the centre. This ensures the model makes predictions using the same scale as the training data, while the variation of a rock mass can also be shown.

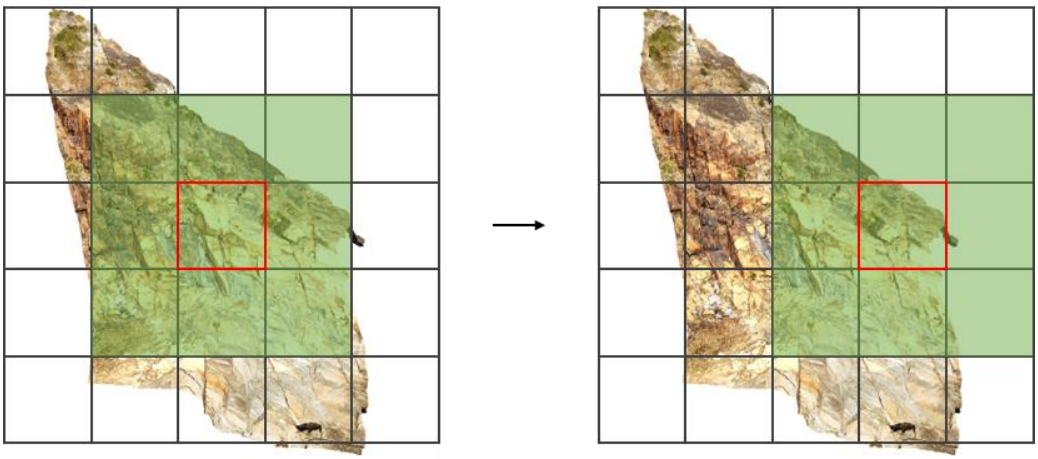


Figure 5: Schematic diagram of the sliding window approach adopted

3 RESULT AND DISCUSSION

3.1 35-class classification scheme

3.1.1 Quantitative results

The results demonstrated that deep learning has the potential to perform rock mass characterization. Figure 6 shows the evolution of classification accuracies of the training and testing data over the 200 epochs, with the best testing accuracy achieved was 29.3%. Figure 7 shows the confusion matrix for testing data.

Firstly, the evolutions of accuracies for both training and testing datasets (Figure 6) were similar, increasing rapidly in the first few epochs and gradually stabilizing at slightly below 30%. This probably indicates that the model did not overfit and successfully learned the features of different rock masses. The relatively low accuracy may suggest that the model struggled to learn the differences between many of the classes, as shown in the confusion matrix (Figure 7).

Secondly, apart from examining the combination of RQD and J_n as a whole, it is also possible to assess the performance in distinguishing different J_n and RQD values. Regarding the performance of classifying different J_n value, the confusion matrix (Figure 7) showed that the model is capable of distinguishing different numbers of major joint sets when the RQD lower than "excellent" (i.e. there are certain number of discontinuities). Nevertheless, the model performed less satisfactory in distinguishing the presence of random sets. One of the possible reasons is that deep leaning models perform classification primarily based on low-frequency signals (i.e. overall appearance of the point cloud). When there are few discontinuities or the presence of random discontinuities, the overall outlook of the rock mass may be very similar. For a human, an engineering geologist will examine the surroundings and make measurements to identify the major discontinuity sets in these cases. On the other hand, when there are a certain number of discontinuities, different numbers of major joint sets usually result in very different block shapes, for example, rock mass with one major discontinuity set (e.g. sedimentary rock) forms layers and rock mass with three orthogonal discontinuity sets forms cubes. The deep learning model is capable of distinguishing these patterns.

Thirdly, regarding the performance of classifying different RQD values, the confusion matrix showed that the model is capable of distinguishing rock mass with good and poor RQD with limited precision, for example, a rock mass with fair RQD is often misidentified as good or poor. One of the possible reasons is that RQD is a continuous variable and the adopted classification was arbitrary, such that rock mass with similar RQD can be classified into two different classes. Nevertheless, for a human to deduce a precise RQD (in the order of 5), it requires a technique including volumetric joint counting and empirical correlation. It appears to be difficult for the computer to develop such a strategy without explicitly incorporating that into the model architecture.

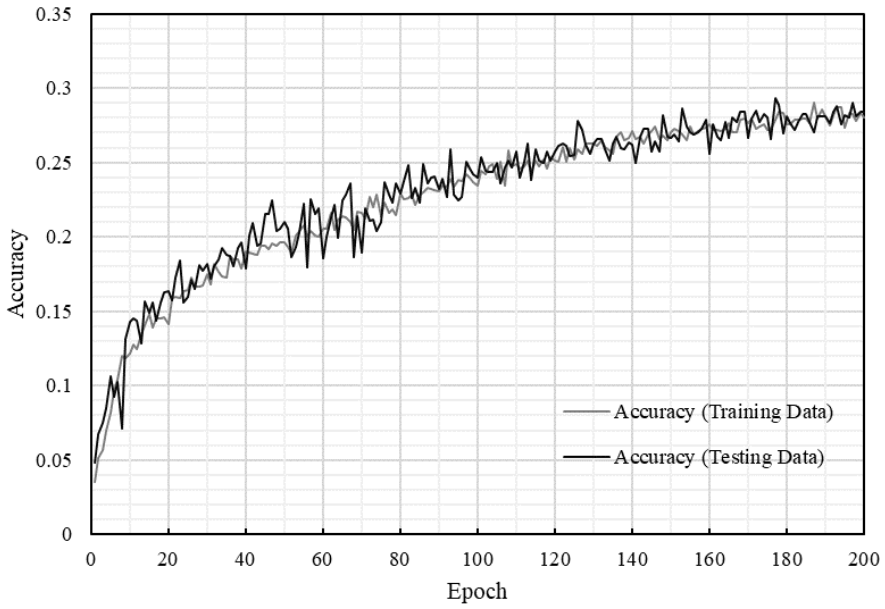


Figure 6: Classification accuracy of training and testing data (35-class classification scheme)

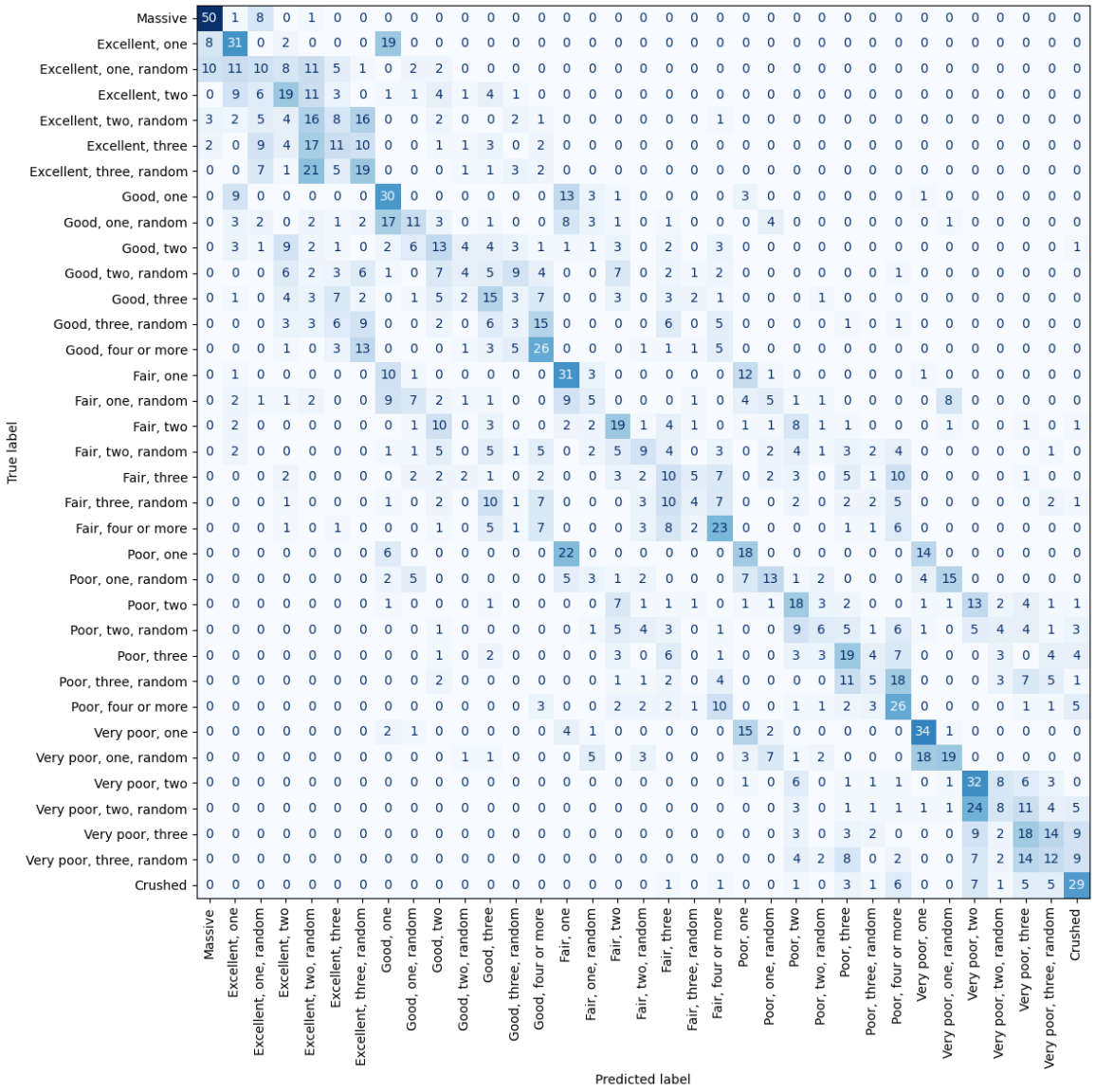


Figure 7: Confusion matrix of testing data (35-class classification scheme). Numbers in the cell denote the number of different combinations of true labels and predicted labels.

3.1.2 Qualitative results

The prediction of RQD/J_n class of Feature Nos. 11SE-B/C249 and 11NW-D/C80 are shown in Figure 8 and Figure 9. The predictions are generally in line with the observations in the field mapping done by GEO (2021).

Field mapping conducted by GEO (2021) identified four major discontinuity sets with spacing between 0.5 m and 1 m in the rock mass of Feature No. 11SE-B/C249. Palmstrom (2005) suggested that the volumetric joint count can be estimated from the joint spacing. In this case, the volumetric joint count (J_v) of the rock mass is around 6 m^{-3}. Next, based on the empirical correlation between volumetric joint count and RQD, proposed by Palmstrom (2005) and also suggested in NGI (2015), the RQD of the rock mass is approximately 95 (i.e. "excellent").

For Feature No. 11SE-B/C249, the RQD/J_n predicted by the deep learning model is broadly consistent with the manual observations by GEO (2021). As shown in Figure 8, the subhorizontal joint set exposes in gentler areas and the rock mass is apparently massive, the deep learning model also predicted those generally as "massive". On the other hand, the deep learning model predicted the steeper areas generally as two different classes, namely "rock mass with excellent RQD and three joint sets with random joints" and "rock mass with good RQD and four or more major joint sets". The model predicted the areas with fewer joints as classes with fewer major discontinuity sets, possibly because the deep learning model may have misidentified the fourth major joint set as random discontinuities. For corners or protruding parts of the rock mass, the model predicted these areas as rock mass with poorer RQD with fewer major joint sets, probably because a smaller rock mass was actually included in the 3 m x 3 m x 3 m.

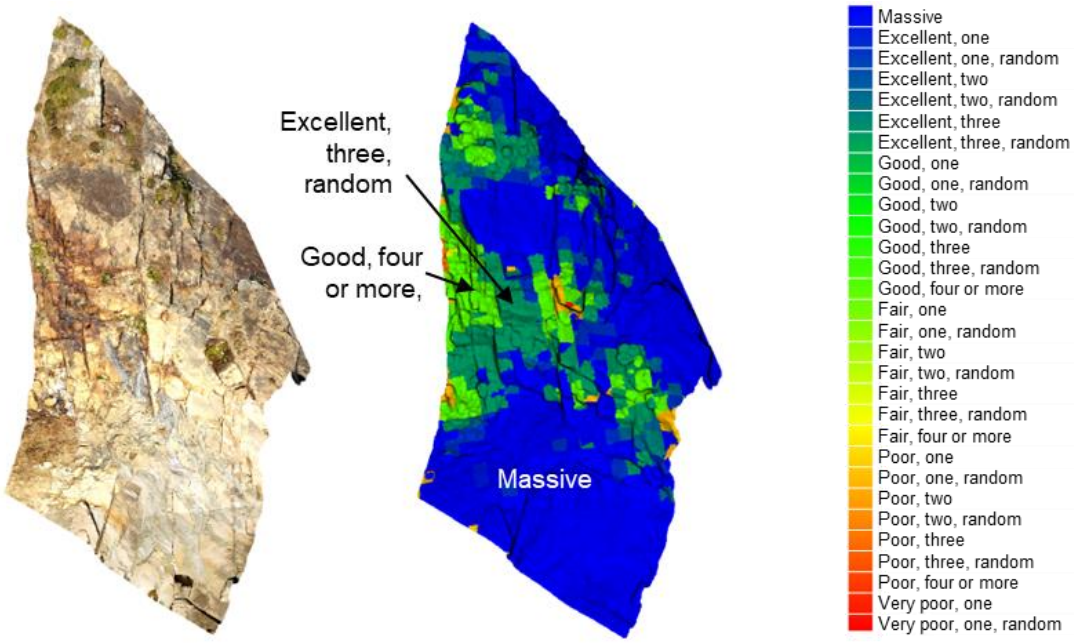


Figure 8: Prediction of RQD/J_n of Feature No. 11SE-B/C249 by the deep learning model

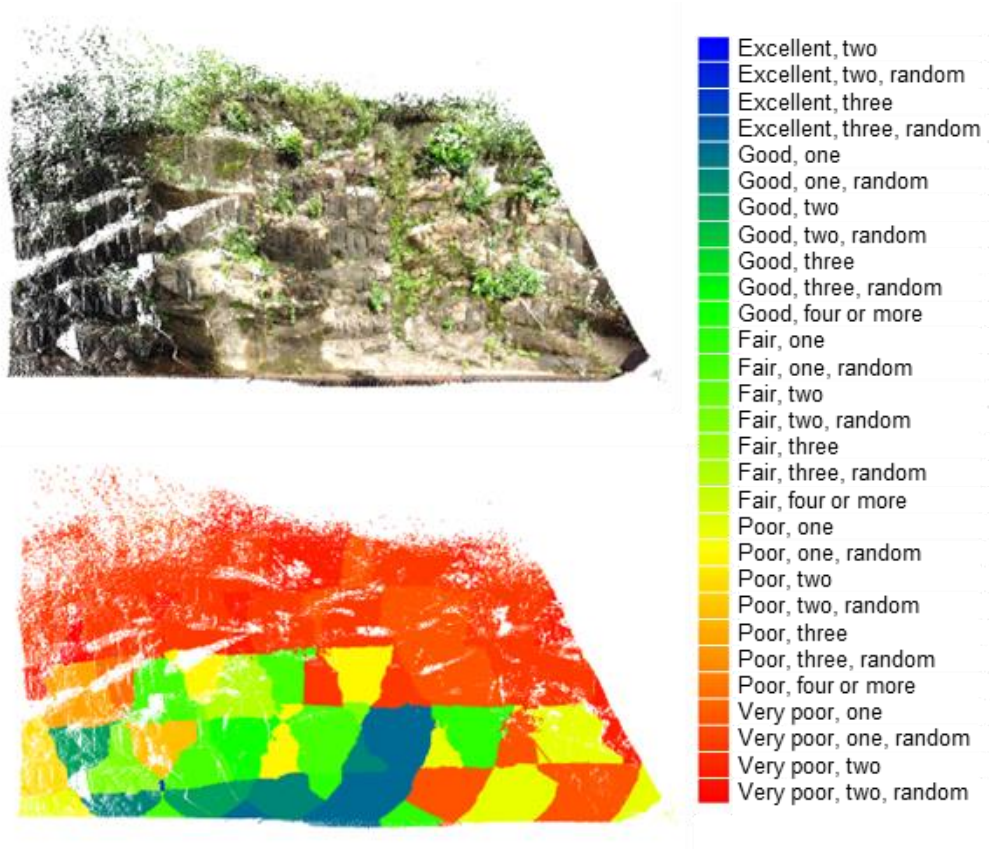


Figure 9: Prediction of RQD/J_n of Feature No. 11NW-D/C80 by the deep learning model

For Feature No. 11NW-D/C80, GEO (2021) also identified four major joint sets, but with a smaller spacing between 0.3 m to 1 m (GEO, 2021). Using the previously approach, J_v of the rock mass is approximately 7.5 m^{-3}, and the RQD is about 90, which falls between "excellent" and "good" classifications.

The RQD/Jn predicted by the deep learning model broadly aligns with the manual observations by GEO (2021). As shown in Figure 9, there is vegetation in the upper part of the rock mass and the model predicted that area as "rock mass with very poor RQD and one major joint set and random joints". On the other hand, the model classified the lower part of the rock mass having one major joint set with/without random joints with RQD between good and poor. Although four major joint sets are presence in the rock mass, only the persistent subhorizontal joint set is well exposed in the lower part of this portion of rock mass. Subvertical joint sets are poorly exposed and may be regarded as "random joints" by the model.

Furthermore, the lower part of the rock mass is also characterized by pre-splitting surfaces, which are subparallel to the slope surface and planar in nature. While these pre-splitting surfaces may resemble discontinuity planes, the model did not seem to count these surfaces as one of the major joint sets. It appears that the model can differentiate between pre-splitting surfaces and natural discontinuity planes; however, further evidence and tests are necessary to confirm whether the model has truly learnt the differences between these two surface types.

3.2 20-class classification scheme

The 20-class classification scheme exhibits an improved classification accuracy of about 44.2%. Figure 10 shows the confusion matrix for the testing data. The model shows better accuracy in classifying rock masses with different J_n classes. The simplified J_n classes may enable the model to focus on learning features created by different numbers of major discontinuity sets. The improvement also indicates that deep learning models perform more robustly when carrying out relatively coarse-grained classification.

However, the model still has relatively low precision in predicting RQD classes, which limits the improvement in classification accuracy. The simplification of J_n classes does not significantly improve the model's capability to distinguish rock masses with different RQD values. As a result, the practical usage of these deep learning models remains limited.

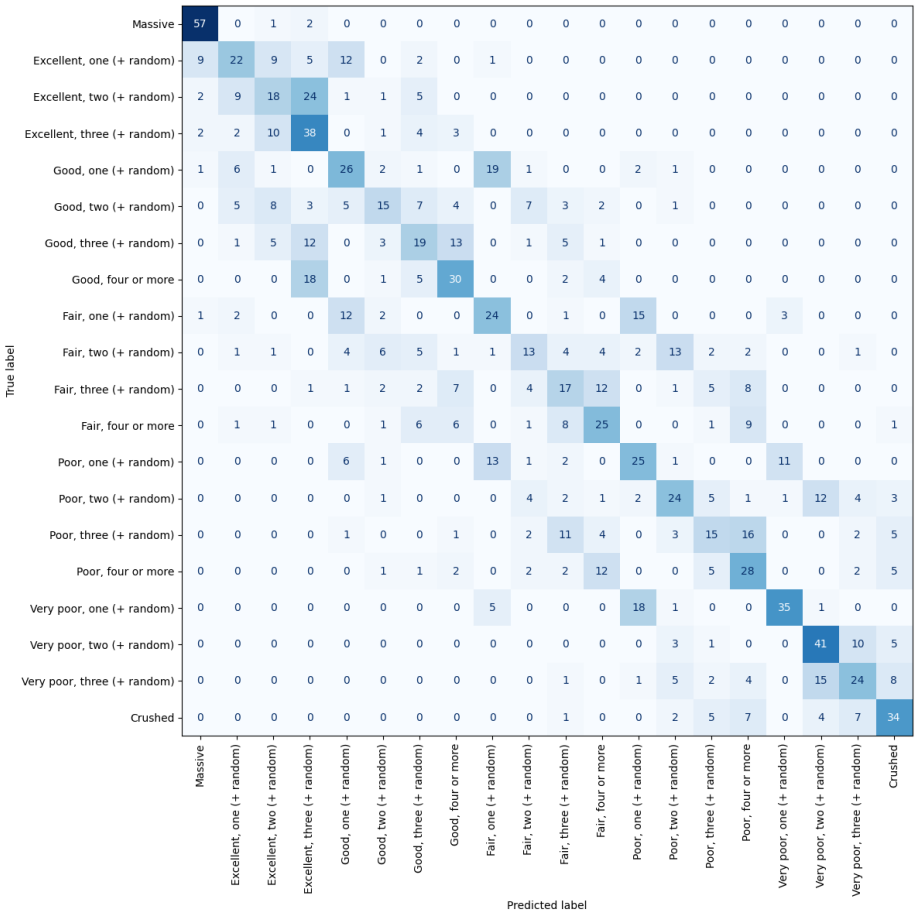


Figure 10: Confusion matrix for testing data (20-class classification scheme). Numbers in the cell denote the number of different combinations of true labels and predicted labels.

3.3 Other observations

During the preparation of training dataset, it was observed that some classes are challenging to generate using the SRMPC algorithm. For example, rock masses with one discontinuity set and very poor RQD were difficult to generate because closely spaced discontinuities are not easily exposed at the resolution of SRMPC. Increasing the resolution of random fractures and the point cloud could alleviate this issue. However, doing so would not only increase generation time, but also raise the requirements for acquiring real data since the resolution of SRMPC was set to be similar to that of typical equipment.

3.4 Synthetic Rock Mass Point Cloud

The results above have demonstrated the feasibility of using synthetic data to train a deep learning model and apply it to real dataset. The SRMPC not only aids in applying deep learning to rock mass characterization, but also supports other machine learning applications in rock mechanics, since a large amount of data with known discontinuity properties can be generated quickly. For example, the SRMPC can be combined with numerical modelling to explore the possibility of predicting stability analysis results based on point cloud data.

3.5 Way forwards

Firstly, classification-based approach can be further explored. State-of-the-art model architectures or pre-trained models, trained with very large datasets, can be adopted. In other fields of machine learning, such as computer vision, “transformer” models trained with vast datasets have become increasingly powerful. For example, the DINOv2 model, trained with an image dataset containing about 142 million images (LVD-142M), exhibited strong performance across various tasks, including image classification, segmentation and monocular depth

estimation (Oquab et al., 2023). When a similar model for performing 3D tasks released in the future, it will be worthwhile to further investigate the classification-based approach.

Secondly, performing discontinuity extraction using a deep learning model can be investigated. In this study, one of the limitations observed in deep learning models is their relatively weak performance in fine-grained interpretation, such as distinguishing the presence of random discontinuities. Deep learning models can first be used to extract all discontinuity planes (i.e., obtaining the complete geometric data), and then RQD and J_n classes can be computed similarly to the existing methods mentioned previously. The extracted discontinuity planes by the deep learning models could potentially also be used in other rock mass classification systems and the generation of DFN models.

4 CONCLUSIONS

This study has demonstrated the potential of deep learning in rock mass characterization. Deep learning models can perform rock mass characterization quickly with fair precision. A simplified 20-class model was also tested, which improved the accuracy but not to a level high enough to be deployed into routine construction workflows. Further research is needed to practically adopt deep learning for routine rock mass characterization. Last but not least, a novel solution called SRMPC was developed in this study to address the scarcity of training data, proving useful for deep learning in rock mass characterization. It also holds potential for application in other machine learning tasks within the field of geological engineering.

ACKNOWLEDGEMENTS

The findings in this paper were based on the Master dissertation of Mr. K.K. CHAN, supervised by Prof. Louis N.Y. WONG at The University of Hong Kong, and a project carried out by the Geotechnical Engineering Office. The authors also gratefully acknowledge the valuable experience from related studies carried out in the Geotechnical Engineering Office. This paper is published with the permission of the Head of the Geotechnical Engineering Office and the Director of Civil Engineering and Development, the Government of the Hong Kong Special Administrative Region.

REFERENCES

Barton, N., Lien, R. & Lunde, J. 1974. Engineering classification of rock masses for the design of tunnel support. *Rock Mechanics*, 6: 189–236.

Barton, N. 2015. Forty Years with the Q-system – Lessons and Developments. Keynote Paper. Institute of Materials, Minerals and Mining, Hong Kong Branch.

Chen, J., Zhu, H., & Li, X. 2016. Automatic extraction of discontinuity orientation from rock mass surface 3D point cloud. *Computers & geosciences*, 95: 18–31

Dershowitz, W. S. 1984. Rock joint systems. Massachusetts Institute of Technology. PhD thesis.

GEO. 2021. Review of Benchmarking Exercise on Digital Rock Mass Discontinuity Survey 2020.

Gigli, G., & Casagli, N. 2011. Semi-automatic extraction of rock mass structural data from high resolution LIDAR point clouds. *International journal of rock mechanics and mining sciences (Oxford, England : 1997)*, 48: 187–198.

Guo, Y., Wang, H., Hu, Q., Liu, H., Liu, L., & Bennamoun, M. 2020. Deep learning for 3d point clouds: A survey. *IEEE transactions on pattern analysis and machine intelligence*, 43(12): 4338-4364.

Hornik, K., & Grün, B. 2014. movMF: An R package for fitting mixtures of von Mises-Fisher distributions. *Journal of Statistical Software*, 58(10): 1-31.

Ivars, D.M., Pierce, M.E., Darcel, C., Reyes-Montes, J., Potyondy, D.O., Young, R.P., & Cundall, P.A. 2011. The synthetic rock mass approach for jointed rock mass modelling. *International Journal of Rock Mechanics and Mining Sciences*, 48: 219–244.

Lei, Q., Latham, J.P., & Tsang, C.F. 2017. The use of discrete fracture networks for modelling coupled geomechanical and hydrological behaviour of fractured rocks. *Computers and Geotechnics*, 85: 151-176.

NGI. 2015. Using the Q-system: Rock Mass Classification and Support Design (handbook). Norwegian Geotechincal Institute, Oslo.

Oquab, M., Darcet, T., Moutakanni, T., Vo, H., Szafraniec, M., Khalidov, V., Fernandez, P., Haziza, D., Massa, F., El-Nouby, A., Assran, M., Ballas, N., Galuba, W., Howes, R., Huang, P.Y., Li, S.W., Misra, I., Rabbat, M., Sharma, V., … Bojanowski, P. 2023. DINOv2: Learning Robust Visual Features without Supervision (arXiv:2304.07193). *arXiv*. http://arxiv.org/abs/2304.07193

Palmstrom, A. 2005. Measurements of and correlations between block size and rock quality designation (RQD). *Tunnelling and Underground Space Technology*, 20(4): 362–377.

Paszke, A., Gross, S., Massa, F., Lerer, A., Bradbury, J., Chanan, G., Killeen, T., Lin, Z., Gimelshein, N., & Antiga, L. 2019. Pytorch: An imperative style, high-performance deep learning library. *Advances in Neural Information Processing Systems*, 32.

Priest, S. D., & Hudson, J. A. 1981. Estimation of discontinuity spacing and trace length using scanline surveys. *International Journal of Rock Mechanics and Mining Sciences & Geomechanics Abstracts*, 18(3): 183–197.

Qi, C.R., Yi, L., Su, H., & Guibas, L.J. 2017. Pointnet++: Deep hierarchical feature learning on point sets in a metric space. *Advances in Neural Information Processing Systems*, 30.

Quilez, I. 2023. Inigo Quilez. https://iquilezles.org/.

Riquelme, A.J., Abellán, A., Tomás, R., & Jaboyedoff, M. 2014. A new approach for semi-automatic rock mass joints recognition from 3D point clouds. *Computers & geosciences*, 68: 38–52.

So, A.C.T., Leung W.K., & Wong J.C.F. 2021. A Novel Method for Measurement of Orientation of Rock Joints from Point Cloud by Facet Amalgamation Approach. The 42nd Asian Conference on Remote Sensing (ACRS2021) 22-24th November, 2021 in Can Tho University, Can Tho city, Vietnam.

Voelcker, H., & Requicha, A. 1977. Constructive solid geometry. University of Rochester.

Wood, A.T. 1994. Simulation of the von Mises Fisher distribution. *Communications in statistics-simulation and computation*, 23(1): 157-164.

Yan, X. 2019. Pointnet/Pointnet++ Pytorch [Python]. https://github.com/yanx27/Pointnet_Pointnet2_pytorch

Development of an AI rock type classification and fracture state characterization web-based application

Louis N.Y. WONG[1], Keith K.C. TSE[1], Joseph S.H. CHEUNG[2] & Lequan YU[3]
[1] *Department of Earth Sciences, The University of Hong Kong*
[2] *Department of Civil Engineering, The University of Hong Kong*
[3] *Department of Statistics & Actuarial Science, The University of Hong Kong*

ABSTRACT

Conventional rock core logging and log checking methods, while dependable, can be labor-intensive and subjective, possibly prone to errors and inconsistencies. This project addresses these limitations by employing computer vision-based deep learning AI technology to improve the accuracy, objectivity, and productivity of rock core logging and log checking processes. A web-based application called PreLogging was developed, capable of classifying common Hong Kong rocks and decomposition grades, identifying fractures, and computing fracture state indices such as Total Core Recovery (TCR), Solid Core Recovery (SCR), Rock Quality Designation (RQD), and Fracture Index (FI). The development of PreLogging involved a multidisciplinary team of researchers, engineers, and industry stakeholders collaborating to produce a tool that addresses the needs of geotechnical engineering. The development process encompassed multiple stages, including the design of a user interface, creation of an alpha version, soliciting feedback from industry stakeholders, incorporating AI computation capabilities, and releasing a stable version. The project team found that collecting feedback from industry stakeholders was crucial in ensuring the application effectively meets the industry's requirements.

1 INTRODUCTION

In the ever-evolving fields of geosciences and geological engineering, the process of rock classification serves as a cornerstone, offering indispensable information required for a wide range of applications and practices. Traditional methods of rock classification have primarily depended on the accumulated experience of experts in the field, which can inadvertently introduce a degree of subjectivity and possible inconsistencies in the classifications. To tackle this challenge and usher in a new era of objectivity, the present study endeavors to harness the cutting-edge advancements in computer vision-based deep learning and artificial intelligence (AI) technologies. The objective is to create a state-of-the-art, web-based platform, known as **PreLogging**, designed to classify both fresh and weathered igneous rocks.

In addition to its primary classification function, the PreLogging platform is also equipped to detect and identify fractures present in rock cores, as well as to derive advanced algorithms for the calculation of fracture indices. By skillfully emulating the innate human capacity to instantaneously and precisely perceive and analyze rock images, PreLogging aspires to significantly enhance the efficiency and objectivity of rock core logging and log checking processes.

Ultimately, the development and deployment of this groundbreaking tool are aimed at providing invaluable support to geologists and engineers in their quest to make well-informed decisions based on reliable and objective data. By minimizing the influence of human subjectivity in rock classification and analysis, PreLogging has the potential to revolutionize the way these professionals approach their work, thereby contributing to the advancement of the geosciences and geological engineering fields as a whole.

2 WEB-BASED PLATFORM DEVELOPMENT

The initial development phase of PreLogging encompasses the creation and implementation of AI-based algorithms and logic for rock type and weathering grade classification (Tse et al., under review). This phase also includes the identification of fractures in rock cores, which will be utilized to calculate fracture indices (Tse et al., under preparation).

PreLogging boasts the ability to classify common Hong Kong rocks and decomposition grades, identify fractures, and compute fracture state indices. The platform's capabilities are as follows:

(1) Rock type prediction/identification: PreLogging supports the following major rock types in Hong Kong (1) Fine grained granite, (2) Medium grained granite, (3) Coarse grained granite, (4) Coarse ash tuff, (5) Fine ash tuff, (6) granodiorite, and (7) feldsparphyric rhyolite and (8) jar.
(2) Weathering grade prediction/identification: PreLogging supports the detection of (1) Grade II, (2) Grade III, (3) Grade IV (Core), (4) Grade V (NR), and (5) Jar.
(3) Quantitative calculation of fracture indices. PreLogging supports the computation of (1) Total Core Recovery (TCR), (2) Solid Core Recovery (SCR), (3) Rock Quality Designation (RQD), and (4) Fracture Index (FI).

Following this early-stage research, a web-based platform is developed. The development process entails the following stages:

(1) An alpha version of the app is created, prioritizing user interface and user experience design.
(2) Collaborating organizations, including the Hong Kong Geological Society and Hong Kong Construction Association – Site Investigation Committee, are invited to provide feedback on the alpha version.
(3) Based on the feedback received, AI computation capabilities are incorporated into the backend, resulting in the release of a beta version.
(4) Several supporting and collaborating organizations are invited to test the beta version. To facilitate the feedback process, an online survey form is created and utilized.
(5) User feedback is collected, and revisions are made to both the app and user manual through multiple internal trials and modifications, ultimately leading to the release of a stable version.

3 USAGE OF PRELOGGING

In this section, the PreLogging's usage workflow is depicted through a series of snapshots (Figures 1 to 11), offering a visual representation of the app's functionality. Detailed descriptions of the key steps can be found within the captions accompanying each figure. This visual guide aims to provide users with a clear understanding of how to effectively utilize PreLogging's advanced capabilities for rock core logging.

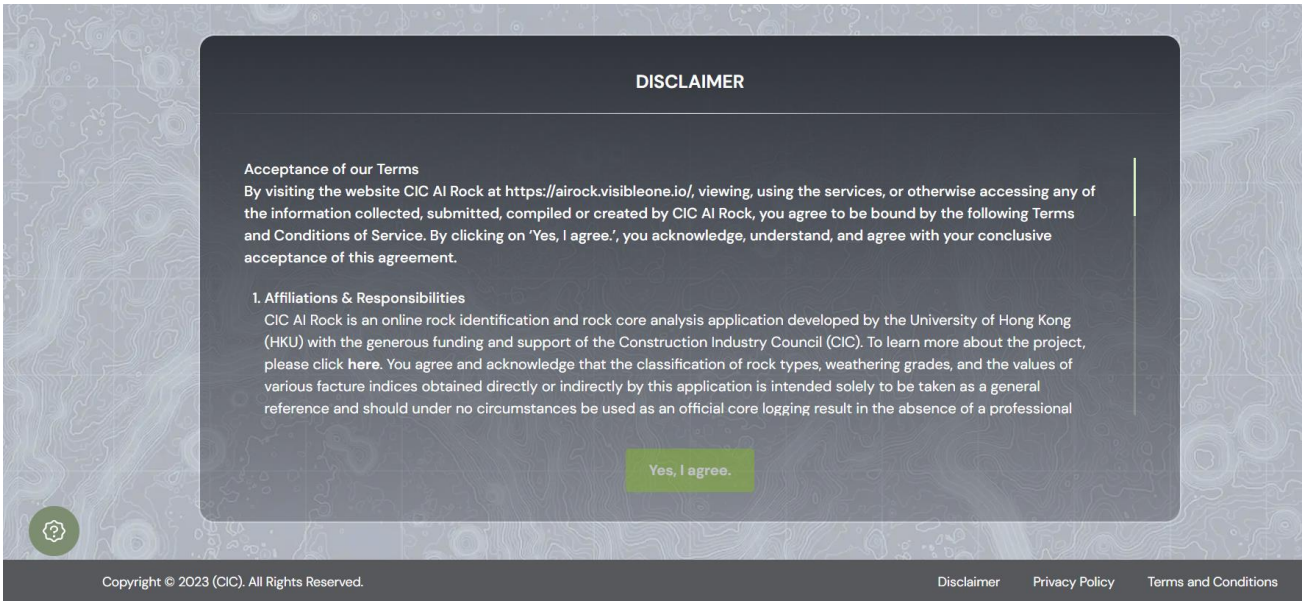


Fig. 1. Displaying disclaimer for user to click "Yes, I agree".

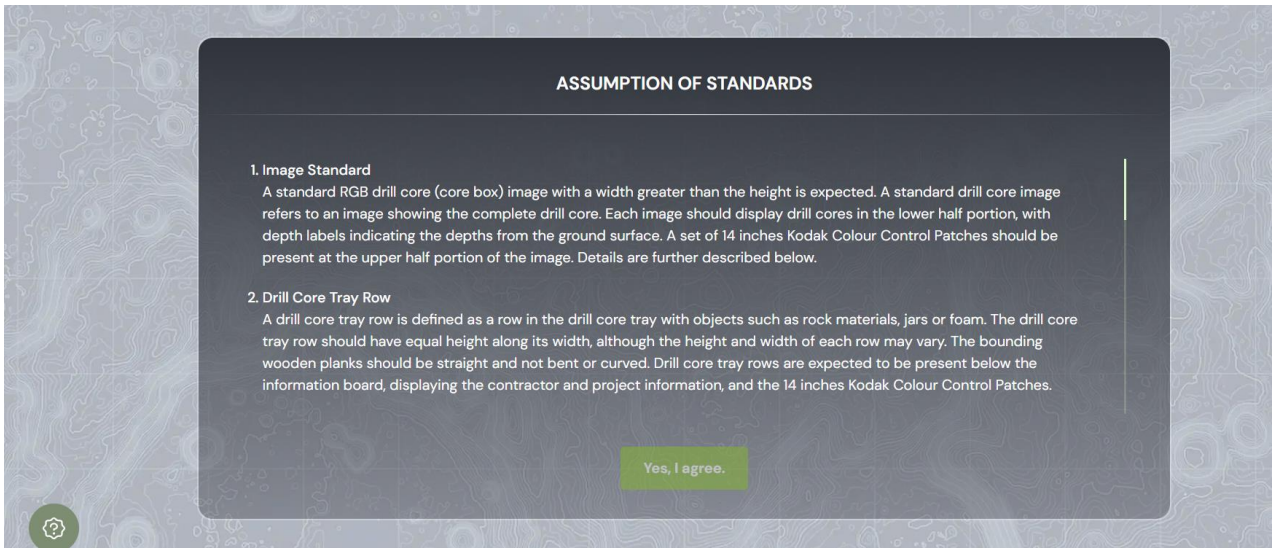


Fig. 2. Displaying assumption of standards.

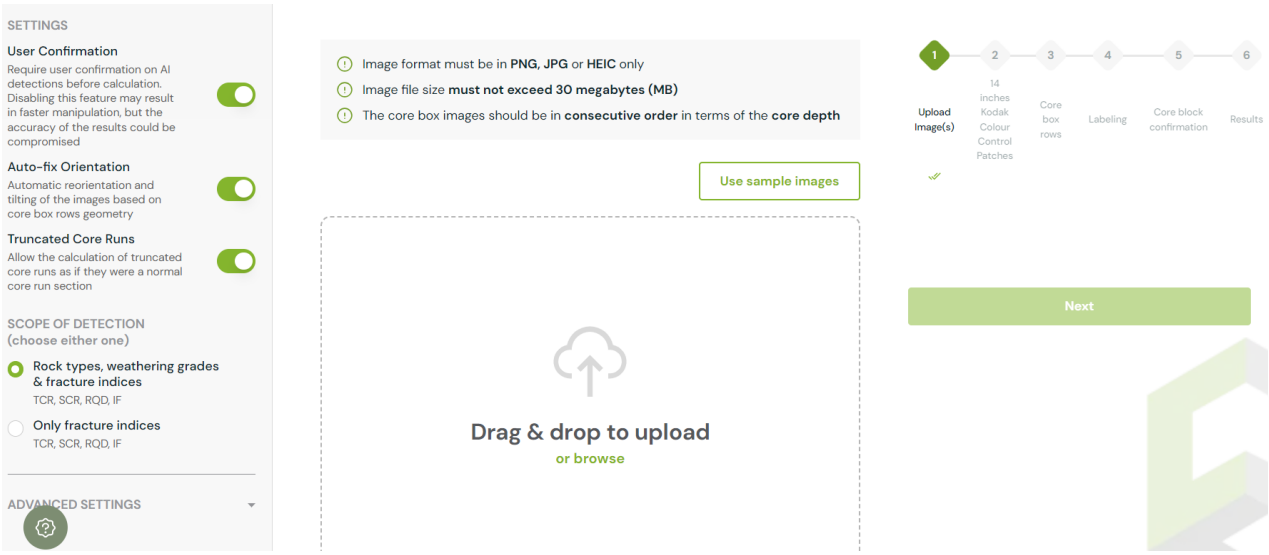


Fig. 3. Prompting user to upload a core box photograph, and to select analysis settings. A standard RGB drill core (corebox) image with a width greater than the height is expected. A standard drill core image refers to an image showing the complete drill core. Each image should display drill cores in the lower half portion, with depth labels indicating the depths from the ground surface.

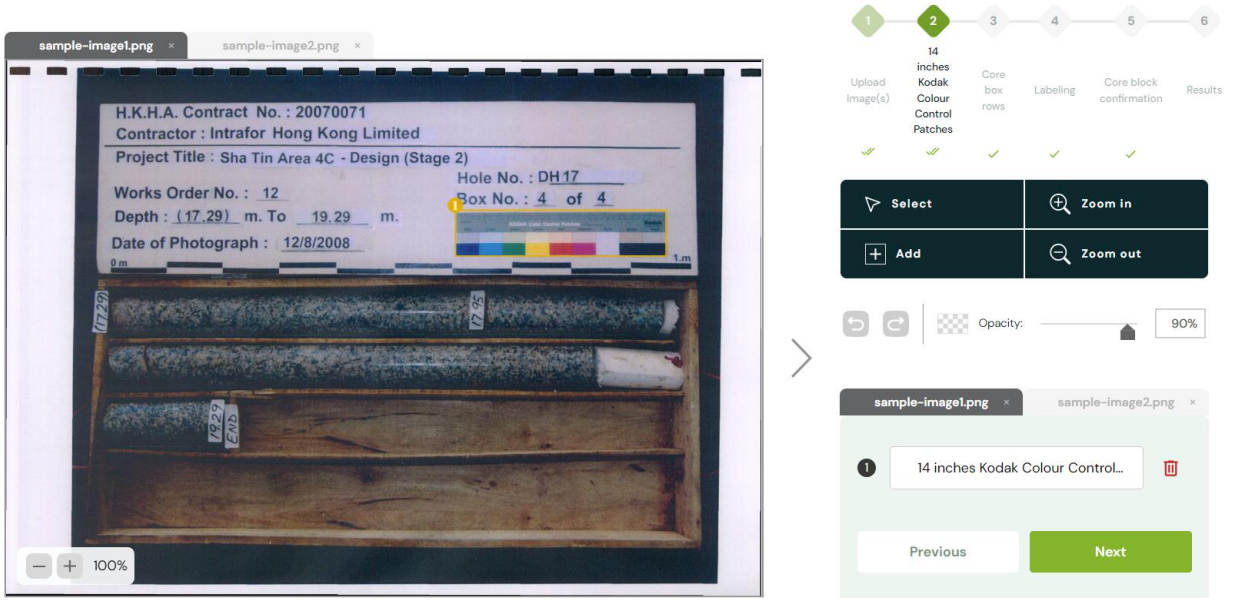


Fig. 4. Automatic identification of length scale. PreLogging takes the set of 14 inches Kodak Colour Control Patches as the length scale, which should be present at the upper half portion of the image. Smaller or non-standard Kodak Colour Control Patches may lead to incorrect calculations.

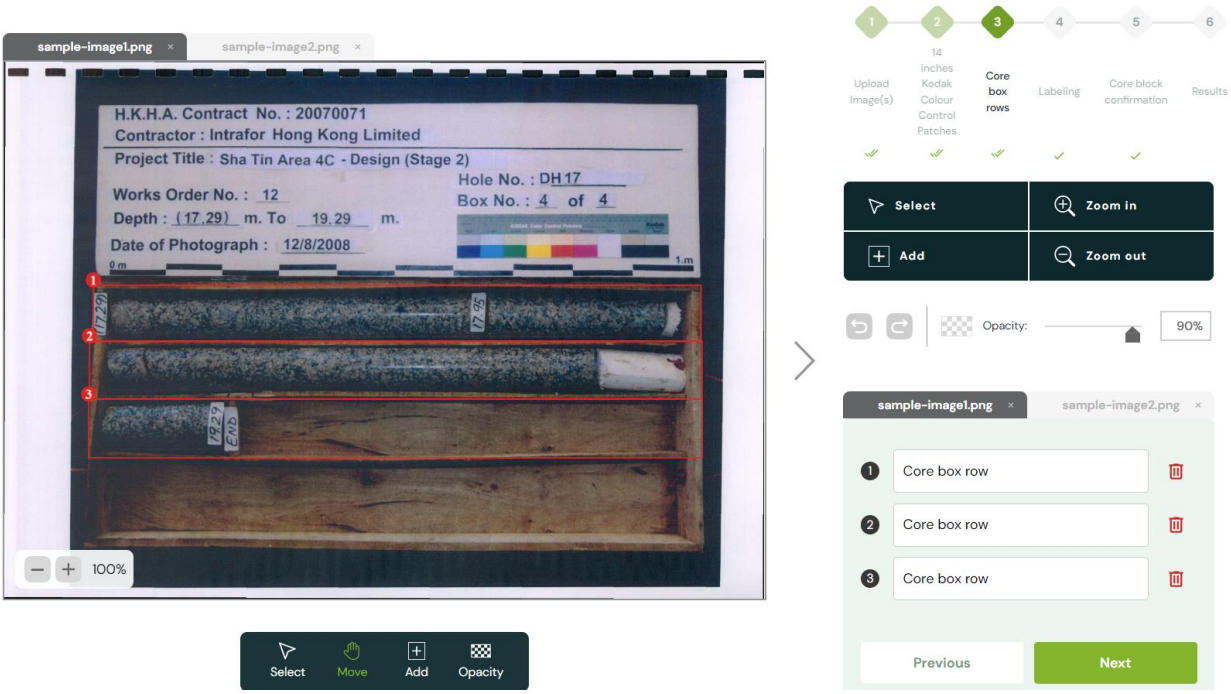


Fig. 5. Automatic identification of corebox rows. A corebox row is defined as a row in the drill core tray with objects such as rock materials, jars or foam. The drill core tray row should have equal height along its width, although the height and width of each row may vary. The bounding wooden planks should be straight and not bent or curved. Drill core tray rows are expected to be present below the information board, displaying the contractor and project information, and the 14 inches Kodak Colour Control Patches.

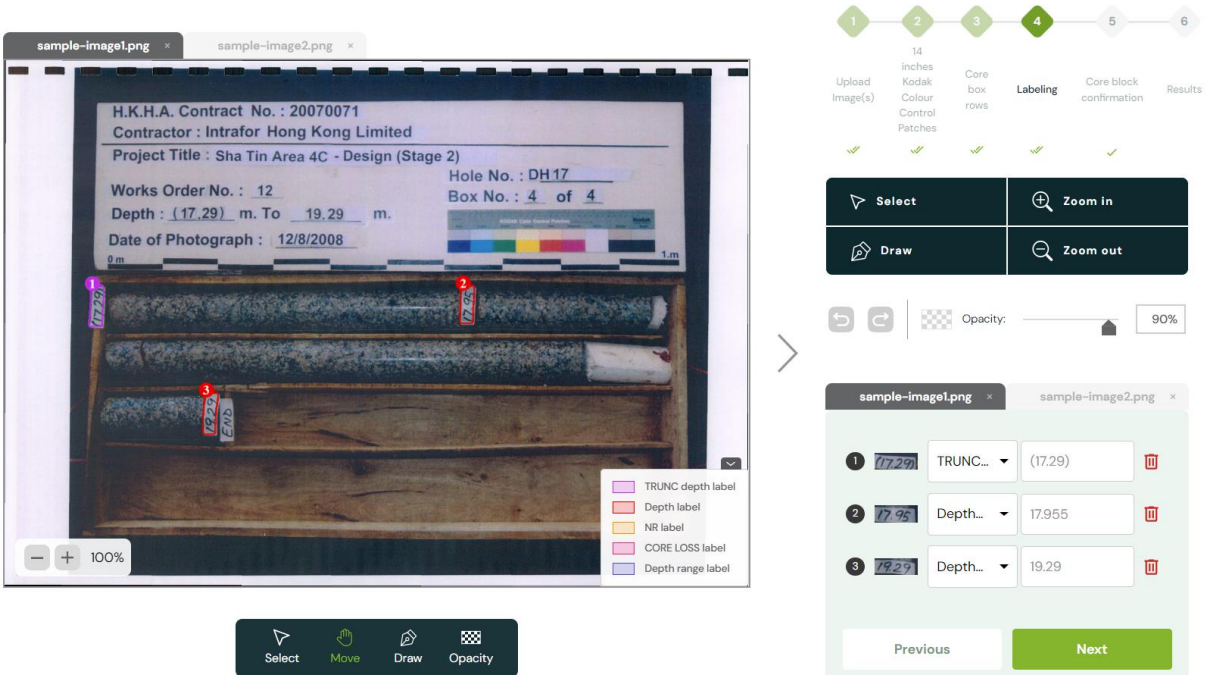


Fig. 6. Automatic identification of depth labels. Depth labels are defined as rectangular white labels displaying depth information or core conditions. The model was trained to identify a variety of hand-written depth labels, as explained below. (1) 'depth label' indicates a depth which refers to the start or end of a core run. (2) 'END label' represents the end of a drillhole. This is not required for the calculation. (3) 'CONTD label' represents that the rock core from the drillhole was put into multiple drill core trays and the drill core tray in the image only shows a portion of the drillhole. This is not required for the calculation. (4) 'TRUNC label' indicates a depth, without any specific implication. The system depends on 'TRUNC label' solely to determine the truncation of the core. (5) 'NR label' represents a section

with no recovery. (6) ‘unrelated label’ represents labels without any specific useful information to the calculation. This is not required for the calculation. Although the model can recognize 'unrelated label', it is suggested not to include them in the image. (7) ‘CORE LOSS label’ contains the same meaning as ‘NR label’, which represents a section with no recovery. (8) ‘depth range label’ indicates a range of depth which is usually used in pair with ‘CORE LOSS label’ or ‘NR label’ to indicate the no recovery range.

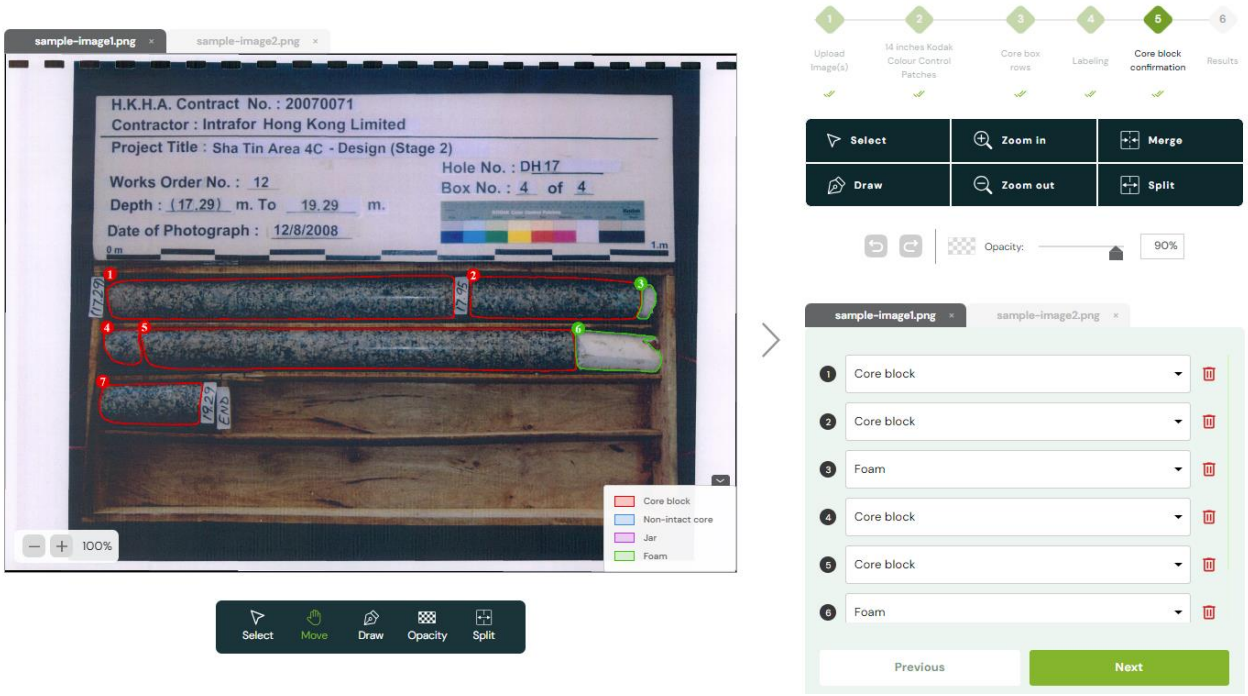


Fig. 7. Automatic identification of object types (core block, non-intact core, jar, foam).

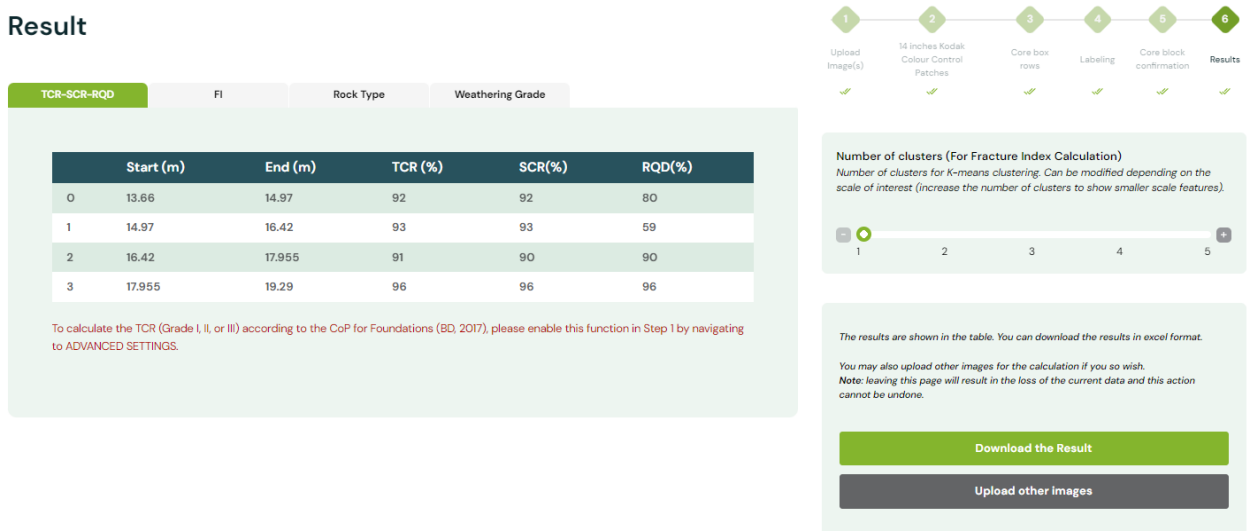


Fig. 8. Displaying results of TCR, SCR and RQD at different depths in a table format.

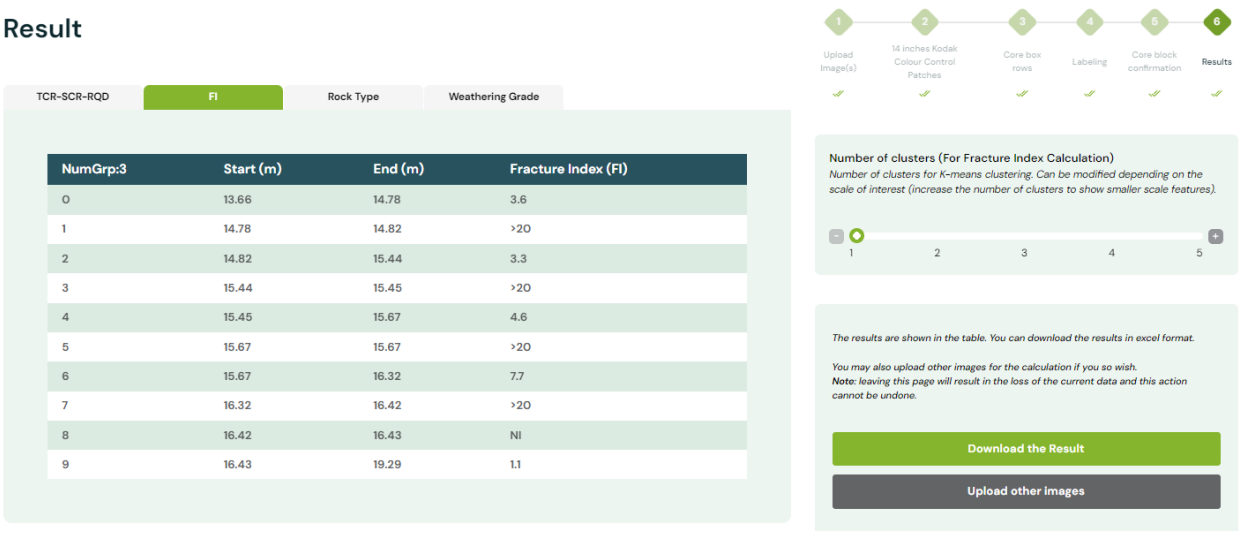


Fig. 9. Displaying results of FI (fracture indice) at different depths in a table format.

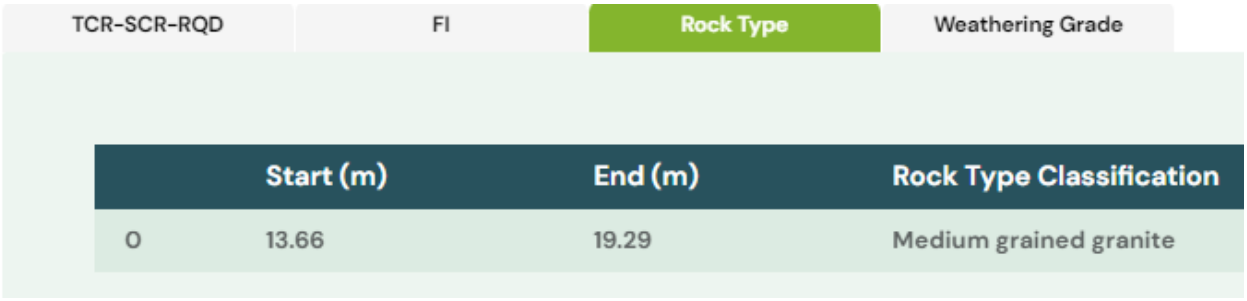


Fig. 10. Displaying results of rock type(s).

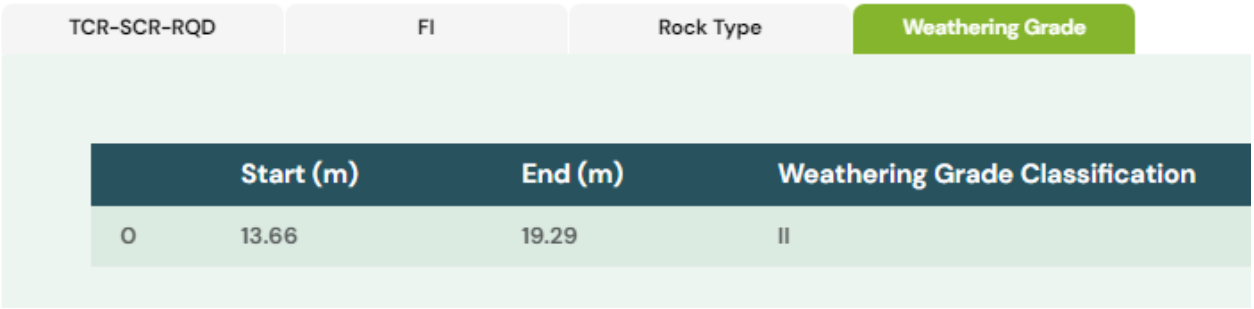


Fig. 11. Displaying results of weathering grade(s).

4 LIMITATIONS

PreLogging is a pioneering tool developed in Hong Kong to aid the ground investigation industry with logging and interpreting borelogs for the civil engineering community. In addition to core logging professionals, potential users of this tool encompass site foreman, structural engineers, civil engineers and project managers. To ensure the efficient and effective usage of PreLogging, it is crucial to acknowledge its limitations and assumptions:

1. PreLogging relies on user-uploaded corebox photographs obtained from ground investigation works in Hong Kong. Currently, the tool is not developed to handle non-corebox images or those taken outside of Hong Kong at present.
2. The predictions and calculations provided by PreLogging are not infallible. As with many AI-powered tools, users must exercise discretion when interpreting and applying the results, as they may

not be entirely accurate. This consideration is particularly critical since PreLogging's underlying principles are based on vision-oriented AI techniques applied to 2D photographs, inherently limiting predictions for concealed or unexposed features. It is important to note that PreLogging is not an X-ray tool with see-through capabilities. Nevertheless, the tool is sensitive to changes in rock types within corebox photographs. Although rock type predictions are not entirely accurate, the results can alert personnel to potential geological changes and problematic areas.

3. PreLogging has been trained using corebox photographs with varying quality levels. However, the system's performance may be compromised if the input images are of extremely poor quality, such as being blurry or having substandard content. It is essential to provide clear and accurate images for optimal results.

5 CONCLUSIONS

In conclusion, the development of PreLogging, a web-based application, has demonstrated the potential for AI and deep learning technologies to improve the accuracy, objectivity, and productivity of rock core logging and log checking processes in the geotechnical engineering field. By leveraging computer vision and AI algorithms, the application is capable of classifying common Hong Kong rocks and decomposition grades, identifying fractures, and computing fracture state indices such as TCR, SCR, RQD, and FI. The collaborative effort between researchers, engineers, and industry stakeholders has proven valuable in ensuring the application meets the requirements of the industry. However, it is important to recognize the limitations of PreLogging, such as its current inability to handle non-corebox images or those taken outside of Hong Kong, and its dependence on user-uploaded corebox photographs. The predictions and calculations provided by the tool may not be infallible, and users should exercise caution when interpreting and applying the results. The performance of the system may also be compromised by poor quality input images. Despite these limitations, PreLogging represents a significant step forward in the application of AI technology for geological engineering and has the potential to revolutionize the rock core logging process in Hong Kong.

ACKNOWLEDGEMENTS

This work was supported by the Construction Industry Council [CICR/01/22]. Its contents are solely the responsibility of the authors and do not necessarily represent the official views of the Construction Industry Council. The authors also gratefully acknowledge the support from the General Research Fund (No. 17206822) of the Research Grants Council (Hong Kong). The first author acknowledges the Postgraduate Scholarship from the University of Hong Kong. A portion of the computations was conducted using the research computing facilities offered by Information Technology Services, the University of Hong Kong. Additionally, Morris Chan, Louis Ng, Calvin Wong and Derek Zhou from the Department of Earth Sciences of the University of Hong Kong offered valuable assistance in this project.

REFERENCES

Tse, K.K.C., Wong, L.N.Y., Cheung, S.H. & Yu, L. under review. Advanced Classification of Drill Core Rock Type and Weathering Grade using Detection Transformer-based Artificial Intelligence Techniques. *Journal of Rock Mechanics and Geotechnical Engineering.*

Tse, K.K.C., Wong, L.N.Y., Cheung, S.H. & Yu, L. under preparation. Automatic analysis of total core recovery, solid core recovery, rock quality designation and fracture index using deep learning.

A Showcase to Components Replacement in Existing Steel Flexible Barrier System

W.L. Wong, P. Cheng & K.K. Chan
AECOM Asia Company Limited, Hong Kong

C.Y. Tang
Housing Department, Government of the Hong Kong SAR, Hong Kong

C.E. Choi
The University of Hong Kong, Hong Kong

ABSTRACT

Steel flexible barrier system is commonly adopted as natural terrain hazard mitigation measures for energy absorption of rockfalls from hillside. The conditions and effectiveness of the steel flexible barrier system installed at hillside may deteriorate with time, so maintenance works including replacement of the components may be required. The original supplier for the main components, such as proprietary energy dissipating devices, may be no longer operated in the market, and the replacement of these main components can only be carried out by using similar products from other available suppliers. To check the compatibility of the replacement components with the original steel flexible barrier system, numerical analysis is carried out to analyze whether the performance of the steel flexible barrier system could be maintained after replacing the components. This paper discusses the steps on how to check the conditions of the existing steel flexible barrier system, and the numerical analysis for assessing the compatibility of the replacement components.

1 INTRODUCTION

A steel flexible barrier system was constructed on the natural hillside above a public housing site in 2002. A specialist supplier was engaged for the design, supply and construction of the steel flexible barrier system to mitigate the potential hazards of the small boulders with dimension less than 1m from natural hillside. The steel flexible barrier system acted as a passive protective barrier system to intercept the trajectory of falling, bouncing, and rolling rocks and retain such falls through a controlled process of energy absorption.

Site reconnaissance was conducted recently to review the existing conditions of the steel flexible barrier system, and rusting was observed at some components including wire clips, thimbles, shackles and energy dissipating devices. Minor rusted components could be repaired by application of rust preventive painting, while some severely rusted components, such as energy dissipating devices, could only be replaced. However, the original supplier for these energy dissipating devices was no longer operated in the market. Therefore, an alternative way was to replace them by using similar components of other brands, and so further numerical analysis for assessing the compatibility of new components was considered necessary.

AECOM has reviewed the available suppliers of energy dissipating devices in Hong Kong, with the consideration of the following criteria to find the appropriate energy dissipating devices as replacement:

- Construction feasibility with minimal disturbance to the existing system
- Similar operation and energy release mechanisms
- Availability and extensive implementation in Hong Kong

After the assessment, two brands were identified and considered in the numerical analysis for comparison with the existing system performance.

2 INITIAL CONDITION REVIEW

The site reconnaissance was carried out on the existing steel flexible barrier system in April 2022. To simplify the repairing works proposal, the overall state of the rusted components was classified into 3 categories and the proposed repairing works were shown in Table 1.

Table 1: Proposed Repairing Works for Different Conditions of Rusting

Category	Condition of Rusting	Proposed Repairing Works
Class 0	No rusting	No works
Class 1	Minor rusting	Painting Works
Class 2	Severe rusting	Replacement of components

According to the results of field inspection, energy dissipating devices, wire clips, thimbles and shackles were in Class 2 severe rusting condition. Therefore, replacement was proposed for those components. For the energy dissipating devices, since they were the main components in steel flexible barrier system, further numerical modelling analysis were carried out.

3 RESULTS FROM PREVIOUS DETAILED DESIGN

The detailed design of steel flexible barrier system to mitigate boulder fall hazard was carried out in 2000. The schematic disposition of steel flexible barrier system upon impact is shown as Figure 1.

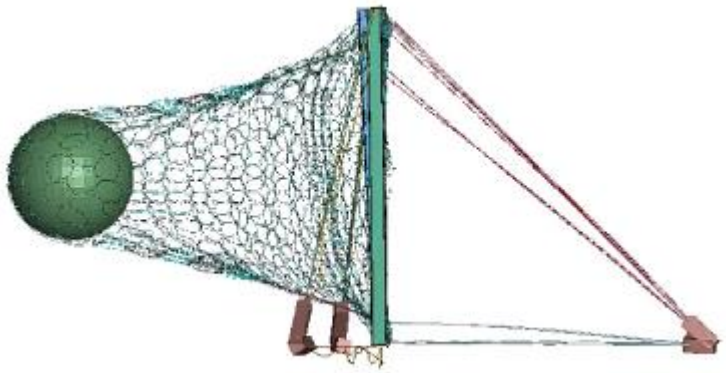


Figure 1: Schematic Deposition of Steel Flexible Barrier System upon Impact

In the design stage, six sections A-A to F-F as shown in Figure 2 were established along the steep slope gradient and significant changes in gradient to represent the most possible and critical boulder flow paths.

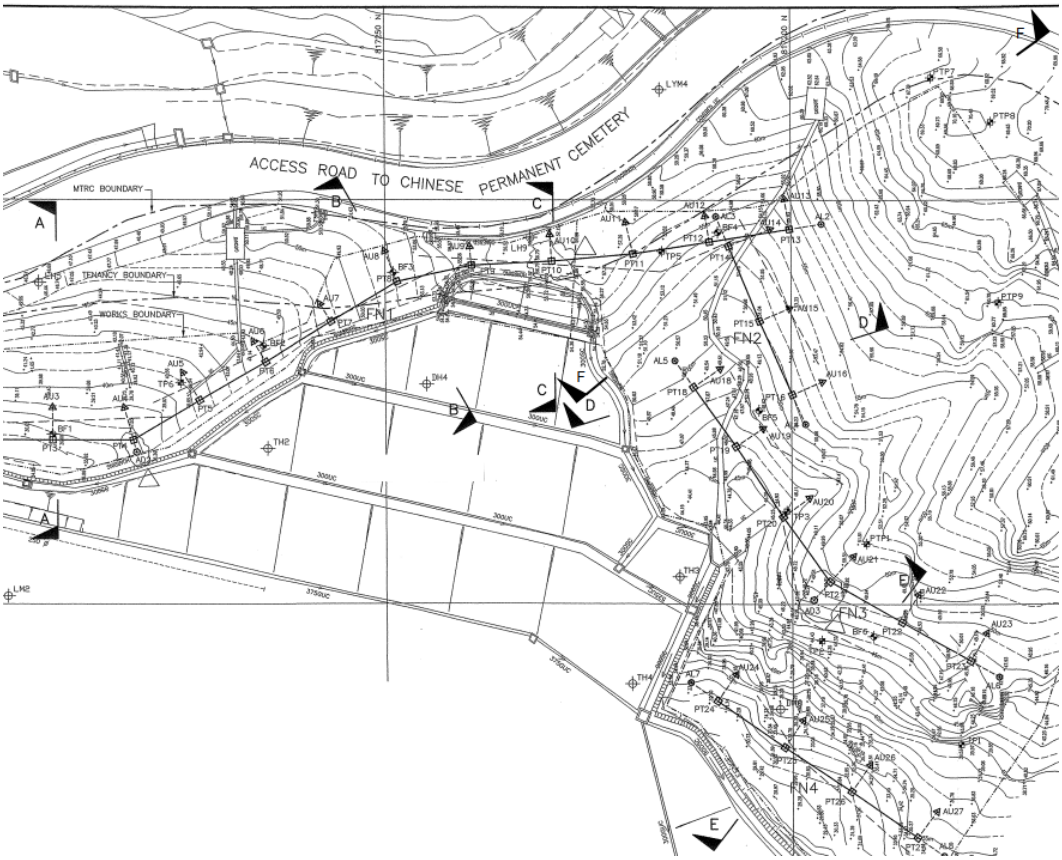


Figure 2: Layout Plan of Natural Hillside with Critical Sections

Two analysis approaches were adopted for finding the maximum kinetic energy and rebounce height:

- In Point Seeder analysis, 300 number of runs were specified at each identified boulder location. One of the six critical sections was analyzed under this approach.
- In Line Seeder analysis, 2000 number of rockfall trials were specified to be randomly over the slope surface to simulate boulder falling at any location along the slope surface. The rockfall behaviours of the six critical sections were analyzed under this approach.

Table 2 summarizes the results computed by the "RocFall" programme for Point Seeder analysis.

Table 2: Point Seeder Analysis Results

Section	Maximum Kinetic Energy (kJ)	Maximum Rebounce Height (m)
E-E	70	1.0

Table 3 summarizes the results computed by the "RocFall" programme for Line Seeder analysis.

Table 3: Line Seeder Analysis Results

Section	Maximum Kinetic Energy (kJ)	Maximum Rebounce Height (m)
A-A	200	3.0
B-B	50	0.5
C-C	100	1.0
D-D	90	1.0
E-E	150	1.0
F-F	700	2.5

The maximum absorption energy of boulder falls at the existing steel flexible barrier system is estimated to be 700kJ based on the "RocFall" program. This value was recommended as the Service Energy Level (SEL) for the steel flexible barrier system.

4 NUMERICAL MODELLING ANALYSIS

In this study, the University of Hong Kong was engaged to use finite-element program LS-DYNA to investigate the response of the steel flexible barrier system under single boulder impact load. Explicit time integration is used to solve the governing equations of mass, momentum and energy conservation for dynamic impact problems involving large deformation. The same numerical model, modelling procedures, and input parameters were adopted as those reported by Koo et al. (2016), which has been validated using field-scale physical data of a rock falling on a flexible barrier as reported by Volkwein (2014).

Figure 2 shows the finite-element model used in this study, which simulates a three-panel segment of the steel flexible barrier system installed at the natural hillside. The barrier is 4-m high and consists of three 10-m wide ring net panels forming the single panel with surface area of 40 m^2. A three-panel configuration was selected to enable comparisons between the design calculations in steel flexible barrier system design report and the full-scale crash tests according to ETAG (2008).

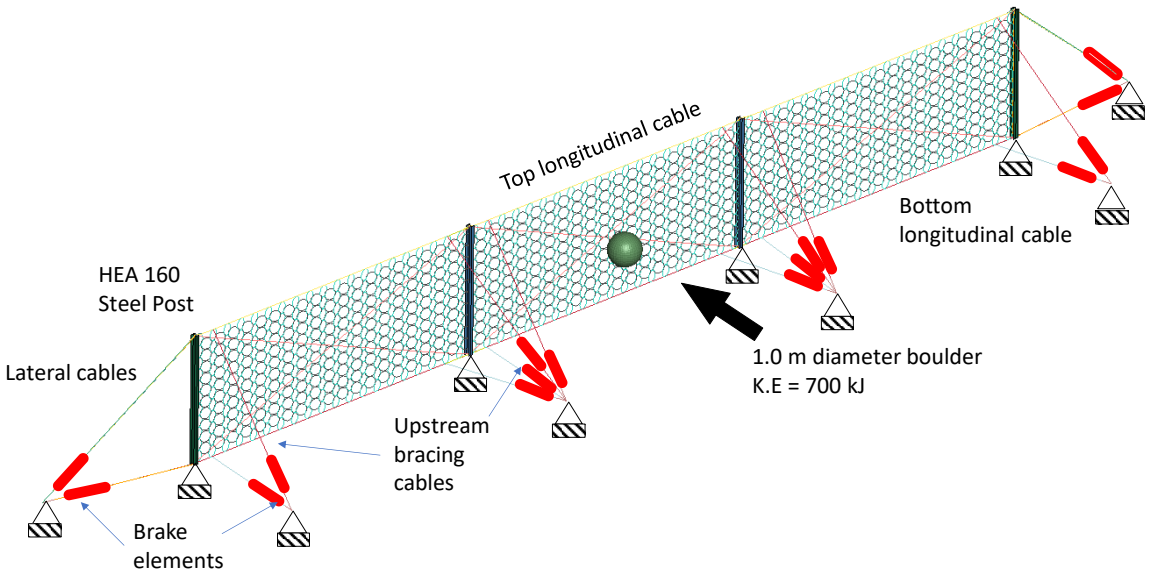


Figure 2: Numerical Model Setup of Steel Flexible Barrier System Oblique 3D with Boulder

The rigid boulder is modelled as a constant stress solid element with reduced integration and hourglass control. The 4-m high steel posts of the barrier were modelled as fully integrated quadrilateral thin shell elements. The steel posts are held in position by upstream and lateral bracing cables anchored to the ground. Longitudinal steel wire ropes running along the top and bottom of the entire barrier are anchored to the ground at both ends of the barrier. Upslope bracing cables are connected via shackles and wire ropes to the top and bottom longitudinal ropes to support the steel posts in their inclined configuration along the slope. Additionally, lateral bracing cables are used to support the steel posts from lateral deflection during impact. All the steel wire rope cables are made of individual wire rope core (IWRC) with yield strength of 1770 MPa. The IWRC steel cable ropes are modelled as resultant beams with cross section integration based on the approach proposed by Reese et al. (2016) to not only capture the axial stiffness but also the bending and flattening behaviour of wire-rope cables.

In a steel flexible barrier system, energy dissipating devices are main components because they limit the peak loads transferred to other barrier components through large elastoplastic deformation. These energy

dissipating devices are typically attached to the main longitudinal cables as well as upstream bracing cables. These devices dissipate energy either by friction, plastic deformation, or a combination of these mechanisms (Castanon-Jano et al., 2017). When subjected to an impact force, these energy dissipating devices are subjected to tensile loading, and they elongate for a long distance at its yield load, thereby gradually absorbing the impact energy and limiting the peak loads. The deformation of the energy dissipating devices also creates an irreversible elongation of the cables, and this further reduces the stiffness of the barrier. Bilinear load-displacement curves were implemented into the finite-element model to simulate the load behavior in Figure 3.

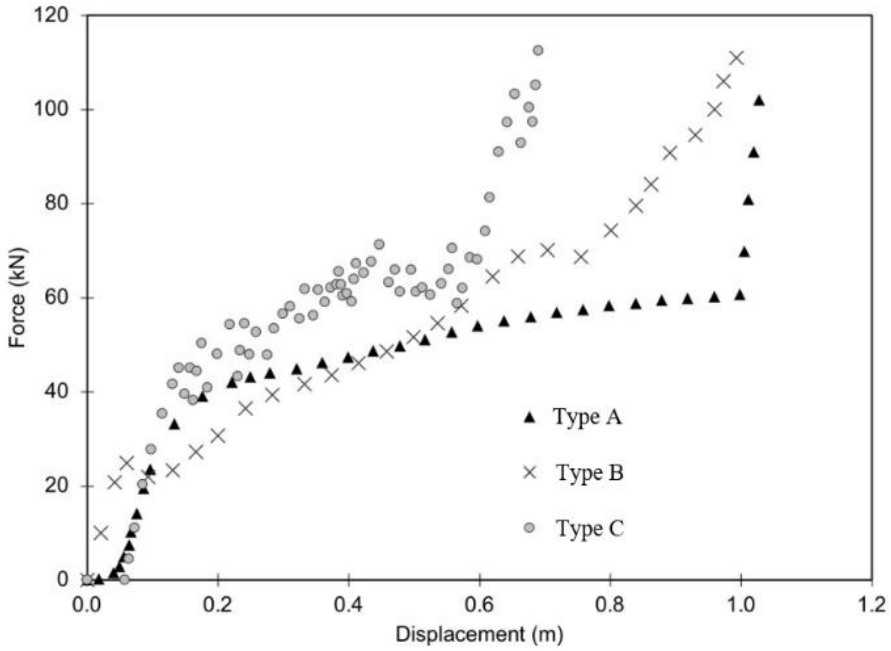


Figure 3: Load-Displacement Curves: (a) Type A - existing energy dissipating device; (b) Type B – Brand A replacement energy dissipating device; and (c) Type C – Brand B replacement energy dissipating device

The interactions between contact surfaces of the rigid boulder and the structural elements are handled using the penalty method discussed by Hallquist (2006). In this approach, the finite-element program searches for intersections between the boulder and the net. It tracks the independent motion of the contacting elements over a small time-step. The penetration of the beam elements into the surface of the boulder results in a normal interface force which is distributed to both elements. The magnitude of this force is proportional to the amount of penetration and is determined using the interface spring stiffness. Furthermore, the sliding of ring nets along the longitudinal wire ropes and lateral cables are modelled using guided cable contact algorithm, which allows frictional sliding of longitudinal rope beam elements along ring net beam nodes.

Based on the detailed design of steel flexible barrier system carried out in 2000, the Maximum Energy Level (MEL) of 1500kJ was selected based on the certified energy absorption capacity for existing steel flexible barrier system. While the impact energy of 700kJ was obtained from the maximum kinetic energy from previous rock fall analysis as the SEL. The input parameters for force and deformation analysis on steel flexible system under MEL and SEL scenarios was shown in Table 4.

Table 4: Summary of Input Parameters

Scenario	Impact Energy (KJ)	Boulder Density (kg/m^3)	Boulder Diameter (m)	Boulder Volume (m^3)	Boulder Mass (kg)	Initial Boulder Velocity (m/s)
MEL	1500	2650	1.5	1.767	4682.94	25.31
SEL	700	2400	1.0	0.524	1256.64	33.37

The computed maximum loads/deformations on each structural member were shown in Table 5.

Table 5: Summary of Simulated Results

Component	From design report	Results in this study using LS-DYNA					
Energy Dissipating Devices	Type A	Type A	Type B	Type C	Type A	Type B	Type C
Impact energy	1545 kJ	1500 kJ	1500 kJ	1500 kJ	700 kJ	700 kJ	700 kJ
Max. deformation	7.0 m	8.1 m	7.7 m	7.7 m	6.2 m	6.2 m	5.6 m
Max. boulder impact force	553 kN	477 kN	591 kN	544 kN	150 kN	276 kN	318 kN
Max. longitudinal cable loads	184 kN	201 kN	200 kN	202 kN	173 kN	119 kN	182 kN
Max. upstream cable loads	145 kN	141 kN	107 kN	145 kN	71 kN	108 kN	101 kN
Max. load on lateral bracing cables	76 kN	125 kN	135 kN	135 kN	94 kN	117 kN	136 kN
Max. load on lateral steel posts	Axial: 208 kN Shear: 137 kN	Axial: 184 kN Shear: 111 kN	Axial: 213 kN Shear: 107 kN	Axial: 256 kN Shear: 120 kN	Axial: 126 kN Shear: 101 kN	Axial: 192 kN Shear: 107 kN	Axial: 185 kN Shear: 104 kN
Max. load on intermediate steel posts	Axial: 132 kN Shear: 137 kN	Axial: 138 kN Shear: 110 kN	Axial: 118 kN Shear: 105 kN	Axial: 244 kN Shear: 101 kN	Axial: 127 kN Shear: 147 kN	Axial: 160 kN Shear: 121kN	Axial: 139 kN Shear: 111 kN

Three conditions for accepting criteria of numerical modelling analysis results were set as below:

- Condition 1: If the results were less than or within 1.2 times of the calculated loads/deformations in design report, it was considered as satisfied condition.
- Condition 2: If the results were more than 1.2 times of the calculated loads/deformations in design report, they were checked against the minimum breaking loads. If the Results were less than the minimum breaking loads, it was considered as satisfied condition.
- Condition 3: If the results were larger than the minimum breaking load / no data specified, they were checked against the structural capacity of each structural member. If the Results were less than the structural capacity, it was considered as satisfied condition.

The results interpretation was summarized in Table 6.

Table 6: Interpretation of Simulated Results

	Satisfied Condition 1	1.2 × From design report	Satisfied Condition 2	Minimum Breaking Load	Satisfied Condition 3	Structural Capacity
Max. deformation	Yes	8.4m	N/A	-	N/A	-
Max. boulder impact force	Yes	663.6kN	N/A	-	N/A	-
Max. longitudinal cable loads	Yes	220.8kN	N/A	-	N/A	-
Max. upstream cable loads	Yes	174kN	N/A	-	N/A	-
Max. load on lateral bracing cables	No	91.2kN	Yes	163 kN	N/A	-
Max. load on lateral steel posts	No	Axial: 249.6 kN Shear: 164.4 kN	No	N/A	Yes	Axial: 1667.11 kN Shear: 327.95 kN
Max. load on intermediate steel posts	No	Axial: 158.4 kN Shear: 164.4 kN	No	N/A	Yes	Axial: 1667.11 kN Shear: 327.95 kN

According to the result of analysis, the magnitude of computed maximum deformation, boulder impact force, longitudinal cable load and upstream cable load were checked satisfied under Condition 1. Although the maximum load on lateral bracing cables exceeded 20%, it was smaller than the minimum breaking loads

specified by the manufacturer, which was also considered as satisfied under Condition 2. For the maximum load on steel posts, no information was found in the previous design report or from manufacturer. Therefore, the structural capacity analysis was carried out, which implied that the loads on the steel posts were satisfied under Condition 3.

In conclusion, the computed loads and deformations were checked satisfied under three accepting criteria, which implied that the replacement components were compatible with the existing steel flexible barrier system. Therefore, repairing the minor rusted components and replacement of the main components, including energy dissipating devices, were thereafter carried out on site.

5 FUTURE INSIGHT

As the experience of energy dissipating devices replacement in a steel flexible barrier system under the new concept in Hong Kong, great challenges were encountered for this project. Ways to classify the severity of rusted components, to ensure the replacement components compatible with the original design requirements, and to supervise the quality and procedures of replacement were the key factors in completing the project.

By collaborating with specialist suppliers and professionals, the more innovative solutions to assess the conditions of existing structures can be discovered. Furthermore, numerical modelling can be implemented by simulating the load-deformation behaviour of the energy dissipating devices to assess the replacement components with equivalent engineering and material properties and structural performance against the original components. Specialist suppliers also offered the on-site demonstration to ensure the acceptance criteria of installation were followed.

This investigation approach helps to improve the maintenance approach for steel flexible barrier system. Also, as the energy dissipating devices were proprietary products, their replacement was limited by the supplier availability. By verification through numerical modelling method, other brands with similar operation and energy releasing mechanism can be used for replacement, which significantly reduces the construction cost and eliminates the risk of supply chain failure, so that maintenance works on rusted steel flexible barrier system in Hong Kong can be promoted on a large scale using similar analysis approach.

6 CONCLUSIONS

According to the recent site reconnaissance of the steel flexible barrier system constructed on the natural hillside above a public housing site, severe rusting on main components were identified. Minor rusting on other components were also identified. Repairing works were recommended including replacement of severely rusted components such as energy dissipating devices and application of rust preventive painting on minor rusted components.

For existing energy dissipating devices with severe rusting, since the original supplier was no longer operated in the market, two other brands were proposed as replacement. After confirmation with the suppliers about the availability, constructability of the replacement components, numerical analysis for assessing the compatibility, serviceability and functionality of the replacement components was conducted. It is concluded that the steel flexible barrier system is checked to have adequate factor of safety with the replaced energy dissipating devices and meet the current geotechnical standards.

ACKNOWLEDGEMENT

The authors gratefully acknowledge the Director of Housing, the Government of the Hong Kong Special Administrative Region, for permission to publish this paper.

REFERENCES

Castanon-Jano, L., Blanco-Fernandez, E., Castro-Fresno, D. & Ballester-Muñoz, F. (2017). *Energy dissipating devices in falling rock protection barriers*. Rock Mech Rock Eng 50, No. 3, 603-619.

ETAG, E. (2008). *027-Guideline for the European Technical Approval of Falling Rock Protection Kits*. EOTA: Brussels, Belgium.

Hallquist, J. O. (2006). *LS-DYNA theory manual*. Livermore Software Technology Corporation *3*, 25-31.

Koo RCH Kwan JSH Lam C Ng CWW Yiu J Choi CE Ng AKL Ho KKS Pun WK (2016). *Dynamic response of flexible rockfall barriers under different loading geometries*. Landslides 14(3):905-916

Reese, L., Qiu, T., Linzell, D. & Rado, Z. (2016). *Field-scale testing and numerical investigation of soil-boulder interaction under vehicular impact using FEM and coupled FEM-SPH formulations*. Int. J. Protect. Struct. 7, No. 1, 77-99.

Volkwein A (2004) *Numerical simulation of flexible rockfall protection systems*. PhD thesis, ETH Zürich, Switzerland, 134 p (in German)

The Pathway to Decarbonisation in LPMitP: Carbon Management Framework

Ryan Yan, Ashley Cheng, David Mak, Thomas Tang, Kenny Yau & Martin Lee
AECOM Asia Co. Ltd., Hong Kong SAR

Yan Tse, Roy Hung, Florence Chu, Jonathan Lau & Natalie Yim
Geotechnical Engineering Office, Civil Engineering and Development Department, Hong Kong SAR

ABSTRACT

In the 2020 Policy Address, the Chief Executive announced that Hong Kong would strive to achieve carbon neutrality before 2050. All stakeholders of the society should take the initiative to work towards this goal. The Landslip Prevention and Mitigation Programme (LPMitP), being a rolling programme, has a role to play in reducing carbon emissions and to exemplify low-carbon practices for geotechnical works. This paper briefly introduces the key concepts of an ongoing framework study on the carbon management of LPMitP, including an introduction of relevant international guidance documents, a review of carbon reduction targets and policies in Hong Kong and some selected countries, the applicability on LPMitP of a commonly adopted carbon management framework possessing the whole life cycle approach, and the philosophy and methodology to establish a carbon baseline intensity of LPMit works. The challenges and opportunities of decarbonisation are identified. With this paper serving as the first episode of disseminating the carbon management study in LPMit works, updates on the study will follow as the journey continues.

1 INTRODUCTION

1.1 Background

Climate change refers to the long-term shifts in temperature and weather patterns (UN 2024). While such shifts can be natural; yet human activities in the past two centuries are well considered to have accelerated climate change. It is generally believed that there is an inevitable linkage between climate change and greenhouse gases (GHGs) concentrations in the Earth's atmosphere which have been significantly increased due to the burning of fossil fuels to boost industrialisation and urbanisation. According to the European Union, the global GHG emissions reached 53.8 Gt-CO2e in 2022, which is 1.4% higher than 2021 and 45.4% higher than 2000 (Crippa et al 2023). The average global temperature on Earth has increased by 1.1°C since the pre-industrial age (NASA 2024). Most of the warming has occurred since 1975 at a rate of about 0.2°C per decade. The impacts of climate change are already being felt around the world from the increase in the intensity and frequency of extreme weather events, including heatwaves, tropical cyclones, flooding and torrential rains which lead to landslides, wildfires, flooding, famines and climate migrations. These subsequently cause physical, social and economic damages. Climate change has been identified as one of the greatest challenges facing the world and will continue to affect us in the future. This drives a growing demand for actions on mitigating climate change. Many of the actions fall into the category of decarbonisation.

In the 2020 Policy Address, the Chief Executive announced that Hong Kong would strive to achieve carbon neutrality before 2050. Hong Kong's Climate Action Plan 2050, published in 2021, set a target to reduce Hong Kong's total carbon emissions by 50% against the 2005 level before 2035. All stakeholders of the society should take the initiative to work towards these targets. The Landslip Prevention and Mitigation Programme

(LPMitP) is no exception. Being a rolling programme with annual output target of upgrading 150 government man-made slopes and implementing risk mitigation works for 30 natural hillside catchments across the territory, the LPMitP has clearly a role to play in reducing carbon emissions and to exemplify low-carbon practices for geotechnical works.

1.2 Carbon management

Carbon management focuses on the identification, quantification, reduction, and removal of carbon dioxide (CO_2) and other GHG emissions from various sources. It aims to (1) achieve a net reduction in CO_2 and GHG emissions by implementing innovative technologies, adopting sustainable practices and fostering interdisciplinary collaboration, (2) promote the transition to a low-carbon economy and (3) create sustainable legacies to *meet the needs and aspirations of the present without compromising the ability of future generations to meet their own needs* (WCED 1987).

1.3 Objectives of the study

This paper briefly introduces an on-going carbon management framework study partnering between the Geotechnical Engineering Office (GEO) of the Civil Engineering and Development Department (CEDD) of the Hong Kong Special Administrative Region (HKSAR) Government and AECOM. The main aims of the study include:

- determine the baseline carbon intensity of current LPMit works,
- recommend practical carbon emissions reduction targets for LPMitP,
- develop and implement decarbonisation measures, and
- formulate the strategy roadmap to realise the carbon emissions reduction targets, thus achieving sustainability in the LPMitP.

While the study is still at its early stage, this paper focuses on presenting an overview of the study attempting to show the geotechnical practitioners different ingredients of the study and to illustrate how a sustainable LPMitP can be achieved via a holistic appraisal of the carbon management of LPMit works.

1.4 Layout of the paper

A brief review will first be provided to highlight some international guidelines and standards which are often referred to when implementing carbon management. The policies and targets of reducing carbon emissions in Hong Kong and some selected countries will be presented to offer the vision and driving engine of the study. A carbon management framework will then be presented illustrating the best practice of the carbon management, how a carbon baseline intensity of LPMit works could be formulated and decarbonisation measures suitable for LPMit works.

2 INTERNATIONAL GUIDELINES AND STANDARDS

The carbon footprint reduction polices, standards, practices and targets related to the construction industry of some selected countries have been reviewed. There are some international policies and standards that are widely referred to or followed by the industries of countries in the endeavour of carbon management, e.g., the Paris Agreement by the United Nations Framework Convention on Climate Change (UNFCCC), ISO 14064-1 (2018), ISO 14064-2 (2019), ISO 14064-3 (2019), PAS 2060 (2014), PAS 2080 (2023), GHG Protocol (www.ghgprotocol.org), etc.

The Paris Agreement, first adopted on 12 December 2015 at the 21st meeting of the Conference of the Parties (COP21), is an agreement within the UNFCCC dealing with the mitigation, adaptation and finance of GHG emissions. The Paris Agreement aims to strengthen the global response to the threat of climate change by keeping a global temperature rise this century well below 2°C above pre-industrial levels and to pursue efforts to limit the temperature increase even further to 1.5°C. As of today, 197 countries and the European Union (EU), representing vast majority of global GHG emissions, have ratified or acceded to the Agreement (UNTC

2024). This includes China and the United States of America (USA) which are two largest GHG emissions country in the world. According to the JRC Science for Policy Report on GHG Emissions of All World Countries (Crippa et al. 2023), China contributed 29.2% while the USA contributed 11.2% of global GHG emissions in 2022. In accordance with the Basic Law of the HKSAR, the Paris Agreement also applies to the HKSAR (UNTC 2024).

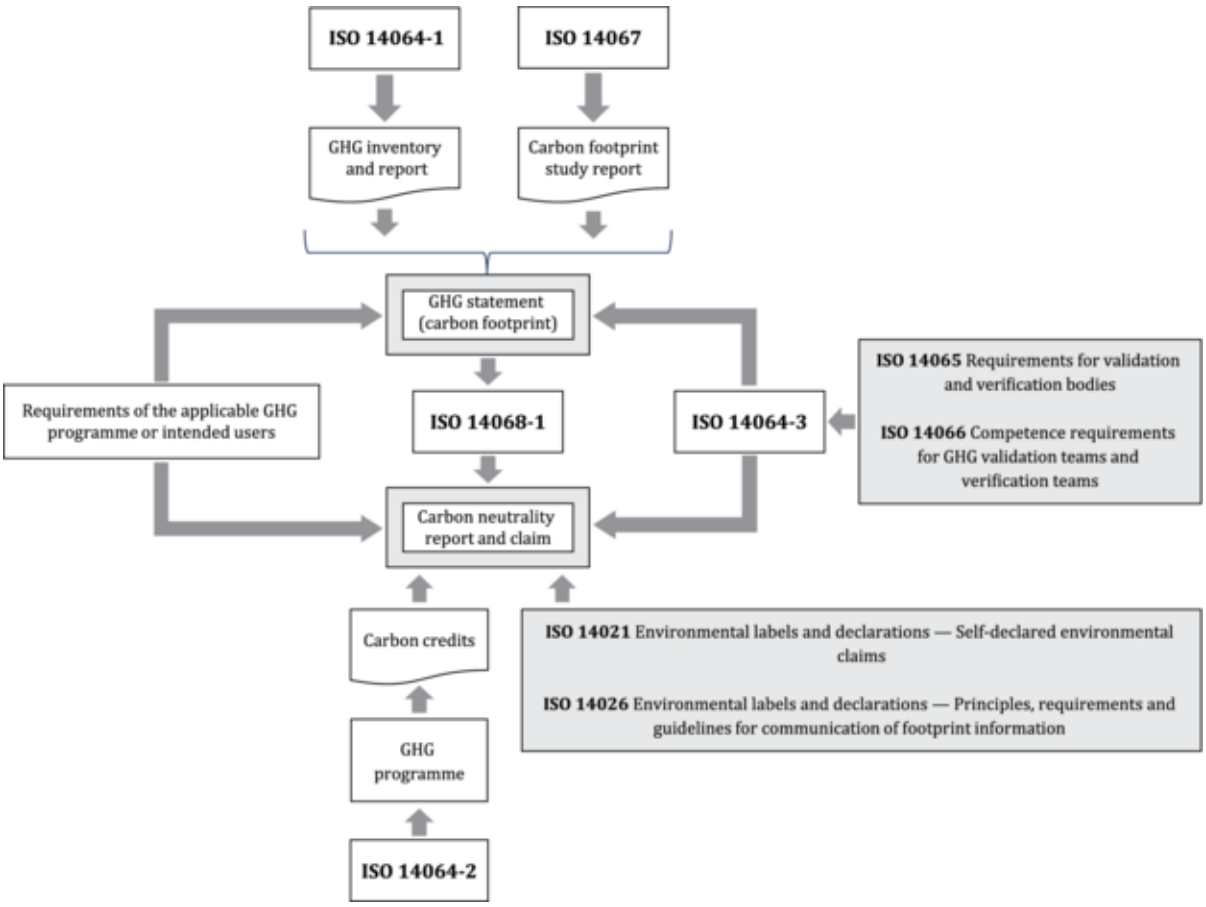


Figure 1: ISO 14068-1 in relation to other International Standards (extracted from ISO 14068-1 (2023))

There are 17 standards published by the ISO/TC207 Subcommittee 7 on greenhouse gas and climate change management and related activities. ISO 14064-1 (2018) provides detailed principles and requirements for designing, developing, managing and reporting organisation-level GHG inventories which includes the requirement for determining GHG emissions and removal boundaries, quantifying an organisation's GHG emissions and removals and identifying specific company actions or activities aiming to improve the GHG management. It also includes the requirements and guidance on inventory quality management, reporting internal auditing and the organisation's responsibilities in verification activities. ISO 14064-2 (2019) details principles and requirements for determining baselines, and monitoring, quantifying and reporting of project emissions. It focuses on GHG projects or project-based activities specifically designed to reduce GHG emissions and/or enhance GHG removals. It provides the basis for GHG projects to be verified and validated. ISO 14064-3 (2019) details requirements for verifying GHG statements related to GHG inventories, GHG projects and carbon footprints of products. It describes the process for verification or validation, including verification or validation planning, assessment procedures, and the evaluation of organisational, project and product GHG statements. ISO 14064 is a well-known GHG accounting framework.

PAS 2060 (2014) is a specification describing how to demonstrate carbon neutrality by a four-stage process: measurement, reduction, offsetting and documentation. It sets out the requirements for quantifying, reducing and offsetting GHG emissions for organisations and products. It is worthy to note that ISO 14068-1 (2023)

was published in November 2023. It provides principles, requirements and guidance for achieving and demonstrating carbon neutrality. It focuses on quantifying, reducing and offsetting carbon footprints, utilizing a hierarchical approach prioritising direct and indirect GHG emission reductions and removal enhancements within the value chain over offsetting. PAS 2060 (2014), therefore, will be withdrawn from use on 20 November 2025. Figure 1 shows the relationships among ISO14068-1 (2023), ISO 14064 family and other related ISO documents.

PAS 2080 (2023) presents a framework looking at the whole value chain aiming to reduce carbon and reduce cost through more intelligent design, construction and use (Figure 2). It ensures carbon is consistently and transparently quantified at key points in infrastructure delivery which promotes sharing of data along the value chain.

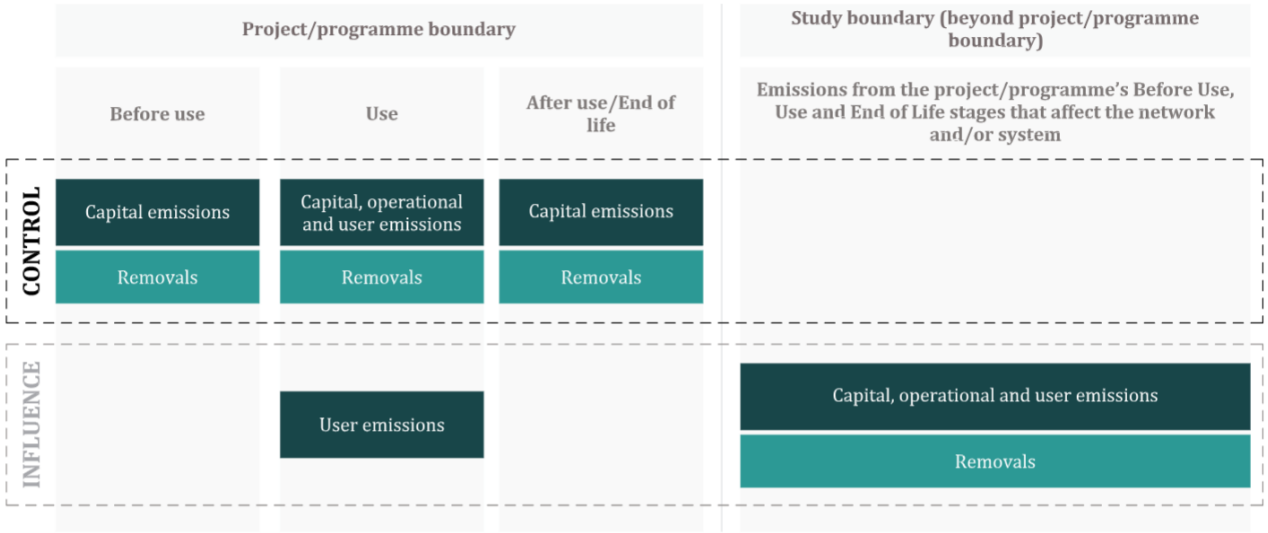


Figure 2: PAS 2080 whole life carbon framework for decision-making (extracted from PAS 2080 (2023))

GHG Protocol, with the joint efforts made by the World Resources Institute (WRI) and the World Business Council for Sustainable Development (WBCSD), provides standards, guidance, tools and training for private and public sector operations to measure and manage GHG emissions (www.ghgprotocol.org). GHG Protocol is another commonly known GHG accounting framework. The GHG Protocol Corporates Standard classifies a company's GHG emissions into three scopes. Scope 1 emissions are direct emissions from owned or controlled sources, e.g., operation of company-owned equipment. Scope 2 emissions are indirect emissions from the generation of purchased energy, e.g., purchased electricity. Scope 1 and 2 are related to company operations. Scope 3 emissions are all indirect emissions, apart from Scope 2, that occur in the value chain (i.e., entire business model) of the company/organisation, including both upstream and downstream emissions, e.g., waste generated in operations, employee commuting, construction, etc.

The ISO 14064 standards and the GHG Protocol are largely overlapping. However, there are some differences which should be highlighted. First, the GHG Protocol constitutes a voluntary standard while the ISO 14064 standards can be used for certification purposes. Second, the GHG Protocol methodology is often adopted by governments, NGOs and other organisations while ISO 14064 standards are mostly used by industrial enterprises. There are also minor differences regarding the setting of organisational boundaries and calculation methods in these two methodologies.

3 TARGETS AND POLICIES

3.1 Carbon reduction target

Hong Kong, the UK, Singapore and Australia have set the long-term target of achieving carbon neutrality or net zero emissions by 2050 while Mainland China has set the same national target to be reached by 2060. Hong Kong has set the regional target to reduce its carbon emissions by 50% against the 2005 level before 2035. The UK has set a series of interim targets and milestones before 2050 that gives a clear descending curve of GHG emissions against time. Singapore targets to reduce carbon emissions to about 60 Mt-CO2e in 2030.

The UK has also set the target of zero avoidable waste in construction sector by 2050. China has published energy efficiency targets for the cement industry and reduce-reuse-recycle targets for construction waste. However, the corresponding progress has not yet been published. Australia has published the progress of GHG emission reduction in the construction sector and in cement industry. However, no carbon reduction targets in the construction sector have been published. It is worth noting that neither carbon emissions target nor progress of the construction sector in Hong Kong or Singapore has been announced.

3.2 Action plans

To understand the regulatory drivers of carbon management, three types of policies and standards are considered as highly relevant to this study. They are:

- National action plans for carbon emission management,
- Action plans, guidelines and standards for low-carbon construction, and
- Design and construction standards for slope upgrading works.

Table 1: List of selected climate action plans

City / Country	Action Plan	Remarks	Link
Hong Kong	Hong Kong's Climate Action Plan 2050	Published in October 2021	https://www.eeb.gov.hk/sites/default/files/pdf/cap_2050_en.pdf
Mainland China	China Action Plan for Carbon Dioxide Peaking Before 2030	Published in October 2021	http://english.scio.gov.cn/topnews/2021-10/27/content_77835815.htm
The United Kingdom (UK)	The Climate Change Act 2008	Became law in November 2008	https://www.legislation.gov.uk/ukpga/2008/27/contents
	Industrial Decarbonisation Strategy	Published in March 2021	https://www.gov.uk/government/publications/industrial-decarbonisation-strategy
	Carbon Budgets	Last updated in July 2021	https://www.gov.uk/guidance/carbon-budgets#setting-of-the-fourth-carbon-budget-2023-2027
	UK Net Zero Strategy: Build Back Greener	Last updated in April 2022	https://www.gov.uk/government/publications/net-zero-strategy
	Decarbonising Transport: A better, Greener Britain	Last updated in January 2023	https://www.gov.uk/government/publications/transport-decarbonisation-plan
Singapore	Mitigation Efforts on National Climate Change Secretariat	Website	https://www.nccs.gov.sg/singapores-climate-action/mitigation-efforts/overview/
	Charting Singapore's Low-Carbon and Climate Resilient Future	Published in April 2020	https://www.nccs.gov.sg/files/docs/default-source/publications/nccsleds.pdf
Australia	Australia's Long-Term Emissions Reduction Plan, A whole-of-economy Plan to Achieve Net Zero Emissions by 2050	Last updated in October 2021	https://www.dcceew.gov.au/sites/default/files/documents/australias-long-term-emissions-reduction-plan.pdf

Table 1 summarises a list of climate action plans from Hong Kong and some selected countries. In 2021, the HKSAR Government announced the Hong Kong's Climate Action Plan 2050. The plan sets the vision of "Zero-carbon Emissions-Liveable City-Sustainable Development" and outlines four major decarbonisation strategies, namely (1) net-zero electricity generation, (2) energy saving and green buildings, (3) green

transport; and (4) waste reduction, which would lead Hong Kong towards the goal of carbon neutrality before 2050. The Government plans to allocate about 240 billion Hong Kong Dollars in next 15 to 20 years to implement climate mitigation and adaptation measures.

China sets ten key tasks to advance actions on carbon dioxide peaking including actions for:

- green and low-carbon energy transition,
- energy saving, carbon emission mitigation and efficiency improvement,
- peaking carbon dioxide emissions in industry sector,
- peaking carbon dioxide emissions in urban-rural development area,
- promoting green and low-carbon transportation,
- promoting circular economy in carbon mitigation purpose,
- advancing green and low-carbon technology innovation,
- consolidating and enhancing carbon sink,
- green and low-carbon society, and
- promoting all regions to peak carbon dioxide emissions hierarchically and orderly.

In the UK, the Climate Change Act 2008 is a legal document which sets a framework for the country to reduce GHG emissions and build capacity to adapt and strengthen resilience to climate risks. The original Act committed the UK to cut its emissions by at least 80% against the 1990 level by 2050. In 2019, the target was amended. The UK now commits the target of net zero emission by 2050. Some of the devolved states have their own policies and targets. For example, Scotland is committed to achieve a net zero target by 2045. The UK is the first country to set legally binding carbon budgets. The budget places a restriction on the total amount of GHGs that the UK is allowed to emit over a 5-year period. The first six carbon budgets cover the period from 2008 to 2037. It implies that every tonne of GHGs emitted between now and 2050 will count and an emission rise in one sector would require a reduction in other sectors. The fourth carbon budget covers from 2023 to 2027 with 1,950 metric tonne CO_2 equivalent (Mt-CO2e), which corresponds to a 52% cut from the 1990 level.

Singapore has committed to achieve net zero emissions by 2050. Four key thrusts are used to accelerate the low-carbon transition for industry, economy, and society. They are:

- catalysing business transformation,
- investing in low-carbon technologies,
- pursuing effective international cooperation, and
- adopting low-carbon practices.

The thrusts are supported by a carbon tax policy, which is the first carbon pricing scheme in Southeast Asia, implemented on 1 January 2019. The carbon tax will increase from five Singapore Dollars per tonne CO_2 equivalent (i.e., S$5/t-CO2e) between 2019 and 2023, to tentatively S$50-80/t-CO2e by 2030.

Australia plans to achieve net zero emissions by 2050 based on five key principles. They are:

- technology not taxes,
- expand choices, not mandates,
- drive down the cost of a range of new energy technologies,
- keep energy prices down with affordable and reliable power, and
- be accountable for progress.

The prioritised essential low emission technologies are clean hydrogen, ultra low-cost solar, energy storage for firming, low emission steel, low emission aluminium, carbon capture and storage and soil carbon. The Australian Government is expected to invest at least 20 billion Australian Dollars to advance low emissions technologies from now to 2030.

3.3 Low-carbon construction

Hong Kong's Climate Action Plan 2050 promotes the environmental perspective in planning for new development areas and urban renewal projects to reduce embodied carbon emissions during the construction process, such as the use of Modular Integrated Construction (MiC) method and electrified machinery.

The Mainland China Government promotes the reduction in using high-carbon construction materials and increase in adopting low-carbon materials including new low-carbon cementitious materials, carbon-sequestration mineral materials and new cementitious materials made from solid wastes. The Government also promotes factory-based precision processing and refined management of building materials to reduce the waste rate of building materials on construction sites by 20% by 2030 against the 2020 level. Besides, the Government also encourages energy-saving construction equipment, energy consumption monitoring of key equipment, and group control management for multiple similar equipment. Furthermore, it prioritises the selection of building material products that have obtained the green building certification and supports the centralisation treatment and graded utilisation of construction wastes.

The UK Government supports the decarbonisation of intermediary industrial products such that the supply chain is gradually supplied with green materials which in turn produces greener final products. The UK Government encourages consumers to make informed choices about the environmental impact of products, so to create pressure feeding upwards to encourage greener purchases throughout the supply chain. It is expected that an annual saving from resource efficiency and material substitution in manufacturing and construction, mostly in cement manufacturing, is 9 Mt-CO2e by 2050. A Timber in Construction Road Map is under planning which promotes the safe use of timber in construction improving carbon capture. Besides, the Low Carbon Concrete Routemap has set out currently available methods of reducing carbon in concrete.

In Singapore, a Green Mark Certification Scheme was launched in 2005 as an initiative to drive Singapore's construction industry towards more environmentally friendly buildings. It is a benchmarking scheme to promote sustainability in the built environment and to raise environmental awareness among developers, designers and builders. The builders are encouraged to use recycled and sustainable materials for non-structural applications, e.g. precast drains, precast road kerbs and wheel stoppers. Solar cells and biodiesel can be used instead of diesel fuels. Besides, the builders are recommended to connect to AC power grids for power supply whenever feasible.

In Australia, Infrastructure Australia is the Australia's independent infrastructure advisor to share knowledge, promote good practice and facilitate collaboration and leadership. It undertakes research and provides advice to the government, industry and community on the infrastructure investment and reforms that will benefit Australians. The 2021 Australian Infrastructure Plan is a practical and actionable roadmap for infrastructure reform. There are 20 recommendations in the Plan, focusing on nine key areas including transport, energy, water and waste.

3.3 Design and construction of slope upgrading works

In Hong Kong, greening of engineered slopes is recommended while vegetation on man-made slopes helps erosion control and serves landscape functions. Guidance for vegetative protection measures is provided in the Geotechnical Manual for Slopes (GEO 2011a). GEO (2011b) presents guidance on good practice of landscape treatments for man-made slopes and engineering works on natural terrain in Hong Kong. On one hand, the role of vegetation on slope stabilisation via complex hydromechanical interaction might be difficult to quantify and be approved in conventional engineering design. On the other hand, the presence of vegetation as a carbon offset over the whole life of the engineered slopes appears attractive from the perspective of carbon management. However, the contribution of each of the commonly adopted slope greening plant species to carbon offset is yet to be quantified.

In Mainland China, the Code for Design of Landslide Stabilisation stipulates the applicability of plant protection engineering which can be used for landscaping. Similar to Hong Kong, engineering design on slope stability should not rely on the potential beneficial effects from vegetation.

4 CARBON MANAGEMENT FRAMEWORK

4.1 Appraisal of carbon management in LPMit works

In 2010, the GEO launched a rolling LPMitP to systematically manage landslide risk associated with both man-made slopes and natural hillsides. Under the LPMitP, the most deserving man-made slopes and natural hillside catchments are selected each year in accordance with a risk-based priority ranking system for further study. The necessary landslip prevention and mitigation works for man-made slopes and natural hillside catchments under Government's maintenance responsibility are implemented under the LPMitP. The target annual outputs of the LPMitP are to: (1) upgrade 150 government man-made slopes, (2) conduct safety-screening studies for 100 private man-made slopes, and (3) implement risk mitigation works for 30 natural hillside catchments (CEDD 2024a). As of 1 March 2024, there are 32 active LPMit works contracts (CEDD 2024b). A brief overview of LPMit works from the perspective of carbon management would identify the major sources of carbon emissions and thus in turn would help to produce a practical decarbonisation strategy. Table 2 summarises a list of major engineering works which are commonly conducted in LPMit works. By examining the construction of each feature, the associated carbon emissions can be quantified. For instance, the construction of soil nails involves materials such as steel and cement grout, site operation such as drilling and formwork construction for soil nail heads.

Table 2: Commonly conducted engineering works in LPMit works

Man-made slopes	Natural hillside catchments
Soil nailing	Flexible barrier
Retaining wall	Rigid barrier, e.g., gabion barrier, concrete barrier
Soil replacement	Deflection structure
Soil compaction	Boulder fence
Surface and subsurface drain	Rock bolt
Surface protection	
Landscaping	

It is expected that most of the carbon emissions would have happened during the construction stage of LPMit works (i.e., embodied carbon). In Hong Kong's slope engineering practice, most of the slope upgrading/stabilisation measures possess low maintenance requirement. In other words, the operational carbon of LPMit works is low when compared to other civil engineering structures such as buildings, tunnels and highways. Furthermore, greening of slopes by vegetation offers an opportunity to offset the embodied carbon. Therefore, it would be crucial to quantify the contribution of slope greening in the carbon management of LPMit works.

4.2 Best practice of carbon management

BS EN 17472 (2022) outlines carbon assessment methodology by establishing the requirements and specific methods for the assessment of environmental, economic and social performance of a civil engineering works while taking into account the civil engineering works' functionality and technical characteristics. The assessment of environmental and economic performance of a civil engineering works is based on the Life Cycle Assessment (LCA), Life Cycle Cost (LCC), Whole-Life Cost (WLC) and other quantified environmental and economic information. The approach to the assessment covers all stages of the civil engineering works life cycle and includes all civil engineering works related construction products, processes and services, used over its life cycle. Figure 3 shows the organisation of the different information modules used for reporting the assessment of the civil engineering works.

In this modular approach, Module A0 covers all the pre-construction stages (Figure 3) including, for example, planning costs, land costs and tax incurred. In general, all costs and impacts before the tender may be included in Module A0. Modules A1 to A3 cover the cradle-to-gate processes for materials and services used in the construction, e.g., the production of steel bar for the construction of soil nails in a slope (i.e., the product stage). Module A1 includes fuel, electricity, direct emissions from extraction and production of raw materials

such as cement, recycled waste, additives, etc. Module A2 includes transportation of the materials. An example would be the fuel consumption to transport materials to the manufacturing plant. Module A3 includes the carbon emissions in the manufacturing process of materials, such as mixing, packaging, curing, etc. Modules A4 and A5 cover carbon emissions associated with construction activities. Module A4 covers the transportation of materials and products from the factory gate to the works site, e.g., the transportation of concrete to the construction site. Module A5 covers the construction/installation process at site including ground works and landscaping, storage of products and transport of persons and construction equipment to and from the site.

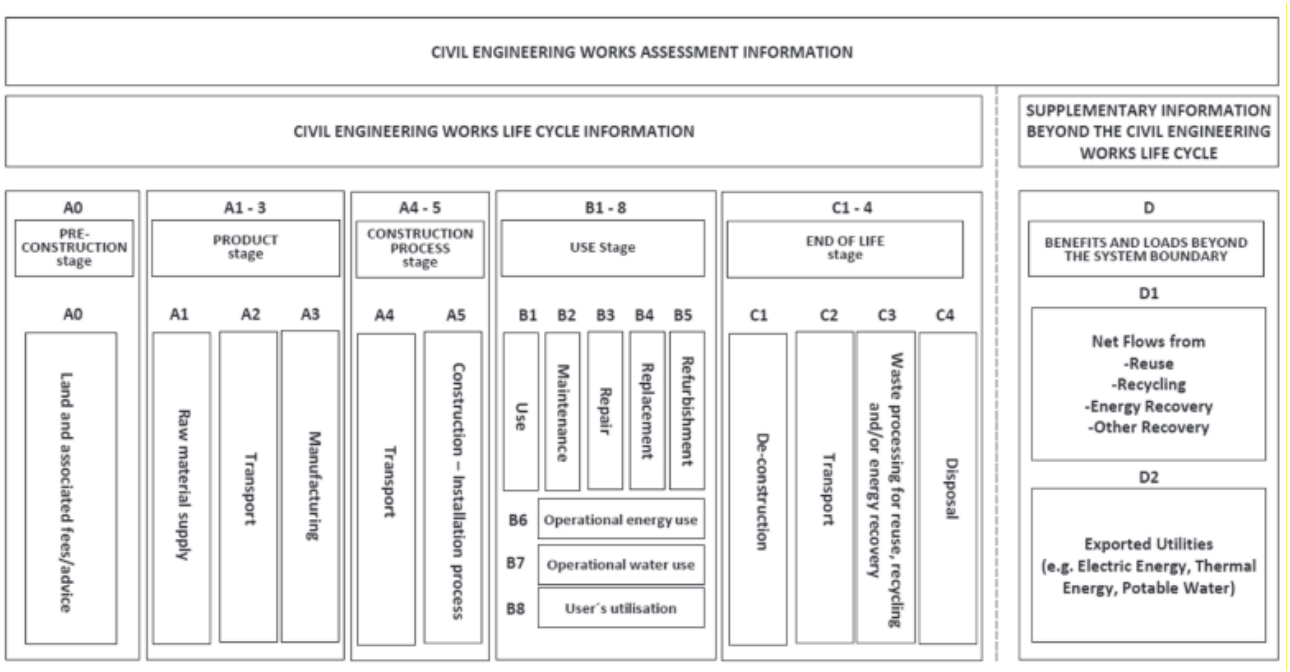


Figure 3: Modular information for different stages of civil engineering works' assessment (extracted from BS EN 17472 (2022))

Modules B1 to B8 relate to the use/operation stage, covering the protection, conservation, moderation, maintenance, control and operation of the object of assessment including works-integrated technical systems. In general, Modules B6 to B8 may be minimal for most LPMit works. For instance, soil nails are considered as maintenance free and do not require any energy to operate. These modules, therefore, can be largely considered as negligible. Yet, some works such as repainting safety access and maintenance inspection would fall into this category.

Modules C1 to C4 belong to the end-of-life stage which starts when the engineering works is decommissioned and not intended to have any further use. At this point, the works' demolition can be considered as a multi-output process that provides a source of materials, products and construction elements that are to be discarded, recovered, recycled, or reused. These modules are scoped out for the carbon management of most LPMit works, as most of the engineering works concerned should have a relatively long service life. It is also challenging to estimate the future decommissioning impacts accurately.

Module D can be divided into two parts: the potential resources for future use (i.e., D1), and the exported energy and other utilities (i.e., D2). These serve as the supplementary information beyond the LPMit works life cycle and are beyond the scope of carbon management in LPMit works.

In general, computation of carbon emissions at the Product Stage (A1-A3) and part of the Use Stage (B1-B5) would need information of material types and quantities. To evaluate carbon emissions at the Construction Process Stage (A4-A5) and part of the Use Stage (B1-B5), one would need fuel consumption of site activities and material transport information.

The current study will follow this modular approach to assess the carbon emissions of whole life cycle of LPMit works. The study will focus on the Product Stage (A1-A3), Construction Process Stage (A4-A5) and Use Stage (B1-B8).

5 COMPUTATION OF CARBON BASELINE INTENSITY

With the appraisal of LPMit works as presented in Section 3.1 and the modular approach following BS EN 17472 (2022) as shown in Section 3.2, a tailor-made data survey form has been prepared to collection site information aiming to evaluate the GHG emissions associated with the construction stage of LPMit works.

The survey form is divided into eight categories as explained in Table 3. Group A questions aim to understand the scale of the site which would be helpful to undertake normalisation, if necessary, at a later stage of the analysis. Group B questions would help further understand the types of engineering works undertaken in the site. Group C questions collect data aiming to evaluate the total amount of construction materials used in the site and help to shed light on the carbon emissions associated with major construction activities. Groups D to F questions collect energy and materials consumption associated with construction activities. Groups G and H questions devote to understand the transport of persons and construction equipment to and from the site.

Table 3: Summary of data survey form

Group	Group description	Items	Potential module following BS EN 17472 (2022)
A	Scale of LPMit site	Size of sites	N/A
B	Engineering works	Soil nail, rock dowel, buttress, rock dentition, drains, fill excavation/replacement, retaining system including rigid and flexible barrier, slope surface protection	A5
C	Material consumption	Cement, concrete, steel, fills, PVC	A1, A2, A3, A4
D	Fuel consumption	Diesel fuel, petrol fuel, biofuel, electricity	A5
E	Water consumption	Water	A5
F	Waste Disposal	Inert and non-inert C&D material	A5
G	Transportation	Electric and Non-electric car	A4
H	Labour	Number of labour	A4

This study will use data collected from active LPMit sites between July 2022 and June 2023 to evaluate the baseline intensity of LPMit works during the construction stage. A generic review of carbon emissions during the operational stage of the works will be conducted separately. Combining the results will give a holistic picture of LPMit works covering both its construction and operational phases.

Carbon emissions of items in Modules A1 to A3 can be calculated using below generic formula:

$$\textit{Amount of GHG emissions} = \textit{Unit of measurement} \times \textit{Density conversion} \times \textit{Emission factor} \quad (1)$$

Carbon emissions of items related to transport of assets and materials can be evaluated using equation (2):

$$\textit{Amount of GHG emissions} = \textit{Weight of materials} \times \textit{Distance travel} \times \textit{Emission factor} \quad (2)$$

Carbon emissions of transportation of labour can be evaluated using equation (3):

$$\textit{Amount of GHG emissions} = \textit{No. of labour} \times \textit{Average distance travel} \times \textit{Emission factor} \quad (3)$$

Carbon emissions of items in Module A5 can be evaluated using equation (4):

$$\textit{Amount of GHG emissions} = \textit{Quantity of consumption} \times \textit{Emission factor} \quad (4)$$

Table 4 shows some examples of emission factor for selected materials. The carbon emission of a one-way economic class flight between the Hong Kong International Airport and the London Heathrow Airport is 1.12 t-CO2e (Cathay Pacific 2024). This serves as an example to give a practical impression of the magnitude of carbon emissions, and thus offers a sense of understanding of the emission factors as shown in Table 4.

Table 4: Examples of emission factor for some commonly used construction materials

Category	Description	Emission factor	Reference
Material	Cement	0.91 kg-CO2e / kg	Zhang et al. 2014
Material	Concrete (C30-C60)	265-429 kg-CO2e / m^3	Gan et al. 2017
Material	Steel (Rebar)	2.25 kg-CO2e / kg	Gan et al. 2017

6 DECARBONISATION: CHALLENGES AND OPPORTUNITIES

Establishment of carbon baseline intensity serves another purpose. It helps to identify items which contribute most to the overall GHG emissions of LPMit works and gives an insightful direction to formulate decarbonisation measures.

In general, decarbonisation measures of LPMit works can be categorised into three aspects, namely:

- Materials
- Workflow
- Energy efficiency

In the material category, consideration should be given to the use of recycled materials, materials sourced from sustainable sources, materials with lower embodied carbon and plants to purify harmful chemicals.

Ground granulated blast furnace slag (GGBS) is a by-product of steel production and can be used to replace cement of up to 80% to form GGBS-based low carbon concrete. Pulverised fly ash (PFA) is a by-product of coal-burning power stations and can be used as a cement substitute to reduce the consumption of cement. Scrap steel recycling has potentials to alleviate carbon emissions.

In the workflow category, one could consider low carbon transportation and digitisation for reducing consumption of paper, MiC for reducing on-site pollution and waste of materials, smart design of LPMit agreements/contracts which groups works sites geographically for minimising travel distance of site staff among slope sites and site depot.

In the energy efficiency category, one could consider the use of clean energy sources for on-site power supply, new energy sources such as hydrogen, equipment with higher energy efficiency, new generation of solar panel, etc.

One of the challenges to decarbonisation includes limited availability and elevated cost of low-carbon materials in the market. However, the situation might be improved by promoting mass production as well as establishing a stable and sustainable supply chain. Besides, with increasing R&D works in new energy such as printable solar panels, electrified and hydrogen-powered construction equipment, more choices of reduced cost green energy should be available in near future.

A unique contribution of LPMit works towards carbon offset is the adoption of vegetated slope cover and wall panels for retaining structures. The whole life cycle of an engineered slope feature is significantly long which could provide an opportunity to offset the embodied carbon during the construction and maintenance stages.

7 CONCLUDING REMARKS

Hong Kong has set out the target to reduce its carbon emissions by 50% against the 2005 level before 2035, and to achieve carbon neutrality by 2050. LPMitP, being a rolling programme, has a role to contribute to the task. This paper introduces a recently commenced study of carbon management of LPMit works. It sets the scene by reviewing international standards, policies and action plans, providing a brief appraisal of LPMit

works, introducing a carbon management framework, suggesting how a carbon baseline intensity can be formulated, and highlighting potential decarbonisation measures suitable for LPMit works. The paper serves as the introductory episode of the entire carbon management journey.

ACKNOWLEDGEMENTS

The paper is published with the permission of the Head of the Geotechnical Engineering Office and the Director of Civil Engineering and Development, the Government of the Hong Kong Special Administrative Region, China.

REFERENCES

BS EN 17472. 2022. Sustainability of construction works. Sustainability assessment of civil engineering works. Calculation methods.

Cathay Pacific. 2024. Offset your carbon emissions, accessed 6 April 2024. https://www.cathaypacific.com/cx/en_HK/about-us/environment/fly-carbon-neutral-fly-greener/offset-your-flights.html

CEDD. 2024a. Report No. 2/2023 on Landslip Prevention and Mitigation Studies and Works Carried out by the Geotechnical Engineering Office, accessed 31 March 2024, https://www.cedd.gov.hk/eng/our-projects/landslip/land_quar/index.html#LPMitP

CEDD. 2024b. Summary of active works contract, accessed 31 March 2024, https://www.cedd.gov.hk/eng/our-projects/landslip/index.html

Crippa, M., Guizzardi, D., Pagani, F., Banja, M., Muntean, M., Schaaf E., Becker, W., Monforti-Ferrario, F., Quadrelli, R., Risquez Martin, A., Taghavi-Moharamli, P., Köykkä, J., Grassi, G., Rossi, S., Brandao De Melo, J., Oom, D., Branco, A., San-Miguel, J., & Vignati, E. 2023. GHG emissions of all world countries, *Publications Office of the European Union*, Luxembourg, 2023, doi:10.2760/953322, JRC134504.

Gan, V. J. L., Chan, C. M., Tse, K. T., Cheng, J. C. P, Lo, I. M. C. 2017. Sustainability analyses of embodied carbon and construction cost in high-rise buildings using different materials and structural form. *HKIE Transactions* 24, 4: 216-227.

GEO. 2011a. Geotechnical manual for slopes. Geotechnical Engineering Office. Civil Engineering and Development Department. Hong Kong SAR.

GEO. 2011b. Technical guidelines on landscape treatment for slopes. GEO Publication No. 1/2011.

ISO 14064-1. 2018. Greenhouse gases. Part 1: Specification with guidance at the organisation level for quantification and reporting of greenhouse gas emissions and removals.

ISO 14064-2. 2019. Greenhouse gases. Part 2: Specification with guidance at the project level for quantification, monitoring and reporting of greenhouse gas emission reductions or removal enhancements.

ISO 14064-3. 2019. Greenhouse gases. Part 3: Specification with guidance for the verification and validation of greenhouse gas statements

ISO 14068-1. 2023. Climate change management - transition to net zero. Part 1: Carbon neutrality.

NASA. 2024. NASA earth observatory: global temperatures, assessed 5 April 2024. https://earthobservatory.nasa.gov/world-of-change/global-temperatures

PAS 2060. 2014. Specification for the demonstration of carbon neutrality.

PAS 2080. 2023. Carbon management in buildings and infrastructure.

UN. 2024. United Nations, assessed 17 May 2024. https://www.un.org/en/global-issues/climate-change

UNTC. 2024. Paris Agreement. United Nations Treaty Collection, accessed 31 March 2024, https://treaties.un.org/pages/ViewDetails.aspx?src=TREATY&mtdsg_no=XXVII-7-d&chapter=27&clang=_en.

WCED. 1987. Our common future. *Report of the World Commission on Environment and Development*. United Nations.

Zhang, J., Cheng, J. C. P., Lo, I. M. C. 2014. Life cycle carbon footprint measurement of Portland cement and ready mix concrete for a city with local scarcity of resources like Hong Kong. *The International Journal of Life Cycle Assessment. 19*: 745-757.

Review on the End Bearing Capacity of Large Diameter Bored Piles founded on Meta-sedimentary Rock in Hong Kong

Terence L Y Yau
C M Wong & Associates Ltd
C K Lau
Sun Hung Kai Architects and Engineers Ltd

ABSTRACT

The HKSAR Government has introduced the Northern Metropolis Development Strategy to transform the northern part of Hong Kong into a metropolitan area for living, working, and traveling. Covering 30,000 hectares, it includes districts like Yuen Long, Tin Shui Wai, Fanling, and Sheung Shui. The strategy aims to increase land availability, improve transport infrastructure, and develop housing, industries, and community facilities. The government has prioritized the Northern Metropolis in its strategic development plans, emphasizing an "industry-driven and infrastructure-led" approach to integrate it with the nation's overall development.

Meta-sedimentary bedrock formations are not uncommon in the Northern Metropolis. A review of the allowable end bearing capacity of this bedrock has been conducted in this paper. The Code of Practice for Foundation 2017 specifies the allowable end bearing capacities for various types of rocks and soils in Hong Kong. For Grade III meta-sedimentary rock, it is limited to 3,000kPa, while for granitic and volcanic bedrock, it has been upgraded to 7,500kPa. To study the behaviour of piles founded on Grade III meta-sedimentary rock, two bored piles were tested each under a load three times the design working load. The test results showed maximum mobilized end bearing pressures exceeds 15,000kPa (i.e. with a factor of safety of 3, the allowable bearing pressure is greater than 5,000kPa). These findings provide valuable insights into pile behavior on meta-sedimentary rock in the Northern Metropolis, suggesting efficient and economical foundation design can be achievable in the new development areas.

Key words: Allowable bearing pressure, Meta-sedimentary rock, Rock Mass Rating

INTRODUCTION

The HKSAR Government introduced the Northern Metropolis Development Strategy in 2021 to transform the northern part of Hong Kong into a metropolitan area for living, working, and traveling. Covering 30,000 hectares, it includes the Yuen Long and North districts, with existing new towns like Yuen Long, Tin Shui Wai, Fanling, and Sheung Shui. The strategy aims to increase land availability, improve transport infrastructure, and develop housing, industries, and community facilities.

The government has prioritized the Northern Metropolis (NM) in its strategic development plans, as highlighted in the 2022 Policy Address. It is envisioned as a new engine for Hong Kong's growth, with an "industry-driven and infrastructure-led" approach emphasized in the 2023 Policy Address to integrate it with the overall development of the country.

Meta-sedimentary rocks are not uncommon in NM. GEO provides a distribution map of Paleozoic rocks (see Figure 1). Late Paleozoic rocks include sedimentary rocks of the Devonian, Carboniferous, and Permian periods, which are distributed in the northern and western parts of Hong Kong. Some of these rocks have undergone thermal and dynamic metamorphism.

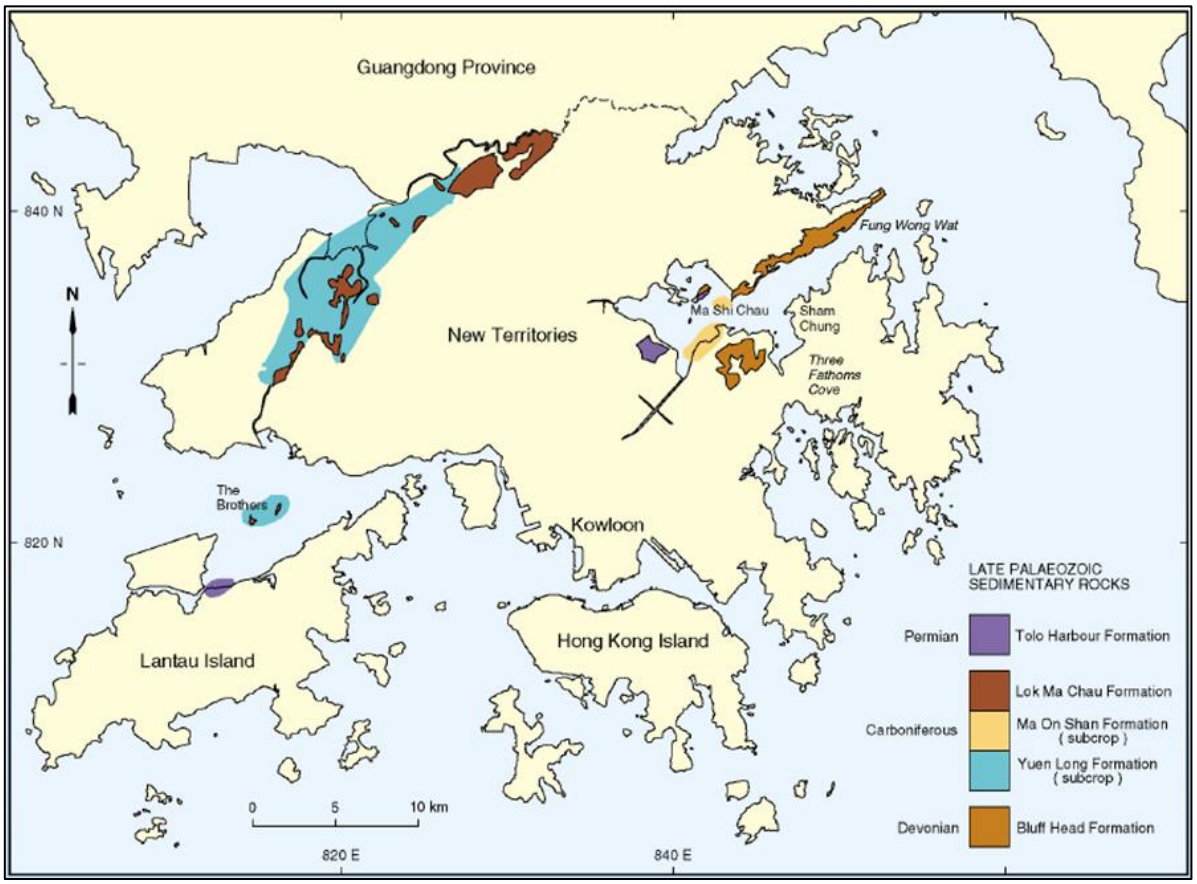


Figure 1 – Distribution of Late Paleozoic sedimentary rocks in Hong Kong

Large scale development will be scheduled in the coming decade in NM. Foundation works would be the

first step for the development. In the current practice, the allowable end bearing pressure of meta-sediment rock for design is significantly lower than that of Granitic or Volcanic rock.

To achieve cost-effective developments in NM, it is necessary to review the allowable end bearing pressure of meta-sedimentary rock. To this end, the authors have carried out load tests on two large diameter bored piles founded on grade III meta-sedimentary rock in Kiu Cheong Road, Tin Shui Wai with an objective to verify that meta-sedimentary rock can provide an allowable bearing capacity of 5,000kPa under the fulfillment of rock strength [(Uniaxial Compressive Strength (UCS) or an equivalent Point Load Index Strength (PLI_{50})] and Total Core Recovery (TCR) not inferior than that of granitic or volcanic rock with the same allowable bearing capacity. In addition, references have also been made to Hill et al (2000) who have reviewed the allowable bearing pressure of rocks for founding of piles in 14 number of pile loading tests conducted for the West Rail Project Phase 1, together with some 20 numbers of full scale loading tests on piles and barrettes in late 1990s. The rocks under Hill's review included also meta-sedimentary rock.

CURRENT DESIGN PRACTICE

Wong (2014) reviewed the development of presumed bearing pressure of granitic and volcanic rock for foundation design in Hong Kong. The foundation design in Hong Kong follows the Code of Practice for Foundation (CoPF) 2017 by the Buildings Department of HKSAR. The allowable bearing pressure (q_a) for pile design is determined based on the categories of rocks. The presumed allowable bearing pressure (qa) for pile design is extracted from Table 2.1 of CoPF 2017 is shown in Table 1 below.

Table 1: Presumed Allowable Bearing Capacity for Foundations (BD, 2017)

Category	Description of rock	q_a (kPa)
1(a)	Grade II or better granite/volcanic rock, TCR of the designated grade = 100%, UCS≥75MPa/PLI_{50}≥3MPa	10,000
1(b)	Grade II or better granite/volcanic rock, TCR of the designated grade ≥ 95%, UCS≥50MPa/PLI_{50}≥2MPa	7,500
1(c)	Grade III or better granite/volcanic rock, TCR of the designated grade ≥ 85%, UCS≥25MPa/PLI50≥1MPa	5,000
1(d)	Grade III or better granite/volcanic rock, TCR of the designated grade ≥ 50%	3,000
2	Grade III or better meta-sedimentary rock, TCR of the designated grade ≥ 85%	3,000

In 2023, Geotechnical Engineering Office (GEO) published a TGN No. 53 which recommends to increase the presumed allowable end bearing pressures of rocks for public works projects (GEO, 2023). The recommendation is now also generally acceptable for private development projects. The updated allowable end

bearing pressures are shown in Table 2 below:

Table 2: Presumed Allowable Bearing Capacity for Foundations (GEO, 2023)

Category	Description of rock	q_a (kPa)
1(a)	Grade II or better granite/volcanic rock, TCR of the designated grade = 100%, UCS≥75MPa/PLI_{50}≥3MPa	12,500
1(b)	Grade II or better granite/volcanic rock, TCR of the designated grade ≥ 95%, UCS≥50MPa/PLI_{50}≥2MPa	10,000
1(c)	Grade III or better granite/volcanic rock, TCR of the designated grade ≥ 85%, UCS≥25MPa/PLI50≥1MPa	7,500
1(d)	Grade III or better granite/volcanic rock, TCR of the designated grade ≥ 50%	3,000
2	Grade III or better meta-sedimentary rock, TCR of the designated grade ≥ 85%	3,000

The TGN has recently revised the presumed allowable bearing capacity of igneous rocks, increasing it from 5,000kPa to 7,500kPa after careful review of past experiences. However, it is crucial to highlight that the presumed allowable bearing pressure for meta-sedimentary rock, as specified in both the CoPF and TGN, has not included the material strength of the rock (UCS/PLT_{50}) as a criterion. Instead, it remains limited to 3,000kPa depending only on rock grade and TCR, which is considered a conservative value.

One of the authors of this study has participated in the West Rail Pile Load Test Programme in the late 1990s, where two instrumented bored piles were subjected to maximum bearing pressures of 25MPa in the Tin Shui Wai Area, specifically on meta-sedimentary rock. The authors believes that the ultimate bearing pressure of the rock is largely dependent on its strength of bearing rock and suggests that the current allowable bearing pressure of 3,000kPa is overly conservative. The authors emphasizes the need for a review of this value based on the availability of more test data.

With the aim of achieving a cost-effective design for a project in Kiu Cheong Road, Tin Shui Wai, the authors have conducted static load tests on piles founded on meta-sandstone. Two instrumented bored piles with a diameter of 813mm were tested at the Kiu Cheong Road site to validate the design assumption of 5,000kPa for meta-sedimentary rocks (Grade III or above with UCS≥25MPa or PLI_{50} ≥1MPa).

LOAD TEST

Ground Conditions of the Site

The site-specific ground investigation reveals that the site is underlain by the superficial deposits typically consist of fill, occasionally with pond deposit, alluvium, and highly to completely decomposed meta-sandstone

and meta-siltstone. Underlying these deposits is moderately to slightly decomposed meta-sandstone and meta-siltstone. The founding bed rock is categorized as Category 2 rock in Table 2.1 of CoPF 2017. The Category (2) bedrock level, which is defined as at least 5m of Grade III or better Rock with Total Core Recovery not less than 85%, varies between -19.8mPD at southern of the site and -48.72mPD at northern of the site respectively. Point load test (PLI50) and uniaxial compression strength (UCS) test were carried out on selected rock core samples retrieved from boreholes during GI stage. The results indicated that the point load index strength PLI50 for meta-sedimentary rock (siltstone/sandstone) ranged from 1.2MPa to 9.9MPa.

Details of the test piles

The authors used the Rock Mass Rating (RMR) method developed by Bieniawski (1974) and Bieniawski (1989) to verify the allowable bearing pressure of the bedrock. Referring to GEO publication No. 1/2006, RMR 50 was adopted as the bearing stratum with an allowable bearing pressure of 5,000kPa. The authors analyzed the borehole logs using RMR and concluded that the two boreholes BH15 and BH22 showed the weakest condition among the 34 boreholes conducted on site. Therefore, two trial piles were conducted at the locations of BH15 and BH22.

Two 813 diameter bored piles were tested to determine the mobilized bearing pressure of under static load. The details of the test piles are shown in Table 3 below.

Table 3: Details of Test Piles

Trial Pile No.	**Reference Boreholes**	**Pile Head Level (mPD)**	**Founding Level (mPD)**	**Pile Length (m)**	**Min. TCR within 3B# below Pile base**	**Bottom Level of Sleeve Casing (mPD)**
BTP-01	BH15	+4.02	-46.34	50.36	93%	-46.34
BTP-02	BH22	+3.92	-29.96	33.88	90%	-29.96

Note: #B is the diameter of pile base

The two 813mm diameter bored piles instrumented with strain gauges (Plate 1) and extensometers were tested to determine the end bearing capacity of meta-sedimentary bedrock. Strain gauges were installed at 8m c/c interval that were used to measure the change in strain along pile shaft and pile base which could estimate the load developed along pile shaft during load testing. The extensometers were aimed at measuring the base movement during load testing. The arrangement of the strain gauges and extensometers are shown in Figure 2.



Plate 1: Strain Gauges installed in the test pile

The test piles, BTP-01 and BTP-02, had lengths of approximately 50m and 34m, respectively. The friction of the pile shaft would take up part of the applied load during testing. To maximize bearing capacity, a left-in casing with a 1mm thick bituminous coating on the outer surface was used as a sleeve. When estimating the applied load for the test, an allowance of 30kPa friction was considered for the shaft resistance along the pile shaft. The arrangements are shown in Figure 2.

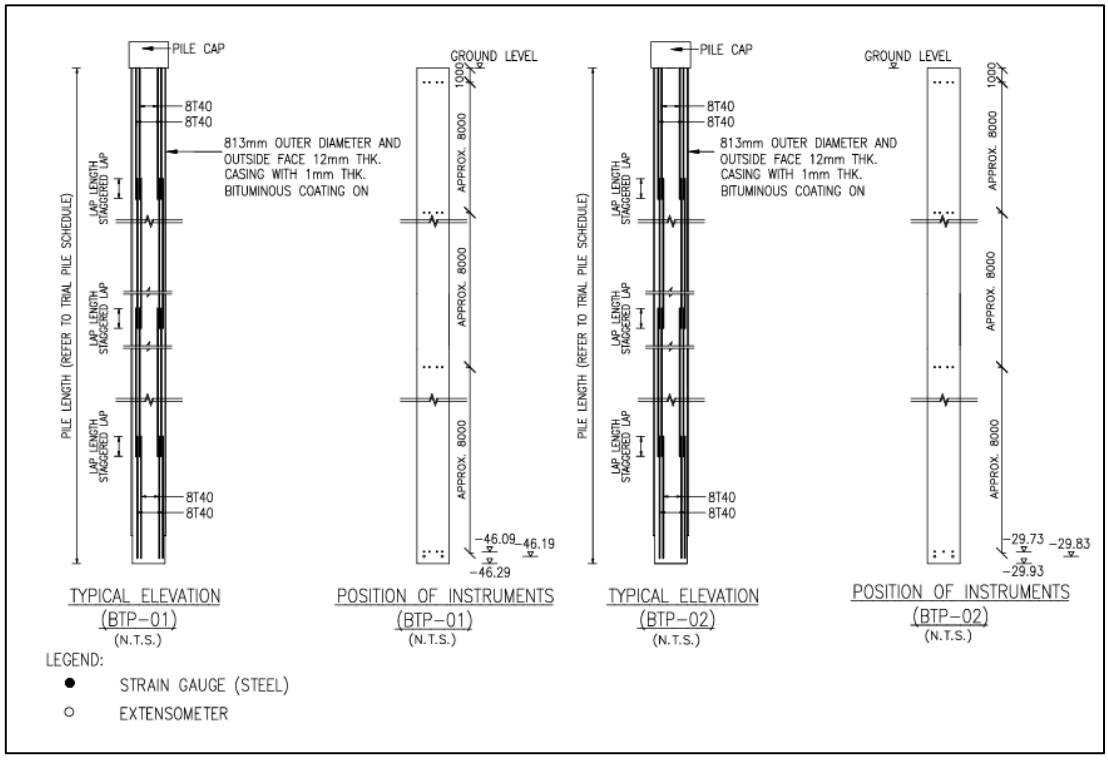


Figure 2: Arrangement of Strain gauges and extensometer for BTP-01 & BTP-02

Based on the pile length, the estimated maximum applied load to the two test piles are summarized in Table 4 below:

Table 4: Summary of estimated apply load for BTP-01 & BTP-02

Test Pile No.	Casing Length (m)	Friction allowance (kN)	End Bearing Force (kN)	Estimate Min. Test Load (kN)
BTP-01	50.31	3,831	7,787	11,618
BTP-02	33.85	2,571	7,787	10,358

The loading tests were conducted in 3 loading cycles. As the aim of the load test was to verify the allowable end bearing pressure of 5,000kPa with a factor of safety of 3, some allowance was also made to cater the shaft friction. The actual applied load at pile head for the two test piles are summarized in Table 5 below:

Table 5: Summary of actual apply load for BTP-01 & BTP-02

Cycle	Design Test Load	Actual Applied Load		Holding time
		BTP-01	BTP-02	
1	1W	4067	3626	-
2	2W	7940	7078	-
3	3W	11814	10531	72 hours

Plates 2 and 3 showing the kentledge setup and loading arrangement for the pile test.



Plate 2: Kentledge set up for load test



Plate 3: Loading arrangement

Pile Load test Results

The load along pile shafts for the two test piles were estimated based on the change of strains measured by strain gauges embedded in the pile shafts. Figures 3 and 4 show the pile loads versus the depths, it is clearly that some loads were taken up the pile shaft frictions and the pile loads at the pile bases were measured by the strain gauges located at 0.2m above the pile base. Based on the test results, the measured shaft friction estimated based on strain gauges were 24kPa and 22KPa for test piles BTP-01 and BTP-02 respectively which were less than the 30kPa assumed in the test proposal. So, the actual mobilized bearing pressure would be greater than 15,000kPa under the maximum test load.

The acceptance criterion of the load test is determined by the pile base settlement. The test is considered acceptable if the pile base settlement is less than 1.5% of pile base diameter under 3 time the working load (FoS of 3). The pile base settlement is measured by extensometers and can also be estimated by the strain gauges readings. The measured pile base settlement is 9.368mm and 9.385mm for BTP-01 and BTP-2 respectively under the maximum test load which is less than the allowable limit of 12.2mm (1.5% of the pile base diameter). The pile head and pile basement movement versus the applied load for BTP-01 and BTP-02 are show in Figure 5 and 6 respectively. The pile load at pile base is estimated by the measured change in strain and thus the mobilized end bearing pressure can be estimated. The estimated bearing pressure under the maximum test loads are 16,254kPa and 16,990kPa for BTP-01 and BTP-02, respectively. Assuming a FoS of 3, the estimated allowable bearing pressure were calculated as 5,418kPa and 5,663kPa, respectively.

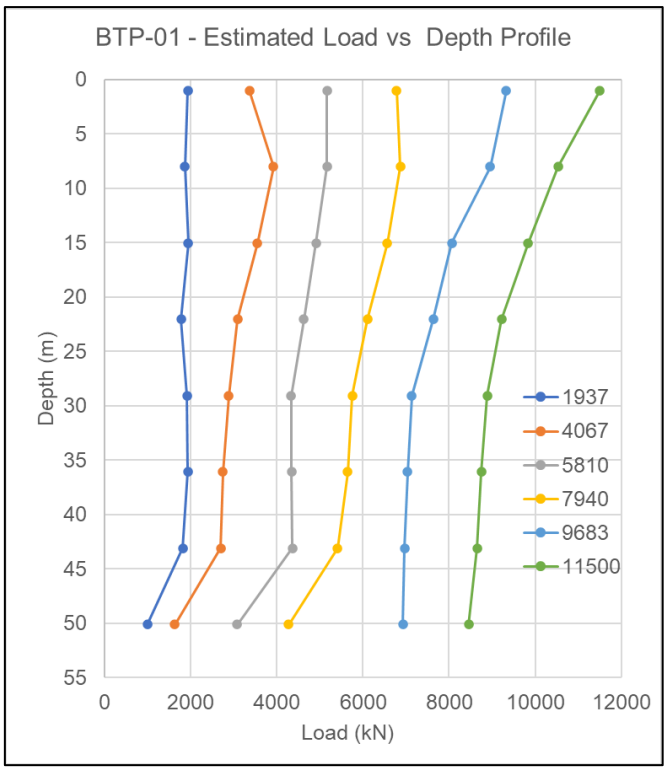


Figure 3: Load vs depth profile of BTP-01

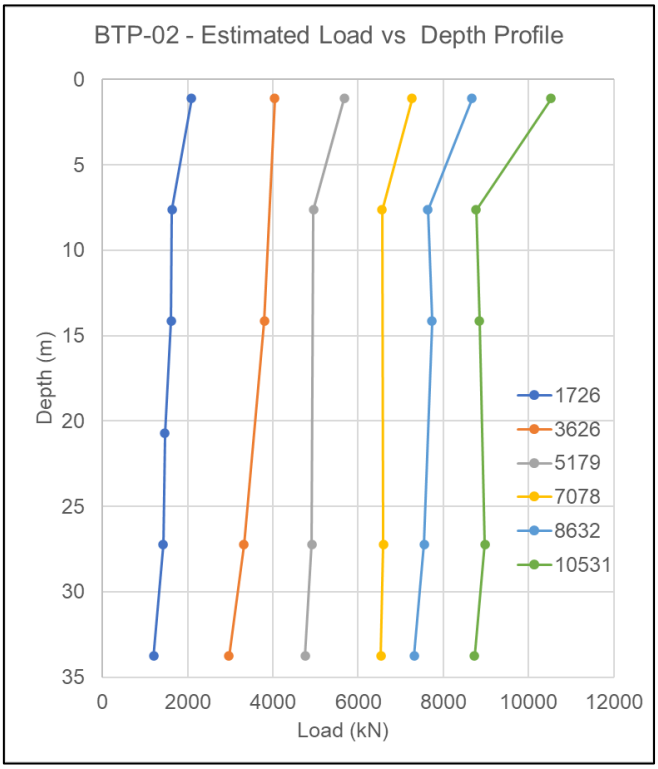


Figure 4: Load vs depth profile of BTP-02

By analysis of the plot of mobilized end bearing pressure against measured pile base movement during the pile loading test (Figures 5 & 6), it is evident that the pile behaved elastically, with no evidence of

plasticity/strain softening even under the maximum test load. Previous results reported by Hill et al. (2000) also showed a mobilized bearing pressure of 26,500kPa for 14mm pile base movement in meta-siltstone, which is significantly higher than the currently adopted bearing pressure (>8,800kPa for a safety factor of 3).

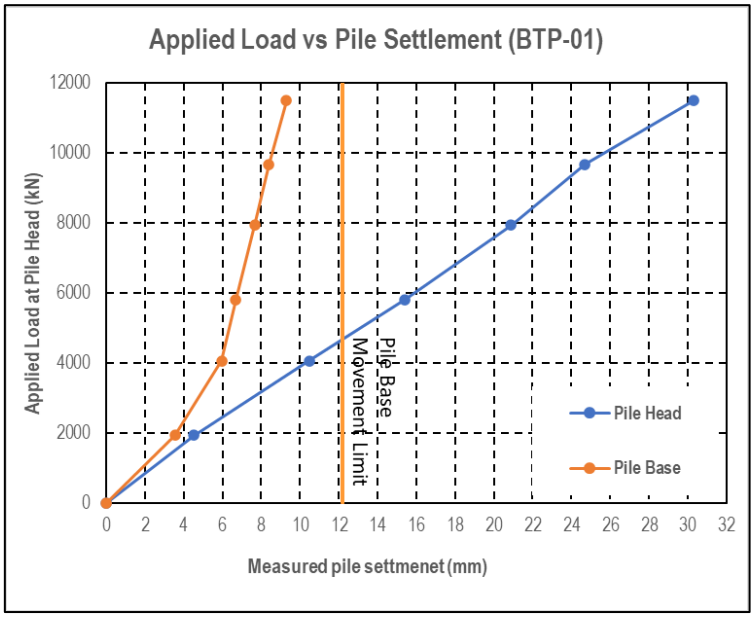


Figure 5: Load and Pile Movement Curve of BTP-01

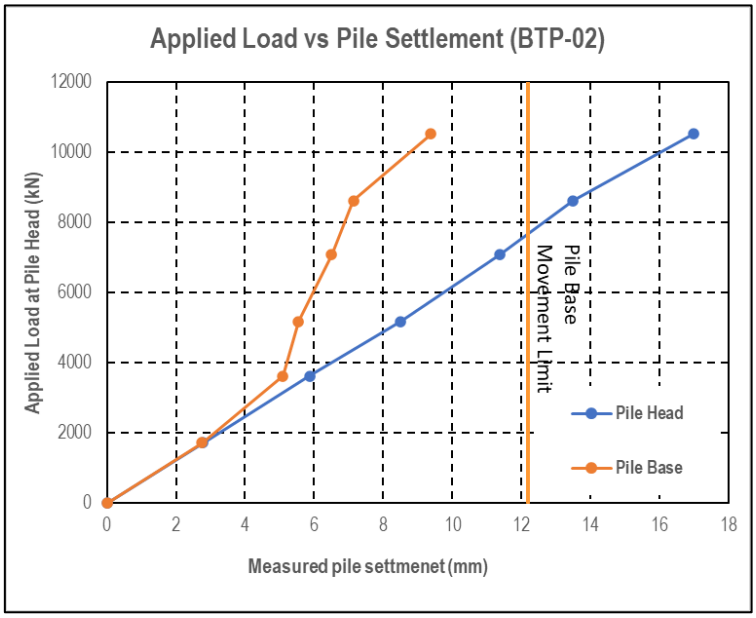


Figure 6: Load and Pile Movement Curve of BTP-02

DISCUSSION

Thorne (1980) proposed that expressing the bearing capacity of rock in relation to the UCS offers a valuable basis for evaluating the performance of foundation on rock. Irfan & Powell (1991) reported that an allowable

bearing stress approximately 0.3 times the UCS would appear to be quite conservative for all rocks except swelling shales. Hill et al (2000), drawing from loading tests conducted during the West Rail Project, suggested a correlation between the ultimate bearing capacity and 1.0 times the UCS, with a maximum limit of 25MPa. It is worth noting that this upper limit represents the maximum bearing pressure demonstrated in the conducted tests.

It is considered that the material strength of rock plays a crucial role in determining the ultimate bearing stress of foundation rock. However, in current design practices, it appears that the end bearing capacity of meta-sedimentary rock is not directly influenced by the material strength of the rock. This phenomenon can be attributed to the challenges associated with acquiring high-quality rock samples for strength testing, primarily due to the presence of closely spaced sub-horizontal joints commonly found in meta-sedimentary rock.

In the context of metasedimentary rocks encountered in the NM, it is frequently observed that these rocks exhibit layered structures with sub-horizontal joints. These rocks tend to preserve the original sedimentary layers present in their pre-metamorphic state, reflecting changes in sedimentary deposition or composition through distinct bands or layers within the rock. It is important to note, however, that not all meta-sedimentary rocks display such layering or sub-horizontal joints. For instance, marble, quartzite, and meta-conglomerate typically lack layered structures.

A comprehensive database of instrumented pile loading test results, encompassing the tests conducted at the West Rail Tin Shui Wai Station, has been compiled in GEO Publication 1/2006 (GEO, 2006). The summarized findings from both the aforementioned tests and those from the Tin Shui Wai Station are presented in Table 6. Notably, all four tests exhibited a maximum mobilized bearing pressure exceeding 15,000kPa, indicating the elastic behaviors of the piles under the maximum test loads.

Table 6: Summary of test results in meta-sedimentary rock

Pile No.	**Pile diameter (mm)**	**Rock Strength (MPa)**	**Mobilized end bearing pressure (kPa)**	**Pile Base settlement (mm)**
TSW1	1200	62 (UCS)	26,530	13.6
TSW2	1350	25.9 UCS)	24,000	2
BTP-01	813	1.8 (PLI_{50})	16,254	9.386
BTP-02	813	50.9 (UCS)	16,989	9.385

CONCLUSION

The instrumented loading tests conducted at the Kiu Cheong Road Site, along with the previous tests at the West Rail Tin Shui Wai Station, suggest that the allowable bearing stress of 3,000kPa for meta-sedimentary rock is very conservative. The two tests discussed in this paper together with the load tests carried out for the West Rail Project for the same rock type are generally consistent and the assumption of 5,000kPa would still be conservative. It is recommended to include the material strength of rock, similar to granitic and volcanic rock

type, as a criterion in determining the presumed allowable bearing pressure of the meta-sedimentary rock. That is, an allowable end bearing stress of 5,000kPa for Grade III or better meta-sedimentary rock with TCR not less than 85% and USC not less than 25MPa/PLI_{50} not less than 1MPa shall be adopted for general foundation design.

REFERENCES

Bieniawski, Z.T. 1974. Geomechanics classification of rock masses and its application in tunnelling. *Proceedings of the Third International Congress of the International Society for Rock Mechanics, Denver, vol. 2A, pp 27-32.*

Bieniawski, Z.T. 1989. "*Engineering Rock Mass Classification*." John Wiley, New York, 251 p.

Buildings Department. 2017. *"Code of Practice for Foundations 2017"*, Buildings Department, Hong Kong

Geotechnical Engineering Office. *"The Geology of Hong Kong (Interactive On-line)"*, Geotechnical Engineering Office, Civil Engineering and Development Department, Hong Kong. www.cedd.gov.hk/eng/about-us/organisation/geo/pub_info/memoirs/geology/pal/index.html

Geotechnical Engineering Office. 2006. *"Foundation Design and Construction"*, GEO Publication No. 1/2006, Geotechnical Engineering Office, Civil Engineering and Development Department, Hong Kong.

Geotechnical Engineering Office. 2023. *"Supplementary Guidelines for Foundation Design and Construction"*, GEO Technical Guidance Note No. 53, Geotechnical Engineering Office, Civil Engineering and Development Department, Hong Kong.

Hill, S.J., Littlechild, B.D., Plumbridge, G.D. & Lee, S.C. 2000. *"End Bearing and Socket Design for Foundation in Hong Kong"*, HKIE Geotechnical Division Annual Seminar 2000, pp 169-178.

Irfan, T.Y. & Powell, G.E. 1991. *"Foundation Design of Caissons on Granitic and Volcanic Rocks"*, GEO Report No. 8, Geotechnical Engineering Office, Civil Engineering Department, Hong Kong.

Thorne, G.P. 1980, "The capacity of piers drilled into rock.", *Proceeding of the International Conference on Structural Foundation on Rock, Sydney, Australia.*

Wong, C.M. 2014. "*Keynote Lectures - Overview of Development and Challenges in Foundation Design and Construction in Hong Kong*", The HKIE Geotechnical Division Annual Seminar 2014, pp 27-52.

Fully Coupled Numerical Methods and a Simple Method for Calculating Settlements of Foundations and Reclamations on Clayey Soils

Jian-Hua YIN, Ze-Jian CHEN, Pei-Chen WU, & Kai LIU

The Hong Kong Polytechnic University, Hong Kong

ABSTRACT

Many foundations are supported by clayey soil ground. Marine reclamations are mostly constructed on seabed consisting of marine clayey soils or marine deposits. The settlement calculation of such foundations and reclamations is needed for their design and performance assessment. In this paper, the authors will firstly give a brief introduction to issues and mechanisms of large settlements of soft clayey soil grounds caused by creep of clayey soil skeleton. The authors will present both Hypothesis A and Hypothesis B methods for calculating consolidation settlements of clayey soils, and the history and equations of the two methods, explaining the inherent logical mistakes of Hypothesis A method. After this, the authors will briefly present fully coupled numerical methods using different Elastic Visco-Plastic (EVP) models for consolidation analysis of clayey soils. They will then introduce a simplified Hypothesis B method, namely simple method, for one-layer and multi-layers of clayey soils. Steps of how to derive this simple method are presented. Two examples of using this simple method by hand calculations or Excel calculations are explained. Verifications of the simple method by comparing with test data and fully coupled numerical methods are presented. Conclusions and remarks are presented at the end.

1 INTRODUCTION

The time-dependent excessive and differential settlement of clayey soil ground are threats to the long-term performance and serviceability of infrastructures such as foundations, road embankments, airports, artificial islands, *etc*. Built on weak soft clay layers, the Leaning Tower of Pisa had suffered from differential settlement since the completion of construction. The uneven distribution of thickness of the clayey soil layer caused the inclination of the tower, costing great effort for stabilization (Burland et al., 2003). The Kansai International Airport in Osaka, Japan consists of two artificial islands constructed over thick layers of marine clayey and sandy soils. The settlement of both islands has exceeded 10 meters, including post-construction settlements of 3 to 6 meters at different positions (http://www.kansai-airports.co.jp). The long-term settlement of the above-mentioned cases is a consequence of the combined effects of consolidation and creep. Rocchi et al. (2006) investigated the long-term settlement of Kansai International Airport on Osaka clay and found that the consolidation analysis without considering creep considerably underestimated its long-term settlement.

Consolidation of soils is induced by the dissipation of excess porewater pressure and the increase of effective stress under loading increment. Creep refers to the time-dependent (visco-plastic) compression of soils under constant effective stress. Viscous compression is a more general term which refers to the time-dependent (visco-plastic) compression of soils under effective stress variations. Other related time-dependent behaviours include stress relaxation and strain rate effects. There are different explanations of creep and other visco-plastic behaviours of clays, most of which have attributed it to the diffuse electrical double layer (bound water) around the negatively charged clay mineral particles. The bound water has significantly different mechanical properties compared with the free water in the soil skeleton. It is believed that creep is related to the viscous movement of the bound water and re-arrangement of soil particles, including but not limited to inter-particle sliding, molecule movements, and inter-particle contact breakdown (Bolt, 1956; Gupta, 1964;

Kuhn & Mitchell, 1993; Le et al., 2012; Mitchell et al., 1968; Mitchell & Soga, 2005; Taylor, 1942; Taylor & Merchant, 1940; Yin, 2015). Double porosity theory was also interpreted as the origin of creep, that the drainage of double-layer water in the micropores is much slower than that of free water in macropores in the soil skeleton (Borja & Choo, 2016; Wang & Xu, 2007; Zeevaert, 1986). In general, researchers have realized that visco-plasticity is a key material property of clayey soils, and should be considered in engineering design. Several design guidelines have adopted fully coupled or simple methods to consider creep during primary consolidation (CGS, 2023; NPRA, 2022).

This paper focuses on the computational/calculation methods to consider such creep effect (or viscous effect in a more general sense) in consolidation settlement analysis of clayey soil ground. The key issues related to two hypotheses (A and B) are clarified, followed by explanations of Elastic Visco-Plastic (EVP) models and the fully coupled analysis methods with these models. Further, a new simple method based on the 1D EVP model is presented with examples considering different over-consolidation ratios and drainage conditions. The effects of several key parameters and coefficients are discussed. The proposed method is verified with field data and fully coupled numerical simulations for a real project in Hong Kong to reveal its validity for multiple soil layers under multi-stage loadings.

2 HYPOTHESIS A, HYPOTHESIS B, ELASTIC VISCO-PLASTIC MODELS, AND FULLY COUPLED METHODS FOR CONSOLIDATION-CREEP ANALYSIS

2.1 Hypothesis A and Hypothesis B

Ladd et al. (1977) first questioned whether creep is a "separate" phenomenon during primary consolidation, which corresponded to different predictions of long-term settlement in the field. If creep is a separate phenomenon caused by the structural viscosity of soils, the EOP ("End-of-Primary consolidation") strain will be dependent on the primary consolidation duration, which is "Curve B" in Figure 1. Otherwise, the EOP strain will be unique, as shown in "Curve A". Jamiolkowski et al. (1985) formally proposed the concept of two hypotheses, in which "Hypothesis A" considers creep only after primary consolidation while "Hypothesis B" considers creep during and after primary consolidation. For Hypothesis A, the EOP strain of soils is thickness-independent. The "primary consolidation" settlement of a thick layer in the field can be directly calculated based on the EOP stress-strain relationship of a thin specimen of oedometer test in the laboratory, and the "secondary compression" is only calculated after EOP using $\varepsilon_{\text{sec}} = C_\alpha / (1+e_0) \cdot \log(t/t_p)$, where C_α is the "secondary consolidation coefficient" and t_p is the time at end of primary consolidation (Mesri & Choi, 1985). For Hypothesis B, the EOP strain of soils is influenced by creep and will be thickness-dependent.

To date, while there are still debates between the two hypotheses (Degago et al., 2011; Mesri & Vardhanabhuti, 2005; Szavits-Nossan, 2015), most researchers now support Hypothesis B that creep should be considered during primary consolidation and the EOP strain is different for different thicknesses (Degago et al., 2011; Grimstad et al., 2022; Kabbaj et al., 1988; Kavazanjian, 1988; Leroueil, 2006; Szavits-Nossan, 2015; Taylor, 1942; Yin & Feng, 2017). Kavazanjian (1988) and Szavits-Nossan (2015) pointed out that the conventional Hypothesis A method that ignores the creep during primary consolidation violated the principles of continuum mechanics. Degago et al. (2011) re-analyzed the previous test data that were considered to support Hypothesis A, and concluded that most of them support Hypothesis B if the initial states of the soils are carefully considered. However, the old Hypothesis A method was widely adopted due to its convenience for settlement calculation in engineering. To use Hypothesis B, the creep effects during the porewater pressure dissipation should be properly analyzed. In the following sections, the fully coupled numerical methods and a simple method that consider creep in consolidation settlement calculations based on Hypothesis B will be presented.

2.2 Elastic Visco-Plastic (EVP) model for clayey soils

A constitutive model describes the relations between different state variables, including strain, effective stress, and others such as strain rates. Reliable constitutive models are essential to the analysis of soil behaviour in the field. There are a series of constitutive models that can consider the creep effects of clayey soils (Adachi

& Oka, 1982; Den Haan, 1994; Vermeer & Neher, 1999; Yin et al., 2002; Yin & Graham, 1989; Yuan & Whittle, 2018) based on the isochrone or isotache concepts (Bjerrum, 1967; Šuklje, 1957).

Figure 2 shows a conceptual diagram of Yin and Graham's 1D EVP model (Yin & Graham, 1989, 1994, 1996). The model proposes an instant time line, reference time line, and equivalent time lines. The visco-plastic strain rate and equivalent time of a soil element are uniquely dependent on the current states of effective stress and vertical strain, but independent of the stress paths. The reference time line describes the soil state when the equivalent time is zero. For a given soil state, the total strain rate $\dot{\varepsilon}_z$ is contributed by elastic strain rate $\dot{\varepsilon}_z^e$ and the visco-plastic strain rate $\dot{\varepsilon}_z^{vp}$, and is calculated as:

$$\dot{\varepsilon}_z = \dot{\varepsilon}_z^e + \dot{\varepsilon}_z^{vp} = \frac{\kappa}{1+e_0}\frac{\dot{\sigma}_z'}{\sigma_z'} + \frac{\psi}{(1+e_0)t_0}\exp\left[\left(\varepsilon_{r0}-\varepsilon_z\right)\frac{1+e_0}{\psi}\right]\left(\frac{\sigma_z'}{\sigma_{r0}'}\right)^{\frac{\lambda}{\psi}} \quad (1)$$

where e_0 is the initial void ratio of the soil when strain is zero, κ is the slope of instant time line in $e-\ln\sigma_z'$, λ is the slope of reference time line in $e-\ln\sigma_z'$ coordinate, $(\sigma_{r0}', \varepsilon_{r0})$ is a fixed point at reference time line, usually taken as the pre-consolidation pressure point $(\sigma_p', \varepsilon_p)$ from oedometer tests, ψ is the creep coefficient (the slope of secondary compression section of $e-\ln t$ curves in oedometer tests), t_0 is the reference time, normally 24 hours in conventional oedometer tests. σ_z', ε_z represent the vertical effective stress and vertical strain in 1D condition. For convenience, the subscript z may be dropped in this paper.

The EVP model has been extended to a three-dimensional (3D) model in general stress-strain space based on the critical state models and overstress theory (Yin et al., 2002; Yin & Graham, 1999).

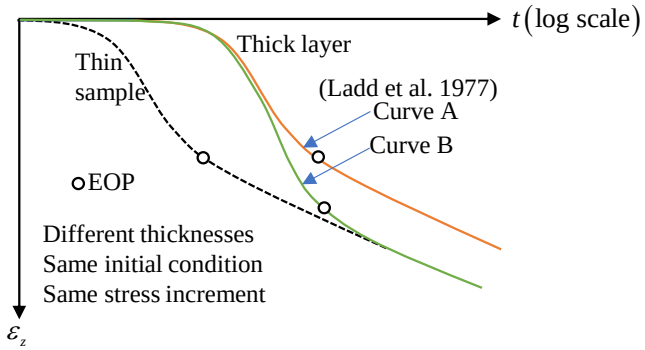


Figure 1: Illustration of Hypothesis A and Hypothesis B in 1D consolidation condition

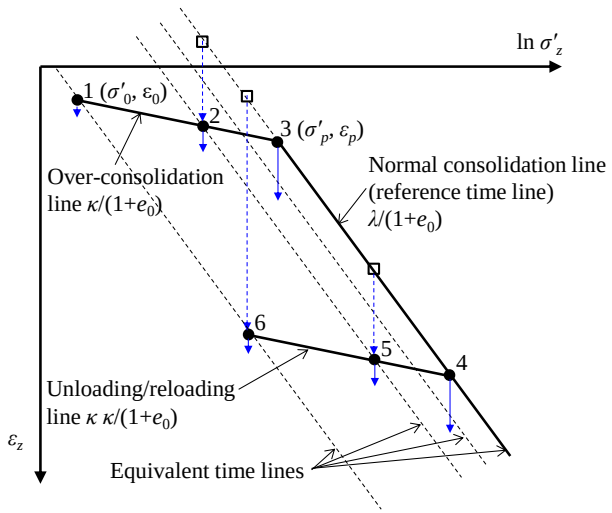


Figure 2: Conceptual diagram of Yin and Graham's 1D EVP model

2.3 Fully coupled numerical simulations based on EVP models

During the consolidation process of soils, the porewater pressure dissipates, and the effective stress is not constant. As shown in Equation (1), the strain rate of the soil is dependent on the stress-strain state. Therefore, creep is coupled with consolidation. A rigorous method is the fully hydro-mechanically coupled numerical simulation, such as finite element method (FEM) or finite difference method (FDM). In the fully coupled method, two sets of partial differential equations are to be solved: (i) a consolidation equation based on mass continuity and Darcy's law; and (ii) a constitutive equation such as Equation (1).

There have been successful applications of Yin and Graham's 1D and 3D EVP models in FDM and FEM, with verifications by measured data (Chen et al., 2021a, 2021b; Yin & Graham, 1996; Yin & Zhu, 1999). Chen et al. (2021a, b) successfully implemented the 3D EVP model in FEM software PLAXIS for analysis of long-term settlement of embankments on multiple layers of soft soils in Canada and Sweden. Another popularly used EVP model in commercial finite element analysis software PLAXIS is the Soft Soil Creep (SSC) model (Vermeer & Neher, 1999). The SSC model which was also called "isotache model" (Degago et al., 2011), shares a high similarity with Yin and Graham's EVP model in both theoretical frameworks and computation results. Besides, in recent years, more complicated EVP models have been developed to further consider the effects of anisotropy (Leoni et al., 2008; Zhou et al., 2005), creep limit (Yin et al., 2002), and temperature (Chen et al., 2023; Laloui et al., 2008).

3 A SIMPLE HYPOTHESIS B METHOD

Although the fully coupled methods for implementing EVP models have been successfully applied, they require a proper numerical programme and related skills, which may be unviable for designers. Conventional design methods by hand calculations or spreadsheets are still widely recommended in many design codes and widely used in engineering. However, these methods are usually developed based on Hypothesis A. As discussed, Hypothesis A underestimates the creep effects during primary consolidation. Therefore, it becomes ungently necessary to develop a proper simple design method based on Hypothesis B and the EVP model.

3.1 Formulations of the simple Hypothesis B method

Yin et al. (2022) proposed a simplified Hypothesis B method for calculating the consolidation settlement of clayey soil ground under different conditions. In this method, the total settlement S_{total} of the soil are analyzed by:

$$S_{total} = US_f + S_{creep} \tag{2}$$

where U is the average degree of consolidation, S_f is the final settlement estimated without considering creep effect, S_{creep} is the creep settlement separated from the "primary consolidation" settlement US_f. In this way, Equation (2) is a "de-coupled" method for creep analysis. S_f is calculated by the compressibility of soils measured from laboratory tests. If the volume compressibility m_v is known, S_f for a soil layer can be calculated by:

$$S_f = m_v \Delta\sigma' H \tag{3}$$

where $\Delta\sigma'$ is the load increment, H is the thickness of the layer. S_f can also be determined from the $e-\log\sigma'$ curves from oedometer tests to consider the nonlinear effective stress-strain behaviour. The $e-\log\sigma'$ curves are obtained at a fixed time t_0 (normally 24 hours). A single layer can be divided into sub-layers. Yin et al. (2022) suggested that a maximal thickness of 0.5m for each sub-layer can achieve enough preciseness. For each sub-layer, $S_{f,j}$ is calculated as:

$$S_{f,j}=\begin{cases} H_j\dfrac{C_r}{1+e_0}\log\dfrac{\sigma_0'+\Delta\sigma_f'}{\sigma_0'} & for\ \sigma_0'<\sigma_0'+\Delta\sigma_f'\le\sigma_p' \\ H_j\dfrac{C_r}{1+e_0}\log\dfrac{\sigma_p'}{\sigma_0'}+H\dfrac{C_c}{1+e_0}\log\dfrac{\sigma_0'+\Delta\sigma_f'}{\sigma_p'} & for\ \sigma_0'\le\sigma_p'<\sigma_0'+\Delta\sigma_f' \\ H_j\dfrac{C_c}{1+e_0}\log\dfrac{\sigma_0'+\Delta\sigma_f'}{\sigma_0'} & for\ \sigma_p'\le\sigma_0'<\sigma_0'+\Delta\sigma_f' \end{cases} \quad (4)$$

where σ_0', σ_p' is the initial effective stress and the pre-consolidation pressure respectively. $C_c=\lambda\ln 10$ is the compression index for the normal consolidation state, and $C_r=\kappa\ln 10$ is the recompression index for the over-consolidation state. The S_f of the whole layer is obtained by superposition of all sublayers, and m_v of the whole layer can then be calculated by

$$m_v=\frac{S_f}{H\Delta\sigma_f'}=\frac{\sum_{j=1}^{n}S_{f,j}}{H\Delta\sigma_f'} \quad (5)$$

It shall be pointed out that m_v above is calculated for the whole layer. The m_v value will be used to calculate the consolidation coefficient $c=k/(\gamma_w m_v)$ where k is hydraulic conductivity of this soil. The c value is then used to calculate the average degree of consolidation U. U can be calculated by classical consolidation theories, such as Terzaghi's 1D consolidation theory, unit cell theory for vertical drains (Hansbo, 1981), and others considering multi-layer profiles (Walker & Indraratna, 2009; Zhu & Yin, 2005), with known consolidation coefficient and thickness.

The other part of the total settlement contributed by creep S_{creep} is calculated using the following equation:

$$S_{creep}=\begin{cases} \alpha U^{\beta}S_{creep,f} & for\ t\ge t_{EOP,lab} \\ \alpha U^{\beta}S_{creep,f}+\left(1-\alpha U^{\beta}\right)S_{creep,d} & for\ t\ge t_{EOP,field} \end{cases} \quad (6)$$

In Equation (6), α,β are empirical coefficients to consider the delayed effective stress during porewater pressure dissipation. $S_{creep,f}$ is a creep settlement calculated under the final effective stress state without considering the delay by porewater pressure. $S_{creep,d}$ is a creep settlement under the final effective stress delayed by the consolidation process, assumed to start after the "End of Primary consolidation" (t_{EOP}). t_{EOP} usually corresponds to the time of $U=90\sim98\%$ based on the engineering practice. α varies from 0 to 1. If $\alpha=0$, the method corresponds to the old Hypothesis A method. According to Yin and Graham's 1D EVP model, $S_{creep,f}$ and $S_{creep,f}$ should be calculated as:

$$\begin{cases} S_{creep,f}=H\dfrac{C_\alpha}{1+e_0}\log\dfrac{t_{ef}+t}{t_{ef}+t_0} \\ S_{creep,d}=H\dfrac{C_\alpha}{1+e_0}\log\dfrac{t_{ef}+t}{t_{ef}+t_{EOP,field}} \end{cases} \quad (7)$$

where $C_\alpha=\psi\ln 10$ is the creep coefficient for log scale, e_0 is the initial void ratio of the soil, t_{ef} is the equivalent time under the final effective stress and final settlement. According to Yin and Graham's EVP model, t_{ef} is calculated by:

$$t_{ef}=\exp\left[-\left(\varepsilon_{r0}-\varepsilon_f\right)\frac{1+e_0}{\psi}\right]\left(\frac{\sigma_f'}{\sigma_{r0}'}\right)^{-\frac{\lambda}{\psi}}-t_0 \quad (8)$$

where σ_f', ε_f is the final effective stress and the final vertical strain based on the $e-\log\sigma'$ curves obtained at a fixed time t_0 (normally 24 hours). If the final state of soil is located at the normal consolidation line (reference time line), such as points 3 and 4 in Figure 2, the equivalent time is zero. If the final state is at an over-consolidation state (such as 2, 5, and 6 in Figure 2), the equivalent time will be larger than zero.

3.2 Verifications for a single layer

The proposed method in 3.1 is easy to implement in a spreadsheet. In this section, verifications on a single layer of clayey soil will be presented. The soil layer is the Hong Kong marine deposit (HKMD), which is a typical clayey soil in Hong Kong (Koutsoftas et al., 1987; Zhu et al. 2001). The parameters are listed in the Table 1. All mechanical parameters of soils can be conveniently obtained from conventional oedometer tests. For example, C_r is fitted as the slope of $e-\log\sigma_v^{'}$ curves at unloading-reloading state, C_c is fitted as the slope of $e-\log\sigma_v^{'}$ curves at normal consolidation state, C_α is fitted as the slope of $e-\log t$ curve of secondary consolidation at normal consolidation state. k_v, k_h are the hydraulic conductivity of undisturbed soils in vertical direction and horizontal direction. k_s represents the hydraulic conductivity of disturbed soils in the smear zone due to drain installation. r_d, r_s, r_e are the radii of vertical drains, smear zone, and the equivalent soil column surrounding each vertical drain respectively. The soil layer is subjected to a uniform vertical load of 20kPa. All of the calculation results are compared with simulations by PLAXIS 2D with the SSC model (i.e., fully coupled method) using the same set of parameters.

Table 1: Parameters of HKMD for the calculation

General parameters	e_0	k_v (m/day)	k_h (m/day)	k_s (m/day)	r_d (m)	r_s (m)	r_e (m)
	2.65	1.90×10^{-4}	1.90×10^{-4}	1.90×10^{-4}	0.027	0.134	0.788
Fully coupled method (PLAXIS)	κ^* $[=2\kappa/(1+e_0)]$	λ^* $[=\lambda/(1+e_0)]$	μ^* $[=\psi/(1+e_0)]$	τ (day)	$c^{'}$ (kPa)	$\varphi^{'}$ (deg)	
	0.02172	0.174	0.0076	1	0.1	30	
Simple method	C_r $[=\kappa\ln(10)]$	C_c $[=\lambda\ln(10)]$	C_α $[=\psi\ln(10)]$	t_0 (day)			
	0.0913	1.4624	0.0639	1			

(a) Calculations for a soil layer with different OCRs with/without vertical drains

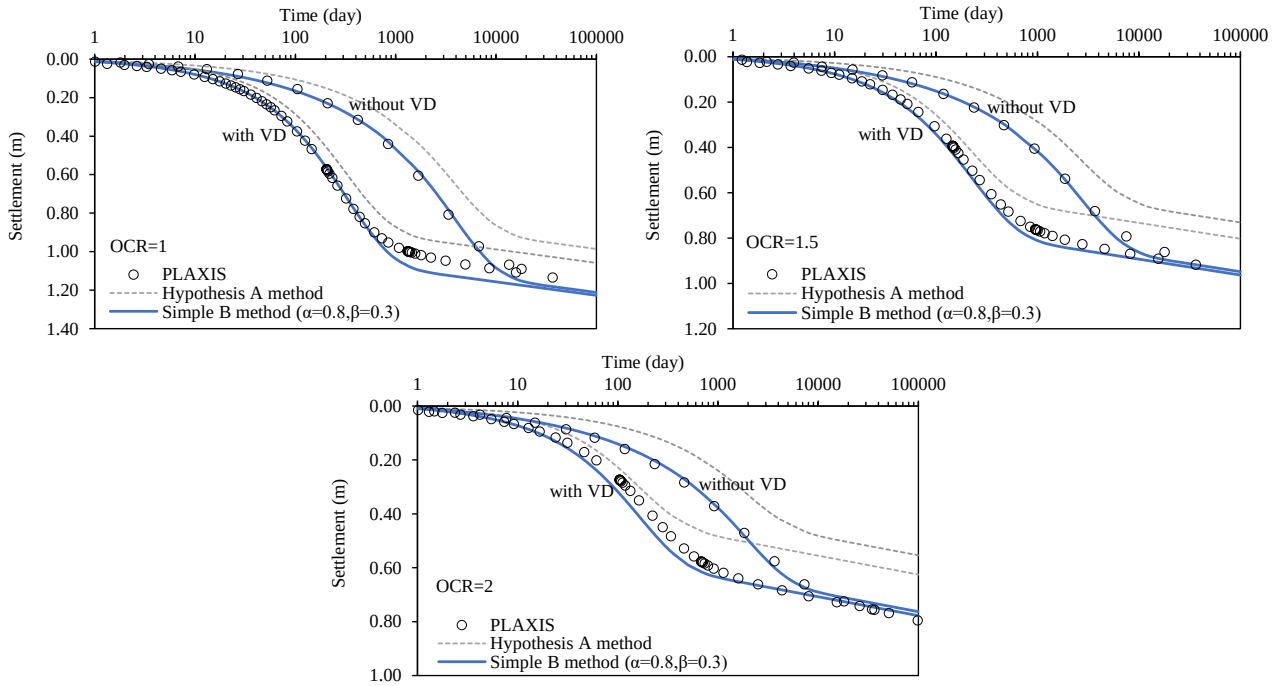


Figure 3: Calculation results by different methods for a clay layer with different OCRs with and without VD

Different initial over-consolidation ratio (OCR) from 1, 1.5, to 2, and drainage conditions with and without vertical drains (VD) are considered in the calculations. OCR is defined as the ratio between $\sigma_p^{'}$ and $\sigma_0^{'}$ for each sub-layer. For soils without VDs, U is calculated using Terzaghi's equations. For soils with VDs, U is analyzed using Hansbo (1981)'s consolidation theory. The radii of drains, smear zone, and equivalent soil are adopted following Zhu et al. (2001). $\alpha = 0.8, \beta = 0.3$ are suggested values in the previous studies. The time achieving $U = 95\%$ is selected as $t_{EOP,field}$.

Figure 3 shows the computation results for these different cases. It can be found that for all cases of an HKMD layer, the calculation results by the simple Hypothesis B method are highly consistent with the fully coupled method by PLAXIS. The old Hypothesis A method always obtains smaller settlements compared with the other two methods. The underestimation of Hypothesis A is more significant in the case without VD than the cases with VD. The reason is that for soils with VDs, the consolidation period is much shorter, and the creep developed during the "primary consolidation" will be smaller, which slightly reduces the error caused by Hypothesis A.

(b) Investigations on the effects of α, β

As discussed in the previous sections, α, β are two constant coefficients, which approximately describe the coupling of consolidation on creep settlement. It is important to verify the robustness and versatility of their values for typical cases. Figure 4 shows the calculation results of the simple method with different values of α (0.6, 0.7, and 0.8). Although there is a small difference at the final stages for different values of α, the computations are all reasonable. For the soil layer with OCR from 1, 1.5, to 2, the best-fitted α may slightly increases from 0.6 to 0.8. Similar results are retained in both VD and non-VD cases.

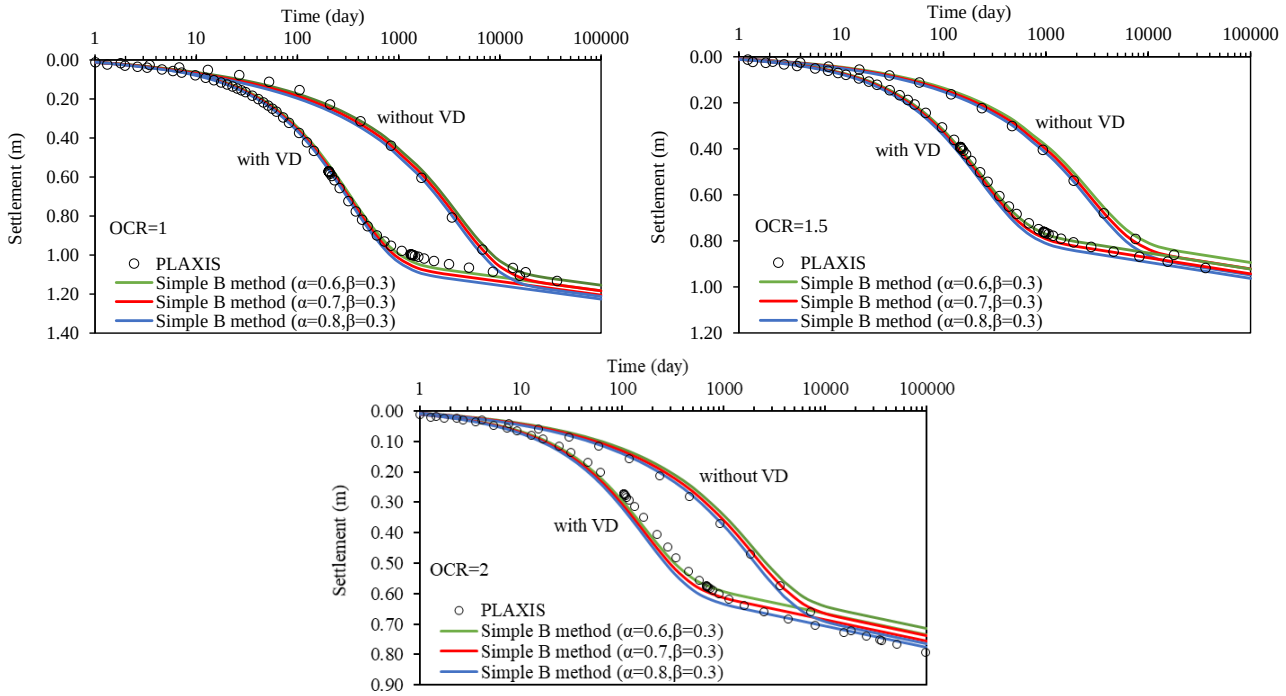


Figure 4: Calculation results by simple methods with different α

Figure 5 shows the calculation results of the simple method with different values of β (0.1, 0.3, and 0.5) under the same α. It can be found that β mainly affects the earlier stages of consolidation, but cannot affect the final stages of consolidation. For the soil layer with OCR from 1, 1.5, to 2, the best-fitted α may slightly increases from 0.6 to 0.8. The influence of β is more significant in the cases without VD than those with VD. Besides, it shows that $\beta = 0.3$ fits the best with the fully coupled analysis in PLAXIS. With increase of β, the

computed settlement tends to decrease. However, as consolidation goes on, the effects of β gradually diminish. Although the influence of OCR exists, $\alpha = 0.8, \beta = 0.3$ can still be used for convenience with OCR from 1 to 2, because the errors are minor. The minor effects of OCR on α, β can be attributed to the smaller compressibility of soils in OC state. With smaller compressibility, the consolidation during OC state is faster, and the differences of creep rates of OC soils during primary consolidation will contribute less to the total creep settlement.

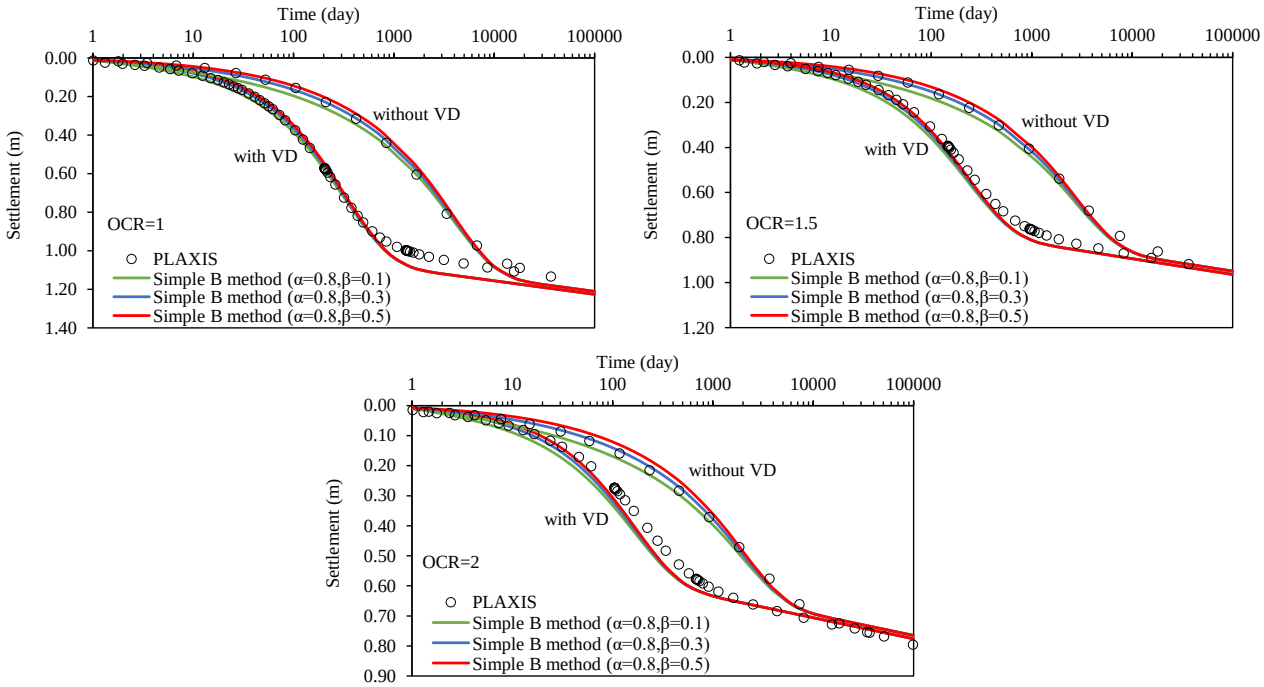


Figure 5: Calculation results by simple methods with different β

(c) Investigations on the criteria degree of consolidation for EOP

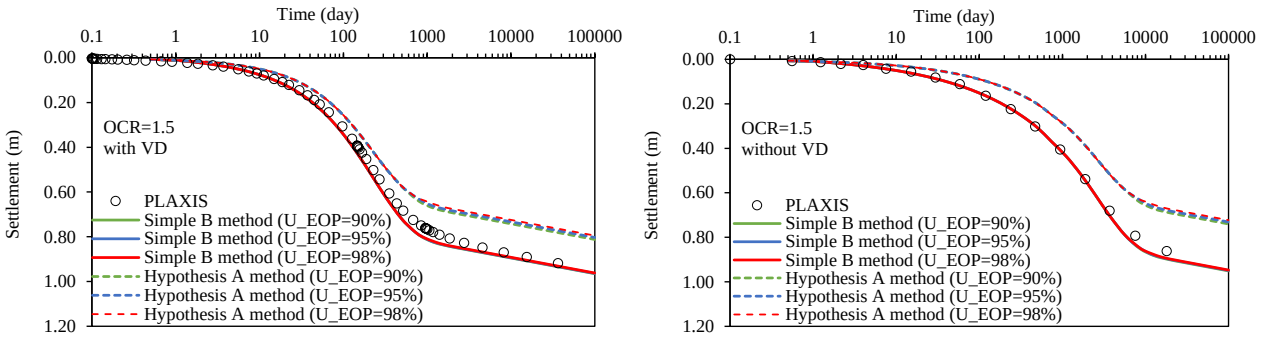


Figure 6: Calculation results by simple methods with different U_{EOP}

According to Equation (6), the determination of t_{EOP} is important. In engineering practice, different criteria could be adopted to determine t_{EOP} by U_{EOP}, which can be 90~98%. In this section, the settlement curves using different U_{EOP} (*i.e.*, 90%, 95%, and 98%) are calculated and compared in Figure 6. It is interesting that within normally adopted ranges, U_{EOP} has little influence on the calculation results. The influence of U_{EOP} is more profound in the Hypothesis A method.

3.3 Verification for multiple clay layers with vertical drains and staged loadings

In real projects, embankments or reclamations can be constructed over multi-layered soils with multi-staged loadings. The proposed method can be applied in analysis of such cases. In this section, the case study on a test embankment for the Hong Kong Chek Lap Kok International Airport is presented.

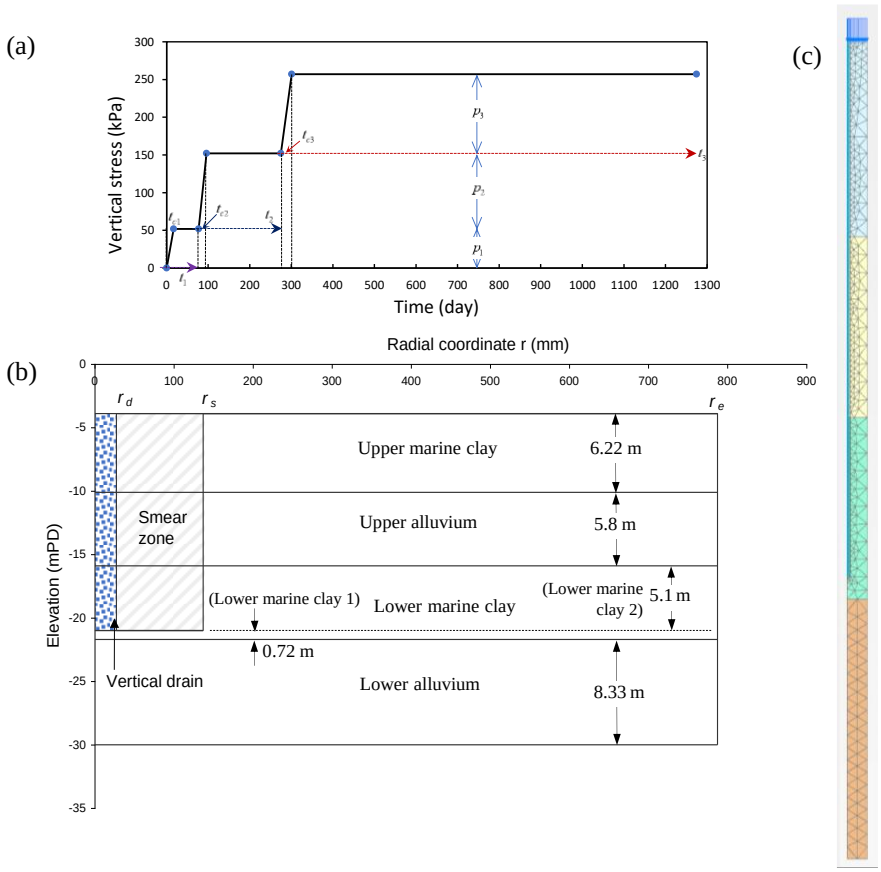


Figure 7: Loading sequence and soil profile of the test embankment (after Zhu et al. 2001): (a) loading history, (b) soil profile and vertical drain dimensions, and (c) axisymmetric finite element model in PLAXIS 2D

The embankment was an artificial island over four layers of marine soils: upper marine clay, upper alluvium, lower marine clay, and lower alluvium. Vertical drains were installed until the lower marine clay layer to accelerate the consolidation. Three stages of loading were applied vertically on the top of the marine clay by gravel filling. Settlement was continuously monitored at four different depths (initially 0, 3, 6, 14.5 meters at depth). The soil profile and loading history are shown in Figure 7. The parameters of each layer of soil are reported in Yin et al. (2022).

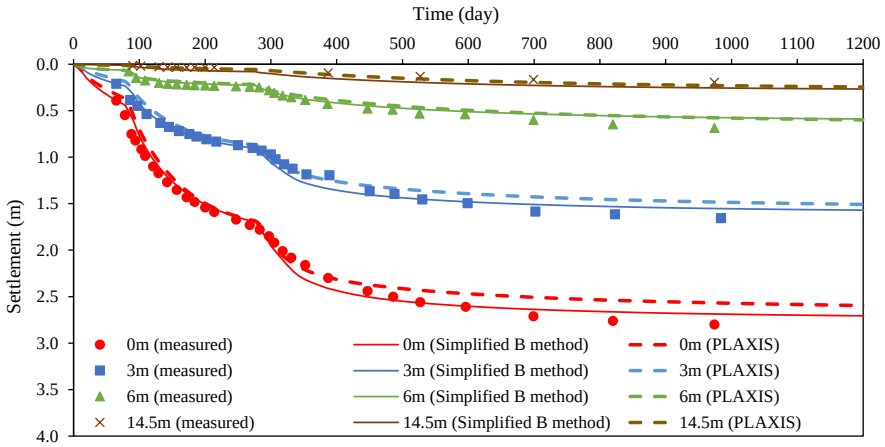


Figure 8: Calculation results of simple method and finite element method compared to measurement for the test embankment of HKIA

The calculation of the multi-layered soil system with vertical drains under each ramp loading is conducted by the spectrum method developed by Walker and Indraratna (2009). The total settlement is calculated by a simple superposition of all different layers and all loading stages. The computed results are compared with the measured data as well as the fully coupled finite element simulations conducted by PLAXIS 2D with SSC model, as shown in Figure 8. The results indicate that the simple Hypothesis B method can provide accurate predictions on the settlement of multi-layered clayey soil ground under multi-staged loadings.

4 CONCLUSIONS

To properly consider the effect of creep, the fully coupled methods and a simple method are presented and verified in this study for both single-layer and multi-layer clayey soils with and without vertical drains. Several conclusions and remarks can be listed as follows.

(i) Creep plays an important role in the time-dependent consolidation settlement of clayey soil grounds. The old Hypothesis A method without properly calculating creep during primary consolidation will underestimate the settlement.

(ii) The proposed simple Hypothesis B method is convenient and efficient for settlement predictions, with high accuracy compared to the fully coupled simulations and the measured data.

(iii) The values of $\alpha = 0.8, \beta = 0.3$ for the simple method are suitable for the typical cases with OCR from 1.0 to 2. Using different degrees of consolidation as criteria of EOP has little influence on the computation results.

ACKNOWLEDGEMENTS

This study is financially supported by General Research Fund (15210020, 15231122, 15226722), Research Impact Fund (R5037-18) from the Research Grants Council of Hong Kong Special Administrative Region Government, and grants (ZDBS, CD7A, CD7J, CD82, BD8U, BDS5) from The Hong Kong Polytechnic University and Research Institute for Land and Space of PolyU.

REFERENCES

Adachi, T., & Oka, F. 1982. Constitutive equations for normally consolidated clay based on elasto-viscoplasticity. *Soils and Foundations*, *22*(4), 57–70.

Bjerrum, L. 1967. Engineering geology of Norwegian normally-consolidated marine clays as related to settlements of buildings. *Géotechnique*, *17*, 81–118. https://doi.org/10.1680/geot.1967.17.2.83

Bolt, G. H. 1956. Physico-chemical analysis of the compressibility of pure clays. *Géotechnique*, *6*(2), 86–93. https://doi.org/10.1680/geot.1956.6.2.86

Borja, R. I., & Choo, J. 2016. Cam-Clay plasticity, Part VIII: A constitutive framework for porous materials with evolving internal structure. *Computer Methods in Applied Mechanics and Engineering*, *309*, 653–679. https://doi.org/10.1016/j.cma.2016.06.016

Burland, J. B., Jamiolkowski, M., & Viggiani, C. 2003. The stabilisation of the Leaning Tower of Pisa. *Soils and Foundations*, *43*(5), 63–80.

CGS. 2023. Section 7.9.2. Methods for consolidation analyses of clayey soils exhibiting viscous compression. *Canadian Foundation Engineering Manual (CFEM), 5th ed.* The Canadian Geotechnical Society (CGS), 228–232.

Chen, Z. J., Feng, W. Q., & Yin, J. H. 2021a. A new simplified method for calculating short-term and long-term consolidation settlements of multi-layered soils considering creep limit. *Computers and Geotechnics*, *138*, 104324. https://doi.org/10.1016/j.compgeo.2021.104324

Chen, Z. J., Feng, W. Q., & Yin, J. H. 2021b. Finite Element Simulations of Clayey Soil Ground with a Three-Dimensional Nonlinear Elastic Viscoplastic Model. *Lecture Notes in Civil Engineering*, *125*(1999), 373–381. https://doi.org/10.1007/978-3-030-64514-4_34

Chen, Z.-J., Feng, W.-Q., Chen, W.-B., & Yin, J.-H. 2023. A thermal elastic visco-plastic model for soft clayey soils. *Canadian Geotechnical Journal*, *61*(2), 208-227. https://doi.org/10.1139/cgj-2022-0279

Degago, S. A., Grimstad, G., Jostad, H. P., Nordal, S., & Olsson, M. 2011. Use and misuse of the isotache concept with respect to creep hypotheses A and B. *Géotechnique*, *61*(10), 897–908. https://doi.org/10.1680/geot.9.P.112

Den Haan, E. J. 1994. *Vertical Compression of Soils*. Delft University.

Grimstad, G., Karstunen, M., Jostad, H. P., Sivasithamparam, N., Mehli, M., Zwanenburg, C., den Haan, E., Ghoreishian Amiri, S. A., Boumezerane, D., Kadivar, M., Ashrafi, M. A. H., & Rønningen, J. A. 2022. Creep of geomaterials – some finding from the EU project CREEP. *European Journal of Environmental and Civil Engineering*, *26*(7), 2521–2536. https://doi.org/10.1080/19648189.2016.1271360

Gupta, B. 1964. *Creep of saturated soil at different temperatures*. University of British Columbia.

Hansbo, S. 1981. Consolidation of fine-grained soils by prefabricated drains. *Proceedings of the International Conference on Soil Mechanics and Foundation Engineering*.

Jamiolkowski, M., Ladd, C. C., Germaine, J. T., & Lancellotta, R. 1985. New development in field and laboratory testing of soils. *Proceedings of the 11th International Conference on Soil Mechanics and Foundation Engineering*, *1*, 57–153.

Kabbaj, M., Tavenas, F., & Leroueil, S. 1988. In situ and laboratory stress-strain relationships. *Géotechnique*, *38*(1), 83–100. https://doi.org/10.1680/geot.1988.38.1.83

Kavazanjian, E. 1988. Discussion: The occurrence of creep during consolidation. *Proceedings of the 11th International Conference on Soil Mechanics and Foundation Engineering*, *5*, 2625.

Koutsoftas, D. C., Foott, R., & Handfelt, L. D. 1987. Geotechnical investigations offshore Hong Kong. *Journal of Geotechnical Engineering*, *113*(2), 87–105. https://doi.org/10.1061/(ASCE)0733-9410(1987)113:2(87)

Kuhn, B. M. R., & Mitchell, J. K. 1993. New perspectives on soil creep. *Journal of Geotechnical Engineering*, *119*(3), 507–524.

Ladd, C., Foott, R., Ishihara, K., Schlosser, F., & Poulos, H. 1977. Stress-deformation and strength characteristics. *State of the Art Report, Proceeding 9th of ISMFE, 2*, 421–494.

Laloui, L., Leroueil, S., & Chalindar, S. 2008. Modelling the combined effect of strain rate and temperature on one-dimensional compression of soils. *Canadian Geotechnical Journal*, *45*(12), 1765–1777. https://doi.org/10.1139/T08-093

Le, T. M., Fatahi, B., & Khabbaz, H. 2012. Viscous behaviour of soft clay and inducing factors. *Geotechnical and Geological Engineering*, *30*(5), 1069–1083. https://doi.org/10.1007/s10706-012-9535-0

Leoni, M., Karstunen, M., & Vermeer, P. A. 2008. Anisotropic creep model for soft soils. *Géotechnique*, *58*(3), 215–226. https://doi.org/10.1680/geot.2008.58.3.215

Leroueil, S. 2006. The isotache approach. Where are we 50 years after its development by Professor Šuklje? (2006 Prof. Šuklje's Memorial Lecture). *Proceedings of the 13th Danube-European Conference on Geotechnical Engineering; Ljubljana*, *2*, 55–88.

Mesri, G., & Choi, Y. K. 1985. The uniqueness of the end-of-primary (EOP): Void ratio-effective stress relationship. *Proceedings of the 11th International Conference on Soil Mechanics and Foundation Engineering*, *2*, 587–590.

Mesri, G., & Vardhanabhuti, B. 2005. Secondary Compression. *Journal of Geotechnical and Geoenvironmental Engineering*, *131*(3), 398–401. https://doi.org/10.1061/(asce)1090-0241(2005)131:3(398)

Mitchell, J. K., Campanella, R. G., & Singh, A. 1968. Soil creep as a rate process. *Journal of the Soil Mechanics and Foundations Division*, *94*(1), 231–253.

Mitchell, J. K., & Soga, K. 2005. *Fundamentals of soil behavior*. Wiley.

NPRA. 2022. *Geoteknikk i vegbygging : veiledning [Håndbok V220]*. Statens vegvesen (Norwegian Public Roads Administration, NPRA).

Rocchi, G., Vaciago, G., Fontana, M., & Plebani, F. 2006. Enhanced prediction of settlement in structured clays with examples from Osaka Bay. *Geomechanics and Geoengineering*, *1*(3), 217–237. https://doi.org/10.1080/17486020600986793

Šuklje, L. 1957. The analysis of the consolidation process by the isotache method. *Proceedings of the 4th International Conference on Soil Mechanics and Foundation Engineering*, *1*, 200–206.

Szavits-Nossan, V. 2015. Consolidation and creep: Hypotheses A and B revisited. *Geotechnical Engineering for Infrastructure and Development*, 3765–3770.

Taylor, D. W. 1942. *Research on consolidation of clays* (Vol. 82). Massachusetts Institute of Technology.

Taylor, D. W., & Merchant, Wilfred. 1940. A theory of clay consolidation accounting for secondary compression. *Journal of Mathematics and Physics*, *19*(4), 167–185.

Vermeer, P. A., & Neher, H. P. 1999. A soft soil model that accounts for creep. *Beyond 2000 in Computational Geotechnics*, 249–261. https://doi.org/10.1201/9781315138206-24

Walker, R., & Indraratna, B. 2009. Consolidation analysis of a stratified soil with vertical and horizontal drainage using the spectral method. *Géotechnique*, *59*(5), 439–449. https://doi.org/10.1680/geot.2007.00019

Wang, Y. H., & Xu, D. 2007. Dual porosity and secondary consolidation. *Journal of Geotechnical and Geoenvironmental Engineering*, *133*(7), 793–801. https://doi.org/10.1061/(asce)1090-0241(2007)133:7(793)

Yin, J., & Graham, J. 1994. Equivalent times and one dimensional elastic viscoplastic modelling of time-dependent stress strain behaviour of clays. *Canadian Geotechnical Journal*, *31*, 42–52. https://doi.org/10.1139/t94-005

Yin, J.-H. 2015. Fundamental Issues of Elastic Viscoplastic Modeling of the Time-Dependent Stress–Strain Behavior of Geomaterials. *International Journal of Geomechanics*, *15*(5), 1–9. https://doi.org/10.1061/(asce)gm.1943-5622.0000485

Yin, J.-H., Chen, Z.-J., & Feng, W.-Q. 2022. A general simple method for calculating consolidation settlements of layered clayey soils with vertical drains under staged loadings. *Acta Geotechnica*, *17*, 3647–3674. https://doi.org/10.1007/s11440-021-01318-2

Yin, J.-H., & Feng, W.-Q. 2017. A new simplified method and its verification for calculation of consolidation settlement of a clayey soil with creep. *Canadian Geotechnical Journal*, *54*(3), 333–347. https://doi.org/10.1139/cgj-2015-0290

Yin, J.-H., & Graham, J. 1989. Visco-elastic-plastic modelling of one-dimentional time-dependent behaviour of clays. *Canadian Geotechnical Journal*, *26*(2), 199–208.

Yin, J.-H., & Graham, J. 1996. Elastic visco-plastic modelling of one-dimensional consolidation. *Géotechnique*, *46*(3), 515–527.

Yin, J.-H., & Graham, J. 1999. Elastic viscoplastic modelling of the time-dependent stress–strain behaviour of soils. *Canadian Geotechnical Journal*, *36*, 736–745.

Yin, J.-H., & Zhu, J.-G. 1999. Elastic viscoplastic consolidation modelling and interpretation of pore-water pressure responses in clay underneath Tarsiut Island. *Canadian Geotechnical Journal*, *36*, 708–717.

Yin, J.-H., Zhu, J.-G., & Graham, J. 2002. A new elastic viscoplastic model for time-dependent behaviour of normally and overconsolidated clays: Theory and verification. *Canadian Geotechnical Journal*, *39*(1), 157–173. https://doi.org/10.1139/t01-074

Yuan, Y., & Whittle, A. J. 2018. A novel elasto-viscoplastic formulation for compression behaviour of clays. *Géotechnique*, *68*(12), 1044–1055. https://doi.org/10.1680/jgeot.16.P.276

Zeevaert, L. 1986. Consolidation in the intergranular viscosity of highly compressible soils. In *Consolidation of soils: Testing and evaluation*. ASTM International.

Zhou, C., Yin, J., Zhu, J., & Cheng, C. 2005. Elastic anisotropic viscoplastic modeling of the strain-rate-dependent stress– strain behavior of K0-consolidated natural marine clays in triaxial shear tests. *International Journal of Geomechanics*, *5*(3), 218–232. https://doi.org/10.1061/(ASCE)1532-3641(2005)5

Zhu, G., & Yin, J.-H. 2005. Solution charts for the consolidation of double soil layers. *Canadian Geotechnical Journal*, *42*(3), 949–956. https://doi.org/10.1139/t05-001

Zhu, G., Yin, J.-H., & Graham, J. 2001. Consolidation modelling of soils under the test embankment at Chek Lap Kok International Airport in Hong Kong using a simplified finite element method. *Canadian Geotechnical Journal*, *38*(2), 349–363. https://doi.org/10.1139/cgj-38-2-349

An Innovative ELS System on Recently Reclaimed Land – Design and Analysis

Jack YIU, Tom S.K. CHAN, Chris C.F. SHUM
Ove Arup & Partners Hong Kong Limited, Hong Kong

Gavin S.H. TOH & C.N. HO
Lambeth Associates Limited, Hong Kong

Oscar Y.N. TSE
Gammon Construction Limited, Hong Kong

ABSTRACT

The Third Runway at Hong Kong International Airport sits on a newly reclaimed land formed by non-dredged method where soft muds remain in place under the reclamation fill. Ground improvement works mainly in the form of Deep Cement Mixing (DCM) were installed within the soft marine clays with embedment into a competent stratum. The APM and BHS tunnels were proposed along the new artificial shoreline. To enable the construction of the cut-and-cover tunnels, it is viable to have an open-cut excavation at landside because of the abundant space. At seaside where space constraints are present, a double-wall system was introduced to retain the earth. The beauty of this system is a strut-free zone can be created, which minimizes the construction constraints and shortens the construction programme significantly. A double-wall system is composed of continuous front wall and discrete back wall connected by steel ties. The front wall relies on the back wall which is anchored into DCM panels. The spacing between the front wall and the back wall varies from 9m to 15m depending on site constraints. The design approach and failure mechanisms are discussed.

1 INTRODUCTION

Excavation and later support system is indispensable to enable the construction of basements and underground structures in Hong Kong, in which steel struts are commonly adopted as the lateral support. It can be attributed to some reasons such as availability and re-usability of high yield steel, better elastic modulus of steel, local construction techniques and practice and compliance with local codes. Although the strutted ELS provides limited space for construction inside the excavation pit, it is a reliable solution in most of the basement and underground construction projects in urban districts where strength and stiffness in the ELS system are usually prioritised.

However, it becomes prominent that an unconventional ELS system is required for the construction of a mega-scale infrastructure in an open area such as a long underground tunnel where the vertical alignment varies along the chainage. Strutted excavations are not an economical or effective solution in case a large open-cut excavation is involved because of the reduced construction efficiency coming from strut installation and removal. Given the temporary nature of the excavation system, large wall deformation may be acceptable as long as the ultimate limit state is designed for. (Lee et al. 2013)

The unconventional and innovative ELS system shall have fewer elements which are prone to changes during construction stage. At the same time, it shall provide abundant construction space to facilitate construction, heavy machinery mobilization and reproducible construction logistics. Therefore, a double wall ELS system without struts is well suited in the aforementioned site setting.

This paper summarises the design and analysis experience of an innovative double wall excavation and lateral support system on a recently reclaimed land at the Hong Kong International Airport between Ove Arup & Partners Hong Kong Limited, Lambeth Associates Limited, and Gammon Engineering and Construction Company Limited.

2 PROJECT BACKGROUND

2.1 Three Runway System (3RS)

Hong Kong International Airport has undergone a transformation into a three-runway system. The Three Runway System (3RS) aims to strengthen Hong Kong's status as an international aviation hub, and to cater for the city's long term air traffic demand.

2.2 Automated People Mover (APM) System and Baggage Handling System (BHS)

The construction of APM and the construction BHS are two of the seven core projects which the 3RS project consists of. The APM and BHS will connect Terminal 2 with the T2 Concourse. The new APM system will operate at a top speed of 80km/h and transport up to 10800 passengers per hour. The new BHS will be capable of handling 9600 bags per hour. Innovative double wall ELS system was adopted in the construction of the new APM and BHS.

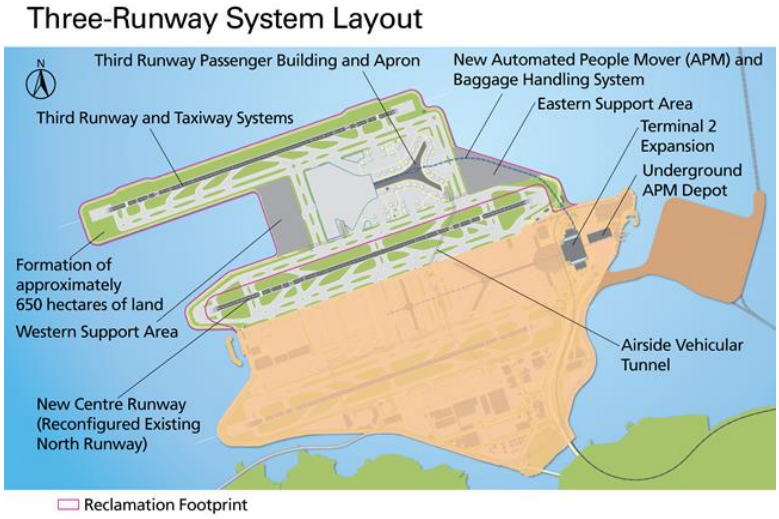


Figure 1: Three-runway system layout (Airport Authority Hong Kong 2021)

3 GROUND CONDITIONS

3.1 Site geology

The site is located offshore of the original Chek Lap Kok Island as well as the existing reclaimed land of the airport area. Marine muds underlain by alluvium layers of different characteristics are present, followed by saprolite and solid rock. The solid geology is predominantly granite – Chek Lap Kok and Lantau Granite of Lamma Suite.

The site was newly reclaimed by non-dredged method that left soft marine deposits in place beneath the reclamation fill. Sand blanket was placed on the seabed followed by ground improvement involving the installation of Deep Cement Mixing (DCM) elements along the tunnel alignment. The area replacement ratio (ARR) of DCM varies with the locations.

3.2 Hydrogeology

The site is on a newly reclaimed land extending from existing reclaimed land. The groundwater regime is expected to be dominated by the seawater level with tidal fluctuation.

4 Site Challenges

4.1 Considerations of Existing DCM Columns

The third runway reclamation adopted the non-dredged "Deep Cement Mixing" (DCM) method, which reduced impact on water quality and marine ecology nearby. DCM method involved the injection of cement slurry from works vessels into the marine mud on the seabed by "mixing" them together. In a DCM treatment zone, DCMs were in the forms of conjoint and non-conjoint columns of different patterns. The seabed was treated in a way that the ground conditions were only improved for the support of future vertical loads such as seawall structures and fill materials to be deposited. When it came to excavation where significant lateral earth pressure was to be supported, considerations of existing DCM were required to be taken into account. For example, the lateral movements and bending of DCM columns had to be assessed to avoid impairing the load-carrying ability of DCMs.

4.2 Under-consolidated Marine Deposit

According to site-specific ground investigation and the interpretation of the cone penetration test (CPT) results, the marine deposit was under-consolidated and only had an undrained shear strength of as low as single digit kilopascal. The weak marine deposit would not only imply that the horizontal elements of the ELS had to be strong and stiff, but it would also require the vertical elements had to be sunk into deeper soil strata such as alluvium and completely decomposed granite from which larger soil strength could be derived.

4.3 As-built seawall and swale in the vicinity

The alignment of the APM and BHS tunnels was close to the seawalls of the third runway reclamation on one side. Due to limited construction space, a more economical conventional open-cut construction method could not be adopted. On the opposite side in the inland area, open-cut construction was possible. However, along the tunnel chainage, the construction space was getting narrower because of the presence of an existing swale between the existing Chap Lap Kok airport island and third runaway reclamation.

5 PROPOSED DOUBLE WALL ELS SYSTEM – DESIGN

5.1 Design Aim

To enable a fast-track construction cycle of APM and BHS tunnel segments, the ELS design was required to accommodate a construction system called travelling formwork. It enabled the repeated construction of structural elements and so was ideally suited to long stretches repetitive concrete forming.

5.2 Choice of Excavation and Lateral Support System

A strutted lateral support system in a conventional ELS would obstruct the deployment of the travelling formwork. On the other hand, a tied-back retaining wall without struts would not be suitable for the ground conditions of the project site. At last, an ELS system with the combination of an open-cut slope on the landside and a double wall system on the seaside was proposed.

Excavation system with double wall set up is not uncommon in neighbouring regions such as mainland China and Taiwan. In China, double row steel sheet pile cofferdam structure was adopted in projects such as Shenzhen-Zhongshan cross-river channel and Shanghai wharf projects. It was particularly favoured in soft soil areas due to its strong resistance to seepage and adaptability according to Jiang et al. (2023). Several excavation projects in Taiwan also involved a double-rail system where two rows of regularly spaced rails were penetrated into the ground as a retaining wall. The front and back rows of rails were usually separated at 600-1200mm. As suggested by Hsieh et al. (2003), this system was applicable to excavation in gravels or sands for single floor basement construction and widening the row spacing of rails can reduce the overall deformation of the retaining system. The design of the double wall ELS system adopted in the APM and BHS tunnel constructions borrowed the successful cases in Taiwan and was further developed to suit the project site.

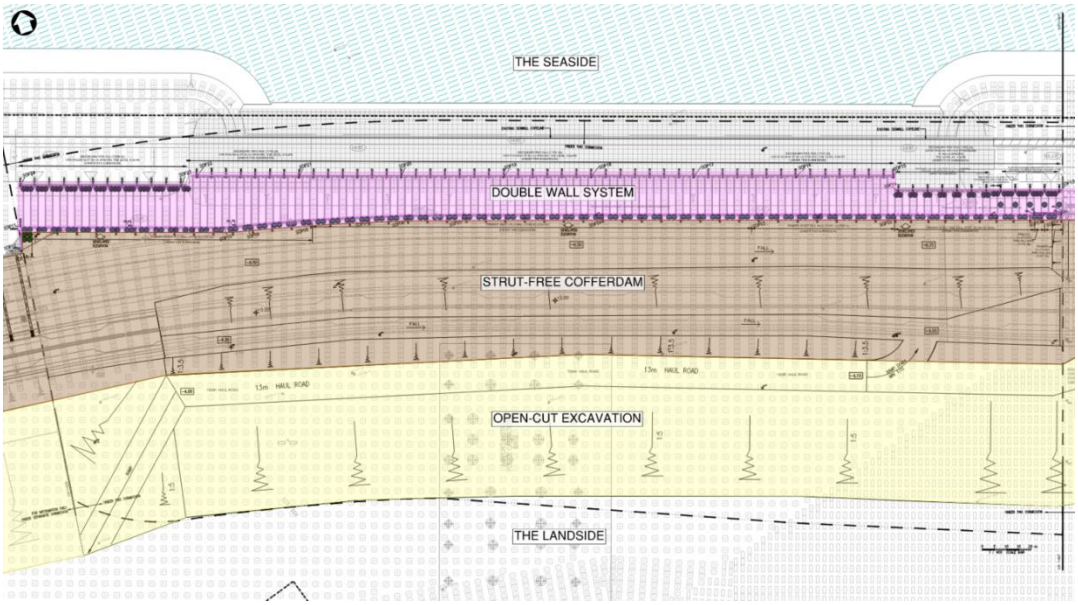


Figure 2: ELS layout plan

5.3 Design Development of Double Wall ELS System

The innovative double wall system was composed of three major elements, the front wall, the tie and the back wall. The idea was borrowed from a deadman anchored retaining wall where a single sheet of wall, referred as "front wall", is held back by deadman anchors installed at the back. Rankine's Theory of Active and Passive Earth Pressure forms the basics of the system. The active earth pressure acts on the "front wall" and the passive earth pressure acts on the "back wall". To maximise the resistance provided by the deadman anchor, the overlapping between the "active zone" and the "passive zone" should be avoided as much as possible. In other words, the angle of internal friction should be fully mobilised in the planes of soil wedges.

The design approach assumed an independent behaviour of the double wall and the soil in between, which was not applicable to the challenges encountered on the site. Such structure should be analysed as a composite structure where the physical interactions between each element were taken into account (Sawaguchi 1974).

In designing the double wall ELS system for the APM and BHS tunnels, PLAXIS 2D and 3D were utilised to study the soil-structure interactions of the double wall ELS system.

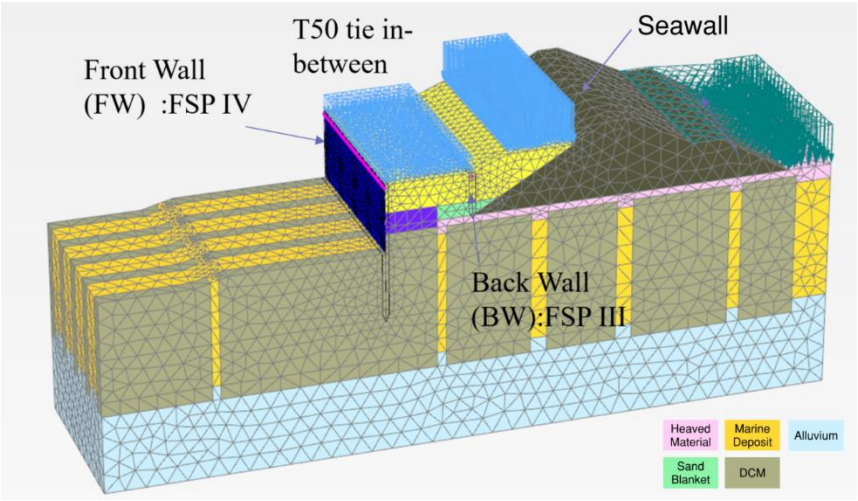


Figure 3: Back wall modelled as deadman anchor in PLAXIS 3D (original approach)

In the APM and BHS tunnel, the deadman anchor was originally designed to be in a form of sheet pile wall, referred to as “back wall”. Due to the close vicinity of the as-built seawall, the separation of the front wall and the back wall was limited. The separation between the front wall and the back wall was 12m in general but it could be as narrow as 9m, which was smaller than the required length of 16-17m to prevent the overlapping between the “active zone” and the “passive zone”.

From PLAXIS safety analysis, there was no distinct difference in soil movement at failure between the double wall, indicating that there might be overlapping and thus the effectiveness of the deadman anchor was reduced. In conventional strutted ELS design, it is typical to enhance the robustness and the ground movement control by using stronger and stiffer vertical and horizontal steel elements and increasing the wall embedment depth, etc. However, these typical methods cannot fully address the overlapping problem which can only be effectively resolved by increasing the separation between the front wall and the back wall.

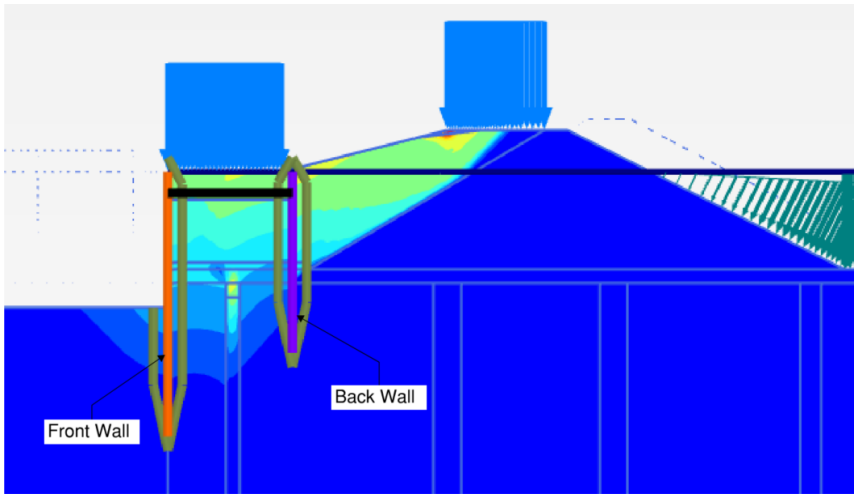


Figure 4: Safety analysis in PLAXIS 2D

After considering the potential failure mode, the double wall design was modified to be less dependent on the passive soil resistance in front the of back wall. Therefore, the modified system changed the back wall from sheet pile to pipe pile. The back wall was rather individual piles than a continuous wall. The pipe piles were designed and positioned to be sunk into the top portion of the DCM columns, which took advantage of the as-built DCM columns in marine deposit. The DCM benefited the modified double wall ELS system in two ways.

Firstly, it treated the marine deposit soil stratum as a whole and improved the strength of the weak and under-consolidated marine deposit. It provided adequate passive soil resistance to the front wall embedded into DCM-treated marine deposit and thus enhanced the toe-kick stability.

Secondly, the individual DCM columns had a uniaxial compressive strength ranging from 800kPa to 1200kPa. It provided strong anchorage for those pipe piles embedded into it. The back wall behaved as laterally loaded piles which did not rely on the passive soil resistance. The potential failure mode of the modified double wall system was changed. The behaviour of the laterally loaded piles was analysed by Oasys Alp and the result was compared with that of PLAXIS 2D to verify the intended working mechanism of the discrete pipe piles.

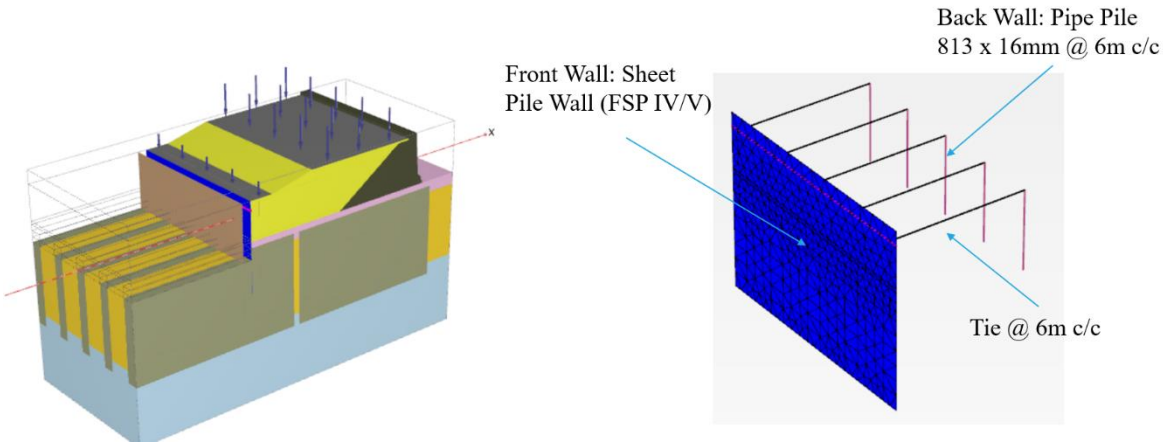


Figure 5: Back wall modelled as individual piles in PLAXIS 3D (modified approach)

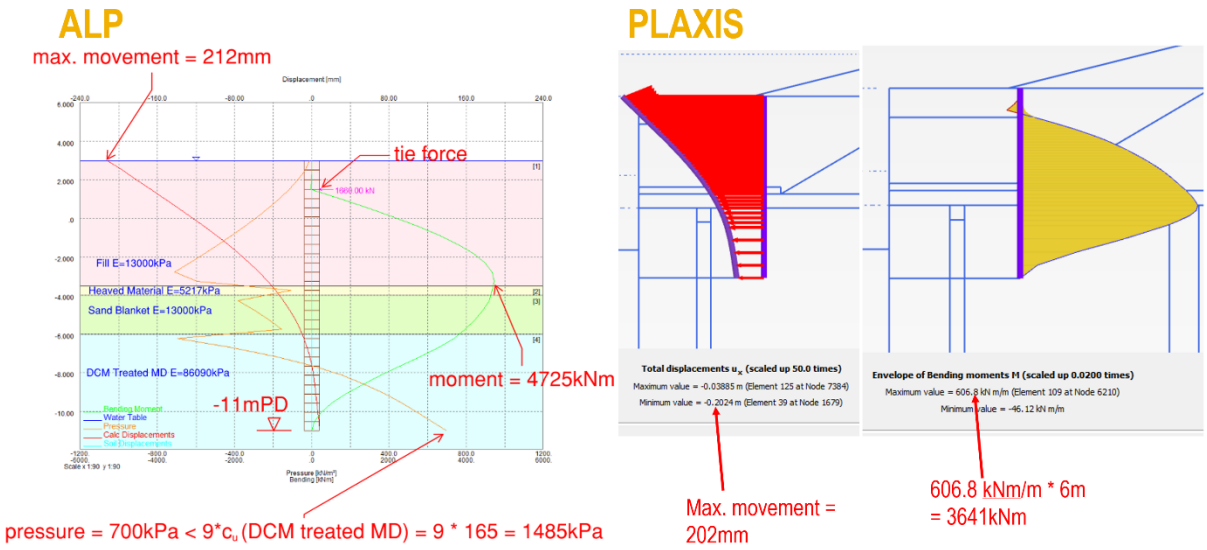


Figure 6: Comparison of results from Oasys Alp and PLAXIS 2D

5.4 Mechanism of the Modified Double Wall ELS System

The front wall was held back by the spaced anchored piles at the back through the connecting tie-backs and acted like a simply supported beam with supports on both ends. It was propped by the tie-backs at the top and the strong DCM-treated marine deposit at the bottom. For ultimate limit state, this ELS system behaved like a singly strutted ELS and the toe stability was checked. For structural check, the front wall, the back piles and the tie-backs were checked against factored forces.

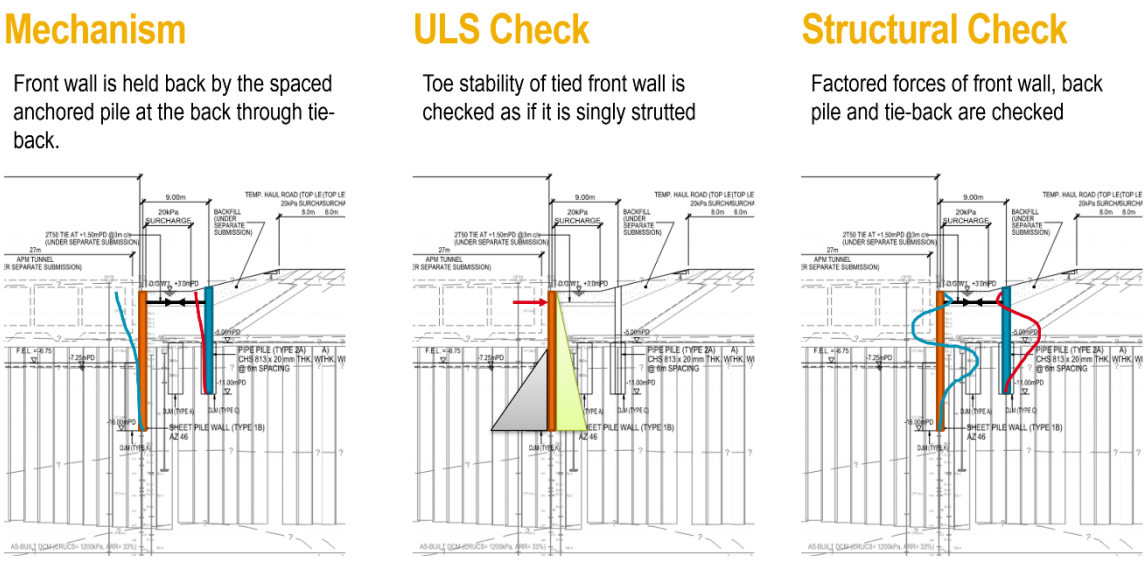


Figure 7: Failure mechanism of double-wall retaining system

6 PROPOSED DOUBLE WALL ELS SYSTEM – NUMERICAL ANALYSIS

The section focuses on the numerical analysis and modelling of the modified double wall ELS systems where different modelling techniques were adopted to validate of design assumptions and verify of the failure mechanism. Improvements on the double wall system have been done with considerations of different potential failure modes.

6.1 Key Design Parameters

The choice and design of ELS system was based on the aforementioned. The design parameters were determined from the site-specific ground investigations that involved extensive in-situ vane shear tests and cone penetration tests. One of the key design parameters that had considerable impact on the design was the undrained shear strength of the marine deposit. It was much weaker than that of the consolidated marine deposits usually encountered in other Hong Kong districts.

6.2 Analysis approach

As DCM columns are surrounded by very weak marine deposits, the ARR of DCM needs to be considered to determine the smeared strength and stiffness for application in PLAXIS 2D with a plane strain assumption. It is a good approximation of behaviour inside a thick composite material loaded in one plane.

Apart from the traditional toe stability check, the overall stability of the system was computed by phi-c reduction in PLAXIS. DCM panels were assumed to have a tensile strength which was directly proportional to their uniaxial compressive strengths (UCS). If the tensile stress exceeded the limit over the course of excavation, the corresponding fractions were replaced with frictional material to mimic the cracked behaviour of DCM. Several iterations were carried out as the stress points might propagate to the surroundings upon the replacement with frictional material. Consequently, safety check was carried out by successively reducing the tensile strength of DCM and shear strength of soils until failure of the structure occurred. It helped identify the critical failure mechanism of the system as well as ensuring the overall stability was up to design requirement.

6.2 Assumptions of back wall

If a continuous back wall was to be adopted, the active wedge of the front wall overlapped greatly with the passive wedge of the back wall, which resulted in a large overall movement of the system. The overall movement was inversely proportional to the distance between the walls. Due to the space constraints of the site, the back

wall was changed from the continuous deadman anchor to laterally-loaded piles anchoring into DCM panels to limit the movement. The laterally-loaded discrete back wall was modelled as embedded beam row in PLAXIS.

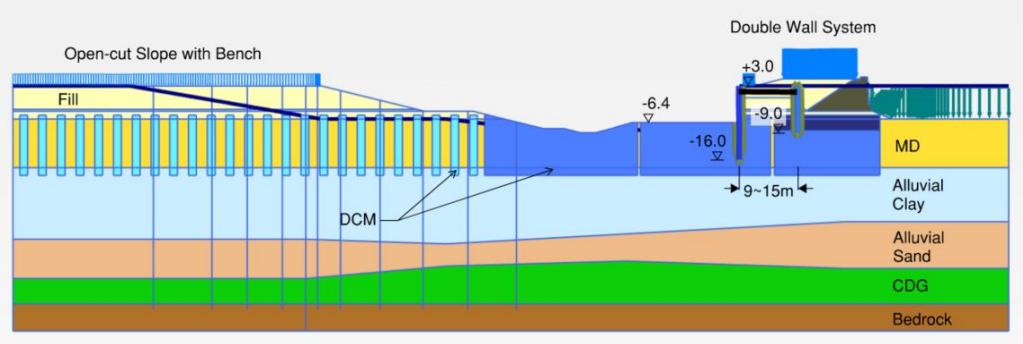


Figure 8: Typical double-wall system setup in PLAXIS 2D

6.3 Interactions with DCM

It was uncertain whether analyses in 2D space were insufficiently conservative in predicting the behaviour of the system as DCM panels are present in rows with compartmentalized marine deposit. The smeared properties might not be representative enough to appraise the local variation in movements and forces of the system. In addition, the back wall was essentially considered discrete because the spacing of the back wall was more than 3 times of the pipe pile diameter. To further verify the accuracy of the 2D model, finite element analysis was conducted in 3 dimensional spaces using PLAXIS 3D at critical and representative locations.

Stress concentration and excessive differential movement was revealed from PLAXIS 3D at the interface of DCM and soft marine clays, which were attributed to the enormous stiffness difference across the different materials. Bending moment of the front wall was found peaking at DCMs along the wall alignment. Additional ground improvement by Dry Jet Mixing (DJM) were proposed at certain soft spots to enhance the robustness of the design. With the addition of DJM columns, the spikes in wall forces were evened out to avoid high local stress concentration which reduced the wall size to yield a cost-effective design and boost the robustness of the system.

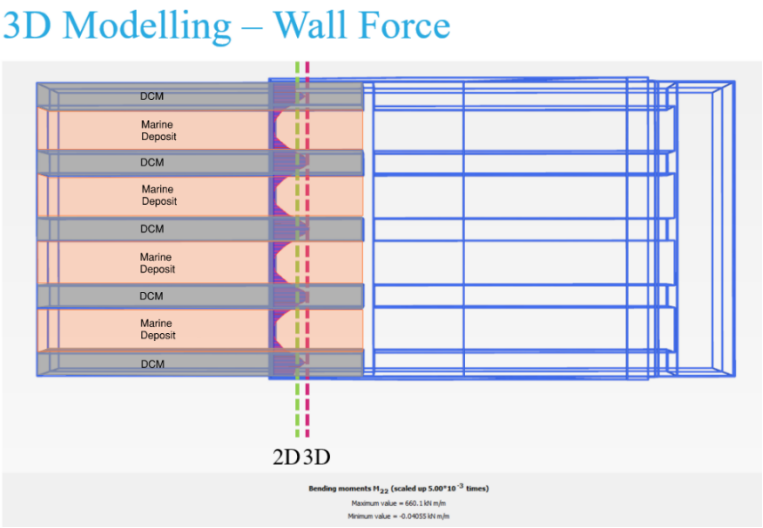


Figure 9: Bending moment of front wall in PLAXIS 3D along wall alignment in absence of additional DJM

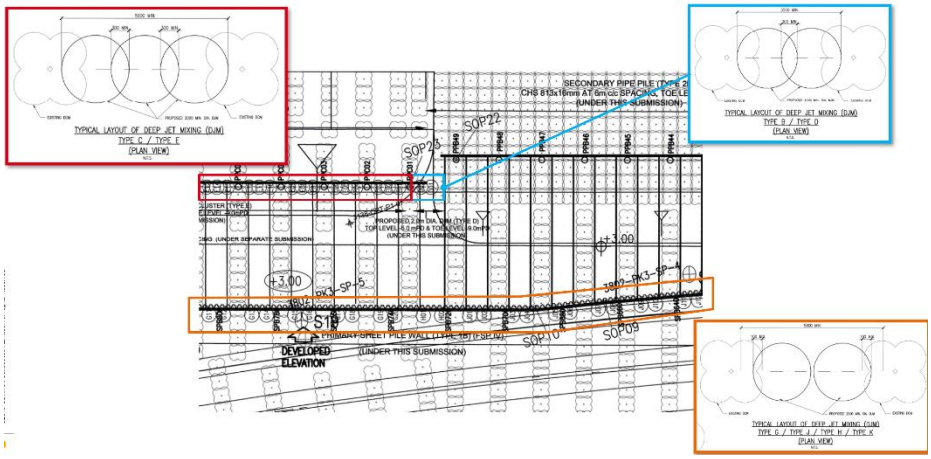


Figure 10: Arrangement of additional DCM/DJM

An approximately 10% increase in wall moment and shear stress was revealed from PLAXIS 3D which confirmed the hypothesis. Hence, modelling in 2D space was considered acceptable by applying a bulk factor to the obtained results. At critical locations, 3D analyses were carried out to countercheck and verify the results in the 2D analysis.

6.4 Transition to strutted cofferdam

The double wall system had great compatibility when it came to interfacing with the conventional strutted excavation. The transition was effortless. However, attention was required to be drawn to the differential movements between the non-strutted wall and the strutted wall during the course of excavation. Grout curtain was recommended to be deployed to the location where transition occurred as precautionary measures to ensure water tightness and to increase robustness at the interface.

7 PERFORMANCE REVIEW DURING CONSTRUCTION STAGE

Different types of monitoring and instrumentation were proposed to monitor the performance of the double-wall system, including ground settlement markers and inclinometers. However, inclinometers were considered key performance indicators as they were less susceptible to disturbance. They were installed in both the front wall and back wall along the wall alignment.

Excavation was carried out progressively by bays along the longitudinal direction of tunnels, with each bay approximately 20m long. At the location where final excavation level was first reached (Day 0), both inclinometers in the front wall and the back wall captured a substantially smaller deflection than the design predicted value. However, the deflection went up significantly as revealed by the next measurement (Day 3). By the time of reporting, the adjacent two bays were proceeding to their FELs. Both the front wall and the back wall deflected by around 50mm more, breaching the alert level. This undue movement had drawn the project team's attention despite the movements were within the predicted value, which eventually led to a performance review. The actual wall deflection profile was checked and compared against the envisaged deflection profile. The depth where largest deflection took place was comparable and it matched with the design expectation. The wall portion socketed into DCM panels had undergone a significantly smaller movement than the predicted value which the integrity of DCM panels was implied. The elongations of tie bars were also found consistent with the prediction. Therefore, it could be concluded that the overall stability and structural integrity were not compromised. The delayed movement might be attributed to the limitations of a staged plane strain analysis. The monitoring of the system movement continued throughout the construction stage and the maximum movement had been within the design limit.

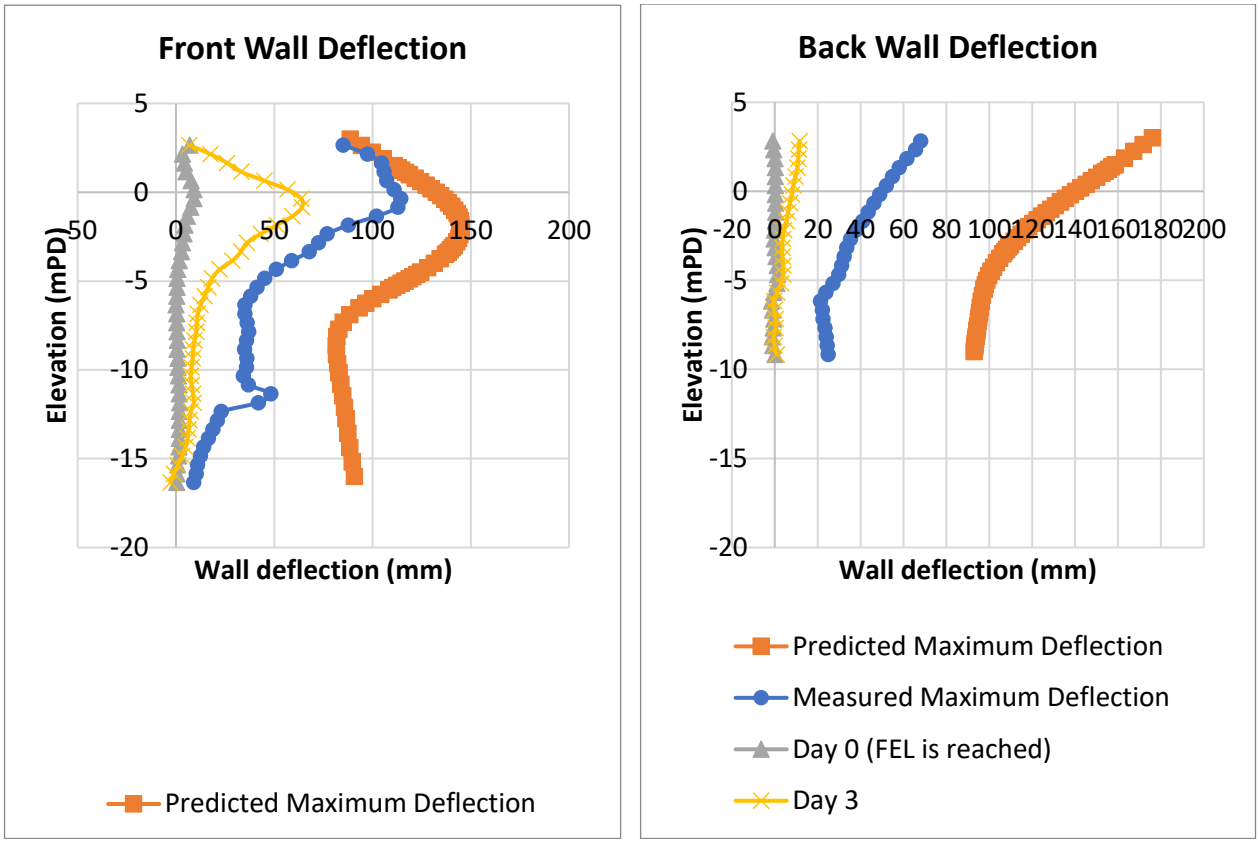


Figure 11: Comparison of predicted and measured wall movement

8 CONCLUSIONS

An innovative design of double-wall system featuring a strutless excavation zone has been carried out for APM/BHS tunnel construction of the Third Runway Project. The double-wall system is the first of its kind in Hong Kong in difficult soft ground conditions. The design principles and envisaged failure mechanisms were discussed in this paper. Careful selection of the analysis methods is required to cater for project specific risks and constraints. The designer shall consider additional measures to ensure the risks are properly mitigated during the design stage as well as the construction stage. Comprehensive instrumentation and monitoring plan for the monitoring and validation of the performance of the double wall ELS system are necessary during construction.

ACKNOWLEDGEMENT

The authors thank the Airport Authority Hong Kong for the permission and kind support to publish this paper. The efforts and participation of the project teams and supervision teams are highly appreciated.

REFERENCES

Lee, C.J., Chen, H.T., Wei, Y.C., Lin, Y.C., Huang, W.S. and Chiang, K.H. 2007. Centrifuge modeling of a self-supported double soldier-piled wall in sandy soil. *J. GeoEng*, 2(3), pp.97-109.

Jiang, Y., Guo, F., Wang, W., Yang, G., Yue, J. and Huang, Y. 2023. Stability Study of a Double-Row Steel Sheet Pile Cofferdam Structure on Soft Ground. *Water*, 15(14), p.2643.

Hsieh, H.S., Shih, C. and Lin, T.M. 2003. A note on the behavior of double-rail earth retaining system. *Sino-geotechnics*, 97, pp.5-14.

Sawaguchi, M. 1974. Lateral behavior of a double sheet pile wall structure. *Soils and foundations*, 14(1), pp.45-59.

Airport Authority Hong Kong 2021. *LC Paper No. CB(4)1696/20-21(01), Legislative Council Panel on Economic Development, Update on the Development of the Three-Runway System at Hong Kong International Airport, 27 October 2021.*